Extreme laser-matter interactions: kinetic modeling of relativistic, ultrarelativistic and radiation dominated plasma

KUMULATIVE HABILITATIONSSCHRIFT

zur

Erlangung des akademischen Grades
doctor rerum naturalium habilitata (Dr. rer. nat. habil.)
der Mathematisch-Naturwissenschaftlichen Fakultät

DER UNIVERSITÄT ROSTOCK

vorgelegt von
Tatyana V. LISEYKINA
geb. am 7. Juni 1973
in Nowosibirsk

Rostock, 2019

Contents

I. Abstract

This cumulative thesis presents a summary of contributions made by the author over the past twelve years and dedicated to the theory of relativistic plasma driven by intense electromagnetic radiation. Starting from the early 90s of the last century, the physics of plasmas has made several considerable steps forward, forming new immense research areas. Physics of laser-driven plasma is one of the central constituents of this progress. The fast and very fruitful development of this research field was triggered by three considerable advances of the last decades. Below we briefly describe these fundamentals of the laser plasma physics.

Firstly, the progress of laser sources boosted by the invention of the chirped pulse amplification technique [1], made routinely possible the generation of electromagnetic fields of ultrahigh intensities exceeding the value of 10^{18} W/cm^2, which makes the motion of electrons relativistic. Such electromagnetic fields are created by laser sources of muti-terawatt (TW) and petawatt (PW) power. Nowadays they are capable of reaching intensities $\sim 10^{21} \div 10^{22}$ W/cm^2. These extreme laser intensities, in combination with short pulse duration typically equal to tenths of femtoseconds (1fs=10^{-15}s), made possible laboratory studies of relativistic and ultra-relativistic collisionless plasmas, which were not accessible at lower intensities and longer pulse duration. As a result, two decades have been essentially dedicated to the experimental and theoretical exploration of the physics of *relativistic classical collisionless plasma*. This exploration brought such phenomena as laser acceleration of charged particles, laser-induced generation of giant electric and magnetic fields and secondary radiation from laser-driven plasma into the scope of the research community. Studies of these effects deliver both new knowledge in fundamental physics and a number of promising applications [2, and references therein]. The current progress in the development and construction of muti-PW laser facilities including APRI [3] (Korea), SULF [4] and CAEP [5] (China), ELI [6] (Europe) and Apollon [7] opens a way to the new level of electromagnetic intensities $\sim 10^{23}$ W/cm^2 and higher. This next generation of laser technology will make possible experimental endeavors in the presently unexplored area of *relativistic radiation-dominated and quantum plasma physics* including such effects as ignition of quantum cascades of elementary particles, creation of coupled electron-positron-photon plasma and a variety of single-particle or collective dynamical phenomena resulting from strong classical or quantum radiation of laser-driven ultra-relativistic plasma. This progress of laser sources has created a great demand of theoretical work and calls for a further development of analytical and numerical methods in this field of physics.

Secondly, the progress in observational astronomy has led to the possibility of quantitative studies of such astrophysical phenomena as jets and shocks and thus, triggered the creation of a new multidisciplinary research field. Known as *laboratory astrophysics* [8, 9], [10, and references therein] it aims at modeling space phenomena in plasma labs using strong lasers and magnetic fields. From the experimental side, the field of laboratory astrophysics employs femtosecond to nanosecond (1ns=10^{-9}s) pulses of high and moderate intensities and strong static or pulsed magnetic fields created by magnets

or by specially designed plasma targets ignited by strong laser radiation. From the theoretical side, it is based on the scalings and similarity parameters, which allow to correctly map micro- and meso-scopic plasma phenomena to those developing on astrophysical and even cosmological scales. Thus, the recently achieved mutual correspondence between the capabilities of the observational astronomy and those of the laser-plasma laboratory experiment provided another strong motivation for studies of the plasma dynamics induced by intense laser radiation.

Finally, the enormous progress in high-performance computing made possible the numerical simulations of complex phenomena, which were totally out of reach twenty or more years ago. For the modeling of classical collisionless plasma dynamics in external fields of femtosecond and picosecond (1ps=10^{-12}s) duration, the Particle-in-Cell method [12, 13], numerically realizing the system of the self-consistent Maxwell-Vlasov equations, remains the main workhorse of the whole field. The orders-of-magnitude acceleration of computer algorithms and a comparable growth of the available memory allowed to extend the area of numerical experiments from the class of toy models to fully realistic three-dimensional interaction setups capable of precisely reproducing experimental data and predicting new nontrivial effects. PIC simulations are being more and more frequently considered as an trustworthy and cheap alternative to laboratory experiments. Experimental observations of new phenomena at ultrahigh laser intensities and, even to a higher extent, the expectations to probe the new physics at intensities exceeding 10^{23} W/cm^2 to be reached at the multi-PW laser facilities, have stimulated a considerable modification of numerical approaches to include new effects in to the scope of numerical experiments. This led to the development of several new PIC- or molecular dynamics-based numerical codes [14, 15, 16, 17, 18, 19, and others] capable of incorporating effects of radiation reaction (classical and quantum) and quantum electrodynamical (QED) processes on plasma dynamics and radiation, including creation of electron-positron pairs. Simultaneously, several PIC codes, which have been tested on a broad variety of plasma problems, have been modified to incorporate radiation reaction and field ionization of gases. These achievements resulted in the creation of an efficient distributed network of advanced open-source numerical codes that are currently being massively used to analyze experimental data, as well as to plan new experiments.

The theoretical work of this cumulative thesis combines these three major subfields of the physics of laser plasma. Its essence in the application of advanced numerical methods realized in the PIC code UMKA originated from the study in [20]. The code has been modified or extended according to the needs of the particular problem, for studies of laser-plasma interactions both at presently accessible parameters and under conditions expected at multi-PW laser facilities of the near future. These studies are devoted to four research topics:
(i) laser acceleration of ions;
(ii) collisionless absorption of laser radiation in plasma and generation of hot electrons;
(iii) interaction of intense laser radiation with microdroplets;
(iv) interaction of laser radiation of extreme intensity with plasma in the radiation-dominated regime.

The first two items belong to the field of research that is currently extensively studied in experiment. Correspondingly, results on (i) and (ii) presented in this thesis have been experimentally verified. Item (iii) also falls into the domain of parameters available for experimental research; possible laboratory realizations of laser-droplet interactions are therefore discussed. Finally, results of (iv) are rather looking into the near and not so near future so that there the discussion of purely theoretical aspects dominates experimental particulars.

II. Abbreviations

1D/2D/3D	one/two/three-dimensional
CP	circular polarization
CSA	collisionless shock acceleration
EM	electromagnetic (wave, energy)
HB	hole-boring RPA regime
IFE	inverse Faraday effect
LAD	Lorentz–Abraham–Dirac (equation)
LL	Landau-Lifshitz (force, equation)
LP	linear polarization
LS	light sail RPA regime
PIC	particle-in-cell (method, code)
QED	quantum electrodynamics
QM	quantum mechanics
RF	radiation friction
RPA	radiation pressure acceleration
TNSA	target normal sheath acceleration
XUV	extreme ultraviolet

III. Notations

$\mathbf{E}$	Electric field
$\mathbf{B}$	Magnetic induction
c	speed of light
$\hbar$	Planck constant
m_e, e	electron mass and charge
m_i, q_i	ion mass and charge
n_e	electron number density
$\omega_{\mathrm{L}}, \lambda_{\mathrm{L}}, T_{\mathrm{L}}, \tau_{\mathrm{L}}$	laser pulse carrier frequency, wavelength, period, duration
E_0	amplitude of the electric field of the laser pulse
$I_{\mathrm{L}} = cE_0^2/4\pi$	laser pulse intensity (linear polarization)
$\mathbf{S}$	Poynting vector
η_{abs}	absorption degree
$n_{\mathrm{cr}} = m_e\omega_{\mathrm{L}}^2/4\pi e^2$	critical plasma density
$\omega_{\mathrm{p}} = \sqrt{4\pi n_e e^2/m_e}$	Langmuir (plasma) frequency
$\mathbf{j}_s$	current density for species s
Λ_D	Debye length
$\delta_{\mathrm{e}} = c/\omega_{\mathrm{p}}$	collisionless skin-depth
$a_0 = eE_0/m_e\omega_{\mathrm{L}}c$	dimensionless amplitude of the laser field
$v_g = \partial\omega/\partial k$	group velocity of the wave
$E_S = m_e^2 c^3/e\hbar$	Schwinger field (critical field of QED)
$\lambda_c = \hbar/m_e c$	Compton wavelength
$v_{\mathrm{osc}} = eE_0/m_e\omega_{\mathrm{L}}$	oscillation (quiver) velocity
$r_{\mathrm{osc}} = eE_0/m_e\omega_{\mathrm{L}}^2$	oscillation amplitude (quiver radius)
v_{th}	thermal velocity
c_{s}	sound velocity
$r_{\mathrm{c}} = e^2/mc^2$	classical electron radius
$\mathcal{E}_{\mathrm{osc}} = m_e c^2(\sqrt{1 + a_0^2/2} - 1)$	electron mean oscillation energy
ν_{ei}	collisional frequency
Δ	foil thickness
T_{hot}	hot electron temperature
$\gamma = 1/\sqrt{1 - v^2/c^2}$	relativistic γ-factor
$\chi = \dfrac{e\hbar}{m^3 c^4}\sqrt{(-(F_{\mu\nu}p^\nu)^2)}$	relativistically invariant quantum parameter

IV. Erklärung

Hiermit erkläre ich, dass ich die vorliegende Habilitationsschrift selbständig verfasst und nur die angegebenen Hilfsmittel verwendet habe. Ich habe bisher noch keinen Habilitationsversuch unternommen.

Unterschrift: _____

Rostock, den _____

1. Introduction

Plasma appears in the Universe in a staggering variety of forms, which are determined by the collective dynamics of charged particles and electromagnetic (EM) fields. This highly non equilibrium[1] matter, dominated by nonlinearities, can produce and manipulate[2] enormous energy density EM fields and electromagnetic radiation on mesoscopic scales in the laboratory as well as on huge spatial scales in the Universe. The possibility to obtain mesoscopic amounts of relativistic, ionized matter in laboratory [21, 22] is due to the recent developments in the generation of laser pulses with ultra-high power. The opportunity to study relativistic plasmas in relatively compact size experiments opens the way to new advances in fields that range [24] from nonlinear dynamics and nonlinear relativistic optics to (i) novel powerful radiation sources at high energy, (ii) alternative particle acceleration techniques, (iii) high energy astrophysics, including relativistic shocks, cosmic ray physics and radiative magnetic reconnection, and finally, (iv) plasma dominated by QED effects, such as quantum recoil and creation of electron-positron pairs. Each of these topics leads to important technological achievements or/and to the creation of interdisciplinary knowledge [25, 26, 27, 28, 29, 30, 31, 32]. The control the dynamics of a relativistic plasma interacting with superintense laser pulses may allow for the spatial and temporal tailoring of the EM field, and thus, achieving frequency up-shift and very tight focusing. In this way, the fields intense enough to probe QED effects even up to the Schwinger limit [33] ($E_S = m_e^2 c^3 / e\hbar \simeq 1.3 \times 10^{16}$V/cm, corresponds to the intensity $I \simeq 10^{29}$ W/cm^2) might be obtained.

The generally adopted framework for the description of dilute laboratory and space plasmas is based on coupling Vlasov's equation to Maxwell's equations for the EM fields. The sources of these fields are not the discrete particles that compose the plasma but a continuous distribution of charges and currents. In this asymptotic mean field description particle correlations and dynamical effects due to incoherent radiation are neglected. At the extreme optical laser intensities, as those foreseen in next-generation experiments ($I > 10^{23}$ W/cm^2), electrons experience extreme accelerations and emit relatively large amounts of high frequency incoherent radiation. Thus, even within the non quantum description, i.e., neglecting quantum recoil and development of electron-positron pair cascades, which may lead to a considerable depletion of a laser pulse [34], the dynamical effects of the radiation friction (RF) force must be addressed. Large projects have been conceived (ELI[6], Apollon [7], SULF [4], CAEP [5], APRI [3]) with the declared objective of reaching even higher EM energy densities inside a macroscopic relativistic medium and probing the physics of plasma regimes dominated by QED effects, in particular, by the generation of electron-positron pair plasmas as the Schwinger field is approached. Besides, the correct treatment of the RF is not only relevant to intense laser plasma interactions. It is also important in astrophysics, e.g., for the description of pulsar winds,

---

[1]in terms of local thermodynamic equilibrium

[2]Relativistic self–focusing of the laser pulse prediced by G. A. Askar'yan in 1962 [23] is one example of such a manipulation. In intense laser-plasma interaction experiments this phenomenon is nowadays regularly observed.

gamma-ray bursts, jets of active galactic nuclei, radiation-dominated relativistic current sheets [35], and the modeling, e.g., of the flaring Crab nebula with high-frequency γ-ray emission [36].

1.1   Intense laser-plasma interaction scenario

One of the most attractive applications of short intense laser pulses is related to the development of new methods of accelerating charged particles. Conventional accelerators are expensive and have approached the maximum reasonable size[3]. These difficulties were evident already more than a half-century ago, yet before the invention of lasers, when V. I. Veksler, G. I. Budker and Ya. B. Fainberg proposed to use *collective* electric fields excited in a plasma to accelerate charged particles [37, 38, 39]. The three key features of the collective acceleration are (i) the accelerating field on each particle is proportional to the number of accelerated particles, (ii) the field is localized in space and *synchronized* in time with the accelerated particles, (iii) in the acceleration process globally charge-neutralized bunches are produced.

In this work we refer to a particular acceleration regime occurring in the interaction of laser light with dense targets. The laser pulse is assumed to be intense enough to ionize target material almost instantaneously. The interaction typically leads to the generation of energetic electrons (more details are given in Section 1.2), which tend to escape from the target, producing the electrostatic charge separation fields at target boundaries ("sheath" regions). These fields in turn accelerate ions and drive the expansion of the plasma. Under suitable conditions, the combination of heating and radiation pressure, acting on the target, can drive nonlinear shock wave which provides an additional acceleration mechanism. The basic mechanisms of ion acceleration, briefly described in Section 1.3, originate from the dominance of each of these effects. In experiments they generally coexist, leading to a complex acceleration scenario [40, 41].

Basic laser-plasma interaction parameters

The interaction geometry is characterized by the angle of incidence of the laser radiation on the plasma surface and by the field polarization, which can be linear, circular or elliptic. In the case of linear polarization and for oblique incidence one distinguishes between S- and P-polarized waves. Let us consider a laser pulse of duration $\tau_{\rm L}$, with electric field amplitude E_0, and carrier frequency $\omega_{\rm L}$. The dimensionless parameter corresponding to the oscillation momentum of a single electron in the electric field of the laser is related to the radiation intensity $I_{\rm L}$ and the wavelength $\lambda_{\rm L} = 2\pi c/\omega_{\rm L}$ by

$$a_0 = \frac{eE_0}{m\omega_{\rm L}c} = \left(\frac{I_{\rm L}[{\rm W/cm}^2]\lambda_{\rm L}^2[\mu{\rm m}^2]}{1.35 \times 10^{18}~{\rm W/cm}^2\mu{\rm m}^2} \right)^{1/2}. \tag{1.1}$$

When $a_0 \ll 1$, the electron oscillation velocity $v_{\rm osc} = eE_0/m_e\omega_{\rm L}$ is small with respect to the speed of light in vacuum, and its oscillation amplitude $r_{\rm osc} = eE_0/m_e\omega_{\rm L}^2$ is much shorter than $\lambda_{\rm L}$. In this case relativistic effects can be safely neglected and the use of the non-relativistic classical approach to describe the interaction is justified. In the opposite limit, when $a_0 \gg 1$, the laser-matter interaction must be described in the framework of the relativistic theory. If the laser field amplitude $a_0~>$

---

[3]The main restriction on the accelerator size is imposed by the critical value of the electric field strength of the order of a few tens of MV/cm. If this value is exceeded an electric discharge forms on the acceleration chamber wall.

$\sqrt{m_i/m_e}$, with m_i being the mass of plasma ions, the processes due to relativistic ion dynamics also come into play.

The plasma density can be characterized by a dimensionless parameter $\alpha = n_e/n_{cr}$, where n_{cr} is the so-called critical density, defined as $n_{cr} = \omega_L^2 m_e/4\pi e^2$. In a plasma with $n_e = n_{cr}$, the frequency of the laser radiation equals the plasma frequency, $\omega_L/\omega_p = \sqrt{n_{cr}/n_e} = 1$. When $\omega_L/\omega_p \gg 1$, the group velocity of the EM waves in such a plasma, $v_g = \partial\omega/\partial k = c\sqrt{1 - (\omega_p/\omega_L)^2}$, is close to the speed of light, and the plasma itself is called "underdense". If instead, $\omega_L/\omega_p < 1$ ("overdense" plasma), the EM wave can only penetrate into such plasma as far as the evanescence length $\delta \sim c/\omega_p$, and the efficiency of the laser field to plasma coupling strongly depends on the inhomogeneity scale of the density. If the density profile is steep, the interaction takes place at the plasma-vacuum interface, where the laser radiation can easily extract the electrons from the plasma and accelerate them towards the vacuum region. This process provides an effective mechanism of laser light *absorption* (see Sec.1.2). Moreover, at a steep plasma-vacuum interface the effective generation of high-order harmonics is possible due to the so called "oscillating mirror" mechanism or due to the nonlinear motion of the electrons in the narrow region near the plasma boundary [42]. Several authors put forward the plasma-mirror concept as the promising tool to enhance the potential of attosecond sources at relativistic, i.e. $a_0 \gg 1$, laser intensities [43]. When the density distribution is smooth, the plasma frequency $\omega_p(\mathbf{r})$ turns to be a function of the coordinates, and the processes that occur in the vicinity of the critical surface $n_e = n_{cr}$, in the region of the plasma resonance $\omega_L = \omega_p(\mathbf{r})$, play a key role [44, 45]. In this region the EM wave resonantly excites strong electric field, localized in a tight area where the laser radiation is absorbed and fast particles are generated.

For $a_0 > 1$ the transmission of the laser pulse through a plasma is modified by relativistic effects and an overdense plasma with $n_e > n_{cr}$ can become transparent. This phenomenon is known as "relativistic transparency". Details depend on the laser and target parameters [46]. According to a simple model applicable in the relativistic regime to targets with thicknesses $\Delta > \lambda_L$, the value of critical density increases as $n_{cr} \to \gamma n_{cr}$ with $\gamma = \sqrt{1 + a_0^2/2}$ [47]. This is equivalent to assume[4] an effective electron mass equal to $m_e\gamma$. If the $\Delta < \lambda_L$, the transparency threshold also depends on Δ. For a foil with a Dirac delta-like density profile [20, 48, 49] the nonlinear reflectivity can be calculated analytically. The onset of relativistic transparency in this case is found to occur for $a_0 > \pi n_e\Delta/(n_{cr}\lambda_L)$. The efficient generation of carbon ion beams with average energies exceeding $10\mathrm{MeV/nucleon}$ has been recently observed in the laser-plasma interaction experiment in the regime of relativistically induced transparency at the LANL Trident Laser [50].

---

[4]The effective mass γm_e is a function of time and position since it depends on the local amplitude $a_0(\mathbf{r}, t)$ of the EM field.

1.2   Collisionless absorption and hot electron generation: a sharp-boundary plasma

Even very intense laser radiation cannot penetrate into the solid density regions of the irradiated target and the absorbed energy is transported to these regions mostly by hot electrons. Here, we define electrons as "hot" if their energy exceeds the mean oscillation energy $\mathcal{E}_{\mathrm{osc}}$ in the electric field in vacuum, $\mathcal{E} > \mathcal{E}_{\mathrm{osc}} = m_e c^2 \left(\sqrt{1 + a_0^2/2} - 1 \right)$. Hot electrons entering solid targets have been observed in many experiments at high intensities for different interaction conditions [51, and references therein]. They play a fundamental role in applications such as laser-driven photonuclear physics, fast ignition of fusion targets, and new radiation sources in the extreme ultraviolet (XUV) domain. Moreover, in most of the laser-plasma experiments reported so far, acceleration of protons and heavier ions is driven by hot electrons. Turning to the possible mechanisms of their production in the absorption of intense light beams, at high intensities collisional absorption is ineffective because the collisional frequency and the inverse Bremsstrahlung rate quickly decrease with increasing electron energy and/or laser intensity as $\nu_{\mathrm{ei}} \sim v_e^{-3}, v_e \simeq \max(v_{\mathrm{th}}, v_{\mathrm{osc}}), v_{\mathrm{th}} \sim T_e^{1/2}, v_{\mathrm{osc}} \sim (I_{\mathrm{L}} \lambda_{\mathrm{L}}^2)^{1/2}$. Thus, in order to ensure a sizable absorption at relativistic and subrelativistic intensities measured in experiments and demonstrated in simulations [51], [52, and references therein], other effects of *non-collisional* nature have to become active. The experimental and theoretical results on the absorption degrees collected up to the year 2009[5] [51] in the regime of intensities $I_{\mathrm{L}} \lambda_{\mathrm{L}}^2 \in [10^{18}, 10^{21}] \ \mathrm{W/cm^2 \mu m^2}$ report absorption degrees ranging from 5% to 95%. Absorption between 35% and 85% is reported at the constant irradiance of $I_{\mathrm{L}} \lambda_{\mathrm{L}}^2 = 6 \times 10^{18} \ \mathrm{W/cm^2 \mu m^2}$. These huge differences can be partially explained by the high sensitivity of hot electron generation to the laser and plasma parameters. For this reason absorption values and charateristics of the hot electron population are often taken into account in a phenomenological way [41], e.g., the hot electron distribution is often assumed to be Maxwellian with a temperature $T_{\mathrm{hot}} \simeq \mathcal{E}_{\mathrm{osc}}$ as a function of the laser intensity.

In terms of basic physics collisionless absorption is understood as a result of an interplay of the oscillating laser field with the space charge field produced in the plasma. In fact, under quasi-steady conditions Poynting's theorem averaged over one laser cycle reduces to

$$\langle \nabla \mathbf{S} \rangle = -\langle \mathbf{j} \cdot \mathbf{E} \rangle. \tag{1.2}$$

Here $\mathbf{S} = \dfrac{c}{4\pi} \mathbf{E} \times \mathbf{B}$ is the Poynting vector, which relates to the intensity as $I_{\mathrm{L}} = \langle \mathbf{S} \rangle$. The current density is $\mathbf{j} = -e n_e \mathbf{v}$, where $\mathbf{v}$ is the mean electron flow velocity. Equation (1.2) decribes both collisional and non-collisional absorption. In the laser field with a mean frequency ω_{L} the electric field evolves in time as $\mathbf{E} \sim \sin \omega_{\mathrm{L}} t$, the current density follows $\mathbf{j} \sim \cos(\omega_{\mathrm{L}} t + \phi)$ and

$$\langle \nabla \mathbf{S} \rangle = -\langle \cos(\omega_{\mathrm{L}} t + \phi) \sin \omega_{\mathrm{L}} t \rangle = -\frac{1}{2} \sin \varphi. \tag{1.3}$$

In collisional absorption the dephasing φ between current and driver field is due to the collisions between electrons and ions,

$$\langle \mathbf{j} \cdot \mathbf{E} \rangle_{\mathrm{collisional}} = \omega_p^2 \frac{\nu_{\mathrm{ei}}}{\omega_p^2 + \nu_{\mathrm{ei}}^2} |\mathbf{E}|^2 > 0.$$

---

[5]See also [53], where the collection of hot electron temperature measurements obtained for subpicosecond laser pulses up to the year 2000 is presented.

As it vanishes at $\nu_{ei} = 0$, any finite phase shift φ for high field intensities can only be of collisionless origin. For the optical laser field with $I_L \sim 10^{19} - 10^{21}$ W/cm^2 this origin is in space charge induced by $\nabla \mathbf{v} \neq 0$ [54]. The compulsory dephasing between current and driver field, that determines the degree of absorption, is provided by the longitudinal space charge field between the oscillating electrons and the quasistatic ions.

Difficulties and complications arise when the degree of absorption has to be *quantified*. Absorption models that have been proposed so far include vacuum heating [55], stochastic electron acceleration in fluctuating fields [56], wave breaking [57], linear and nonlinear Landau damping [58], anomalous skin effect [59], Brunel (sharp-egde) absorption [60], ponderomotive heating (longitudinal [61] and trasverse [62]), $\mathbf{j} \times \mathbf{B}$ heating [63], surface plasmon excitation [64, 65] and "laser dephasing heating" [66]. These models are either based on simulations only or they are in disagreement with basic properties observed in experiments and simulations [51, 53, 67]. For example, the anomalous skin-effect at high laser intensities yields an absorption of a few percent only. Absorption by excitation of surface plasmons requires corrugated [65] or grating targets [68], while in flat targets [64] the coupling is very delicate and unlikely to occur. The best know non-collisional candidate, the resonance absorption at oblique incidence[6][44], is sensitive to the density scale length $n_e/|\nabla n_e|$ because the driving force is evanescent in the resonance region, but in the interaction of the high intensity laser pulses with good contrast ratios with solid targets, there is no time to form a preplasma in front of an irradiated sample that could couple to a resonantly excited plasma wave[7].

The first successful proposal able to explain a sizable absorption in a sharp boundary solid-density target was the so-called $\mathbf{j} \times \mathbf{B}$ heating. The results of PIC simulations [63] have shown that appreciable absorption, target heating, and production of superthermal electrons at any density above n_{cr} for normal laser pulse incidence is due to the the Lorentz force, which induces *non-resonant* electron oscillations at frequency $2\omega_L$ normal[8] to the target surface. However, at that point no attempt was made to explain how the observed absorption comes into play. A notable step in understanding high-power collisionless absorption (offering within limits of a laminar electron flow dynamics the first physical explanation of the $\mathbf{j} \times \mathbf{B}$ heating at $2\omega_L$) was made by F. Brunel [60]. Brunel proposed an electrostatic model of electron heating at a step-boundary plasma and has shown that the resonance absorption concept [44] could be adapted to steep, highly overdense plasma profiles. In this case significant absorption is achieved under oblique incidence despite total absence of plasma resonance at $\omega_L = \omega_p$ and no possibility for a plasma wave to propagate into a shallow preplasma in front of the target. Until recently Brunel's model has been the only successful attempt to explain efficient collisionless absorption on physical grounds under a minimum of assumptions and simplest geometry [69].

An accurate analysis of Brunel's model [69] has revealed essential aspects of collisionless absorption, such as prompt generation of fast electrons during one laser cycle or a fraction of it under P-polarization, insensitivity of absorption with respect to the target density well above n_{cr}, simplicity, and robustness. The splitting of the electron energy spectrum into the two groups of slow and of fast electrons, observed in experiments and simulations, also comes about in the most natural

---

[6]The resonance absorption at oblique incidence consists of the direct conversion of laser light into an electron plasma wave resonantly excited at the critical electron density where $\omega_L = \omega_p$.

[7]It is worth mentioning that in most high intensity experiments the main interaction pulse is preceded by prepulses which cause early plasma formation and expansion so that the short-pulse interaction does not occur with a sharp-boundary, solid-density plasma.

[8]Electron motion parallel to the laser field defines a perfectly reversible process. Absorption is due to the motion perpendicular to the target surface induced by the magnetic field $\mathbf{B}$.
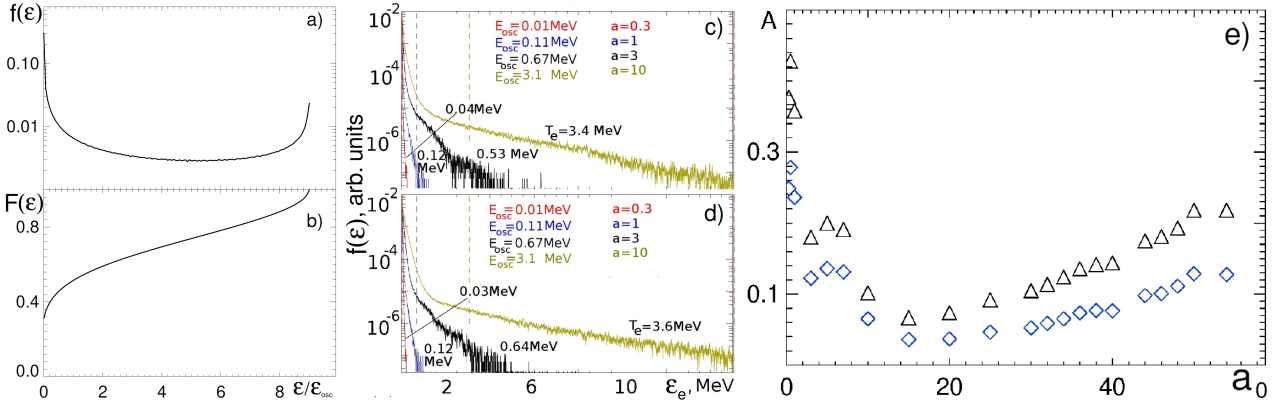
Figure 1.1: *Collisionless absorption* – (a) Electron spectrum $f(\mathcal{E})$ from Brunel's nonrelativistic model [60], (b) – $F(\mathcal{E}) = \int_0^{\mathcal{E}} f(E')dE'$. Energy $\mathcal{E}$ in units of mean oscillation energy in vacuum, energy cutoff is at $\mathcal{E} = 9.1\mathcal{E}_{\text{osc}}$. (c)-(d) Electron energy spectra $f(\mathcal{E})$ in logarithmic scale obtained in 1D simulations of the interaction of laser pulse irradiating a dense plasma slab (initial enectron density $n_e = 100\,n_{\text{cr}}$) at $45°$ incidence angle. The spectra are calculated at $t = 30 \times 2\pi/\omega_{\text{L}}$ and $t = 45 \times 2\pi/\omega_{\text{L}}$ cycles after the beginning of the interaction. Vertical dashed lines mark the mean oscillation energies. The hot electrons follow a Maxwellian distribution. (e) Total absorption (triangles) and the absorption by electrons (blue diamonds) as a function of a_0 obtained from 1D PIC simulations. Figure is adapted from [54].

way. However, in the geometry of Brunel's model, PIC simulations unambiguously show that the hot electron spectrum is broad and can be reasonably well described with an exponential function $f(\mathcal{E}_{\text{hot}}) \propto \exp(-\mathcal{E}_{\text{hot}}/k_B T_{\text{hot}})$, extended up to a cutoff of a few times $k_B T_{\text{hot}}$, (see Fig. 1.1(c)-(d) showing the energy spectra of the electrons for different laser pulse amplitudes), and that the fraction of hot electrons is a few percent only. On the contrary, the spectrum of Brunel electrons is non-Maxwellian with a pronounced maximum at $\mathcal{E} = 9.1\mathcal{E}_{\text{osc}}$, followed by a sharp cutoff, Fig.1.1(a)-(b), and the resulting percentage of fast electrons is nearly two orders of magnitude bigger than the values obtained in PIC simulations. The scaling of the absorption coefficient with intensity in Brunel's model is $A \sim (I_{\text{L}}\lambda_{\text{L}}^2)^{1/2}$. It reaches unity at incidence $\theta = 86°$ (no solution exist beyond) and at intermediate angles of incidence it is considerably smaller, than the values measured in experiments [70] so that the absorption in Brunel's mechanism is inefficient below very oblique incidence. Finally, the average energy of the hot electrons in Brunel's model is proportional to the intensity, which is dramatically different from the experiment, performed under Brunel's conditions [70], as well as from relevant results in the literature [71, 72, 73, 74, 75, 76, 77].

The further investigation of statistical ensembles of electron orbits, extracted from 1D PIC simulations [54], showed that the absorption process is localized at the ion-vacuum interface and in the skin layer. Contrary to the laminar dynamics assumed in Brunel's model, the electron flow becomes highly turbulent. Single electrons enter into resonance with the laser field thereby undergoing a phase shift which causes orbit crossing and breaking of Brunel's laminar flow. This anharmonic resonance [77] is responsible for the formation of a Maxwellian tail in the electron energy spectrum. Most remarkable results of the study reported in [54] are the Brunel-like spectra of hot electrons at the relativistic threshold, the minimum of absorption, Fig.1.1 (e), at $I_{\text{L}} \sim (0.3 - 1.2) \times 10^{21}$ W/cm^2 in plasma targets of $n_e \simeq 100\,n_{\text{cr}}$, the drastic reduction of the number of hot electrons in the same intensity range and their reappearance in the highly relativistic domain.

As for the most controversially discussed subject in the relevant literature, the scaling of the hot elec-

tron energy with the laser intensity, early 1D PIC simulations [71] obtained a scaling $\mathcal{E}_{\text{hot}} \sim \sqrt{I_{\text{L}}}$, which has been reconfirmed by independent simulations [78] and by experiments [79], but seems to be in contrast with other experimental data [72] and more sophisticated analysis [75]. Analogous scaling laws have been proposed by other authors [70, 73, 76]. Nevertheless, there is no convergence towards a definite scaling yet [41, 49, 54, 80].

Note that for S-polarization or/and normal incidence the laser electric field vector does not have a component perpendicular to the target surface. However, for high intensities the magnetic force term $\mathbf{v} \times \mathbf{B}$ becomes important and may drive the electron oscillation along the density gradient also for normal incidence. In this case the generation of hot electrons will occur twice per laser period if the polarization is linear. For circular polarization (CP) and normal incidence the generation of hot electrons might be strongly suppressed because the perpendicular to the surface oscillating $\mathbf{j} \times \mathbf{B}$ component vanishes for CP (see also discussion in Sec. 1.3). A more detailed analysis shows that electron heating is quenched when the ellipticity exceeds some threshold value [81, 82].

Although we believe that the reported phenomena will survive in 2D and 3D also, the 2D simulations reveal additional effects, such as the deformation of the plasma surface due to "hole-boring" driven by the radiation pressure, which changes the local angle of incidence [71]. This effect leads to an increased absorption and provides a dynamic effect of collimating the electron flow inside the target [83]. A similar effect takes place in microcone targets [84, 85, 86, 87, 88, 89]. Absorption and fast electron generation in solid density targets are also sensitive to sub-wavelength density gradients and structuring of the interaction surface [90]. However, in order to exploit this effect experimentally, e.g., to enhance and optimize the ion acceleration, the use of high contrast laser systems is strictly necessary.

1.3   Ion acceleration

The progress in laser technology has led already to light sources delivering pulses of focused intensities exceeding $10^{21} \mathrm{W/cm^2}$ [91]. Even higher intensities are foreseen with the new generation of laser sources expected to come into operation in the nearest years [6, 7]. When such a pulse impinges on a solid target[9] both electrons [92] and *ions* [93, 94, 95, 96] can be accelerated up to hundreds of MeV or even GeV energies.

The first succesful experiments on laser acceleration of protons with beam-like properties and multi-MeV energies were reported almost two decades ago [26, 96, 97]. Since then multi-Mev proton and ion beams with ultrashort burst emission, high brilliance and low emittance have been obtained over a wide range of laser[10] and target parameters. The recently reported maximum proton energy approach 100 MeV [98]. Widely accepted basic scenarios of ion acceleration are the "target normal sheath acceleration" (TNSA) (see e.g. [96, 97, 99, 100] and references therein) and the "radiation pressure acceleration" (RPA) [101]. In the former, laser-driven fast electrons escape from the rear side of a thin foil and drag ions behind, in the latter electrons and ions are accelerated together. Under suitable conditions, the combination of heating and radiation pressure can drive nonlinear shock waves and lead to "collisionless shock acceleration" (CSA).

Most of the observations of ion acceleration cannot be fully explained in terms of TNSA, RPA or CSA. Depending on the laser and target parameters, the acceleration mechanism may be of hybrid nature and combine aspects of all the three "basic" acceleration concepts. In addition, in the literature there are many proposals of particular schemes, employing, e.g., complex target configurations. Although these proposals are ordinarily supported by numerical simulations, only very few of them have been realized in the laboratory so far. Extensive surveys on the underlying physical principle of the main ion acceleration mechanisms along with related experimental indications are given in the reviews [40, 41, 102, 103].

Target Normal Sheath Acceleration – The most successful, although qualitative, description of the TNSA [99] was proposed to explain the first experimental results on multi MeV proton acceleration from solid targets [26, 96, 97]. In the intensity regime of relevance, i.e. for $I_\mathrm{L}\lambda_\mathrm{L}^2 > 10^{18} \mathrm{W/cm^2}\mu m^2$, the laser pulse can efficiently accelerate electrons. The average energy of the hot electrons is of the order of MeV, their collisional range is much larger than the target thickness, so that they can propagate to the *rear* side of the target and drive the acceleration of ions from surface layers via the charge separation field. While only a limited number of very energetic electrons will definitely leave the target, most of hot electrons will be held back within it by the space charge. These electrons will form a sheath of a Debye length from the initially unperturbed rear surface. According to the model developed in [97], the accelerating sheath field E_sheath is defined by the temperature T_hot and density n_hot of the hot electrons and is given by

$$E_\mathrm{sheath} \sim \frac{k_B T_\mathrm{hot}}{e \Lambda_D} \sim \sqrt{n_\mathrm{hot} k_B T_\mathrm{hot}}.$$

If a scaling $T_\mathrm{hot} \sim \sqrt{I_\mathrm{L}\lambda_\mathrm{L}^2}$ [53, 60, 69] and a roughly 10% fractional absorption in hot electrons are assumed, the strength of the sheath field will be $E_\mathrm{sheath} \sim 10^{10} \mathrm{V/cm}$ for $I_\mathrm{L}\lambda_\mathrm{L}^2 = 10^{19} \mathrm{W/cm^2}\mu m^2$.

---

[9]In this work we refer to ion acceleration occurring in the interaction of intense laser light with the solid targets, where the electron density significantly exceeds the critical density n_cr.

[10]Experiments on ion acceleration use ultrashort (few tens of fs) laser systems, typically based on solid state Ti:Sa technology, as well as high energy picosecond laser systems (Nd:glass). Some experiments employ also $C0_2$ lasers.
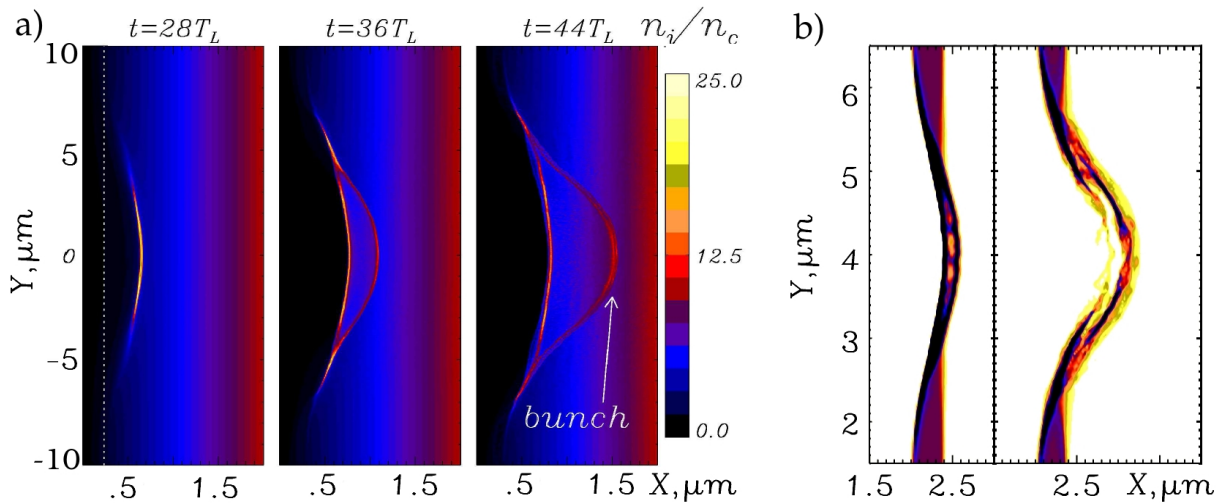
Figure 1.2: *Hole-boring and light sail acceleration by a circularly polarized laser pulse* – (a) Snapshots of the ion density from a 2D PIC simulation for a linear density profile rising from 0 to $10n_{cr}$ over $2\lambda_L$. The white dotted line indicates the initial position of the $n_e = n_{cr}$ surface. The arrow indicates the location of the short dense ion bunch. The divergence of the bunch is about $4°$. Picture is adapted from [110]; b) Snapshots (at $t = 75$ fs and $t = 100$ fs) of ion density from a 3D PIC simulation of a thin hydrogen foil $\Delta = 0.4\lambda$, irradiated by a tightly focused CP laser pulse with $I_L = 3.4 \times 10^{19}$ W/cm^2. Pictures are adapted from [126].

This large field will backhold most of the escaping electrons, ionize atoms at the *rear* surface of the target, and accelerate ions up to energy in the MeV range. Under appropriate conditions, including the right combination of target thickness and laser pulse duration, the energy of the ions can be enhanced by the recirculation of the hot electrons through the target during the ion acceleration process [104]. The energy of the TNSA accelerated ions scales with the laser pulse intensity roughly[11] as $\sim \sqrt{I_L}$. Concerning the properties of the accelerated ion beam, in both simulations and experiments the energy spectrum is found to be quasi-thermal with a cutoff at a maximum energy. The angular distribution of the ions is also quite broad, the average divergence is in the range $10°$-$20°$ with the high energy ions having smaller divergence. Note that while TNSA can accelerate any ion species present in the surface layer, in most experimental settings it results in preferential acceleration of light ions from contaminant layers, with protons being the dominant component of the TNSA-accelerated ion beams. Removing hydrocarbon contaminants, e.g., by resistive heating [105], may suppress the dominant proton acceleration. It should be noted that even though in ultra-high contrast laser pulses a symmetric acceleration from the front side (in backward direction) has also been observed [107], the front-TNSA efficiency is drastically reduced if the front preplasma formation is not inhibited.

Radiation Pressure Acceleration – The possibility of an ion contribution originating from the *front* surface of the target was considered already in the first reported measurements of MeV protons accelerated in the *forward* direction [96, 97]. The mechanisms of acceleration, alternative or complementary to TNSA and efficient in the front target regions, have been extensively investigated. The incidence of an EM wave of intensity I_L on a plane target leads to absorption of its linear momentum and produces at the front surface a pressure P_{rad}. The maximum of this pressure (for normal inci-

---

[11]The power-law scalings of the ion energy $\propto I_L^\nu$, with $\nu \in [1/3, 1]$ depending on the laser pulse duration have been inferred by reviewing the data from different laser laboratories [40] and performing parametric studies on a single laser system [106].

dence) is obtained for an ideally reflecting target surface and reads $P_{rad} = 2I_L/c$. For sufficiently high intensity this *radiation pressure* may overcome the thermal pressure and push an *overdense* target inward, leading to the steepening of the density profile, bending of the surface and recession of the interaction surface, see Fig.1.2a). This process is called "hole-boring" and the velocity of the surface is known as the "hole boring" (HB) velocity v_{HB}. It can be estimated, assuming the balance between the flows of EM and kinetic momentum at the surface. For $v_{HB}/c \ll 1$ the resulting expression [108] reads $v_{HB} = \sqrt{I_L/\rho c}$, where $\rho \simeq nm_i$ is the mass density[12]. The balance of mass and momentum flows at the moving surface implies that there must exist a flow of ions "reflected" from the recession front at twice v_{HB}. This results in an ion population with *energy per nucleon* equal to

$$\mathcal{E}_{HB} = \frac{1}{2}m_p \cdot (2v_{HB})^2 = 2m_p\frac{I_L}{\rho c} = 2m_e c^2 \frac{\mathcal{Z}n_{cr}}{\mathcal{A}n_e} \cdot a_0^2. \tag{1.4}$$

Here $\mathcal{Z}$ and $\mathcal{A}$ are the charge and mass numbers of the plasma ions. Since $I_L \propto a_0^2$, the scaling of $\mathcal{E}_{HB}$ with the intensity (1.4) is more favorable than the $\sqrt{I_L}$ scaling for TNSA. The scaling with the density $\mathcal{E}_{HB} \propto n_e^{-1}$ implies, however, that higher energies are achievable if the target density is reduced to relatively small values slightly exceeding n_{cr}. For values typical for solid targets ($n_e > 100\ n_{cr}$) only modest energies may be obtained. Combining low-density targets with laser pulses at fore-seeable intensities $I_L > 10^{22}$ W/cm^2 may allow reaching > 100 MeV energies, as investigated theoretically [111]. Note that for moderate laser intensities the hole-boring efficiency is strongly reduced because of the generation of fast electrons. They decrease the reflectivity of the plasma and produce a strong thermal pressure which counteracts the radiation pressure. Only at high intensities $I_L > 5 \times 10^{21}$ W/cm^2 RPA starts to dominate over TNSA for any laser polarization, as was shown first by PIC simulations [101]. A dominance of RPA over TNSA may be, however, obtained at much lower intensity if a laser pulse with circular polarization at normal incidence, instead of linear polarization (LP), is used [108, 110]. In fact, under such conditions the acceleration of "fast" electrons at the laser-plasma interface is suppressed, ruling out TNSA. The suppression of fast electrons for CP can be understood by recalling that models of electron acceleration at a sharp plasma surfaces require the driving force having an oscillating component along the density gradient. For normal incidence such component is given by the part of the term $\mathbf{j} \times \mathbf{B}$, ocillating at $2\omega_L$, which vanishes for CP. The numerical studies [108] confirmed this prediction and showed that in the interaction of a CP laser pulse with $I_L < 10^{19}$ W/cm^2 all the ions in the skin layer get accelerated and the fastest ones produce a very dense bunch directed in the forward direction. In Fig.1.2a) a single, ultrashort ion bunch generated in the interaction of a CP laser pulse of intensity $I_L = 5.5 \times 10^{18}$ W/cm^2 and $\tau_L = 33$ fs duration with slightly overdense plasma is shown. The ion acceleration initially occurs near the cutoff layer where $n_e = n_{cr}$ and produces a dense, $n_i > 10\ n_{cr}$, ion bunch with a narrow energy spectrum.

The first successful experiment of HB acceleration has been performed at the Accelerator Test Facility of Brookhaven National Laboratory using a CO$_2$ infrared laser with $\lambda = 10\mu$m ($n_{cr} \simeq 10^{19}$cm^{-3}) and $I_L \simeq 6.4 \times 10^{15}$ W/cm^2 (corresponding to $a_0 \simeq 0.5$) and a hydrogen jet target with the density a few times n_{cr}. In this experiment a spectral peak at energy $\mathcal{E} \simeq 1.2$ MeV have been obtained [112]. The hole-boring velocity has been measured later in a similar experiment [113]. Experimental evidence of HB acceleration in solid targets is at present less clear [41]. But signatures of such acceleration have been associated with the interferometric observation of collimated plasma jets in PW

---

[12]The relativistic expression [109] reads $v_{HB}/c = \dfrac{\sqrt{I_L/\rho c}}{c + \sqrt{I_L/\rho c}}$.

laser pulse interactions with a few μm thick targets [114].

HB-PRA applies to targets with thicknesses much larger than the skin layer, in which ion acceleration occurs. If the target is thin, such that $\Delta \ll v_{\text{HB}}\tau_{\text{L}}$, the HB front reaches the rear side of the target before the end of the pulse duration and the whole target is accelerated[13], Fig.1.2b). In this case the laser pulse can further accelerate ions since they are not screened by the background plasma anymore [115, 116, 117]. This regime in its simplest form can be modeled as a thin mirror, boosted by radiation pressure, and is called "light sail" (LS) acceleration. The characteristic features of LS-RPA, such as high conversion efficiency in the relativistic limit and the possibility to reach very high energies with foreseeable laser and target technologies, may be qualitatively understood within the simple model of a perfectly reflecting mirror accelerated by a normally incident plane wave. Due to the Doppler effect the frequency ω_{L} of each incoming photon reflected by the mirror moving with the velocity $V = \beta c$ in the laboratory frame is downshifted to ω', according to the relation $\omega' = \omega_{\text{L}}(1 - \beta)/(1 + \beta)$, so that almost all of the energy $\hbar\omega_{\text{L}}$ of the photon is delivered to the target in the limit $\beta \rightarrow 1$. Since the number of photons is conserved for a perfect mirror, a complete conversion of the wave energy into mechanical energy is obtained for $\beta \rightarrow 1$. For a given surface density $\rho \cdot \Delta$ of the sail, its reflectivity drops down due to the onset of relativistic transparency for the field amplitude $a_0 > \pi n_e \Delta/n_{\text{cr}}\lambda_{\text{L}}$. This effect suggests $a_0 = \pi n_e \Delta/n_{\text{cr}}\lambda_{\text{L}}$ as an optimal condition for LS acceleration [48, 118, 119].

The interest in the LS-RPA acceleration regime was greatly stimulated by the results of the 3D PIC simulations of a thin ($\Delta = \lambda_{\text{L}}$) dense ($n_e = 49\ n_{\text{cr}}$) hydrogen foil boosted by an ultra short ($8 \times 2\pi/\omega_{\text{L}}$) ultra intense ($I_{\text{L}} = 1.4 \times 10^{23}\ \text{W/cm}^2$) laser pulse [101]. These simulations demonstrated that most of the ions in the foil were accelerated coherently up to energies $\mathcal{E} \sim 1.5$ GeV and that the temporal dependence and typical values of the ion energy were well described by the LS model. Later theoretical studies addressed the issue of target stability during LS-RPA. 2D [110, 117, 120] and 3D [121] PIC simulations in the ultraintense regime showed a bending instability, Fig.1.2b), which has been interpreted to be of the Rayleigh–Taylor (RT) type. Some experimental evidence of radiation-pressure-driven RT instability in thin targets has been also reported [122]. The first experimental investigations of the LS-RPA regime [123] showed several issues, such as non monoenergetic ion spectra, weak dependence of the energy cutoff on polarization, and non-uniformity of the accelerated beam. An experiment performed recently on the GEMINI laser with a short intense pulse ($\tau_{\text{L}} = 45$ fs, $I_{\text{L}} = 6 \times 10^{20}\ \text{W/cm}^2$) and ultrathin ($\Delta = 0.01 - 0.1\ \mu$m) amorphous Carbon targets has given evidence of much higher Carbon ion energies for CP, where the ions energy cutoff 25 MeV has been observed. For LP the cutoff energy has been measured at 10 MeV [124].

Although some authors have proposed the RPA of a thin foils as a way to generate high-energy proton beams, this approach is most interesting for the acceleration of higher-$\mathcal{Z}$ ions. While it seems technologically unfeasible to have an ultrathin target made of hydrogen only, in a target made of multiple species all the ions will be accelerated to the same velocity, resulting in higher energies for the heavier species. However, an analysis of the LS dynamics beyond the rigid mirror model [48] shows that for pulses of finite duration only part of the target ions are accelerated as a monoenergetic bunch, and under proper conditions this part may contain only the target protons. In addition, the formation of a region of an accelerating field ahead of the target related to "leaking" transmission of the laser pulse may also accelerate protons [125].

Collisionless Shock Acceleration – This mechanism of ion acceleration, often associated with astrophysical scenarios, in laser-plasma interaction is related to the collisionless shock generated in the plasma due to the HB process. Its investigation is still relatively preliminary compared to that

---

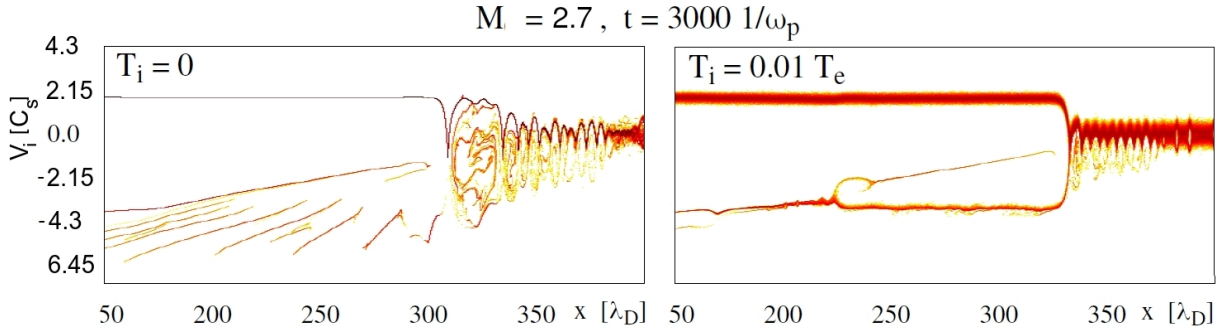[13]The transverse size of the accelerated region corresponds roughly to the focal spot-size of the laser pulse.

Figure 1.3: *Electrostatic shock with reflected ions* – (a) The distribution of ions on the (x, v_x) phase plane. An electrostatic shock wave with $M = v_{\rm sh}/c_s \simeq 2.7$ propagates to the left. Strong reflection (left frame) leads to the broad ion spectrum. True shock is formed in the presence of a sufficiently warm ion distribution and the steady ion reflection occurs. 1D PIC non relativistic simulations have been performed by A. Hanusch.

of TNSA, though collisionless shock experiments using laser produced plasmas have a long history [127]. In [128], a collisionless shock was produced by irradiating a solid target mounted inside a pinch device filled with low-density plasma. In [129], the supersonic flow of a laser ablated plasma, which got past a stationary obstacle, was investigated. Several recent experiments [130] have detailed the propagation of collisionless electrostatic shocks driven by the laser ablation of thin metal foils in a low density plasma. As a mechanism of ion acceleration, potentially leading to the generation of ion beams with exceptionally narrow spectral distribution in superintense laser interaction with μm-scale plasma targets, CSA was proposed on the basis of PIC simulations [131, 132]. These simulations have demonstrated the generation of shock waves with sonic Mach number $M = v_{\rm sh}/c_s = 2 - 3$ and the production of energetic ions of velocity $\sim 2v_{\rm sh}$. The sound speed c_s was estimated as $c_s = \sqrt{\mathcal{Z}T_{\rm hot}/\mathcal{A}m_p}$, with the temperature of the hot electrons being $T_{\rm hot} \simeq \mathcal{E}_{\rm osc}$. The charge separation field at the shock front acts as a potential barrier for the ions in the plasma, accelerating some of them by reflection up to twice the shock velocity. If the velocity of the shock is kept constant, this results in monoenergetic ion beam with energy per nucleon

$$\mathcal{E}_{\rm CS} = \frac{1}{2}m_p \cdot (2v_{\rm sh})^2 = 2m_p M^2 c_s^2 = 2\frac{\mathcal{Z}T_{\rm hot}}{\mathcal{A}}M^2. \tag{1.5}$$

In the experiment reported in [133], CSA has been indicated as the mechanism responsible for the proton acceleration in the interaction of a CO_2 laser pulse with a gas-jet target. A proton beam with $\sim$20 MeV energy per particle and only 1% energy spread and low emittance has been obtained. The number of accelerated protons in this experiment was, however, approximately three orders of magnitude lower than the number of protons accelerated via the HB mechanism in similar laser and target conditions [112]. It should be noted here that the number of CSA accelerated ions *must* be low if one aims for a monoenergetic ion beam (see Fig. 1.3). In fact, the particle reflection strongly depends on the amplitude of the shock (overshoot of electrostatic potential), which depends on the shock speed [134, 135, 136] in the first place. The reflected particles alter the shock amplitude and speed (momentum conservation), and thus the reflection threshold, causing the ion spectrum to broaden. The demonstration of CSA with optical lasers, which allow for a much higher intensity but require for the efficient acceleration higher target density, has been achieved so far by simulations only. The recent 3D PIC parametric studies [137, 138] have shown that the control of the target density profile is crucial to achieve multi MeV protons with PW laser systems.

The extensive research interest in laser-accelerated ion beams is stimulated by their exceptional properties, including high brightness, high spectral cutoff, high directionality, laminarity, and ultrashort duration. These properties make laser-driven ion beams suitable for any technological application which requires an extremely localized energy deposition [139, 140]. Moreover, if significant improvements over present laser plasma accelerators were achieved, they could become attractive for medical purposes both for oncological ion beam therapy [26, 28] and short-lived radioisotope production [27, 102, 103, 141]. Nowadays ions in the energy range of hundreds of MeV are routinely used for cancer treatment in several[14] medical facilities in the world. In the medical centers for hadrontherapy, the ion beams with the required parameters are obtained with conventional accelerators. A necessary and the most expensive element in such centers is the gantry system, i.e. a huge device for the irradiation of the lying patient from different directions. Compared to conventional accelerators of charged particles the laser ion acceleration would be more advantageous due to compactness and relatively low cost of the accelerator itself, and due to the possibility to develop an optical scheme to transport and rotate photon beams instead of magnetic transportation lines and gantry for high energy ions [28]. However, before plasma based accelerators could compete with traditional accelerators in this field, several important improvements seem to be necessary. In particular, the cutoff energy of the laser-accelerated ions is still too low to be of medical interest, and their spectra are too broad. But the major difficulty is related to the reliability of the plasma based acceleration systems leaving much to be desired. In this context the application of long wavelength CO_2 laser as a driver enables the use of a flowing gas target, which may simplify high repetition rate operation compared to a solid target, which needs to be mechanically replaced or displaced in a very short time. However, in order to reach the ion energy range suitable for medical applications, the CO_2 laser intensity should be increased by two orders of magnitude. Some development projects and required technical advances are discussed in the literature [143].

The low emittance of laser-acceleted protons favored their application for imaging [144]. The broad energy spectrum combined with the short duration of the proton bunch generated via TNSA has enabled the development of a single-shot detection of EM fields generated in laser-plasma interaction, with picosecond temporal resolution [145]. This innovative application has provided much valuable information on the nonlinear dynamics of plasmas, including the proton acceleration mechanism itself [146].

---

[14]As of 2014, there were 40 centers worldwide and about the same number under construction. Now (November 2019) about 100 centers operate and more than 30 are under construction [142].

1.4   Droplets in intense laser field

While laser-based particle acceleration shows an unprecedented efficiency as far as particle energy per acceleration length is concerned, the beam quality is not yet sufficient for many applications. In order to be useful specifically for medical purposes the ion spectrum should be monochromatic, tunable, and reproducible. For any useful application one needs moreover a high repetition rate and a debris free target system. In this context, finite-size mass-limited targets are of particular interest because they can be used to confine the absorbed energy, obtaining thus higher temperatures. In a well know example the interaction of ultrashort moderate intensity laser pulses with subwavelength clusters resulted in the acceleration of ions up to energies sufficient to drive deuterium–deuterium nuclear fusion reactions [147]. An obvious limitation on the use of such clusters as ion sources is the isotropic ion emission and the resulting low brilliance [41]. Enhancement of the conversion efficiency and proton cutoff energy has been observed recently in isolated droplets [148, 149, 150] and in foils with limited (tens of microns) transverse extension [151]. In a recent experiment [152], a plasma produced from a 1 μm diameter levitated plastic sphere positioned with micrometer precision in the focus of a PW laser pulse has been used to generate a single proton bunch with narrow energy spread. Central energies for consecutive laser shots were found in the range from 20 to 40 MeV.

Among various technique to generate ultrashort *electron* bunches, which in turn have potential applications in attosecond electron diffraction experiments or as sources of attosecond X-ray pulses, mass-limited targets in general and micro-droplets in particular may offer a number of advantages. Attosecond control of the collective electron motion and directional emission from isolated dielectric nanoparticles with phase stabilized two-cycle laser pulses have been demonstrated experimentally, supported by the microscopic analysis of the electron emission [153]. Electron acceleration from micro and nanodroplets has been extensively investigated numerically. Narrow electron bunches have been observed in 3D PIC simulations of the interaction of a short ($\tau_{\mathrm{L}} = 30$ fs), intense ($I_{\mathrm{L}} = 2 - 8 \times 10^{18}$ W/cm^2), linearly polarized plane-wave laser pulse with helium micro-droplets [154]. The spatial width of the generated bunches is much smaller than the wavelength, therefore their temporal structure is already in the attosecond domain. The bunches are emitted each half-cycle, Fig. 1.4, under plus or minus a certain angle in the polarization plane. The preferred electron emission angles and the kinetic energies in the multi-MeV range arising due to local field enhancements at the droplet surface can be calculated using Mie theory. A parametric study with respect to the droplet size for a similar setup but much shorter laser pulses ($\tau_{\mathrm{L}} = 5$ fs) has been performed in [155]. Significant disagreement with Mie theory has been reported for electron bunch emission from droplets, whose radii R satisfy the condition $\delta_r < R < 10\delta_r$, where $\delta_r = \sqrt{\gamma}\delta_e$ is the relativistic skin depth. This effect has been attributed to the induced relativistic transparency. PIC simulations with the synchrotron radiation module incorporated [156] demonstrated the generation of bright fs X-rays by irradiating a liquid helium micro-droplet with an intense CP laser pulse at intensity $I_{\mathrm{L}} = 6 \times 10^{19}$ W/cm^2 [157]. The possibility to obtain tunable X-rays with required brightness and energy by an appropriate choice of the laser and droplet parameter has been discussed.

Heating mechanisms and ionization in laser-illuminated clusters have been systematically investigated in the last two decades [147, 158, 159, and references therein]. The ionization dynamics in wavelength-sized targets irradiated by LP laser pulses of intensity $I_{\mathrm{L}} \simeq 5 \times 10^{17}$ W/cm^2 has been addressed in [160] by parametric 3D PIC simulations with field ionization included, and the fractional ionization degrees for various droplet and laser parameters have been obtained. The results of the simulations have shown that a strong near-infrared or optical laser pulse interacting with an ini-
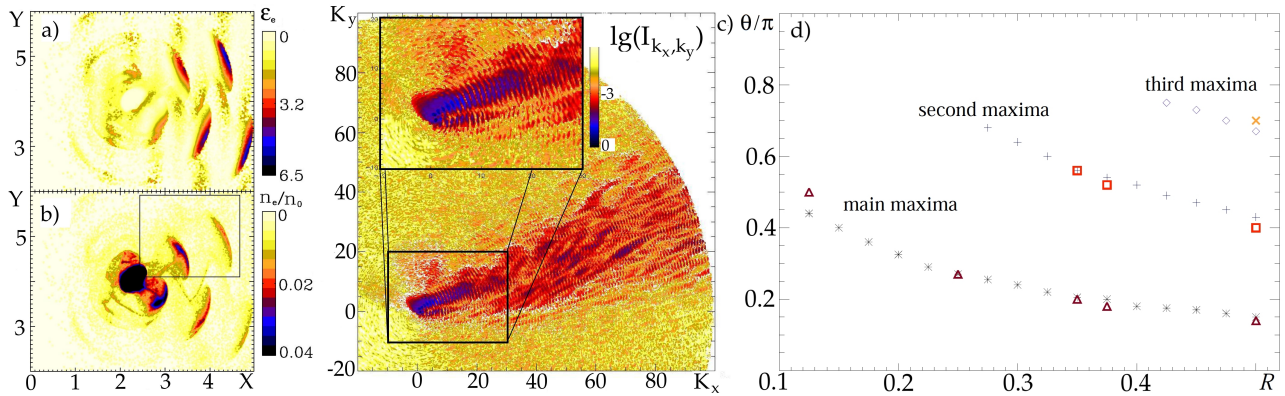
Figure 1.4: *Helium droplet in intense laser fields* – Kinetic electron energy in MeV (a) and density (b) contour plots of the He droplet in a laser pulse of intensity $I_{\mathrm{L}} = 8 \times 10^{18}$ W/cm^2. In the bunch ejected around the pulse maximum, the maximum electron energy is ~ 6 MeV. (c) - Spectral distribution of the radiation, emitted by the two bunches in the black rectangle in frame (b). (d) - Angles of the electron emission vs droplet radius R: PIC simulations (colored symbols) and Mie results. Lengths are normalized to λ_{L}. Frames (a) and (b) are adapted from [160].

tially neutral, wavelength-sized spherical He-droplet may generate a charge density distribution that neither is homogeneous throughout the droplet nor created only within a thin skin layer at the surface. The time-dependent field and density distributions inside the droplet are not accessible to standard Mie theory and fall into the realm of extreme nonlinear optics. At higher laser intensities a qualitatively similar ionization dynamics is expected for higher-$\mathcal{Z}$ materials. The resulting inhomogeneous charge distribution may be probed via scattering of short-wavelength radiation [161].

1.5   Dynamics of charged particles and radiation in laser-plasma interactions at ultrahigh intensities: collective effects

Within the immense research field of the interaction of extreme fields with plasma, elementary particles and even with vacuum [2, 162, 163], a new area of classical and quantum dynamics in the radiation-dominated regime has recently emerged. Here we refer to the radiation-dominated regime whenever radiation of photons by accelerated elementary particles significantly affects the individual dynamics of these particles, as well as the collective dynamics of the plasma [164, and references therein]. Apparently, the distortion of the particles' dynamics influences the process of radiation itself, making the whole problem self-consistent and, due to the extreme intensities of the applied laser fields highly nonlinear and even nonperturbative. Until recently, the theoretical studies of elementary particles and plasma strongly coupled to their radiation were remote from possible experimental verification of the related effects and remained on the level of academic interest. With the new generation of laser sources expected to come into operation in the nearest years [3, 4, 5, 6, 7] or in the foreseeable future [165, 166, 167, 168], this research became of topical interest and already resulted in a number of new fundamental findings. Below we briefly mention the reasons, justifying a constantly growing interest in effects of radiation friction (RF)[15] in the interaction of ultra-intense laser fields with matter.

Firstly, the influence of RF on the dynamics of individual charged particles or plasma becomes more significant as the laser intensity increases. Therefore, a number of laser-plasma phenomena, as well as single-particle effects for ultra relativistic electrons in strong EM fields, have to be revisited taking RF into account. In the last 15 years, this reconsideration has resulted in extensive work on RF effects in nonlinear Thomson- [170] and Compton scattering [171], in Raman spectra [172], in radiative trapping [173], in electron and ion acceleration in vacuum [174], and in X-ray emission from plasma targets [175]. Recent experiments based on Thomson scattering of a superintense laser pulse by a high-energy electron bunch [176, 177, 178] have provided a first (albeit weak) evidence for deviations from classical predictions in the radiation spectrum. In the modeling of the experiments, a so-called "semiclassical" approach based on a modification of the Landau-Lifshitz RF force [179] appeared to provide a better agreement than a "quantum" approach where the emission of radiation is described stochastically. This finding has been explained by the possible breakdown of approximations underlying the quantum model, as also suggested by a different experiment [180], and attempts are being pursued to overcome the approximations in the quantum model [181, 182, 183]. This scenario suggests that identifying different RF signatures and test their sensitivity to the onset of quantum effects is important in order to improve the theoretical and numerical modeling.

Second, at present the understanding of RF is far from being complete, because some principal questions of the theory of this phenomenon are still not answered. Even within the classical treatment, several not exactly equivalent expressions for the RF force are discussed [184]. The situation becomes even more complicated for very energetic particles and very high field strengths when classical electrodynamics do not apply. One has to admit that presently, a comprehensive QED theory of RF does not exist.

Finally, there are qualitative effects whose very existence results from the RF force. Such phenomena, if observed experimentally, can provide an unambiguous proof of the crucial role RF plays at high intensities of laser fields and high energies of plasma electrons. In a recent paper [185], it has been

---

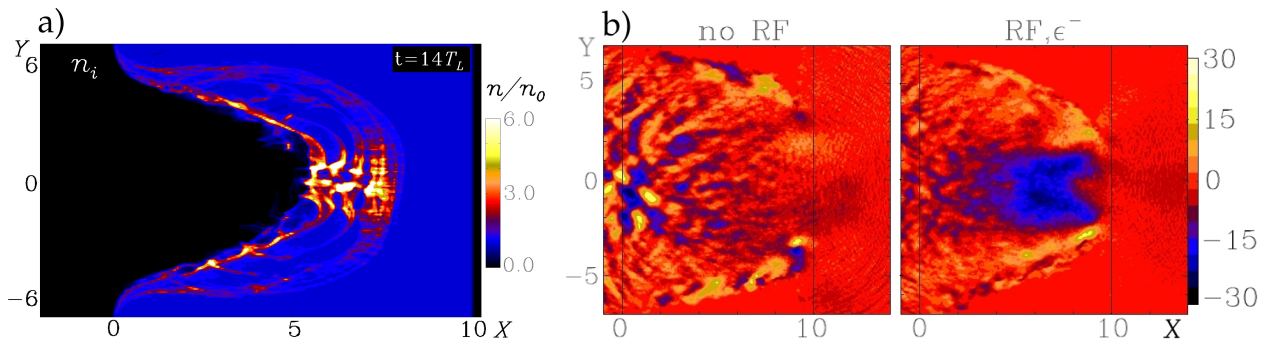[15]RF arises from the back-action on the accelerated electron of the EM field generated by the electron itself [169].

Figure 1.5: *Inverse Faraday effect driven by radiation friction* – (a) The distribution of ion density at $t = 14 \times 2\pi/\omega_{\mathrm{L}} \simeq 37$ fs and (b) axial magnetic field B_x (normalized to $B_0 = 1.34 \times 10^8$ Gauss) at $t = 32 \times 2\pi/\omega_{\mathrm{L}} \simeq 100$ fs after the beginning of the interaction (left: without RF, right: with RF included). The distributions are shown in the (x, y) plane, very similar patterns are observed in the (x, z) plane. The CP laser pulse of $I_{\mathrm{L}} = 7.6 \times 10^{23}$ W/cm^2 ($a_0 = 600$) is incident along the x-axis from the left side on the target with density $n_e = 1.55 \times 10^{23}$ cm^{-3}. The thin black lines denote the boundaries of the target. The coordinates are normalized to λ_{L}. Picture on frame b) is adapted from [185].

shown that RF induces a specific form of the inverse Faraday effect (IFE), i.e., the generation of magnetic fields due to absorption of EM angular momentum into a plasma. From a classical viewpoint, in the presence of dissipative effects, the EM angular momentum carried by a circularly polarized laser pulse is transferred to the plasma electrons, which acquire a torque and produce an azimuthal current and an axial magnetic field. From a quantum viewpoint, the RF-induced absorption of angular momentum is due to the annihilation of $N \gg 1$ polarized laser photons needed to generate a single high-energy photon so that an angular momentum amount equal to $(N - 1)\hbar \simeq N\hbar$ ($\hbar$ being the photon spin independent of the photon energy) is transferred to the orbital motion of electrons. In a regime of interaction with high-density plasmas, the conversion efficiency of laser energy into incoherent radiation may be a few ten percent, which results in axial quasistatic magnetic fields up to gigagauss values at intensities $\simeq 10^{24}$ W/cm^2, as observed in 3D PIC simulations with classical RF included [185], see. Fig.1.5. Such huge magnetic fields, besides affecting the plasma dynamics, provide an unambigous signature of RF effects and may be measured by polarimetry methods.
Based on the equations of macroscopic electrodynamics and conservation laws, a description of IFE in the field of an intense laser pulse [185] predicts the maximal amplitude of the quasistatic longitudinal magnetic field excited on the axis of a laser beam to be linear with respect to the laser magnetic field amplitude B_{L} and to the fraction of the laser energy η associated with the irreversible transfer of angular momentum from the laser field to the plasma:

$$B_{xm} = C\eta a_0 B_0 \equiv C\eta B_{\mathrm{L}}. \tag{1.6}$$

Here

$$a_0 = \frac{E_0}{B_0}, \qquad B_0 = \frac{mc\omega_{\mathrm{L}}}{e} = 1.34 \times 10^8 \text{ G} \tag{1.7}$$

are the dimensionless laser field amplitude and the characteristic magnetic filed, respectively. The dimensionless coefficient C is determined by the shape of the laser pulse envelope and has typical values $C \simeq 0.1 \div 0.2$. The structure of Eq. (1.6) is consistent with the general theory of IFE [186, 187]. The absorption coefficient η reads

$$\eta = \frac{\omega_{\mathrm{L}} L_{\mathrm{abs}}}{U_{\mathrm{L}}}, \tag{1.8}$$

where L_{abs} is the angular momentum absorbed by the plasma and $U_{\mathrm{L}} = A\lambda_{\mathrm{L}}^3 a_0^2 B_0^2$ is the energy stored in the laser pulse. The dimensionless coefficient A is determined by the pulse duration, time envelope and focusing. Equations (1.6)–(1.8) are insensitive to a particular physical mechanism of the angular momentum transfer. In particular, Eq. (1.6) applies independently of the impact of quantum effects on the plasma dynamics. In the high-field regime, radiation by plasma electrons is the only mechanism for energy absorption, thus $\omega_{\mathrm{L}} L_{\mathrm{abs}} = U_{\mathrm{rad}}$ where U_{rad} is the radiation energy emitted by the electrons, and Eq.(1.8) reads

$$\eta \equiv \eta_{\mathrm{rad}} = \frac{U_{\mathrm{rad}}}{U_{\mathrm{L}}} \equiv \frac{\int d^3r \int dt P_{\mathrm{rad}}(\mathbf{r}, t) n_e(\mathbf{r}, t)}{U_{\mathrm{L}}} \leq 1. \tag{1.9}$$

Here, P_{rad} is the emission power for a single electron moving under the action of the local EM field with a given time- and space-dependent envelope, and n_e is the electron density. The *conversion efficiency* η_{rad} is the key value for the determination of magnetic field amplitude.

In [185], the scaling of η_{rad} with the laser intensity agreed reasonably with the results of 3D PIC simulations of the laser-plasma interaction, up to intensities approaching 7×10^{23} W/cm^2. Beyond this limit, the model predicts values of $\eta_{\mathrm{rad}} > 1$ because neither the modification of the radiating electron trajectories due to RF nor the depletion of the laser pulse is taken into account. In addition, at those intensities the classical description becomes questionable and quantum effects are expected to become relevant.

The further development of the classical model for the calculation of radiation losses [188] included a self-consistent picture of the IFE, accounting for RF effects on the electron motion via the Zeldovich model [189], for the plasma motion driven by radiation pressure in the hole boring regime, and for an inhomogeneous distribution of the laser intensity. This improved model predicts values of η_{rad} in good agreement with the PIC simulations and it is found to be robust with respect to assumptions on the particular shape of electron and ion density distributions in the radiating layer despite of its analytic simplicity. The effect of the RF force, in combination with the global HB motion of the plasma and of the laser field in space and time resulted in a slower increase of the conversion efficiency with the laser intensity, compared to predictions made in [185], so that ultimately it appears to be on the level of $\eta_{\mathrm{rad}} \simeq 0.2$ for $I_{\mathrm{L}} = 10^{24}$ W/cm^2, leading to an upper limit $B_{\mathrm{xm}} \approx 3.2 \times 10^9$ G at such intensities.

The significant relative suppression of the radiation losses leads to a specific freezing of the electron lateral motion for $a_0 > a_{\mathrm{cr}} = (4\pi r_c/3\lambda_{\mathrm{L}})^{-1/3}$ so that the relativistic γ factor grows much slower $\gamma \sim a_0^{1/4}$ than in the perturbative domain, where the RF force is negligible. Here, $r_c \equiv e^2/mc^2 \simeq 2.8 \times 10^{-9}$ μm is the classical electron radius. This in turn shifts the border between the classical and the quantum regime of interaction to considerably higher intensities. The significance of QED effects is determined by the value of the relativistically invariant quantum parameter

$$\chi = \frac{e\hbar}{m^3 c^4} \sqrt{(-(F_{\mu\nu} p^\nu)^2)} = \frac{E_{\mathrm{L}}'}{E_S}, \tag{1.10}$$

which equals the ratio of the external (laser) electric field in the electron rest frame E_{L}' to the critical field of quantum electrodynamics, $E_S = m^2 c^3/e\hbar$. Here, $F_{\mu\nu}$ is the EM field tensor and p^ν is the four-momentum vector. The asymptotic value[16] of χ is found to be [188]

$$\chi_{a_0 \to \infty} \simeq \frac{3}{2\alpha} \left(\frac{a_0 \xi^2}{2\sqrt{\mu}} \right)^{1/4},$$

---

[16]in the strong field limit $a_0 \to \infty$, when the hole-boring velocity approaches the speed of light

where $\mu = \mathcal{Z}n_{cr}m_e/\mathcal{A}n_e m_p$, $\xi = 4\pi r_c/3\lambda_{\mathrm{L}} = a_{cr}^{-3}$ and $\alpha = e^2/\hbar c = 1/137$ is the fine-structure constant. In the weak field regime, $a_0 \ll a_{cr}$, a quantum parameters χ turns to be equal to

$$\chi = \frac{3}{2\alpha}\xi a_0^2.$$

In the range of $a_0 \in [200, 800]$, corresponding to the range of intensities $I_{\mathrm{L}} \in [1.7, 27] \times 10^{23}\,\mathrm{W/cm}^2$, and for the parameters of the simulations performed in [185, 188] ($\lambda_{\mathrm{L}} = 800$ nm, $n_e = 90 n_{cr}$, $\mathcal{A}/\mathcal{Z} = 2$) the value of χ increases from 0.092 to 0.436, and even for an "extreme" amplitude of $a_0 = 2000$ the value $\chi \simeq 0.636$ is obtained. This shows that the onset of a full radiation-dominated regime is prevented and a classical description of the dynamics and radiation of electrons is applicable, at least on a qualitative level. This prediction may be tested by simulations with QED effects included.

1.6   Particle-in-Cell simulations

The complexity of the laser-plasma interaction related to the high dimensionality of the problem, to the disparity of the involved scales, to the lack of symmetry and to the importance of nonlinear and kinetic effects prevent analytical methods from providing a detailed description of the phenomena that take place in one or another interaction setup. The unfolding of rich and complex dynamics of such an interaction, involving collective and self-organization effects, requires therefore the use of self-consistent numerical simulations. The interaction of intense and super-intense coherent radiation with plasmas poses some of the most challenging problems for numerical physics. This is because the most important and interesting phenomena are multiscale and cannot be described hydrodynamically. The first feature imposes the use of very large numerical grids since the spatial size and/or evolution time of the system are much larger than the smallest spatial and temporal scales to be resolved[17]. The second one implies that a hydrodynamic description in real space must be abandoned and much more demanding kinetic equations in phase space have to be solved. To this end, the PIC method [12, 13] is by far the most commonly used approach because it allows a great saving of memory in allocating the momentum space with respect to a purely Eulerian approach. However, even with a PIC method a *realistic* simulation would require a three-dimensional spatial grid with thousands of grid-points in each spatial direction, resulting in a total number of grid-points exceeding some tens of billions. Moreover, thousands of particles per cell may be needed to properly resolve high energy tails in the distribution [190] as well as sharp density gradients, which always occur in intense laser-plasma interactions. Thus, the progress in this area is directly related to the possibility to access larger high performance computer resources. Nowadays, large-scale multidimensional PIC simulations running on parallel supercomputers are an effective support for the design and interpretation of laser-plasma acceleration experiments, although fully realistic simulations in three spatial dimensions and for experimentally achievable laser pulse and target parameters are most of the time still beyond computational capabilities [49, 191].

The PIC approach is a means to solve the Vlasov-Maxwell system of equations

$$\frac{df_i}{dt} = \frac{\partial f_i}{\partial t} + \mathbf{v} \cdot \nabla_{\mathbf{r}} f_i + \frac{q_i}{m_i} \left(\mathbf{E} + \frac{\mathbf{v}}{c} \times \mathbf{B} \right) \cdot \nabla_{\mathbf{p}} f_i = 0, \tag{1.11}$$

$$\frac{1}{c} \frac{\partial \mathbf{B}}{\partial t} = -\nabla \times \mathbf{E}, \qquad \frac{1}{c} \frac{\partial \mathbf{E}}{\partial t} + \frac{4\pi}{c} \mathbf{J} = \nabla \times \mathbf{B}, \tag{1.12}$$

$$\nabla \cdot \mathbf{E} = 4\pi\rho, \qquad \nabla \cdot \mathbf{B} = 0, \tag{1.13}$$

using pseudo particles of the same charge-to-mass ratio as the real particles in the plasma. The distribution function is sampled as

$$\tilde{f}(\mathbf{r}, \mathbf{p}, t) = \sum_{j=1}^{J} R(\mathbf{r}, \mathbf{r}_j(t)) \delta(\mathbf{p} - \mathbf{p}_j) \tag{1.14}$$

so that the charge and current densities can be obtained from

$$\tilde{\rho}(\mathbf{r}, t) = \sum_{j=1}^{J} q_j R(\mathbf{r}, \mathbf{r}_j(t)), \; \tilde{\mathbf{j}}(\mathbf{r}, t) = \sum_{j=1}^{J} q_j \mathbf{v}_j R(\mathbf{r}, \mathbf{r}_j(t)). \tag{1.15}$$

---

[17]In the laser-plasma acceleration setup the smallest scales are the laser and/or plasma wavelength ($\sim 0.1 \div 100\mu$m), and the largest scale is the acceleration distance, which may range from a few centimeters to meters or even kilometers.

The weighting function $R(\mathbf{r}, \mathbf{r}')$ obeys the normalization condition $\int_V R(\mathbf{r}, \mathbf{r}')\mathrm{d}\mathbf{r} = 1$. For symmetric $R(\mathbf{r}, \mathbf{r}') = R(\mathbf{r}', \mathbf{r})$ the trajectories of the pseudo particles

$$\frac{d\mathbf{r}_j}{dt} = \frac{\mathbf{p}}{\gamma m_j}, \ \frac{d\mathbf{p}_j}{dt} = q_j \left(\mathbf{E} + \frac{\mathbf{v}}{c} \times \mathbf{B}\right), \tag{1.16}$$

coincide with the characteristics of the Vlasov equation. The electric and magnetic fields in a PIC code are calculated on a numerical grid. For propagation, each time-step the current-density on the grid and the field values at the particle positions need to be calculated through a position-to-grid mapping procedure.

The number of pseudo particles in a "numerical plasma" is usually significantly smaller than the number of particles in a real plasma. Therefore, it is important to bear in mind that the characteristic properties of these two plasmas can also be very different. Let a value $\alpha = n/n' \gg 1$ be the ratio of real and model plasma densities. Hereinafter, the symbol $'$ indicates the values of the model plasma. From the conservation of total charge and mass it follows that $q' = \alpha q, m' = \alpha m$, where m, q and m', q' are the masses and charges of individual particles in real and model plasma, respectively. In this case, the particle dynamics indeed does not change, $q'/m' = q/m$. The electron and ion plasma frequencies are also conserved $\omega'_\mathrm{p} = \sqrt{4\pi q' n'^2/m'} = \omega_\mathrm{p}$. If we assume that the Debye length is invariant [13] $\Lambda'_D = \sqrt{T'_e/4\pi e'^2 n'_e} = \Lambda_D$ then the model and real plasma temperatures will be different $T' = \alpha T$ though the thermal velocities remain the same $v'_T = \sqrt{T'/m'} = v_T$. Finally, for the mean interparticle distance, mean free path, number of particle in the Debye sphere and the collisional frequency of the model plasma we have $\langle r' \rangle = n'^{-1/3} = \alpha^{1/3} \langle r \rangle, \ \langle r'_{col} \rangle = \langle r_{col} \rangle / \alpha, \ N' = n' \Lambda'_D = N/\alpha, \ \nu' = \alpha\nu$. Since $\alpha \gg 1$, the collisional frequency in the numerical plasma can be significantly bigger and the mean free path, in turn, significantly smaller then the corresponding values in a real plasma. This brings the model plasma closer a state where the particle collisions should be rather taken into account. Fortunately, in many simulation setups the inequality $\langle r'_{col} \rangle \gg L'$, where L' is the characteristic spatial scale of the model plasma, still can hold, and a collisionless simulation is possible.

Most of the numerical studies discussed in this Thesis were performed with the Supercomputers at the John von Neumann Institute for Computing (NIC, Jülich, Germany) and at the CINECA Supercomputer facility (Bologna, Italy) using the fully electromagnetic PIC code UMKA originated from the study reported in [20]. UMKA employs state of the art, widely used numerical algorithms such as an Yee Cartesian lattice for EM fields, the time-reversible, semi-implicit Boris pusher to integrate the Lorentz force and the current reconstruction scheme [192] to satisfy the continuity equation. In the following we briefly present the peculiarities of the state of the art version of this code.

Ionization dynamics – The "standard" PIC codes start with a preformed plasma of a certain density profile and temperature, which means that ionization both by the electric field and by collisions is neglected. This approach is adequate for relativistic laser-field intensities and relatively light target material so that it turns into a dilute plasma with a well defined ionization degree within a fraction of the laser-pulse period. In a more general situation the charge state and density distributions are expected to be sensitive to the ionization dynamics and have to be calculated self-consistently. Moreover, in targets that turn overdense in the course of ionization the skin-effect prevents the laser from penetrating further so that a complicated space and time-dependent charge distribution develops [160, 193]. Such interactions of laser pulses with rapidly self-generated plasmas have already found

applications, e.g., as "plasma mirrors", which are routinely used to increase the pulse contrast for intense laser-matter experiments [194]. Note that molecular dynamics is a powerful tool that is widely used to describe the ionization dynamics in small laser-driven targets, e.g., clusters [195]. However, for wavelength-sized or bigger targets the influence of the target on the propagation of the incident EM wave needs to be taken into account self-consistently. This requires the solution of Maxwell's equations together with the equations of motion for the charged particles. In the case of weakly coupled plasmas, the problem can be reduced to the solution of the Vlasov-Maxwell system of equations, which is efficiently achieved using PIC codes.

In the UMKA code, the ionization of an ion with charge state $\mathcal{Z} - 1$ and ionization potential I due to the electric field E is implemented using the tunneling ionization rate formula [196]

$$w(E) = \left(\frac{2E_{ch}}{|E|} \right)^{2n^*} \frac{k^2 \hbar}{m} \frac{|E|}{E_{ch}} \exp \left(-\frac{2E_{ch}}{3|E|} \right) \tag{1.17}$$

with $k = \frac{\sqrt{2mI}}{\hbar}$, $E_{ch} = \frac{\hbar^2 k^3}{me}$, $n^* = \mathcal{Z}\sqrt{\frac{I_H}{I}}$. Here, m is the electron mass and I_H is the ionization potential of atomic hydrogen. The ionization probability for the ith ion during time τ is then calculated[18] from $P_i = \tau w(E)$. When an ionization event takes place a free electron at rest is created at the position of the ion. The energy needed for ionization is taken out of the field via an "ionization current" $\mathbf{j}_{\text{ion}}$ parallel to the electric field at the ion location. The value of $\mathbf{j}_{\text{ion}}$ is such that $\mathbf{j}_{\text{ion}} \cdot \mathbf{E}$ is the work spent on ionization per time step [198]. Energy conservation is accounted for during the whole process; if the remaining field energy in a cell is insufficient for further ionization, this cell is not considered anymore during the current time step [199].

In order to address the process of impact ionization, we use tabulated data of impact ionization cross-sections $\sigma_i(v_e)$ [200]. The total collision ionization frequency of an electron with velocity v_e is then calculated from $\nu_{\text{tot}}(v_e) = v_e \sum_{i=0}^{\mathcal{Z}-1} \sigma_i(v_e) n_i$, and the total collisional ionization probability is $P_e = \tau \nu_{\text{tot}}$. When an ionization event takes place, the charge state of the ion under consideration is changed, and a free electron is created at rest at the position of the ion. The value of the impacting electron's velocity is reduced in order to ensure energy conservation. Numerically, we use the Monte-Carlo null collision method [201] for the treatment of electron impact ionization. Excited electronic states are not considered, neither are recombination processes. Self-consistency requires that collisional absorption is taken into account along with the collisional ionization, as in the PIC codes described in Refs. [17, 18, 202]. A microscopic PIC code [19, 203] bridges the gap between PIC and molecular dynamics and is also capable of incorporating collisional ionization and collisional absorption, albeit so far only for small targets.

Classical radiation friction – At optical laser intensities exceeding $I_{\text{L}} \sim 10^{23}$ W/cm^2, the plasma electrons become ultrarelativistic within a fraction of the laser wave period. They experience a very strong acceleration and emit relatively large amounts of EM radiation, rendering radiation friction effects [169] more important as the laser intensity increases. First PIC simulation that included RF [204] on the level of the Lorentz–Abraham–Dirac (LAD) equation with the RF force that is exact for a point particle [205], showed that RF effects become important at intensities exceeding 5×10^{22} W/cm^2, and are thus expected to play a crucial role in experiments soon. It is therefore

---

[18]This method has the drawback of restricting the time step to very small values in order to properly describe the field ionization in sufficiently strong fields. A multiple ionization scheme proposed in [197] may help to relax this constraint.

important to incorporate RF in PIC simulations of laser-plasma by an appropriate modeling, taking the essential RF effects into account while retaining at the same time the capability to perform large-scale simulations. In order to do so one should solve the LAD equation. This equation, however, suffers from inconsistencies such as the existence of the so-called "runaway" solutions, in which the electron momentum grows exponentially in the absence of external fields. In the realm of classical electrodynamics, i.e., neglecting quantum effects, the LAD equation

$$mc\frac{du^\mu}{d\tau} = eF^{\mu\nu}u_\nu - e\tau_0\left(\frac{d^2u^\mu}{d\tau^2} + u^\mu u^\nu \frac{d^2u_\nu}{d\tau^2}\right), \tau_0 = 2e^2/(3mc^3) \tag{1.18}$$

can be consistently approximated by the Landau–Lifshitz (LL) equation

$$mc\frac{du^\mu}{d\tau} = eF^{\mu\nu}u_\nu + e\tau_0\left[u_\nu u^\alpha \partial_\alpha F^{\mu\nu} + \frac{e}{mc}F^{\mu\nu}F_{\nu\alpha}u^\alpha + \frac{e}{mc}\left(F^{\nu\beta}u_\beta F_{\nu\alpha}u^\alpha\right)u^\mu\right],$$

which is obtained by inserting the unperturbed Lorentz acceleration in Eq. (1.18) [206]. This removes the third order derivative of the position and thus runaway solutions, and gives a more conventional phase space description. In 3D notation, the above equation reads

$$\frac{d\mathbf{p}}{dt} = e\left(\mathbf{E} + \frac{\mathbf{v}}{c}\times\mathbf{B}\right) + e\tau_0\gamma\left[\left(\frac{\partial}{\partial t} + \mathbf{v}\cdot\nabla\right)\mathbf{E} + \frac{\mathbf{v}}{c}\times\left(\frac{\partial}{\partial t} + \mathbf{v}\cdot\nabla\right)\mathbf{B}\right]$$
$$+ \tau_0\frac{e^2}{mc}\left\{\left[\left(\mathbf{E} + \frac{\mathbf{v}}{c}\times\mathbf{B}\right)\times\mathbf{B} + \left(\frac{\mathbf{v}}{c}\cdot\mathbf{E}\right)\mathbf{E}\right] - \gamma^2\left[\left(\mathbf{E} + \frac{\mathbf{v}}{c}\times\mathbf{B}\right)^2 - \left(\frac{\mathbf{v}}{c}\cdot\mathbf{E}\right)^2\right]\frac{\mathbf{v}}{c}\right\}.$$

As long as a classical description is adequate, RF effects are relevant, and quantum effects are subdominant, the expression for the RF force given in textbooks [206] can be safely used,

$$\mathbf{F}_{\text{RF}} \simeq -\frac{2}{3}r_c^2\left[\gamma^2\left(\mathbf{F}_{\text{L}}^2 - \left(\frac{\mathbf{v}}{c}\cdot\mathbf{E}\right)^2\right)\frac{\mathbf{v}}{c} - \mathbf{F}_{\text{L}}\times\mathbf{B} - \left(\frac{\mathbf{v}}{c}\cdot\mathbf{E}\right)\mathbf{E}\right]. \tag{1.19}$$

Here, $\mathbf{F}_{\text{L}} = \mathbf{E} + \frac{\mathbf{v}}{c}\times\mathbf{B}$, and the small terms containing the temporal derivatives of the fields are dropped .

To account self-consistently for the effect of radiation emission on the *electron dynamics* we implemented in UMKA the radiation reaction via the LL approach, using a numerical scheme [208] based on the assumption that the acceleration of particles is dominated by the Lorentz force, with the RF force giving a smaller, albeit non-negligible contribution[19]. The numerical implementation [208, 209] allows the addition of RF effects to any PIC code, which uses the standard Boris pusher algorithm for the acceleration of the particles, at a small computational cost. We emphasize that the inclusion of the radiation loss as a dissipative process via the RF force requires the following assumptions: (i) the dominant frequencies in the escaping radiation are much higher than the highest frequency that can be resolved on the numerical grid, (ii) the radiation at such frequencies is incoherent, (iii) the plasma is transparent to such frequencies [185, 208].

The above presented approach discards the effect of quantum recoil on the spectrum of emitted radiation. One one hand, the quantum parameter χ, Eq. (1.10), remains smaller than unity up to intensities $\sim 10^{25}$ W/cm^2, making a classical description of dynamics and radiation of electrons applicable at

---

[19]For a benchmark with other approaches see [207] M. Vranic, J. L. Martins, R. A. Fonseca, L. O. Silva, *Classical Radiation Reaction in Particle-In-Cell Simulations*, Computer Physics Communications 204, 141-151 (2016).

least on a qualitative level. On the other hand, the spectrum of emitted photons appears considerably modified by quantum effects already for $\chi \approx 0.1$ [210, 211]. For the targets with $n_e \sim 100 n_{\mathrm{cr}}$ this is achieved for $I_{\mathrm{L}} \simeq 1.9 \times 10^{23}$ W/cm^2 so that quantum corrections to the radiated power may become numerically important. To account for the suppression of the radiation power due to the off-set in the emission spectrum we introduce[20] the quantum factor $g(\chi)$. To that end we have further modified our code by incorporating the parameter χ in the expression for the radiation friction force $\tilde{\mathbf{F}}_{\mathrm{RF}} = g(\chi)\mathbf{F}_{\mathrm{RF}}$. The quantum parameter χ is calculated at each time step by taking the values of electric and magnetic fields at the position of each electron.

Finally, the PIC code UMKA allows simulations in 1D, 2D and 3D Cartesian geometries. The simulation grid is rectangular, and the grid spacings $\Delta x, \Delta y, \Delta z$ may be different. It is possible to choose between periodic and open boundary conditions. UMKA allows to perform simulations with a "moving window", which may be useful in several cases (laser wakefield acceleration, RPA acceleration by long laser pulses). The implementation of complex target geometries, as well as complex target compositions having different ion species with a given $\mathcal{A}/\mathcal{Z}$ ratios, is sraightforward. For a non-standard initial geometry, such as foam-targets used in [213], it is possible to load an external file, containing the coordinates and radii of a collection of spheres.

The locality of the PIC methods allows for an efficient parallelization obtained via a domain decomposition technique. In the UMKA code, parallelization is implemented by a decomposition in the (y, z)-discretized coordinates, perpendicular to the propagation of the laser pulse in x direction. This choice provides an initially balanced partition of the particles for problems where the particle density is initially uniform in the (y, z)-plane. A dynamical load-balancing keeps the data partition balanced as particles move across different domains. The distribution of numerical data among the processing units and the mutual exchanges are handled by MPI routines. No special libraries or packages are needed by the code. Recent simulations performed with UMKA on JURECA (NIC, Jülich) and Marconi (CINECA, Bologna) show a fully parallel performance up to 13600 cores.

The material presented below in this work is organized as follows. In Chapter 2, the papers discussing the analytical and simulation work on both the hole-boring (HB) and light sail (LS) regimes of radiation-pressure-dominant acceleration of ions by circularly polarized laser pulses are collected. These include a parametric study of the optimal target thickness in the LS case, evaluation of pre-plasma effects, investigation of the absorption of the angular momentum of the laser pulse by dense plasma. Papers devoted to the study of collisionless absorption of the laser radiation and generation of hot electrons are presented in Chapter 3. The contributions to the research of the radiation friction effects that emerge in the interaction of super intense laser radiation with plasma are collected in Chapter 4. These include a comprehensive presentation of an approach to a kinetic description of laser-plasma interaction with radiation reaction effects being included via the Landau-Lifshitz force, a detailed study of polarization and radiation reaction effects in the radiation pressure dominated acceleration regime and a proposal to an alternative approach to investigate radiation friction in the laboratory, namely to search for the regimes where collective effects in the laser-plasma interaction boost radiation friction losses and the radiation friction signatures become strong and unambiguous. In Chapter 5, the results of the study of the interplay between ionization, pulse propagation and particle acceleration in intense laser-droplet interaction are shown. In Chapter 6, the papers are included that arose from the collaboration with the experimental team of the Queen's University of Belfast (UK).

---

[20]General formulas for the quantum factor $g(\chi)$ can be found in the literature [210]. For practical calculations we use a fit [212] $g(\chi) = (1 + 12\chi + 31\chi^2 + 3.7\chi^3)^{-4/9}$.

Author contribution statement

RADIATION PRESSURE ACCELERATION OF IONS

1 <u>T. V. Liseikina</u> and A. Macchi
Features of ion acceleration by circularly polarized laser pulses
Appl. Phys. Lett. **91**, 171502 (2007)
T. V. L. contributed to the design and implementation of the research, designed the model and computational framework, performed the numerical calculations, contributed to the analysis of the results and to the writing of the manuscript.

2 A. Macchi, A. Bigongiari, F. Ceccherini, F. Cornolti, <u>T. V. Liseikina</u>, M. Borghesi, S. Kar and L. Romagnani
Ion dynamics and coherent structure formation following laser pulse self-channeling
Plasma Phys. Contr. Fusion , **49**, B71 (2007)
T. V. L. contributed to the design and implementation of the theoretical part of research, designed the numerical model and computational framework, performed the numerical calculations, contributed to the analysis of the results and to the writing of the manuscript.

3 <u>T. V. Liseikina</u>, D. Prellino, F. Cornolti, A. Macchi
Ponderomotive Acceleration of Ions: Circular Versus Linear Polarization
IEEE Transaction of Plasma Science **36**, 1866-1871 (2008)
T. V. L. contributed to the design and implementation of the research, designed the model and computational framework, performed 2D numerical calculations, contributed to the analysis of the results and to the writing of the manuscript.

4 <u>T. V. Liseykina</u>, M. Borghesi, A. Macchi, S. Tuveri
Radiation pressure acceleration by ultraintense laser pulses
Plasma Phys. Contr. Fusion , **50**, 124033 (2008)
T. V. L. contributed to the design and implementation of the research, designed the model and computational framework, performed 2D and 3D numerical simulations, contributed to the analysis of the results and to the writing of the manuscript.

5 A. Macchi, <u>T. V. Liseikina</u>, S. Tuveri, S. Veghini
Theory and simulation of ion acceleration with circularly polarized laser pulses
C. R. Physique **10**, 207–215 (2009)
T. V. L. contributed to the design and implementation of the research, designed the model and computational framework, performed 3D numerical simulations, contributed to the analysis of the results and to the writing of the manuscript.

6 A. Macchi, S. Veghini, T. V. Liseykina, F. Pegoraro
Radiation pressure acceleration of ultrathin foils
New J. Phys. , **12**, 045013 (2010)
T. V. L. contributed to the design and implementation of the research, designed the model and computational framework, contributed to the analysis of the results and to the writing of the manuscript.

7 M. Tamburini, A. Di Piazza, T. V. Liseykina, C. H. Keitel
Plasma-based generation and control of a single few-cycle high-energy ultrahigh-intensity laser Pulse
Phys. Rev. Lett. , **113**, 025005 (2014)
T. V. L. designed the numerical model and computational framework for the 2D simulations, contributed to the analysis of the results and to the writing of the manuscript.

- HOT ELECTRON GENERATION

8 P. Mulser, S.M. Weng, T. Liseykina
Analysis of the Brunel model and resulting hot electron spectra
Phys. Plasmas , **19**, 043301 (2012)
T. V. L. designed the numerical model and computational framework for the PIC simulations, contributed to the analysis of the results and to the writing of the manuscript.

9 T. Liseykina, P. Mulser, M. Murakami
Collisionless absorption, hot electron generation, and energy scaling in intense laser-target interaction
Phys. Plasmas , **22**, 033302 (2015)
T. V. L. contributed to the design and implementation of the research, designed the numerical model and computational framework, performed numerical simulations, contributed to the analysis of the results and to the writing of the manuscript.

- RADIATION FRICTION EFFECT IN LASER-PLASMA INTERACTIONS

10 M. Tamburini, F. Pegoraro, A. Di Piazza, C. H. Keitel, T. V. Liseykina, A. Macchi
Radiation reaction effects on electron nonlinear dynamics and ion acceleration in laser–solid interaction
Nuclear Instruments & Methods in Physics ResearchA **653**, 181–185 (2011)
T. V. L. contributed to the design and implementation of the research, designed the numerical model and computational framework for 2D PIC simulations, contributed to the analysis of the results and to the writing of the manuscript.

11 M. Tamburini, T. V. Liseykina, F. Pegoraro, A. Macchi
Radiation-pressure-dominant acceleration: Polarization and radiation reaction effects and energy increase in three-dimensional simulations
Phys. Rev. E , **85**, 916407 (2012)
T. V. L. contributed to the design and implementation of the research, designed the numerical

model and computational framework for 2D and 3D PIC simulations, carried out the implementation of the radiation friction force in the 3D PIC code, contributed to the analysis of the results and to the writing of the manuscript.

12 T. Liseykina, S. Popruzhenko, A. Macchi
    Inverse Faraday effect driven by radiation friction
    New J. Phys. , **18** 072001 (2016)
    T. V. L. contributed to the design and implementation of the research, designed the model and computational framework, performed the numerical calculations, contributed to the analytical calculations, to the analysis of the results and to the writing of the manuscript.

13 S. Popruzhenko, T. Liseykina, A. Macchi
    Efficiency of radiation friction losses in laser-driven "hole boring" of dense targets
    New J. Phys. , **21**, 033009 (2019)
    T. V. L. contributed to the design and implementation of the research, designed the model and computational framework, performed the numerical calculations, contributed to the analytical calculations, to the analysis of the results and to the writing of the manuscript.

- HE-DROPLETS IN INTENSE LASER FIELD

14 T.V. Liseykina, S. Pirner, D. Bauer
    Relativistic Attosecond Electron Bunches from Laser-Illuminated Droplets
    Phys. Rev. Lett. , **104**, 092002 (2010)
    T. V. L. contributed to the design and implementation of the research, designed the model and computational framework for the 3D PIC simulations, performed 3D simulations, contributed to the analysis of the results and to the writing of the manuscript.

15 T.V. Liseykina, D. Bauer
    Plasma-Formation Dynamics in Intense Laser-Droplet Interaction
    Phys. Rev. Lett. , **110**, 145003 (2013)
    T. V. L. contributed to the design and implementation of the research, designed the model and computational framework for the 3D PIC simulations, carried out the implementation of the field ionization in 3D PIC code, performed 3D simulations, contributed to the analysis of the results and to the writing of the manuscript.

16 P. Sperling, T. Liseykina, D. Bauer, R. Redmer
    Time-resolved Thomson scattering on high-intensity laser-produced hot dense helium plasmas
    New J. Phys. , **15**, 025041 (2013)
    T. V. L. design the model and computational framework for the 3D PIC simulations, contributed to the analysis of the results and to the final version the manuscript.

- NUMERICAL SUPPORT TO THE EXPERIMENTAL STUDIES

17 S. Kar, M. Borghesi, C. A. Cecchetti, L. Romagnani, F. Ceccherini, T. V. Liseykina, A. Macchi,
    R. Jung, J. Osterholz, O. Willi, L. A. Gizzi, A. Schiavi, M. Galimberti, & R. Heathcote
    Dynamics of charge-displacement channeling in intense laser-plasma interactions

New J. Phys. , **9**, 402 (2007)
T. V. L. contributed to the modeling (designed the numerical framework and performed the 2D PIC simulations) and interpretation of laser beam self-channeling experimentally observed thanks to the use of laser-driven proton beams as a time and space–resolved probe of electromagnetic fields, contributed to the writing the manuscript.

18 K. Quinn, P. A. Wilson, C. A. Cecchetti, B. Ramakrishna, L. Romagnani, G. Sarri, L. Lancia, J. Fuchs, A. Pipahl, T. Toncian, O. Willi, R. J. Clarke, D. Neely, M. Notley, P. Gallegos, D. C. Carroll, M. N. Quinn, X. H. Yuan, P. McKenna, T. V. Liseykina, A. Macchi, & M. Borghesi
Laser-driven ultrafast field propagation on solid surfaces
Phys. Rev. Lett. , **102**, 194801 (2009)
T. V. L. contributed to the modeling (designed the numerical framework and carried out 2D PIC simulations) of giant current pulses of k-Ampere intensity and picosecond duration, observed after the high-intensity irradiation of metal targets, contributed to the final version of the manuscript.

19 L. Romagnani, A. Bigongiari, S. Kar, S. V. Bulanov, C. A. Cecchetti, T. Zh. Esirkepov, M. Galimberti, R. Jung, T. V. Liseykina, A. Macchi, J. Osterholz, F. Pegoraro, O. Willi, & M. Borghesi
Observation of magnetized soliton remnants in the wake of intense laser pulse propagation through plasmas
Phys. Rev. Lett. , **105**, 175002 (2010)
T. V. L. contributed to the modeling (designed the numerical framework and performed the 2D PIC simulations) and interpretation of coherent electromagnetic structures formation in the wake of an intense laser pulse, which was experimentally observed thanks to the use of laser-driven proton beams as a time and space–resolved probe of electromagnetic fields, contributed to the final version of the manuscript.

20 G. Sarri, A. Macchi, C. A. Cecchetti, S. Kar, T. V. Liseykina, X. H. Yang, M. E. Dieckmann, J. Fuchs, M. Galimberti, L. A. Gizzi, R. Jung, I. Kourakis, J. Osterholz, F. Pegoraro, A. P. L. Robinson, L. Romagnani, O. Willi, & M. Borghesi
Dynamics of self-generated, large amplitude magnetic fields following high-intensity laser matter interaction
Phys. Rev. Lett. , **109**, 205002 (2012)
T. V. L. contributed to the modeling (designed the numerical framework and performed the 2D PIC simulations) and interpretation magnetic field generation experimentally observed thanks to the use of laser-driven proton beams as a time and space–resolved probe of electromagnetic fields, contributed to the writing of the manuscript.

2. Radiation pressure acceleration of ions

The list of publications:

T. V. Liseikina and A. Macchi, *Features of ion acceleration by circularly polarized laser pulses*, Appl. Phys. Lett. **91**, 171502 (2007)

A. Macchi, A. Bigongiari, F. Ceccherini, F. Cornolti, T. V. Liseikina, M. Borghesi, S. Kar and L. Romagnani, *Ion dynamics and coherent structure formation following laser pulse self-channeling*, Plasma Phys. Contr. Fusion **49**, B71 (2007)

T. V. Liseikina, D. Prellino, F. Cornolti, A. Macchi, *Ponderomotive Acceleration of Ions: Circular Versus Linear Polarization*, IEEE Transaction of Plasma Science **36**, 1866-1871 (2008)

T. V. Liseykina, M. Borghesi, A. Macchi, S. Tuveri, *Radiation pressure acceleration by ultraintense laser pulses*, Plasma Phys. Contr. Fusion **50**, 124033 (2008)

A. Macchi, T. V. Liseikina, S. Tuveri, S. Veghini, *Theory and simulation of ion acceleration with circularly polarized laser pulses*, C. R. Physique **10**, 207–215 (2009)

A. Macchi, S. Veghini, T. V. Liseykina, F. Pegoraro, *Radiation pressure acceleration of ultrathin foils*, New J. Phys. **12**, 045013 (2010)

M. Tamburini, A. Di Piazza, T. V. Liseykina, C. H. Keitel, *Plasma-based generation and control of a single few-cycle high-energy ultrahigh-intensity laser Pulse*, Phys. Rev. Lett. **113**, 025005 (2014)

Features of ion acceleration by circularly polarized laser pulses

T. V. Liseikina[a)]
Dipartimento di Fisica "E. Fermi," Università di Pisa, Pisa I-56127, Italy

A. Macchi[b)]
polyLAB, CNR-INFM, and Dipartimento di Fisica "E. Fermi," Università di Pisa, Pisa I-56127, Italy

The characteristics of a MeV ion source driven by superintense, ultrashort laser pulses with circular polarization are studied by means of particle-in-cell simulations. Predicted features include high efficiency, large ion density, low divergence, and the possibility of femtosecond duration. A comparison with the case of linearly polarized pulses is made. © *2007 American Institute of Physics*. [DOI: 10.1063/1.2803318]

The short-duration, multi-MeV ion beams produced in the interaction of high-intensity laser pulses with solid targets have proven to be effective for applications such as proton radiography,[1,2] diagnostic of highly transient electromagnetic fields,[2–4] isochoric heating of matter,[5] isotope production,[6] and nuclear activation.[7] Foreseen future applications to medicine,[8] nuclear fusion[9] or particle physics[10] will require improvements in factors such as the conversion efficiency, peak ion energy, beam monochromaticity, and collimation. Recent experiments performed with these aims[11–13] are based on sheath acceleration (SA) of ions on a surface layer at the rear side of the target.[14] SA is driven by the space-charge field of high-energy "fast" electrons expanding in vacuum. Numerical simulations have also explored different regimes, such as "shock acceleration,"[15] "laser-piston,"[16] "skin-layer ponderomotive acceleration,"[17] or acceleration by circularly polarized laser pulses.[18–20] In these latter studies, as a common feature ion acceleration occurs at the target front side and is in principle dominated by the effect of the radiation pressure of the laser pulse. These regimes based on radiation pressure acceleration (RPA) might be the leading ones at ultrahigh intensities[16] or be most suitable for specific applications.[17]

Here we report a numerical study on ion acceleration with circularly polarized (CP) pulses with the aim to show the peculiar features of the ion source (high efficiency, large ion density, short duration, and good collimation) which may be advantageous for specific applications. A comparison with the case of linearly polarized (LP) pulses is made to evidentiate the differences with CP and to provide a deeper understanding of RPA mechanisms. This is possible because using CP at normal incidence fast electron generation is almost suppressed,[18] thus related effects (such as SA) can be separated by those based on radiation pressure (such as RPA).

We compare two one-dimensional (1D) particle-in-cell (PIC) simulations performed for LP and CP, respectively. Assuming a pulse wavelength $\lambda_L = 1$ μm, the LP and CP simulations have same duration ($\tau_L = 26T_L = 86$ fs, where $T_L = \lambda_L/c$) and intensity $I = 3.5 \times 10^{20}$ W cm^{-2}. To ensure that I is the same, the peak field amplitude in the CP case, $a_L = 11.3$, is lower by a factor of $\sqrt{2}$ than in the LP case

$a_L = 16$. Here, a_L is the dimensionless pulse amplitude given by $a_L = 0.85\sqrt{(I\lambda^2)_{18}/\alpha}$, where $(I\lambda^2)_{18}$ is the irradiance in units of 10^{18} W cm^{-2} and $\alpha = 1$ (2) for LP (CP). The plasma parameters are the same for both simulations (proton plasma slab of 20 μm thickness and electron density $n_e = 10n_c$, where $n_c = 1.1 \times 10^{21}$ cm^{-3} is the cutoff density). The parameters of the LP case are close to those of simulations reported by Silva *et al.*[15] to address "shock" acceleration. The temporal and spatial resolutions are given by $\Delta x = c\Delta t = \lambda_L/400$ and 32 particles per cell are used. The high spatiotemporal resolution is necessary to ensure convergence of the results, since very sharp gradients are generated during the interaction, e.g., at the ion density spiking discussed below and elsewhere.[18,21]

Figure 1 compares the ion density profiles and the phase space of ions and electrons for CP and LP. For LP, strongly relativistic electrons with momenta p_{ex} up to $\simeq 30m_ec$ are generated. The ion phase space shows at least three "groups:" ions accelerated by SA both at the front and the rear side, with momenta p_{ix} up to $\simeq 0.3m_ic$, and ions accelerated at the front surface propagating into the plasma with similar momentum values. For CP, electrons are relatively "cold," since typical momenta are more than one order of magnitude lower than for LP. This is due to the fact that the net force on electrons is small as the ponderomotive force of the laser pulse (whose integral over the target depth gives the total radiation pressure) and the electrostatic force produced by charge separation almost cancel each other.[18] Due to the absence of "fast" electrons, no significant SA ions are ob-
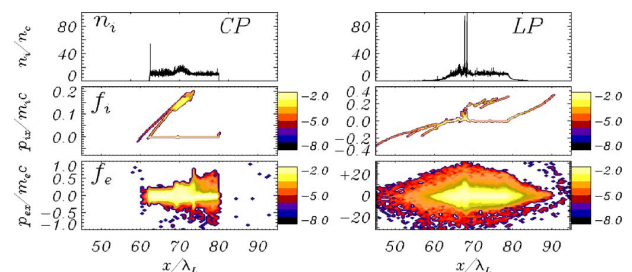

FIG. 1. (Color online) Snaphsots at $t=140T_L=467$ fs of the ion density n_i (top) and the (x,p_x) phase space projections of ions (f_i, middle) and electrons (f_e, bottom) from 1D PIC simulations in the CP (left) and LP (right) cases. The laser pulse propagates from left to right. Length scales are normalized to $\lambda_L=1$ μm, the density to n_c, and momenta to mc. Notice the different scales on the momentum axes between the CP and LP cases.

[a)]On leave from Institute for Computational Technologies, SD-RAS, Novosibirsk, Russia.
[b)]Electronic address: macchi@df.unipi.it

34

171502-2   T. V. Liseikina and A. Macchi   Appl. Phys. Lett. **91**, 171502 (2007)
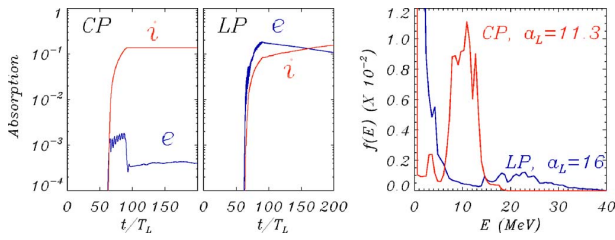
FIG. 2. (Color online) Comparison of absorption efficiency into ions and electrons vs time (left) and of ion energy spectra (right) from 1D PIC simulations of ion acceleration with LP or CP pulses for the same plasma parameters and laser energy and duration.
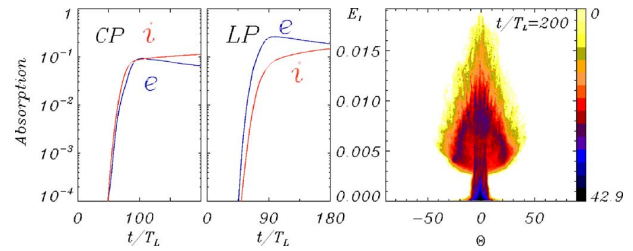

FIG. 3. (Color online) 2D simulation results. Left: comparison between CP and LP of absorption efficiency into ions and electrons vs time. Right: energy vs angle distribution of ions for the CP case. The pulse radius is r_L =2 μm. Other parameters are the same of the 1D runs of Figs. 1 and 2.

served, and most of the accelerated ions are located in a bunch with longitudinal momentum $p_x \simeq 0.15 m_i c$.

Figure 2 compares the absorption efficiency and the ion spectrum obtained in the CP and LP cases, respectively. The absorption into bunch ions is 13.7% for CP and is constant after the laser pulse, confirming that all ions are accelerated by RPA; absorption into electrons is negligible. For LP, absorption into electrons is dominant during the interaction with the laser pulse; later, energy transfer toward ions occurs and the conversion efficiency into ion energy has a value similar to CP, but including all the three ion groups observed in Fig. 1. The ion spectrum for CP is relatively narrow and peaked around 10 MeV, while the LP spectrum is more thermal-like, with a broad maximum around 20 MeV. A series of simulations with parameters in the a_L=1–15 and n_e=5–100 ranges confirm that these features are robust and indicate a scaling of both the peak ion velocity and the absorption efficiency into ions proportional to a_L.[22]

While RPA is the only effective ion acceleration channel in the CP case, for LP its contribution overlaps with SA, and the same analytical model proposed for the CP case[18] may be used if the longitudinal force on ions is considered to be a temporal average. Thus, the forward accelerated ions at the front surface observed for LP may be simply attributed to RPA (rather than to shock acceleration[15]). However, the strong absorption into electrons for LP reduces the total radiation pressure and so the RPA efficiency. An estimate of the relative contributions of SA and RPA is provided by an analysis of particle energy versus position, showing that at the time corresponding to Fig. 1 the energy belonging to ions located within the original plasma slab position (60 μm$<x$ $<$80 μm) is 76% of the total energy for LP (with 10% and 14% being the contributions of ions emitted from the front and rear sides, respectively) and almost 100% for CP.

The reason why the RPA peak in the ion energy spectrum is much more prominent for CP than for LP is attributed to the fact that the ponderomotive force tends to focus the ion spatially at the end of the skin layer, creating a very sharp density peak.[18,21] For LP, the strong electron pressure counteracts the piling up of the ions, leading to "explosion" of the proton bunch and to a broader energy spectrum; the maximum ion energy is higher for LP than for CP, as a few of the RPA ions gain additional energy from the fast electrons. The comparison with the CP simulation shows that in this latter case it is the relatively low electron temperature which allows for a narrow ion energy spectrum.

The comparison of 1D, plane-wave simulations best enlightens the different regimes of ion acceleration between LP and CP and the particular features of RPA versus SA. For a

realistic laser pulse with a finite spot size, the differences between LP and CP are somewhat weakened by the effects of pulse focusing which introduces electric field components normal to the target surface at the edges of the spot, leading to electron heating. Figure 3 shows the effect on fractional absorption in 2D simulations with the same parameters of the 1D case, and a tightly focused pulse with a Gaussian intensity distribution and a spot radius r_L=2λ_L. In the 2D case a_L gives the peak amplitude at the center of the spot. The differences between LP and CP and between ion and electron absorptions in the latter case are less dramatic as expected, but still substantial. The ion energy and the conversion efficiency into ions (11.3%) observed in 2D simulations are close to the values expected from the 1D analysis.

The angular spread of ions depends on their energy E. The $f(E,\Theta)$ distribution of ions in Fig. 3, where Θ is the emission angle with respect to the target normal, shows that the most energetic the ions the most collimated they are: for instance, ions having energy exceeding $0.01 m_i c^2$ are found within a cone with an aperture angle of about 10°. Wider spot sizes or smoother intensity profiles may yield a lower divergence.

The narrow ion energy spectrum of the CP case is a necessary condition to obtain a dense ion bunch with very short duration, in addition to the requirement of a laser pulse with duration of the order of the bunch acceleration time.[18] These particular features of ions accelerated using CP pulses may be useful for ultrafast, localized energy deposition in matter, and are essential for a proposed concept of sources of fusion neutrons with duration of a few femtoseconds.[23]

The production of a single, ultrashort ion bunch can be observed in the simulation of Fig. 4 (for which I=5.5 $\times 10^{18}$ W cm^{-2}, τ_L=33 fs, and r_L=4 μm) where, in addition, a linear density profile was used instead of a steplike one to address the effect of early plasma production by a prepulse in experiments. We observe that ion acceleration initially occurs near the cutoff layer where n_e=n_c and produces at t $\simeq 30 T_L$ a narrow ion bunch with a density larger than $10 n_c$. The divergence of the bunch ions is about 4°.

To our knowledge no laser-plasma interaction experiments investigating RPA with CP have been reported so far. Our results suggests that this regime may lead to high efficiency and large numbers of ions which can be useful for applications requiring fast deposition of energy in matter. At the same time, recent works[19,20] suggest that the acceleration of very thin targets for sufficiently long times using CP pulses may lead to very high ion energies and monoenergetic spectra. Since no unaffordable problem seems to prevent the use of high-intensity CP pulses at normal incidence for laser-
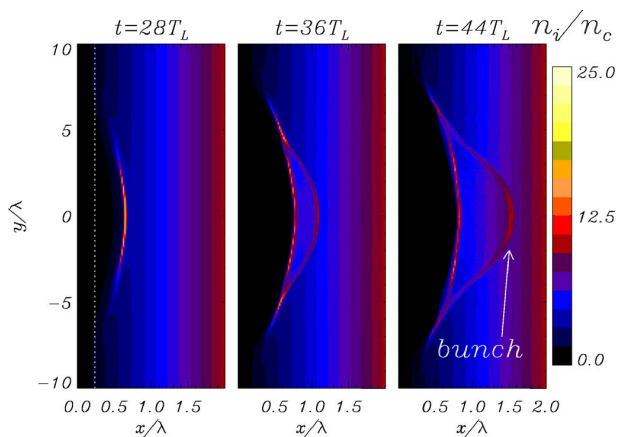
FIG. 4. (Color online) Snapshots of ion density from a 2D, CP simulation for a linear density profile rising from 0 to $10n_c$ over 2λ. Laser pulse parameters are $a_L=2$, $\tau_L=10T_L$, and $r_L=4\lambda$. The white dotted line indicates the initial position of the $n_e=n_c$ surface. The arrow indicates the location of the short ion "bunch" at $t=44T_L$.

plasma interactions, the regime of RPA with CP pulses may be investigated in present-day experiments allowing progress in the use of laser-accelerated ions for specific applications.

[1]J. A. Cobble, R. P. Johnson, T. E. Cowan, N. R.-L. Galloudec, and M. Allen, J. Appl. Phys. **92**, 1775 (2002).

[2]A. J. Mackinnon, P. K. Patel, D. W. Price, D. Hicks, L. Romagnani, and M. Borghesi, Appl. Phys. Lett. **82**, 3188 (2003).

[3]M. Borghesi, L. Romagnani, A. Schiavi, D. H. Campbell, M. G. Haines, O. Willi, A. J. MacKinnon, M. Galimberti, L. Gizzi, R. J. Clarke, and S. Hawkes, Appl. Phys. Lett. **82**, 1529 (2003).

[4]C. K. Li, F. H. Seguin, J. A. Frenje, J. R. Rygg, R. D. Petrasso, R. P. J. Town, P. A. Amendt, S. P. Hatchett, O. L. Landen, A. J. MacKinnon, P. K. Patel, V. A. Smalyuk, T. C. Sangster, and J. P. Knauer, Phys. Rev. Lett.

[continued]
97, 135003 (2006).

[5]P. K. Patel, A. J. MacKinnon, M. H. Key, T. E. Cowan, M. E. Foord, M. Allen, D. F. Price, H. Ruhl, P. T. Springer, and R. Stephens, Phys. Rev. Lett. **91**, 125004 (2003).

[6]K. Nemoto, A. Maksimchuk, S. Banerjee, K. Flippo, G. Mourou, D. Umstadter, and V. Y. Bychenkov, Appl. Phys. Lett. **78**, 595 (2001).

[7]P. McKenna, K. E. D. Ledingham, T. McKanny, R. P. Singhal, I. Spencer, E. L. Clark, F. N. Beg, K. Krushelnick, M. S. Wei, J. Galy, J. Magill, R. J. Clarke, K. L. Lancaster, P. A. Norreys, K. Spohr, and R. Chapman, Appl. Phys. Lett. **83**, 2763 (2003).

[8]V. Malka, S. Fritzler, E. Lefebvre, E. d'Humieres, R. Ferrand, G. Grillon, C. Albaret, S. Meyroneinc, J. P. Chambaret, A. Antonetti, and D. Hulin, Med. Phys. **31**, 1587 (2004).

[9]S. Atzeni, M. Temporal, and J. J. Honrubia, Nucl. Fusion **42**, L1 (2002).

[10]F. Terranova, S. V. Bulanov, J. L. Collier, H. Kiriyama, and F. Pegoraro, Nucl. Instrum. Methods Phys. Res. A **558**, 430 (2006).

[11]B. M. Hegelich, B. J. Albright, J. Cobble, K. Flippo, S. Letring, M. Paffett, H. Ruhl, J. Schreiber, R. K. Schulze, and J. C. Fernandez, Nature (London) **439**, 441 (2006).

[12]H. Schwoerer, S. Pfotenhauer, O. Jaeckel, K. U. Amthor, B. Liesfeld, W. Ziegler, R. Sauerbrey, K. W. D. Ledingham, and T. Esirkepov, Nature (London) **439**, 445 (2006).

[13]T. Toncian, M. Borghesi, J. Fuchs, E. d'Humieres, P. Antici, P. Audebert, E. Brambrink, C. A. Cecchetti, A. Pipahl, L. Romagnani, and O. Willi, Science **312**, 410 (2006).

[14]S. C. Wilks, A. B. Langdon, T. E. Cowan, M. Roth, M. Singh, S. Hatchett, M. H. Key, D. Pennington, A. MacKinnon, and R. A. Snavely, Phys. Plasmas **8**, 542 (2001).

[15]L. O. Silva, M. Marti, J. R. Davies, R. A. Fonseca, C. Ren, F. S. Tsung, and W. B. Mori, Phys. Rev. Lett. **92**, 015002 (2004).

[16]T. Esirkepov, M. Borghesi, S. V. Bulanov, G. Mourou, and T. Tajima, Phys. Rev. Lett. **92**, 175003 (2004).

[17]J. Badziak, S. Jablonski, and S. Glowacz, Appl. Phys. Lett. **89**, 061504 (2006).

[18]A. Macchi, F. Cattani, T. V. Liseykina, and F. Cornolti, Phys. Rev. Lett. **94**, 165003 (2005).

[19]X. Zhang, B. Shen, X. Li, Z. Jin, and F. Wang, Phys. Plasmas **14**, 073101 (2007).

[20]A. P. L. Robinson, M. Zepf, S. Kar, R. G. Evans, and C. Bellei, e-print arXiv:0708.2040.

[21]Y. Sentoku, T. E. Cowan, A. Kemp, and H. Ruhl, Phys. Plasmas **10**, 2009 (2003).

[22]T. V. Liseikina, D. Prellino, F. Cornolti, and A. Macchi, *Proceedings of the Laser and Plasma Accelerators Workshop 2007, Azores, Portugal, 2007* [IEEE Trans. Plasma Sci. (to be published)].

[23]A. Macchi, Appl. Phys. B: Lasers Opt. **82**, 337 (2006).

Ion dynamics and coherent structure formation following laser pulse self-channeling

Andrea Macchi[1,2]**, Alessandra Bigongiari**[2]**, Francesco Ceccherini**[2]**,
Fulvio Cornolti**[2]**, Tatiana V Liseikina**[2]**, Marco Borghesi**[3]**,
Satyabrata Kar**[3] **and Lorenzo Romagnani**[3]

[1] polyLab, CNR-INFM, Pisa, Italy
[2] Dipartimento di Fisica 'Enrico Fermi', Università di Pisa, Largo Bruno Pontecorvo 3, I-56127 Pisa, Italy
[3] School of Mathematics and Physics, the Queen's University of Belfast, Belfast BT7 1NN, UK

E-mail: macchi@df.unipi.it

Abstract
The propagation of a superintense laser pulse in an underdense, inhomogeneous plasma has been studied numerically by two-dimensional particle-in-cell simulations on a time scale extending up to several picoseconds. The effects of the ion dynamics following the charge-displacement self-channeling of the laser pulse have been addressed. Radial ion acceleration leads to the 'breaking' of the plasma channel walls, causing an inversion of the radial space-charge field and the filamentation of the laser pulse. At later times a number of long-lived, quasi-periodic field structures are observed and their dynamics is characterized with high resolution. Inside the plasma channel, a pattern of electric and magnetic fields resembling both soliton- and vortex-like structures is observed.

(Some figures in this article are in colour only in the electronic version)

1. Introduction

The propagation of superintense laser pulses through low-density plasmas gives rise to a variety of nonlinear electromagnetic phenomena [1, 2]. As a general issue the response of the plasma is nonlinear due to both relativistic effects (hence the definition of 'relativistic optics' [3]) and the intense ponderomotive force (i.e. the radiation pressure), which strongly modifies the local plasma density. Probably, the example of such dynamics which has been mostly investigated is the self-focusing, channeling and filamentation of the laser pulse [4–10]. Another prominent effect is the generation of coherent structures such as electromagnetic solitons or vortices. Numerical simulations (see e.g. [11–13]) show that such structures are generated during the interaction with the laser pulse on an ultrafast (femtosecond) time scale, but they may lead to typical field structures which last for much longer times (e.g. 'post-solitons') [12], i.e. in the picosecond range, allowing for their experimental observation [14]. On such a scale

the temporal evolution of such field structures must be studied including the effects of the motion of the plasma ions. Stability and evolution of coherent structures on the ion time scale has been studied theoretically and numerically in several papers, for various regimes and dimensionalities [11–13, 15–20].

In this paper we report a theoretical study of nonlinear effects during and after the propagation of a superintense laser pulse in an underdense, longitudinally inhomogeneous plasma. The work was motivated by experiments on laser propagation in a low-density plasma where the dynamics of self-generated, slowly varying electromagnetic fields was investigated using the proton diagnostic technique [21]. In this paper we focus on the simulation results and on their theoretical interpretation, while a comparison with the experimental results will be reported elsewhere [22, 23].

2. Simulation set-up

The laser–plasma interaction simulations were performed using a particle-in-cell (PIC) code in 2D with Cartesian geometry. Reduction to 2D was dictated by the need to address relatively long spatial and temporal scales, close to the experimental ones. Moreover (as will be clear from the discussion of the results) during the interaction sharp gradients in the field and current patterns are generated. Thus, a reasonable resolution is mandatory to resolve such details, pushing the memory requirements in 3D much beyond present-day supercomputing capabilities. Among the set of 2D simulations that were performed for this study, the largest ones employed a 7750×2400 grid, with spatial resolution $\Delta x = \Delta y = \lambda/10$ (where λ is the laser pulse wavelength) and 16 particles per cell for both electrons and ions, requiring a total of 5000 CPU hours on 100 processors to simulate more than 1500 laser periods of the interaction. The code is fully parallelized and the simulations were performed at the CINECA supercomputing facility in Bologna (Italy).

In the following, lengths are given in units of λ, times in units of $T_L = \lambda/c = 2\pi/\omega$, electric and magnetic fields in units of $E_0 = m_e \omega c/e$, and densities in units of $n_c = m_e \omega^2/4\pi e^2$. For $\lambda = 1\,\mu\text{m}$, $E_0 = 3.213 \times 10^{10}\,\text{V cm}^{-1} = 107.1\,\text{MG}$ and $n_c = 1.11 \times 10^{21}\,\text{cm}^{-3}$. The dimensionless parameter a_L, giving the peak field amplitude of the laser pulse normalized to E_0, is related to the laser intensity I and the wavelength by $a_L = 0.85(I\lambda^2/10^{18}\,\text{W cm}^{-2}\,\mu\text{m}^2)^{1/2}$.

In all the 2D simulations reported below, the plasma is inhomogeneous along the x axis, i.e. in the direction of propagation of the laser pulse. The electron density profile rises linearly from zero value at $x = 25\lambda$ to the peak value $n_0 = 0.1n_c$ at $x = 425\lambda$, and then remains uniform. The pulse duration τ_L was either 150 or 300 T_L, corresponding to 0.5 and 1 ps, respectively, for $\lambda = 1\,\mu\text{m}$.

The laser pulse was *S*-polarized, i.e. the electric field of the laser pulse was in the z direction perpendicular to the simulation plane. In the following we restrict the discussion to the *S*-polarization case which has some advantages for the data analysis and visualization (for instance, the space-charge field generated in the radial (y) direction during self-channeling is separated by the electromagnetic field E_z, which is representative of the pulse evolution). It is known, however, that at high intensity the details of nonlinear effects in pulse propagation depend on the polarization leading to differences between the *S*- and *P*-polarization cases in 2D geometry and to asymmetry effects in 3D for what concerns self-focusing [24] and also to differences in the type and stability of solitons and vortices [[2, 3] and references therein]. A preliminary simulation performed for *P*-polarization showed slight, but no substantial differences for what concerns the early self-channeling evolution which we discuss in section 3.1. The discussion of the effect of different polarizations on the coherent structures generation and evolution is more involved and will be addressed in future work.
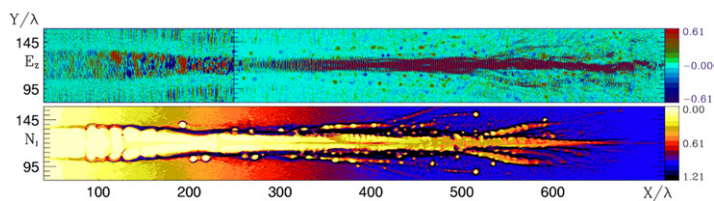
Figure 1. Contours of the electric field of the laser pulse E_z and the ion density n_i from a 2D PIC simulation, at $t = 1000T_L$, showing the self-channeling and filamentation of the laser pulse and the generation of isolated solitary structures and of field patterns. The laser pulse propagates from the left to the right. In the E_z frame, the contour levels in the leftmost region ($50 < x < 250$) has been rescaled by a factor of 3 to show the presence of field structures with relatively low amplitudes. The laser pulse parameters are $a_L = 2.7$, $r_L = 8\lambda$ and $\tau_L = 300T_L$.

3. Results

To illustrate the variety of nonlinear effects observed in the simulation results, figure 1 shows snapshots at $t = 10^3 T_L$ of the ion density (n_i) and the electric field of the laser pulse (E_z) over nearly the whole length of the plasma, for a simulation with $a_L = 2.7$ and $\tau_L = 300T_L$. Figure 1 contains most of the prominent features we observed throughout the set of our simulations, which may be summarized as follows.

In the low-density region, the laser pulse bores a single charge-displacement channel, which in the higher density region breaks up into three main channels and a few secondary, narrow filaments. In the following (see section 3.1) we trace back the appearance of the 'trifurcated' channel to the effects of radial ion acceleration, which lead to the 'breaking' of the channel walls.

Different types of electromagnetic structures are observed in regions of different density. In the lower density region (approximately between $x = 100$ and $x = 150$ in figure 1) a pattern of fields with approximate axial symmetry is observed. A detailed analysis of the electric and magnetic fields, including an estimate of their characteristic frequency from the simulation (see section 3.4), shows that this type of structures combines both features of low-frequency electromagnetic post-solitons or 'cavitons' and steady current vortices. In the higher density region a number of slowly evolving field structures, either appearing as 'solitary' structures or organized into patterns, are observed both outside the main low-density channels and inside the latter. There is some experimental indication of the growth of regularly spaced field structures into the main channel [23].

3.1. Ion and electric field dynamics following self-channeling

For intensities up to $a_L \simeq 2$, in the early stage of the interaction the laser pulse bores a regular charge-displacement channel in the inhomogeneous region of the plasma, i.e. at densities $n_e < 0.1n_c$. This is the case for the simulation of figure 2 ($a_L = 2$, $\tau_L = 300T_L$, transverse width $r_L = 4\lambda$), which shows a snapshot of the ion density n_i and the electric field components E_z and E_y (results from this simulation are also reported in [22]). The laser pulse undergoes self-focusing as indicated both by the reduction of its transverse radius to $\simeq 3\lambda$ and by the increase in its amplitude by a factor $\simeq 1.2$.

In the leading edge of the channel the transverse field E_y is in the outward direction from the axis, indicating that the channel is positively charged due to the radial expulsion of electrons. In the trailing part of the pulse, the radial profile of E_y changes qualitatively, as two ambipolar fronts appear on each side of the channel. On the inner side of the ambipolar fronts
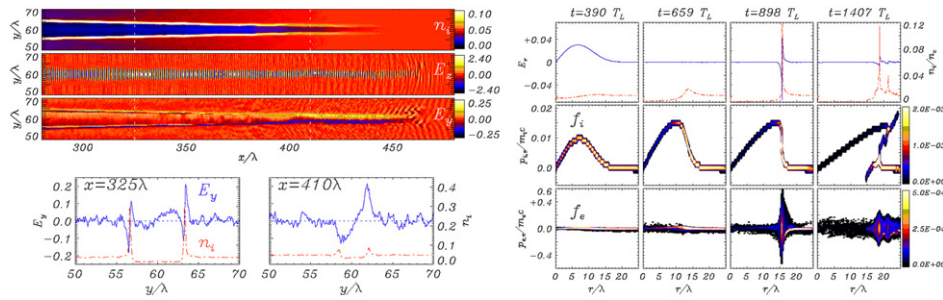
Figure 2. Simulation results addressing electric field dynamics following self-channeling, showing the transition in the radial field profile [22]. Left column: 2D PIC results. Top frame: ion density (n_i) and electric field components (E_z and E_y) at $t = 600T_L$. Bottom frame: lineout of E_y (blue) and n_i (red) along the y-axis at two different x-positions. Parameters are $a_L = 2$, $\tau_L = 300T_L$, $r_L = 4\lambda$. Right column: snapshots at various times of radial electric field E_r (blue, thick line) and ion density n_i (red, dashed–dotted line), and the phase space distributions of ions $f_i(r, p_r)$ and electrons $f_e(r, p_r)$ from 1D simulations using a ponderomotive, electrostatic model [25]. Parameters are $a_L = 2.7$, $n_e/n_c = 0.01$, $r_L = 7.5\lambda$, $\tau_L = 300T_L$.

E_y now points in the inward direction, i.e. towards the axis. The onset of an 'inversion' in the radial field has been noticed in experimental investigations of channel dynamics [22].

3.2. One-dimensional modeling and the electric field 'echo'

The dynamics leading to the evolution of the radial electric field can be studied in detail using a one-dimensional, electrostatic PIC model where the laser pulse action is taken into account only via the ponderomotive force. The model assumes a non evolving radial profile of the laser pulse and cylindrical symmetry taking only the radial, cycle-averaged dynamics of electron and ions into account. Details about the model and its results are reported elsewhere [25]. Here we focus on the most prominent features of electric field dynamics.

Figure 2 shows snapshots of the radial electric field E_r and the ion density n_i at various times, for a 1D simulation in the same regime of 2D electromagnetic runs. Initially, the ponderomotive force F_p pushes electrons away from the axis, creating a back-holding space-charge field which is found to balance F_p almost exactly. At the end of the pulse, when $F_p = 0$, E_r has almost vanished. However, E_r appears back at a later time, with an ambipolar profile very similar to that observed in the 2D simulations. This 'echo' effect originates from the ion dynamics of ions which are accelerated by the electric force $ZeE_r = ZF_p$ during the laser pulse. The spatial profile of F_p is such that the ions are focused towards a very narrow region at the edge of the channel, producing a very sharp spike of the ion density and leading to hydrodynamical breaking as the fastest ions overturn the slowest ones. Looking at the profile of the ion density we observe that the latter may be said to 'break' in literal meaning, as a secondary density spike moving outwards is formed. The process is also accompanied by strong heating of electrons near the breaking point, leading to the appearance of an ambipolar sheath field around the density spike. The negative field is strong enough to slow down and invert the velocity of the slowest ions, which are directed back to the axis where they are found to form a local density maximum at later times.

3.3. Laser beam breakup

A simple analytical model shows that the time required for the ions in the channel to reach the 'breaking' point is proportional to the channel radius and inversely proportional to the
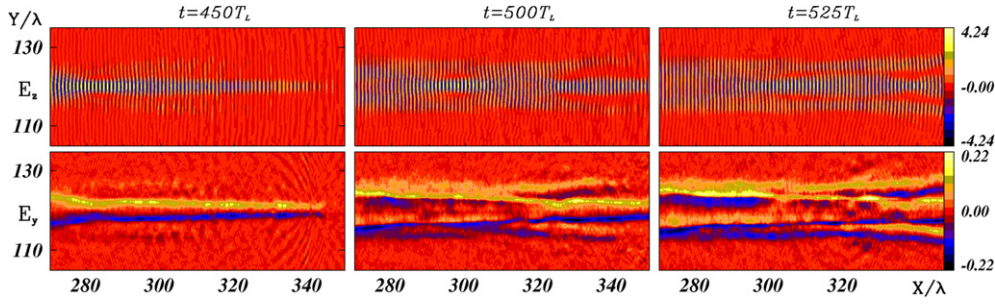
Figure 3. Evolution of the laser field E_z at different times showing the breakup of the laser pulse into three main beams. The two secondary beams propagating in the oblique direction originate from near the location of the 'breaking' of the channel walls. The laser pulse parameters are $a_L = 2.7$, $r_L = 8\lambda$ and $\tau_L = 150T_L$.

laser field amplitude [25]. For high intensities, the 'breaking' effect due to ion acceleration may occur early during the laser pulse, i.e. when the electromagnetic energy density inside the channel is very high, and cause a fast, strong variation of the density at the edge of the channel. In turn, this may affect the propagation of the laser pulse, similarly to what would happen in a wave guide where a sudden 'leak' in its walls occurs. A possible signature of this effect is the appearance of two secondary beams, propagating in the oblique direction, and originating near the point where the breaking of the channel walls occurs, as can be observed in figure 3.

From the 'leaking waveguide' picture we roughly estimate these secondary beams to propagate at an angle θ with respect to the axis given by $\tan \theta \simeq k_y/k_x$, where $k_y \simeq \pi/d$ is the transverse wavevector of the guided mode, d is the local channel diameter and $k_x \simeq \sqrt{\omega^2/c^2 - k_y^2}$. In this estimate the pulse in the channel is modelized as a TE mode of lowest order in a square guide. From the simulation result we get $\tan \theta \simeq 0.065$, while with $d \simeq 7\lambda$ we obtain $k_y/k_x \simeq (\pi/7\lambda)/(2\pi/\lambda) = 0.071$.

3.4. Slowly varying electromagnetic structures

As already noted in figure 1 an impressive number of localized, slowly varying structures are generated in the interaction. In the denser plasma region, the several small-scale structures whose most evident signature is a strong depression in the plasma density are likely to be rather similar to the so-called post-solitons [12, 14] having zero propagation velocity and slowly expanding due to ion acceleration driven by the internal radiation pressure. They may be described as small cavities trapping electromagnetic radiation whose frequency is less than the plasma frequency of the surrounding plasma (hence they may be also appropriately named as 'electromagnetic cavitons'). We notice that we do not observe a drift of such structures towards the low-density region. This difference from the observations of [11] might be ascribed to the smoother electron gradient in our case.

The regular structures, forming an axially symmetrical row, observed in the low-density region near the plasma boundary (far left side in figure 1) have indeed features which are similar to both electromagnetic cavitons and magnetic vortices. This 'dual' nature can be observed in figure 4, which shows the components of the fields E_z and B_z perpendicular to the simulation plane as a contour plot and the components in the (x, y) plane as a vector plot. By analyzing the frequency spectrum of the fields inside the density depression, we find that the fields E_z, B_x and B_y are oscillating at a frequency of approximately 0.1ω, lower than the local value
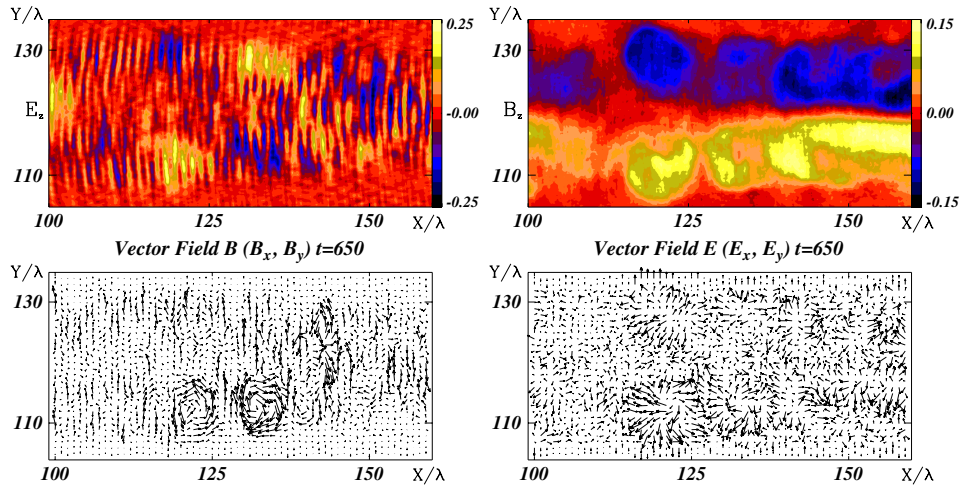
Figure 4. (Anti-)symmetrical row of slowly varying structures in the low-density region of the plasma at $t = 625T_L$. The left column shows the fields E_z (contour plot) and $B_x + B_y$ (vector plot) oscillating at a frequency $\simeq 0.1\omega$. The right column shows the quasi-static fields B_z (contour plot) and $E_x + E_y$ (vector plot). The laser pulse parameters are $a_L = 2.7$, $r_L = 8\lambda$ and $\tau_L = 150T_L$.

of the plasma frequency (for unperturbed plasma) $\omega_p \simeq 0.15\omega$. Qualitatively, the oscillating fields are similar to those of the lowest TM resonant mode in a cylindrical cavity.

The frequency analysis of E_x, E_y and B_z shows that these field components are quasi-static, their spectrum being peaked around zero frequency. The electric field components E_x and E_y are in the radial direction with respect to the axis of the structure, as it is expected for a cavity expanding under the action of the radiation pressure of the trapped radiation. The static magnetic field component B_z is associated with current rings flowing around the axis of the structure.

Apart from being associated with 'post-soliton'-like structures, the fact that the magnetic vortices form a symmetrical row and are localized near the boundary of the channel makes them different from those observed in the wake of a much shorter laser pulse, for which the creation of a low-density channel does not occur, and which seem to form an antisymmetrical row [1,26]. It is nevertheless possible that the current filamentation instability discussed in [26] plays a role in vortex formation also in the present case. In the early stage we observe a strong electron current in the main channel and two narrow return current sheets just outside the channel boundaries; later, the current layers seem to bend locally forming vortices around magnetic field maxima.

The axial symmetry of these particular structures suggests that in 'realistic' 3D geometry they may have a toroidal or 'donut' shape. To get an impression of such a 3D structure one should imagine the field patterns of the 2D simulations rotating around the x-axis. This particular type of coherent structure would be characterized by azimuthal components of $\boldsymbol{E}$ (oscillating) and $\boldsymbol{B}$ (quasi-static) directed along the torus circumference, a solenoidal and oscillating magnetic field coiled up round the torus and by an electrostatic field component perpendicular to the torus surface. The 3D soliton discussed in [13] has a toroidal magnetic field and a poloidal magnetic field; however, in our case we have no clear indication of the charge oscillations inside the solitons observed in [13].

Inside the main and secondary low-density channels generated in the denser region of the plasma, the growth of field patterns which are less regular than those of figure 4, but
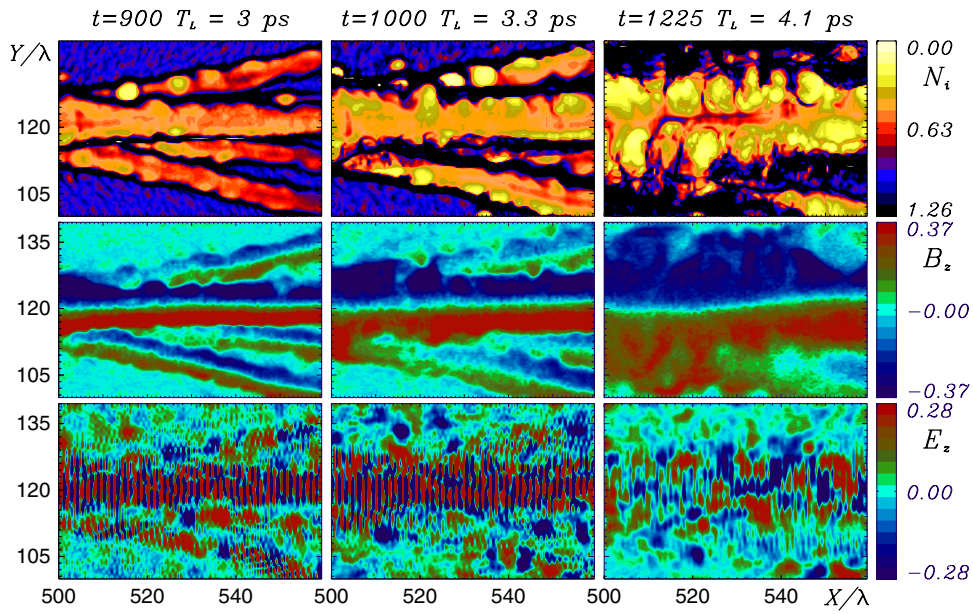
Figure 5. Details of the evolution of field structures in the denser region of the plasma, from the simulation of figure 1. The laser pulse parameters are $a_L = 2.7$, $r_L = 8\lambda$ and $\tau_L = 300 T_L$.

qualitatively similar, can be observed. Figure 5 gives details of their evolution. We observe a tendency of this type of structures to grow inside the channels and to be correlated with rippling and bending of the channel walls. Theoretical work will be required to address the physics of formation of such structure patterns.

4. Conclusions

The main results emerging from the series of 2D PIC simulations reported in this paper may be summarized as follows. Ion acceleration due to the space-charge field in the channel drilled by the laser pulse leads to hydrodynamical breaking of the plasma profile at the channel walls. Two side effects of the ion-driven 'breaking' have been identified: a change in the radial profile of the electrostatic field (including a sort of 'echo' effect for pulses shorter than the breaking time) and a breakup of 'long' laser pulses due to the sudden 'leak' generated in the channel walls. The evolution of coherent, slowly varying field structures has been monitored in time up to thousands of laser cycles, corresponding to several picoseconds in 'real' experiments. Patterns of multi-peak structures appear inside low-density channels, and the formation of structures having both oscillating and static field components with a hybrid soliton-vortex nature has been observed. These results, and the perspective of experimental investigations of such field patterns, support the view of relativistic 'laser plasmas' as environments showing a high degree of self-organization and a wealth of coherent structures, which are thus of great interest for the physics of nonlinear systems.

References

[1] Askaryan G A *et al* 1997 Magnetic interaction of ultrashort high-intensity laser pulses in plasmas *Plasma Phys. Control. Fusion* **39** A137

[2] Bulanov S V *et al* 2001 Relativistic interaction of laser pulses with plasmas *Rev. Plasma Phys.* **22** 227

[3] Mourou G A, Tajima T and Bulanov S V 2006 Optics in the relativistic regime *Rev. Mod. Phys.* **78** 309

[4] Sun G Z, Ott E, Lee Y C and Guzdar P 1987 Self-focusing of short intense pulses in plasmas *Phys. Fluids* **30** 526

[5] Mori W B, Joshi C, Dawson J, Forslund D W and Kindel J M 1998 Evolution of self-focusing of intense electromagnetic waves in plasmas *Phys. Rev. Lett.* **60** 1298

[6] Borisov A B *et al* 1992 Relativistic and charge-displacement self-channeling of intense ultrashort laser pulses in plasmas *Phys. Rev. A* **45** 5830

[7] Monot P *et al* 1995 Experimental demonstration of relativistic self-channeling of a multiterawatt laser pulse in an underdense plasma *Phys. Rev. Lett.* **74** 2953

[8] Borghesi M *et al* 1997 Relativistic channeling of a picosecond laser pulse in a near-critical preformed plasma *Phys. Rev. Lett.* **78** 879

[9] Krushelnick K *et al* 1997 Plasma channel formation and guiding during high intensity short pulse laser plasma experiments *Phys. Rev. Lett.* **78** 4047

[10] Sarkisov G S *et al* 1997 Observation of the plasma channel dynamics and Coulomb explosion in the interaction of a high-intensity laser pulse with a He gas jet *JETP Lett.* **66** 828

[11] Sentoku Y *et al* 1999 Burst of superreflected laser light from inhomogeneous plasmas due to the generation of relativistic solitary waves *Phys. Rev. Lett.* **83** 3434

[12] Naumova N M *et al* 2001 Formation of electromagnetic postsolitons in plasmas *Phys. Rev. Lett.* **87** 185004

[13] Esirkepov T, Nishihara K, Bulanov S V and Pegoraro F 2002 Three-dimensional relativistic electromagnetic subcycle solitons *Phys. Rev. Lett.* **89** 275002

[14] Borghesi M *et al* 2002 Macroscopic evidence of soliton formation in multiterawatt laser-plasma interaction *Phys. Rev. Lett.* **88** 135002

[15] Farina D and Bulanov S V 2001 Relativistic electromagnetic solitons in the electron-ion plasma *Phys. Rev. Lett.* **86** 5289

[16] Lontano M, Passoni M and Bulanov S V 2003 Relativistic electromagnetic solitons in a warm quasineutral electron-ion plasma *Phys. Plasmas* **10** 639

[17] Lehmann G, Laedke E W and Spatschek K H 2006 Stability and evolution of one-dimensional relativistic solitons on the ion time scale *Phys. Plasmas* **13** 092302

[18] Weber S, Lontano M, Passoni M, Riconda C and Tikhonchuk V T 2005 Electromagnetic solitons produced by stimulated brillouin pulsations in plasmas *Phys. Plasmas* **12** 112107

[19] Riconda C, Weber S, Tikhonchuk V T, Adam J-C and Heron A 2006 Two-dimensional particle-in-cell simulations of plasma cavitation and bursty brillouin backscattering for nonrelativistic laser intensities *Phys. Plasmas* **13** 083103

[20] Baiwen Li, Ishiguro S, Skoric M M and Sato T 2007 Stimulated trapped electron acoustic wave scattering, electromagnetic soliton and ion vortices in intense laser interaction with subcritical plasmas *Phys. Plasmas* **14** 032101

[21] Borghesi M *et al* 2001 Proton imaging: a diagnostic for inertial confinement fusion/fast ignitor studies *Plasma Phys. Control. Fusion* **43** A267–76

[22] Kar S *et al* 2007 Dynamics of charge-displacement channeling in intense laser-plasma interactions (*preprint* physics/0701332)

[23] Liseykina T V *et al* 2007 Generation and observation of coherent, long–lived structures in a laser–plasma channel (*preprint* physics/0702177)

[24] Naumova N M *et al* 2001 Polarization, hosing and long time evolution of relativistic laser pulses *Phys. Plasmas* **8** 4149–55

[25] Macchi A, Ceccherini F, Cornolti F, Kar S and Borghesi M 2007 Ponderomotive laser ion acceleration and electric field dynamics following charge–displacement channeling (*preprint* physics/0701139)

[26] Bulanov S V, Lontano M, Esirkepov T Zh, Pegoraro F and Pukhov A M 1996 Electron vortices produced by ultraintense laser pulses *Phys. Rev. Lett.* **76** 3562
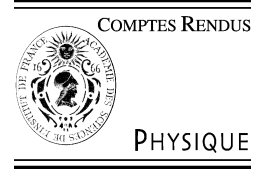
Laser acceleration of particles in plasmas / Accélération laser de particules dans les plasmas

Theory and simulation of ion acceleration with circularly polarized laser pulses

Andrea Macchi [a,b,*], Tatiana V. Liseikina [c,1], Sara Tuveri [b], Silvia Veghini [b]

[a] *CNR/INFM/polyLAB, 56127 Pisa, Italy*
[b] *Department of Physics "E. Fermi", University of Pisa, Largo B. Pontecorvo 3, 56127 Pisa, Italy*
[c] *Max Planck Institute for Nuclear Physics, 69029 Heidelberg, Germany*

Available online 29 April 2009

Abstract

Ion acceleration driven by the radiation pressure of circularly polarized pulses is investigated via analytical modeling and particle-in-cell simulations. Both thick and thin targets, i.e. the "hole boring" and "light sail" regimes are considered. Parametric studies in one spatial dimension are used to determine the optimal thickness of thin targets and to address the effects of preformed plasma profiles and laser pulse ellipticity in thick targets. Three-dimensional (3D) simulations show that "flat-top" radial profiles of the intensity are required to prevent early laser pulse breakthrough in thin targets. The 3D simulations are also used to address the issue of the conservation of the angular momentum of the laser pulse and its absorption in the plasma. ***To cite this article: A. Macchi et al., C. R. Physique 10 (2009).***
© 2009 Académie des sciences. Published by Elsevier Masson SAS. All rights reserved.

Résumé

Théorie et simulation de l'accélération des ions par impulsions laser à polarisation circulaire. L'accélération des ions par la pression de radiation des impulsions laser avec polarisation circulaire a été étudiée à l'aide de modèles analytiques et de simulations "*particle-in-cell*". Les deux régimes de cibles épaisses et minces, c'est-à-dire de "*hole boring*" et "*light sail*" ont été considérés. Des études paramétriques dans une dimension spatiale ont été réalisées afin de déterminer l'épaisseur optimale des cibles minces et pour étudier l'effet des profils de densité plasma préformés et l'effet de l'ellipticité de l'impulsion dans cibles épaisses. Les simulations tridimensionnelles (3D) montrent que des impulsions avec des profils radiaux plats en intensité sont nécessaires pour prévenir la pénétration de l'impulsion à travers la cible. Les simulations 3D ont aussi été utilisées pour étudier la conservation du moment angulaire de l'impulsion laser et son absorption dans le plasma. ***Pour citer cet article : A. Macchi et al., C. R. Physique 10 (2009).***
© 2009 Académie des sciences. Published by Elsevier Masson SAS. All rights reserved.

Keywords: Laser–plasma acceleration; Ion acceleration; Radiation pressure; Circular polarization

Mots-clés : Accélération laser–plasma ; Accélération des ions ; Pression de radiation ; Polarisation circulaire

* Corresponding author at: Department of Physics "E. Fermi", University of Pisa, Largo B. Pontecorvo 3, 56127 Pisa, Italy.
  E-mail address: macchi@df.unipi.it (A. Macchi).
  URL: http://www.df.unipi.it/~macchi (A. Macchi).
[1] On leave from Institute of Computational Technologies, SD-RAS, Novosibirsk, Russia.

1. Introduction

Radiation Pressure Acceleration (RPA) is a possible route to the acceleration of ions up to energies in the relativistic domain (GeV/nucleon), alternative to the Target Normal Sheath Acceleration (TNSA) mechanism which explains ion acceleration from thin solid targets in present-day experiments (see [1] for a review). The interest in RPA was stimulated by Particle-In-Cell (PIC) simulations of Esirkepov et al. [2,3] showing that at intensities $I > 5 \times 10^{21}$ W cm^{-2} RPA starts to dominate over TNSA, and that at $I \gtrsim 10^{23}$ W cm^{-2} and using a thin foil target, an efficient generation of GeV ions and a linear scaling of ion energy vs. the pulse energy may be obtained. These characteristic features of RPA, very appealing for foreseen applications of ion acceleration, may be qualitatively understood using the simple model of a perfectly reflecting mirror accelerated by a normally incident plane wave. Due to the Doppler effect, the frequency ω of each incoming photon reflected by the mirror moving at the velocity $V = \beta c$ in the laboratory frame is downshifted to ω' according to the relation $\omega' = \omega(1 - \beta)/(1 + \beta)$, so that almost all of the energy $\hbar\omega$ of the photon is delivered to the target in the limit $\beta \to 1$ and, since the number of photons is conserved for a perfect mirror, a complete conversion of the wave energy into mechanical energy is obtained.

Intensities exceeding 10^{23} W cm^{-2} are not available yet, but a dominance of RPA over TNSA may be already obtained at much lower intensity if a laser pulse with circular polarization (CP), instead of linear polarization (LP), is used. In fact, in such conditions the acceleration of "fast" electrons at the laser–plasma interface is almost suppressed, ruling out TNSA which is driven from the space charge produced by energetic electrons escaping in vacuum. The suppression of fast electrons for CP can be understood by noting that models of electron acceleration at a sharp plasma surface ([4,5] and references therein) require the driving force to have an *oscillating* component along the density gradient. For normal incidence, such component is given by the $\mathbf{J} \times \mathbf{B}$ term at 2ω (with experimental evidence given by Ref. [6]) which however vanishes for CP (see Section 2 for a discussion based on a simple model).

Radiation Pressure Acceleration using Circular Polarization (CP-RPA) was first studied by our group [7,8] by considering "thick" targets, such that during the laser pulse only a finite layer of the target at its front surface is accelerated, forming a dense bunch of ions (neutralized by "cold" electrons) entering the target. Dramatic differences in ion acceleration were observed between CP and LP [7,8]. Later, three groups [9–12] studied the acceleration of "thin" foils, such that the whole target is accelerated. In this regime, the use of CP is particularly important to prevent the foil expansion due to the "thermal" pressure of electrons, allowing the acceleration of the target as a single "rigid" object and preserving the inherent monoenergeticity after the acceleration stage. In good accordance with the predictions of the "mirror" model, it was found that sub-micrometric targets may be accelerated up to energies corresponding to GeV/nucleon using petawatt pulses with picosecond duration, which are feasible with current technology. This perspective has stimulated additional theoretical and numerical investigations [13–16].

In this article, we review our analytical and simulation work [7,8,17,18] on both the "thick" and "thin" regimes of CP-RPA which are also named "hole boring" (HB) and "light sail" (LS) regimes, respectively. Most recent work from our group included a) a study of the "optimal" target thickness in the LS case, b) a preliminary evaluation of "preplasma" effects, and c) three-dimensional (3D) simulations of CP-RPA to address in particular the issue of the absorption of the angular momentum of the laser pulse by the plasma.

2. The role of the pulse polarization: a simple model

A simple and possibly pedagogical "minimal" model to show the role of the polarization in laser interaction with an overdense plasma at normal incidence may be described as follows. We assume a plane, elliptically polarized wave of frequency ω incident on an overdense plasma with a step-like profile of the electron density $n_e(x) = n_0 \Theta(x)$, and $\omega_p > \omega$ being $\omega_p = \sqrt{4\pi n_0 e^2/m_e}$ the plasma frequency. For sufficiently low intensity (neglecting relativistic and strong charge separation effects) the vector potential inside the plasma has the form

$$\mathbf{A}(x,t) = \frac{A(0)}{\sqrt{1+\epsilon^2}} e^{-x/d_p} (\hat{y} \cos\omega t + \epsilon \hat{z} \cos\omega t) \tag{1}$$

where $d_p = c/\sqrt{\omega_p^2 - \omega^2}$ and ϵ is the ellipticity ($0 < \epsilon < 1$). The longitudinal force on electrons due to the $\mathbf{v} \times \mathbf{B}$ term is then obtained as

$$F_x = -\frac{e^2}{2m_e c^2} \partial_x \mathbf{A}^2 = F_0 e^{-2x/d_p} \left(1 + \frac{1-\epsilon^2}{1+\epsilon^2} \cos 2\omega t\right) \tag{2}$$

where $F_0 = (e^2 A(0)^2/2d_p m_e c^2)$. By solving the equations of the longitudinal motion of electrons for the secular and 2ω components we obtain the electric field and the electron density perturbation

$$E_x = \frac{F_0}{e} e^{-2x/d_p} \left(1 + \frac{1 - \epsilon^2}{1 + \epsilon^2} \frac{\cos 2\omega t}{1 - 4\omega^2/\omega_p^2} \right), \quad \delta n_e = -\frac{1}{4\pi e} \partial_x E_x \tag{3}$$

The denominator in the oscillating term of E_x arises from the resonant excitation of plasma oscillations when $2\omega = \omega_p$. For LP ($\epsilon = 0$), the peak amplitude of the oscillating term is larger than the secular term, and as a consequence some electrons are dragged into the vacuum side, as can be evidenced by calculating the quantity

$$\Delta N_e(t) = \int_0^{+\infty} \delta n_e \, dx = \frac{F_0}{4\pi e^2} \left(1 + \frac{1 - \epsilon^2}{1 + \epsilon^2} \frac{\cos 2\omega t}{1 - 4\omega^2/\omega_p^2} \right) \tag{4}$$

When $\Delta N_e(t) > 0$, electrons are piling up inside the plasma and a positive surface charge appears to ensure quasineutrality. However, if the oscillating term becomes larger than the secular one (and this always happens if $\epsilon = 0$, i.e. for LP), $\Delta N_e(t) < 0$ occurs implying that some electrons cross the $x = 0$ surface entering the vacuum side. In this case a regular, periodic solution does not exist anymore. This is a signature of the onset of self-intersection of electron trajectories in vacuum leading to heating and appearance of fast electron "jets" twice per laser cycle. For CP ($\epsilon = 1$), however, the oscillating terms vanish, the electric force on electrons balances the ponderomotive force ($F_x - eE_x = 0$) and no electron heating occurs. The model suggests an ellipticity threshold $\epsilon_T = (\omega_p^2/2\omega^2 - 1)^{-1/2}$ such that for $\epsilon > \epsilon_T$ we have $\Delta N_e(t) > 0$ at any t, and "vacuum heating" should be inhibited.

These conclusions can be verified to hold also at higher intensity with numerical methods. For example, a PIC simulation with fixed ions and a CP, semi-infinite laser pulse with a sufficiently slow rising edge shows that the equilibrium profiles of E_x and δn_e are in excellent agreement with an exact analytical solution including relativistic and strong charge separation effects [19,20].

3. Thick targets: density breaking and ion bunch generation

The electrostatic field E_x created by the electron displacement accelerates ions modifying the density profile. A self-consistent, time-dependent solution of the wave penetration is not available. In Ref. [7] a phenomenological model giving simple analytical solutions and accounting for the most prominent features observed in simulations for the "thick" target or "hole boring" regime was obtained by taking an "ad hoc" spatial and temporal profile of the ponderomotive force F_x and assuming the quasi-equilibrium condition for electrons to hold as the ions move. A brief description of the model is given in Fig. 1 and its caption.

The equations of motion are valid until the time τ_b at which all the ions initially located in the layer of electron compression ($x_d < x < x_s$ in Fig. 1) reach the point $x = x_s$; here, the ion density becomes singular and the fastest ions overcome the slowest ones so that hydrodynamical or "wave" breaking for the ion fluid occurs. At the time t_i, the maximum ion velocity and the corresponding energy for a laser pulse of constant intensity are given by

$$\frac{v_{im}}{c} = 2\sqrt{\frac{Z}{A} \frac{m_e}{m_p} \frac{n_c}{n_e}} a_L, \quad \mathcal{E}_m = \frac{1}{2} m_i v_{im}^2 = 2Z m_e c^2 \frac{n_c}{n_e} a_L^2 \tag{5}$$

where $a_L = 0.85(I\lambda^2/10^{18} \text{ W} \mu\text{m}^2/\text{cm}^2)^{1/2}$ is the laser amplitude in dimensionless units. These formulas are valid for non-relativistic ion velocities; relativistic corrections are considered in Ref. [16].

The details of the ion spectrum depend on the highly transient stage of wave breaking and may be studied mostly via simulations. Fig. 1b) shows three snapshots from a 1D PIC simulation, showing the generation of the electrostatic field, the very strong spiking of the ion density at the instant of wave breaking and the formation of a short-duration, high-density "bunch" moving in the forward direction at velocity $\simeq v_{im}$. The heating of electrons is significant only around the "breaking" event and the electron energies are lower by nearly two order of magnitudes than the value observed for LP interaction at the same intensity [7,8]. A detailed study of the dynamics of wave breaking in a very similar context has been reported in Ref. [21].
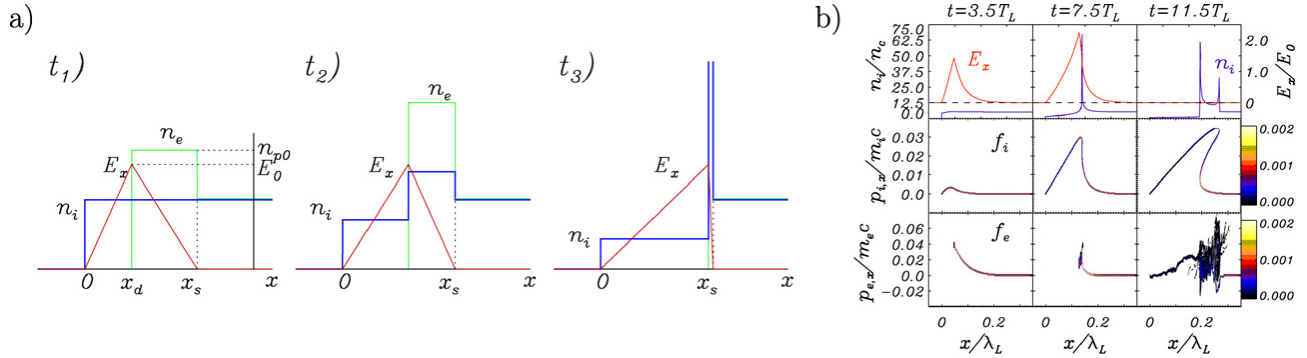
A. Macchi et al. / C. R. Physique 10 (2009) 207–215

Fig. 1. a): model for RPA of ions at the front target surface [7,17]. The plots show the spatial profiles of E_x (red), n_i (blue) and n_e (green) at three different times. The ponderomotive force $F_x = eE_x$ in the region where $n_e \neq 0$. Due to conservation laws, model parameters are related by $E_0 = 4\pi e n_0 x_d$, $n_0 x_s = n_{p0}(x_s - x_d)$, and $E_0 e n_{p0}(x_s - x_d)/2 \simeq 2I/c$ where $x_s - x_d \simeq c/2\omega_p$. At the time t_1, ions have not moved yet and electrons have been pushed creating the charge separation field; at t_2, E_x accelerates ions and pile them up in the evanescence region, while electrons rearrange themselves to keep the force balance condition; at t_3, the density peaks up to infinite values since all ions starting from the $x_d < x < x_s$ get to the point $x = x_s$ at the same time, and "wave breaking" occurs. b): 1D PIC simulation of the interaction of a short CP laser pulse with an overdense, step-boundary plasma [17]. The figure shows n_i and E_x (top row) and the (x, p_x) phase space distribution for ions (f_i, middle row) and electrons (f_e, bottom row) at different times in units of the laser period T_L. The laser pulse has peak amplitude $a = 2$ and duration $\tau = 6T_L$ (FWHM). The initial density is $n_0 = 5n_c$ where n_c is the cut-off density. The x coordinate is normalized to λ, the density to n_c, the electric field to $m_e \omega c/e$ and the momenta to $m_e c$ and $m_i c$, respectively.

Some further insight into the dynamics of ion bunch formation is obtained by looking at simulations with *elliptical* polarization for different values of the ellipticity ϵ, since this allows to vary the relative importance of secular and oscillating components in the accelerating fields. They are also of interest to test the sensitivity of the RPA regime to values of $\epsilon < 1$ as it may occur in experiments. The snapshots shown in Fig. 2 for simulations having the same plasma target and a laser pulse of fixed energy and duration but different values of ϵ show the tendency to the formation of multiple ion "bunches". This effect may be explained by noting that, due to the oscillating component in E_x, ions now cross the evanescence point at different times corresponding to positive maxima of E_x. The phase space for $\epsilon = 0.5$ shows the "X"-type structure whose origin has been discussed in Ref. [21]. The electron heating is observed to increase as ϵ decreases from 1 (CP) to 0 (LP). Very recently a similar study has been reported in Ref. [22], showing a "threshold" value for ϵ which depends weakly on the laser intensity. This is in qualitative agreement with our simple model (Section 2) where the intensity dependence may arise in the resonant denominator due to the relativistic correction to the plasma frequency $\omega_p^2 \rightarrow \omega_p^2 / \sqrt{1 + a^2}$.

Parametric 1D runs were also performed to study the effect of a "preplasma", i.e. a density profile smoother than a step-like one, which could be typically produced in experiments by a prepulse preceding the ultrashort, superintense pulse. Such study is also of interest because the scaling laws (5) predict the ion energy to be inversely proportional to the density. Although these relations have been obtained for a step-like profile, they suggest that in a preplasma the interaction occurs near the $n_e \simeq n_c$ layer leading to higher ion energies. This effect was confirmed in the preliminary simulations shown in Ref. [18], which show that ion bunch formation occurs also in a preplasma, suggesting the possible use of prepulse control to achieve higher energies. The dependence of ion energy and conversion efficiency (defined as the ratio of the total energy of the ions over the energy of the laser pulse) on the density scalelength $L = n_c/|\partial_x n_0|_{n_0 = n_c}$ for a given laser pulse are shown in Fig. 2b).

In general, because of the large value of n_e/n_c ($\sim 10^2$) for solid densities and the typical laser wavelength ~ 1 µm, any possibility (e.g., by special target materials) to achieve a laser–plasma interaction at smaller values of n_c/n_e would be important to obtain high ion energies in the "hole boring" regime. We note that, usually, 2D and in particular 3D simulations are performed for relatively small values of n_e/n_c because of computational limitations, since the need to resolve length scales smaller than $c/\omega_p \sim 1/\sqrt{n_e}$ and density regions where $n_e < n_c$ forces to use large numbers of small cells and large numbers of particles. At least, an estimate of the scaling of all relevant quantities such as ion energy and conversion efficiency with n_e is thus needed to extrapolate simulation results to feasible experimental parameters.
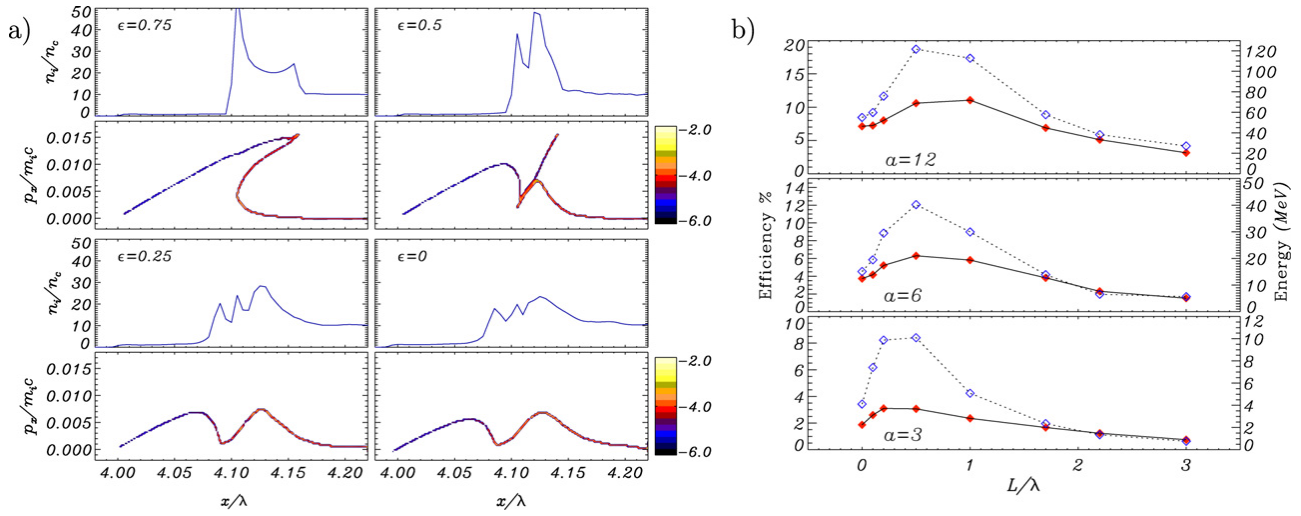
Fig. 2. Results from parametric 1D simulations. a): snapshots of n_i and $f_i(x, p_x)$ (in $\log_{10}$ scale) from simulations with different ellipticity ϵ. Common parameters to all runs are $n_0 = 10n_c$, $a = 2$, and $\tau = 12T_L$. b): interaction with preformed plasmas [18]. Conversion efficiency (red filled diamonds, solid line) and peak energy (blue empty diamonds, dashed line) of ions as a function of the density scalelength L in preplasma and the laser amplitude a. The density profile is described by a $\sim(x - x_0)^4$ function up to a peak density $n_0 = 16n_c$. The pulse duration $\tau = 9T_L$.

4. Thin targets: optimal thickness and heating effects

The analysis of the RPA dynamics for "thick" targets outlined above now allows us to define "thin" targets in this context. In thick targets, after wave breaking the fastest ions overturn the slowest ones, penetrate into the overdense plasma and are not accelerated anymore. To obtain high energies the laser pulse must be able to repeat the acceleration stage over the same ions. Thus, the target thickness must be close to the depth of the compression layer (the parameter $\ell_s = x_s - x_d$ in Fig. 1) in order for repeated or "cyclic" RPA to occur. If the solid target contains hydrogen ions, they will gain higher velocity in a first stage, but overturning other ions they will be screened by the laser pulse until heavier ions reach them. Thus, ions of different Z/A ratio will tend to ultimately be accelerated to the same velocity, so that RPA of thin foils appears to be most suitable for the acceleration or ions heavier than protons, e.g., carbon.

Although due to the above considerations the target may not be considered as a "rigid" object, the accelerating mirror or "light sail" model gives reasonable estimates for the target velocity $V = \beta c$ as a function of the laser pulse energy. The equations of motion are

$$\frac{d(\gamma\beta)}{dt} = \frac{2I(t - X/c)}{\rho d c^2} \frac{1 - \beta}{1 + \beta} R(\omega'), \quad \frac{dX}{dt} = \beta c \tag{6}$$

where ρ and d are the mass density and thickness of the mirror and R is its reflectivity, which can be written as a function of the pulse frequency in the rest frame ω'. An analytical solution is found for $R = 1$ and constant intensity

$$\gamma\beta = \left[\sinh\psi(t) - \frac{1}{4\sinh\psi(t)}\right], \quad \psi(t) = \frac{1}{3}\operatorname{arcsinh}\left(\frac{6It}{\rho d c^2} + 2\right) \tag{7}$$

Higher velocities and efficiency are expected for lighter targets, but as ρd decreases the target tends to become transparent to the laser light. One thus expect to find an "optimal" thickness d_{opt} to exist for a given laser intensity. Fig. 3a) shows a set of 1D parametric simulations in a range of presently accessible intensities (10^{19}–10^{21} W cm^{-2}). It is found that d_{opt} increases with pulse intensity (presumably due to induced relativistic transparency) and has typical values of $\approx 10^{-2}$ µm. Such ultrathin targets are technologically feasible but will require the complete suppression of prepulses in experiments.

We obtained an analytical solution for the motion of the mirror even in the case of partial reflectivity by using for the latter the model of a "delta-like" foil [23] and including the effects of self-induced transparency. The resulting energy per nucleon as a function of the target thickness and the pulse fluence (energy per unit surface) is shown in Fig. 3b). There is qualitative agreement with the numerical simulations although the model predicts lower ion energies.
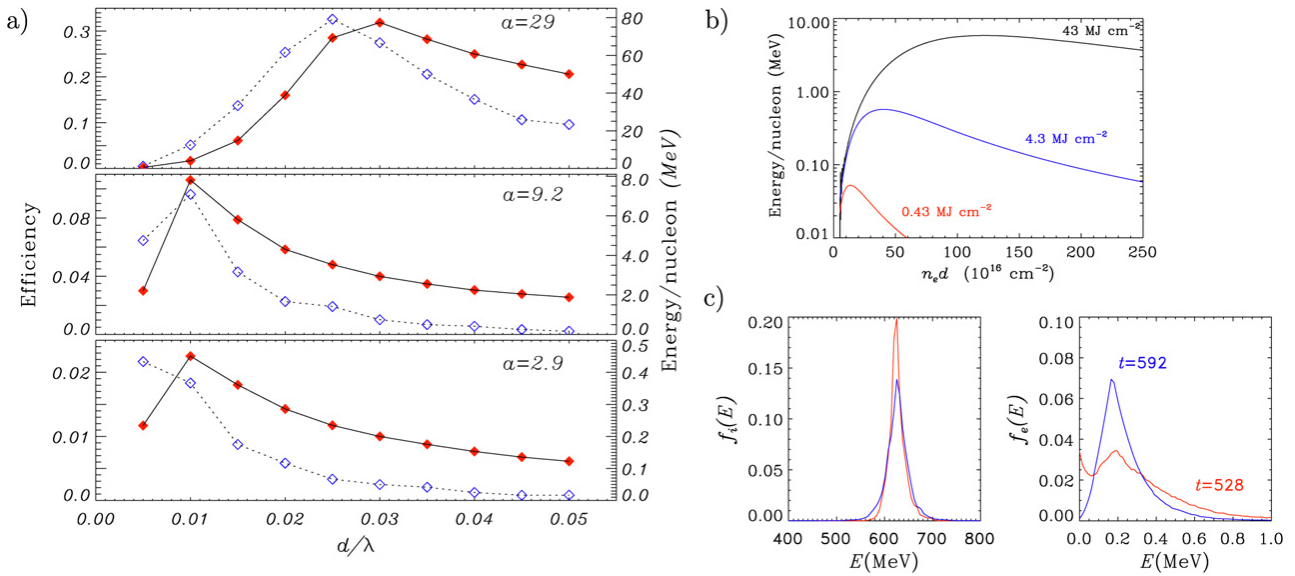
Fig. 3. a): energy conversion efficiency (red filled diamonds) and peak energy per nucleon (blue empty diamonds) as a function of the target thickness d and pulse amplitude a from 1D PIC simulations [18]. Common parameters to all runs are $\tau = 9T_L$, $n_e = 250n_c$ and $Z/A = 1/2$. b): analytical calculation of the energy per nucleon as a function of the areal density $n_e d$ of the target and of the pulse fluence. c): energy spectra of ions and electrons from a simulation of the interaction of a 400 fs, 1.8×10^{20} W cm^{-2} pulse with a 0.056 μm thick carbon target ($n_e = 250n_c$), for two different times (in fs).

A simple energy balance argument shows that to accelerate a solid target of "optimal" thickness $\approx 10^{-2}$ μm up to velocities corresponding to energies per nucleon ≈ 1 GeV, a pulse energy per unit surface $\approx 10^8$ J cm^{-2} is needed. The width of the energy spectrum is also an issue. The simulation results shown in Fig. 3c) show that a spectrum with $\simeq 5\%$ spread is obtained at the end of the laser pulse. However, some broadening of the energy spectrum is observed also after the acceleration stage. This seems to be related to a relatively abrupt increase of the absorption fraction into electrons near the end of the laser pulse, as the radiation pressure decreases. The resulting electron "temperature", although orders of magnitude lower than the quiver energy, may be sufficient to cause some expansion of the thin foil and to broaden the ion spectrum.

5. Multi-dimensional effects

The above analysis is based on 1D modeling and simulations, which for example do not account for effects related to the finite transverse size of the laser pulse. As an obvious consequence, the intensity distribution implies that the radiation pressure on the plasma is inhomogeneous, leading to a broader ion energy spectrum, with less energetic ions at the periphery of the laser spot. Moreover, a finite pulse waist of radius r_L implies longitudinal field components $E_\parallel \approx (\lambda/r_L)E_\perp$ at the edge of the spot, causing local heating of electrons. The bending of the plasma surface caused by hole boring or foil deformation also increases the electron heating because the local angle of incidence does not vanish anymore. However, 2D simulations [7,8,11,12] show that these effects do not cause a failure of the CP-RPA, and the differences with the LP case are still evident [8]. It has been shown that pulses with a "flat-top" (e.g., supergaussian) [11] intensity profile allow to preserve a narrow ion spectrum and a very low divergence (a few degrees).

The onset of surface instabilities, e.g. of density rippling, has also been studied by 2D simulations. A Rayleigh–Taylor-like instability driven by radiation pressure has been characterized in Ref. [24] for thin foils accelerated by LP pulses. However, the comparison of thick targets simulations for CP and LP show that the surface instability is weaker for CP [17]. This suggests that additional effects besides RPA contribute to the dynamics of the instability.

Since a CP wave carries a net angular momentum, conservation of the latter poses an additional constraint on the interaction. This gives a specific motivation for 3D simulations of CP-RPA. The issue of angular momentum absorption in the plasma has been studied in the past mostly for underdense plasmas and in close connection with the Inverse Faraday Effect, i.e. the generation of axial magnetic fields, and apparently it has often been a subject of controversy and misunderstanding (see e.g. [25,26] and references therein). In the present context it is noticeable
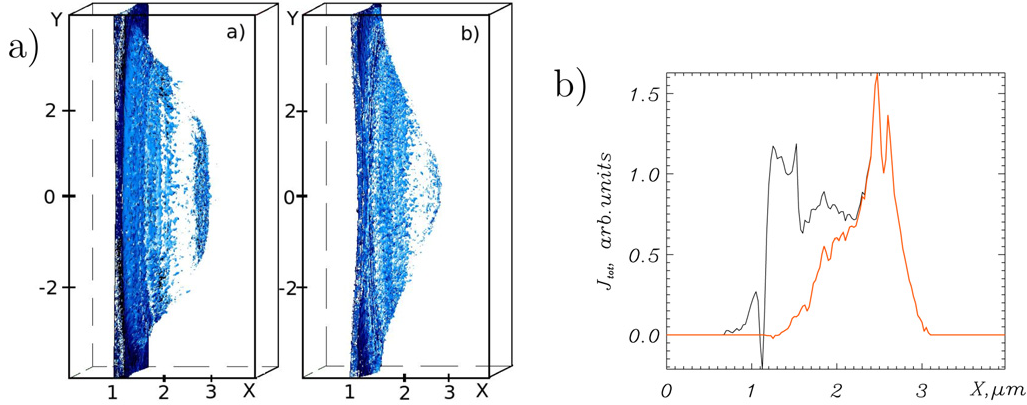
Fig. 4. Three-dimensional simulations of CP-RPA of a thin foil target. a): the ion density n_i at $t = 40T_L$ for two different radial profiles of the laser intensity, a supergaussian $\sim\exp(-r^4/r_s^4)$ or "flat-top" (left) and a Gaussian $\sim\exp(-r^2/r_g^2)$ (right) profile, with $r_s = 2.5\lambda$ and $r_g = 2.4\lambda$. Common simulation parameters are $n_0 = 16n_c$, $d = 0.4\lambda$, $a = 5$ and $\tau = 10T_L$. b): the azimuthal ion current $J_{i,\varphi}$ averaged over the transverse plane (y, z), t=130 fs versus longitudinal coordinate, showing the angular momentum absorption into ions [18]. The black and red lines correspond to an average over a circle with radius $r = 4.5\lambda$ and 2.5λ, respectively, around the x-axis.

that, according to the accelerating mirror model, absorption of angular momentum by the target may vanish even for nearly complete energy absorption. In fact, the photon "spin" is $\hbar$ and independent from the frequency, while in the reflection of a photon from the mirror the direction of the spin is not reversed (as it happens for the momentum), so that the conservation of photon number in any frame implies that no angular momentum is absorbed by the target at all. Thus, the amount of angular momentum absorbed during CP-RPA gives an indication of non-adiabatic or dissipative processes at play in the laser–plasma interaction.

Fig. 4a) shows a 3D snapshot of the ion density for two simulations having identical parameters but different radial profiles of the intensity, i.e. a Gaussian and a supergaussian "flat-top" profile. The thickness of the target was chosen to be close to the "optimal" value inferred from the 1D parametric study. However, for the Gaussian pulse case, the lateral expansion of the central region of the target causes an early breakthrough of the laser pulse through the plasma, with a detrimental effect on the ion acceleration. The use of a "flat-top" pulse prevents the breakthrough and leads to an ion beam with very low divergence and energy values close to those inferred from the 1D analysis.

The fraction A_L of the angular momentum of the pulse transferred to the plasma was evaluated directly from the phase space distribution of the particles and compared to the energy absorption A_E. It is found that $A_L \lesssim A_E$ showing that a substantial part of the energy is absorbed via non-adiabatic processes (i.e. violating the conservation of photon number). It is noticeable that the density of axial angular momentum of the incident pulse is given by $\ell_x = \ell_x(r) = -\frac{r}{2c\omega}\partial_r I(r)$, which peaks at the edge of the beam where the axial components of the oscillating electric field have their maximum, i.e. where most of the electron heating occurs. Thus, non-adiabatic heating of electrons at the edge of the beam is likely to provide a channel for angular momentum absorption. However, the simulations show that eventually, after the end of the laser pulse, most of the absorbed angular momentum is given to ions. The absorption of angular momentum should lead to a torque on the ions and to the appearance of a steady azimuthal current. Such a net current can be evidenced by an average over the transverse plane, as in Fig. 4b), as the actual distribution is rather complicated. No regular magnetic field is found on the axis, i.e. there is no significant Inverse Faraday Effect associated to CP-RPA.

6. Discussion

The "light sail" regime of CP-RPA is very attractive for the possibility to accelerate a large number of ions (presumably of carbon or heavier elements) to GeV energies. The scheme requires ultrathin targets and, consequently, laser pulses with extremely high contrast [27]. Our simulations show that, in addition, flat-top intensity profiles may be crucial to reach the highest energies as well as to achieve high collimation and a monoenergetic spectrum.

The thick target or "hole boring" regime allows one to reach much lower energies with present-day intensities and solid target densities. However, this regime requires less critical conditions than the "light sail", and may be useful for applications requiring high densities of ions with moderate energies (up to a few MeV). Moreover, our preliminary

study of RPA in preformed plasma profiles suggest that the scaling with density allows to obtain energies higher than the values expected for solid densities and same pulse parameters. It might be also of interest to investigate RPA with CO_2 pulses in gas jets, where the gas density can be tuned to be only slightly over n_c and, in addition, high repetition rates would be possible.

Presently, no experimental results on CP interaction at normal incidence (or in conditions significantly close to such "optimal" conditions) have been reported yet in publications, but devoted experiments are planned or have been proposed in several facilities. For interactions with linearly polarized pulses, radiation pressure effects have been claimed to play a dominant role in a few experiments for different conditions [28–30] as well as in several phenomena observed in simulations (e.g. "laser piston" [2], surface rippling [24] or "shock acceleration" [31]). The study of circularly polarized interactions, besides its potential for ion acceleration, may be very useful for a detailed understanding of radiation pressure effects as these latter can be separated from effects due to fast electrons.

Acknowledgements

References

[1] M. Borghesi, J. Fuchs, S.V. Bulanov, A.J. MacKinnon, P.K. Patel, M. Roth, Fusion Sci. Technol. 49 (2006) 412.
[2] T. Esirkepov, M. Borghesi, S.V. Bulanov, G. Mourou, T. Tajima, Phys. Rev. Lett. 92 (2004) 175003.
[3] T. Esirkepov, M. Yamagiwa, T. Tajima, Phys. Rev. Lett. 96 (2006) 105001.
[4] P. Gibbon, Short Pulse Laser Interactions with Matter: An Introduction, Imperial College Press, London, 2005.
[5] D. Bauer, P. Mulser, Phys. Plasmas 14 (2007) 023301.
[6] S.D. Baton, J.J. Santos, F. Amiranoff, H. Popescu, L. Gremillet, M. Koenig, E. Martinolli, O. Guilbaud, C. Rousseaux, M. Rabec Le Gloahec, T. Hall, D. Batani, E. Perelli, F. Scianitti, T.E. Cowan, Phys. Rev. Lett. 91 (2003) 105001.
[7] A. Macchi, F. Cattani, T.V. Liseykina, F. Cornolti, Phys. Rev. Lett. 94 (2005) 165003.
[8] T.V. Liseikina, A. Macchi, Appl. Phys. Lett. 91 (2007) 171502.
[9] X. Zhang, B. Shen, X. Li, Z. Jin, F. Wang, Phys. Plasmas 14 (2007) 073101.
[10] X. Zhang, B. Shen, X. Li, Z. Jin, F. Wang, M. Wen, Phys. Plasmas 14 (2007) 123108.
[11] A.P.L. Robinson, M. Zepf, S. Kar, R.G. Evans, C. Bellei, New J. Phys. 10 (2008) 013021.
[12] O. Klimo, J. Psikal, J. Limpouch, V.T. Tikhonchuk, Phys. Rev. ST Accel. Beams 11 (2008) 031301.
[13] X.Q. Yan, C. Lin, Z.M. Sheng, Z.Y. Guo, B.C. Liu, Y.R. Lu, J.X. Fang, J.E. Chen, Phys. Rev. Lett. 100 (2008) 135003.
[14] Y. Yin, W. Yu, M.Y. Yu, A. Lei, X. Yang, H. Xu, V.K. Senecha, Phys. Plasmas 15 (2008) 093106.
[15] M. Chen, A. Pukhov, Z.M. Sheng, X.Q. Yan, Phys. Plasmas 15 (2008) 113103.
[16] A.P.L. Robinson, P. Gibbon, M. Zepf, S. Kar, R.G. Evans, C. Bellei, Plasma Phys. Controlled Fusion 51 (2009) 024004.
[17] T.V. Liseikina, D. Prellino, F. Cornolti, A. Macchi, IEEE Trans. Plasma Sci. 36 (2008) 1866.
[18] T.V. Liseikina, M. Borghesi, A. Macchi, S. Tuveri, Plasma Phys. Controlled Fusion 50 (2008) 124033.
[19] F. Cattani, A. Kim, D. Anderson, M. Lisak, Phys. Rev. E 62 (2000) 1234.
[20] D. Prellino, Master's thesis, University of Pisa, Italy, 2007.
[21] A. Macchi, F. Ceccherini, F. Cornolti, S. Kar, M. Borghesi, Plasma Phys. Controlled Fusion 51 (2009) 024005.
[22] S.G. Rykovanov, J. Schreiber, J. Meyer-ter-Vehn, C. Bellei, A. Henig, H.C. Wu, M. Geissler, New J. Phys. 10 (2008) 113005.
[23] V.A. Vshivkov, N.M. Naumova, F. Pegoraro, S.V. Bulanov, Phys. Plasmas 5 (1998) 2727.
[24] F. Pegoraro, S.V. Bulanov, Phys. Rev. Lett. 99 (2007) 065002.
[25] I.V. Sokolov, Sov. Phys. Usp. 34 (1991) 925.
[26] M.G. Haines, Phys. Rev. Lett. 87 (2001) 135005.
[27] C. Thaury, F. Quéré, J.-P. Geindre, A. Levy, T. Ceccotti, P. Monot, M. Bougeard, F. Réau, P. d'Oliveira, P. Audebert, R. Marjoribanks, Ph. Martin, Nat. Phys. 3 (2007) 424.
[28] J. Badziak, S. Glowacz, S. Jablonski, P. Parys, J. Wolowski, H. Hora, J. Krása, L. Láska, K. Rohlena, Plasma Phys. Controlled Fusion 46 (2004) B541.

[29] S. Kar, M. Borghesi, S.V. Bulanov, M.H. Key, T.V. Liseykina, A. Macchi, A.J. Mackinnon, P.K. Patel, L. Romagnani, A. Schiavi, O. Willi, Phys. Rev. Lett. 100 (2008) 225004.

[30] K.U. Akli, S.B. Hansen, A.J. Kemp, R.R. Freeman, F.N. Beg, D.C. Clark, S.D. Chen, D. Hey, S.P. Hatchett, K. Highbarger, E. Giraldez, J.S. Green, G. Gregori, K.L. Lancaster, T. Ma, A.J. MacKinnon, P. Norreys, N. Patel, J. Pasley, C. Shearer, R.B. Stephens, C. Stoeckl, M. Storm, W. Theobald, L.D. Van Woerkom, R. Weber, M.H. Key, Phys. Rev. Lett. 100 (2008) 165002.

[31] L.O. Silva, M. Marti, J.R. Davies, R.A. Fonseca, C. Ren, F.S. Tsung, W.B. Mori, Phys. Rev. Lett. 92 (2004) 015002.

Ponderomotive Acceleration of Ions: Circular Versus Linear Polarization

Tatiana V. Liseikina, Domenico Prellino, Fulvio Cornolti, and Andrea Macchi

Abstract—**Ponderomotive (or radiation pressure) acceleration is a route to the generation of high-energy ions in laser–solid interactions, which does not rely on the generation of fast electrons. It may be optimized by the use of circularly polarized (CP) laser pulses rather than linearly polarized (LP) ones, since for CP, fast electron generation is strongly inhibited, quenching competing mechanisms such as target normal sheath acceleration. We present a comparison of 1-D and 2-D particle-in-cell simulations for CP and LP, which shows the potential of CP pulses for ion acceleration. The comparison also enables us to discriminate "pure" ponderomotive effects from those due to fast electrons, aiding the understanding of basic mechanisms of ion acceleration and surface rippling.**

Index Terms—**Circular polarization (CP), ion acceleration, laser–plasma accelerators, ponderomotive force (PF), radiation pressure acceleration (RPA).**

I. INTRODUCTION

WHEN a laser pulse with intensity typically in the 10^{17}–10^{20} W/cm^2 range impinges on a solid target, there is more than one possible route to energy transfer from the laser pulse to ions. The laser–plasma interaction at the front surface of the target can generate large numbers of "fast" electrons with several MeV of energy, which attempt to escape outside the target, creating a very strong electric field. At the rear side of the target, the electric field efficiently accelerates ions initially located on the surface, in particular, protons from hydrogen contaminants. This is the basis of the target normal sheath acceleration (TNSA) mechanism, leading to the production of proton beams with remarkable properties and several possible applications (see [1] for a review). Recent results have suggested that appropriate target engineering can improve the beam quality and control for both protons [2], [3] and heavier ions [4].

Another route to ion acceleration is based on the fundamental concept of the radiation pressure exerted by the laser pulse on the target. In an elementary description, the target may be represented by a mirror boosted by the total force $F \simeq (2I/c)S$, where I is the laser intensity, and S is the mirror surface. In a more detailed description, and within the assumption of adiabatic and quasi-equilibrium dynamics, the local force acting on ions is given by $Z\mathbf{f}_p$, where Z is the ion charge, and $\mathbf{f}_p$ is the steady ponderomotive force (PF) acting on electrons. In general, $\mathbf{f}_p = -m_e c^2 \nabla (1 + \langle \mathbf{a}^2 \rangle)^{1/2}$, where $\mathbf{a} = e\mathbf{A}/m_e c$, $\mathbf{A}$ is the vector potential, and the brackets denote a cycle average. Several theoretical studies on ion acceleration at the front surface are based on a ponderomotive picture where the ions "directly" gain momentum from the laser pulse [5]–[7]. A phenomenological description [6] shows that ion acceleration driven by the PF occurs at the front side of the target as a sequence of short ion bunches.

While in most of present-day experiments ion acceleration from solid targets is dominated by TNSA, the interest in ponderomotive or, more generally speaking, radiation pressure acceleration (RPA) arises from theoretical and simulation studies predicting that RPA becomes dominant at intensities exceeding 10^{23} W/cm^2 [8] and leads to very efficient production of highly collimated ions with energies approaching GeV values. The required intensities may become available in the next decade due to the building of novel laser facilities such as the Extreme Light Infrastructure.

It is, however, possible to obtain a regime of RPA dominance with present-day laser systems using circularly polarized (CP) pulses, instead of linearly polarized (LP) ones, at normal incidence. In fact, in this configuration, the generation of fast electrons is almost suppressed [6], strongly quenching TNSA and other effects driven by energetic electrons. Simulations of ion acceleration with CP in a thick overdense plasma target show high conversion efficiency, strong collimation, and the possibility of the ultrashort duration of the ion bunch [6], [9]. The use of ultrathin targets may further increase the ion energy and may lead to a mononergetic spectrum [10]–[12].

In this paper, we review our previous results on ion acceleration with CP, emphasizing the differences with the LP case. We also discuss more recent works related to issues such as analytical modeling, scaling laws for ion energy and conversion efficiency, and rippling instabilities at the target surface.

T. V. Liseikina is with the Dipartimento di Fisica "Enrico Fermi," Universitá di Pisa, 56127 Pisa, Italy, with the Institute of Computational Technologies, Siberian Division, Russian Academy of Sciences (SD RAS), 630090 Novosibirsk, Russia, and also with the Max Planck Institute for Nuclear Physics, 69117 Heidelberg, Germany.

D. Prellino was with the Dipartimento di Fisica "Enrico Fermi," Universitá di Pisa, 56127 Pisa, Italy. He is now with the German Cancer Research Center, 69120 Heidelberg, Germany.

F. Cornolti is with the Dipartimento di Fisica "Enrico Fermi," Universitá di Pisa, 56127 Pisa, Italy.

A. Macchi is with the polyLAB, CNR/INFM, 56127 Pisa, Italy and also with the Dipartimento di Fisica "Enrico Fermi," Universitá di Pisa, 56127 Pisa, Italy (e-mail: macchi@df.unipi.it).

Color versions of one or more of the figures in this paper are available online at http://ieeexplore.ieee.org.

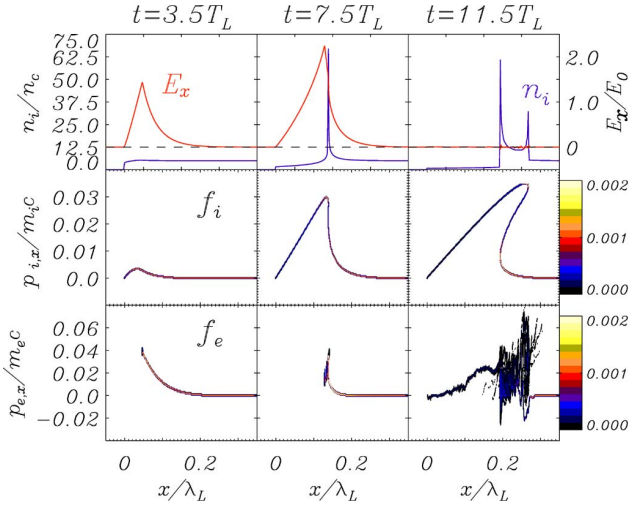Digital Object Identifier 10.1109/TPS.2008.927141

Fig. 1. One-dimensional PIC simulation of the interaction of a short CP laser pulse with an overdense step-boundary plasma. The figure shows the (top row, solid line) ion density n_i, (top row, dotted) electrostatic field E_x, and (x, p_x) phase-space distribution for (middle row) ions f_i and (bottom row) electrons f_e at different times in laser cycles. For a laser wavelength $\lambda_L = 1$ μm, the laser and plasma parameters correspond to an irradiance $I\lambda_L^2 = 5.5 \times 10^{18}$ W $\cdot$ μm^2/cm^2, a pulse duration $\tau_L = 20$ fs, and an initial electron density $n_e = 5.5 \times 10^{21}$ cm^{-3}. The x-coordinate is normalized to $\lambda_L = 1$ μm, the density to $n_c = 1.1 \times 10^{21}$ cm^{-3}, and the momenta to $m_e c$ and $m_i c$, respectively. The electric field is normalized to $E_n = m_e \omega_L c / e$.

II. THEORY

The physical basis for the difference between LP and CP when a laser pulse impinges at normal incidence on an overdense plasma (density $n_e > n_c$, where $n_c = m_e \omega_L^2 / 4\pi e^2$ is the cutoff density for an EM wave of frequency ω_L) is the absence of the oscillating component (at frequency $2\omega_L$) in the longitudinal $\mathbf{J} \times \mathbf{B}$ force for CP. In fact, fast electron generation at normal incidence is due to forced nonadiabatic oscillations of electron driven by the oscillating component, which is present only for LP. For CP, the $\mathbf{J} \times \mathbf{B}$ force has only the secular cycle-averaged component (i.e., the PF). Hence, the comparison between LP and CP is useful to separate effects due to the PF (i.e., due to radiation pressure) from those due to fast electrons. A simple phenomenological model of ponderomotive acceleration by ultrashort laser pulses was then formulated [6] on the basis of the dynamics observed in particle-in-cell (PIC) simulations.

Fig. 1 shows three snapshots from the interaction of a short CP pulse with an overdense plasma slab. In the early stage, we observe the generation of a strong electrostatic field due to the pushing of electrons by the PF. It can be shown that the PF and the electrostatic force produced by charge separation almost cancel each other, so that a quasi-equilibrium dynamics for electrons can be assumed and no substantial electron heating occurs, as can be observed in the phase-space distribution. The electrostatic field accelerates ions, leading to the formation of a very sharp peak of the ion density at the end of the skin layer, i.e., near the evanescence point of the EM field. When the fastest ions (coming from the target surface) overturn the slowest ones, hydrodynamical breaking occurs (which is apparent in the ion phase-space plot) and the density peak "splits" in

two parts, creating a narrow bunch of ions propagating into the target. We also observe that longitudinal heating of electrons (up to the modest energies) occurs after the "breaking" of the ion fluid. It may be interesting to notice that a rather similar dynamics has been observed in simulations of radial ponderomotive acceleration by a laser pulse propagating in an underdense ($n_e < n_c$) plasma [13].

The simple model accounting for the ion density spiking and subsequent breaking and providing scaling laws for ion bunch generation is described as follows: A linear profile of E_x is assumed both in the depletion layer ($E_x = E_0 x/d$ for $0 < x < d$) and in the compression region ($E_x = E_0[1 - (x - d)/l_s]$ for $d < x < d + l_s$), and a self-consistent uniform electron density n_{p0} is assumed in this latter region [see Fig. 2(a)]. The parameters E_0, n_{p0}, d, and l_s are related by the equations $E_0 = 4\pi e n_0 d$ (due to Poisson equation), $n_0(d + l_s) = n_{p0} l_s$ (due to global charge conservation), and $E_0 e n_0 l_s / 2 \simeq 2 I_L / c$ (due to the balance between the total radiation and electrostatic pressures). The "evanescence length" l_s can be chosen as the only free parameter. It can be estimated by a proper approximation of the exact initial equilibrium profile of PF for immobile ions, which can analytically be found [14], by the "*ad hoc*" profiles of Fig. 2. This approximation yields $l_s \simeq c/2\omega_p$ in the limit $d \ll l_s$ and shows a relatively weak dependence of l_s on the laser intensity and plasma density [15].

Starting from this configuration, the equations of ion motion are solved in Lagrangian coordinates, keeping the assumption of quasi-equilibrium between the PF and the electrostatic force. Since the electric field on a Lagrange particle is a constant in 1-D, this implies that the PF behaves in a similar way. Solving the equations of motion, it is easily found that the ions pile up in the region between the laser–plasma interface and the evanescence point [Fig. 2(b)], all reaching the latter at the same time τ_i. Here, the fastest ions overrun the slower ones, the density becomes singular [Fig. 2(c)], and hydrodynamical breaking occurs. After τ_i, the fluid description becomes inadequate, and a kinetic approach is needed. However, at least the fastest ions keep the velocity acquired before τ_i; thus, their energy can be estimated using the fluid model. The maximum ion velocity v_{im} and the breaking time τ_i [6] are given in the limit $d \ll l_s$ by

$$\frac{v_{\mathrm{im}}}{c} = 2\sqrt{\frac{Z}{A}\frac{m_e}{m_p}\frac{n_c}{n_e}}a_L \quad \tau_i \simeq \frac{1}{2\omega_L a_L}\sqrt{\frac{A}{Z}\frac{m_p}{m_e}}. \quad (1)$$

Here, $a_L = 0.85(I\lambda_L^2/10^{18}$ W $\cdot$ μm^2/cm$^2)^{1/2}$ is the dimensionless laser amplitude. Noting that the number of accelerated
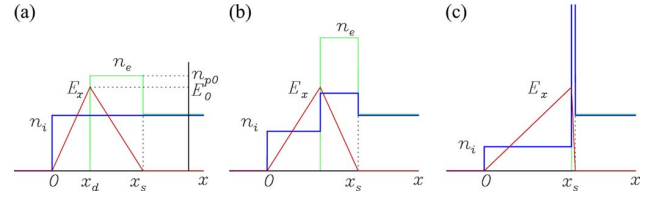

Fig. 2. Simple model of ponderomotive acceleration. (a) Initial equilibrium configuration with immobile ions. (b) Ion acceleration leads to compression of the ion profile. (c) Density peaks up to infinite values since all ions get to the point $x = d + l_s$ at the same time.
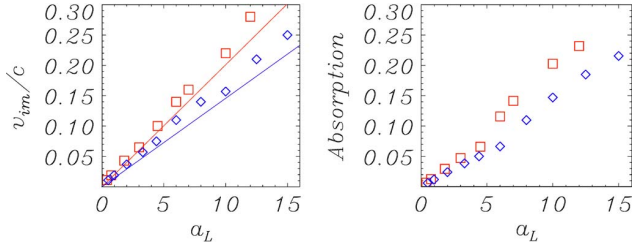
Fig. 3. Maximum ion velocity and energy conversion efficiency into ions versus laser pulse amplitude and plasma density from a set of parametric 1-D PIC simulations. (Red squares) Electron density $n_e = 5.4n_c$. (Blue diamonds) $n_e = 10.3n_c$. The straight lines in the velocity plot correspond to (1) for v_{im}. The simulations have been obtained for a pulse with a constant intensity starting from a configuration of an initial equilibrium with fixed ions.

ions per unit surface is $\simeq n_0 l_s$, the ion energy flux can be estimated as $\simeq m_i(v_m/2)^2 n_0 l_s/2$, corresponding to the energy conversion into ions $\simeq v_m/c$. If d is not small with respect to l_s, the model predicts a less favorable scaling of v_m versus a_L.

The predicted scalings have been tested by a set of parametric 1-D simulations. To separate a possible dependence upon the pulse duration, an initial equilibrium with fixed ions and a constant laser intensity are assumed in the simulations. To achieve the equilibrium configuration in the simulations, the laser pulse is switched off, adiabatically keeping the ions immobile; ions are released after the fields have reached the equilibrium profile (corresponding to the analytical solutions of [14]. Results are shown in Fig. 3 for two values of the plasma densities. The aforementioned linear dependence of ion velocity and conversion efficiency on the laser amplitude a_L is observed up to high amplitudes, beyond the range where $d \ll l_s$ may be assumed. These observed scalings (indeed promising for ponderomotive acceleration) suggest that a refinement of the simple model is required for very high intensities.

We conclude this section by noting that, since the secular component is also present in the LP case, the aforementioned model may also be used to estimate the contribution of ponderomotive acceleration at the front side for LP if the longitudinal force on ions is considered to be a temporal average over the laser cycle. Features such as the sharp spiking of the ion density (see, e.g., [16]) or the generation of dense bunches of ions with energies similar to what is predicted by the model (see next section) are also indeed observed in simulations with LP. However, the simultaneous presence of fast electrons affects the dynamics of ponderomotive acceleration, as, for example, the strong absorption into electrons reduces the total radiation pressure on the target, whereas the compression of ions into a single density spike can be counteracted by the strong thermal pressure of electrons.

III. CP VERSUS LP

To show the fundamental differences between the LP and CP cases, we compare simulations having the same target parameters (i.e., the same electron density n_e, charge-to-mass ratio Z/A, and target thickness L), as well as pulse intensity I and duration τ_L, the only difference being the laser polarization. The chosen parameters are close to those of simulations by
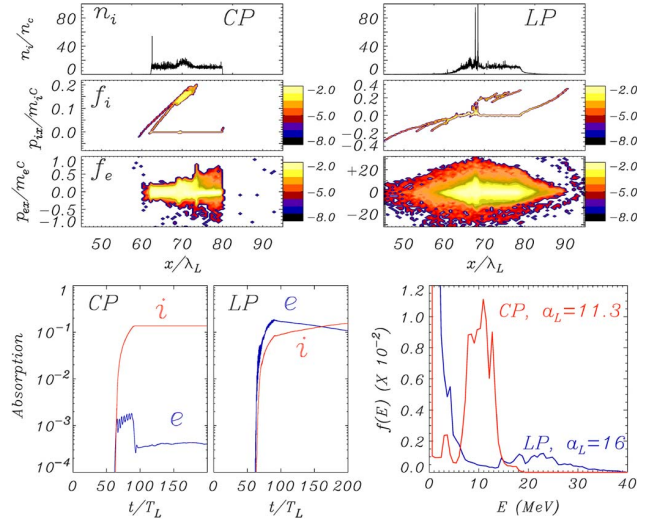

Fig. 4. Comparison of 1-D simulation results for CP and LP. (Top frame) Snapshots of the ion density n_i and the (x, p_x) phase-space projections of ions f_i and electrons f_e for (left column) CP and (right column) LP. The time $t = 467$ fs is measured from the instant at which the front of the laser pulse (propagating from left to right) reaches the target. Normalizations are as in Fig. 1. (Bottom frame) Energy conversion efficiency into ions and electrons versus (left) time and (right) energy spectrum of ions. Simulation parameters are $\tau_L = 86$ fs, $I = 3.5 \times 10^{20}$ W/cm^2, $n_e = 10^{22}$ cm^{-3}, $L = 20$ μm, and $Z/A = 1$.

Silva et al. [5], where (using LP) it is claimed that the ion acceleration due to the generation of a collisionless shock wave is dominant over TNSA. We compare the simulation results for CP and LP both in 1-D and 2-D geometries. Details of the simulation setup are reported in [9].

A. 1-D Simulations

Fig. 4 compares the ion density profiles and the phase-space projection $f(x, p_x)$ of ions and electrons for CP and LP. For CP, at the chosen irradiance $I = 3.5 \times 10^{20}$ W $\cdot \mu$m^2/cm^2, a very few electrons with a longitudinal momentum larger than $0.5m_e c$ are found. In contrast, for LP, the generation of strongly relativistic electrons with maximum longitudinal momenta $p_{ex} \simeq 30m_e c$ is observed. In the ion phase-space plot, for CP, we observe only one population of "fast" ions, with typical momenta $p_x \simeq 0.15m_i c$. No ions accelerated by TNSA are found. For LP, ions accelerated by TNSA are observed both at the front and rear sides of the target, with similar momentum values (up to $\simeq 0.3m_i c$). This "symmetric" feature of TNSA occurs when the density gradient at the front side is as sharp as at the rear side and has recently been experimentally confirmed by prepulse-free measurements [17]. A third group of ions, accelerating at the front side and propagating inside the target at the time shown, is observed and attributed to ponderomotive acceleration.

The conversion efficiency of laser pulse energy into ion energy (Fig. 4, left bottom frame) for CP is close to 0.14, whereas the conversion into electron energy is negligible. Notice that the ion energy remains constant after the laser pulse is over. In contrast, for LP, the conversion into electron energy is dominant at early times, and ions continue to acquire energy
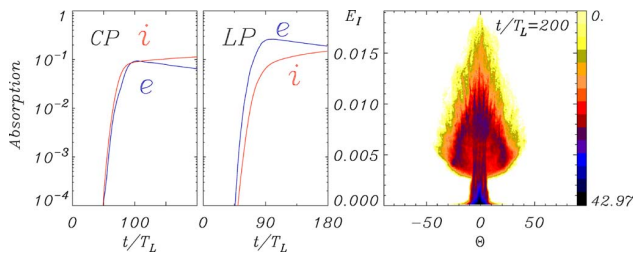
Fig. 5. Comparison of 2-D simulation results for CP and LP. (Left) Energy conversion efficiency into ions and electrons versus time. (Right) Energy versus angle distribution of ions. The laser pulse profile is Gaussian with a waist radius $r_L = 2\ \mu$m. The peak intensity on axis is equal to the intensity of the 1-D case. Other parameters are the same as in Fig. 4.

at late times due to TNSA. The conversion efficiency for the ponderomotively accelerated ions is, however, also relatively high (around 0.1) for LP. Strong differences are also noticeable in the ion energy spectra (Fig. 4, right bottom frame), showing for CP a peak around 10 MeV but a thermal-like spectrum for LP overlapping over a broad maximum around 20 MeV.

B. 2-D Simulations

The absence of oscillating forces driving electrons across the sharp laser–plasma interface for CP pulses is strictly true only for a plane wave. A laser pulse focused to a spot size of a few wavelengths has off-axis longitudinal electric field components oscillating at the laser frequency ω_L, whose amplitude is on the order of λ_L/r_L times the peak field amplitude, where r_L is the waist radius. However, 2-D simulations show that even for tightly focused pulses, electron heating indeed occurs at distances $\simeq r_L$ from the axis and increases energy absorption into electrons, but weakly affects the features of ion acceleration with CP. This can be noticed in Fig. 5(a), which shows the energy conversion into ions and electrons for 2-D simulations with the same plasma parameters and the same pulse duration of the 1-D case (see Fig. 4) and a Gaussian transverse profile with $r_L = 2\lambda_L$. The intensity at the center of the spot in 2-D simulations is equal to the intensity in 1-D simulations. The efficiency of energy conversion into ions is about 0.1 in the 2-D CP case. Fig. 5(b) shows the $f(E, \Theta)$ distribution of ions, where Θ is the emission angle with respect to the target normal. Ions with energy $> 0.01 m_i c^2$ have an angular spread of $\simeq 10°$.

C. Surface Rippling

The 2-D simulations also show that the onset of density rippling at the target surface is affected by the pulse polarization. The comparison between CP and LP results in Fig. 6 shows that at early times ($t = 80$ laser cycles), surface ripples are much deeper for LP than for CP, and that the density in the region near the surface evolves in a more "turbulent" state in the LP case. For CP, density rippling is also evident, but the structures are more regular and less deep than in the LP case.

Rippling of the front surface was already observed in early simulations of high-intensity laser pulse interaction with over-
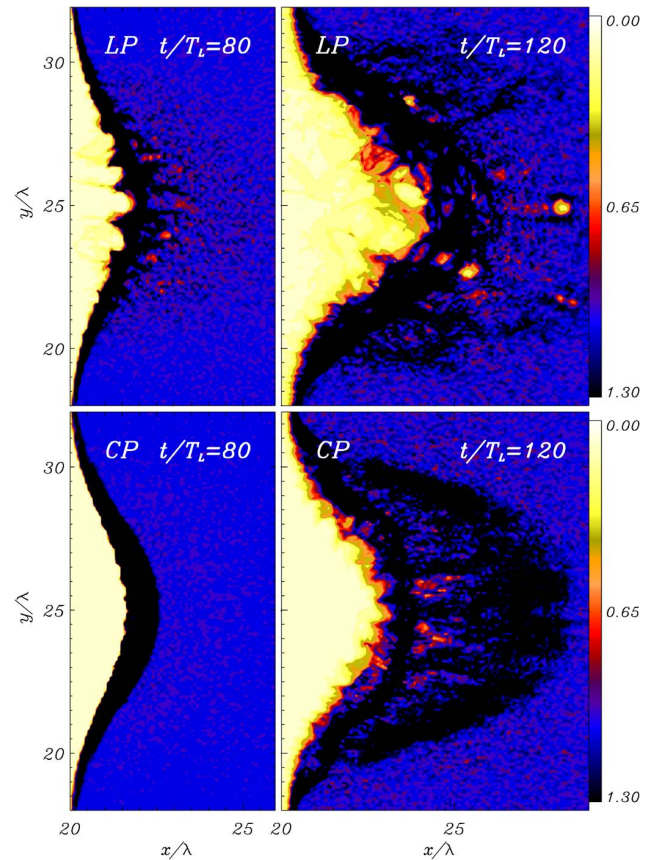

Fig. 6. Contours of the ion density from 2-D simulation results for CP and LP at two different times, showing the growth of surface rippling at the laser-irradiated surface. Simulation parameters are the same as in Fig. 5.

dense plasmas [18], [19]. Recently, this topic has been revisited for thin plasma foils accelerated in the radiation-pressure-dominated regime [20]. Explanations of the surface rippling have mostly been based on Rayleigh–Taylor-like instabilities due to the strong acceleration of the target driven by the radiation pressure. To test such theoretical description and its scaling with laser and plasma parameters, the case of CP interaction is most adequate as radiation pressure dominance holds at any intensity. On the other hand, the difference observed between CP and LP suggests that additional effects are at play for LP. These effects might be due to fast electrons or stimulated surface instabilities [21].

The surface rippling appears to affect ion acceleration at the front surface. In the density plot for CP at $t = 120$ cycles in Fig. 6, the curved front of ponderomotively accelerated ions is clearly visible, which is consistent with the quite regular angular distribution shown in Fig. 5. No well-defined ion front is observed for LP. In this latter case, we also notice the generation of density "holes" (e.g., at $(x, y) \simeq (31, 25)$ for $t = 120$). Analysis of electromagnetic fields inside such holes shows that they behave as "optical microcavities," trapping radiation at a frequency lower than the plasma frequency of the surrounding plasma. These structures are similar to the so-called "postsolitons" (see, e.g., [22]), which, however, have mostly been studied in underdense plasmas so far.

IV. Discussion and Conclusion

The use of CP, instead of LP, at normal incidence strongly affects the dynamics of ion acceleration in laser interaction with overdense plasmas. Due to the quenching of fast electron generation, using CP, a regime of purely ponderomotive acceleration, i.e., of radiation pressure dominance, may already be obtained at moderate intensities. Our theoretical and simulation studies of "thick" targets showed that the ponderomotively accelerated ions may have properties such as high efficiency, large density, and good collimation, which may be interesting for specific applications.

The CP radiation-pressure-dominated regime should extend over a wide range of intensities above the typical values, where collective effects, instead of collisional ones, dominate the laser–plasma interaction. This is usually the case at intensities above 10^{18} W/cm^2. The scaling of ion energy and conversion efficiency that have been inferred from parametric PIC simulations look promising for experiments at higher intensities. It is possible that CP represents an optimal choice for ion acceleration in the ultrahigh-intensity regimes, where ions become relativistic [8], [23]. However, our theoretical picture may not anymore be appropriate at such intensities. For example, as the ions become faster while electrons acquire increased relativistic inertia in the laser fields, the two species tend to stick together, and it is not anymore justified to assume different temporal scales for their motion. In addition, as the threshold for induced relativistic transparency is reached for a given density, the laser pulse penetrates into the plasma, and the laser–plasma coupling completely changes.

From the point of view of theoretical understanding, the use of CP in simulations is useful to separate purely ponderomotive (radiation pressure) effects from those due to fast electrons. For example, as we have shown in 2-D simulations, this may help unfold mechanisms driving surface rippling of the plasma. It is interesting to notice that for LP, where ion acceleration due to TNSA occurs, a significant fraction of ponderomotively accelerated ions at the front surface are observed in simulations. One may then wonder why so far in experiments the observed generation of MeV ions (mostly protons) has successfully been explained by the effect of TNSA only, leaving weak or no evidence for ponderomotive acceleration. In addition to checking if the interaction conditions and the diagnostics in the experiments allowed the detection of such ions, a possible explanation is due to the fact that ions accelerated at the front surface in the forward direction have to cross the target at solid density. Thus, collisional stopping may play an important role, particularly if the ponderomotively accelerated ions are not protons from the surface but bulk ions at higher Z, as would probably be the case for an interaction affected by prepulse effects. Thus, quite thin targets (on the order of 1 μm) would probably be required to observe ponderomotively accelerated ions. Ultrathin targets (typically less than one tenth of a micrometer thick) may be accelerated as a whole by CP pulses and, under proper conditions, allow one to reach very high ion energies [10]–[12]. Finally, we note that these claims have also been made in another recent paper [24], where, however, in our opinion, no substantially new result or concept has been reported with respect to a previous work.
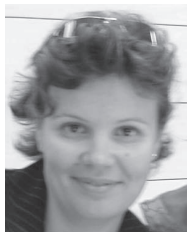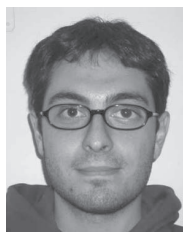
References

[1] M. Borghesi, J. Fuchs, S. V. Bulanov, A. J. MacKinnon, P. K. Patel, and M. Roth, "Fast ion generation by high-intensity laser irradiation of solid targets and applications," *Fusion Sci. Technol.*, vol. 49, no. 3, pp. 412–439, 2006. [Online]. Available: http://www.ans.org/pubs/journals/fst/va-49-3-412-439

[2] H. Schwoerer, S. Pfotenhauer, O. Jaeckel, K. U. Amthor, B. Liesfeld, W. Ziegler, R. Sauerbrey, K. W. D. Ledingham, and T. Esirkepov, "Laser–plasma acceleration of quasi-monoenergetic protons from microstructured targets," *Nature*, vol. 439, no. 7075, pp. 445–448, Jan. 2006. [Online]. Available: http://dx.doi.org/10.1038/nature04492

[3] T. Toncian, M. Borghesi, J. Fuchs, E. d'Humierers, P. Antici, P. Audebert, E. Brambrink, C. A. Cecchetti, A. Pipahl, L. Romagnani, and O. Willi, "Ultrafast laser driven microlens to focus and energy-select mega-electron volt protons," *Science*, vol. 312, no. 5772, pp. 410–413, Apr. 2006. [Online]. Available: http://dx.doi.org/10.1126/science.1124412

[4] B. M. Hegelich, B. J. Albright, J. Cobble, K. Flippo, S. Letring, M. Paffett, H. Ruhl, J. Schreiber, R. K. Schulze, and J. C. Fernandez, "Laser acceleration of quasi-monoenergetic MeV ion beams," *Nature*, vol. 439, no. 7075, pp. 441–444, Jan. 2006. [Online]. Available: http://dx.doi.org/10.1038/nature04400

[5] L. O. Silva, M. Marti, J. R. Davies, R. A. Fonseca, C. Ren, F. S. Tsung, and W. B. Mori, "Proton shock acceleration in laser–plasma interactions," *Phys. Rev. Lett.*, vol. 92, no. 1, p. 015 002, 2004. [Online]. Available: http://link.aps.org/abstract/PRL/v92/e015002

[6] A. Macchi, F. Cattani, T. V. Liseykina, and F. Cornolti, "Laser acceleration of ion bunches at the front surface of overdense plasmas," *Phys. Rev. Lett.*, vol. 94, no. 16, p. 165 003, 2005. [Online]. Available: http://link.aps.org/abstract/PRL/v94/e165003

[7] J. Badziak, S. Jablonski, and S. Glowacz, "Generation of highly collimated high-current ion beams by skin-layer laser–plasma interaction at relativistic laser intensities," *Appl. Phys. Lett.*, vol. 89, no. 6, p. 061 504, 2006. [Online]. Available: http://link.aip.org/link/?APL/89/061504/1

[8] T. Esirkepov, M. Borghesi, S. V. Bulanov, G. Mourou, and T.Tajima, "Highly efficient relativistic-ion generation in the laser–piston regime," *Phys. Rev. Lett.*, vol. 92, no. 17, p. 175 003, 2004. [Online]. Available: http://link.aps.org/abstract/PRL/v92/e175003

[9] T. V. Liseikina and A. Macchi, "Features of ion acceleration by circularly polarized laser pulses," *Appl. Phys. Lett.*, vol. 91, no. 17, p. 171 502, 2007. [Online]. Available: http://link.aip.org/link/?APL/91/171502/1

[10] X. Zhang, B. Shen, X. Li, Z. Jin, and F. Wang, "Multistaged acceleration of ions by circularly polarized laser pulse: Monoenergetic ion beam generation," *Phys. Plasmas*, p. 073 101, vol. 14, no. 7, 2007. [Online]. Available: http://link.aip.org/link/?PHP/14/073101/1

[11] A. P. L. Robinson, M. Zepf, S. Kar, R. G. Evans, and C. Bellei, "Radiation pressure acceleration of thin foils with circularly polarized laser pulses," *New J. Phys.*, vol. 10, no. 1, p. 013 021, 2008. [Online]. Available: http://stacks.iop.org/1367-2630/10/013021

[12] O. Klimo, J. Psikal, J. Limpouch, and V. T. Tikhonchuk, "Monoenergetic ion beams from ultrathin foils irradiated by ultrahigh-contrast circularly polarized laser pulses," *Phys. Rev. ST Accel. Beams*, vol. 11, no. 3, p. 031 301, Mar. 2008. [Online]. Available: http://link.aps.org/abstract/PRSTAB/v11/e031301

[13] A. Macchi, F. Ceccherini, F. Cornolti, S. Kar, and M. Borghesi, *Ponderomotive Laser Ion Acceleration and Electric Field Dynamics Following Charge-Displacement Channeling*, 2007. e-print arXiv:physics/0701139. [Online]. Available: http://arxiv.org/abs/physics/0701139

[14] F. Cattani, A. Kim, D. Anderson, and M. Lisak, "Threshold of induced transparency in the relativistic interaction of an electromagnetic wave with overdense plasmas," *Phys. Rev. E, Stat. Phys. Plasmas Fluids Relat. Interdiscip. Top.*, vol. 62, no. 1, pp. 1234–1237, Jul. 2000. [Online]. Available: http://link.aps.org/abstract/PRE/v62/p1234

[15] D. Prellino, "Ponderomotive acceleration of ions via laser–plasma interaction," M.S. thesis, Univ. Pisa, Pisa, Italy, 2007.

[16] Y. Sentoku, T. E. Cowan, A. Kemp, and H. Ruhl, "High energy proton acceleration in interaction of short laser pulse with dense plasma target," *Phys. Plasmas*, vol. 10, no. 5, pp. 2009–2015, 2003. [Online]. Available: http://link.aip.org/link/?PHP/10/2009/1

[17] T. Ceccotti, A. Levy, H. Popescu, F. Reau, P. D'Oliveira, P. Monot, J. P. Geindre, E. Lefebvre, and P. Martin, "Proton acceleration with high-intensity ultrahigh-contrast laser pulses," *Phys. Rev. Lett.*, vol. 99, no. 18, p. 185 002, 2007. [Online]. Available: http://link.aps.org/abstract/PRL/v99/e185002

[18] S. C. Wilks, W. L. Kruer, M. Tabak, and A. B. Langdon,"Absorption of ultra-intense laser pulses," *Phys. Rev. Lett.*, vol. 69, no. 9, pp. 1383–1386, 1992. [Online]. Available: http://link.aps.org/abstract/PRL/v69/p1383

[19] S. C. Wilks and W. L. Kruer, "Absorption of ultrashort, ultra-intense laser light by solids and overdense plasmas," *IEEE J. Quantum Electron.*, vol. 33, no. 11, pp. 1954–1968, Nov. 1997. [Online]. Available: http://dx.doi.org/10.1109/3.641310

[20] F. Pegoraro and S. V. Bulanov, "Photon bubbles and ion acceleration in a plasma dominated by the radiation pressure of an electromagnetic pulse," *Phys. Rev. Lett.*, vol. 99, no. 6, p. 065 002, 2007. [Online]. Available: http://link.aps.org/abstract/PRL/v99/e065002

[21] A. Macchi, F. Cornolti, F. Pegoraro, T. V. Liseikina, H. Ruhl, and V. A. Vshivkov, "Surface oscillations in overdense plasmas irradiated by ultrashort laser pulses," *Phys. Rev. Lett.*, vol. 87, no. 20, p. 205 004, 2001. [Online]. Available: http://link.aps.org/abstract/PRL/v87/e205004

[22] M., Borghesi, S. Bulanov, D. H. Campbell, R. J. Clarke, T. Z. Esirkepov, M. Galimberti, L. A. Gizzi, A. J. MacKinnon, N. M. Naumova, F. Pegoraro, H. Ruhl, A. Schiavi, and O. Willi, "Macroscopic evidence of soliton formation in multiterawatt laser–plasma interaction," *Phys. Rev. Lett.*, vol. 88, no. 13, p. 135 002, 2002. [Online]. Available: http://link.aps.org/abstract/PRL/v88/e135002

[23] F. Pegoraro, S. V. Bulanov, F. Califano, T. Z. Esirkepov, T. V. Liseikina, N. M. Naumova, H. Ruhl, and V. A. Vshivkov, "Ion acceleration regimes in underdense plasmas," *IEEE Trans. Plasma Sci.*, vol. 28, no. 4, pp. 1177–1183, Aug. 2000. [Online]. Available: http://dx.doi.org/10.1109/27.893311

[24] X. Q. Yan, C. Lin, Z. M. Sheng, Z. Y. Guo, B. C. Liu, Y. R. Lu, J. X. Fang, and J. E. Chen, "Generating high-current monoenergetic proton beams by a circularly polarized laser pulse in the phase-stable acceleration regime," *Phys. Rev. Lett.*, vol. 100, no. 13, p. 135 003, 2008. [Online]. Available: http://link.aps.org/abstract/PRL/v100/e135003

Domenico Prellino was born in 1981. He received the B.S. and M.S. degrees in physics from the Universitá di Pisa, Pisa, Italy, in 2005 and 2007, respectively, with an M.S. thesis on "Ponderomotive acceleration of ions via laser–plasma interaction." He is currently working toward the Ph.D. degree at the German Cancer Research Center, Heidelberg, Germany, focusing on theoretical and numerical modeling of biological systems.

Fulvio Cornolti was born in 1949. He received the M.S. degree from the Universitá di Pisa, Pisa, Italy, in 1974.

He is currently an Associate Professor of plasma physics and nonlinear models in physics with the Dipartimento di Fisica "Enrico Fermi," Universitá di Pisa. His main interests are plasma physics, nonlinear optics, and laser–matter interactions.

Tatiana V. Liseikina was born in 1973. She received the M.S. degree from Novosibirsk State University, Novosibirsk, Russia, in 1995 and the Ph.D. degree in physics and mathematics from the Institute of Theoretical and Applied Mechanics, Siberian Division, Russian Academy of Sciences (SD RAS), Novosibirsk, in 1998.

She has been a Senior Researcher with the Institute of Computational Technologies, SD RAS, since 2004. Since 2007, she has been a Visiting Scientist with the Dipartimento di Fisica "Enrico Fermi," Universitá di Pisa, Pisa, Italy. Since April 2008, she has been a Visiting Scientist with the Max Planck Institute for Nuclear Physics, Heidelberg, Germany. Her current research interests are the theory and simulation of laser–plasma interactions, as well as the development of algorithms and numerical codes for the simulation of many-particle systems.

Andrea Macchi was born in 1970. He received the M.S. degree from the Universitá di Pisa, Pisa, Italy, in 1995 and the Ph.D. degree in physics from the Scuola Normale Superiore, Pisa, in 1999.

He has been a Research Fellow with the Italian National Research Council–National Institute for the Physics of Matter (CNR–INFM), Pisa, Italy, since 2003 and has been affiliated with the polyLAB since 2005. His current research interests are the theory and simulation of laser–plasma interactions, particularly ion acceleration and generation of coherent electromagnetic structures.

Radiation pressure acceleration by ultraintense laser pulses

Tatiana V Liseykina[1,2]**, Marco Borghesi**[3]**, Andrea Macchi**[3,4,5] **and Sara Tuveri**[5]

[1] Max Planck Institute for Nuclear Physics, Heidelberg, Germany
[2] Institute of Computational Technologies SD RAS, Novosibirsk, Russia
[3] School of Mathematics and Physics, the Queen's University of Belfast, Belfast, UK
[4] polyLab, CNR-INFM, Pisa, Italy
[5] Dipartimento di Fisica 'Enrico Fermi', Università di Pisa, Pisa, Italy

E-mail: Tatyana.Liseykina@mpi-hd.mpg.de

Abstract
The future applications of the short-duration, multi-MeV ion beams produced in the interaction of high-intensity laser pulses with solid targets will require improvements in the conversion efficiency, peak ion energy, beam monochromaticity and collimation. Regimes based on radiation pressure acceleration (RPA) might be the dominant ones at ultrahigh intensities and most suitable for specific applications. This regime may be reached with present-day intensities using circularly polarized (CP) pulses thanks to the suppression of fast electron generation, so that RPA dominates over sheath acceleration at any intensity. We present a brief review of a previous work on RPA with CP pulses and a few recent results. Parametric studies in one dimension were performed to identify the optimal thickness of foil targets for RPA and to study the effect of a short-scalelength preplasma. Three-dimensional simulations show the importance of 'flat-top' radial intensity profiles to minimize the rarefaction of thin targets and address the issue of angular momentum conservation and absorption.

(Some figures in this article are in colour only in the electronic version)

1. Introduction

In 1962, Forward considered the possibility of interstellar travel by a rocket propelled by an Earth-based laser beam (see [1] and references therein). The concept is as simple as follows: the rocket's engine and fuel are replaced by a light sail, i.e. a mirror, and the force exerted on the sail due to the radiation pressure of the laser light boosts the rocket. In 1966, Marx [2] found that the *efficiency* of the system, i.e. the ratio between the mechanical energy of the object accelerated by the laser beam and the energy contained in the laser beam itself, would

T V Liseykina *et al*

approach unity as the velocity of the object approaches the speed of light. An heuristic (though incomplete) argument might be given in terms of light quanta, i.e. photons, although the system can be described as entirely classical: let us consider a 'perfect' mirror irradiated by a monochromatic light wave of frequency ω, which contains a certain number N of photons and thus has a total energy $N\hbar\omega$. The mirror reflects photons conserving their number in any reference frame. If the mirror has an (instantaneous) velocity $V = \beta c$ in the laboratory frame, the frequency of the reflected photons is $\omega' = \omega(1 - \beta)/(1 + \beta)$. Thus, since N is invariant, the energy of the reflected pulse tends to zero if $V \rightarrow c$, so that a mirror moving at a speed close to c absorbs almost all the energy of the incident pulse.

Marx paper's conclusions turned out to be right although its approach needed a critical revision, as can be found in the rigorous and pedagogical description of [3]. According to the formulas in [3] it would take three years for a 10 TW laser to accelerate a 10^3 kg rocket to $V = (4/5)c$. Scaling this result to the typical parameters of superintense laser pulses and micro-targets, we obtain that about 5×10^{10} carbon ions might be accelerated to the same speed in 1 ps by a 1 PW laser, which is within the capabilities of the present technology. Note that the required acceleration length would be of the order of 100 μm, which is a suitable value for the Rayleigh length, so that laser pulse diffraction should not be a strong limiting factor on the achievable energies. This makes the perspective of radiation pressure acceleration (RPA) attractive for applications requiring large numbers of relativistic ions.

Nearly all of the experiments reported in the last decade on the acceleration of ions (mainly protons) by superintense laser pulses (see e.g. [4, 5] and references therein) are not based on RPA but instead on the target normal sheath acceleration (TNSA) mechanism, in which ions are accelerated by space-charge fields created by multi-MeV electrons escaping into vacuum. The dominance of RPA over TNSA in thin solid targets irradiated at intensities higher than those of present-day experiments has been claimed by Esirkepov and coworkers [6, 7], on the basis of simulations showing a transition occurring at some intensity value above 10^{21} W cm^{-2}, with a strong dominance leading to the so-called 'piston' regime over 10^{23} W cm^{-2}. Such an intensity may be available only in several years from now thanks to the development of advanced laser facilities. Experimentally, a preliminary indication of RPA effects in thin targets at intensities approaching 10^{20} W cm^{-2} has been published recently [8] (some experimental results on ion acceleration at intensities $\leqslant 10^{18}$ W cm^{-2} were also interpreted in terms of purely ponderomotive, i.e. radiation pressure effects [9]).

The question then arises whether it is possible to achieve an RPA-dominated regime already at lower intensity; this corresponds in practice to quenching the generation of high-energy electrons which drive TNSA but do not contribute to RPA. This may be possible using circularly polarized (CP) laser pulses at normal incidence because the *oscillating* components of the Lorentz force in the direction perpendicular to the sharp density gradient vanish (for a plane wave) or are relatively small (for a finite laser spot size): as a consequence, the motion of electrons at the interaction surface is predominantly adiabatic and electron heating is strongly reduced, while the space-charge field created to balance the local radiation pressure (i.e. the ponderomotive force) accelerates ions.

The strong differences between the cases of linearly polarized (LP) and CP pulses have been evidenced in some papers by our group [10, 11], mostly for the case of 'thick' targets, i.e. thicker than the skin layer. These studies showed that for CP the interaction accelerates all the ions in the skin layer and the fastest ones produce a very dense 'bunch' with a narrow energy spectrum, directed in the forward direction.

Recently, the experimental availability of ultrathin targets (i.e. with thickness down to a few nanometers) and high contrast laser pulses (see, e.g. [12–14]) has called for studies of CP-RPA

with such pulses and targets. The simulations performed independently by several groups [15–19] suggest that indeed the whole target may be accelerated, leading to efficient generation of large numbers of ions with monoenergetic spectra in the near-GeV range. Presently, no experiment using CP pulses at normal incidence has been reported in publications yet, but several related proposals have been made, so that the CP-RPA concept is expected to be explored soon.

    This paper reviews the main issues of CP-RPA and reports novel numerical results on parametric studies in one spatial dimension (1D), showing the role of the target thickness and the case of RPA in short-scalelength preformed plasmas, as well as first results in fully 3D geometry where, in particular, the issue of angular momentum conservation can be addressed.

2. Theory and earlier work

Firstly we shall provide a brief description of the interaction in the case of a thick target. The ponderomotive force of the laser pulse causes the electrons to pile up in the skin layer until it is balanced by the charge separation field that accelerates the ions. The ions produce a sharp density spike at the end of the skin layer where hydrodynamical breaking occurs, with the faster ions creating a dense bunch (with a narrow spectrum) that moves ballistically into the plasma (a rather similar dynamics has been noted in the case of radial ponderomotive acceleration of ions in an underdense plasma [20]). A detailed physical description and a simple model of RPA in thick targets (assuming *a priori* non-relativistic ions) have been given in previous works [10, 21]. The model provides the following scaling, valid for sub-relativistic ion velocities, for the maximum ion velocity (which almost corresponds to the bunch velocity) and the corresponding energy:

$$\frac{v_{\mathrm{im}}}{c} = 2\sqrt{\frac{Z}{A}\frac{m_{\mathrm{e}}}{m_{\mathrm{p}}}\frac{n_{\mathrm{c}}}{n_{\mathrm{e}}}}a_{\mathrm{L}}, \qquad \mathcal{E}_{\mathrm{m}} = \frac{m_{\mathrm{i}}}{2}v_{\mathrm{im}}^2 = 2m_{\mathrm{e}}c^2 Z\frac{n_{\mathrm{c}}}{n_{\mathrm{e}}}a_{\mathrm{L}}^2, \tag{1}$$

where $n_{\mathrm{c}} = m_{\mathrm{e}}\omega^2/4\pi e^2 = 1.1 \times 10^{21}\,\mathrm{cm}^{-3}$ is the cut-off density for the laser wavelength $\lambda = 2\pi c/\omega$, n_{e} is the background electron density, $a_{\mathrm{L}} = eE_{\mathrm{L}}/m_{\mathrm{e}}\omega c = 0.85(I\lambda^2/10^{18}\,\mathrm{W\,cm}^{-2})$ is the dimensionless amplitude of the laser pulse with electric field E_{L} and intensity I and other symbols are standard. Actually, this result has been derived in the limit of a relatively low intensity, but this scaling has been found to hold up to a much higher intensity in parametric 1D simulations [21].

    The ion bunch is formed in a time of the order of $\sim c/\omega_{\mathrm{p}}v_{\mathrm{im}}$ (where ω_{p} is the plasma frequency) after which it exits the skin layer accompanied by neutralizing electrons, and the laser pulse may accelerate a new layer. If energies higher than the above estimate must be reached, it is necessary to repeat the acceleration stage on the same ions, i.e. the target must be thin enough in order to bunch and accelerate all ions via several cycles. Simulation results on the acceleration of ultrathin targets have been interpreted with the model of the accelerating mirror [17] (where the mirror is assumed to be a 'rigid' object, neglecting any internal dynamics).

    Although a few authors have proposed the RPA of a thin foil as a way to generate high-energy protons, this approach seems to be most interesting for the acceleration of higher-Z ions. In fact, while it seems technologically unfeasible to have an ultrathin target made of hydrogen only, in a target made of multiple species all the ions will be accelerated to the same velocity, resulting in higher energies for the heavier species. If a lighter species (e.g. hydrogen) is present, these ions will be first accelerated overtaking the heavier ones. This will cause them to decouple from the laser pulse, which is screened by the heavier ion layer. The

heavier ions will be accelerated until they reach the lighter ions, allowing the laser to reach them and accelerate them further. In the end all species will have the same velocity. Due to this effect, for an ultrathin target of a single material (e.g. carbon) a monoenergetic ion spectrum is expected.

The above picture of the acceleration dynamics should change when the ions finally reach a speed close to c, as they will no longer be separated from the electrons. The 'laser-piston' regime investigated by Esirkepov *et al* [6] corresponds to conditions in which the ions are promptly accelerated to relativistic velocities and stick to the electrons, which may not be assumed to be in a mechanical quasi-equilibrium anymore. In this paper we restrict our analysis to the regime of non-relativistic ions because near-term experiments on RPA are unlikely to have the potential to accelerate ions up to strongly relativistic energies.

The theoretical picture and the predicted scalings have been supported by 1D simulations. So far multi-dimensional effects have been addressed at most by 2D simulations for both thick [10, 11, 21] and thin [17–19] targets. In the thick target cases, the energy spectrum is basically determined by the convolution of the 1D scaling law with the intensity profile of the pulse. The angle of emission of ions is energy dependent, but a good collimation is already obtained for a Gaussian pulse profile [11]. For thin targets, the use of a flat-top profile increases the monoenergeticity and collimation and quenches the heating of electrons, as expected [17, 18].

The issue of target stability during RPA has been addressed in thin foil 2D simulations for CP [18] and also for linear polarization in the ultraintense regime [22], showing a bending instability which has been interpreted to be of the Rayleigh–Taylor type and hence can be described in terms of the radiation pressure only. Simulations for thick targets, however, have shown that surface instabilities are weaker for CP pulses than for the LP ones. The quality of the ion beam is expected to be lower for linear polarization [21].

3. 1D simulations

3.1. The role of the target thickness

We performed a parametric study to determine the optimal values of target thickness d to obtain a higher efficiency and/or ion energy for given laser parameters. In order to be able to cover a quite wide range of parameters and to simulate 'realistic' target densities we used 1D simulations, which in the CP-RPA regime have so far proved to yield efficiency and ion energy values close to those from 2D or 3D simulations for those cases where a comparison is possible (i.e. for moderate density values). Results are shown in figure 1. The electron density of the target and the pulse duration were kept constant for all runs and corresponded, for a laser wavelength $\lambda = 0.8\,\mu$m, to $n_e = 4.3 \times 10^{23}\,\mathrm{cm}^{-3}$ and $\tau_L = 24$ fs. The three values of the dimensionless amplitude that were studied ($a = 2.9$, 9.2 and 29) corresponded to intensities $I = 1.8 \times 10^{19}\,\mathrm{W\,cm}^{-2}$, $1.8 \times 10^{20}\,\mathrm{W\,cm}^{-2}$ and $1.8 \times 10^{21}\,\mathrm{W\,cm}^{-2}$, respectively.

The values of d for which efficiency and ion energy have their maximum are close to each other and, as expected, they correspond to ultrathin, sub-micrometer targets. The strong decrease in efficiency and energy for smaller values of d may be explained with the onset of relativistically induced transparency in the thin foil when $d \simeq \lambda a (n_c/n_e)$ [23], so that the total radiation pressure on the target decreases. This point will be further discussed below when three-dimensional effects are addressed (section 4).

The energy per nucleon reported in figure 1 can be scaled to all species with $Z/A = 1/2$. For carbon ($A = 12$) the highest energy of 0.96 GeV is obtained for $a = 29$ and $d = 0.025\lambda$. Note that these are 'peak' energies which correspond to a distinct maximum in the ion
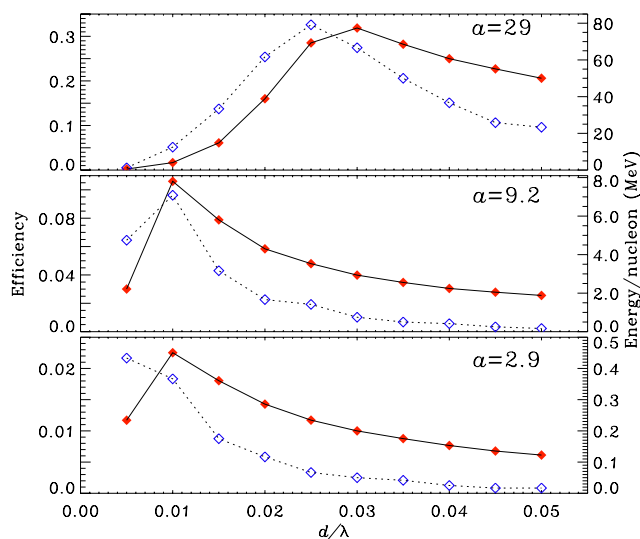
Figure 1. Energy conversion efficiency into ions (red filled diamonds) and the 'peak' energy per nucleon (blue empty diamonds) as a function of the target thickness, investigated by parametric 1D PIC simulations. The top, middle and bottom plots are for a pulse amplitude $a = 29$, 9.2 and 2.9, respectively. In all the runs, the laser pulse had a duration of 9 cycles (FWHM), the electrons density was $n_e = 250 n_c$ and the charge-to-mass ratio was $Z/A = 1/2$.

spectra. However, depending on the interaction parameters some tail of higher energy ions appears. Moreover, the width of the ion energy peak also varies throughout the simulations and does not remain constant in time, as some broadening is observed after the laser pulse is over. This broadening appears to be related to electron heating which occurs at the end of the acceleration stage, creating 'warm' electrons which are much less energetic than those produced for LP interaction but may already drive the expansion of the thin plasma foil. Hence, monoenergeticity of ions appears to be a non-trivial issue already in 1D.

In higher dimensionality it is known that the intensity distribution in the laser spot gives rise to an energy spread correlated with the direction of laser-accelerated ions [11], so that a 'flat-top' distribution, whenever feasible, may improve monoenergeticity as well as beam collimation (see e.g. 2D simulations in [17]). Additional effects of the pulse profile are also discussed in section 4.

3.2. RPA in preformed plasmas

The use of ultrathin targets in experiments will require the use of systems with an extremely high contrast ratio, otherwise the prepulse preceding the main interaction pulse will destroy the target completely. Interaction experiments in such a regime appear to be presently possible [12, 14], thanks, for example, to the use of plasma mirrors to improve the contrast [13]. Such conditions are optimal to test the CP-RPA of ultrathin targets, provided that the strategies implemented to improve the pulse contrast are compatible with preserving the circular polarization of the pulse. It is also worth stressing that the need for normal pulse incidence might also be non-trivial to be experimentally satisfied due to the danger of back-reflection from the overdense plasma.

It is interesting in any case to consider the possibility of the interaction of the CP pulse with a non-uniform preplasma, as this may be present in experiments where the contrast ratio
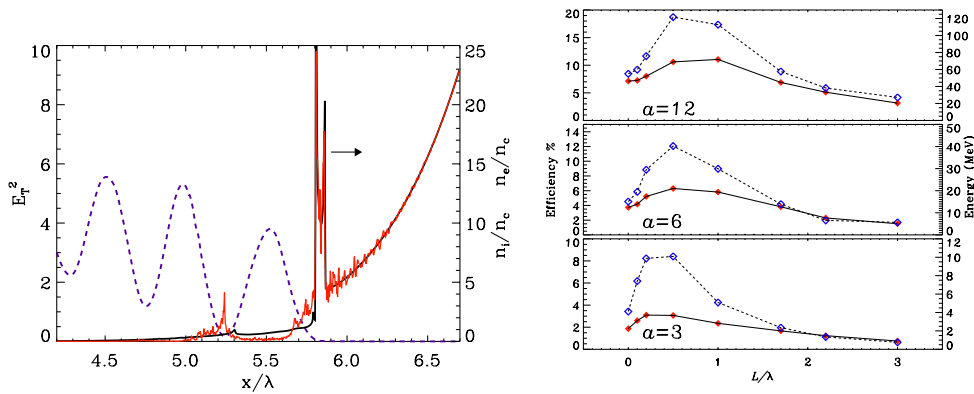
Figure 2. Interaction with preformed plasmas. Left: snapshots of the profiles of $E_T^2 = E_y^2 + E_z^2$ (dashed blue line), n_i (thick black line) and n_e (thin red line) soon after the formation of the 'fast' ion bunch (evidenced by the arrow). The pulse intensity was $a = 3$ corresponding to $1.2 \times 10^{19}\,\mathrm{W\,cm^{-2}}$ for $\lambda = 1\,\mu\mathrm{m}$, the density profile was rising with a $\sim (x - x_0)^9$ law up to a peak density $n_0 = 40n_c$. Right: conversion efficiency (red filled diamonds, solid line) and peak energy (blue empty diamonds, dashed line) of ions as a function of the density scalelength L, for three values of the laser amplitude a. In all the simulations the laser pulse had a duration of 9 cycles (FWHM) and the density profile was rising with a $\sim (x - x_0)^4$ law up to a peak density $n_0 = 16n_c$ and then remained constant.

is modest. Moreover, the expected scaling of the ion energy with the inverse of the plasma density suggests that, in a preformed plasma, a given laser pulse may produce a lower total number of ions but with higher energy, as the interaction occurs with the layer at the cut-off density n_c which is typically less than one hundredth of the solid density.

We performed a set of parametric 1D simulations assuming initial density profiles of the power-law type (i.e. $n_0(x) \sim (x - x_0)^k$ for $x > x_0$) and different values of the density scalelength at the cut-off layer, $L = n_c / |\partial_x n_0|_{n_0 = n_c}$. The snapshot of the ion density n_i in figure 2 shows that n_i undergoes spiking and 'breaking' and that a 'fast' bunch forms near the cut-off density layer, with features very similar to the case of a sharply rising density (no preplasma) [10]. The bunch density is several times n_c. As a function of L, both the maximum ion energy and the conversion efficiency have their maxima for a very short scalelength $L \simeq 0.5\lambda$, as also shown in figure 2 where $L = 0$ corresponds to the case of no preplasma, i.e. a step-like profile. When compared with the energy scaling (1), the observed ion energy would correspond to a density value intermediate between n_c and the peak density ($16n_c$) of the profile. The decrease in energy and efficiency for larger values of L might be related to the weaker coupling of the laser pulse to the cut-off layer; a relevant part of the pulse energy is found to be absorbed in the underdense plasma, e.g. by excitation of plasma waves, causing the absorption degree into electrons to be higher than into ions and consequently decreasing the total radiation pressure. The stronger heating of electrons may account for the broad energy spectrum that is observed for non-optimal values of L; figure 2 reports the maximum or cut-off energy, but several and broad 'peaks' may appear in the spectrum under such conditions, while the spectrum is narrow for the case of absolute maximum energy. These preliminary results suggest that RPA may be strongly affected by prepulse effects. However this may allow one to achieve dense bunches of multi-MeV ions using ultrashort pulses with controlled contrast. For longer pulses (hundreds of femtoseconds), this approach may become ineffective because of strong steepening effects during the rise of the pulse, decreasing the value of L_c. The width of the target layer that remains undamaged by the prepulse may also play a
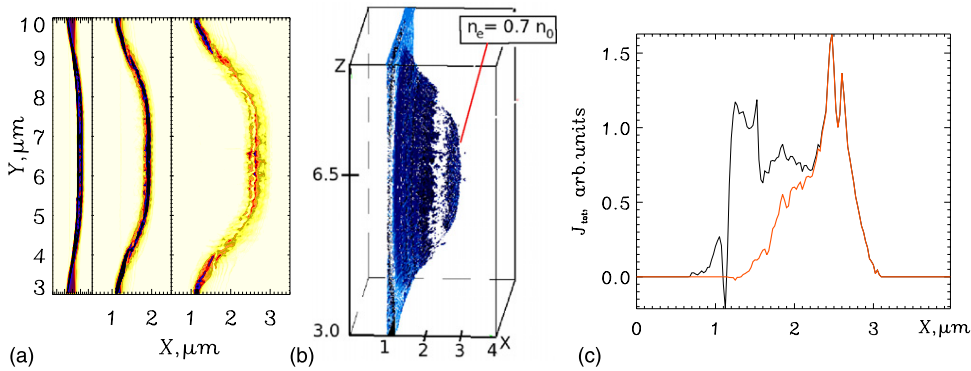
Figure 3. (*a*) The distribution of ion the density at $t = 75, 100$ and 130 fs in the (xy) plane, (*b*) the distribution of the ion density at $t = 130$ fs (the laser pulse is over), (*c*) the integral of the ion poloidal current $\oint J_\varphi \, \mathrm{d}y \, \mathrm{d}z$ at $t = 130$ fs versus longitudinal coordinate, showing the angular momentum absorption: black line for the region with radius $r = 4.5 \, \mu$m around the x-axis; red line for the $r = 2.5 \, \mu$m region around the x-axis.

role because the ions may undergo relevant collisional losses while crossing the solid-density region (see, e.g. the discussion in [8]).

4. 3D simulations

As is always the case for computational plasma physics, 3D simulations would be required for a 'realistic' description, but the limits of computing power force the restriction to a narrow set of 'feasible' parameters. This is the case for CP-RPA where, furthermore, the resolution must be high enough to resolve effects such as the strong spiking of the density observed in 1D and 2D. Thus, only a few 3D runs could be performed and for plasma densities much less than solid-density values, though well above n_c.

The comparison with 1D and 2D results is also important because a CP pulse carries a net angular momentum whose conservation law appears as an additional constraint in 3D. Note that, despite the strong absorption of pulse energy, no absorption of angular momentum is expected, at least as long as the acceleration is adiabatic (as is assumed in the 'perfect mirror' model). In fact, coming back to the heuristic argument of the introduction, if the number of photons is conserved and the reflected beam conserves helicity (which can be shown to hold), no angular momentum is left in the target because the 'spin' of any photon is $\hbar$, independent of the frequency.

In order to study these issues in detail, we performed several 3D simulations. In all the runs discussed here the normally incident laser pulse was CP with a peak intensity of $3.4 \times 10^{19} \, \mathrm{W \, cm^{-2}}$ and ~ 60 fs duration and the target consisted of electrons and protons. Figure 3 presents the results of the interaction of a laser pulse with a 'flat-top' intensity profile of $6 \, \mu$m width with a target of density $n_e = 16 n_{cr} = 1.7 \times 10^{22} \, \mathrm{cm^{-3}}$ and $0.3 \, \mu$m thick. Figure 3(*a*) shows the projected 2D distributions of ion density at $t = 75, 100$ and 130 fs and (*b*) the 3D plot of the ion density when the laser pulse is over. The density of the 'bunch' is approximately 0.7 of the initial density of the target, the peak energy of ions in this bunch is ~ 4 MeV the number of accelerated ions is $\sim 4 \times 10^{10}$. When the laser pulse is over most of the absorbed angular momentum ($\sim 4\%$) is transferred to the ions (the energy absorption in this case was $\sim 7\%$). To prove that a torque on the plasma ions exists, we plot in figure 3(*c*) the integral (over (y, z)) of the poloidal current J_φ of the ions. We thus see that on average there
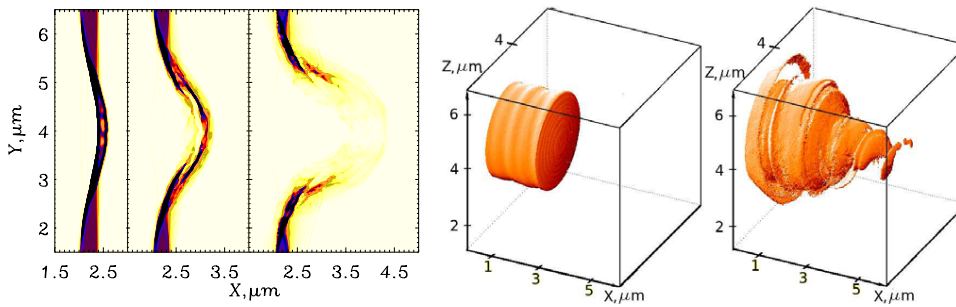
7

T V Liseykina *et al*

Figure 4. The distribution of ion density at $t = 75$, 100 and 130 fs and the electromagnetic energy at $t = 50$ fs and $t = 100$ fs in the case of tightly focused (3 μm width) laser pulse interaction with an ultrathin foil.

is a net 'rotation' of the ions, while the same plot for the electron current shows that the latter averages over x almost to zero. The poloidal ion current is concentrated near the edge of the laser spot where the angular momentum density has a maximum.

Angular momentum absorption in laser–plasma interactions has been mostly studied so far in underdense plasmas as a problem closely related to the generation of a steady magnetic field (inverse Faraday effect). Haines [24] reported a short critical review of a previous work and discussed the effects leading to a torque on the plasma ions. The issue of angular momentum absorption in overdense plasmas has received much less attention so far. In the present context, the observation of some degree of angular momentum absorption is a signature of non-adiabatic or 'dissipative' effects (which are an interesting issue in collisionless systems) not included in the 'perfect mirror' model of RPA. They may be related to the onset of hydrodynamical breaking during the acceleration process [10], violating the adiabaticity condition.

In figure 4 the results of the interaction of a tightly focused (3 μm width) Gaussian laser pulse with a target of density $n_e = 9n_{cr} = 1 \times 10^{24}$ cm^{-3} and thickness of 0.4 μm are shown. In this case the pulse focusing was tight enough to contribute dramatically to the induced transparency of the target.

In both cases presented here the density and the width of the targets were chosen in a way to ensure their opacity on the basis of the 1D analysis. However, 3D effects decrease the transparency threshold because the foil tends to expand in the perpendicular direction. For the tightly focused Gaussian laser pulse this effect is very pronounced so that the foil becomes transparent even if initially it was opaque. Since the use of a target with densities not very far from the transparency threshold is more suitable to achieve an efficient acceleration rate, the shape of the laser pulse becomes a critical issue and the use of 'flat-top' laser pulses, whenever possible, may help.

Acknowledgments

Radiation pressure acceleration of ultrathin foils

Andrea Macchi[1,2,6]**, Silvia Veghini**[1]**, Tatyana V Liseykina**[3,4] **and Francesco Pegoraro**[1,5]

[1] Department of Physics 'E. Fermi', Largo B Pontecorvo 3, 56127 Pisa, Italy
[2] CNR, Istituto Nazionale di Ottica (INO), Pisa, Italy
[3] Max Planck Institute for Nuclear Physics, Heidelberg, Germany
[4] Institute of Computational Technologies, SD-RAS, Novosibirsk, Russia
[5] Consorzio Nazionale Interuniversitario per le Scienze Fisiche della Materia (CNISM), unità di ricerca di Pisa, Italy
E-mail: macchi@df.unipi.it

Abstract. The acceleration of sub-wavelength, solid-density plasma foils by the ultraintense radiation pressure of circularly polarized laser pulses is investigated analytically and with simulations. An improved 'Light Sail' or accelerating mirror model, accounting for nonlinear self-induced transparency effects, is used for estimating the optimal thickness for acceleration. The model predictions are in good agreement with one-dimensional simulations. These latter are analyzed in detail to unfold the dynamics and self-organization of electrons and ions during the acceleration. Two-dimensional simulations are also performed to address the effects of target bending and of laser intensity inhomogeneity.

[6] Author to whom any correspondence should be addressed.

Contents

1. Introduction

Present-day laser systems may deliver at their focal spot intensities up to $10^{22}\,\mathrm{W\,cm^{-2}}$, and possibly even higher in the near future. The radiation pressure on a reflecting object corresponding to such intensities would exceed terabar values, driving strong compression and acceleration of matter. A few experiments have already given some evidence of strong radiation pressure (or ponderomotive) effects in various regimes [1]–[3]. The possibility to develop laser-driven sources of high-energy ions based on radiation pressure acceleration (RPA) is of particular interest. Theoretical studies [4]–[6] have shown that in the interaction with ultrathin (sub-micrometric) foils at intensities exceeding $10^{23}\,\mathrm{W\,cm^{-2}}$, the dominant mechanism of ion acceleration may be RPA instead of target normal sheath acceleration (TNSA), which has been intensively investigated experimentally (see [7] for a review). A regime of radiation pressure dominance may also exist at lower intensities, if circular polarized (CP) laser pulses at perpendicular incidence on the target are used. In such conditions, TNSA may be ruled out by the strong quenching of high-energy electron generation for CP pulses [8]. The regime of RPA with CP pulses has been recently investigated in many theoretical papers for different laser and target conditions, including thick targets ('hole boring' regime) [8]–[13], structured or composite targets [14]–[18], and ultrathin foils [19]–[29]. The effects of elliptical polarization were also studied [30, 31]. First experimental results were communicated recently [32]–[34].

In this paper, we focus on ultrathin foil targets. Although experimentally challenging, such a regime appears to be feasible due to the present possibility of both manufacturing targets as thin as a few nanometers, e.g. diamond-like carbon (DLC) foils, and avoiding early disruption of such targets by prepulse effects thanks to the use of techniques such as the plasma mirror to obtain extremely 'clean' pulses [35]. Early theoretical studies both for linearly polarized pulses in the radiation pressure-dominated regime [4] and for CP pulses at lower intensities [19]–[22] suggested that an ultrathin foil may be accelerated as a whole, leading to a monoenergetic spectrum of ions. In addition, the acceleration process is highly efficient and the energy per nucleon scales favorably with the laser pulse energy. These features are in agreement with the predictions of the simplest model of thin-foil acceleration, which assumes the thin foil target to be a perfectly reflecting, undeformable, plane mirror boosted by the radiation pressure of an electromagnetic (EM) plane wave (corresponding to the laser pulse) at perpendicular incidence.

This regime of RPA has also been named 'Light Sail' (LS), and in the following we refer to the 'accelerating mirror' model as the LS model.

This paper is organized as follows. In section 2, we present an analytical model that improves the basic LS model by including the effect of the nonlinear self-induced transparency (SIT) of the foil at 'relativistically' strong laser intensities. It is found that SIT effects determine an 'optimal' value of the foil thickness for which, given a laser pulse, the foil velocity is highest. The predictions of the model are found to be in good agreement with one-dimensional (1D) particle-in-cell (PIC) simulations for what concerns the energy of the spectral peak of 'monoenergetic' ions and the conversion efficiency.

In section 3, the dynamics of thin-foil RPA is analyzed in 1D PIC simulations. It is found that the distribution of electrons and ions undergoes a dynamic self-organization to maintain an equilibrium condition for electrons where the electrostatic and ponderomotive forces balance each other. It is found that in general the spectral peak contains just a fraction of the total ions, the actual value depending on the target and pulse parameters.

In the final section 4, the acceleration of foils with thicknesses close to the 'optimal value' is further investigated with two-dimensional (2D) simulations, addressing the effects of target bending and of laser intensity inhomogeneity.

2. Thin-foil modeling

2.1. Review of the LS model

The LS model takes into account an EM plane wave of frequency ω and intensity $I = I(t)$, perpendicularly incident on a foil of mass density ρ, thickness ℓ and reflectivity $R = R(\omega)$. In the rest frame of the foil, neglecting dissipative effects, the radiation pressure is given by

$$P_{\text{rad}} = 2R\frac{I}{c}. \tag{1}$$

Note that equation (1) is different from the known expression for the case of incidence on a semi-infinite medium

$$P_{\text{rad}} = (1 + R)\frac{I}{c}, \tag{2}$$

which does not vanish if $R = 0$ because the transmitted wave does not leave the target and deliver all its momentum there.

By a Lorentz transformation of the force on the foil and of the intensity and frequency of the EM wave, the following equations of motion for the foil in the laboratory frame are obtained:

$$\frac{\text{d}}{\text{d}t}(\beta\gamma) = \gamma^3\frac{\text{d}\beta}{\text{d}t} = \frac{2I(t - X/c)}{\rho\ell c^2}R(\omega')\frac{1 - \beta}{1 + \beta}, \tag{3}$$

$$\frac{\text{d}X}{\text{d}t} = \beta c, \tag{4}$$

where $\beta = V/c$ is the velocity of the foil in units of the speed of light c, $\omega' = \omega\sqrt{(1 - \beta)/(1 + \beta)}$ is the EM wave (laser) frequency in the rest frame and $\gamma = (1 - \beta^2)^{-1/2}$.

For $R = 1$, i.e. taking the foil as a perfectly reflecting mirror, the model yields a simple solution for $\beta = \beta(w)$, where $w = t - X/c$ is the retarded time, as a function of the pulse fluence $\mathcal{F}$ (the pulse energy per unit surface) [36, 37]:

$$\beta(w) = \frac{[1 + \mathcal{E}(w)]^2 - 1}{[1 + \mathcal{E}(w)]^2 + 1}, \tag{5}$$

$$\mathcal{E}(w) = \frac{2\mathcal{F}(w)}{\rho \ell c^2}, \qquad \mathcal{F}(w) = \int_0^w I(w')\,\mathrm{d}w'. \tag{6}$$

This expression can also be retrieved from the more general derivation given in section 2.3. The corresponding energy per nucleon is

$$E(w) = m_{\mathrm{p}} c^2 [\gamma(w) - 1] = m_{\mathrm{p}} c^2 \frac{\mathcal{E}^2(w)}{2[\mathcal{E}(w) + 1]}. \tag{7}$$

The instantaneous efficiency η, i.e. the ratio between the mechanical energy delivered to the foil and the incident pulse energy, is also a simple function of β [36, 37] or, equivalently, of $\mathcal{E}$:

$$\eta = \frac{2\beta(w)}{1 + \beta(w)} = 1 - \frac{1}{[\mathcal{E}(w) + 1]^2}. \tag{8}$$

Thus, $\eta \to 1$ when $\beta(w) \to 1$, i.e. when $\mathcal{E} \to \infty$.

The final velocity of the foil β_{f} and the corresponding energy per nucleon E_{n} are obtained trivially by rewriting equations (5)–(7) as a function of the total energy, i.e. by taking $\mathcal{E} = \mathcal{E}(\infty)$. In practical units,

$$\mathcal{E} \simeq 2.2 \frac{\mathcal{F}}{10^8\,\mathrm{J\,cm^{-2}}} \left(\frac{\rho}{1\,\mathrm{g\,cm^{-3}}}\right)^{-1} \left(\frac{\ell}{10\,\mathrm{nm}}\right)^{-1}. \tag{9}$$

It is also useful to rewrite $\mathcal{E}$ as a function of the relevant dimensionless parameters: the amplitude of the pulse $a_0 = \sqrt{I/m_{\mathrm{e}} c^3 n_{\mathrm{c}}}$ (with $n_{\mathrm{c}} = m_{\mathrm{e}} \omega^2 / 4\pi e^2$ the cutoff density), the surface density $\zeta = \pi (n_{\mathrm{e}}/n_{\mathrm{c}})(\ell/\lambda)$ (with $\lambda = 2\pi c/\omega$ the laser wavelength) and the duration of the laser pulse τ in units of the laser period $T = 2\pi/\omega = \lambda/c$. By estimating the total fluence $\mathcal{F} \simeq I(T\tau) = m_{\mathrm{e}} c^3 n_{\mathrm{c}} T (a_0^2 \tau)$, we obtain for $\mathcal{E}$

$$\mathcal{E} \simeq \frac{2 m_{\mathrm{e}} c^2 n_{\mathrm{c}} a_0^2 \tau \lambda}{m_{\mathrm{i}} n_{\mathrm{i}} \ell c^3} = 2\pi \frac{Z}{A} \frac{m_{\mathrm{e}}}{m_{\mathrm{p}}} \frac{a_0^2 \tau}{\zeta}. \tag{10}$$

Figure 1 shows β_{f} and E_{n} as a function of $a_0^2 \tau$ and ζ ($Z/A = 1/2$ has been assumed). To convert from/to practical units, for a laser wavelength $\lambda = 0.8\,\mu\mathrm{m}$ and a fully ionized DLC target ($\rho = 2.2\,\mathrm{g\,cm^{-3}}$, $n_{\mathrm{e}}/n_{\mathrm{c}} = 384$), we find $a_0^2 \tau = 1.73 \mathcal{F}/(10^4\,\mathrm{J\,cm^{-2}})$ and $\zeta = 1.5 \ell/(1\,\mathrm{nm})$.

2.2. Nonlinear reflectivity

To include the effects or partial reflectivity ($R < 1$) and SIT into the LS model, we first look for a suitable analytical expression of R. We use the model of a delta-like 'thin foil' [38], i.e. a plasma slab located at $x = 0$ with electron density $n_{\mathrm{e}}(x) = n_0 \ell \delta(x)$. The model gives the following expression for R in the rest frame of the foil:

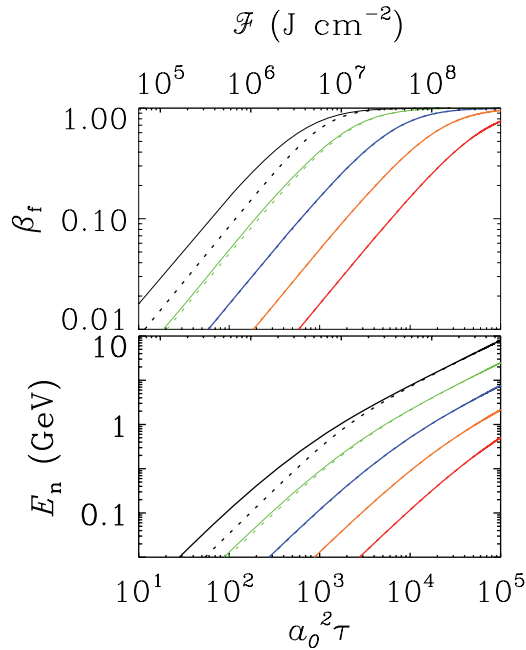$$R = \frac{1}{1 + \zeta^{-2} \Gamma^2}, \tag{11}$$

Figure 1. Analytical results from the LS model. The final velocity of the foil β_f and the corresponding energy per nucleon E_n are given as a function of the dimensionless pulse fluence $a_0^2 \tau$ and for the values of surface density of the foil $\zeta = 1$ (black line), 3.16 (green), 10 (blue), 31.6 (orange) and 100 (red). The values on the upper horizontal axis give the fluence in $\mathrm{J\,cm^{-2}}$ corresponding to $a_0^2 \tau$ for $\lambda = 0.8\,\mu\mathrm{m}$. For a DLC target, $\zeta = 2.6\ell/(1\,\mathrm{nm})$. The solid lines correspond to equation (5) i.e. to the case of a 'perfect' mirror with reflectivity $R = 1$. The dotted lines correspond to equation (17) where the effects of pulse transmission through the foil have been taken into account (for $\zeta \geqslant 10$, solid and dotted lines cannot be distinguished).

$$\Gamma = \frac{1 + a_0^2 - \zeta^2}{2} + \sqrt{\left(\frac{1 + a_0^2 - \zeta^2}{2}\right)^2 + \zeta^2}, \tag{12}$$

which is very well approximated by

$$R \simeq \begin{cases} 1/(1 + \zeta^{-2}) & (a_0 < \sqrt{1 + \zeta^2}), \\ \zeta^2/a_0^2 & (a_0 > \sqrt{1 + \zeta^2}). \end{cases} \tag{13}$$

Note that Γ is the relativistic factor for electrons in the thin foil (calculated self-consistently with the EM fields). It is thus apparent that the SIT is due to the relativistically increased inertia of electrons, as m_e is replaced by $m_e \Gamma$ in their equation of motion. The expression for $a_0 < \sqrt{1 + \zeta^2}$ corresponds to that obtained in the linear regime, i.e. for sub-relativistic intensities.

Equations (11) and (13) for R are both plotted in figure 2, showing that the transition from the linear to the nonlinear regime is quite sharp and that equation (13) provides an excellent approximation. We may thus define a threshold condition for relativistic SIT as $a_0 = \sqrt{1 + \zeta^2} \simeq \zeta$ when $\zeta \gg 1$, i.e. in most cases of interest. Combining equations (1) and (13), the total radiation pressure P_{rad} on the target becomes *independent* of a_0 for $a_0 > \zeta$. Thus, $a_0 \simeq \zeta$
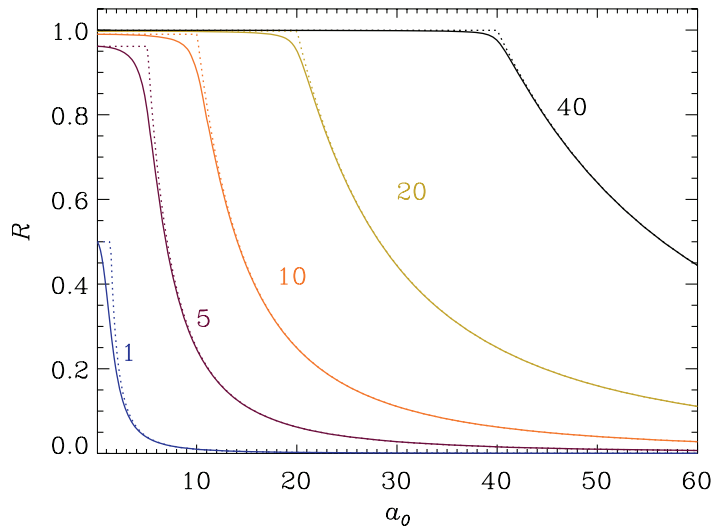
Figure 2. Nonlinear reflectivity R as a function of incident wave amplitude a_0 and for several values of the 'optical thickness' ζ. Thick and dashed lines correspond to the 'exact' formula (11) and to its approximation (13), respectively.

gives the condition of maximum radiation pressure on the (immobile) foil, and one would expect the RPA of the foil to saturate for $a_0 > \zeta$. Actually, simulations show that in this regime the interaction is rather dominated by the effect of expulsion of electrons from the foil, leading to a transition from RPA to a Coulomb explosion [28]. Hence, the LS model is appropriate for $a_0 < \zeta$.

2.3. Improved LS formula

According to equation (11), the reflectivity R is independent of a_0 in the $a_0 < \sqrt{1+\zeta^2}$ range, and for $\zeta \gg 1$, corresponding to most cases of experimental relevance, $R \simeq 1$ is a very good approximation. Nevertheless, thin-foil manufacturing technology seems able even to approach values of ζ not much larger than unity; hence it is of some interest to consider how the LS formulae are modified in the $a_0 > \zeta \gtrsim 1$ regime.

Using $R \simeq (1+\zeta^{-2})^{-1}$ and switching to the retarded time w, equation (3) becomes

$$\frac{d\beta}{dw} = \frac{2}{\rho \ell c^2} I(w) \gamma^{-3} (1+\beta)^{-1} \left(1 + \zeta^{-2} \frac{1-\beta}{1+\beta} \right) \tag{14}$$

(note that $dw = (1-\beta)dt$). By switching to the variable $b(w) = \sqrt{(1-\beta)/(1+\beta)}$, we obtain

$$b^{-2}(w) \left[1 + b^2(w)\zeta^{-2} \right] \frac{db}{dw} = -\frac{2}{\rho \ell c^2} I(w), \tag{15}$$

which can be integrated with the initial condition $b(0) = 1$, corresponding to $\beta(0) = 0$, to yield

$$b^{-1}(w) - 1 - \zeta^{-2} b(w) + \zeta^{-2} = \frac{2}{\rho \ell c^2} \int_0^w I(w') \, dw' = \mathcal{E}(w). \tag{16}$$
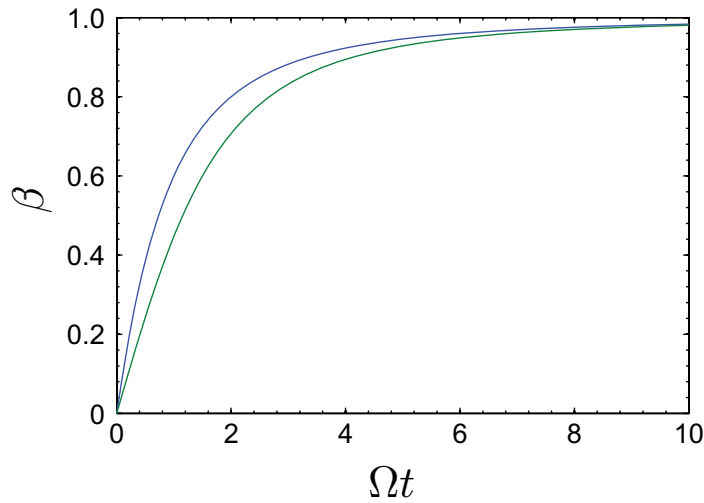
Figure 3. Foil velocity as a function of Ωt defined in (18) for $\zeta = 1$ (green lower curve) and for $\zeta^2 = \infty$, i.e. a perfectly reflecting foil (blue upper curve).

By solving (16) for $b(w)$ and rewriting the result for β, we obtain

$$\beta(w) = \frac{[1 + \mathcal{E}(w) - \zeta^{-2}]^2 \left(1 + \sqrt{1 + 4\zeta^{-2}[1 + \mathcal{E}(w) - \zeta^{-2}]^{-2}}\right) + 2\zeta^{-2} - 2}{[1 + \mathcal{E}(w) - \zeta^{-2}]^2 \left(1 + \sqrt{1 + 4\zeta^{-2}[1 + \mathcal{E}(w) - \zeta^{-2}]^{-2}}\right) + 2\zeta^{-2} + 2}. \tag{17}$$

In the limit of $\zeta \to \infty$, i.e. $R \to 1$, one recovers equation (5). As shown in figure 1, the difference between (5) and (17) (and between the corresponding energies) is important for $\zeta \sim 1$.

For a constant intensity I, i.e. for a 'flat-top' temporal profile of the laser pulse, the fluence can be written as a function of time as

$$\mathcal{E}(t) = \frac{2It}{\rho \ell c^2} = 2\pi \frac{Z}{A} \frac{m_e}{m_p} \frac{a_0^2}{\zeta} \frac{t}{T} \equiv \Omega t, \tag{18}$$

where T is the period of the laser radiation. In this case, explicit analytical expressions for $\beta(t)$ and $X(t)$ can be given as a function of ζ and Ωt [39]. The result for $\beta(t)$ is shown in figure 3 for the two cases $\zeta = 1$ and $\zeta = \infty$. The latter corresponds to the known solution for a perfectly reflecting mirror [4, 21], which is formally identical to the solution of the longitudinal motion of a charge during Thomson scattering from a plane wave [40].

2.4. Optimal thickness for ion acceleration

We now use the LS model with SIT effects included to provide an estimate for the value of foil surface density ζ_{max} (corresponding to thickness ℓ_{max} for a given target material), which, for a given laser pulse, leads to the highest foil velocity. In the regime of sub-relativistic intensity, ζ_{max} may be obtained by differentiating (17) with respect to ζ at fixed pulse fluence. However, for very high intensities, ζ_{max} is ultimately determined by SIT effects; thus the complete nonlinear expression for R (11) must be used. In the LS equation of motion (3), the expression for $R(\omega')$

IOP Institute of Physics Φ DEUTSCHE PHYSIKALISCHE GESELLSCHAFT

now reads

$$R(\omega') = R(\beta) = \frac{1}{1 + \zeta^{-2}\Gamma^2(\beta)(1-\beta)/(1+\beta)}, \tag{19}$$

$$\Gamma = \frac{1 + a_0^2 - \zeta^2(1+\beta)/(1-\beta)}{2} + \sqrt{\left(\frac{1 + a_0^2 - \zeta^2\frac{1+\beta}{1-\beta}}{2}\right)^2 + \zeta^2\frac{1+\beta}{1-\beta}}. \tag{20}$$

By using the variable $b(w)$ as in equation (15), we now obtain

$$[b^{-2}(w) + \Gamma^2(b)\zeta^{-2}]\frac{\mathrm{d}b}{\mathrm{d}w} = -\frac{2}{\rho\ell c^2}I(w), \tag{21}$$

which can be integrated for a constant intensity $I(w) = I$:

$$b^{-1}(w) - 1 - \zeta^{-2}\int_1^b \Gamma(b')\,\mathrm{d}b' = E(w). \tag{22}$$

Using the implicit equation (22), $b(w)$ and $\beta(w)$ can be obtained numerically. By differentiating (22) with respect to ζ at a fixed acceleration time τ (which should approximately correspond to the duration of the laser pulse), it can be shown [39] that $\zeta_{\max}$ lies in the interval

$$\sqrt{\left(\frac{\Omega\tau}{2\pi}\right)^2 + 1 + a_0^2} - \frac{\Omega\tau}{2\pi} < \zeta_{\max} < \sqrt{1 + a_0^2}, \tag{23}$$

where Ω has been defined in (18). Equation (23) shows that for $\Omega\tau \ll 1$ the optimal thickness is $\zeta_{\max} \simeq \sqrt{1 + a_0^2} \simeq a_0$, corresponding to the maximum radiation pressure on the immobile thin foil as found in section 2.2. As $\Omega\tau \gtrsim 1$ increases, e.g. for increasing pulse duration (keeping other parameters fixed), $\zeta_{\max}$ may become smaller than a_0. This effect may be ascribed to the increase of the reflectivity and the decrease of the intensity in the rest frame of the foil as it is accelerated to high values of β. Since $\Omega^{-1} \simeq 6 \times 10^2\,\mathrm{T}(\zeta/a_0^2)$, this effect is relevant only for long (hundreds of periods) pulses. We may thus conclude that the condition of 'optimal' thickness, given by our improved LS model with SIT effects included for a pulse of constant amplitude a_0, is given by

$$\zeta_{\max} \simeq a_0. \tag{24}$$

In figure 4, the energy per nucleon E_n and the efficiency η obtained from the numerical solution of (22) for $\beta(\infty)$ are compared with the results of the 1D PIC simulations that were previously shown in figure 1 of [24]. In these simulations, η is calculated as the ratio between the total energy of the ions and the energy of the laser pulse. Both E_n and η are shown as a function of the target thickness ℓ and for three different values of the peak pulse amplitude a_0. For all simulations, $n_e = 250n_c$, $Z/A = 1/2$ and the pulse has a full-width at half-maximum (FWHM) duration of 9 periods with a $\sin^2$ envelope for the field. A fairly good agreement between the model and simulations is found. Part of the discrepancy may be ascribed to the effect of the pulse envelope; for simulations with a flat-top envelope (i.e. a nearly constant amplitude), the observed 'optimal' thickness is in closer agreement with equation (24).

Several other authors give for the optimal thickness the same scaling of equation (24) but often with different numerical coefficients. Yan *et al* [23] give the following range,

$$\frac{\zeta}{\pi(1+R)^{1/2}} \sim a_0 \lesssim 2\zeta, \tag{25}$$

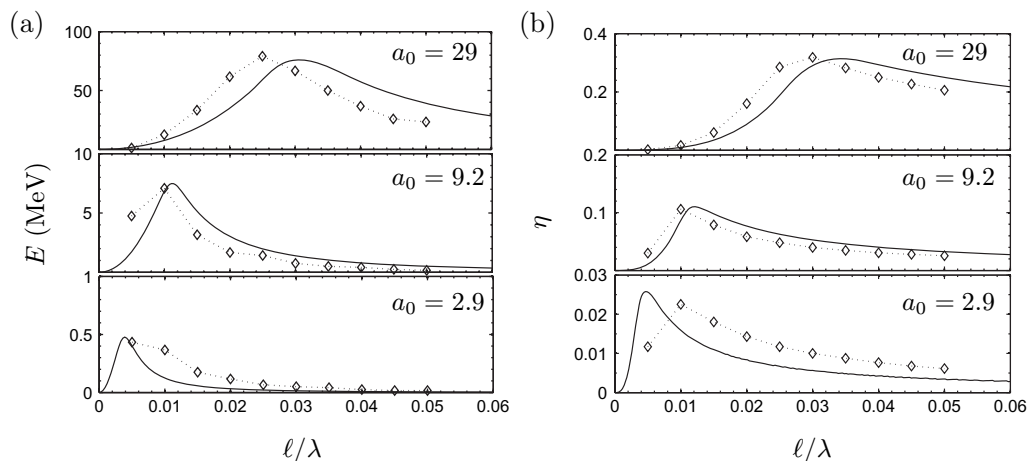**Figure 4.** Energy per nucleon (a) and efficiency of energy conversion into ions (b) obtained as a function of target thickness ℓ and pulse amplitude a_0 for a laser pulse of duration $\tau = 9$ cycles and an electron density $n_e = 250 n_c$. The solid line gives the values corresponding to the numerical solution of (22) for β. The diamonds give the values obtained from parametric 1D PIC simulations.

using an argument of pressure balance but not accounting for SIT effects, since equation (2) is used for P_{rad}. A critical comment by Ji *et al* [41] about the $a_0 \lesssim 2\zeta$ condition appears to originate from a missing 2 factor [42]. Tripathi *et al* [26] give a condition identical to equation (24), accounting for the 'relativistic' modification of the plasma refractive index but using a calculation for a semi-infinite plasma profile. Finally, Esirkepov *et al* [5] observe in multi-parametric simulations a condition of the form $\zeta_{\text{max}} \simeq 3\pi + b\sqrt{I}$, where b is an appropriate constant factor, and notice its similarity with the SIT condition of a thin foil; however, the simulations are performed for linearly polarized pulses and for parameters not corresponding to the radiation pressure-dominated regime. An additional source of difference may be indeed the 2D (instead of 1D) nature of the simulations, as we also find ζ_{max} to be larger than indicated by equation (24) in 2D simulations (see section 4 below).

3. Electron and ion dynamics in one dimension

The comparison with 1D PIC simulation results shown in figure 4 shows that the simple LS model of section 2 is remarkably successful in predicting ion energy as a function of pulse energy and foil thickness. Moreover, for $a_0 \lesssim \zeta_{\text{max}}$ the further simplifying assumption of a totally reflecting foil ($R = 1$) is appropriate. The dynamics underlying the RPA of the thin foil is, however, more complex than what the simple 'mirror' model might suggest. Unfolding such dynamics with the help of simulations helps to explain why some of the observed features seem to be in contrast with the model assumptions. Such features have been discussed in [28]. In the following, we start by recalling the results we obtained in [28] and go a step further in the analysis.

   The LS model assumes the foil as a 'rigid' object, so that all the ions and electrons move coherently at the same velocity $V = \beta c$ of the foil. However, the 1D simulations show that the spectral peak, centered at the energy predicted by the LS model, contains only a fraction of the
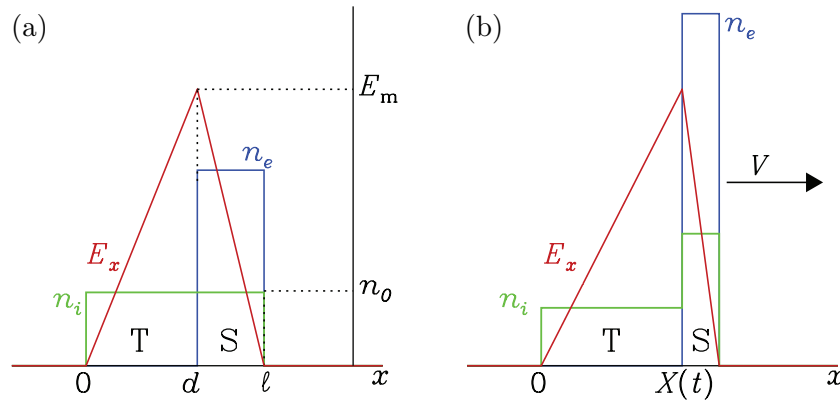
Figure 5. Cartoon showing how two ion populations are formed. The schematic profiles of the ion density n_i (green), electron density n_e (blue) and electrostatic field E_x (red) are shown at two different times. Part (a) corresponds to the early stage of the interaction where ions have not moved yet, so that their density equals the initial value n_0, and electrons have piled up under the action of the ponderomotive force f_p in the $d < x < \ell$ or 'Sail' (S) region. The $0 < x < d$ region of electron depletion is named as the 'Tail' (T) region. Part (b) shows the stage of ion acceleration. Ions in the T region are accelerated by their own space-charge field as in a Coulomb explosion, so that the ion density decreases in this region. Ions in the S region ($x > X(t)$) are bunched and accelerated by E_x, which in this region equals f_p/e, and move with the electrons at velocity V.

total number of the ions. Those 'monoenergetic' ions originate from a layer at the rear surface of the foil. The rest of the ions form an exponential-like 'pedestal' in the spectrum.

We explain the formation of the two ion populations with the help of the cartoon in figure 5. As the laser pulse impinges on the overdense plasma, the electrons are pushed by the steady ponderomotive force $\mathbf{f}_p$, whose integral over the whole target depth equals the radiation pressure. Thus, electrons pile up in the region $d < x < \ell$ of figure 5, which we call the 'Sail' region. The electron displacement generates the space-charge field $E_x \simeq f_p/e$ to balance the ponderomotive action. (If $R \simeq 1$, almost no electrons are pushed out of the foil, because the EM field and the ponderomotive force vanish at the rear surface of the foil; the electron compression does not change R in 1D since the product $n_e\ell$ is constant.) Ions in the Sail are accelerated and bunched by E_x [8, 28] and move together with electrons. The Sail is thus negatively charged during the acceleration because it contains all of the electrons in the foil but just a fraction $F \simeq 1 - d/\ell$ of the ions. An estimate for the condition of pressure equilibrium gives $F \simeq 1 - a_0/\zeta$, showing that F can be significantly smaller than unity as a_0 approaches ζ.

The analysis of 1D simulations confirms the above-described scenario. Typical snapshots of density and field profiles are shown in figure 6(a) for a simulation with $a_0 = 12$, $\tau = 9$, $n_e/n_c = 100$ and $\ell = 0.05$, so that $\zeta = 15.7$. Both a fine spatiotemporal resolution ($\Delta x = c\Delta t = \lambda/2000$) and a high number of particles per cell were used to resolve accurately the dynamics, and in particular the density variation that involves both the strong spiking in the Sail region and the rarefaction in the Tail region.

The Sail moves with a well-defined velocity V, so that ions in the Sail are monoenergetic. The velocity V satisfies the LS equation (3), where, according to the comparison with
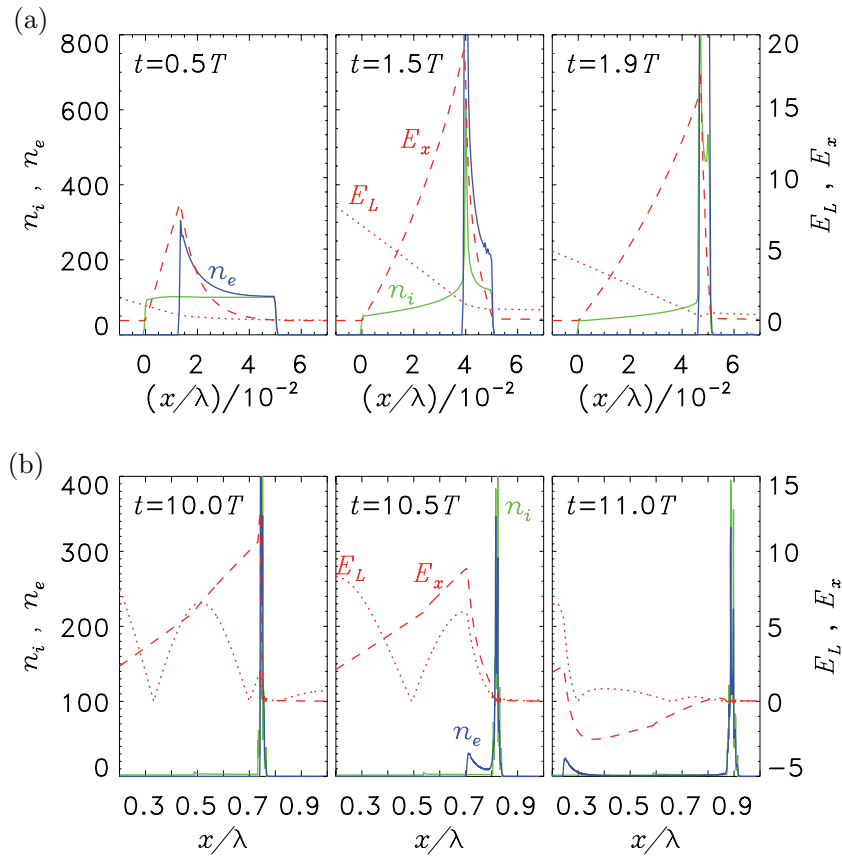
Figure 6. Snapshots from a 1D PIC simulation of the interaction of a laser pulse with a thin plasma slab. Ion density n_i (green), electron density n_e (blue), longitudinal electric field E_x (red, dashed) and pulse field amplitude $E_L = \sqrt{E_y^2 + E_z^2}$ (red, dotted) are shown. Plots in row (a) correspond to the early stage of the interaction when electrons pile up at the rear side of the foil and a charged layer at the rear side is accelerated. Plots in row (b) correspond to later times when the laser pulse decouples from the foil and excess electrons are accelerated backward leaving the charged layer. Note that the scales of the x and $n_{e,i}$ axes have been changed in (b) with respect to (a) for better visibility. The target left boundary is at $x = 0$ where the pulse impinges at $t = 0$. Times are normalized to the laser period T, fields to $E_0 = m_e \omega c / e$ and densities to $n_c = m_e \omega^2 / 4\pi e^2$. The laser pulse has peak amplitude $a_0 = 12$ and a 'flat-top' profile with a duration of $9T$ (FWHM) and $1T$ rise and fall times, the foil thickness is $\ell = 0.05\lambda$, the electron density $n_e = 100 n_c$ and $Z/A = 1/2$.

simulations, the *total* thickness ℓ of the foil, i.e. the total mass, must be used. This may actually sound surprising because the Sail's mass is $\simeq F$ times the total mass and the total pressure on ions is lower than P_{rad}. In fact, in 1D the equilibrium condition for electrons is

$$\int (-e) n_e E_x \, \mathrm{d}x = \int n_e f_p \, \mathrm{d}x = P_{\text{rad}}, \qquad (26)$$
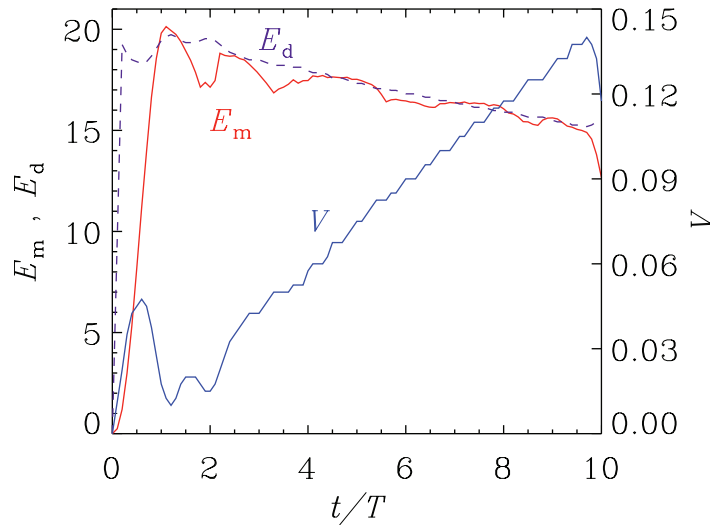
Figure 7. Red solid line: temporal evolution of the peak of the electrostatic field E_x from the same simulation of figure 6, $E_m(t) = E_x(x = X(t))$. Blue solid line: velocity of the peak position $V(t) = dX/dt$. Purple dashed line: function $E_d(t) = E_m(0)(1 - V/c)/(1 + V/c)$.

while the total electrostatic pressure P_{es} on ions is given by

$$P_{es} = \int Z e n_i E_x \, dx \tag{27}$$

(the ponderomotive force on ions is smaller than f_p by a factor $\sim m_e/m_i$ and is thus negligible). Only in the case of local charge neutrality $Zn_i = n_e$, would we obtain $P_{es} = P_{rad}$. However, in the Sail, $Zn_i < n_e$, so that $P_{es} < P_{rad}$. The calculation of P_{es} from the approximate initial profiles of n_i and E_x (figure 5(a)) in equilibrium conditions shows that $P_{es} = F P_{rad}$ [28]; thus the equation of motion for the Sail can be written as

$$\frac{d}{dt}(\beta\gamma) = \frac{P_{es}}{\rho \ell F c^2} = \frac{P_{rad} F}{\rho \ell F c^2} = \frac{P_{rad}}{\rho \ell c^2}, \tag{28}$$

which is equivalent to equation (3).

In the $0 < x < d$ region, which we call the 'Tail' region, complete electron depletion occurs. In the Tail, ions are accelerated by their own space-charge field, as in a Coulomb explosion, resulting in an ion density that decreases with time and in a broad energy spectrum. Actually, not all the ions in the Tail remain at all times behind the Sail front, i.e. in the $x < X(t)$ region. This is related to maintaining a mechanical quasi-equilibrium for electrons during the acceleration. As the Sail is accelerated toward higher velocities, the radiation pressure decreases by the factor $(1 - \beta)/(1 + \beta)$. Thus, the field E_x must decrease by the same factor to keep the electrons in equilibrium. This is evident in figure 7, where we plot the peak field $E_m(t) = \max[E_x(x, t)] = E_x(x = X(t))$ and show that $E_m(t) \simeq E_m(0)(1 - \beta(t))/(1 + \beta(t))$, so that the pressure equilibrium is maintained. In 1D, the value of E_x at a point x' is proportional to the amount of charge contained in the $x < x'$ region; thus, there must be a positive current through the $x = X(t)$ surface during the acceleration stage. By computing the total number of ions in the $x > X(t)$ region, we find that there is a flow of ions in the forward direction at the
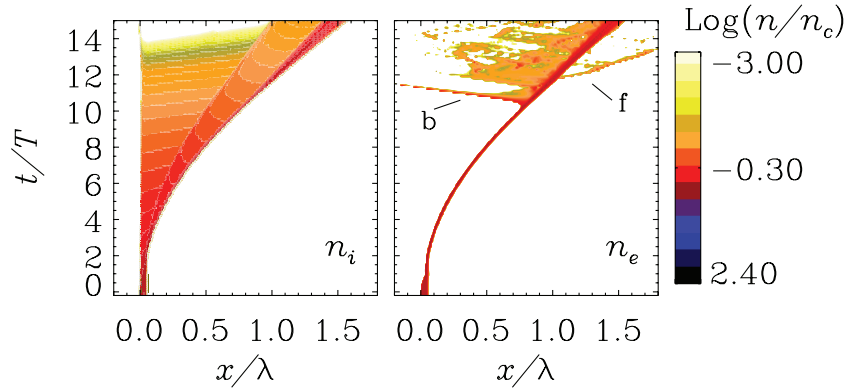
Figure 8. Space–time contours of $n_\mathrm{i} = n_\mathrm{i}(x, t)$ and $n_\mathrm{e} = n_\mathrm{e}(x, t)$ from the same simulation of figure 6, in logarithmic scale. Labels 'b' and 'f' indicate two electron bunches leaving the Sail in the backward and forward direction, respectively, at $t \simeq 11$.

$x = X(t)$ surface. These ions are accelerated by the space-charge field in the Tail region and overturn the position of the Sail front.

The number of electrons in the Sail remains constant up to near the end of the laser pulse, i.e. when the laser amplitude at the foil surface drops down. At a certain time, P_rad does not balance P_es anymore and thus electrons no longer remain in mechanical equilibrium. As a consequence, a bunch of electrons is accelerated *backward* by E_x, as shown in figure 6(b). Some other electrons leave the Sail at later times and also in the forward direction, acquiring a larger velocity than the Sail. This dynamics is best visualized by plotting the space–time contours of $n_\mathrm{i}(x, t)$ and $n_\mathrm{e}(x, t)$ in logarithmic scale, as in figure 8. The detachment of excess electrons eventually leaves the Sail neutral. At the same time, the loss of mechanical equilibrium causes heating of the electrons, driving in turn the expansion of the Sail (which can be noticed in figure 8) and the broadening of the ion spectrum.

Despite the formation of two ion populations, of which the 'monoenergetic' one may be less numerous, the fraction of laser pulse energy converted into kinetic energy of the ions is still in good agreement with the LS efficiency η given by equation (8), which in turn depends only on the Sail velocity. Since work has to be done by the laser pulse to push the negatively charged Sail against the electrostatic field E_x generated by the ions in the Tail, part of the energy is stored as electrostatic energy [28] and eventually converted into kinetic energy of ions in the Tail.

In a recent similar study, Eliasson *et al* [27] also noticed the formation of two ion populations. In their work, ions in the Sail are referred to as 'trapped' in an effective potential in the Sail frame. Using an argument of force balance (instead of pressure balance), they estimate the fraction of ions initially trapped as $F \simeq 1 - (a_0^2/\zeta^2)/2$.

4. 2D simulations

The analysis of the two preceding sections is based on a 1D approach, which may be accurate only under certain conditions, i.e. when the intensity distribution of the laser pulse in the focal plane is flat-top and the foil displacement is smaller than the focal spot radius. To check the predictions of the 1D model, we performed 2D simulations for laser and target parameters close
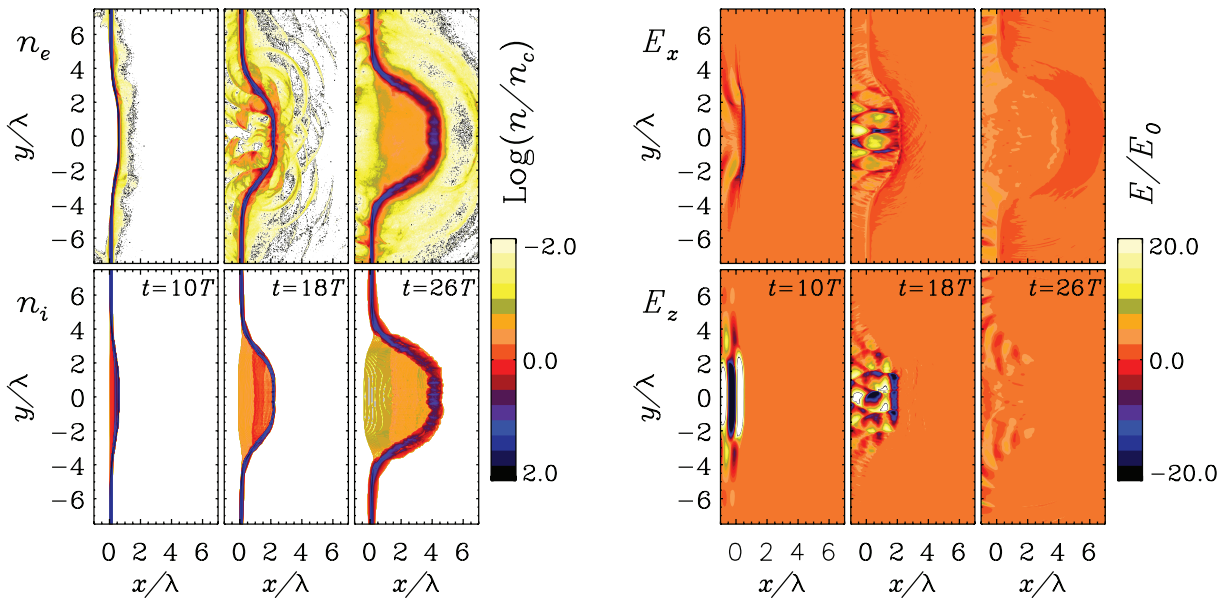
Figure 9. 2D simulation results. Snapshots of n_e, n_i and electric field components E_x and E_z are shown at three different times. The laser pulse has eight cycle duration and eight wavelength diameter (both FWHM) and peak amplitude $a_0 = 20$. The plasma foil has initial density $n_e = 50 n_c$ and thickness $\ell = 0.2\lambda$. Normalizations are as in figure 6.

to the optimal thickness condition (24). In 2D geometry, several effects of possible relevance are taken into account, including e.g. laser intensity distribution, bending of the target, increased heating of electrons due to longitudinal components of the electric field out of the laser axis and onset of surface rippling instabilities. A few groups also reported 3D simulations of thin-foil RPA [4, 14, 24]. These simulations are generally very demanding numerically, also because, as shown by the 1D analysis, high values of the spatial resolution and of the number of particles per cell are needed to resolve the huge density variations in the plasma. With respect to the 2D case, in 3D geometry the additional physical constraint of the conservation of the angular momentum delivered by the circularly polarized laser pulse is taken into account. A theoretical analysis [24] shows that angular momentum absorption in the plasma may occur only via dissipative effects; thus, in general it does not provide the generation of an axial magnetic field, according to the mechanism hypothesized in [26].

Figure 9 shows snapshots of ion and electron densities and of E_x and E_z field components from 2D simulations. The laser pulse has a peak amplitude $a_0 = 20$ and a fourth-order supergaussian (i.e. an $\exp(-u^4)$ function) profile both in the longitudinal (x) and in the transverse (y) directions, with eight cycle duration and eight wavelength width (both FWHM). The foil target has initial electron density $n_e = 50 n_c$ and thickness $\ell = 0.2\lambda$ so that $\zeta = 31.4$.

At the intermediate time $t = 18$, the formation of the low-density Tail of ions can be noticed in the contour plot of n_i. The electron density distribution is more complicated due to 2D effects. As the foil is accelerated by the laser pulse, owing to target deformation the laser pulse incidence is effectively oblique at the edges of the laser spot. Moreover, as soon as the foil displacement is a few times λ, the light reflected from one edge is incident back on the opposite
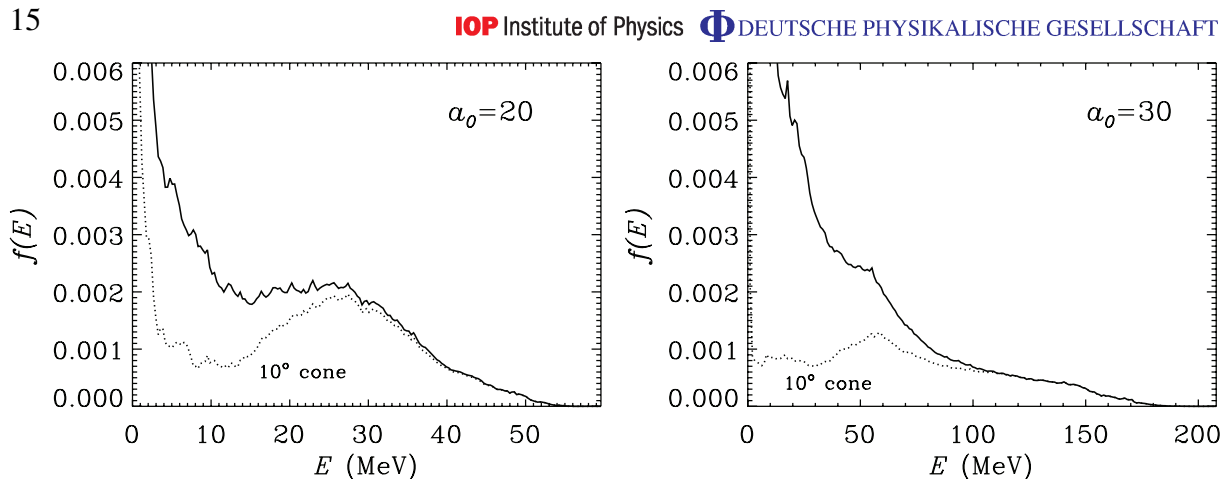
Figure 10. Ion spectra (in energy per nucleon) from the simulations of figure 9 ($a_0 = 20$) and figure 11 ($a_0 = 30$). The dotted line gives the spectrum where only ions inside a $10°$ cone around the axis are included. Both spectra correspond to the latest time in figures 9 and 11.

side, and a standing wave-like pattern is observed ($t = 18\,\text{T}$). These effects enhance electron heating, driving the formation of a low-density electron cloud around the target and leading to broadening of the ion spectrum due to thermal expansion of the foil. In turn, absorption into electrons and oblique incidence reduce the radiation pressure at the edges of the focal spot, and may thus enhance the effect of the inhomogeneous distribution of the laser intensity. A similar dynamics is also noticed for even 'flatter' intensity profiles (e.g. eighth-order supergaussian).

As a likely consequence of stronger electron heating in 2D, the ion spectrum shown in figure 10 is quite broad, even when only ions moving into a $10°$ cone around the axis are considered. According to these results, to obtain a monoenergetic spectrum is a challenging issue. In two recent papers, Chen *et al* investigated strategies to improve monoenergeticity based on tailoring either the laser intensity distribution [12] or the thickness of the target [14].

It also appears that 2D effects make the optimal thickness condition (24) more stringent, so that a lower intensity is required. Figure 11 shows snapshots from simulations with the same parameters as in figure 9, but with the pulse amplitude $a_0 = 30$, close to the value of $\zeta = 31.4$. We observe a strong transmission of the laser pulse, causing a strong turbulence in the electron density. The strong transmission appears to be correlated with a strong rarefaction of the electron density out of the axis (around $y = \pm 2\lambda$ as in figure 11), leaving a denser bunch of ions along the axis. The corresponding spectrum shows that the RPA peak is barely distinguishable from the exponential-like background.

5. Conclusions

We reported an analytical and simulation study of RPA of ultrathin foils. The effects of the nonlinear SIT of the foil were addressed and incorporated into the 1D 'LS' model for foil acceleration. The model predictions for ion energy and conversion efficiency as a function of target thickness were in fairly good agreement with the result of 1D simulations. The latter were further analyzed to unfold the dynamics and self-organization of foil acceleration. 2D simulations for parameters close to the 'optimal' thickness value given by the 1D theory showed
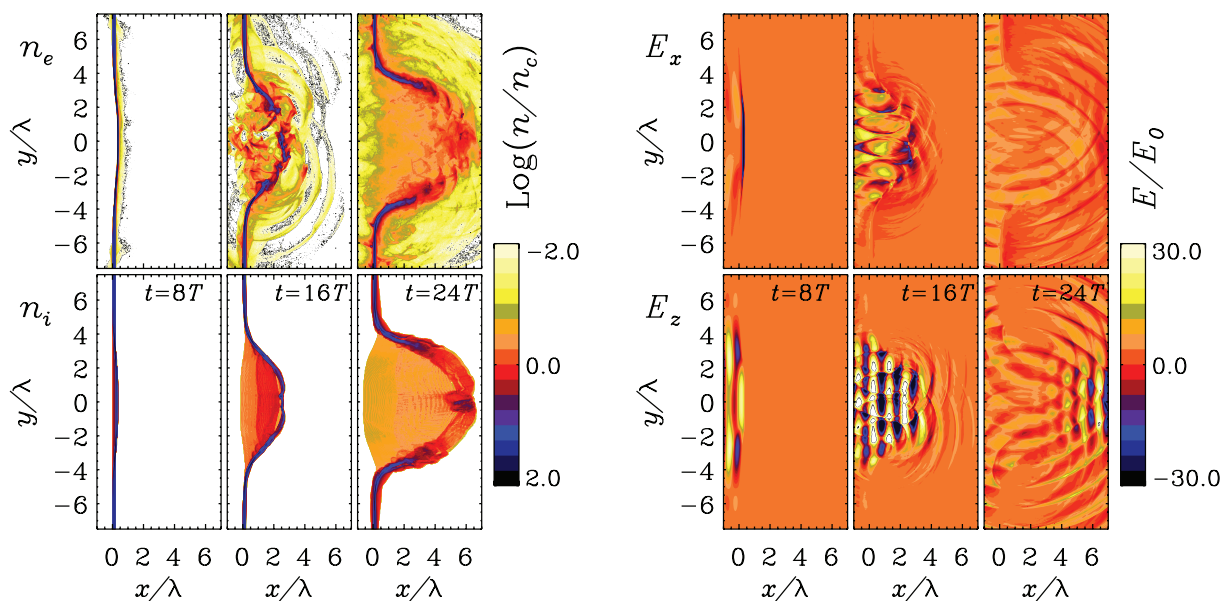
16

Figure 11. Same as figure 9, but for a pulse amplitude $a_0 = 30$.

that deformation of the target causes strong heating of electrons, leading to a broad ion spectrum and giving a lower threshold for the penetration of the laser pulse through the foil.

Acknowledgments

References

[1] Badziak J, Glowacz S, Jablonski S, Parys P, Wolowski J, Hora H, Krása J, Láska L and Rohlena K 2004 Production of ultrahigh ion current densities at skin-layer subrelativistic laser-plasma interaction *Plasma Phys. Control. Fusion* **46** B541–55

[2] Kar S *et al* 2008 Plasma jets driven by ultraintense-laser interaction with thin foils *Phys. Rev. Lett.* **100** 225004

[3] Akli K U *et al* 2008 Laser heating of solid matter by light-pressure-driven shocks at ultrarelativistic intensities *Phys. Rev. Lett.* **100** 165002

[4] Esirkepov T, Borghesi M, Bulanov S V, Mourou G and Tajima T 2004 Highly efficient relativistic-ion generation in the laser-piston regime *Phys. Rev. Lett.* **92** 175003

[5] Esirkepov T, Yamagiwa M and Tajima T 2006 Laser ion-acceleration scaling laws seen in multiparametric particle-in-cell simulations *Phys. Rev. Lett.* **96** 105001

[6] Pegoraro F and Bulanov S V 2007 Photon bubbles and ion acceleration in a plasma dominated by the radiation pressure of an electromagnetic pulse *Phys. Rev. Lett.* **99** 065002

[7] Borghesi M, Fuchs J, Bulanov S V, MacKinnon A J, Patel P K and Roth M 2006 Fast ion generation by high-intensity laser irradiation of solid targets and applications *Fus. Sci. Technol.* **49** 412

[8] Macchi A, Cattani F, Liseykina T V and Cornolti F 2005 Laser acceleration of ion bunches at the front surface of overdense plasmas *Phys. Rev. Lett.* **94** 165003

[9] Liseikina T V and Macchi A 2007 Features of ion acceleration by circularly polarized laser pulses *Appl. Phys. Lett.* **91** 171502

[10] Robinson A P L, Gibbon P, Zepf M, Kar S, Evans R G and Bellei C 2009 Relativistically correct hole-boring and ion acceleration by circularly polarized laser pulses *Plasma Phys. Control. Fusion* **51** 024004

[11] Naumova N, Schlegel T, Tikhonchuk V T, Labaune C, Sokolov I V and Mourou G 2009 Hole boring in a DT pellet and fast-ion ignition with ultraintense laser pulses *Phys. Rev. Lett.* **102** 025002

[12] Chen M, Pukhov A, Sheng Z M and Yan X Q 2008 Laser mode effects on the ion acceleration during circularly polarized laser pulse interaction with foil targets *Phys. Plasmas* **15** 113103

[13] Yin Y, Yu W, Yu M Y, Lei A, Yang X, Xu H and Senecha V K 2008 Influence of target thickness on the generation of high-density ion bunches by ultrashort circularly polarized laser pulses *Phys. Plasmas* **15** 093106

[14] Chen M, Pukhov A, Yu T P and Sheng Z M 2009 Enhanced collimated GeV monoenergetic ion acceleration from a shaped foil target irradiated by a circularly polarized laser pulse *Phys. Rev. Lett.* **103** 024801

[15] Zhang X, Shen B, Ji L, Wang F, Jin Z, Li X, Wen M and Cary J R 2009 Ion acceleration with mixed solid targets interacting with circularly polarized lasers *Phys. Rev. Sel. Top. Accel. Beams* **12** 021301

[16] Robinson A P L, Kwon D-H and Lancaster K 2009 Hole-boring radiation pressure acceleration with two ion species *Plasma Phys. Control. Fusion* **51** 095006

[17] Gonoskov A A, Korzhimanov A V, Eremin V I, Kim A V and Sergeev A M 2009 Multicascade proton acceleration by a superintense laser pulse in the regime of relativistically induced slab transparency *Phys. Rev. Lett.* **102** 184801

[18] Grech M, Skupin S, Nuter R, Gremillet L and Lefebvre E 2009 High-quality ion beams by irradiating a nano-structured target with a petawatt laser pulse *New J. Phys.* **11** 093035

[19] Zhang X, Shen B, Li X, Jin Z and Wang F 2007 Multistaged acceleration of ions by circularly polarized laser pulse: monoenergetic ion beam generation *Phys. Plasmas* **14** 073101

[20] Zhang X, Shen B, Li X, Jin Z, Wang F and Wen M 2007 Efficient GeV ion generation by ultraintense circularly polarized laser pulse *Phys. Plasmas* **14** 123108

[21] Robinson A P L, Zepf M, Kar S, Evans R G and Bellei C 2008 Radiation pressure acceleration of thin foils with circularly polarized laser pulses *New J. Phys.* **10** 013021

[22] Klimo O, Psikal J, Limpouch J and Tikhonchuk V T 2008 Monoenergetic ion beams from ultrathin foils irradiated by ultrahigh-contrast circularly polarized laser pulses *Phys. Rev. Sel. Top. Accel. Beams* **11** 031301

[23] Yan X Q *et al* 2008 Generating high-current monoenergetic proton beams by a circularly polarized laser pulse in the phase-stable acceleration regime *Phys. Rev. Lett.* **100** 135003

[24] Liseykina T V, Borghesi M, Macchi A and Tuveri S 2008 Radiation pressure acceleration by ultraintense laser pulses *Plasma Phys. Control. Fusion* **50** 124033

[25] Qiao B, Zepf M, Borghesi M and Geissler M 2009 Stable GeV ion-beam acceleration from thin foils by circularly polarized laser pulses *Phys. Rev. Lett.* **102** 145002

[26] Tripathi V K, Liu C S, Shao X, Eliasson B and Sagdeev R Z 2009 Laser acceleration of monoenergetic protons in a self-organized double layer from thin foil *Plasma Phys. Control. Fusion* **51** 024014

[27] Eliasson B, Liu C S, Shao X, Sagdeev R Z and Shukla P K 2009 Laser acceleration of monoenergetic protons via a double layer emerging from an ultra-thin foil *New J. Phys.* **11** 073006

[28] Macchi A, Veghini S and Pegoraro F 2009 'Light Sail' acceleration reexamined *Phys. Rev. Lett.* **103** 085003

[29] Yan X Q, Wu H C, Sheng Z M, Chen J E and Meyer–ter–Vehn J 2009 Self-organizing GeV, nanocoulomb, collimated proton beam from laser foil interaction at 7×10^{21} W cm^{-2} *Phys. Rev. Lett.* **103** 135001

[30] Rykovanov S G, Schreiber J, Meyer–ter–Vehn J, Bellei C, Henig A, Wu H C and Geissler M 2008 Ion acceleration with ultra-thin foils using elliptically polarized laser pulses *New J. Phys.* **10** 113005

[31] Macchi A, Liseikina T V, Tuveri S and Veghini S 2009 Theory and simulation of ion acceleration with circularly polarized laser pulses *C. R. Phys.* **10** 207–15

[32] Borghesi M 2009 Talk at the *Coulomb09 Workshop Ion Acceleration with High Power Lasers: Physics and Applications (Senigallia, Italy, June 15–18, 2009)*

Plasma-Based Generation and Control of a Single Few-Cycle High-Energy Ultrahigh-Intensity Laser Pulse

M. Tamburini,[1,*] A. Di Piazza,[1] T. V. Liseykina,[2] and C. H. Keitel[1]

[1]*Max-Planck-Institut für Kernphysik, Saupfercheckweg 1, D-69117 Heidelberg, Germany*
[2]*Institut für Physik, Universität Rostock, D-18051 Rostock, Germany*

A laser-boosted relativistic solid-density paraboloidal foil is known to efficiently reflect and focus a counterpropagating laser pulse. Here we show that in the case of an ultrarelativistic counterpropagating pulse, a high-energy and ultrahigh-intensity reflected pulse can be more effectively generated by a relatively slow and heavy foil than by a fast and light one. This counterintuitive result is explained with the larger reflectivity of a heavy foil, which compensates for its lower relativistic Doppler factor. Moreover, since the counterpropagating pulse is ultrarelativistic, the foil is abruptly dispersed and only the first few cycles of the counterpropagating pulse are reflected. Our multidimensional particle-in-cell simulations show that even few-cycle counterpropagating laser pulses can be further shortened (both temporally and in the number of laser cycles) with pulse amplification. A single few-cycle, multipetawatt laser pulse with several joules of energy and with a peak intensity exceeding 10^{23} W/cm^2 can be generated already employing next-generation high-power laser systems. In addition, the carrier-envelope phase of the generated few-cycle pulse can be tuned provided that the carrier-envelope phase of the initial counterpropagating pulse is controlled.

A wide range of novel studies in nonlinear optics as well as the major new regimes of extreme field physics require laser pulses which simultaneously exhibit the following three key features: few-cycle duration, high-energy, and ultrahigh intensity. Already in nonrelativistic atomic physics, it has been demonstrated that quantum processes can be controlled by manipulating the pulse shape of few-cycle laser pulses [1]. In order to achieve the same goal also in the ultrarelativistic regime and in the realm of nonlinear QED, few-cycle laser pulses with tunable carrier-envelope phase (CEP) are required with peak intensities largely exceeding 10^{20} W/cm^2 [2–4]. At such high intensities, for example, the nonlinear Compton emission spectrum is expected to show pronounced pulse-shape effects [5,6].

Although next-generation 10-PW optical laser systems are expected to generate laser pulses with 150–300 J energy and 15–30 fs duration [4,7] [full width at half maximum (FWHM) of the pulse intensity], the limited bandwidth renders the generation of few-cycle pulses with multijoule energy very challenging [8,9]. Indeed, the only laser system aiming at 1-PW power and few-cycle duration is the Petawatt Field Synthesizer [10]. Several methods for further shortening and amplifying laser pulses have been proposed, e.g., Raman [11,12] and Brillouin [13,14] backscattering, interaction with plasma waves [15,16] and ionization induced self-compression effects [17,18]. However, none of the pulses generated employing the above-mentioned methods simultaneously exhibit few-cycle duration, multijoule energy, and ultrarelativistic intensity. In fact, the initial intensity is bounded to

relatively moderate values and the generated pulses are transversely and temporally modulated, which might prevent their subsequent focusing to ultrarelativistic intensities. In addition, the CEP control, which is crucial for many applications, has not been demonstrated in any of the above-mentioned methods.

In this Letter, we put forward the concept of a laser-boosted solid-density paraboloidal relativistic "mirror," interacting with a superintense counterpropagating laser pulse, to generate a CEP tunable few-cycle pulse with multijoule energy and peak intensity exceeding 10^{23} W/cm^2. Contrary to intuition, it is found that a heavy and therefore relatively slow "mirror" should be employed to maximize the intensity and the energy of the reflected pulse, since its larger reflectivity compensates for the lower velocity. Furthermore, the short duration of the reflected pulse is achieved by employing a superintense incident pulse, which abruptly disperses the plasma mirror after only the first few cycles. Multidimensional particle-in-cell (PIC) simulations indicate both the feasibility of the presented setup by employing next-generation multi-PW laser systems and a considerable shortening with amplification even for already few-cycle laser pulses.

In the proposed setup, a "driver" pulse with frequency ω and (average) intensity I_d accelerates a "mirror" to relativistic velocities along the positive x direction and a "reflected" pulse is generated in the collision of the mirror with a counterpropagating "source" pulse, also with frequency ω and with intensity I_s. Here and below, the subscript s (d) and the upper (lower) sign refer to the

PHYSICAL REVIEW LETTERS

source (driver) pulse counterpropagating (copropagating) with respect to the mirror, and $T = 2\pi/\omega$ ($\lambda = cT$) is the laser period (wavelength). Our aim here is to determine the conditions for maximizing both the intensity and the energy of the reflected pulse. In order to develop an analytical model, for the thin foil we employ the Dirac-δ density profile $n(x) = n_e \ell \delta(x)$ [19,20], where n_e and ℓ are the foil density and thickness, respectively. If the foil moves with velocity $v_x = \beta c > 0$, its reflectivity is given by $\mathcal{R}_{s/d} = \zeta_{s/d}^2/(\zeta_{s/d}^2 + \Gamma_{s/d}^2)$ [20], where $\Gamma_{s/d}^2 = \{1 + a_{s/d}^2 - \zeta_{s/d}^2 + [(1 + a_{s/d}^2 - \zeta_{s/d}^2)^2 + 4\zeta_{s/d}^2]^{1/2}\}/2$ and $\zeta_{s/d} \equiv \zeta_0/D^{\pm}$. Here we have introduced the normalized (average) field amplitude $a_{s/d}^2 \equiv I_{s/d}/I^*$ with $I^* \equiv m_e^2 \omega^2 c^3/4\pi e^2$, the Doppler factors $D^{\pm} = \sqrt{(1 \pm \beta)/(1 \mp \beta)} \gtrless 1$, and the surface density $\zeta_0 \equiv \pi n_e \ell/n_c \lambda$, with $n_c \equiv m_e \omega^2/4\pi e^2$ being the critical density. Notice that for a linearly polarized (LP) pulse the peak intensity $\hat{I}$ is approximately twice the intensity I, whereas they coincide for a circularly polarized (CP) pulse. If both the source and the driver pulse fields are ultrarelativistic ($a_{s/d} \gg 1$), the reflectivity can be approximated as [20,21] $\mathcal{R}_{s/d} \approx 1$ if $\zeta_{s/d} > a_{s/d}$ and $\mathcal{R}_{s/d} \approx \zeta_{s/d}^2/a_{s/d}^2$ if $\zeta_{s/d} < a_{s/d}$, which presents the reflectivity with accuracy better than 2% for $a_{s/d} > 50$. Hence, the condition $\zeta_{s/d} > a_{s/d}$ has to be fulfilled to secure $\mathcal{R}_{s/d} \approx 1$.

In our model the foil is initially at rest and it is accelerated along the positive x direction by the driver pulse. In order to determine the value of the Doppler factor after the acceleration phase D_0^+, we assume that $\zeta_0 > a_d$ and thus $\mathcal{R}_d \approx 1$. The velocity of a foil accelerated by the radiation pressure [22] of the driver pulse can be calculated analytically by employing the "light sail" equation for a perfectly reflecting mirror [20,21,23] and the result for D_0^+ is $D_0^+ = 1 + \mathcal{E}_d/\zeta_0$, where $\mathcal{E}_d = 2\pi Z m_e \int a_d^2(w)dw/Am_p$ is the "effective" energy of the driver pulse. Here Z (A) is the ion atomic number (weight) and $a_d^2(w) = I_d(w)/I^*$ is the field amplitude as a function of the foil phase $w = [t/T - x(t)/\lambda]$.

Since the foil undergoes a recoil due to the radiation pressure of the source pulse, the Doppler factor D^+ of the foil at the maximum of the source pulse intensity is smaller than D_0^+. On this respect it is convenient to employ a sharp-rising, high-contrast source pulse, as those generated with the plasma mirror technique [24,25]. By proceeding as for the calculation of D_0^+, we obtain

$$D^+ = \frac{D_0^+}{1 + D_0^+ \mathcal{E}_s/\zeta_0} = \frac{\zeta_0(\zeta_0 + \mathcal{E}_d)}{\zeta_0^2 + \mathcal{E}_s(\zeta_0 + \mathcal{E}_d)}, \quad (1)$$

where $\mathcal{E}_s = 2\pi Z m_e \int a_s^2(w)dw/Am_p$ which, for a sharp-rising pulse, is the part of the source pulse energy before the source pulse intensity reaches its maximum (see below for details). Since we seek $\mathcal{R}_s \approx 1$, we require $\zeta_s > a_s$, which provides the constraint $\zeta_0 > \zeta_{0,m}$ with

$$\zeta_{0,m} = a_s[1 - \epsilon + \sqrt{(1-\epsilon)(1-\epsilon+4\mathcal{E}_d/a_s)}]/2, \quad (2)$$

where $\epsilon \equiv \mathcal{E}_s/a_s$ accounts for the effect of the recoil. In order to maximize the energy and the intensity of the reflected pulse at $\mathcal{R}_s \approx 1$ for fixed driver and source pulses, we have to maximize the Doppler factor D^+ as a function of ζ_0 with the condition $\zeta_0 > \zeta_{0,m}$. From Eq. (1), $D^+(\zeta_0)$ has a maximum at $\zeta_0^* = \mathcal{E}_d\sqrt{\mathcal{E}_s}/(\sqrt{\mathcal{E}_d} - \sqrt{\mathcal{E}_s})$ and monotonically decreases for $\zeta_0 > \zeta_0^*$. Assuming sufficiently small recoil [$\epsilon < 1/2$ and $\mathcal{E}_d > \mathcal{E}_s(1-\epsilon)^2/(1-2\epsilon)^2$], then $\zeta_{0,m} > \zeta_0^*$ and the maximum $D^+(\zeta_0)$ compatible with $\zeta_0 > \zeta_{0,m}$ is at $\zeta_{0,m}$, and it is $D_m^+ = \zeta_{0,m}/a_s$.

Note that, for a flat foil and fixed driver and source pulses, both the maximum intensity $I_r = D^{+4}\mathcal{R}_s I_s$ and energy $E_r \approx I_r S \Delta t_s/D^{+2}$ of the reflected pulse are achieved at the minimum ζ_0 such that $\zeta_s > a_s$, i.e., at $\zeta_{0,m}$. Here S is the surface area of the focal spot and Δt_s is the source pulse duration. In fact, for $\zeta_s < a_s$ the reflectivity is $\mathcal{R}_s \approx \zeta_s^2/a_s^2$ thus $I_r = D^{+2}\zeta_0^2 I^*$ and $E_r \approx \zeta_0^2 I^* S \Delta t_s$, which are monotonically increasing functions of ζ_0. The fact that there exists an optimal value of the surface density has a simple physical interpretation: for fixed driver and source pulses, if ζ_0 is too large, the foil slows down and the Doppler factor is small. If ζ_0 becomes too small, the velocity of the foil increases and the reflectivity rapidly decreases because ζ_s tends to vanish. Moreover, at $\zeta_{0,m}$ the reflected pulse energy $D_m^{+2} I_s S \Delta t_s$ is a monotonically increasing function of I_s. If $\epsilon < 1/3$ and $\mathcal{E}_d < a_s(1-\epsilon)^2(1-3\epsilon)/4\epsilon^2$, i.e., if the effect of the recoil is sufficiently small, the maximum reflected pulse intensity $D_m^{+4} I_s$ is also a monotonically increasing function of I_s. For fixed source pulse, the above conditions account for the slowdown of the foil due to the recoil, which becomes increasingly important for increasing foil velocity [see Eq. (1)]. In a three-dimensional geometry, a paraboloidal mirror can focus the source pulse to its diffraction limit. Since the laser wavelength is Doppler reduced in the rest frame of the foil, the reflected pulse can be focused down to λ^2/D^{+2} and the intensity at the focus is $I_{r,f} = D^{+6}\mathcal{R}_s I_s S/\lambda^2$. If $\zeta_0 > \mathcal{E}_d$, $\epsilon < 1/4$ and $\mathcal{E}_d < 2a_s(1-\epsilon)^2(1-4\epsilon)/(1+2\epsilon)^2$, the maximum of the intensity at the focus $I_{r,f}$ is achieved at $\zeta_{0,m}$ and it is an increasing function I_s. In other cases, the maximum of $I_{r,f}$ can be a decreasing function of I_s or the maximum of $I_{r,f}$ can be achieved at $\mathcal{R}_s < 1$. However, in these cases a higher intensity *at the focus* is achieved at the expense of a lower reflected pulse power $P_r = D^{+4}\mathcal{R}_s I_s S$ and energy $E_r \approx D^{+2}\mathcal{R}_s I_s S \Delta t_s$.

For simplicity, we first consider a driver and source pulse with one-cycle $\sin^2$-function rise and fall, and with a five-cycle constant plateau. Figure 1 reports the maximum reflected pulse amplitude $\sqrt{D^{+4}\mathcal{R}_s I_s/I^*}$ as a function of ζ_0 for $a_d = 130$ and for $a_s = 130, 100, 80$. In each case the reflected pulse amplitude initially increases for increasing
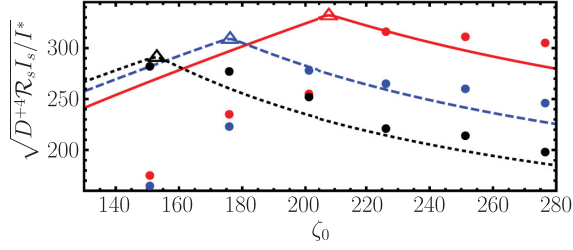
FIG. 1 (color online). The maximum amplitude of the reflected pulse $\sqrt{D^{+4}\mathcal{R}_s I_s/I^*}$ as a function of ζ_0 for $a_d = 130$ and $a_s = 130$ (solid red line), $a_s = 100$ (dashed blue line) and $a_s = 80$ (dotted black line). See the text for further details.

ζ_0, reaches its maximum at $\mathcal{R}_s \approx 1$, and then decreases as the Doppler factor decreases. The three triangles in Fig. 1 are centered at $(\zeta_{0,m}, \sqrt{D_m^{+4}I_s/I^*})$ and their position coincides with the maximum of the reflected pulse amplitude, confirming our analytical estimates. Since in all cases $\mathcal{E}_d < a_s(1-\epsilon)^2(1-3\epsilon)/4\epsilon^2$, the maximum reflected amplitude rises for increasing I_s (see Fig. 1). The results of one-dimensional PIC simulations with CP driver and source pulses are also reported in Fig. 1 (colored circles), the foil being a slab of fully ionized carbon with $n_e = 400n_c$. The spatial resolution is $\lambda/4000$ and the number of particles per cell per species 1000. Our PIC simulation results agree with the model predictions at $\zeta_0 > \zeta_{0,m}$, i.e., at $\mathcal{R}_s \approx 1$.

In a multidimensional geometry, the onset of transverse Rayleigh-Taylor-like (RT) [22] instabilities renders the foil "porous" to the source pulse. RT instabilities in the radiation pressure acceleration regime have been investigated analytically [26,27], numerically [26–28] and experimentally [29]. In particular, in Refs. [26,27] it was shown that in the linear approximation the RT instability grows as $\exp[\Phi_d(w)]$ with $\Phi_d(w) = \int_0^w 2\pi[Zm_e a_d^2(u)\lambda/Am_p\zeta_0\lambda_{\rm RT}]^{1/2}du$ where $\lambda_{\rm RT}$ is the wavelength of the perturbation. Our simulations indicate that in order to effectively reflect the source pulse, $\Phi_d(w) \lesssim 5.7$ for $\lambda_{\rm RT} \approx \lambda$ [29], which can be fulfilled by increasing the value of $\zeta_0 > \zeta_{0,m}$.

In our two-dimensional PIC simulations both the driver and the source pulse have a $\sin^2$-function temporal field profile with 15.5 fs duration (FWHM of the intensity), Gaussian transverse profile and wavelength $\lambda = 800$ nm. The driver (source) pulse is CP (LP with the electric field along the y axis) with intensity $I_d \approx 3.4 \times 10^{22}$ W/cm^2 ($I_s \approx 5.6 \times 10^{22}$ W/cm^2) and spot radius $\sigma_d = 3.8\lambda$ ($\sigma_s = 1.2\lambda$), corresponding to a power $P_d \approx 9.9$ PW ($P_s \approx 1.6$ PW). These parameters are envisaged at the APOLLON laser system [4,7,30]. The foil consists of fully ionized carbon with electron density $n_e = 400n_c$ and it is initially shaped transversely with a thickness distribution $\ell = \max[\ell_1, \ell_0 \exp(-y^2/2\sigma_f^2)]$, with $\ell_1 = 0.02\lambda$, $\ell_0 = 0.20\lambda$, $\sigma_f = 2.6\lambda$ and localized at $x = 5\lambda$. Note that the properties of such carbon foils can be engineered with high precision nowadays [31,32]. It has been shown that Gaussian pulses and shaped foils can be employed to generate collimated ion beams [33,34]. Here we propose to use shaped foils to generate paraboloidal relativistic mirrors. Indeed, for $\sigma_d > \sqrt{2}\sigma_f$ the acceleration factor $a_d^2(y)/\zeta_0(y)$ [33] is larger in the outer part of the foil, which therefore takes a focusing profile for the source pulse. Since for many applications slow focusing and defocusing are desirable, we have set $\sigma_d \approx \sqrt{2}\sigma_f$ so the relativistic mirror is nearly flat before interacting with the source pulse (see Fig. 2). The size of the computational box is $20\lambda(x) \times 20\lambda(y)$, the corresponding grid is $20\,000(x) \times 8000(y)$ and 900 particles per cell for each species are used.

Figure 2 displays the evolution of the square root of the energy density $u = \sqrt{(\mathbf{E}^2 + \mathbf{B}^2)/2}$ and of the electron density distribution n_e. The driver (source) pulse reaches the edge of the foil at $t \approx 0$ (10T). An accurate synchronization between two laser pulses can be achieved, e.g., by generating the two pulses from the same seed pulse before the amplification stage. Although instabilities have developed ($\Phi_d \approx 4.7$ with our parameters) and density fluctuations are clearly visible before the source pulse impinges on the foil, the foil remains sufficiently compact to reflect the first part of the source pulse (see Fig. 2 at $t \leq 16T$ and the Supplemental Material [35] for a movie of the laser-foil interaction). As the source pulse amplitude at the foil
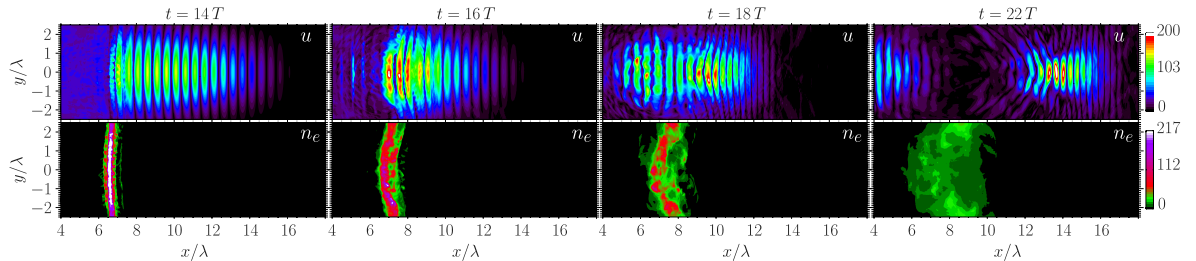

FIG. 2 (color online). Snapshots of $u = \sqrt{(\mathbf{E}^2 + \mathbf{B}^2)/2}$ (first row) and n_e (second row) in normalized units. See the text for details.

position increases, the source pulse "digs through" the lower-density regions and abruptly disperses the foil, which becomes transparent to the remaining part of the pulse (see Fig. 2 from $t = 16T$ to $t = 18T$). Finally, at $t = 22T$ a single few-cycle reflected pulse separated from the foil remnants is observed. The peak intensity and peak power of the reflected pulse are: $\hat{I}_r \approx 2.3 \times 10^{23}$ W/cm^2 (for the source pulse $\hat{I}_s \approx 9.6 \times 10^{22}$ W/cm^2), and $\hat{P}_r \approx 2.2$ PW, with 5.8 fs duration and 6.8 J energy [see Fig. 3(c)]. Figure 3(a) displays the y component of the electric field of the reflected pulse along the central axis for the case of zero (solid black line) and $\pi/2$ (dotted red line) CEP of the source pulse showing that the reflected pulse *inherits* the CEP of the source pulse. Inclusion of radiation reaction (RR) effects, according to Refs. [36,37], does not significantly alter the reflected pulse [see Fig. 3(b)]. Our explanation is that when the reflected pulse is generated, the foil density is still high and the fields inside the foil are much smaller than in vacuum [36]. Moreover, we ensured that the probability of electron-positron pair production remains negligible. The influence of a randomly distributed preplasma on the front surface of the foil is also considered in Fig. 3(b) (dashed red line). The preplasma thickness corresponds to 10% of the foil thickness and its average density is $n_e/2$. The presence of the preplasma reduces the peak intensity, peak power and energy of the reflected pulse to $\hat{I}_r \approx 1.8 \times 10^{23}$ W/cm^2, $\hat{P}_r \approx 2.0$ PW and 5.8 J, respectively. This can be explained by the increased electron heating due to the enhanced penetration of the driver pulse into the preplasma. The modulus of the Fourier transform of the y component of the electric field along the central axis $|E_{r,y}(k_x)|$, where k_x denotes the wave number and $k \equiv 2\pi/\lambda$, is reported in Fig. 3(d) (solid black line) showing that the reflected pulse is chirped and peaked at $\lambda_r \approx 593$ nm. For comparison, the spectra of two Gaussian pulses with the

same wavelength and with two (dotted red line) and three (dashed blue line) cycles FWHM of the *field* profile are also reported [see Fig. 3(d)].

In order to account for the slowly rising profile of the source pulse and estimate the wavelength λ_r and peak intensity $\hat{I}_r$ of the reflected pulse, we approximate the sin^2-function field profile with a linearly rising profile b_0w/N. Here N is the number of cycles before the source pulse maximum and $b_0 = 3a_s/2\sqrt{2}$ so the source pulse and its linear profile approximation have the same duration and energy before their maximum. Assuming $\mathcal{R}_s \approx 1$, the maximum reflected intensity is achieved at min$[N, \hat{w}]$ with $\hat{w} = [4Am_pN^2\zeta_0/15\pi Zm_eD_0^+a_s^2]^{1/3}$. For a slowly-rising profile $\hat{w} \leq N$, thus $\hat{\mathcal{E}}_s(\hat{w}) = \zeta_0/5D_0^+$ which *does not* depend on the source pulse parameters. Hence, from Eq. (1) we get $\hat{D}^+(\hat{w}) = 5D_0^+/6$. By inserting our numerical parameters we obtain: $\lambda_r \approx 656$ nm and $\hat{I}_r \approx 1.2 \times 10^{23}$ W/cm^2 for the linearly rising profile, and $\lambda_r \approx 593$ nm and $\hat{I}_r \approx 1.4 \times 10^{23}$ W/cm^2 for the more realistic sin^2-function profile. While λ_r is in good agreement with the two-dimensional simulation results, $\hat{I}_r$ is underestimated because, by definition, the one-dimensional model does not include focusing effects. Indeed, our simulations show that increasing the ratio σ_d/σ_f by reducing σ_f from 2.6λ to 2.4λ improves the focusing and further enhances $\hat{I}_r$ from 2.3×10^{23} W/cm^2 to 2.8×10^{23} W/cm^2. In addition, higher intensities are expected in a fully three-dimensional geometry, where, in contrast to two-dimensional simulations, the source pulse is focused also along the z axis. We also mention that increasing $P_{s/d}$ by doubling $\sigma_{s/d}^2$ and σ_f^2 with the other parameters as reported above enhances $\hat{P}_r$ to 3 PW but reduces the intensity enhancement $\hat{I}_r/\hat{I}_s$ from 2.4 to 1.8 because the pulse focusing decreases.

Finally, we stress that even a few-cycle source pulse can be further shortened and amplified. Indeed, by employing a $\ell_0 = 0.17\lambda$, $\sigma_f = 2.1\lambda$ shaped foil and a driver (source) pulse with 15.5 fs (5.8 fs) duration, $I_d \approx 5.1 \times 10^{22}$ W/cm^2 ($I_s \approx 5 \times 10^{22}$ W/cm^2) intensity and $\sigma_d = 3.1\lambda$ ($\sigma_s = 1\lambda$) radius [corresponding to a driver (source) power $P_d \approx 9.9$ PW ($P_s \approx 1$ PW)], a single 1.5 cycles (2.1 fs duration), 2 J energy, $\hat{P}_r \approx 1.8$ PW and $\hat{I}_r \approx 1.4 \times 10^{23}$ W/cm^2 reflected pulse is generated ($\hat{I}_s \approx 7 \times 10^{22}$ W/cm^2). Moreover, in contrast to the previous case of a relatively long source pulse, a 2.7 fs duration, 1.3 J energy 1 PW peak power and 4.7×10^{22} W/cm^2 peak intensity transmitted pulse is also generated (see the movies in the Supplemental Material [35]). Similar parameters for the driver and source pulses are envisaged at the Extreme Light Infrastructure [4,38].
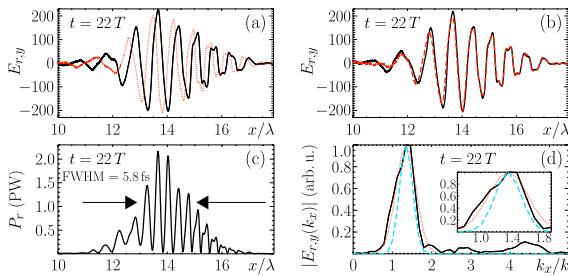

FIG. 3 (color online).   (a) $E_{r,y}$ along the central axis for zero (solid black line) and $\pi/2$ (dotted red line) CEP of the source pulse. (b) $E_{r,y}$ with RR effects (solid black line) and with a preplasma on the front surface of the foil (dashed red line). (c) Power contained in a spot with 1λ radius centered on the axis. (d) $|E_{r,y}(k_x)|$ (solid black line) and the corresponding quantity for a Gaussian pulse with two (dotted red line) and three (dashed blue line) cycles FWHM of the *field* profile. The inset shows a zoom of the main peak region.

*matteo.tamburini@mpi-hd.mpg.de

[1] F. Krausz and M. Ivanov, Rev. Mod. Phys. **81**, 163 (2009).

[2] S. Meuren and A. Di Piazza, Phys. Rev. Lett. **107**, 260401 (2011).

[3] A. I. Titov, H. Takabe, B. Kämpfer, and A. Hosaka, Phys. Rev. Lett. **108**, 240406 (2012).

[4] A. Di Piazza, C. Müller, K. Z. Hatsagortsyan, and C. H. Keitel, Rev. Mod. Phys. **84**, 1177 (2012).

[5] F. Mackenroth and A. Di Piazza, Phys. Rev. A **83**, 032106 (2011).

[6] M. Boca, V. Dinu, and V. Florescu, Phys. Rev. A **86**, 013414 (2012).

[7] A. V. Korzhimanov, A. A. Gonoskov, E. A. Khazanov, and A. M. Sergeev, Phys. Usp. **54**, 9 (2011).

[8] D. Herrmann, L. Veisz, R. Tautz, F. Tavella, K. Schmid, V. Pervak, and F. Krausz, Opt. Lett. **34**, 2459 (2009).

[9] S. Witte and K. Eikema, IEEE J. Sel. Top. Quantum Electron. **18**, 296 (2012).

[10] "Petawatt Field Synthesizer," http://www.attoworld.de/Mainpages/Light_and_matter/index.html#42 (2014).

[11] V. M. Malkin, G. Shvets, and N. J. Fisch, Phys. Rev. Lett. **82**, 4448 (1999).

[12] Z. Toroker, V. M. Malkin, and N. J. Fisch, Phys. Rev. Lett. **109**, 085003 (2012).

[13] L. Lancia, J.-R. Marquès, M. Nakatsutsumi, C. Riconda, S. Weber, S. Hüller, A. Mančić, P. Antici, V. T. Tikhonchuk, A. Héron, P. Audebert, and J. Fuchs, Phys. Rev. Lett. **104**, 025001 (2010).

[14] S. Weber, C. Riconda, L. Lancia, J.-R. Marquès, G. A. Mourou, and J. Fuchs, Phys. Rev. Lett. **111**, 055004 (2013).

[15] J. Faure, Y. Glinec, J. J. Santos, F. Ewald, J.-P. Rousseau, S. Kiselev, A. Pukhov, T. Hosokai, and V. Malka, Phys. Rev. Lett. **95**, 205003 (2005).

[16] J. Schreiber, C. Bellei, S. P. D. Mangles, C. Kamperidis, S. Kneip, S. R. Nagel, C. A. J. Palmer, P. P. Rajeev, M. J. V. Streeter, and Z. Najmudin, Phys. Rev. Lett. **105**, 235003 (2010).

[17] N. L. Wagner, E. A. Gibson, T. Popmintchev, I. P. Christov, M. M. Murnane, and H. C. Kapteyn, Phys. Rev. Lett. **93**, 173902 (2004).

[18] S. A. Skobelev, A. V. Kim, and O. Willi, Phys. Rev. Lett. **108**, 123904 (2012).

[19] V. A. Vshivkov, N. M. Naumova, F. Pegoraro, and S. V. Bulanov, Phys. Plasmas **5**, 2727 (1998).

[20] A. Macchi, S. Veghini, T. V. Liseykina, and F. Pegoraro, New J. Phys. **12**, 045013 (2010).

[21] A. Macchi, S. Veghini, and F. Pegoraro, Phys. Rev. Lett. **103**, 085003 (2009).

[22] P. Mulser and D. Bauer, *High Power Laser-Matter Interaction*, Springer Tracts in Modern Physics Vol. 238 (Springer, New York, 2010), Chap. 4.2.

[23] T. Esirkepov, M. Borghesi, S. V. Bulanov, G. Mourou, and T. Tajima, Phys. Rev. Lett. **92**, 175003 (2004).

[24] C. Thaury, F. Quere, J.-P. Geindre, A. Levy, T. Ceccotti, P. Monot, M. Bougeard, F. Reau, P. d'Oliveira, P. Audebert, R. Marjoribanks, and P. Martin, Nat. Phys. **3**, 424 (2007).

[25] C. Rödel, M. Heyer, M. Behmke, M. Kübel, O. Jäckel, W. Ziegler, D. Ehrt, M. Kaluza, and G. Paulus, Appl. Phys. B **103**, 295 (2011).

[26] F. Pegoraro and S. V. Bulanov, Phys. Rev. Lett. **99**, 065002 (2007).

[27] S. V. Bulanov, T. Z. Esirkepov, F. Pegoraro, and M. Borghesi, C.R. Phys. **10**, 216 (2009).

[28] M. Chen, N. Kumar, A. Pukhov, and T.-P. Yu, Phys. Plasmas **18**, 073106 (2011).

[29] C. A. J. Palmer *et al.*, Phys. Rev. Lett. **108**, 225002 (2012).

[30] G. Chériaux, F. Giambruno, A. Fréneaux, F. Leconte, L. P. Ramirez, P. Georges, F. Druon, D. N. Papadopoulos, A. Pellegrina, C. Le Blanc, I. Doyen, L. Legat, J. M. Boudenne, G. Mennerat, P. Audebert, G. Mourou, F. Mathieu, and J. P. Chambaret, AIP Conf. Proc. **1462**, 78 (2012).

[31] A. V. Krasheninnikov and F. Banhart, Nat. Mater. **6**, 723 (2007).

[32] W. van Dorp, C. Hagen, P. Crozier, B. van Someren, and P. Kruit, Microelectron. Eng. **83**, 1468 (2006).

[33] M. Chen, A. Pukhov, T. P. Yu, and Z. M. Sheng, Phys. Rev. Lett. **103**, 024801 (2009).

[34] M. Chen, T.-P. Yu, A. Pukhov, and Z.-M. Sheng, New J. Phys. **12**, 045004 (2010).

[35] See the Supplemental Material at http://link.aps.org/supplemental/10.1103/PhysRevLett.113.025005 for a movie of the laser-foil interaction with the parameters corresponding to those of Fig. 2 (Movie_long_source_pulse.gif) and with the parameters reported in the last paragraph of the Letter (Movie_few-cycle_source_pulse.gif).

[36] M. Tamburini, F. Pegoraro, A. Di Piazza, C. H. Keitel, and A. Macchi, New J. Phys. **12**, 123005 (2010).

[37] M. Tamburini, T. V. Liseykina, F. Pegoraro, and A. Macchi, Phys. Rev. E **85**, 016407 (2012).

[38] "Extreme Light Infrastructure," http://www.eli-laser.eu/ (2014).

3. Hot electron generation and Brunel's model

The list of publications:

P. Mulser, S.M. Weng, T. Liseykina, "*Analysis of the Brunel model and resulting hot electron spectra*, Phys. Plasmas **19**, 043301 (2012)

T. Liseykina, P. Mulser, M. Murakami, *Collisionless absorption, hot electron generation, and energy scaling in intense laser-target interaction*, Phys. Plasmas **22**, 033302 (2015)

Analysis of the Brunel model and resulting hot electron spectra

P. Mulser,[1,a)] S. M. Weng,[1,b)] and Tatyana Liseykina[2]

[1]*Theoretical Quantum Electronics (TQE), Technische Universität Darmstadt, D-64289 Darmstadt, Germany*
[2]*Institut für Physik, Universität Rostock, Universitätsplatz 3, D-18051 Rostock, Germany*

Among the various attempts to model collisionless absorption of intense and superintense ultrashort laser pulses, the so-called Brunel mechanism plays an eminent role. A detailed analysis reveals essential aspects of collisionless absorption: Splitting of the electron energy spectrum into two groups under *p*-polarization, prompt generation of fast electrons during one laser cycle or a fraction of it, insensitivity of absorption with respect to target density well above n_c, robustness, simplicity, and logical coherence. Such positive aspects contrast with a non-Maxwellian tail of the hot electrons, too low energy cut off, excessively high fraction of fast electrons, and inefficient absorption at moderate angles of single beam incidence and intensities. Brunel's pioneering idea has been the recognition of the role of the space charges induced by the electron motion perpendicular to the target surface that make irreversibility possible. By setting the electrostatic fields inside the overdense target equal to zero, anharmonic resonance and mixing of layers leading to Maxwellianization are excluded. To what extent the real electron spectra and their scaling on laser intensity are the product of the interplay between Brunel's mechanism and anharmonic resonance is still an open question. © *2012 American Institute of Physics*. [http://dx.doi.org/10.1063/1.3696034]

I. INTRODUCTION

Despite nearly three decades of research on superintense laser-target interaction collisionless absorption is not yet understood. Simple estimates show that from intensities of $I = 10^{16}$ W/cm² on collisional heating becomes less and less important and the excellent degree of absorption at relativistic and subrelativistic intensities, demonstrated by experiments and simulations, has to rely on collisionless processes.[1] Various mechanisms and models have been proposed: Anomalous skin effect,[2,3] vacuum heating,[4,5] wave breaking,[6] Landau damping,[7] diffusive heating,[8] stochastic electron acceleration in fluctuating fields,[9] $\mathbf{j} \times \mathbf{B}$ heating,[10] surface plasmon excitation,[11,12] and "laser dephasing heating."[13] The models are either based on simulations only ($\mathbf{j} \times \mathbf{B}$ heating, "laser dephasing"), or they are in disagreement with basic properties observed in experiments and simulations. The anomalous skin effect at high intensities yields an absorption of a few percentage only. In addition, the assumption of regular or diffuse electron reflection at the target-vacuum interface is severely modified by electron trapping in front of the target as well as in its interior.[14] Absorption by excitation of surface plasmons requires corrugated targets.[12] In flat targets,[11] coupling is very delicate and unlikely to occur. For a discussion in more detail, the reader may consult Refs. 1, 14, and Sec. 8.3.2 in Ref. 15.

One of the prominent features of collisionless absorption in intense laser beam-dense matter interaction is the generation of fast electrons. Energetic electrons in the MeV region are observed in all computer simulations of particle in cell (PIC), Vlasov and molecular dynamics type, and appear in all corresponding experiments as well. As several applications are connected with this phenomenon, like efficient generation of intense electron and ion beams by novel techniques, fast ignition of inertial fusion pellets, new radiation sources in the extreme ultraviolet (XUV) domain, cancer therapy, the spectral composition of the fast electrons, their maximum energy, and the question of possible tailoring of the spectra is in the focus of common interest. Nevertheless, no systematic spectral investigations on the experimental site hitherto exist and, on the other hand, the theoretical understanding of the electron spectra is far from being satisfactory. Even worse, no general agreement exists on how the fast electrons are created in the laser field.

In long laser pulses of ps duration and subrelativistic intensities, several collisionless processes may be responsible for absorption and fast electron generation as soon as a rarefaction density profile has formed, to mention first resonance absorption at critical electron density[16] and subsequent electron trapping in the electron plasma wake (Landau damping). Collisionless absorption becomes particularly complex owing to crater formation at late times and the evolution of instabilities, Secs. 2.3 and 6.2 in Ref. 15. The study of collisionless absorption in the general 3-dimensional (3D) case with no restrictions on symmetry is the domain of simulations and experiments. Both need interpretation; simulations do not reveal the underlying physics either. Nevertheless, the situation is not hopeless. Basic understanding means prediction of the degree of absorption, of the origin of fast electrons and their spectrum, their percentage and scaling of the "temperature" on laser intensity as well as the mean energy of the slow electrons. What we have to aim at is similar to atomic physics once when understanding the hydrogen spectrum led to understanding the complex spectrum of iron. In plane target geometry, there is the hope to arrive at such a hydrogen atom analogy, i.e., at a simple picture of physics

---

[a)]Electronic mail: Peter.Mulser@physik.tu-darmstadt.de.
[b)]Present address: Institute of Laser Engineering, Osaka University, Osaka 565-0871, Japan.

governing collisionless absorption of intense pulses (a) when their length is of sub 100 fs duration and the ions may be considered as fixed or (b) in the (sub)ps domain when their intensity is relativistic. In both cases, the electron dynamics of the critical region may be limited to 1D of a sharp edged plasma, owing to the absence of a rarefaction wave (a) or because of the extreme profile steepening and almost absence of subcritical plasma, Sec. 5.3.1 in Ref. 15 (b). Fortunately, there exist 1D single beam experiments showing absorption up to 78% under oblique incidence and 1D PIC single beam simulations reproducing them.[17] Important hints for a simple model may come from simulations. In detail, simulations show that the fast electrons are generated (1) first before the slow electrons; (2) nearly instantaneously, i.e., the single electron during one laser cycle; and (3) efficiently, regardless of how overdense the target is. In contrast, an absorption mechanism of diffusive type, e.g., electron-ion collisions and collisions of the electrons with the fluctuating electromagnetic field according to the fluctuation-dissipation theorem, is slow and extends over a high number of cycles. Hence, fast electron generation is not of diffusive type.

In 1987, Brunel proposed an absorption model for oblique incidence of a *p*-polarized sub-relativistic laser beam onto a step-like highly overdense flat target, $n_e \gg n_c, n_e$ electron density, $n_c = \epsilon_0 m_e \omega^2/e^2$ critical density, m_e electron mass, ω laser frequency, and e electron charge.[18] As we shall see in Sec. II, this model is capable of explaining several features of collisionless absorption in a much more convincing way than others mentioned above. In the strongly relativistic domain, the zero vector potential mechanism perhaps may assume a similar role.[19] Indeed, until recently Brunel's model has been the only successful attempt so far to explain efficient collisionless absorption on physical grounds under a minimum of assumptions and simplest geometry. For normal incidence, $\mathbf{j} \times \mathbf{B}$ heating is generally invoked.[10] However, the reader must be aware that no explanation was given for it by the authors, absorption was found by simulations only. Nevertheless, it is a pioneering paper, similar to Brunel's, because the authors recognized that electron motion strictly parallel to the laser field would define a perfectly reversible process. Irreversibility comes from the motion perpendicular to the target surface induced by the magnetic field **B** and its discontinuity there, in analogy to Brunel's model for oblique incidence. Brunel's model occupies a special place. Therefore, it is indicated to subject it to a thorough analysis, never given before, the author included, with particular attention to its predictions on fast electron generation. It seems to be believed by a majority of researchers that the fast electrons are "Brunel electrons." In this context here, an electron is defined fast somewhat arbitrarily when its energy exceeds the mean oscillation energy it has got in the laser beam in vacuum.

The analysis of Brunel's model will be done in Sec. II. By comparing with measurements, it will be shown to what extent this model is able to make valid predictions and by which simple additions partial improvement in absorption could be achieved. Subsequently, we shall compare with PIC simulations and discover also serious shortcomings and we shall indicate the main reason for them. The purpose of the

analysis is to make a further step towards understanding the physics of collisionless absorption and the splitting of the electron spectrum into a low energetic main part and a hot tail. Incidentally, the detailed study of the plasma layer dynamics in Brunel's model will reveal already a qualitative understanding of the existence of two spectral groups. Contrary to the general believe that all electrons are pushed back to the target by the laser field after reversion, half of them (the slow ones) return against the laser field. Finally, it will result that the belief of the fast electrons being of Brunel origin is of very limited validity.

II. BRUNEL'S MODEL IN DETAIL

A highly overdense, e.g., solid target of constant electron density $n_e = n_0$ and zero temperature filling the half space $x \geq 0$ is given. From the vacuum, the laser field component $E(\tau) = E_0 \sin\tau$ is normally incident onto its surface, $\tau = \omega t$. From Poisson's law follows that the skin depth at time τ_l is

$$x_{0l} = \frac{\epsilon_0 E_0 \sin\tau_l}{e n_0}, \tag{1}$$

see Fig. 1. With the amplitude of the oscillation velocity $v_0 = eE_0/(m_e\omega)$ in *x* direction, the normalized velocity $w_l = v/v_0$ of the layer number *l* is given by

$$w_l(\tau) = (\cos\tau - \cos\tau_l) + (\tau - \tau_l)\sin\tau_l; \quad \tau \geq \tau_l. \tag{2}$$

Correspondingly, the normalized trajectory $s_l = x_l\omega/v_0$ results as

$$s_l(\tau) = (\sin\tau - \sin\tau_l) - (\tau - \tau_l)\cos\tau_l + \frac{1}{2}(\tau - \tau_l)^2 \sin\tau_l$$
$$+ \frac{x_{0l}\omega}{v_0}; \quad \tau \geq \tau_l. \tag{3}$$

The number of particles per unit cross section that move during one cycle follows from Eq. (1) as $N_0 = n_0 x_0 = \epsilon_0 E_0/e$.
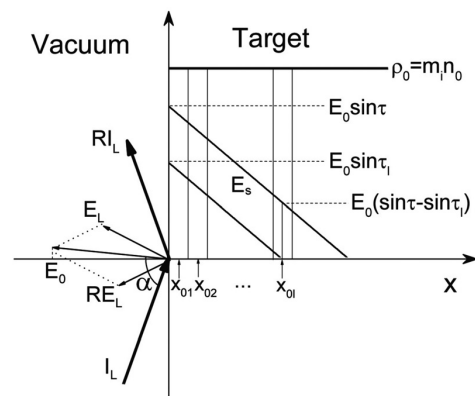

FIG. 1. Configuration of Brunel's absorption model. A *p*-polarized plane laser wave E_L (intensity I_L) impinges under angle α and is partially reflected as RE_L under α. At time instant $\tau_l = \omega t_l$, the resulting *x* component $E_0(\tau_l)$ penetrates up to the position x_{0l} given by Eq. (1). At the instant τ, its magnitude there is $E_0(\sin\tau - \sin\tau_l)$ for $|\sin\tau| > |\sin\tau_l|$ and zero for $|\sin\tau| \leq |\sin\tau_l|$.

97   ANALYSIS OF THE BRUNEL MODEL

043301-3   Mulser, Weng, and Liseykina   Phys. Plasmas **19**, 043301 (2012)

A. The genuine model

Owing to the smallness of x_{0l} in a high density target in comparison to the oscillation amplitude v_0/ω, it is set zero. When the lth particle is driven back to the target surface at the instant $\tau = \tau_f$, it enters the region $x > 0$ that is assumed to be field-free. Thus, it has gained the kinetic energy $m_e v_0^2 w_l^2(\tau_f)/2$ from the laser field. For Eqs. (2) and (3) to hold the orbits are not allowed to cross. A sufficient condition for this is that

$$\frac{\partial s_l}{\partial \tau_l} = \frac{1}{2}(\tau - \tau_l)^2 \cos\tau_l \qquad (4)$$

does not change sign. In the interval $0 \le \tau_l \le \pi/2$, it is satisfied.

In Fig. 2, representative orbits starting in the first interval $0 \le \tau_l \le 2\pi$ are shown. All of the N_0 electrons are pulled out into the vacuum during the first quarter time period $0 \le \tau_l < \pi/2$ (see upper picture). In the second quarter period, the two free fall terms $(\tau - \tau_l)\cos\tau_l$ and $(\tau - \tau_l)^2\sin\tau_l/2$ in Eq. (3) prevail on the laser field term, so that all s_l result positive (see lower picture) and have to be ignored. The change of sign in velocity w_l occurs exactly at $\tau_l = \pi/2$. In fact, for $\tau - \tau_l = \epsilon > 0$ and $\tau = \pi/2$, it follows $w_l = -\sin\epsilon + \epsilon\cos\epsilon = -\epsilon^2/2 < 0$. In contrast, $\tau_l = \pi/2$ yields $w_l = \epsilon^3/3! > 0$. In the second half period $\pi < \tau_l < 2\pi$, the driving laser field is reversed and neutralized by the (infinitely) strong space charge field. Thus, when considering only particles with reentry times $\tau \le 2\pi$, no crossing of orbits happens. Figure 2, upper plot, shows that not all particles return during one period of τ. The front layer drifts away into the vacuum at the speed v_0 because of missing free fall term. The closer a layer is positioned to the front, the longer is its reentry time. This gives rise to some orbit crossing for reentry times larger than one cycle.

In Fig. 3, the number of particles returning up to time τ in units of N_0 is plotted. It shows that $N_0/2$ particles reenter
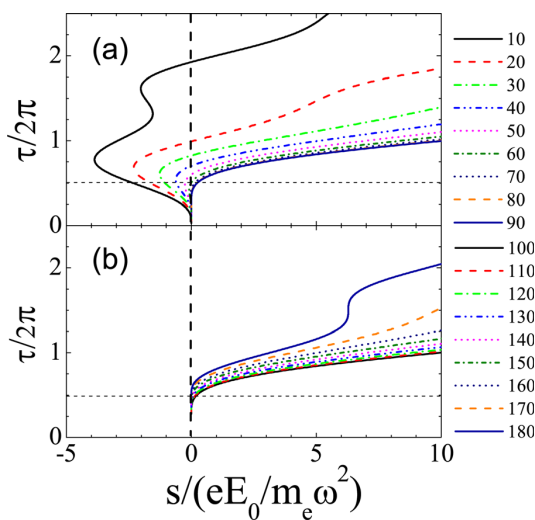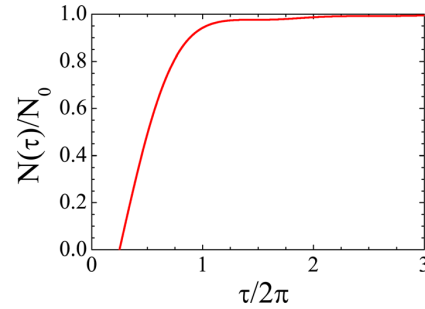

FIG. 3. Number of particles per unit area $N(\tau)$ returned to the target in the interval $[0, \tau]$.

in the interval $\pi/2 < \tau \le \pi$ but only a small fraction (2.2%) comes back after one period 2π.

The velocity w_f at which a particle enters the target is shown as a function of τ_l in Fig. 4. The maximum reaches $w_f = 2.13$. High-speed electrons in the neighborhood of the maximum of w_f return late. Particles lifted into vacuum at $\tau_l < 13° = 13\pi/180$ come back only after two periods and show strongly oscillating reentry velocities.

Of particular interest is the absorbed energy as a function of τ. The dashed curve in Fig. 5 shows the average reentry energy E in units of the mean oscillation energy $m_e v_0^2/4$ in the interval $[0, \tau]$. If normalization is done by the number of all particles N_0 that have been moved during one laser cycle, the solid line is obtained. The results do not differ much from each other because the electrons $N_0/2$ reentering during the second quarter period contribute energetically by less than 1%. If summation is extended to all particles N_0 pulled out into the vacuum during one period, the result is the dotted line. All N_0 electrons contribute to absorption. However, the target is heated directly by the laser only by those coming back during the duration of the laser pulse. Crossing of trajectories does not occur in the interval $\pi < \tau \le 5\pi/2$. In order to obtain a measure for target heating, we extend the integration over a whole cycle from π to 3π, although intersection of orbits occurs for $\tau > 5\pi/2$, invalidating in principle Eqs. (2) and (3) (Brunel[18] does the integration from $\pi/2$ to $5\pi/2$). However, according to Fig. 3, only 0.5% of electron orbits show crossing. This is a too small number to influence the equations of motion (2) and (3) by their space charge. Together with Fig. 5 follows that the energetic contribution from the extension remains below
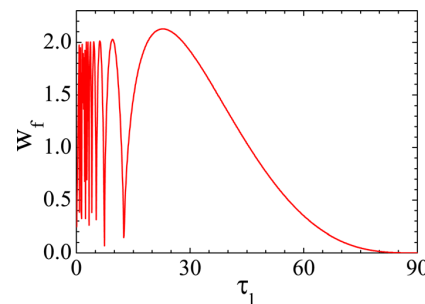

FIG. 2. Single layer displacement $s(\tau)$. The individual layer starts from position $x_{0l} \simeq 0$ at the time τ_l, indicated in degrees on the ordinate at the right $(10, 20, ..., 90 \Longleftrightarrow \pi/2, 100, ...)$. Only displacements $x(\tau) \le 0$ are physically real (a). In the region $x > 0$, the electric field $E_0(\tau)$ is zero at all times τ (b).

FIG. 4. Reentry velocity component w_f normal to the target of a layer started at τ_l.
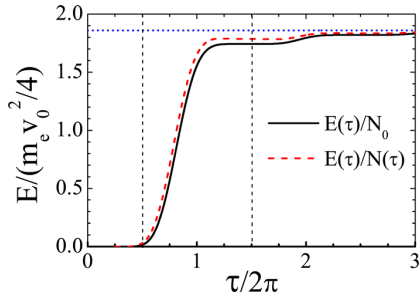
FIG. 5. Normalized average reentry energy as a function of reentry time τ. Bold curve: average over all particles pulled into vacuum during one laser cycle; and dashed curve: average over $N(\tau)$ from Fig. 3.

1% and that the strongly oscillating fraction in Fig. 4 contributes even considerably less. From Fig. 5 for the average energy $\eta_h m_e v_0^2/4$ gained per electron heating the target in the interval $[\pi, 3\pi]$, one reads $\eta_h = 1.74$ (Brunel: $\eta_h = 1.57$). The corresponding factor η_t of all electrons contributing to absorption is $\eta_t = 1.87$. One could think that the run away electrons could accumulate over several cycles and disturb the dynamics Eqs. (2) and (3). This may not happen because, in three dimensions, the space charge cloud rarefies rapidly and may also be quickly neutralized by a return current within the target.

Let us come now to the two most interesting questions, namely to the energy spectrum of the electrons and to the absorption coefficient in Brunel's model. The fastest electron of $w_f = 2.13$ finds back to the target at $\tau \simeq 2\pi$ corresponding to the cut off energy $E_f = (2w_f^2 = 9.07) \times m_e v_0^2/4$. The spectral distribution $f(E)$ normalized to unity is presented in Fig. 6. Its peculiarity is the peak of f at the cut off energy exceeding the flat minimum by a factor of 7.5. If only non intersecting orbits are considered, i.e., $\tau \leq 5\pi/2$, almost no change is observed; in particular, cut off energy and the peak there in $f(E)$ are preserved.

As the only free parameter is ν_0, this spectrum is self-similar and universal. Equating the energy gain by the reentering electrons per period 2π to the energy supplied to the target,
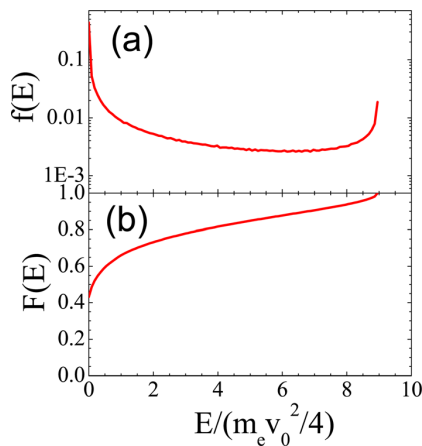

FIG. 6. Electron spectra $f(E)$ and $F(E) = \int f(E')dE'$.

$$\frac{1}{4} N_0 \eta_h m_e v_0^2 = \mathcal{A} I \cos \alpha \frac{2\pi}{\omega}, \tag{5}$$

α angle of incidence, the absorption coefficient $\mathcal{A}$ is

$$\mathcal{A} = \frac{1}{2} \eta_h \frac{v_0}{c} \frac{E_0^2}{E_L^2} \frac{1}{2\pi \cos \alpha}, \tag{6}$$

E_L laser field amplitude. With the help of the reflection coefficient R, the field component E_0 follows from Fig. 1 as $E_0 = (1 + \sqrt{R})E_L \sin\alpha$. Introducing the electron oscillation amplitude in vacuum $v_{os} = eE_L/m_e\omega$, $v_0 = v_{os}(1 + \sqrt{R})\sin\alpha$, the heating and total absorption coefficients (indexes h, t) read

$$\mathcal{A} = \frac{1}{4\pi} \eta_{h,t} \frac{v_{os}}{c} (1 + \sqrt{R})^3 \frac{\sin^3\alpha}{\cos\alpha} \sim (I\lambda^2)^{1/2};$$
$$\frac{\eta_h}{4\pi} = 0.138, \quad \frac{\eta_t}{4\pi} = 0.149. \tag{7}$$

In general, the connection between $\mathcal{A}$ and R may be complex. In the simplest case, $R = 1 - \mathcal{A}$ may be set and Eq. (7) may be solved for $v_{os}/c = 0.3$ as a function of α. The result is presented in Fig. 7 for η_t. For $\alpha = 86°$, total absorption is reached and no solution exists beyond. At relativistic intensities, an effective Lorentz factor γ has to be introduced. As a rule, for $\alpha \leq 60°$, Eq. (7) yields only modest absorption in p-polarization. Even setting $v_{os} = c$ (weakly relativistic case) and $R = 1$ produces collisionless absorption not exceeding $\mathcal{A} = 120\sin^3\alpha/\cos\alpha\%$ at moderate angles of incidence ($\alpha \leq 25°$). On the other hand, for $\alpha = 82°$ $\mathcal{A}$ exceeds unity at $v_{os}/c = 1$. In the subrelativistic intensity range, the absorbed energy scales like $(I\lambda^2)^{3/2}$.

Equation (7) can directly be compared with measurements and PIC simulations of the angular absorption dependence in p polarization for $I = 2 \times 10^{16}$ W/cm^2 Ti:Sa,[17] see Table I, $\mathcal{A}_C$ in the 1st row. They are taken with a few cycle Ti:Sa laser and correspond to the conditions of Brunel's model, i.e., no prepulse, no hydrodynamic motion. The last values (80°) refer to $I = 5 \times 10^{16}$ W/cm^2. The Brunel values $\mathcal{A}_B$ in the 2nd row are calculated from Eq. (7) under the condition $\mathcal{A} + R = 1$.

In the 3rd row under $\mathcal{A}_E$, older measurements at $I = 3 \times 10^{16}$ W/cm^2 twice the harmonic of the fundamental Ti:Sa frequency are reported for additional comparison.[20] In
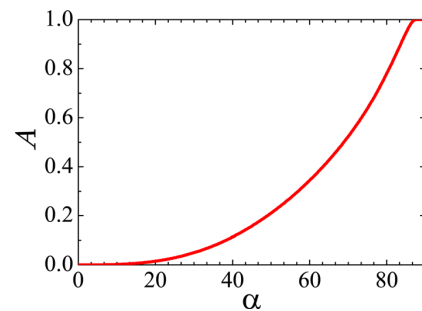

FIG. 7. Absorption coefficient $\mathcal{A}$ as a function of angle of incidence α for $v_{os}/c = 0.3$ under condition $R = 1 - \mathcal{A}$; v_{os}/c electron oscillation amplitude in vacuum normalized to light speed c.

TABLE I. Comparison of the absorption coefficients as functions of the incident angle from two experiments ($\mathcal{A}_C$, $\mathcal{A}_E$) and from Brunel's model ($\mathcal{A}_B$, $\mathcal{A}_{BE}$). The meaning of $\mathcal{A}_C$, $\mathcal{A}_B$, $\mathcal{A}_E$, and $\mathcal{A}_{BE}$ is given in the text. $\mathcal{A}_B$ and $\mathcal{A}_{BE}$ obey the condition $\mathcal{A} + R = 1$.

α	20°	30°	40°	50°	60°	70°	80°
$\mathcal{A}_C$	0.12	0.17	0.20	0.30	0.40	0.60	0.77
$\mathcal{A}_B$	0.003	0.012	0.028	0.054	0.098	0.171	0.334
$\mathcal{A}_E$	0.11	0.12	0.24	0.38	0.50	0.49	—
$\mathcal{A}_{BE}$	0.006	0.020	0.046	0.089	0.155	0.262	0.476

this latter case, the plasma density scale length L in units of the fundamental laser wavelength $L/\lambda = 5\% - 6\%$ is estimated. The table shows good agreement between the two experiments, in addition $\mathcal{A}_C$ is in agreement with PIC simulations, see Ref. 17. However, the predictions on absorption $\mathcal{A}_B$ from Brunel's genuine model differ drastically. Only near grazing incidence realistic values are obtained for $\mathcal{A}_B$; for all angles below the $\mathcal{A}_B$ values are far too low, i.e., the model works inefficiently in this intensity range. From Eq. (7), the scaling $\mathcal{A}_B \sim I^{1/2}$ is deduced. Owing to the universal character of the spectrum in Fig. 6, except slight modifications due to R, this is also the scaling of the fast electrons. The scaling extracted from Ref. 17 is $\mathcal{A}_B \sim I^{0.12 \pm 0.02}$. The scaling of the average energy of the fast electrons ("electron temperature T_e") in Brunel's model results proportional to the intensity I, whereas in the experiments, simulations, and theory, the state of the art is $T_e \sim I^{1/2}$ to $I^{1/3}$ with tendency to a 1/4 exponent in the strong relativistic domain, see Refs. 21–26. Thus, the Brunel mechanism predicts very different scalings for the total absorption coefficient and the absorbed total energy; these quantities in turn are proportional to the number and the energy of the hot electrons in Brunel's model.

There is a natural subdivision of the electron spectrum into a low energy and a high energy group, separated by a smooth transition zone. Where does it originate from? With a view on Figs. 2–6 and bearing in mind what has been stated on particle dynamics in the combined space charge and laser fields, in particular on reentry, the decay of the electron energies into a slow and into a fast group has to be attributed to the following characteristics of Brunel's model. The particles returning to the target from vacuum during the second
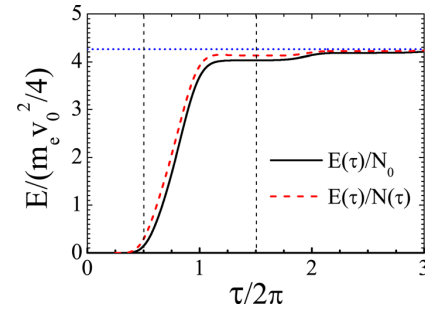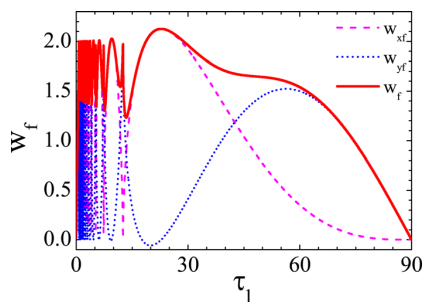

FIG. 8. Extended Brunel model, corresponds to Fig. 4 with motion w_y parallel to the target surface included. Dashed: genuine Brunel model, $w_f = (w_{yf}^2 + w_{xf}^2)^{1/2}$.

FIG. 9. Normalized average reentry energy from the extended Brunel model, corresponds to that from the Brunel model in Fig. 5.

quarter cycle $(\pi/2, \pi)$ are those closer to the target. They feel a weakly screened space charge field and a weakened laser field. As a consequence, they are not pushed far out into to vacuum and return already when the two fields are opposed to each other. This results into a low energy gain for half the total number N_0 of particles lifted into the vacuum (see Figs. 3, 5, and 9). We give them the name "free falling particles." For the N_0 particles reentering the target in the interval $(\pi, 2\pi)$, the situation is reversed; they are effectively accelerated back by the two fields in phase.

B. Extended Brunel model

In the sharp-edged plasma, the energy gained by the single electron and absorbed in the field-free region is given by the sum of the contributions from w_l normal and w_y parallel to the target rather than by w_l alone, thus

$$\frac{1}{2}m_e w_f^2 = \frac{1}{2}m_e(w_l^2 + w_y^2), \quad w_y = \frac{eE_0(1-\sqrt{R})\cos\alpha\sin\tau_l}{m_e\omega v_0}.$$
(8)

If not stated differently, in the following two pictures, the angle of incidence is chosen $\alpha = 45°$, and $R = 0$ is set for direct comparison with Figs. 4–6. The significant contribution to w_f by the extension is seen in Fig. 8 from the bold curve. There is a significant change for $\tau_l < \pi/12$, as closer inspection shows, but on the same ground as in Fig. 4, it does not contribute noticeably to the average reentry energy. However, the extension has a strong impact on it around $\tau = \pi/6$, compare the dotted and dashed graphs. As a consequence, the absorbed energy per electron is increased considerably, $\eta_h = 4.04$ and $\eta_t = 4.27$ now, see the change of scale almost by a factor of 2.5 in Fig. 9 compared to Fig. 5, both *under $R = 0$.* Only its shape is basically preserved owing to w_f reducing to zero for τ_l approaching $\pi/2$.

Again, the most interesting aspect is the energy distribution function $f(E)$ and its integral $F(E)$. The number of slow electrons $(E < 1)$ is decreased and there is a significant increase of hot electrons over the entire spectral range with a pronounced maximum around $E = 2$, Fig. 10. Needless to mention that it is far from Maxwellian. The location of the local maximum of $f(E)$ is very sensitive to the reflection coefficient R. The fraction of the fast electrons has increased from 34% to 71%.
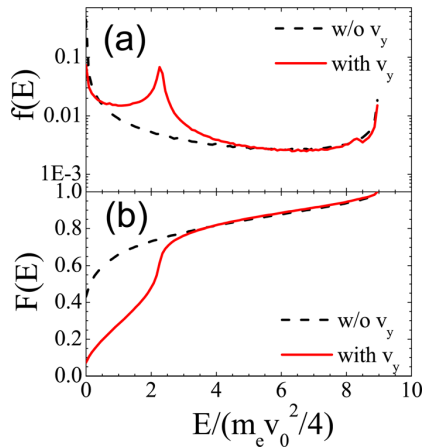
FIG. 10. Electron spectra $f(E)$ and $F(E) = \int f(E')dE'$ from the extended Brunel model under the condition $\mathcal{A} + R = 1$ (solid line). Dashed line from Fig. 5 for comparison.

In Fig. 7, $\mathcal{A}$ is calculated self consistently fulfilling the condition $\mathcal{A} + R = 1$. The same should be done in the extended model for w_f from Eq. (8). This is much more involving because now η_h depends on angle of incidence α and on R. For $v_{os}/c = 0.3$, the numerical result is shown in Fig. 11. The difference to the genuine Brunel model is 45% at $\alpha = 60°$, see Fig. 11, bold curve, with dashed curve taken from Fig. 7. It shifts into the right direction, but not enough at moderate intensities, as, in particular, the 4th row of Table I illustrates with $\mathcal{A}_{BE}$ self consistently determined for the parameters of $\mathcal{A}_B$ of the 2nd row for intensities $v_{os}/c \lesssim 0.1$. The extension introduced here is not as successful one would have hoped with a view on the drastically increased values of η_h and η_t. It is a consequence of the minus sign in Eq. (8). If, as a test, the R values are chosen from Ref. 17, the experimental values from there are reproduced; however, this is inconsistent. The situation with the spectrum of the fast electrons deteriorates in the extended model owing to the presence of the local maximum at normalized $E = 2$.

III. THE PROBLEM OF THE FAST ELECTRON SPECTRA AND THE MISSING PHYSICS IN BRUNEL'S MODEL

Among the various attempts to arrive at a quantitative description of the angular dependence of absorption, there is
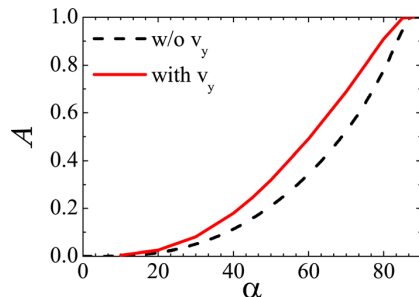

FIG. 11. Absorption coefficient $\mathcal{A}$ from the extended Brunel model for $v_{os}/c = 0.3$ (solid line) and from Fig. 7 (dashed).

the one dimensional hydrocode MULTI-fs (Ref. 27) that can handle linear resonance absorption. It has been widely used in the past and has still a non ignorable group of supporters. In a first trial, it was also applied to the experiment in Ref. 17 with the result that it reproduced the experimental values $\mathcal{A}_C$ as well as the PIC simulations could do or even slightly better. Nevertheless for that experiment, it had to be discarded because as a test showed almost all absorption, locally given by **jE** cycle-averaged, took place in a preplasma in front of the target of density by orders of magnitude lower than that of the target. This is unphysical and is due to the artificial viscosity introduced in the code to prevent hydrodynamic breaking of flow, in the experiment under consideration occuring two orders below the intensity used. It could be shown in general that collisionless absorption was reproduced when introducing a collision frequency ratio $\nu/\omega > 2$ artificially. A realistic estimate for the critical region led to ratios ν/ω not exceeding 10^{-2}. Hence, when using MULTI-fs, it must be separately tested that absorption occurs in the right place and is not produced by the artificial viscosity term. Such caution is in order when reexamining any papers on absorption of ultrashort laser pulses where "good agreement" is found of MULTI with experiments.

So far, there are several arguments in favor of the extended Brunel model: (1) simplicity and coherence, (2) prompt generation of the fast electrons within a fraction of a laser cycle, (3) increased absorption values for nearly relativistic intensities at angles from which on the electric force prevails on the Lorentz force ("$\mathbf{j} \times \mathbf{B}$ heating"), and (4) absorption efficiency not depending on the target density as soon as it is much higher than the critical density. At the same time, there are severe cons against the model: (1) absorption exceeding 100% at grazing incidence, (2) wrong absorption scaling on intensity, (3) wrong prediction of the fraction of fast electrons, and (4) energy spectrum far from Maxwellian with a cutoff that is too low. In this respect, the extension presented here on physical grounds makes the situation even considerably worse; compare Figs. 6 and 10.

In the geometry of the Brunel model, the PIC simulations unambiguously show that the hot electron spectrum is Maxwellian, $f_h(E) \sim \exp(-\beta E)$, $\beta = $ const, and that its fraction is a few percent only. Examples of $f(E)$ and $F(E)$ from a 1D simulation for Nd pulses of constant intensity $I\lambda^2 = 1.37 \times 10^{18} a^2$ W/cm$^{-2}\mu$m^2, $a = eE_L/m_e c\omega = 0.3, 1.0, 3.0,$ and 10 at oblique incidence of $\alpha = 45°$ after 40 fs are presented in Fig. 12. The normalization of $f(E)$ is done on all electrons having been exposed once to the laser light before escaping into the target and having got energies superior to $E = \epsilon \times E_{os}$, $E_{os} = m_e v_0^2/4, \epsilon = 0, 10^{-4}, 10^{-3}, 10^{-2}$. The resulting percentage of the fast electrons is seen from $F(E = E_{os})$. It is nearly 2 orders of magnitude lower than in Brunel's model. It clearly shows that the bulk of electrons is heated up to low temperature.

The question arises: What part of physics is missing in Brunel's model? To give a first answer, Eqs. (2) and (3) may be solved numerically by decomposing the overdense target into a number of layers and determining the driving field in the evanescent region from Poisson's law. This is an easily solvable system having all advantages of dynamics of
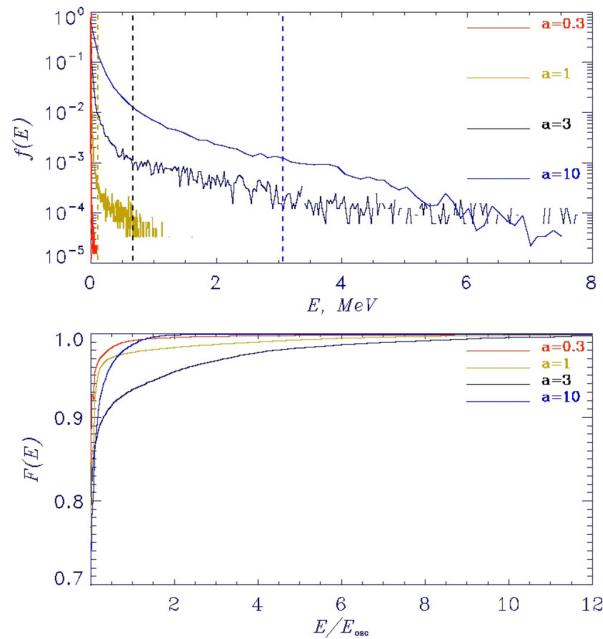
FIG. 12. 1D PIC simulation of collisionless absorption of constant intensities a = 0.3, 1.0, 3.0, and 10 under 45° p-polarized incidence. (a) Spectral energy distribution $f(E)$ of the electrons; vertical line marks the position of E equalizing the mean electron oscillation energy. (b) $F(E)$ total number of electrons having energies greater than $\epsilon \times E_{os}$ and less or equal E; $\epsilon = 10^{-2}$. The number of fast electrons amounts to a few percentage.

Hamiltonian character. The answer has been given in Ref. 28. The system shows a chaotic behavior which manifests itself in a continuous crossing of layers and stochastic order of reentering, see their order given there. Closer inspection then shows that single layers happen to resonate anharmonically, thereby undergoing a phase shift by π or a fraction of it and moving against the bulk. This is a very efficient process of wave breaking, introduced first in Ref. 28 ("resonant breaking of flow"), and generator of a high level of fluctuations. This fact shifts the question of missing physics in Brunel's model to the search for the origin of the exclusion of resonance. In fact, as shown by our sufficient condition Eq. (4) for non-crossing of orbits, the model is mathematically correct as long as each particle undergoes one oscillation only, in contrast to what the numerical Hamiltonian treatment shows. When an electron is displaced by the weak evanescent laser field, it undergoes small forced oscillations that later may become resonant when entering the nonlinear regime. Thus, by assuming zero electrostatic potential inside the target ($x > 0$), all electrons undergo one single oscillation only with the consequence that resonance and chaos are excluded automatically in Brunel's model, with the severe impact above on the hot electron spectrum. From test runs with the potential inside the target set equal zero in the Hamiltonian model, the absorption decreased by more than an order of magnitude. Such a boundary condition is equivalent to the assumption of an instantaneous onset of the neutralizing return current. In reality, the building up of the return current takes time according to its inertia which involves many layers in contrast to the few layers driven in the evanescent laser front.
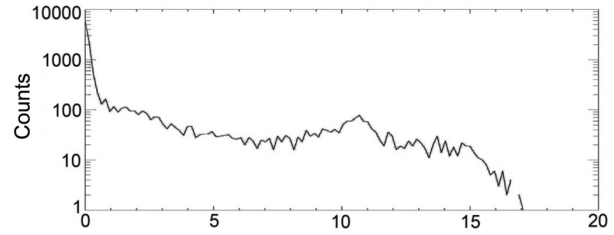

FIG. 13. Electron energy spectrum $f(E)$ from Hamiltonian dynamics of a layered target under the action of the Lorentz force from a p-polarized laser beam of intensity $I = 10^{17}$ Wcm^{-2} Nd under 45° incidence. The local fields are calculated from Fresnel's formulas. Anharmonic resonance allows for mixing of layers. Energy cutoff occurs at $E = 17 \times E_{os}$ and $E_{os} = m_e v_0^2/4$.

Going one step further by calculating correctly the laser field in each layer with the help of Fresnel formulas for thin layers (thickness much less than the local wavelength) and including the Lorentz force term in Eqs. (2) and (3), one is led at additional insight on when a layer reenters the target and on the spatial distribution in vacuum where this disruption-like motion originates from Ref. 29. We show the resulting electron spectrum in Fig. 13: There is the bulk of cold electrons, similar to the slope of the main fraction of cold Brunel electrons in Fig. 6(a), however continued to the right now by a fast Maxwellian like tail extending up to $17E_{os}$. Recirculation of electron layers enabling even higher cut offs is excluded in the model. The percentage of the particles in the tail is below 10%. Although the Hamiltonian multilayer model is physically richer and more complete in the spectrum of Fig. 13 remnants of Brunel's original spectrum are still present, like the concave shape of the hot electron distribution and an attenuated maximum shifted now from normalized $E = 9.3$ to $E = 11$.

IV. SUMMARY AND DISCUSSION

An analysis of the Brunel model has revealed essential aspects of collisionless absorption: Prompt generation of fast electrons during one laser cycle or a fraction of it under p-polarization, insensitivity of absorption with respect to target density well above n_c, robustness, and simplicity. Finally, the characteristic splitting of the electron energy spectrum into the two groups of slow and of fast electrons, observed in all experiments and simulations, PIC and Vlasov, comes about in the most natural way. Such positive aspects contrast with a non-Maxwellian tail of the hot electrons, too low cut off, unrealistic fraction of fast electrons, scaling of mean electron energy with intensity drastically different from the experiment by Cerchez et al.[17] under Brunel conditions, as well as from relevant findings in the literature so far,[21–26] and inefficient absorption below very oblique incidence. These are clear indications of some essential physics missing in Brunel's model. It is difficult to see which effect has been overlooked in this simple mechanism that the consequences are such a strong scaling of the absorption coefficient $\mathcal{A}_B \sim I^{1/2}$ on intensity, and, in particular, the astonishing dependence of the energy absorbed per cycle $\sim I^{3/2}$. In tendency, it looks like energy production from vacuum.

Brunel's pioneering idea has been the recognition of the space charges induced by the electron motion perpendicular to

the target surface that make irreversibility possible. However, one essential root of failure evidently is setting the electrostatic fields inside the overdense target equal to zero. It implies the neglect of any inertia and resistivity of the cold return current as well as of excitation of plasmons by the jets of the hot electrons and their mutual energy transfer. It must be kept present that in the skin layer, the total density of electron currents streaming into the vacuum and coming back undergo strong rarefaction compared to the situation in the target interior, i.e., the return current undergoes strong acceleration, accomplished by an intense electrostatic field. Even more significant seems to be the following effect. When the dynamics of the Brunel layers is studied properly as in Refs. 28 and 29, they undergo several oscillations before escaping into the target interior. In Brunel's model, they are suppressed with the consequence of inhibition of anharmonic resonance and, in concomitance, of mixing of layers ("resonant breaking of flow"). Mixing produces stochastic motion, longer life time in front of the target, the tendency towards Maxwellization and fast tail formation of the energetic electrons and a natural reduction of the reentry currents. We think that exactly here there is space for improvements. Hence, it remains to be investigated next to which extent the Brunel effect and anharmonic resonance compete and mix up to generate the correct electron spectra seen in simulations and experiments and to produce higher absorption at moderate angles of incidence in p-polarization. Furthermore, the Brunel mechanism and anharmonic resonance have a different impact on the symmetry of fast electron flows into the target and towards the irradiating laser. Brunel is extremely unidirectional into the target, the anharmonic resonance mechanism tends, like PIC simulations, to a more symmetric distribution of electron flows into the target and into the vacuum. In the latter case, target normal sheath acceleration (TNSA) yields similar maximum ion energies in front and behind the solid target of suitable thickness.[30]

Finally, one additional consideration on viscosity and MULTI may be in order. Perhaps stimulated by the fluid-like treatment of $\mathbf{j} \times \mathbf{B}$ heating in its analytical part in Ref. 10, one could be tempted to think of absorption being connected somehow with the nonlinear motion and bunching of the electron fluid, here assumed as collisionless. On a fluid scale, this can only be modeled by introducing an artificial viscosity or by an analogous technique. However, whatever the nonlinear motion of an ideal fluid is it does not lead to any absorption as long the flow represents a continuous mapping in space, i.e., as long breaking and/or splitting into beamlets for example is absent.

V. CONCLUSION

Collisionless absorption in overdense plasma cannot be treated in the framework of ideal fluid dynamics.

[1]J. R. Davies, Plasma Phys. Controlled Fusion **51**, 014006 (2009).
[2]T.-Y. B. Yang, W. L. Kruer, R. M. More, and A. B. Langdon, Phys. Plasmas **2**, 3146 (1995).
[3]W. Rozmus and V. T. Tikhonchuk, Phys. Rev. A **42**, 7401 (1990).
[4]P. Gibbon and A. R. Bell, Phys. Rev. Lett. **68**, 1535 (1992).
[5]L. M. Chen *et al.*, Phys. Plasmas **8**, 2925 (2001).
[6]D. Umstadter, J. Phys. D **36**, R151 (2003).
[7]D. F. Zaretsky, Ph. A. Korneev, S. V. Popruzhenko, and W. Becker, J. Phys. B **37**, 4817 (2004); Ph. A. Korneev, S. V. Popruzhenko, D. F. Zaretsky, and W. Becker, Laser Phys. Lett. **2**, 452 (2005).
[8]V. S. Rastunkov and V. P. Krainov, Laser Phys. **15**, 262 (2005).
[9]Y. Sentoku *et al.*, Appl. Phys. B **74**, 207 (2002).
[10]W. L. Kruer and K. Estabrook, Phys. Fluids **28**, 431 (1985).
[11]A. Macchi, F. Cornolti, F. Pegoraro, T. V. Liseikina, H. Ruhl, and V. A. Vshivkov, Phys. Rev. Lett. **87**, 205004 (2001); A. Macchi, F. Cornolti, and F. Pegoraro, Phys. Plasmas **9**, 1704 (2002).
[12]S. Kahaly, S. K. Yadav, W. M. Wang, S. Sengupta, Z. M. Sheng, A. Das, P. K. Kaw, and G. R. Kumar, Phys. Rev. Lett. **101**, 145001 (2008).
[13]C. Jungreuthmayer, M. Geissler, J. Zanghellini, and T. Brabec, Phys. Rev. Lett. **92**, 133401 (2004).
[14]D. Bauer and P. Mulser, Phys. Plasmas **14**, 023301 (2007).
[15]P. Mulser and D. Bauer, *High-Power Laser-Matter Interaction* (Springer, Heidelberg, 2010).
[16]A. D. Piliya, Sov. Phys. Tech. Phys. **11**, 609 (1966); H.-J. Kull, Phys. Fluids **26**, 1881 (1983).
[17]M. Cerchez, R. Jung, J. Osterholz, T. Toncian, O. Willi, P. Mulser, and H. Ruhl, Phys. Rev. Lett. **100**, 245001 (2008).
[18]F. Brunel, Phys. Rev. Lett. **59**, 52 (1987).
[19]T. Baeva, S. Gordienko, A. P. L. Robinson, and P. A. Norreys, Phys. Plasmas **18**, 056702 (2011).
[20]K. Eidmann, R. Rix, T. Schlegel, and K. Witte, Europhys. Lett. **55**, 334 (2001).
[21]F. N. Beg, A. R. Bell, A. E. Dangor, C. N. Danson, A. P. Fews, M. E. Glinsky, B. A. Hammel, P. Lee, P. A. Norreys, and M. Tatarakis, Phys. Plasmas **4**, 447 (1997).
[22]C. D. Chen, J. A. King, M. H. Key, K. U. Akli, F. N. Beg, H. Chen, R. R. Freeman, A. Link, A. J. Mackinnon, A. G. MacPhee, P. K. Patel, M. Porkolab, R. B. Stephens, and L. D. Van Woerkom, Rev. Sci. Instrum. **79**, 10E305 (2008).
[23]A. G. MacPhee, K. U. Akli, F. N. Beg, C. D. Chen, H. Chen, R. Clarke, D. S. Hey, R. R. Freeman, A. J. Kemp, M. H. Key, J. A. King, S. Le Pape, A. Link, T. Y. Ma, H. Nakamura, D. T. Offermann, V. M. Ovchinnikov, P. K. Patel, T. W. Phillips, R. B. Stephens, R. Town, Y. Y. Tsui, M. S. Wei, L. D. Van Woerkom, and A. J. Mackinnon, Rev. Sci. Instrum. **79**, 10F302 (2008).
[24]S. C. Wilks, W. L. Kruer, M. Tabak, and A. B. Langdon, Phys. Rev. Lett. **69**, 1383 (1992).
[25]M. G. Haines, M. S. Wei, F. N. Beg, and R. B. Stephens, Phys. Rev. Lett. **102**, 045008 (2009).
[26]T. Kluge, T. Cowan, A. Debus, U. Schramm, K. Zeil, and M. Bussmann, Phys. Rev. Lett. **107**, 205003 (2011).
[27]K. Eidmann, J. Meyer-ter-Vehn, Th. Schlegel, and S. Hüller, Phys. Rev. E **62**, 1202 (2000).
[28]P. Mulser, D. Bauer, and H. Ruhl, Phys. Rev. Lett **101**, 225002 (2008).
[29]P. Mulser and D. Bauer, AIP Conf. Proc. **1209**, 75 (2010).
[30]T. Ceccotti *et al.*, Phys. Rev. Lett. **99**, 18502 (2007).

Collisionless absorption, hot electron generation, and energy scaling in intense laser-target interaction

T. Liseykina,[1,2,a)] P. Mulser,[3] and M. Murakami[4]

[1]*Institut für Physik, Universität Rostock, Universitätsplatz 3, 18051 Rostock, Germany*
[2]*Institute of Computational Technologies SD RAS, Acad. Lavrentjev Ave. 6, 630090 Novosibirsk, Russia*
[3]*Theoretical Quantum Electronics, Technische Universität Darmstadt, 64289 Darmstadt, Germany*
[4]*Institute of Laser Engineering, Osaka University, Osaka 565-0871, Japan*

Among the various attempts to understand collisionless absorption of intense and superintense ultrashort laser pulses, a whole variety of models and hypotheses has been invented to describe the laser beam target interaction. In terms of basic physics, collisionless absorption is understood now as the interplay of the oscillating laser field with the space charge field produced by it in the plasma. A first approach to this idea is realized in Brunel's model the essence of which consists in the formation of an oscillating charge cloud in the vacuum in front of the target, therefore frequently addressed by the vague term "vacuum heating." The investigation of statistical ensembles of orbits shows that the absorption process is localized at the ion-vacuum interface and in the skin layer: Single electrons enter into resonance with the laser field thereby undergoing a phase shift which causes orbit crossing and braking of Brunel's laminar flow. This anharmonic resonance acts like an attractor for the electrons and leads to the formation of a Maxwellian tail in the electron energy spectrum. Most remarkable results of our investigations are the Brunel like spectral hot electron distribution at the relativistic threshold, the minimum of absorption at $I\lambda^2 \cong (0.3 - 1.2) \times 10^{21}$ Wcm$^{-2}\mu$m^2 in the plasma target with the electron density of $n_e\lambda^2 \sim 10^{23}cm^{-3}\mu$m^2, the drastic reduction of the number of hot electrons in this domain and their reappearance in the highly relativistic domain, and strong coupling, beyond expectation, of the fast electron jets with the return current through Cherenkov emission of plasmons. The hot electron energy scaling shows a strong dependence on intensity in the moderately relativistic domain $I\lambda^2 \cong (10^{18} - 10^{20})$ Wcm$^{-2}\mu$m^2, a scaling in vague accordance with current published estimates in the range $I\lambda^2 \cong (0.14 - 3.5) \times 10^{21}$ Wcm$^{-2}\mu$m^2, and again a distinct power increase beyond $I = 3.5 \times 10^{21}$ Wcm$^{-2}\mu$m^2. The low energy electrons penetrate normally to the target surface, the energetic electrons propagate in laser beam direction. © 2015 AIP Publishing LLC.
[http://dx.doi.org/10.1063/1.4914837]

I. INTRODUCTION

Intense and superintense laser beam interaction with dense matter is characterized by one prominent phenomenon, that is, the generation of superthermal high energy electrons and ions. It leads to the spontaneous question as to the effects that generate them in the absorption process of intense monochromatic light beams. Latest when the kinetic temperature reaches $10^3 Z^2$ eV in the plasma, Z ion charge, collisional absorption is ineffective and other effects of non-collisional nature have to become active in order to ensure absorption. The best known non-collisional candidate so far was resonance absorption at oblique laser incidence.[1,2] It consists in the direct conversion of laser light into an electron plasma wave resonantly excited at the critical electron density where the laser frequency ω equals the plasma frequency ω_p. High intensity laser pulses in the intensity domain $I = 10^{16}$–10^{22} Wcm^{-2} with good contrast ratio are so fast rising that there is no time to form a preplasma in front of an irradiated solid sample that could couple to a resonantly excited plasma wave. Therefore, the search begun for new collisionless

absorption processes. The first successful proposal was the so-called $\mathbf{j} \times \mathbf{B}$ heating.[3] The authors could show by particle-in-cell (PIC) simulations that at normal incidence the Lorentz force induces non-resonant electron oscillations at 2ω normal to the target surface which lead to appreciable absorption, target heating, and production of superthermal electrons at any density above critical. However, no attempt was made to explain how the observed absorption, i.e., irreversibility, comes into play. Not long after, a remarkable step forward was made by Brunel[4] in understanding high-power collisionless absorption. He could show after introducing a few modifications that the resonance absorption concept could be adapted to steep highly overdense plasma profiles and significant absorption could be achieved under oblique incidence despite total absence of plasma resonance at $\omega = \omega_p$ (not-so-resonant, resonant absorption[4]) and no possibility for a plasma wave to propagate into a shallow preplasma in front of the target. Instead, now the energy imparted to the electrons is transported into the target and deposited there. Under the assumptions of cold (i) infinitely dense plasma (ii) with discontinuous interface to vacuum (iii) Brunel could formulate the laser-matter interaction dynamics in the vacuum in front of the target in terms of three ordinary differential

a)Electronic mail: tatyana.tiseykina@uni-rostock.de

equations. Perhaps, for this reason, Brunel's mechanism of the electrons pulled out into the vacuum and then pushed back into the field-free target interior is frequently identified with the term "vacuum heating," an expression coined later for the particles forming a kind of thermal cloud at the vacuum-ion interface in PIC simulations.[5]

To be more specific, the reason why the term vacuum heating played an ominous role in the past and partially still does presently is because, often invoked as the leading collisionless absorption mechanism, it has never been defined properly. To introduce some rating in this respect, it seems that two groups of authors can be distinguished. By the concept of vacuum heating, the first group addresses the electrons in front of the sharp-edged target that circulate in the vacuum and do not cross the interface during one laser cycle.[5,6] Identification of vacuum heating with Brunel's mechanism is made by the second group[7,8] to contrast with anomalous skin layer absorption.[9–11] By the latter, all motion is strictly confined to the target inside. Sometimes, vacuum heating is interpreted as a consequence of unspecified wave breaking.[12,13] Meanwhile, it has been clarified that Brunel/vacuum heating prevails distinctly on skin layer absorption and that vacuum heating in the restricted sense, i.e., the contribution to absorption of the electrons not entering the target with the periodicity of the laser, is almost insignificant.[14]

Only recently, a detailed analysis and discussion of Brunels's model has been given in Ref. 15. With a view on the means of the present paper, a compact summary of the results may be of interest. The laser field component perpendicular to the target is assumed to have the structure $E(t) = E_0 \sin \omega t$. It generates electron jets of periodicity $\tau = 2\pi/\omega$. All of them are ejected during the first quarter period, and all, except 2.2%, return to the target during the second half period $(\pi, 2\pi)$. During the remaining 3/4 period, no further electron ejection is possible as a consequence of partial screening by the outer layers and driver field inversion. Contrary to a common believe that all electrons in one jet are pushed back by the inverted field, only half of them, lifted in the interval $(0, \pi/4)$, are in phase with the driver, the other half experience a weakened driver due to screening and fall back to the target, attracted by the immobile ions, before the laser field has changed direction. This leads quite naturally to a classification into energetic and less energetic electrons. If not specified differently, throughout the paper, we define, somehow arbitrarily, those electrons as hot whose return energy exceeds the quiver energy E_{os} of the free electron. Accordingly, 34% of the Brunel electrons are hot and carry 82% of the energy in the single jet. In contrast to PIC simulations, the Brunel spectrum is non-Maxwellian with a pronounced maximum at $E = 9.1 E_{os}$, followed by a sharp cut off (see Fig. 1). Absorption $A = I_{abs}/I$ is considerably lower than measured at intermediate angles of incidence[16] but reaches unity at 86° of incidence. A and the absorbed energy scale like $I^{1/2}$ and $I^{3/2}$, respectively. Evidently, this is the price Brunel pays for oversimplification. We want to stress that in Brunel's model, crossing of layers among each other during the laser action is excluded, except a few front layers whose contribution to absorption is negligible. In other words, the electron flow dynamics is laminar, no wave
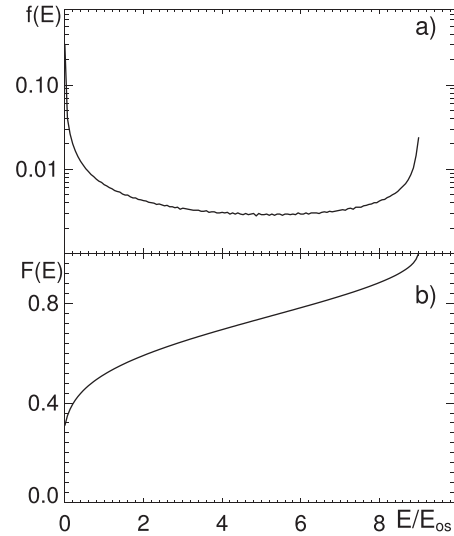

FIG. 1. (a) Electron spectrum $f(E)$ from Brunel's nonrelativistic model;[4] (b) $F(E) = \int f(E')dE'$. Energy E in units of mean oscillation energy in vacuum; energy cut off is at $E = 9.1 E_{os}$.

breaking or, more appropriate in the context, no breaking of flow occurs. Brunel's model offered, within limits, the first physical explanation of $\mathbf{j} \times \mathbf{B}$ heating at 2ω. And yet, Brunel's model does not give a direct physical feeling for the absorption process. The numerous wrong, at least inexact interpretations of it that are still around are a direct indicator (example: "all electrons are pushed back by the laser field" contrasts with the true "free fall" of half of them).

From an early sional (1D) PIC simulation, the energy scaling $E_{hot} \sim I^{1/2}$ has been extracted for the hot electrons;[17] it has been re-"confirmed" by independent simulations[18] and apparently by experiments.[19,20] However, the scaling seems to be questionable for its too strong dependence on intensity; it contrasts with other experiments[21] and more sophisticated analysis.[22] In turn, corrections to the latter have been given recently on the basis of a relativistic kinematic model.[23] Analogous scaling laws have been proposed by numerous other authors.[16,24–26] Nevertheless, there is no convergence towards a definite scaling.[27] In order to achieve further progress, the investigation has to start from a discussion of collisionless absorption, a flow analysis of the absorbed energy into the various plasma components, a definition of the hot electron component, and completed by analytical modeling in combination with concomitant simulations. In what follows, we present our considerations on the degree of understanding collisionless laser beam absorption, the process of fast electron generation, and their interaction with the low electron energy component in order to arrive at more firmly validated scaling relations in forthcoming work. The analysis will enable us also to get insight into shortcomings of the existing models for intense laser-dense matter interaction.

II. COLLISIONLESS ABSORPTION BASICALLY UNDERSTOOD

Let us consider the phenomenon of collisionless absorption of high-power laser beams from a more fundamental

point of view. Under quasi-steady state conditions, Poynting's theorem averaged over one laser cycle reduces to

$$\overline{\nabla \mathbf{S}} = -\overline{\mathbf{jE}}. \tag{1}$$

The energy flux density is the Poynting vector $\mathbf{S} = \varepsilon_0 c^2 \mathbf{E} \times \mathbf{B}$; it relates to the laser intensity by $I = \bar{\mathbf{S}}$. With n_e the electron density and $\mathbf{v}$ the mean electron flow velocity, the current density is $\mathbf{j} = -en_e\mathbf{v}$. Equation (1) describes all kinds of absorption, collisional, noncollisional, classical, or quantized; in the latter case, the current density and the electric field $\mathbf{E}$ are to be substituted by their operators acting on the corresponding state vector $|\psi\rangle$. In the intense laser field, despite the high particle densities involved, the classical picture is an excellent approximation. If the laser field evolves in time as $\mathbf{E} \sim \sin\omega t$, the current density follows as $\mathbf{j} \sim \cos(\omega t + \phi)$ and

$$\overline{\nabla \mathbf{S}} = -\overline{\mathbf{jE}} \sim -\overline{\cos(\omega t + \phi)\sin\omega t} = -\frac{1}{2}\sin\phi. \tag{2}$$

Dephasing between driver field and current determines the degree of absorption. Thus, collisionless absorption reduces to the problem of finding out which effects lead to a finite phase shift in $\mathbf{j}$. In collisional absorption, it is the friction originating from the collisions between electrons and ions,

$$\overline{\mathbf{jE}} = \varepsilon_0 \omega_p^2 \frac{\nu}{\omega^2 + \nu^2} |\mathbf{E}|^2 > 0, \tag{3}$$

ν collision frequency. At $\nu = 0$, the collisional phase shift vanishes and any finite ϕ can only be of dynamic origin. Up to $I = 5 \times 10^{20}$–10^{21} Wcm^{-2}, this dynamic origin is found in the space charge induced by $\nabla \mathbf{v} \neq 0$. The space charge generates an electrostatic field that, superposed to the laser field, determines the electron motion and leads to the desired finite phase shift ϕ. This can be seen most immediately with a constant electric field $\mathbf{E}_0$. It yields per electron

$$\overline{\mathbf{jE}} = \frac{2\pi e^2 \mathbf{E}_0{}^2}{m_e\omega} > 0. \tag{4}$$

It is interesting to note, and it can be formally shown; however, it is also physically evidents that $\overline{\mathbf{j}(\mathbf{E}_{\text{Laser}} + \mathbf{E}_{\mathbf{s}})} = \overline{\mathbf{jE}}_{\text{Laser}}$; all work is done by the driver field; the space charge field $\mathbf{E}_{\mathbf{s}}$ is inert; it provides for the phase shift only. Some authors may attribute absorption to the Brunel like abrupt reduction of the laser wave amplitude in the skin layer. Due to this asymmetry, the energy gained by an electron in the vacuum cannot be given back anymore to the wave when entering the evanescent region. However, for this picture to work, an electrostatic field component is needed too; transverse and longitudinal components cannot be isolated from each other. In the standard resonance absorption, at the critical density, it is the space charge field of the electron plasma wave that provides for collisionless absorption up to 49% through a phase shift $\phi \neq 0$.[2] On the fundamental level of Eqs. (2) and (4), collisionless absorption of superintense ultrashort laser pulses may be classified as fully understood now for $I < 10^{21}$ Wcm^{-2} for optical wavelengths.

All kinds of difficulties and complications arise when the degree of absorption has to be quantified. This step can only be done by introducing appropriate models. Numerous attempts into this direction have been undertaken with the intention to explain (i) the origin of the hot and the warm electron components, (ii) when and how they are created, during one laser period by direct resonant and nonresonant acceleration, or by stochastic processes over several laser cycles, and (iii) where is absorption localized, in vacuum or in the skin layer. Correspondingly, the existing absorption models may be characterized as statistic or as dynamic. Examples of the first class are vacuum heating in the restricted sense,[28,29] wave breaking,[12,13] and skin layer absorption, e.g., Ref. 9, linear and nonlinear Landau damping.[30,31] Candidates of the second class are, first of all, sharp edge absorption,[4] longitudinal[32] and transverse[33] ponderomotive heating, "zero vector potential mechanism,"[18] relativistic kinematic model,[23] and anharmonic resonance.[34] Let our PIC simulations decide on questions (i)–(iii) and to what degree statistics is involved in the dynamics induced by the laser in dense targets.

Now, after three decades of intense studies on superintense laser-matter interaction, one would expect that such basic questions (i)–(iii) as labeled above should have found a final answer. The numerous models presented on performed experiments tell the opposite and show that no convergence has been reached yet. It is instructive to have a look at over 100 experimental and theoretical results on the absorption degree collected up to 2009 in Ref. 35, (Fig. 1 in Ref. 35), in the irradiance regime from $I\lambda^2 = 10^{18}$ Wcm$^{-2}\mu$m^2, to 10^{21} Wcm$^{-2}\mu$m^2. The absorption degrees range from 5% to 95%, and yet, at the constant irradiance of 6×10^{18} Wcm$^{-2}\mu$m^2, absorption between 35% and 85% is reported. It drastically reflects the difficulties encountered in performing unambiguous experiments with all essential parameters well defined. It is this situation that justifies still basic 1D simulations in order to learn more about which are the essential parameters defining the underlying physical processes. For example, a good portion of difficulties and uncertainties arising in the context of hot electron scaling have their origin in different understanding of when an electron is "hot."

III. LOCALIZATION OF ABSORPTION AND ORIGIN OF FAST ELECTRONS

We consider always linear polarized (in y-direction) laser pulses impinging under 45° angle of incidence onto strongly overdense fully ionized cold hydrogen targets with initial electron density n_{e0} such that $n_{e0}\lambda^2 \simeq 10^{23}$ cm$^{-3}\mu$m^2. The interaction of the laser beam with the target is studied by 1D relativistic PIC simulations using the boost technique.[36] If not specified differently, throughout the text, we call all electrons with energies E exceeding their mean oscillation energy E_{os} "hot" or "fast,"

$$E > E_{\text{os}} = m_ec^2\left[(1 + a^2/2)^{1/2} - 1\right]; \quad a = \frac{e|\hat{\mathbf{A}}|}{m_ec},$$

$$I\lambda^2 = 1.37 \times 10^{18}a^2 \text{ W/cm}^2\mu\text{m}^2,$$
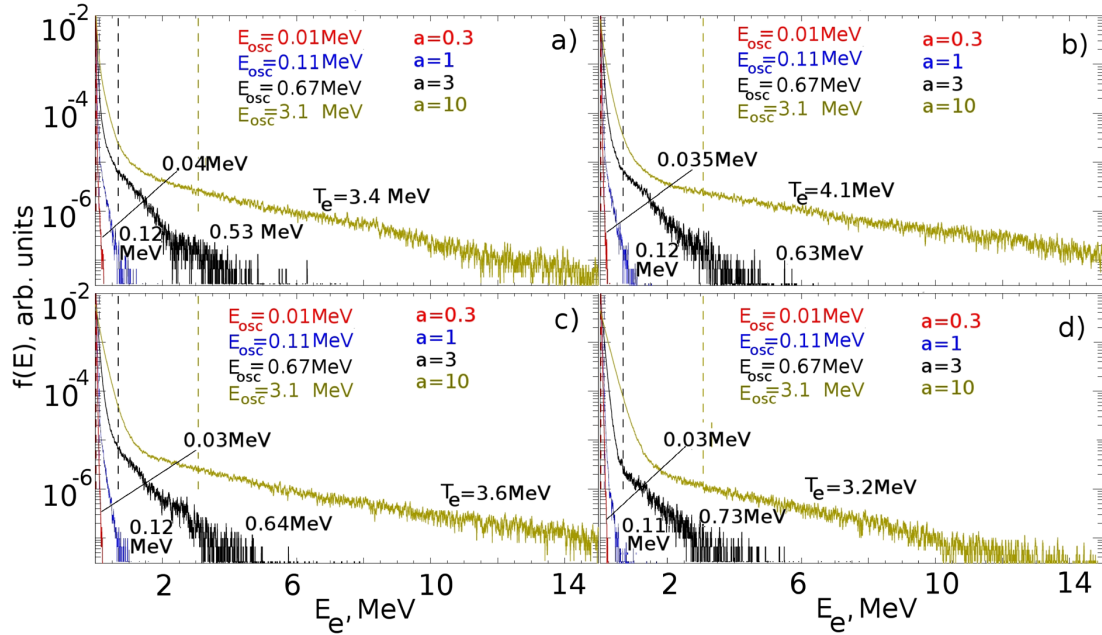
$\hat{\mathbf{A}}$ maximum vector potential amplitude.

106

033302-4   Liseykina, Mulser, and Murakami   Phys. Plasmas **22**, 033302 (2015)

FIG. 2. Electron energy spectra $\ln f(E)$ at (a) 30, (b) 35, (c) 40, and (d) 45 cycles after the beginning of the interaction. A $\sin^4$ laser pulse of peak amplitude $a = 0.3, 1, 3, 10$ and full width of 50 cycles impinges under $45°$ onto a hydrogen target with electron density n_{e0} such that $n_{e0}\lambda^2 = 9 \times 10^{22} \text{cm}^{-3}\mu\text{m}^2$. The pulses are identical in all four frames. Target thickness varies from 40 to 60 λ. Vertical dashed lines mark the mean oscillation energies. The hot electrons follow a Maxwellian distribution. The maximum mean energies $k_B T_e$ for $a \geq 1$ are by the factors 1.04, 1.09, 1.7 higher than the associated E_{os}. $k_B T_e$ increases during the evolution of laser pulse for $a = 3$; for $a = 10$, it decreases. Power scaling $k_B T_e \sim I^\alpha$, $\alpha \geq 0$ not detected.

A. Brunel model and vacuum heating

The energy spectra $f(E)$ of the hot electrons assume the typical shape of Fig. 2, here, for an $I \sim \sin^4$ laser pulse of full width 50 cycles and $a = 0.3, 1, 3, 10$ after 30, 35, 40, and 50 laser cycles. The straight lines of $\ln f(E)$ starting from the energy E between $2E_{os}/3$ for $a = 10$ and from $E = E_{os}$ for $a \leq 3$ are a clear signature of a Maxwellian type distribution function, $f(E) \sim \exp(-E/k_B T_e)$, k_B Boltzmann constant (for example, the genuine nonrelativistic Maxwellian contains the degeneracy factor $\sqrt{E}$ to be subtracted from $\ln f(E)$ to yield a straight line, see related argument in Sec. V). From the slope, an electron "temperature" T_e is determined, with the significance of $k_B T_e$ the mean energy if the straight lines are extrapolated down to $E = 0$. In the figure, T_e is indicated in units of MeV. For $a = 10$, one notices already cooling by energy transfer to the cold electrons and beginning plasma expansion during laser irradiation. Similar hot electron spectra have been reported by other authors, for example, in Ref. 37.

The interaction of intense laser beams with dense targets is very complex and rich of peculiar facets. On the other hand, consequences of basic effects, like collisionless interaction under non-harmonic resonance, are not clarified as they should. Here, we report on phenomena which we believe will survive in 2D and 3D also. Let us tentatively identify vacuum heating with the energy gained by all Brunel-like electrons (Brunel electrons). It is the sum of energies gained during the excursion into vacuum. This energy fraction is identified as "vacuum heating" and compared with the energy absorbed by all electrons. The target thickness is chosen such that no particles are reflected from the target backside and falsify the

statistics. The laser beam intensity rises during one laser cycle to its full intensity, is subsequently held constant for 30 cycles, and then sinks to zero during another full cycle. In Fig. 3, the energies of all Brunel particles and of all particles that have crossed the skin layer at a depth of half a vacuum wavelength are plotted at their crossing time for $a = 1$ and $a = 60$. The salient feature is their jet like structure predicted by the Brunel model. At the low intensity ($a = 1$), there is a clear distinction between the Brunel electrons and all electrons having undergone heating. The increase of the energy maxima from $6.5E_{os}$ to $8E_{os}$ and the more diffuse energy profiles of the jets at half wavelength in depth is a clear indication that some heating is localized in the skin layer, in contrast to the Brunel mechanism. At high intensity ($a = 60$), the jets assume a pronounced double structure due to the increased $\mathbf{v} \times \mathbf{B}$ heating operating at 2ω, but the patterns of the two groups appear equally diffuse. The increase in energy of the fastest electrons is almost no longer visible (increase by $0.5E_{os}$). For $a > 1$, the fraction of Brunel electrons results
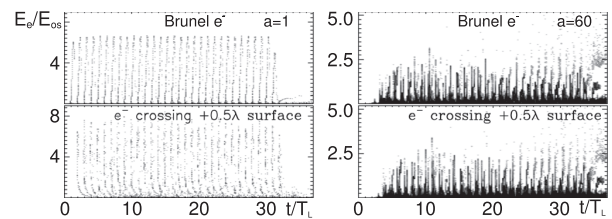

FIG. 3. Energy spectra of Brunel jets (upper pictures) and jets at depth $\lambda/2$ as function of time (units in laser cycles) for $a = 1$ and $a = 60$. Double structure is due to $\mathbf{v} \times \mathbf{B}$ acceleration. Strong reduction of E_{max}/E_{os} with increasing a is noticeable.

always higher than the fraction of electrons moving inward and crossing the boundary at $\lambda/2$ in the skin layer. The reason for the difference is to seek in the accumulation of Brunel electrons in the skin layer with increasing laser cycle number, randomized there and repeatedly crossing the target-vacuum interface before disappearing in the depth of the target. It is instructive to analyze the spectral distribution function $f(E)$ of the Brunel electrons and all electrons just when crossing positions $x = 0.5\lambda$, λ, 1.5λ, and 2λ for the laser intensities corresponding to $a = 1$, 7, 30, and 60, see Fig. 4. Surprising enough, at low intensity ($a = 1$) and, to a minor degree, also at $a = 7$, the Brunel electrons from the PIC simulations resemble much Brunel's analytical spectrum from Fig. 1: The sharp cut offs and the adjacent maxima of $f(E)$ are reproduced; their positions, however, lie at much lower energies. The maximum of $f(E)$ is still clearly visible for $a = 15$ (not in the figure), this time at $E = E_{os}$, but the sharp cut off changes into a transition extending over $0.4 E_{os}$. The formation of a Maxwellian tail in the fast electron spectrum occurs in the skin layer and even deeper inside the target. From $a \simeq 20$, on no difference in the spectra from Brunel and total electrons can be observed, they are all "thermalized." At $a = 30$, the spectra extend up to $1.4 E_{os}$; at $a = 60$, the maximum energy is shifted to $E = 3.7 E_{os}$. This is in agreement with the dependence of the fast electron number on laser intensity, see Sec. IV A. From Fig. 3, we conclude that at moderate intensities ($a \leq 15$), the skin layer contributes sensitively to the production of the most energetic electrons, either by laser-space charge resonance and/or by stochastic Brunel electron-plasmon interactions.

B. Localization and mechanism of heating

Plasma density and velocity distributions as functions of time are the natural outcome in standard PIC simulations. Additional insight in the heating mechanism is obtained
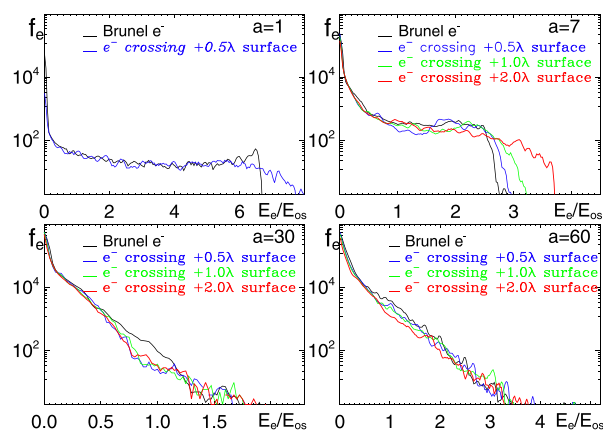
from the orbits $\mathbf{x}(t)$ of randomly chosen electrons. We have analyzed numerous such computer runs each with 200 trajectories stochastically selected from (i) all particles heated by the laser and (ii) from the set of the hot electrons only. In Fig. 5, their time histories are depicted for the intensities $a = 7$ (left) and $a = 60$ (right). The salient features characteristic of the two groups are the following:

(1) Heating of the energetic electrons is well localized at the vacuum-target interface and takes place during one laser cycle or a fraction of it. This excludes stochastic heating of the hot electrons. Only a low fraction of them get the high energy in the skin layer without ever emerging into vacuum.

(2) Contrary to the standard assumption, the "slow" return current is highly irregular as a consequence of the interaction of the jets from Fig. 3 with the background. It is clearly recognized in Fig. 5 that irregular flow sets in just with the arrival of the first jets and it becomes the more irregular the more jets it is exposed to. The jets are accompanied by strong localized electrostatic fields that force electrons from the return current to reverse their direction towards the back of the target or, if they succeed to cross the charge cloud of an incoming jet, they are heavily accelerated towards the target front to interact further with the laser field. In short words, the laminar flow of the return current is heavily perturbed by the Cherenkov emission of the plasmons excited by the jets. The stochastic interaction, both, return electron acceleration and deceleration, has been observed in test particle models in the past.[14]

(3) The plasma flow in the skin layer breaks (like "wave breaking"), i.e., the orbits cross each other, in contrast to Brunel's laminar model of infinite target density.

(4) Excursion into vacuum (vacuum heating) of the energetic electrons decreases continuously with a increasing to reach a minimum at around $a = 30$ and then to increase
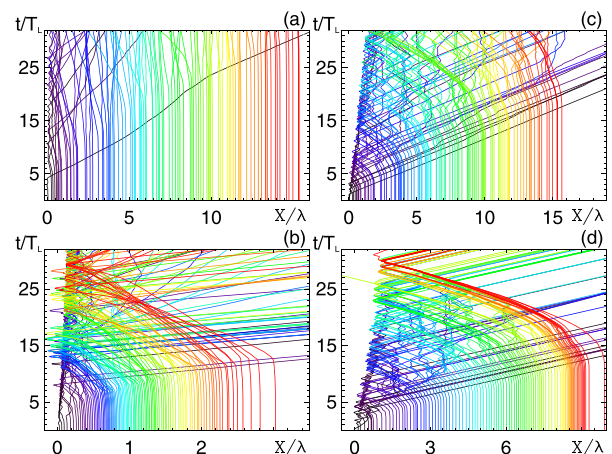

FIG. 4. Energy distributions $f(E)$ of Brunel electrons and of electrons crossing positions $x = 0.5\lambda$, 1λ, 1.5λ, and 2λ at intensities $a = 1$, 7, 30, and 60. The distributions are taken after 37 laser cycles when all electrons have returned to position $x = 2\lambda$. The non-Maxwellian structure of the Brunel electrons is preserved up to $a = 15$. For higher intensities, there is almost no difference between electrons heated in the vacuum and additional heating in the skin layer region.

FIG. 5. Arbitrary selection of orbits $x_i(t)$, $i = 1$–100, for $a = 7$ (a) and $a = 60$ (c). The lower (b) and (d) show the same number of stochastically chosen orbits from the hot electrons only with $E \geq E_{os}$. Their analysis shows acceleration, i.e., heating almost during one laser cycle or a fraction of it in the laser field at the target front and their strong interaction with the return current.

again. Owing to the significance of effects (1)–(3) for localization and understanding hot electron generation, and understanding collisionless laser beam absorption in general, we analyze further the acceleration process. In Brunel's model, the density of the target is assumed infinite. Consequently, all electrons start from the same position and no crossing of orbits occurs; the particle flow into vacuum and back to the target is laminar. Despite Brunel's oversimplification, his model explains basic properties of the collisionless interaction: formation of steady state jets (Fig. 3), two groups of electron energies (energetic electrons co-moving with the laser field, slow free fall electrons), majority of fast electrons stemming from the excursion into vacuum, and dominant fraction of laser energy delivered to hot electrons. If therefore "vacuum heating" is identified with Brunel's mechanism, it acquires a precise meaning. However, there is the missing link to the physics of acceleration in this simple model. Not to forget that in Brunel's model, all heated electrons are lifted into vacuum only during the first quarter laser period. The reality with skin layer included is different: The phase for lifting is stochastic, as expected from broken flow; period doubling, tripling, quadrupling, etc., of electron oscillations occurs in the skin layer (see Fig. 5); acceleration to high energies is a resonance effect. To see this, we must concentrate once more in detail on single orbits selected statistically. In Fig. 6, the time history of four particles starting from different depth in the target together with the electric field (white traces) they "see" during their motion is depicted for $a = 1$, i.e., the orbits $x(t)$ and the momenta $p_x/m_e c$ normal to the target. Resonant interaction in the first two pictures is clearly recognized by the abrupt changes in $x(t)$ and $p_x(t)$. Out of resonance, the phase difference between field and momentum is $\pi/2$, see $p_x(t)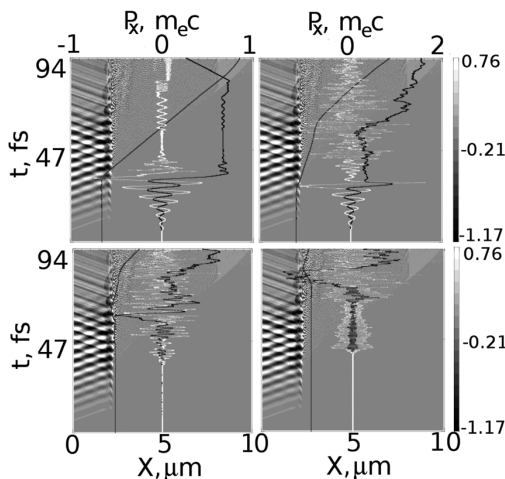$ and laser field (white line) in the first two pictures. The transition to resonance, i.e., field and momentum antiparallel, occurs during half a cycle or less in the kink of $x(t)$, seen best by zooming Fig. 6. The essential point of this resonance is its anharmonic character. In contrast to the harmonic oscillator in the oscillator with anharmonic potential resonance is an attractor: Given an excitation by the periodic laser, above a certain threshold, transition to resonance is unavoidable. The reason for this behavior is as follows. The harmonic potential is the only one in which the degree of excitation does not change its periodicity, and therefore, it either is driven in or out of resonance. The average stochastically perturbed space charge potential of the plasma is flatter than harmonic, and so, depending on the excitation level, its eigenfrequency changes continuously from the high level ω_p at low excitation down below the laser frequency ω. At the crossing point, resonance occurs. It has two consequences: (i) Driver, when in phase with the electron displacement, transforms it into a runaway particle in general;[34] (ii) the resonant phase switch forces the electron to move against the bulk, the plasma flow breaks. Breaking of flow or wave breaking, respectively, often invoked as acceleration or absorption mechanism[12,13] is never their origin, it is their consequence.

We conclude that at $I < (5 \times 10^{20}$–$10^{21})$ Wcm^{-2}, the majority of energetic electrons is produced by resonant interaction of the laser field with the longitudinal space charge field over a fraction of one laser cycle in the vacuum as well as in the skin layer. However, there is also indirect acceleration of stochastic nature of the target background, evidenced by the last two pictures in Fig. 6 with electrons heated stochastically by the plasmons emanating from the jets. The rapidly oscillating stochastic field of the plasmons increases with the number of jets produced; its influence on stochastic acceleration of electrons is evident in the last two pictures of Fig. 6.

IV. FAST ELECTRONS AND ENERGY PARTITION

As seen in Sec. III, there are several thermalizing mechanism: breaking of flow, skin layer noise, and Cherenkov plasmons from jets. As a consequence, one would expect that such effects dominate the low energy component of the electrons and that this should propagate mainly normally to the target. The more energetic an electron is, the more it feels the Lorentz force in $\mathbf{v} \times \mathbf{B}$ direction forcing its motion into laser beam direction, 45° in this paper. For the single free electron starting from rest in a traveling plane wave, the maximum energy gain $\Delta\mathcal{E}$ and the lateral angular spread $\tan\alpha$ of the velocity component v_k in propagation direction to the velocity component in the $\mathbf{E}$ field direction v_E are[38]

$$\Delta\mathcal{E} = \frac{1}{2} a^2 m_e c^2, \quad \tan\alpha = \left|\frac{v_E}{v_k}\right| = \frac{2}{a}, \tag{5}$$

thus confirming this tendency. In Fig. 7, the momenta p_y parallel to the target vs p_x along the target normal of the heated electrons are depicted for $a = 1, 7, 15, 60,$ and 100. The

FIG. 6. Anharmonic electron resonance and stochastic interaction.[34] Regular shadow structure: laser field; black trajectory: orbit $x(t)$ (left) and momentum $p_x(t)$ (right), white traces: electromagnetic/electrostatic field at the particle's position. Primary interaction is by resonance between transverse and longitudinal field during a fraction of laser cycle. Particles in the last two pictures experience stochastic acceleration by plasmons only.
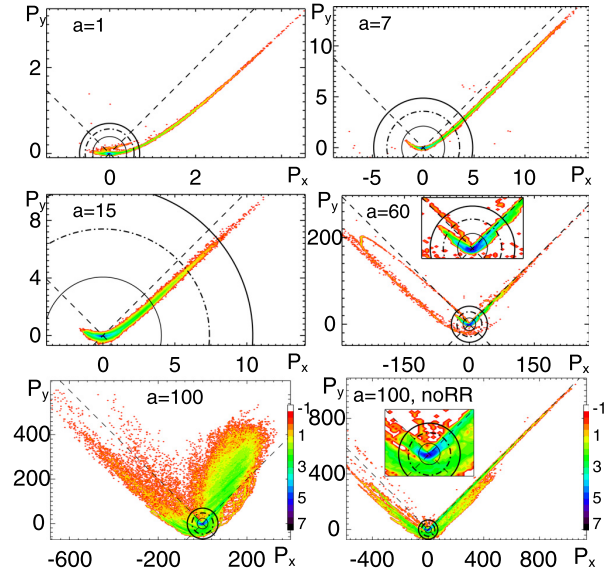
FIG. 7. Direction of heated electrons: Momenta $p_y/m_e c$ vs $p_x/m_e c$ for $a = 1$, 7, 15, 60, and 100 (left picture $a = 100$: with radiation damping, right: without) at the end of the standard laser pulse. Electron energies: $E < E_{os}/3$ within inner black circle, $E \in [1/3, 2/3]E_{os}$ within dashed circle, $E \in [2/3, 1]E_{os}$ within bold circle, $E > E_{os}$ (hot electrons) outside. Circles in the last pictures are very small; therefore, see the two insets). The color of the particles in this pictures indicates their number according to the color bar. Low energy electrons within the inner circle (majority in number) penetrate the target normally; energetic electrons follow the laser beam direction (dashed black lines), in $a = 60$, 100 also along the reflected laser beam.

corresponding distributions of the momenta p_x normal to the target over the space coordinate are shown in Fig. 8. From the pictures, it is not directly seen that the majority of slow electrons move in the direction of the target normal; however, as expected from (5), with increasing energy the electrons follow, indeed, the direction of the laser beam. In addition, at $a = 60$ and 100, an appreciable percentage is accelerated into specular direction. The reduction of the absolute number of hot electrons with increasing intensity, their almost vanishing at $a = 15$, and their impressive reappearance towards $a = 100$ is particularly striking. This effect will have direct impact on every attempt to formulate scaling laws for the "hot electron" production. We have counted their number as a function of intensity; the result is reported in Table I. Drop and increase with intensity are beyond expectation.

The formation of spatial spikes within groups of energies and laser intensities is depicted in Fig. 8. It has to be seen as complementary to the spike distribution in time in Fig. 3. At low laser intensity, only the fastest electrons form jets in space as long as they are "young." As they travel further into the target, they become increasingly diffuse as a consequence of their interaction with the Cherenkov plasmons. The electrons of varying velocity undergo mixing in phase space, see uniform background in Figs. 3 and 8; the spikes only are accompanied by strong electrostatic fields. Their damping by friction is given through the collision frequency $\nu_{coll} = 2(e^4 n_{e0}/\epsilon_0 m_e^2 v_e^3 \gamma) \ln \Lambda$. With the Lorentz factor, $\gamma = 1$, $v_e = c$, and $n_{e0} = 10^{23} \text{cm}^{-3}$, this results in
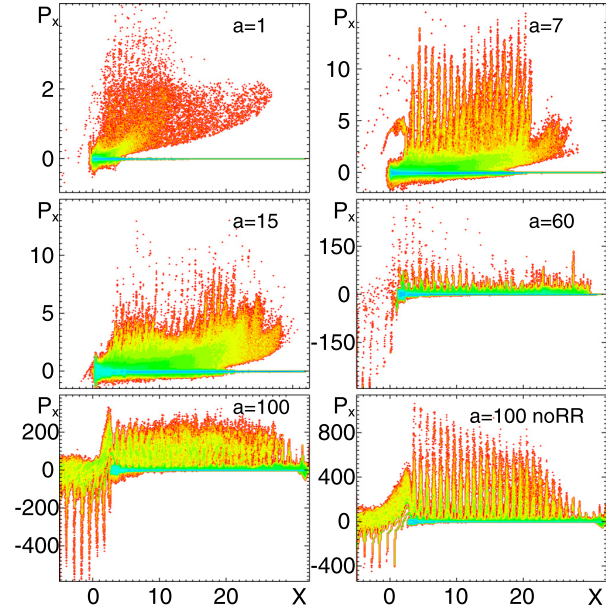

FIG. 8. Energy distribution of heated electrons: Momentum $p_x/m_e c$ vs target normal x for $a = 1$, 7, 15, 60, and 100 (left: with radiation damping, right: without) at the end of the standard laser pulse. The color of the particles indicates their number according to the color bar of Fig. 7. The spiky structure is a rough indicator of relativistic jets.

$\nu_{coll} = 5 \times 10^{10} \ln \Lambda \, \text{s}^{-1}$; hence, collisional damping of spikes is unimportant. Anomalous interaction of the laser heated electrons with the background has been studied recently.[39] All electrons after having entered the distinctly relativistic regime show a neat spiky structure because they all fly at light speed and behave much stiffer now against their concomitant space charge field. The inclination of groups of spikes with respect to the normal to the abscissa at subrelativistic speeds is self-explaining. We note also that the excursion of the slow electrons into vacuum (p_x negative) reduces with increasing a.

A. Partition of the absorbed energy

Sometimes, it is claimed (at least in the past) that all electrons are "hot" in intense laser-solid target interaction. This rises the question on the percentage of the hot electrons with respect to number, to average energy, or to average flux density. Here, we must stress that a percentage in particle number cannot be given, neither in the experiment nor in the simulation for the simple reason that the fraction depends very sensitively on the total number of particles involved: Where to put the lower threshold? Should the shock heated portion of the target be counted also, or is it reasonable to restrict counting on those electrons that have "seen" the laser at least once? However, the situation is totally different with

TABLE I. Number of hot electrons per unit area (arbitrary units) in dependence of a for $n_{e0} = 100 n_c = 100 m_e \omega^2 \epsilon_0 / e^2$.

a	1	3	7	15	30	60
N_{hot}	7819	7991	17 464	147	265	19 273

respect to energy fractions because no ambiguity arises on that. In Table II, we present such an absorbed energy partition as a function of laser intensity (parameter $a \sim I^{1/2}$) for two overdense targets, $n_{e0} = 100 n_c$ and $n_{e0} = 200 n_c$ (for $a = 15$ also $n_{e0} = 400 n_c$): overall fraction of absorption I_{abs}; percentage of energy which is found in the electrons; total fraction of energy absorbed by the hot electrons, $E \geq E_{os}$ and by hot + medium hot electrons of $E > E_{os}/2$ (warm e^-); energy fraction transmitted to the ions; energy fraction found in the electrostatic space charge field (fields). A first view on the table tells that the main absorption is accomplished by the energetic electrons (see 5th and 6th column). The absorption by the ions (protons in the table) remains modest for $a \leq 15$, however, Cherenkov plasmons (fields) assume a non negligible portion of laser energy, more than we predicted.

The increase in ion energy beyond $a = 15$ is due to the deeper penetration of the laser as a consequence of the recession of the electrons by the radiation pressure and hence, increased energy coupling to the ions.

The overall absorption drops continuously with increasing laser intensity. In contrast to the runaway energy $\mathcal{E}$ in (5), the free quiver energy at fixed oscillation center is $E_{os} = mc^2[\sqrt{1 + a^2/2} - 1] \sim I^{1/2}$. However, this reduction is counterbalanced by the relativistic increase of the critical density, $n_{cr} \sim \gamma n_c$. As the speed of the moderately hot electrons approaches c, the absorption into energetic electrons, which is the major portion, should not change; the drop must have a different, nonrelativistic origin. Although the scaling of E_{os} and n_{cr} may be oversimplified (see Ref. 40 for n_{cr} scaling), it is correct in its tendency. Our current explanation attributes the very pronounced reduction of absorption to the limiting effect of the electrostatic field on the oscillation amplitude of the single electron: With increasing intensity I, the electrons are pushed more and more inward by the radiation

pressure. The electron oscillating in the neighborhood of the vacuum-ion interface oscillates in a narrow anharmonic potential, the half width of which towards the target interior is a small fraction of the wavelength (profile steepening). A similar reduction of absorption has been reported for normal incidence, with an explanation that agrees qualitatively with ours.[41] Latest, beyond $I \simeq 10^{21}$ Wcm^{-2}, absorption by the fastest electrons increases again. They are runaway electrons. The electrostatic potential is strong but finite. The phase at which the electrons enter the laser beam is stochastic. Within them, there will some of them happen to be in resonance with the field and subject to the Doppler shift

$$\omega' = \gamma(\omega - \mathbf{k v}), \tag{6}$$

with γ Lorentz factor, $\mathbf{k}$ wave vector. If such an electron is moving inward from the vacuum, it sees the incident wave at a Doppler downshifted low frequency and is accelerated over a longer distance, whereas the reflected wave is seen at a highly upshifted frequency and represents merely a high frequency disturbance. For an electron moving outward towards the vacuum, the accelerating field is that of the reflected wave. The proof of this acceleration mechanism is based on the study of single particle motions, and is directly confirmed by the appearance of energetic electrons flowing into vacuum in the reflected wave direction in the picture for $a = 60$ and $a = 100$ of Fig. 7. To give a numerical example of electron displacement lengthening $\Delta x/\lambda$ in a plane TN:SA laser wave ($\lambda = 800$ nm) during a forth cycle $\Delta \varphi = \pi/2$: $\Delta x/\lambda = 3$ at $I = 10^{21}$ Wcm^{-2} and $\Delta x/\lambda = 30$ at 10^{22} Wcm^{-2}. For comparison, at $I = 10^{18}$ Wcm^{-2}, this shift is 0.03 only. Beyond $I = 10^{22}$ Wcm^{-2} radiation, reaction on the electron motion has to be taken into account.[43–45] A summary of absorption into all plasma channels (electrons, ions, plasmons), its fraction into electrons, the decrease of absorption towards a pronounced minimum close to zero at $a \simeq$ 15–20, and its rise beyond is presented in Fig. 9.

V. ON SCALING LAWS OF THE "HOT ELECTRONS"

From intensity scaling, the experimentalist and theoretician expect analytical formulas of the shape of the electron spectrum as a function of the laser intensity. As such, a goal

TABLE II. Partition of the incident laser energy: fraction of absorbed intensity I_{abs} transmitted to the electrons, the hot and warm electrons, and the ions and the plasmons (fields) at the end of the standard laser pulse.

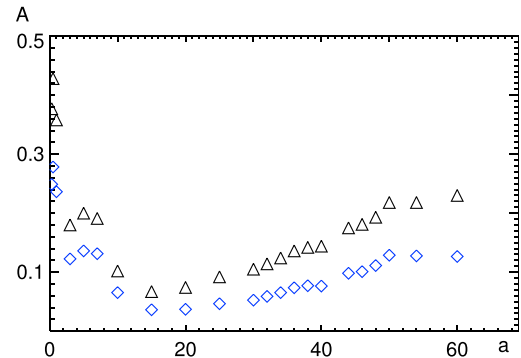| a_0	n_{e0}/n_c	A	All e^-	Hot e^-	Warm e^-	Ions	Fields
0.3	100	0.377	0.25	0.213	0.217	0.009	0.118
	200	0.313	0.24	0.161	0.167	0.007	0.066
0.5	100	0.43	0.28	0.228	0.233	0.01	0.138
1	100	0.358	0.238	0.2	0.211	0.008	0.112
	200	0.354	0.24	0.199	0.206	0.0077	0.106
3	100	0.18	0.122	0.08	0.092	0.003	0.055
	200	0.18	0.123	0.08	0.092	0.003	0.054
5	100	0.2	0.136	0.088	0.102	0.0033	0.061
	200	0.2	0.136	0.089	0.103	0.0026	0.061
7	100	0.19	0.131	0.073	0.089	0.0033	0.056
	200	0.19	0.132	0.076	0.093	0.0025	0.055
15	100	0.067	0.036	0.0002	0.003	0.01	0.021
	200	0.051	0.028	0.0005	0.003	0.007	0.016
	400	0.064	0.039	0.0022	0.008	0.0057	0.019
30	100	0.105	0.0525	0.0002	0.0018	0.0206	0.032
	200	0.045	0.0168	0	0.00012	0.0168	0.011
60	100	0.23	0.126	0.01	0.027	0.033	0.071
	200	0.092	0.031	0.00006	0.0003	0.034	0.027

FIG. 9. Total absorption (triangles) of a 30 cycles standard laser pulse (see text) and the absorption by electrons (blue diamonds) is given as a function of a. The reduction is due to oscillation inhibition by the induced electrostatic field; its rise beyond is mainly a consequence of entrainment (runaway electrons).

seems to be beyond reach; at present, the high power laser community has limited its focus on the energetic electrons. There, the generation of a Maxwellian tail is one of the characteristics of high power interaction. It is also the most interesting part of the spectrum because, as seen from Table II, it contains the main part of the absorbed energy and, last but not least, it is relevant to applications for collective ion acceleration, radiation sources, medical applications, and others. It is aimed at how the number of energetic electrons, the degree of absorption, and the mean energy scale with intensity. On the basis of present knowledge, scaling of the first two quantities is not feasible. Regarding the mean energy, or the hot temperature $k_B T_{hot}$, respectively, despite the frequent attempts in experiment and theory, no convergence has been achieved so far at all. In the light of our foregoing analysis, there is not much surprise about.

The frequently invoked ponderomotive scaling (Wilks' scaling)[17] of $T_{hot} \sim I^{1/2}$ is based on the idea that each laser cycle energetic electrons with energy average in the range of about $E_{os} = m_e c^2 (\sqrt{1 + a^2/2} - 1)$ are generated. Subsequently, this scaling has been recognized as too strong and, in first place guided by experiments,[21] has been replaced by the milder power law[46] $T_{hot} \sim I^{0.34-0.4}$ in the intensity range 10^{18}–10^{21} Wcm^{-2}. It is intended as to be applied to the unidirectional Maxwellian electrons reaching the analyzer at time $t = \infty$. The search for the right mean energy scaling is equivalent to the search for the process of absorption. In the absence of the stochastic element inherent in collisions, it is important to understand whether a Maxwellian tail is one of the signatures of the interaction and, if it is, why.

To arrive at a Maxwellian distribution in an ensemble, it is sufficient to know that, given a certain amount of particles n_{hot} containing the amount of energy $\mathcal{E}_{hot}$, all possible states in the relevant phase space are equally likely and that the Hamiltonian is given by the sum

$$H = \sum_{i=1}^{n_{hot}} \sqrt{m_e^2 c^4 + c^2 \mathbf{p}_i^2}; \quad |H| = \mathcal{E}_{hot}, \qquad (7)$$

which expresses the property that the single electrons are uncorrelated. If the relevant phase space is $\{(\mathbf{p}, \mathbf{q})\}$, as—for example—in statistical thermodynamics, the resulting distribution is the Maxwellian momentum distribution $f(E) \sim \sqrt{E} \exp(-E/k_B T_{hot})$, in disagreement with Fig. 2. However, as outlined in the foregoing chapters, fast electron generation is by anharmonic resonance. This has the important properties: (i) resonance is an attractor for all electrons above a certain oscillation energy, in contrast to harmonic resonance; the always present crossing of trajectories is a clear indicator of it. (ii) All n_{hot} electrons have the same chance to resonate anharmonically regardless of their phase with respect to the laser driver. This makes it very likely that the relevant phase space is the energy acquired at resonance rather than the momentum. Then, from (i) and (ii) follows that collisionless absorption is accompanied by a Maxwellian tail of energetic electrons (consequence of anharmonic attractor) and the spectrum scales like

$f(E) \sim \exp(-E/k_B T_{hot})$, without a degeneracy factor $\sqrt{E}$. This is what we also deduce from Fig. 2.

Let us first examine Fig. 2 for pulses $I \sim \sin^4$ in the intensity range 10^{18}–10^{20} Wcm^{-2}. The uncertainties on the mean energy (slope of log scale) in pictures (a) (30 cycles) and (c) (40 cycles) are considerable; nevertheless, we can conclude with certainty that neither Wilks' original ponderomotive scaling[17] ($I^{0.5}$) nor its improved version is met to some extent. They are far too weak. However, the analysis shows that the assumption $k_B T_{hot} = \kappa \times E_{os}$ with the constant κ not far from unity works. This means that at these relatively low intensities (from $a \simeq 3$ to $a = 10$), the scaling is

$$k_B T_{hot} \sim \sqrt{1 + a^2/2} - 1, \qquad (8)$$

in agreement with Ref. 42. From $a = 12$ on, E_{os} is well approximated by $m_e c^2 a \sim I^{1/2}$. In Fig. 10, we extended the search for scaling from $a = 10$ up to $a = 60$; the latter is already in the runaway regime of absorption. Satisfactory agreement with Ref. 42 is obtained for I from 10^{20} to 10^{21} Wcm^{-2}. Beyond the change in the absorption mechanism and the stiffer, coupling to the ions is noticeable in the increase of slope relative to Ref. 42.

VI. SUMMARY AND CONCLUSION

The focus of the present paper is on the physics of collisionless absorption of intense laser beams in dense targets in the intensity domain $I = 10^{18}$–10^{22} Wcm^{-2} for optical wavelengths, on the variation of the spectral composition of the energetic electrons with intensity and on their scaling with the latter. Most remarkable results are the Brunel like spectral hot electron distribution at the relativistic threshold, the minimum of absorption at $a \cong 15 - 30$, the drastic reduction of the number of hot electrons in this domain and their reappearance beyond, the strong coupling with the return current beyond expectation, a strong hot electron scaling in $a \cong 1 - 10$, and a
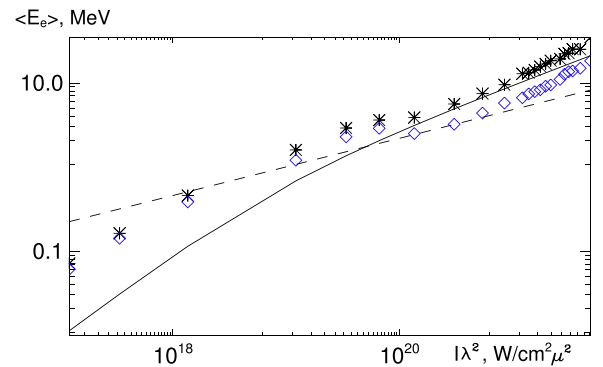
FIG. 10. Hot and warm electron energy scaling $\langle E_e \rangle$ with laser intensity $I = 10^{17} - 5 \times 10^{21}$ Wcm^{-2}, standard pulse. Stars: $E_e \geq E_{os}$ (hot electrons); diamonds: $E_e \geq 0.5 E_{os}$ (warm electrons). In contrast to Fig. 2, here, $\langle E_e \rangle$ is the average taken over the single energies E_e. Solid line: scaling after,[42] $k_B T_{hot} = m_e c^2 [\sqrt{1 + (I\lambda^2)/(2.74 \times 10^{18})} - 1]$. Dashed line: scaling after,[21] $k_B T_{hot} = m_e c^2 [I\lambda^2/(1.37 \times 10^{18})]^{0.34}$.

scaling in vague accordance with current published estimates in $a \cong 10 - 50$ and a strong increase beyond.

On a fundamental level understanding, collisionless absorption is equivalent to the search for the non-orthogonality of induced current density to the laser field. The answer is found in the interplay of the laser field with the space charge field induced by it. The idealized model of Brunel works already on this basis. It is capable of explaining important effects at the relativistic intensity threshold and below, like the generation of two groups of electrons, a hot and a cold component. The non-Maxwellian spectrum predicted by the model is found in our simulations at the relativistic threshold and below; with the increase in a, it is washed out. By following test orbits, we are able to localize absorption at the vacuum-target interface and skin layer for all intensities below the radiation reaction limit at $I \cong 10^{22}\,\mathrm{Wcm}^{-2}$ in linear polarization, in agreement with Brunel for non relativistic intensities. If, therefore, the ominous "vacuum heating" is invoked as responsible for absorption, this is correct if it is identified with Brunel's mechanism. What it does not explain, and Brunel does not either, is the underlying physics, i.e., the phase shift and, in concomitance, orbits crossing.

An explanation in terms of physics has to show that (i) such a breaking of flow is not by accidence and (ii) a hot Maxwellian tail in the spectrum is a natural outcome from strong drivers. Anharmonic resonance is currently the best model explaining both aspects. It rules stochastic heating and "weave breaking" out automatically. Anharmonic resonance constitutes an attractor (fix point). This kind of resonance always happens in presence of a sufficiently strong driver at any laser frequency and any target density, in contrast to harmonic resonance, which is bound to $\omega = \omega_p$. When crossing resonance, the momentum of an electron undergoes a phase shift by π or a fraction of it with respect to the bulk of the plasma. Wave breaking, here more appropriately called breaking of flow owing to profile steepening on lengths of a small fraction of a laser wavelength, is a consequence of absorption and energetic electron generation, not its origin.

From $I \cong 5 \times 10^{21}\,\mathrm{Wcm}^{-2}$, anharmonic resonance is strengthened by the generation of runaway electrons due to trapping in both, the incident and the reflected laser wave. The reduction up to nearly disappearance of hot electrons $E \geq E_{\mathrm{os}}$ is attributed to oscillation inhibition by the ponderomotive space charge field. In the whole intensity domain considered, the major fraction of laser energy is deposited in the hot and moderately hot electrons. The next significant portion goes into Cherenkov plasmons excited by the periodic plasma jets. From the analysis of the test trajectories, their coupling to the neutralizing return current is apparent. We consider it as an important aspect when modeling anomalous transport of heat and fast electrons in compressed matter.

Finally, we reexamined the hot electron scaling in 1D, perhaps the most controversially discussed subject in the pertinent literature. Acceptable coincidence with the leading approximations is only found in the intensity range 10^{20}–10^{21}. The deviations below $a \cong 10$ are to be attributed

mainly to the imprecise proportionality between E_{os} and $I \sim a^2$. In the runaway absorption regime, the governing scaling law is still to be discovered. The main reason for the current misunderstandings and disagreements have to be attributed to the poor knowledge of the electron energy spectrum $f(E)$. What is missing most at present in the experiment and in the theory is a clear definition of what means "hot" and "cold" electrons. In order not to fall into this deficiency, we define electrons as "hot" and "moderately hot" if their energy is higher than E_{os} and $(0.5 - 2/3)E_{\mathrm{os}}$. It is approximately the range of the Maxwellian tail. The commonly used terminology "Maxwellian" is misleading because it refers to the electron velocities **v** or momenta with a distribution law $df(E) = v^2 \exp(-E/k_B T_{\mathrm{hot}})dv \sim \sqrt{E}\exp(-E/k_B T_{\mathrm{hot}})dE$. This differs from our findings (and, implicitly, others) of a Boltzmann distribution $df(E) = \exp(-E/k_B T_{\mathrm{hot}})dE$ for the relevant restricted phase space of total energies $\mathcal{E} = \sum E_i$.

ACKNOWLEDGMENTS

[1] A. D. Piliya, Sov. Phys. Tech. Phys. **11**, 609 (1966).
[2] H.-J. Kull, Phys. Fluids **26**, 1881 (1983).
[3] W. L. Kruer and K. Estabrook, Phys. Fluids **28**, 430 (1985).
[4] F. Brunel, Phys. Rev. Lett. **59**, 52 (1987); Phys. Fluids **31**, 2714 (1988).
[5] P. Gibbon and A. R. Bell, Phys. Rev. Lett. **68**, 1535 (1992).
[6] P. Gibbon, Phys. Rev. Lett. **73**, 664 (1994).
[7] L. M. Chen, J. Zhang, Q. L. Dong, H. Teng, T. J. Liang, L. Z. Zhao, and Z. Y. Whei, Phys. Plasmas **8**, 2925 (2001); Q. Dong and J. Zhang, Sci. China **46**, 71 (2003); D. Umstadter, J. Phys. D **36**, R151 (2003); S. Kato, J. Plasma Fusion Res. **6**, 658 (2004).
[8] A. V. Getz and V. P. Krainov, J. Exp. Theor. Phys. **101**, 80 (2005).
[9] W. Rozmus and V. T. Tikhonchuk, Phys. Rev. A **42**, 7401 (1990); W. Rozmus, V. T. Tikhonchuk, and R. Cauble, Phys. Plasmas **3**, 360 (1996).
[10] T.-Y. B. Yang, W. L. Kruer, R. M. More, and A. B. Langdon, Phys. Plasmas **2**, 3146 (1995); T.-Y. B. Yang, W. L. Kruer, A. B. Langdon, and T. W. Johnston, Phys. Plasmas **3**, 2702 (1996).
[11] G. Ferrante, M. Zarcone, and S. A. Uryupin, Phys. Plasmas **9**, 4560 (2002).
[12] S. Kato, B. Bhattacharyya, A. Nishiguchi, and K. Mima, Phys. Fluids B **5**, 564 (1993).
[13] H.-B. Cai, Phys. Plasmas **13**, 063108 (2006).
[14] D. Bauer and P. Mulser, Phys. Plasmas **14**, 023301 (2007).
[15] P. Mulser, S.-M. Weng, and T. Liseykina, Phys. Plasmas **19**, 043301 (2012).
[16] M. Cerchez, R. Jung, J. Osterholz, T. Toncian, O. Willi, P. Mulser, and H. Ruhl, Phys. Rev. Lett. **100**, 245001 (2008).
[17] S. C. Wilks, W. L. Kruer, M. Tabak, and A. B. Langdon, Phys. Rev. Lett. **69**, 1383 (1992).
[18] T. Baeva, S. Gordienko, A. P. L. Robinson, and P. A. Norreys, Phys. Plasmas **18**, 056702 (2011).
[19] G. Malka and J. L. Miquel, Phys. Rev. Lett. **77**, 75 (1996).
[20] P. McKenna, F. Lindau, O. Lundh, D. C. Carroll, R. J. Clarke, K. W. D. Ledingham, T. McCanny, D. Neely, A. P. L. Robinson, L. Robson, P. T.

Simpson, C.-G. Wahlström, and M. Zepf, Plasma Phys. Controlled Fusion **49**, B223 (2007).

[21]F. N. Beg, A. R. Bell, A. E. Dangor, C. N. Danson, A. P. Fews, M. E. Glinsky, B. A. Hammel, P. Lee, P. A. Norreys, and M. Tatarakis, Phys. Plasmas **4**, 447 (1997).

[22]M. G. Haines, M. S. Wei, F. N. Beg, and R. B. Stephens, Phys. Rev. Lett. **102**, 045008 (2009).

[23]P. Gibbon, A. A. Andreev, and K. Yu. Platonov, Plasma Phys. Controlled Fusion **54**, 045001 (2012).

[24]C. D. Chen, J. A. King, M. H. Key, K. U. Akli, F. N. Beg, H. Chen, R. R. Freeman, A. Link, A. J. Mackinnon, A. G. MacPhee, P. K. Patel, M. Porkolab, R. B. Stephens, and L. D. Van Woerkom, Rev. Sci. Instrum. **79**, 10E305 (2008).

[25]A. G. MacPhee, K. U. Akli, F. N. Beg, C. D. Chen, H. Chen, R. Clarke, D. S. Hey, R. R. Freeman, A. J. Kemp, M. H. Key, J. A. King, S. Le Pape, A. Link, T. Y. Ma, H. Nakamura, D. T. Offermann, V. M. Ovchinnikov, P. K. Patel, T. W. Phillips, R. B. Stephens, R. Town, Y. Y. Tsui, M. S. Wei, L. D. Van Woerkom, and A. J. Mackinnon, Rev. Sci. Instrum. **79**, 10F302 (2008).

[26]T. Kluge, T. Cowan, A. Debus, U. Schramm, K. Zeil, and M. Bussmann, Phys. Rev. Lett. **107**, 205003 (2011).

[27]A. Macchi, *A Superintense Laser-Plasma Interaction Theory Primer* (Springer, New York, 2013), Chap. 4, Sec. 2.

[28]Y. Sentoku, V. Y. Bychenkov, K. Flippo, A. Maksimchuk, K. Mima, G. Mourou, Z. M. Sheng, and D. Umstadter, Appl. Phys. B **74**, 207 (2002).

[29]V. S. Rastunkov and V. P. Krainov, Laser Phys. **15**, 262 (2005).

[30]D. F. Zaretsky, Ph. A. Korneev, S. V. Popruzhenko, and W. Becker, J. Phys. B **37**, 4817 (2004).

[31]Ph. A. Korneev, S. V. Popruzhenko, D. F. Zaretsky, and W. Becker, Laser Phys. Lett. **2**, 452 (2005).

[32]A. V. Sofronov and V. P. Krainov, J. Phys. B **37**, L329 (2004).

[33]A. Pukhov, Rep. Prog. Phys. **66**, 47 (2003).

[34]P. Mulser, D. Bauer, and H. Ruhl, Phys. Rev. Lett. **101**, 225002 (2008).

[35]J. R. Davies, Plasma Phys. Controlled Fusion **51**, 014006 (2009); Nucl. Instrum. Methods Phys. Res. A **544**, 61 (2005).

[36]P. Gibbon, A. A. Andreev, E. Lefebvre, G. Bonnaud, H. Ruhl, J. Delettrez, and A. R. Bell, Phys. Plasmas **6**, 947 (1999).

[37]A. J. Kemp, Y. Sentoku, and M. Tabak, Phys. Rev. E **79**, 066406 (2009).

[38]P. Mulser and D. Bauer, *High Power Laser-Matter Interaction* (Springer, Heidelberg, 2010), p. 356.

[39]M. Sherlock, E. G. Hill, R. G. Evans, and S. J. Rose, Phys. Rev. Lett. **113**, 255001 (2014).

[40]S. M. Weng, P. Mulser, and Z. M. Sheng, Phys. Plasmas **19**, 022705 (2012).

[41]J. Sanz, A. Debayle, and K. Mima, Phys. Rev. E. **85**, 046411 (2012).

[42]H. Chen, S. C. Wilks, W. Kruer, P. Patel, and R. Shepherd, "Hot electron energy distributions from ultra-intense laser solid interactions," Phys. Plasmas **16**, 020705 (2009).

[43]N. Naumova, T. Schlegel, V. T. Tikhonchuk, C. Labaune, I. V. Sokolov, and G. Mourou, Phys. Rev. Lett. **102**, 025002 (2009).

[44]M. Tamburini, T. V. Liseykina, F. Pegoraro, and A. Macchi, Phys. Rev. E **85**, 016407 (2012); M. Tamburini, F. Pegoraro, A. Di Piazza, C. H. Keitel, and A. Macchi, New J. Phys. **12**, 123005 (2010).

[45]L. L. Ji, A. Pukhov, I. Yu. Kostyukov, B. F. Shen, and K. Akli, Phys. Rev. Lett. **112**, 145003 (2014).

[46]S. C. Wilks and W. L. Kruer, IEEE J. Quantum Electron. **33**, 1954 (1997).

4. Radiation friction effect in laser-plasma interactions

The list of publications:

M. Tamburini, F. Pegoraro, A. Di Piazza, C. H. Keitel, T. V. Liseykina, A. Macchi, *Radiation reaction effects on electron nonlinear dynamics and ion acceleration in laser–solid interaction*, Nuclear Instruments & Methods in Physics Research A **653**, 181–185 (2011)

M. Tamburini, T. V. Liseykina, F. Pegoraro, A. Macchi, *Radiation-pressure-dominant acceleration: Polarization and radiation reaction effects and energy increase in three-dimensional simulations*, Phys. Rev. E **85**, 916407 (2012)

T. Liseykina, S. Popruzhenko, A. Macchi, *Inverse Faraday effect driven by radiation friction*, New J. Phys. **18** 072001 (2016)

S. Popruzhenko, T. Liseykina, A. Macchi, *Efficiency of radiation friction losses in laser-driven "hole boring" of dense targets*, New J. Phys. **21**, 033009 (2019)

Radiation reaction effects on electron nonlinear dynamics and ion acceleration in laser–solid interaction

M. Tamburini [a,*], F. Pegoraro [a], A. Di Piazza [b], C.H. Keitel [b], T.V. Liseykina [c,d], A. Macchi [a,e]

[a] Dipartimento di Fisica "E. Fermi", Università di Pisa, Largo Bruno Pontecorvo 3, I-56127 Pisa, Italy
[b] Max-Planck-Institut für Kernphysik, Saupfercheckweg 1, D-69117 Heidelberg, Germany
[c] Institute of Computer Technologies, SD-RAS, Novosibirsk, Russia
[d] Institute of Physics, University of Rostock, Germany
[e] Istituto Nazionale di Ottica, CNR, Research unit "A. Gozzini", Pisa, Italy

ARTICLE INFO

ABSTRACT

Radiation Reaction (RR) effects in the interaction of an ultra-intense laser pulse with a thin plasma foil are investigated analytically and by two-dimensional (2D3P) Particle-In-Cell (PIC) simulations. It is found that the radiation reaction force leads to a significant electron cooling and to an increased spatial bunching of both electrons and ions. A fully relativistic kinetic equation including RR effects is discussed and it is shown that RR leads to a contraction of the available phase space volume. The results of our PIC simulations are in qualitative agreement with the predictions of the kinetic theory.

© 2010 Elsevier B.V. All rights reserved.

1. Introduction

Current laser systems may deliver intensities up to 10^{22} W cm^{-2} [1] and intensities up to 10^{26} W cm^{-2} are expected at the Extreme Light Infrastructure (ELI). In such ultrahigh-intensity regime and for typical laser wavelength $\lambda \sim 0.8$ μm the motion of electrons in the laser field is ultra-relativistic and Radiation Reaction (RR) effects may become important. The RR force describes the back-action of the radiation emitted by an accelerated electron on the electron itself and accounts for the loss of the electron energy and momentum due to the emission of such radiation. Apart from the need of including RR effects in the dynamics of laser–plasma interactions in the ultra-relativistic regime, the latter also offers for the first time the opportunity to detect RR effects experimentally [2,3].

In this paper we present an approach to a kinetic description of laser–plasma interactions where RR effects are included via the Landau–Lifshitz (LL) force [4]. Some properties of the kinetic equation with RR are discussed and in particular it is proved that the RR force leads to a *contraction* of the phase space volume. Then, Particle-In-Cell (PIC) simulations are used to study RR effects on the acceleration of a thin plasma foil in the regime of Radiation Pressure dominance [5]. Numerical simulations [5] suggested that Radiation Pressure Acceleration (RPA) becomes the dominant mechanism of ion acceleration at intensities exceeding 10^{23} W cm^{-2}. Such RPA regime is attractive because of the foreseen high efficiency, the quasi-monoenergetic features expected in the ion energy spectrum and the possibility to achieve a potentially "unlimited" acceleration [6]. Previous PIC simulations [7] showed signatures of RR effects at intensities exceeding 5×10^{22} W cm^{-2} and increasing nonlinearly with the laser intensity. More recent simulations studies of RPA both for thick targets [8,9] and ultrathin targets [10] suggested that the inclusion of the RR force cools the electrons and may improve the quality of the ion spectrum.

Our approach to the inclusion of RR effects in a PIC code has been discussed in detail in Ref. [11] where one-dimensional (1D) simulations of RPA have been also reported. In the present paper we report both additional 1D simulations and first two-dimensional (2D) simulations using parameters similar to those of Ref. [12] where, in particular, the impact of a Rayleigh–Taylor-like instability on a thin foil acceleration was studied.

In classical electrodynamics, the effect of RR can be included by means of the LL force [4]:

$$\mathbf{F}_R = -\left(\frac{4\pi}{3}\frac{r_e}{\lambda}\right) \cdot \left\{ \gamma \left[\left(\frac{\partial}{\partial t} + \mathbf{v} \cdot \boldsymbol{\nabla}\right)\mathbf{E} + \mathbf{v} \times \left(\frac{\partial}{\partial t} + \mathbf{v} \cdot \boldsymbol{\nabla}\right)\mathbf{B} \right] \right.$$
$$\left. - [(\mathbf{E} + \mathbf{v} \times \mathbf{B}) \times \mathbf{B} + (\mathbf{v} \cdot \mathbf{E})\mathbf{E}] + \gamma^2 \left[(\mathbf{E} + \mathbf{v} \times \mathbf{B})^2 - (\mathbf{v} \cdot \mathbf{E})^2 \right] \mathbf{v} \right\} \quad (1)$$

where $\mathbf{v}$ is the electron velocity, γ is the relativistic factor, $r_e \equiv e^2/mc^2 \approx 2.8 \times 10^{-9}$ μm is the classical electron radius, $\lambda = 2\pi c/\omega$ is the laser wavelength and we use dimensionless quantities as in the PIC code: time, space and momentum are normalized in units of ω^{-1}, $c\omega^{-1}$ and mc, respectively. Consequently, EM fields are normalized in units of $m\omega c/|e|$ and densities in units of the critical density $n_c = m\omega^2/4\pi e^2$.

* Corresponding author.
E-mail addresses: matteo.tamburini@gmail.com, tamburini@df.unipi.it (M. Tamburini).

The LL approach holds in the classical framework and quantum effects are neglected. As pointed out in Ref. [11], the first term of the LL force Eq. (1) i.e. the one containing the *derivatives* of the electric and magnetic fields, should be neglected because its effect is smaller than quantum effects such as the spin force. However, in Eq. (2) we show the effect of each term of the LL force Eq. (1) on the rate of change of the phase space volume.

2. The kinetic equation with Radiation Reaction

In this section, a fully relativistic kinetic equation that includes the RR effects is discussed. We show a few basic properties of the kinetic equation pointing out the peculiarities of the RR force whose main new feature is that it *does not* conserve the phase space volume.

Generalized kinetic equations for non-conservative forces and in particular for the RR force have been known since late 60s for the Lorentz–Abraham–Dirac (LAD) equation [13,14] and late 70s for the LL equation [15]. Recently, the generalized kinetic equation with the LL force included has been used to study the RR effects on thermal electrons in a magnetically confined plasma [16] and to develop a set of closed fluid equations with RR [17–19]. In this paper, we give the kinetic equation in a non-manifestly covariant form, see Refs. [15,16] for the kinetic equation in a manifestly Lorentz-covariant form.

The relativistic distribution function $f = f(\mathbf{q}, \mathbf{p}, t)$ evolves according to the collisionless transport equation:

$$\frac{\partial f}{\partial t} + \nabla_{\mathbf{q}} \cdot (f\mathbf{v}) + \nabla_{\mathbf{p}} \cdot (f\mathbf{F}) = 0 \tag{2}$$

where $\mathbf{q}$ are the spatial coordinates, $\mathbf{v} = \mathbf{p}/\gamma$ is the three-dimensional velocity, $\gamma = \sqrt{1 + \mathbf{p}^2}$ is the relativistic factor and $\mathbf{F} = \mathbf{F}_L + \mathbf{F}_R$ is the mean force due to external and collective fields ($\mathbf{F}_L \equiv -(\mathbf{E} + \mathbf{v} \times \mathbf{B})$ is the Lorentz force and $\mathbf{F}_R$ is given in Eq. (1)). Physically, Eq. (2) implies the conservation of the number of particles.

The new key feature compared to the usual Vlasov equation is that for the RR force $\mathbf{F}_R$ we have $\nabla_{\mathbf{p}} \cdot \mathbf{F}_R \neq 0$. Using Lagrangian coordinates $\mathbf{q}(t)$, $\mathbf{p}(t)$, Eq. (2) can be recast in the equivalent form:

$$\frac{d \ln f}{dt} = -\nabla_{\mathbf{p}} \cdot \mathbf{F}. \tag{3}$$

According to Eq. (3), $\nabla_{\mathbf{p}} \cdot \mathbf{F}$ provides the percentage of variation of the distribution function f within the characteristic time scale ω^{-1}. Integrating Eq. (3) along its characteristics, we find that the distribution function f remains positive as required.

Introducing the entropy density in the phase space $s(\mathbf{q}, \mathbf{p}, t) = -f(\mathbf{q}, \mathbf{p}, t) \ln f(\mathbf{q}, \mathbf{p}, t)$, from Eq. (2) we get the equation for the evolution of the entropy density:

$$\frac{\partial s}{\partial t} + \nabla_{\mathbf{q}} \cdot (s\mathbf{v}) + \nabla_{\mathbf{p}} \cdot (s\mathbf{F}) = f \nabla_{\mathbf{p}} \cdot \mathbf{F}. \tag{4}$$

Integrating Eq. (4) in the phase space, we get the rate of variation of the total entropy $S(t) = \int d^3q \, d^3p \, s(\mathbf{q}, \mathbf{p}, t)$:

$$\frac{dS(t)}{dt} = \int d^3q \, d^3p \, f \nabla_{\mathbf{p}} \cdot \mathbf{F}. \tag{5}$$

The Lorentz force $\mathbf{F}_L \equiv -(\mathbf{E} + \mathbf{v} \times \mathbf{B})$ gives $\nabla_{\mathbf{p}} \cdot \mathbf{F}_L = 0$ identically thus $\nabla_{\mathbf{p}} \cdot \mathbf{F} = \nabla_{\mathbf{p}} \cdot \mathbf{F}_R$. Moreover, the distribution function $f(\mathbf{q}, \mathbf{p}, t)$ is always non-negative $f \geq 0$ thus the sign of dS/dt is given by $\nabla_{\mathbf{p}} \cdot \mathbf{F}_R$ solely.

From the LL force Eq. (1) we get [20]

$$\nabla_{\mathbf{p}} \cdot \mathbf{F}_R = -\left(\frac{4\pi}{3}\frac{r_e}{\lambda}\right) \left\{ \left[\nabla_{\mathbf{q}} \cdot \mathbf{E} - \mathbf{v} \cdot \left(\nabla_{\mathbf{q}} \times \mathbf{B} - \frac{\partial \mathbf{E}}{\partial t}\right)\right] \right.$$
$$\left. + 2\left[\frac{\mathbf{E}^2 + \mathbf{B}^2}{\gamma}\right] + 4\gamma[(\mathbf{v} \times \mathbf{E})^2 + (\mathbf{v} \times \mathbf{B})^2 - 2\mathbf{v} \cdot (\mathbf{E} \times \mathbf{B})] \right\}. \tag{6}$$

In a plasma, the kinetic equation is coupled with the Maxwell equations for the self-consistent fields:

$$\nabla_{\mathbf{q}} \cdot \mathbf{E} = \frac{\rho}{\rho_c} = \frac{1}{n_c} \sum_{j=e,i} Z_j \int d^3p f_j(\mathbf{q}, \mathbf{p}, t) \tag{7}$$

$$\nabla_{\mathbf{q}} \times \mathbf{B} - \frac{\partial \mathbf{E}}{\partial t} = \frac{\mathbf{j}}{j_c} = \frac{1}{n_c c} \sum_{j=e,i} Z_j \int d^3p \, \mathbf{v} f_j(\mathbf{q}, \mathbf{p}, t) \tag{8}$$

where $\rho_c \equiv |e| n_c$, $j_c \equiv |e| n_c c$, $\int d^3q \, d^3p f_j(\mathbf{q}, \mathbf{p}, t) = N_j$ is the total number of particles for each species ($j = e$ electrons, $j = i$ ions) and Z_j is the charge of the particle species in units of $|e|$ (for electrons $Z_e = -1$). For a plasma, Eq. (6) can be recast as

$$\nabla_{\mathbf{p}} \cdot \mathbf{F}_R = -\left(\frac{4\pi}{3}\frac{r_e}{\lambda}\right) \left\{ \left[\frac{\rho}{\rho_c} - \mathbf{v} \cdot \frac{\mathbf{j}}{j_c}\right] + 2\left[\frac{\mathbf{E}^2 + \mathbf{B}^2}{\gamma}\right] \right.$$
$$\left. + 4\gamma[(\mathbf{v} \times \mathbf{E})^2 + (\mathbf{v} \times \mathbf{B})^2 - 2\mathbf{v} \cdot (\mathbf{E} \times \mathbf{B})] \right\}. \tag{9}$$

The terms of Eq. (9) proportional to the charge density ρ and to the current density $\mathbf{j}$ come from the first term of the LL force Eq. (1) i.e. the term containing the derivatives of the fields. In general, these terms can give either a positive or negative contribution to $\nabla_{\mathbf{p}} \cdot \mathbf{F}_R$. The second term of Eq. (9) i.e. the term proportional to $(\mathbf{E}^2 + \mathbf{B}^2)$ has always a negative sign, its effect decreases with increasing electron energy and it is typically negligible. The third term of Eq. (9) comes from the strongly anisotropic "friction" term of the LL force i.e. the term proportional to γ^2 in Eq. (1) (see Ref. [11] for a detailed discussion of this term) and dominates in the ultra-relativistic limit $\gamma \gg 1$.

It is possible to prove [20] the following statement: for any $\mathbf{v}$ such that $|\mathbf{v}| \in [0,1[$ then

$$\left[(\mathbf{v} \times \mathbf{E})^2 + (\mathbf{v} \times \mathbf{B})^2 - 2\mathbf{v} \cdot (\mathbf{E} \times \mathbf{B})\right] + \left[\frac{\mathbf{E}^2 + \mathbf{B}^2}{2\gamma^2}\right] \geq 0 \tag{10}$$

therefore according with Eqs. (5, 9), the terms of the LL force Eq. (1) that *do not* depend on the derivatives of the fields always lead to a *contraction* of the available phase space volume $dS/dt \leq 0$. In a few special cases, the effect of the terms of the LL force Eq. (1) that depend on the derivatives of the fields (i.e. the terms proportional to ρ and $\mathbf{j}$ in Eq. (9)) might lead to an expansion of the phase space volume. Anyway, their effect should be negligible compared to quantum effects as discussed in Ref. [11].

We show explicitly the contraction of the phase space in the special case of a small bunch of electrons interacting with a plane wave where collective fields are assumed to be negligible compared with the plane wave fields. Assuming an initial distribution $f = g(\mathbf{q})\delta^3(\mathbf{p} - \mathbf{p}_0)$, from Eqs. (5, 9) we have

$$\frac{dS(t)}{dt} = -\left(\frac{4\pi}{3}\frac{r_e}{\lambda}\right) \int d^3q \, g(\mathbf{q}) \left\{ 2\left[\frac{\mathbf{E}^2 + \mathbf{B}^2}{\gamma(\mathbf{p}_0)}\right] + 4\gamma(\mathbf{p}_0) \right.$$
$$\left. \cdot [(\mathbf{v}_0 \times \mathbf{E})^2 + (\mathbf{v}_0 \times \mathbf{B})^2 - 2\mathbf{v}_0 \cdot (\mathbf{E} \times \mathbf{B})] \right\} \tag{11}$$

where $\mathbf{v}_0 = \mathbf{p}_0/\gamma(\mathbf{p}_0)$. If the electron bunch counter propagates with the plane wave ($[\mathbf{v}_0 \cdot (\mathbf{E} \times \mathbf{B})] < 0$) or propagates in the transverse direction ($[\mathbf{v}_0 \cdot (\mathbf{E} \times \mathbf{B})] = 0$), from Eq. (11) it is clear that RR leads to a contraction of the phase space. In particular, in the case of counter-propagation (using $|\mathbf{E}| = |\mathbf{B}|$, $\mathbf{E} \cdot \mathbf{B} = 0$) we have $\nabla_{\mathbf{p}} \cdot \mathbf{F}_R = -(4\pi r_e/3\lambda)4\mathbf{E}^2[2\gamma(\mathbf{p}_0)|\mathbf{v}_0|(1 + |\mathbf{v}_0|) + 1/\gamma(\mathbf{p}_0)]$. On the other hand, if the bunch propagates in the same direction of the plane wave ($\mathbf{v}_0$ parallel to $\mathbf{E} \times \mathbf{B}$), then the contribution of the friction term (proportional to γ in Eq. (9)) becomes comparable with the contribution of the second term (proportional to $(\mathbf{E}^2 + \mathbf{B}^2)$ in Eq. (9)) and we have $\nabla_{\mathbf{p}} \cdot \mathbf{F}_R = -(4\pi r_e/3\lambda)[4\mathbf{E}^2/(1 + |\mathbf{v}_0|)^2 \gamma^3(\mathbf{p}_0)]$

which still leads to a contraction of the phase space but with a rate γ^4 smaller than the case of counter-propagation. This reinforces the evidence of the strongly *anisotropic* features of the LL force Eq. (1) (see Ref. [11] for further details).

The physical interpretation of the above properties is that the RR force acts as a cooling mechanism for the system: part of the energy and momentum are radiated away and the spread in both momentum and coordinate space may be reduced. This general prediction is confirmed by our PIC simulations (see Section 3) where we found that RR effects lead to both an increased bunching in space and to a noticeable cooling of hot electrons.

Finally, it is worthwhile mentioning that Eq. (2) is more general than the Vlasov equation but the PIC approach is still valid i.e. the PIC approach provides a solution for Eq. (2) and it not limited to the Vlasov equation [20].

3. PIC simulations

Suitable approximations to the LL force and our approach to its inclusion in a PIC code are described in Ref. [11]. The numerical approach is based on the widely used Boris particle pusher and it can be implemented in codes of any dimensionality. Inclusion of RR effects via this method in PIC simulations leads to only a $\sim 10\%$ increase in CPU time, which may be essential to perform large-scale simulations with limited computing power.

3.1. 1D simulations

We first report one-dimensional (1D3P) PIC simulations with laser and plasma parameters similar to Ref. [5]. Previous 1D simulations in this regime have been reported in Ref. [11] where a detailed comparison with other work is also made. In the present paper we review the basic observations in the 1D case and we include results at intensities higher than those investigated in Ref. [11].

The target is a plasma foil of protons with uniform initial density $n_0 = 100 n_c$ and thickness $\ell = 1\lambda$ where $\lambda = 0.8\,\mu m$ is the laser wavelength and $T = \lambda/c \approx 2.67\,fs$ is the laser period. In these simulations, the laser pulse front reaches the edge of the plasma foil at $t = 0$, the profile of the laser field amplitude has a "trapezoidal" shape in time with one cycle, $\sin^2$-function rise and fall and a five cycles constant plateau. We considered three intensities $I = 2.33 \times 10^{23}, 5.5 \times 10^{23}$, and $10^{24}\,W\,cm^{-2}$ for both Circular (CP) and Linear (LP) polarization of the laser pulse.

In the CP case, we found that RR effects on the ion spectrum are negligible even at intensities of $I = 10^{24}\,W\,cm^{-2}$ as shown in Fig. 1. For CP, electrons pile up and the numerical density grows exceeding thousand of times the critical density n_c. The laser pulse does not penetrate deeply into the target (i.e. the effective skin depth is a very small fraction of the foil thickness) and electrons move in a field much weaker than the vacuum field.

In Ref. [5] it was expected that RR effects in the radiation-pressure dominated acceleration of the thin foil would have been weak because in this regime the whole foil becomes quickly relativistic, hence in the foil frame the laser wavelength λ' increases and the typical strength of the RR parameter $\sim r_e/\lambda$ [see Eq. (1)] decreases. The present case of acceleration with CP pulses appears to confirm this picture. The weakness of RR effects may also be explained on the basis of the LL equation for an electron moving into a plane wave [21]. As electrons move in the forward direction coherently with the foil (while rotating in the transverse plane in the CP field) and the amplitude of the reflected wave is weak when the foil is strongly relativistic, the situation is similar to an electron co-propagating with the plane wave at a velocity close to c, for which the LL force almost vanishes [11]. The relativistic motion of the foil also prevents the onset of Self-Induced Transparency by
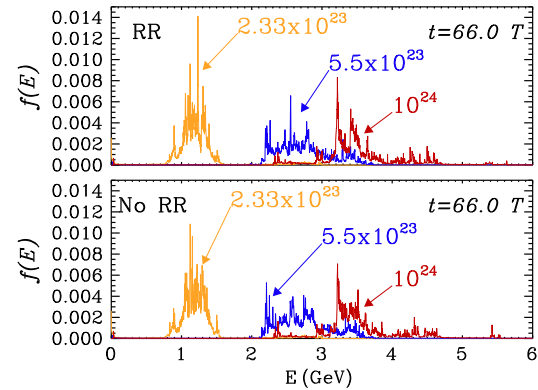

Fig. 1. Ion energy spectra at $t = 66\,T$ with (top) and without (bottom) RR for Circular Polarization. The laser intensity I is $2.33 \times 10^{23}\,W\,cm^{-2}$ (yellow), $5.5 \times 10^{23}\,W\,cm^{-2}$ (blue), $10^{24}\,W\,cm^{-2}$ (red) and the target thickness is $\ell = 1\lambda$. (For interpretation of the references to color in this figure legend, the reader is referred to the web version of this article.)
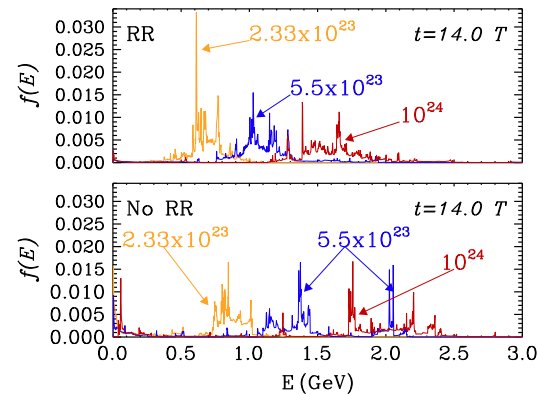

Fig. 2. Ion energy spectra at $t = 14\,T$ with (top) and without (bottom) RR for Linear Polarization. The laser intensity I is $2.33 \times 10^{23}\,W\,cm^{-2}$ (yellow), $5.5 \times 10^{23}\,W\,cm^{-2}$ (blue), $10^{24}\,W\,cm^{-2}$ (red) and the target thickness is $\ell = 1\lambda$. (For interpretation of the references to color in this figure legend, the reader is referred to the web version of this article.)

increasing the optical thickness parameter $\zeta = \pi n_0 \ell/n_c \lambda$ in the foil frame (see Ref. [22] and references therein). For smaller target thickness, breakthrough of the laser pulse occurs and RR effects are greatly enhanced also for CP [11].

It may be worth noticing that, at the highest intensity considered $I = 10^{24}\,W\,cm^{-2}$, in principle one would expect the classical approach to RR to break down due to the onset of quantum electrodynamics (QED) effects, as discussed in Ref. [11]. However, it can be shown by a direct analysis of the simulation data that the threshold condition for QED effect is not violated in the CP case.

For linear polarization (LP), differently from the CP case, we found that RR effects are important leading to a reduction of the maximum achievable ion energy and to some narrowing of the width of the ion spectrum as shown in Fig. 2. This different dynamics for LP is correlated with the strong longitudinal oscillatory motion driven by the oscillating component of the $\mathbf{j} \times \mathbf{B}$ force which is suppressed in the CP case. This allows a deeper penetration of the laser pulse into the foil with a significant fraction of electrons on the front surface moving in a strong electromagnetic field of the same order of vacuum fields [11]. The relative reduction in the ion energy when RR is included is close to the percentage of the laser pulse energy which is lost as high-energy radiation escaping from the plasma.

The results for LP (Fig. 2) are shown for the same intensity values of the CP case (Fig. 1) for a direct comparison. However, at least for the highest intensity case, the LP results must be taken with some caution as the condition for the validity of a classical approach tends to be significantly violated. In such regime, an analysis based on quantum RR effects might be necessary [23,24].

3.2. 2D simulations

We report preliminary two-dimensional (2D3P) PIC simulations with laser and plasma parameters similar to Ref. [12]. To the best of our knowledge, this is the first paper reporting results of two-dimensional PIC simulations with RR effects included.

The target is a plasma slab of fully ionized deuterium ($Z/A = 1/2$) of width 40λ, density $n_0 = 169n_c$ and thickness $\ell = 0.5\lambda$. The size

of the computational box is $95\lambda \times 40\lambda$ with a spatial resolution $\Delta x = \Delta y = \lambda/80$ and 625 quasi-particles per cell corresponding to a total of 8×10^7 quasi-particles for each species. The laser pulse is s-polarized with the electric field along the z-axis. Its normalized amplitude is $a_0 = 320$ corresponding to an intensity $I = 1.4 \times 10^23$ W cm^{-2} with a wavelength $\lambda = 1.0$ μm and period $T = \lambda/c \approx 3.3$ fs. The pulse has a Gaussian transverse profile of width 20λ FWHM and a sin^2 longitudinal profile of length 40λ FWHM. In these simulations, the front of the laser pulse reaches the foil at $t = 0$.

Comparing the results of our simulations with and without RR (see Fig. 3, we report the results at $t = 70$ T) it is apparent that RR leads to both an increased electron and ion bunching and to a strong cooling of electrons. These results are qualitatively consistent with our expectations from the kinetic theory that we have discussed in Section 2 and in particular with the prediction of a contraction of the electrons available phase space volume.

A qualitative understanding of these results can be achieved by recalling that the RR force Eq. (1) is mainly a strongly anisotropic and non-linear friction-like force that reaches its maximum for electrons that counter-propagate with the laser pulse [11]. The backward motion of electrons is thus impeded by RR, more electrons and consequently ions are pushed forward leading to an enhanced clumping that improves the efficiency of the RPA mechanism. In fact, the ion spectrum with RR shows a region between about 300 and 600 MeV with a significant increase in the number of ions compared to the case without RR (Fig. 3). This picture is confirmed by both the enhancement of the longitudinal electric field E_x and the formation of denser bunches in the ion density compared to the case without RR (see Fig. 3). However, for linear polarization, hot electrons are always generated by the oscillating component of the $\mathbf{j} \times \mathbf{B}$ force. The generation of hot electrons provides a competing acceleration mechanism to RPA and ultimately leads to the generation of the fraction of ions with the highest energy. The noticeable suppression of the $\mathbf{j} \times \mathbf{B}$ heating mechanism due to the RR force therefore leads to a lower maximum cut-off energy both in the electron and in the ion spectrum (see Fig. 3).

These preliminary results for two-dimensional simulations with RR effects included suggest that, in the LP case, the trends found in one-dimensional simulations hold qualitatively even for higher dimensions. More detailed studies and quantitative comparisons between one-dimensional and two-dimensional PIC simulations are left for forthcoming publications.

4. Conclusions

We summarize our results as follows. Radiation Reaction effects on the electron dynamics in the interaction of an ultra-intense laser pulse with a thin plasma foil were studied analytically and by one-dimensional and two-dimensional PIC simulations. The details of the numerical implementation of the RR force in our PIC code were described in Ref. [11].

In one-dimensional simulations, we checked RR effects for three different intensities: $I = 2.33 \times 10^{23}$, 5.5×10^{23} and 10^{24} W cm^{-2} comparing the results for Circular and Linear Polarization of the laser pulse. For CP, we found that RR effects are not relevant even at intensity of $I = 10^{24}$ W cm^{-2} whenever the laser pulse does not break through the foil. In contrast, for LP we found that RR effects are important reducing the ion energy significantly.

In two-dimensional simulations, we found that RR reduces the $\mathbf{j} \times \mathbf{B}$ heating mechanism leading to a lower maximum cut-off energy both in the electron and in the ion spectrum. Moreover, RR increases the spatial bunching of both electrons and ions which are collected into denser clumps compared to the case without RR. This might lead to a somewhat beneficial effect with a longer and more efficient radiation pressure acceleration phase whose signature would be an ion energy spectrum peaking at an intermediate energy.
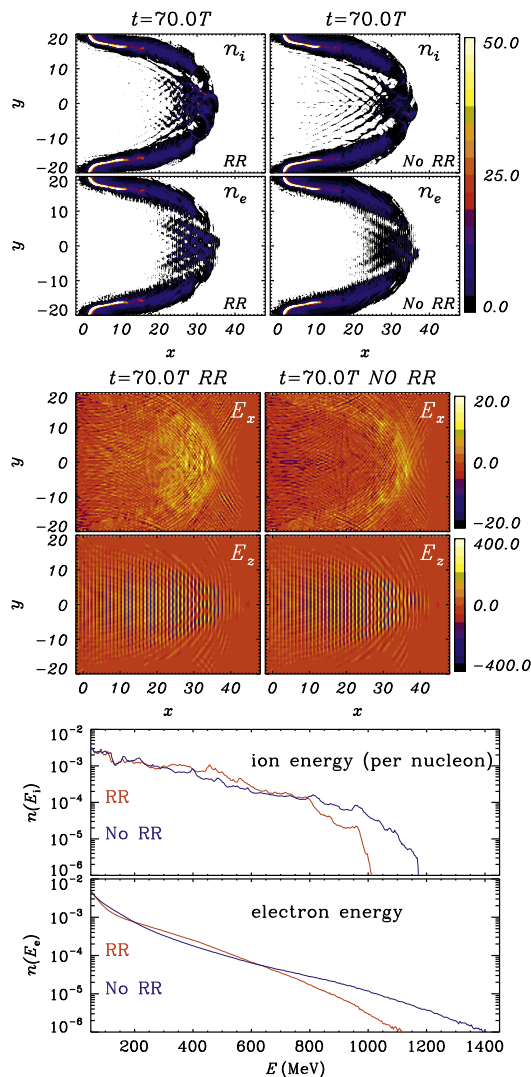
Fig. 3. Plots of the 2D PIC simulations at $t = 70$ T. The laser pulse is s-polarized with an intensity $I = 1.4 \times 10^{23}$ W cm^{-2} and the target thickness is $\ell = 0.5\lambda$. From top to bottom, ion n_i and electron n_e density distributions with (left column) and without (right column) RR, longitudinal E_x (first row) and transverse E_z (second row) electric field, ion and electron spectrum with (red) and without (blue) RR. (For interpretation of the references to color in this figure legend, the reader is referred to the web version of this article.)

A generalized relativistic kinetic equation including RR effects has been discussed and we have shown that RR leads to a contraction of the available phase space volume. This prediction is in qualitative agreement with the results of our PIC simulations where we observed both an increased spatial bunching and a significant electron cooling as discussed above.

Acknowledgment

References

[1] V. Yanovsky, V. Chvykov, G. Kalinchenko, P. Rousseau, T. Planchon, T. Matsuoka, A. Maksimchuk, J. Nees, G. Cheriaux, G. Mourou, K. Krushelnick, Opt. Express 16 (2008) 2109.
[2] C.H. Keitel, C. Szymanowski, P.L. Knight, A. Maquet, J. Phys. B 31 (1998) L75.
[3] A. Di Piazza, K.Z. Hatsagortsyan, C.H. Keitel, Phys. Rev. Lett. 102 (2009) 254802.
[4] L.D. Landau, E.M. Lifshitz, The Classical Theory of Fields, second ed., Elsevier, Oxford, 1975, p. 76.
[5] T. Esirkepov, M. Borghesi, S.V. Bulanov, G. Mourou, T. Tajima, Phys. Rev. Lett. 92 (2004) 175003.
[6] S.V. Bulanov, E.Yu. Echkina, T.Zh. Esirkepov, I.N. Inovenkov, M. Kando, F. Pegoraro, G. Korn, Phys. Rev. Lett. 104 (2010) 135003.
[7] A. Zhidkov, J. Koga, A. Sasaki, M. Uesaka, Phys. Rev Lett. 88 (2002) 185002.
[8] N. Naumova, T. Schlegel, V.T. Tikhonchuk, C. Labaune, I.V. Sokolov, G. Mourou, Phys. Rev. Lett. 102 (2009) 025002.
[9] T. Schlegel, N. Naumova, V.T. Tikhonchuk, C. Labaune, I.V. Sokolov, G. Mourou, Phys. Plasmas 16 (2009) 083103.
[10] M. Chen, A. Pukhov, T.P. Yu, Z.M. Sheng, Plasma Phys. Control Fusion 53 (2011) 014004, arXiv:0909.5144v1, doi:10.1088/0741-3335/53/1/014004.
[11] M. Tamburini, F. Pegoraro, A. Di Piazza, C.H. Keitel, A. Macchi, New J. Phys. 12 (in press) 123005, arXiv:1008.1685v2, doi:10.1088/1367-2630/12/12/123005.
[12] F. Pegoraro, S.V. Bulanov, Phys. Rev. Lett. 99 (2007) 065002.
[13] R. Hakim, A. Mangeney, J. Math. Phys. 9 (1968) 116.
[14] R. Hakim, A. Mangeney, Phys. Fluids 14 (1971) 2751.
[15] L.S. Kuz'menkov, Dokl. Akad. Nauk. Arm. SSR 241 (1978) 322;
L.S. Kuz'menkov, Sov. Phys. Dokl. 23 (1978) 469.
[16] R.D. Hazeltine, S.M. Mahajan, Phys. Rev. E 70 (2004) 046407.
[17] V.I. Berezhiani, R.D. Hazeltine, S.M. Mahajan, Phys. Rev. E 69 (2004) 056406.
[18] R.D. Hazeltine, S.M. Mahajan, Phys. Rev. E 70 (2004) 036404.
[19] V.I. Berezhiani, S.M. Mahajan, Z. Yoshida, Phys. Rev. E 78 (2008) 066403.
[20] M. Tamburini, Ph.D. Thesis, in preparation.
[21] A. Di Piazza, Lett. Math. Phys. 83 (2008) 305.
[22] A. Macchi, S. Veghini, T.V. Liseykina, F. Pegoraro, New J. Phys. (2010) 045013.
[23] A. Di Piazza, K.Z. Hatsagortsyan, C.H. Keitel, Phys. Rev. Lett. 105 (2010) 220403 in press, arXiv:1007.4914v1, doi:10.1103/105.220403.
[24] I.V. Sokolov, J.A. Nees, V.P. Yanovsky, N.M. Naumova, G.A. Mourou, Phys. Rev. E 81 (2010) 036412.

Radiation-pressure-dominant acceleration: Polarization and radiation reaction effects and energy increase in three-dimensional simulations

M. Tamburini,[1,2,*] T. V. Liseykina,[3] F. Pegoraro,[2,1] and A. Macchi[1,2]

[1]*Istituto Nazionale di Ottica, CNR, research unit "A. Gozzini," Pisa, Italy*
[2]*Dipartimento di Fisica "E. Fermi," Università di Pisa, Largo Bruno Pontecorvo 3, I-56127 Pisa, Italy*
[3]*Institut für Physik, Universität Rostock, D-18051 Rostock, Germany*

Polarization and radiation reaction (RR) effects in the interaction of a superintense laser pulse ($I > 10^{23}$ W cm^{-2}) with a thin plasma foil are investigated with three dimensional particle-in-cell (PIC) simulations. For a linearly polarized laser pulse, strong anisotropies such as the formation of two high-energy clumps in the plane perpendicular to the propagation direction and significant radiation reactions effects are observed. On the contrary, neither anisotropies nor significant radiation reaction effects are observed using circularly polarized laser pulses, for which the maximum ion energy exceeds the value obtained in simulations of lower dimensionality. The dynamical bending of the initially flat plasma foil leads to the self-formation of a quasiparabolic shell that focuses the impinging laser pulse strongly increasing its energy and momentum densities.

I. INTRODUCTION

The radiation pressure generated by ultraintense laser pulses may drive strong acceleration of dense matter, as experimentally shown in various regimes [1]. Thus, radiation pressure may be an effective mechanism for the generation of high-energy ions, especially in the regime of extremely high intensities and relativistic ion energies as foreseen with the ELI project. In the case of solid-density thin foil targets, pioneering particle-in-cell (PIC) simulations showed that at intensities exceeding 10^{23} W cm^{-2} and for linear polarization of the laser pulse radiation pressure dominates the acceleration yielding linear scaling with the laser pulse intensity, high efficiency and quasimonoenergetic features in the ion energy spectrum [2]. More recent two-dimensional (2D) simulations for a small disk target suggested a potentially "unlimited" energy gain for the fraction of ions that get phase locked with the laser pulse [3].

The above-mentioned studies showed that the radiation pressure dominant acceleration (RPDA) regime is very appealing as a route to the generation of relativistic ions, but they leave several theoretical issues open. First, transverse instabilities [4] and multidimensional effects may play a crucial role as shown by 2D simulations [3]. Second, the use of circular polarization (CP) instead of linear polarization (LP) quenches the generation of high-energy electrons [5], allowing radiation pressure to dominate even at intensities below 10^{23} W cm^{-2} and leading to efficient acceleration of ultrathin foils [6]; it has not been shown yet whether the use of CP is advantageous also at ultrahigh intensities ($I > 10^{23}$ W cm^{-2}), i.e., when the radiation pressure generated by the laser pulse becomes the dominant mechanism of acceleration both for CP and LP. Finally, it has been shown by one-dimensional (1D) simulations that radiation reaction (RR) effects may significantly affect the dynamics of radiation pressure acceleration both for

thick [7] and thin targets [8,9], and also depend strongly on the polarization [8]. All of these phenomena may be affected by the dimensionality of the problem, and a fully three-dimensional (3D) approach is ultimately needed because, e.g., in 2D simulations and for LP the laser-plasma coupling is different for *S* and *P* polarization (i.e., for the electric field of the laser pulse either perpendicular or parallel to the simulation plane, respectively) and the constraint of the conservation of angular momentum carried by CP pulses holds in 3D only.

In this paper, we address the role of polarization and RR effects in the RPDA regime using fully 3D PIC simulations. To our knowledge, these are the first 3D simulations of ion acceleration in the RPDA regime with RR effects included and among the largest and most accurate 3D simulations reported so far. Our results show that even in the RPDA regime CP leads to higher ion energies and better collimation than LP, for which an anisotropic ion distribution is observed. It is also found that the bending of the foil leads to a self-generated parabolic shell that focuses the impinging pulse down to an almost λ^3 volume and that the energy density at the focus largely exceeds the initial peak energy density. Compared to 2D simulations with analogous parameters, the pulse focusing effect is remarkably enhanced and the cut-off energy of ions is increased. Radiation reaction effects on the ion spectrum are found to be negligible for CP but quite relevant for LP where they increase the energy cutoff.

II. MODELING AND SIMULATION SET-UP

Our approach is based on the numerical solution of kinetic equations for the phase-space distributions of electrons and ions, where RR is included in the motion of electrons via the Landau-Lifshitz (LL) force [10]. Details of our RR modeling and numerical implementation in a PIC code are given in Refs. [8,11]. The effective equation of motion for electrons, after neglecting terms that are negligible in the classical limit

[8], is

$$\frac{d\mathbf{p}}{dt} = -e\left(\mathbf{E} + \frac{\mathbf{v}}{c} \times \mathbf{B}\right) + \mathbf{f}_R,$$

$$\mathbf{f}_R = \frac{2r_c^2}{3}\left\{-\gamma^2\left[\left(\mathbf{E} + \frac{\mathbf{v}}{c} \times \mathbf{B}\right)^2 - \left(\frac{\mathbf{v}}{c} \cdot \mathbf{E}\right)^2\right]\frac{\mathbf{v}}{c}\right.$$

$$\left. + \left[\left(\mathbf{E} + \frac{\mathbf{v}}{c} \times \mathbf{B}\right) \times \mathbf{B} + \left(\frac{\mathbf{v}}{c} \cdot \mathbf{E}\right)\mathbf{E}\right]\right\}, \qquad (1)$$

where $r_c = e^2/m_e c^2$. The RR force contribution is important for ultrarelativistic electrons and it is usually dominated by the first term, while the second term ensures the on-shell condition [8]. Notice that the dominant term has almost the same form also in different approaches to RR modeling [7,9]. For a plane wave propagating along the x axis, the RR force is maximum or zero for counterpropagating ($v_x/c \to -1$) or copropagating ($v_x/c \to +1$) electrons, respectively.

In order to clarify the new qualitative features due to RR effects, we recall that the phase-space volume element J evolves according to $dJ/dt = J\nabla_\mathbf{p} \cdot \mathbf{f}_R$. It has been shown [11] that $\nabla_\mathbf{p} \cdot \mathbf{f}_R \leqslant 0$ and, therefore, the RR force leads to a *contraction* of the available phase-space volume. The physical interpretation of this property is that the RR force acts as a cooling mechanism for the system accounting for the emission of high-energy photons. These photons are assumed to escape from the plasma freely, carrying away energy and entropy [11].

We present a total of four 3D simulations each with the same physical and numerical parameters but different polarization, with and without RR effects. In these simulations, the laser field amplitude has a $\sin^2$-function longitudinal profile with 9λ full width at half-maximum (FWHM) (where $\lambda = 0.8\ \mu$m is the laser wavelength) while the transverse radial profile is Gaussian with 10λ FWHM and the laser pulse front reaches the edge of the plasma foil at $t = 0$. The peak intensity at the focus is $I = 1.7 \times 10^{23}\ \mathrm{W\,cm^{-2}}$, which corresponds to a normalized amplitude $a_0 = 280$ for LP and $a_0 = 198$ for CP. The target is a plasma foil of electrons and protons with uniform initial density $n_0 = 64n_c$ (where $n_c = \pi m_e c^2/e^2\lambda^2$ is the critical density), thickness $\ell = 1\lambda$, and initially located in the region $10\lambda \leqslant x \leqslant 11\lambda$. The density $n_0 \simeq 1.1 \times 10^{23}\ \mathrm{cm^{-3}}$ is slightly lower than that of solid targets but the areal density $n_0\ell$ has fully realistic values. Moreover, laser pulses of ultrahigh contrast are now available [[12], and references therein] to avoid early plasma formation effects by the prepulse, thus, a thin plasma with steplike profile is not an unrealistic assumption.

The simulation grid is $1320 \times 896 \times 896$ and the spatial step is $\lambda/44$ for each direction. The time step is $T/100$ where $T = \lambda/c = 2.67$ fs is the laser period. We use 216 particles per cell for each species and the total number of particles is 1.526×10^{10}. The runs were performed using 1024 processors each one equipped with 1.7 GB of memory of the IBM-SP6 cluster at the CINECA supercomputing facility in Bologna, Italy.

III. RESULTS AND DISCUSSION

Figure 1 shows the ion and the electron 3D spatial distributions [13] at $t = 20T$ for the LP case without (a) and with (b) RR and for the CP case without (c) and with (d) RR. The color (grayscale) corresponds to the range in kinetic energy. For CP, the ion spatial distribution follows the spatial intensity profile of the initial laser pulse, has rotational symmetry around the central axis, and a distribution in energy monotonically decreasing with increasing radial distance. The most energetic ions are located near the axis. The number of ions having energy $\mathcal{E} \geqslant 1100$ MeV and $\mathcal{E} \geqslant 800$ MeV are 2.3×10^{10} and 9.4×10^{10}, respectively. The electron spatial distribution has a helicoidal shape with step λ; Figs. 1(c),
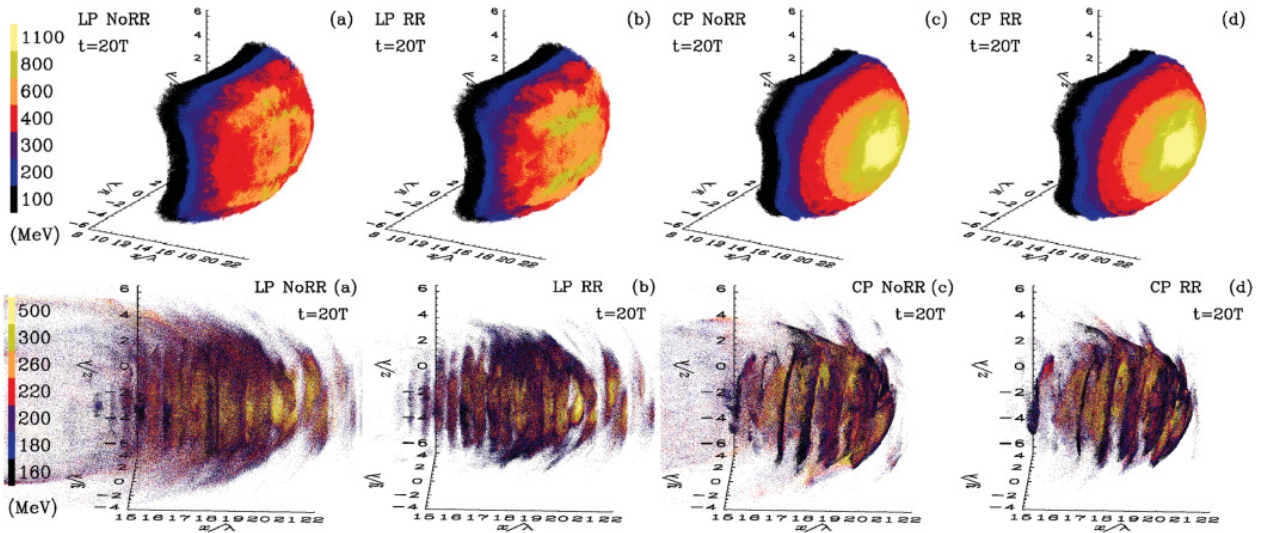

FIG. 1. (Color online) Spatial distributions of ions (upper row) and electrons (lower row) at $t = 20\ \mathrm{T}$ and in the region ($|y|,|z|) \leqslant 5.7\lambda$, for LP without (a) and with (b) RR and for CP without (c) and with (d) RR. Ions and electrons are divided into seven populations according to their kinetic energy, with the color bar (grayscale) reporting the lower bound of the energy interval. In the LP case [(a) and (b)], the polarization is along the y axis.
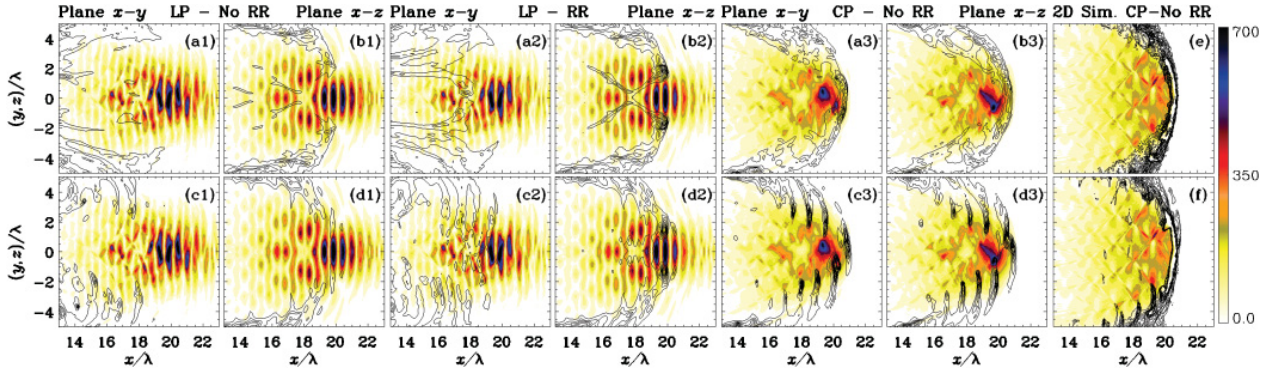
FIG. 2. (Color online) (x,y) and (x,z) sections of the 3D simulations of the laser pulse-foil interaction [(a1)–(a3), (b1)–(b3), (c1)–(c3), and (d1)–(d3)] and 2D simulations for CP and without RR with the same parameters as the 3D simulations [(e) and (f)], all at $t = 20T$. Each frame reports the color (grayscale) contours of $\sqrt{\mathbf{E}^2 + \mathbf{B}^2}$ (normalized units) in the xy plane at $z = 0$ [(a1)–(a3) and (c1)–(a3)], in the xz plane at $y = 0$ [(b1)–(b3) and (d1)–(d3)] and in the simulation plane [(e) and (f)] in the 2D case. Line contours of the ion and electron densities are superimposed in the upper and lower frames, respectively. The CP case with RR is almost identical to the CP case without RR and it is not reported.

and 1(d). Radiation reaction effects play a minor role for CP, affecting only a small fraction of ultrarelativistic electrons [mostly removing fast electrons *behind* the foil with almost no influence on the ion distribution as seen by comparing Figs. 1(c) and 1(d)].

The (x,y) and (x,z) sections of the total electromagnetic energy density and of the ion and electron densities for the CP case in Fig. 2 [(a3)–(b3) and (c3)–(d3)] evince a self-generated parabolic shell wrapping the laser pulse and focusing it up to nearly a λ^3 volume, so both the energy and the momentum densities at the focus reach values more than 8 times their peak value in the initial laser pulse. This effect is much weaker in 2D simulations with the same parameters as shown in Figs. 2(e)–2(f). Along the axis, the peak value and width of the ion density profile are $\simeq 10 n_c$ and $\simeq 0.5\lambda$, showing a strong rarefaction due to the transverse expansion, potentially leading to enhanced acceleration as described in Ref. [3].

For LP, the peak ion energy is lower than for CP, the ion distribution is anisotropic, and RR effects are much stronger. The most energetic ions (800–1100 MeV) are grouped into two off-axis clumps lengthened and aligned along the polarization direction, and their number is increased in the case with RR as seen by the comparison of Figs. 1(a) and 1(b) and also in Figs. 2 [(a1),(a2) and (b1),(b2)] where sections of the ion density in the (x,y) and (x,z) planes are shown. The contours of the electromagnetic (EM) energy density in Figs. 2 [(a1),(a2) and (b1),(b2)] show that near the axis most of the laser pulse has been transmitted through the target. The increased bunching and higher density observed in the case with RR may be related to the higher ion energies since the local increase of the density and, therefore, of the reflectivity leads to a longer and more efficient RPDA phase. This is consistent with observing in Figs. 2(b1) and 2(b2) that the EM energy density is higher behind the two high-density clumps, which correspond to the most energetic ions and are similar to the ion lobes observed in Ref. [14] at lower intensity and in a regime of strong pulse penetration through the foil. The pulse focusing effect by the self-generated parabola is present also in the LP case although weaker than in the CP case and presumably reduced as the laser pulse breaks through the parabolic shell.

The differences between CP and LP in the acceleration dynamics are well explained, for planar geometry and non-relativistic ions, by the absence of the oscillating component of the $\mathbf{J} \times \mathbf{B}$ force for CP [5], which maximizes the effect of the radiation pressure strongly suppressing the electron heating. The absence of the oscillating component of the $\mathbf{J} \times \mathbf{B}$ force also accounts for the very different RR effects. For CP, a steady push of the foil and weak pulse penetration are observed and most of the electrons move coherently with the foil and in the same direction as the laser pulse so the RR force becomes very small in accordance with Eq. (1) since the electrons effectively copropagate with the laser pulse (see also Refs. [2,8]). For LP, the $\mathbf{J} \times \mathbf{B}$-driven oscillations allow electrons to collide with the counterpropagating laser pulse twice per cycle producing temporal maxima in the RR force in agreement with Eq. (1). Our present results indicate that CP leads to more efficient acceleration, producing higher energy and collimated ion beams, and making RR effects negligible also in the 3D case, accounting for target bending and pulse focusing effects, and for relativistic ions.

Large-scale 3D PIC simulations are limited by the size and availability of computational resources both in the number of runs that may be performed and in the achievable numerical resolution. This last issue may raise doubts on the accuracy of 3D results. To gain confidence on this side, as well as to compare the 3D results to those obtained in lower dimensionality, we performed 2D simulations both with numerical parameters similar to those of 3D runs and with higher resolution. The effect of increasing resolution and particle number on the ion spectra in 2D simulations is shown in Fig. 3 where 2D results are reported for the three different polarization cases (CP, LP-S, and LP-P) and compared with the 3D results for both LP and CP. The spectra are normalized to unity both in the 2D and 3D cases. In the CP case both numerical and RR effects on the spectrum are smaller while in the P-polarization case these effects are larger. Changing the spatial resolution from $\lambda/44$ to $\lambda/80$ and increasing the number of particles-per-cell for each species from 256 to 625 shifts the energy cutoff by $\sim 2\%$ in the CP case and by $\sim 15\%$ ($\sim 20\%$) in the P-polarization case without RR (with RR). The stronger
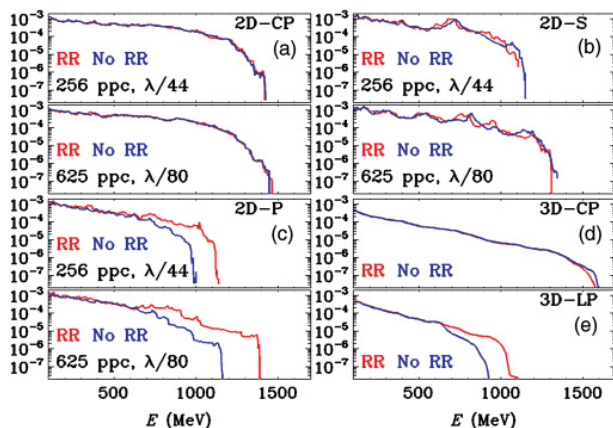
FIG. 3. (Color online) Ion spectra from 2D [(a)–(c) and 3D [(d)–(e)] simulations with same physical parameters, all at $t = 20T$. The 2D spectra are reported for circular [CP, panel (a)] and linear (LP) "S" [panel (b)] and "P" [panel (c)] polarization cases. In each plot, the blue (dark gray) and red (light gray) curves correspond to simulations without and with radiation reaction (RR) effects, respectively. In the upper plots of panels (a)–(c) the numerical resolution (number of particles per cell and of points per wavelength) is similar to those of the 3D simulations in panels (d) and (e), while in the lower plots the results for higher resolution are shown.

effect of the inclusion of RR for the higher resolution case may be explained by noticing that RR mostly affects the highest energy electrons [8], which are located in the high-energy tail of the distribution function that needs a very large number of particles to be resolved properly. Nevertheless, the limited resolution does not qualitatively affect prominent features in ion spectra, such as the higher ion energy for CP and the relevance of RR effects for LP only, leading for this latter case to an *higher* energy of ions with respect to the case of no RR as observed in 1D simulations [8]. As a novel feature of 2D simulations, P polarization leads to much stronger RR effects than S polarization. In fact, for P polarization the electric field can drag a large fraction of electrons out in vacuum and toward the laser pulse as the plasma foil begins to bend, enhancing the RR effect.

For CP, the maximum ion energy is higher in the 3D case ($\simeq 1600$ MeV) than in the 2D case ($\simeq 1400$ MeV). In turn, the latter value is higher than what found in 1D, plane-wave simulations, for which we find a broad spectral peak which at $t = 20$ extends up to $\simeq 1100$ MeV and is centered around a value of $\simeq 870$ MeV. The latter value corresponds to the energy $\mathcal{E}_{LS} = (\gamma - 1)m_p c^2$, where $\gamma = 1/\sqrt{1 - \beta^2}$ and β are obtained from the "light sail" model [[15], and references therein] by numerically integrating the 1D equations of motion

for the foil

$$\frac{d\gamma\beta}{dt} = \frac{2I(t - X/c)}{n_0 \ell m_p c^2}\left(\frac{1 - \beta}{1 + \beta}\right), \qquad \frac{dX}{dt} = \beta c. \quad (2)$$

From the 1D modeling we also evaluate a final ion energy for the spectral peak of $\simeq 1700$ MeV that is reached at $t \simeq 90$. The 3D simulations could not be extended up to the end of the acceleration stage (estimated up to $\sim 90T$ in 1D simulations) but, since the efficiency of RPDA increases with the foil velocity, the energy gain is expected to be even larger at the later times (provided that 3D effects do not cause an early stop of the acceleration). Hence, the comparison at $t = 20$ shows an overall *increase* of the ion energy in the 3D case with respect to 1D and 2D cases. Part of the energy enhancement can be attributed to the reduction of the areal density $n_0\ell$ due to the transverse expansion, as was noticed in 2D simulations supporting the model of "unlimited" acceleration [3]. An additional contribution may come from the above-described focusing of the laser pulse by the deformed foil, which is stronger in 3D geometry. This latter effect was absent in the simulations of Ref. [3] because a target with a radius smaller than the pulse waist was considered.

IV. CONCLUSIONS

In conclusion, with three-dimensional particle-in-cell simulations of ultraintense laser interaction with solid-density foils we showed that circular polarization improves ion acceleration also in the radiation pressure dominant regime, confirming and extending previous results obtained for lower intensity and/or lower dimensionality. In detail, circular polarization leads to the highest ion energies, to a symmetrical and collimated distribution, and to negligible effects of radiation reaction. In addition, the maximum energy of ions in 3D is larger than observed in corresponding 1D and 2D simulations. This enhancement is attributed both to the density decrease in the target, as noticed in the "unlimited acceleration" model [3], and to the strong focusing of the laser pulse by the parabolically deformed foil. In the linear polarization case, lower maximum energies are achieved, the most energetic ions are grouped anisotropically into two off-axis clumps and radiation reaction effects significantly affect the energy spectrum. We expect these findings to be of relevance for the design of future experiments on laser acceleration of ions up to relativistic (GeV) energy.

[1] S. Kar *et al.*, Phys. Rev. Lett. **100**, 225004 (2008); K. U. Akli *et al.*, *ibid.* **100**, 165002 (2008); A. Henig *et al.*, *ibid.* **103**, 245003 (2009); C. A. J. Palmer *et al.*, *ibid.* **106**, 014801 (2011).

[2] T. Esirkepov, M. Borghesi, S. V. Bulanov, G. Mourou, and T. Tajima, Phys. Rev. Lett. **92**, 175003 (2004).

[3] S. V. Bulanov, E. Y. Echkina, T. Z. Esirkepov, I. N. Inovenkov, M. Kando, F. Pegoraro, and G. Korn, Phys. Rev. Lett. **104**, 135003 (2010)

[4] F. Pegoraro and S. V. Bulanov, Phys. Rev. Lett. **99**, 065002 (2007).

[5] A. Macchi, F. Cattani, T. V. Liseykina, and F. Cornolti, Phys. Rev. Lett. **94**, 165003 (2005).

[6] X. Zhang, B. Shen, X. Li, Z. Jin, and F. Wang, Phys. Plasmas **14**, 073101 (2007); A. P. L. Robinson, M. Zepf, S. Kar, R. G. Evans, and C. Bellei, New J. Phys. **10**, 013021 (2008); O. Klimo, J. Psikal, J. Limpouch, and V. T. Tikhonchuk, Phys. Rev. ST Accel. Beams **11**, 031301 (2008).

[7] N. Naumova, T. Schlegel, V. T. Tikhonchuk, C. Labaune, I. V. Sokolov, and G. Mourou, Phys. Rev. Lett. **102**, 025002 (2009).

[8] M. Tamburini, F. Pegoraro, A. D. Piazza, C. H. Keitel, and A. Macchi, New J. Phys. **12**, 123005 (2010).

[9] M. Chen, A. Pukhov, T.-P. Yu, and Z.-M. Sheng, Plasma Phys. Contr. Fusion **53**, 014004 (2011).

[10] L. D. Landau and E. M. Lifshitz, *The Classical Theory of Fields*, 2nd ed. (Elsevier, Oxford, 1975).

[11] M. Tamburini, F. Pegoraro, A. D. Piazza, C. Keitel, T. Liseykina, and A. Macchi, Nucl. Inst. Methods A **653**, 181 (2011).

[12] C. Thaury *et al.*, Nat. Phys. **3**, 424 (2007); C. Rödel, M. Heyer, M. Behmke, M. Kübel, O. Jäckel, W. Ziegler, D. Ehrt, M. Kaluza, and G. Paulus, Appl. Phys. B: Lasers Opt. **103**, 295 (2011).

[13] See Supplemental Material at http://link.aps.org/supplemental/ 10.1103/PhysRevE.85.016407 for high-quality pictures of the three-dimensional electron and ion spatial distributions reported in Fig. 1.

[14] L. Yin, B. J. Albright, K. J. Bowers, D. Jung, J. C. Fernández, and B. M. Hegelich, Phys. Rev. Lett. **107**, 045003 (2011).

[15] A. Macchi, S. Veghini, T. V. Liseykina, and F. Pegoraro, New J. Phys. **12**, 045013 (2010).

New Journal of Physics

The open access journal at the forefront of physics

CrossMark

FAST TRACK COMMUNICATION

Inverse Faraday effect driven by radiation friction

T V Liseykina[1,5], S V Popruzhenko[2] and A Macchi[3,4]

1   Institute of Physics, University of Rostock, D-18051 Rostock, Germany
2   National Research Nuclear University, Moscow Engineering Physics Institute, Kashirskoe Shosse 31, 115409, Moscow, Russia
3   CNR, National Institute of Optics (INO), Adriano Gozzini research unit, Pisa, Italy
4   Enrico Fermi Department of Physics, University of Pisa, largo Bruno Pontecorvo 3, I-56127 Pisa, Italy
5   On leave from Institute of Computational Technologies, SD RAS, 630090 Novosibirsk, Russia.

E-mail: andrea.macchi@ino.it

Abstract

A collective, macroscopic signature to detect radiation friction in laser–plasma experiments is proposed. In the interaction of superintense circularly polarized laser pulses with high density targets, the effective dissipation due to radiative losses allows the absorption of electromagnetic angular momentum, which in turn leads to the generation of a quasistatic axial magnetic field. This peculiar 'inverse Faraday effect' is investigated by analytical modeling and three-dimensional simulations, showing that multi-gigagauss magnetic fields may be generated at laser intensities $>10^{23}$ W cm^{-2}.

1. Introduction

The development of ultrashort pulse lasers with petawatt power has opened new perspectives for the study of high field physics and ultra-relativistic plasmas [1, 2]. In this context, the longstanding problem of radiation friction (RF) or radiation reaction has attracted new interest. RF arises from the back-action on the electron of the electromagnetic (EM) field generated by the electron itself and plays a dominant role in the dynamics of ultra-relativistic electrons in strong fields. A considerable amount of work has been devoted both to revisiting the RF theory [3, 4] and to its implementation in laser–plasma simulations [5–9], as well as to the study of radiation-dominated plasmas in high energy astrophysics, see e.g. [10–12].

While RF is still an open matter both for classical and quantum electrodynamics [2], RF models have not been discriminated experimentally yet. This circumstance led to several proposals of devoted experiments providing clear signatures of RF, e.g. in nonlinear Thomson scattering [13–18], Compton scattering [19], modification of Raman spectra [20], electron acceleration in vacuum [21–23], radiative trapping [24–26] or γ-ray emission from plasma targets [27, 28]. Most of these studies are based on single particle effects, and RF signatures are found in modifications of observables such as emission patterns and spectra when RF is included in the modeling. Detecting such modifications may require substantial improvements in reducing typical uncertainties in laser–plasma experiments. At very high intensities, RF losses may affect the collective dynamics, e.g. by modifying the spectra of accelerated ions in the radiation pressure dominated regime [29, 30, and references therein] or the dynamics of magnetic field generation by the filamentation instability in laser-generated colliding pair plasmas [31]. However, also in this case the modifications are quantitative, rather than qualitative, and relatively modest so that it may be difficult to discriminate RF effects.

Instead, in this paper we identify a collective, macroscopic effect induced by RF, namely the generation of multi-gigagauss, quasi-steady, axial magnetic fields in the interaction of a circularly polarized (CP) laser pulse with a dense plasma. This is a peculiar form of the inverse Faraday effect (IFE) [32–35] and may be more accessible experimentally than single-particle effects. In fact, the IFE has been previously studied in different regimes of laser–plasma interactions [36–42, and references therein]. By using three-dimensional (3D) particle-in-cell (PIC) simulations, we find that at laser intensities foreseeable with next generation facilities producing multi-petawatt [43] or even exawatt pulses [44, 45], the magnetic field created by the RF-driven IFE in dense

plasma targets reaches multi-gigagauss values with a direction dependent on the laser polarization, which confirms its origin from the 'photon spin'. The magnetic field is slowly varying on times longer than the pulse duration and may be detected via optical polarimetry techniques [46–50]. This would provide an unambiguous signature of the dominance of RF effects, since the axial magnetic field disappears in the absence of RF. The effect might also be exploited to create strongly magnetized laboratory plasmas in so far unexplored regimes (see e.g. [51]).

2. Role and modeling of radiative losses

The IFE is due to absorption of EM angular momentum[6], which in general is *not* proportional to energy absorption. As an example of direct relevance to the present work, let us consider a mirror boosted by the radiation pressure of a CP (with positive helicity, for definiteness) laser pulse. From a quantum point of view, the laser pulse of frequency ω propagating along $\hat{\mathbf{x}}$ corresponds to N incident photons with total energy $N\hbar\omega$ and angular momentum $N\hbar\,\hat{\mathbf{x}}$. If the mirror is perfect, N is conserved in any frame. If the mirror moves along $\hat{\mathbf{x}}$, the reflected photons are red-shifted leading to EM energy conversion into mechanical energy (up to 100% if the mirror velocity $\sim c$) but there is no spin flip for the reflected photons, hence no absorption of angular momentum. However, if the electrons in the mirror emit high-frequency photons, a greater number of incident low-frequency photons must be absorbed with their angular momentum. From a classical point of view, absorption of angular momentum requires some dissipation mechanism [42] which, in our example, implies a non-vanishing absorption in the rest frame of the mirror.
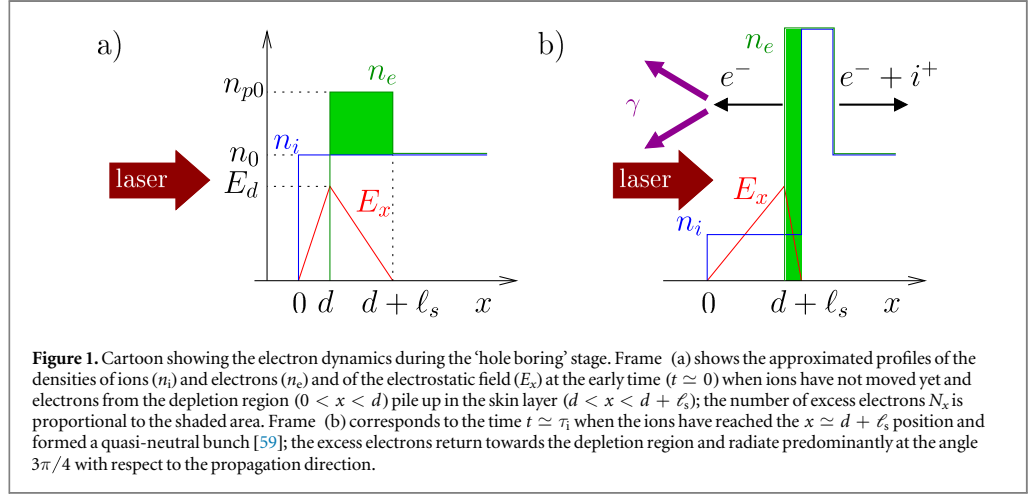
In the case here investigated, effective dissipation is provided by the RF force which makes the electron dynamics consistent with the radiative losses. In order to demonstrate IFE induced by RF, we consider a regime of ultra-high laser intensity $I_L > 10^{23}$ W cm^{-2} and thick plasma targets (i.e. with thickness much greater than the evanescence length of the laser field) where the radiative energy loss is a significant fraction of the laser energy as shown by simulations with RF included [29, 30, 54–56]. We use a simple model to account for such losses and provide a scaling law with the laser intensity. The power radiated by an electron moving with velocity v_x along the propagation axis of a CP pulse of amplitude $E_L = (m_e \omega c/e) a_0 \equiv B_0 a_0$ (with ω the laser frequency) is

$$P_{\mathrm{rad}} = \frac{2e^2\omega^2\gamma^2a_0^2}{3c}\left(1 - \frac{v_x}{c}\right)^2. \tag{1}$$

The classical RF force on an electron is defined in order that the work done per unit time equals P_{rad}. In our simulations the Landau–Lifshitz (LL) expression for the RF force has been used [57]. Consistently with equation (1) the LL force in a plane wave vanishes for $v_x = c$, and has a maximum for $v_x = -c$. The spectrum of the emitted radiation peaks at frequencies $\omega_{\mathrm{rad}} \simeq \gamma^3\omega$, with γ the relativistic factor of electrons which can be estimated as $\gamma \simeq a_0\omega$. At such frequencies the radiation from the plasma is incoherent (see also the discussion in section 3), thus the total radiated power by N comoving electrons will be NP_{rad}. For thin targets accelerated by the CP laser pulse ('light sail' regime), all electrons move with the foil at $v_x \simeq c$, and there is no high-frequency oscillation driven by the $\mathbf{v} \times \mathbf{B}$ force. Thus the radiation is strongly suppressed by the factor $(1 - v_x/c)^2 \ll 1$, as observed in simulations [7, 58]. In contrast, RF losses become much larger for thick targets [29, 30, 54] ('hole boring' regime) because the acceleration of the plasma surface has a pulsed nature [55, 59, 60] with a dense bunch of electrons being periodically dragged towards the incident laser pulse, i.e. in a counterpropagating configuration ($v_x < 0$).

In order to estimate the number of radiating electrons per unit surface we consider the dynamic picture of hole boring [59, 61]. As illustrated in figure 1, at the surface of the plasma the radiation pressure generates a positively charged layer of electron depletion (of thickness d) and a related pile-up of electrons in the skin layer (of thickness ℓ_s), i.e. the evanescent laser field region. Ions are accelerated in the skin layer leaving it at a time τ_i at which an ion bunch neutralized by accompanying electrons is formed. At this instant, the equilibrium between ponderomotive and electrostatic forces is lost and the excess electrons in the skin layer will quickly return back towards the charge depletion region. The number per unit surface of returning electrons is $N_x = (n_{p0} - n_0)\ell_s$ where n_{p0} is the electron density in the skin layer at the beginning of the acceleration stage. Using the model of [59, 61], N_x may be estimated from the balance of electrostatic and radiation pressures: $eE_d n_{p0}\ell_s/2 = 2I_L/c$, where $E_d = 4\pi e n_0 d$ is the peak field in the depletion region, and $n_{p0}\ell_s = n_0(d + \ell_s)$ because of charge conservation. Eliminating d from these equations yields for the density compression ratio in the skin layer

---

[6] Here we consider only the absorption of intrinsic angular momentum or photon 'spin'. For studies on orbital angular momentum absorption and IFE in laser–plasma interaction see, e.g., [52, 53].

Figure 1. Cartoon showing the electron dynamics during the 'hole boring' stage. Frame (a) shows the approximated profiles of the densities of ions (n_i) and electrons (n_e) and of the electrostatic field (E_x) at the early time ($t \simeq 0$) when ions have not moved yet and electrons from the depletion region ($0 < x < d$) pile up in the skin layer ($d < x < d + \ell_s$); the number of excess electrons N_x is proportional to the shaded area. Frame (b) corresponds to the time $t \simeq \tau_i$ when the ions have reached the $x \simeq d + \ell_s$ position and formed a quasi-neutral bunch [59]; the excess electrons return towards the depletion region and radiate predominantly at the angle $3\pi/4$ with respect to the propagation direction.

$$\frac{n_{p0}}{n_0} = \frac{1}{2} + \left(\frac{1}{4} + 4\left(\frac{n_c}{n_0}\frac{c}{\omega\ell_s}a_0\right)^2\right)^{1/2}, \tag{2}$$

where $n_c = m_e\omega^2/(4\pi e^2)$. In our conditions the laser field is evanescent, thus $(c/\omega\ell_s) > 1$, and we consider a range of parameters such that $a_0 n_c/n_0 > 1$. We thus obtain $n_{p0}/n_0 \approx 2a_0 (n_c/n_0)^{1/2} \gg 1$, in agreement with a detailed theory of nonlinear wave propagation (see e.g. [62]) and numerical simulations. Thus, by writing $I_L = m_e c\omega^2 a_0^2/(4\pi r_c)$ (where $r_c = e^2/m_e c^2$) we obtain $N_x \simeq a_0/r_c\lambda$ (where $\lambda = 2\pi c/\omega$ is the laser wavelength), independently on the initial density[7].

The total radiated intensity is $I_{rad} = P_{rad}N_x$. In order to compare the radiated energy with the laser pulse energy we take into account that the radiation is emitted as bursts corresponding to the periodic return of electrons towards the laser, i.e. for a fraction $f_\tau \simeq \tau_e/(\tau_e + \tau_i)$ of the interaction stage where τ_e is the time interval during which the electrons move backwards. Analysis of laser piston oscillations in [55] suggests that $\tau_e \simeq \tau_i$ so we take $f_\tau \simeq 1/2$ for our rough estimate. Since $(1 - v_x/c)^2 \gtrsim 1$ for returning electrons, we obtain for the fraction of radiated energy to the laser pulse energy

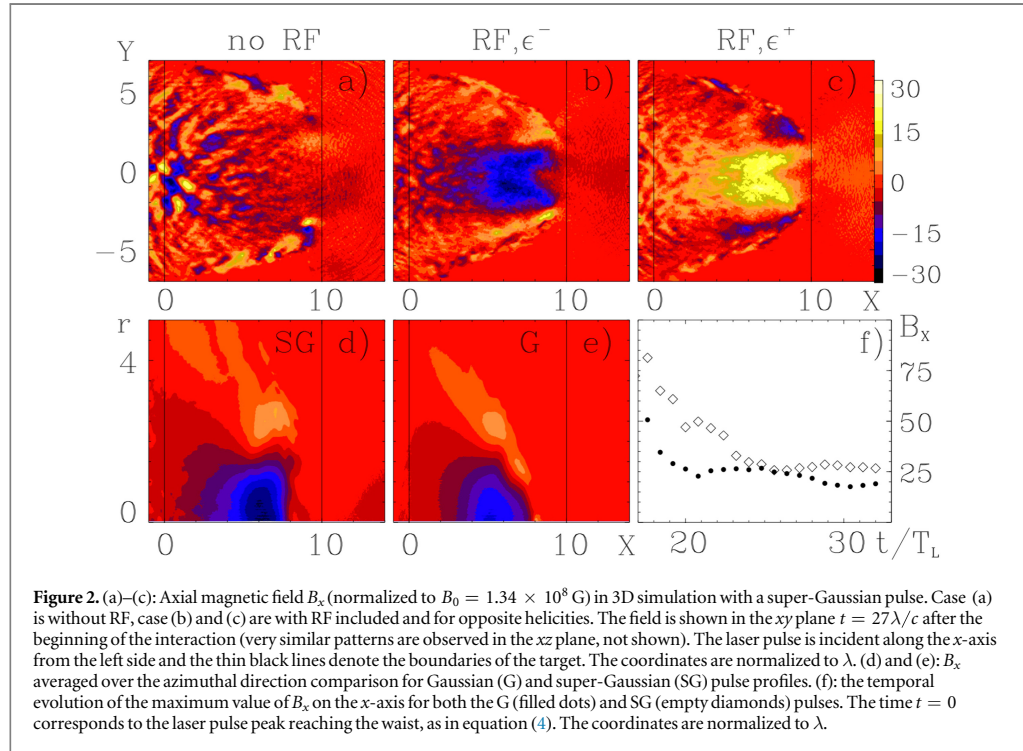$$\eta_{rad} \simeq \frac{4\pi}{3}\frac{r_c}{\lambda}a_0\gamma^2. \tag{3}$$

If the energy of electrons is mainly due to the motion in the laser field, then $\gamma \simeq (1 + a_0^2)^{1/2} \simeq a_0$ for $a_0 \gg 1$ and $\eta_{rad} \propto a_0^3$. For $\lambda = 0.8$ μm, $\eta_{rad} \sim 1$ for $a_0 \sim 400$, corresponding to $I_L \sim 7 \times 10^{23}$ W cm^{-2}. This order-of-magnitude estimate implies that for such intensities a significant part of the laser energy is lost as radiation, strongly affecting the interaction dynamics. A more precise estimate would require to account both for the energy depletion of the laser and for the trajectory modification of the electrons due to the RF force.

3. Simulation results

A 3D approach is essential to model the phenomena of angular momentum absorption and magnetic field generation, thus we rely on massively parallel PIC simulations in which RF is implemented following the approach described in [7], based on the LL equation (see [9] for a benchmark with other approaches). We remark that the inclusion of the radiation loss as a dissipative process via the RF force requires the following assumptions: (i) the dominant frequencies in the escaping radiation are much higher than the highest frequency that can be resolved on the numerical grid, (ii) the radiation at such frequencies is incoherent, (iii) the plasma is transparent to such frequencies. Since, as also stated above, for radiation in the field of a plane CP wave of ultrarelativistic intensity the radiation spectrum peaks at frequencies of the order of $\omega_{rad} \approx a_0^3\omega$, all the above assumptions are well-satisfied in our conditions.

The laser pulse is initialized in a way that at the waist plane $x = 0$ (coincident with the target boundary) the normalized amplitude of the vector potential $\mathbf{a} = e\mathbf{A}/m_e c^2$ would be

---

[7] The scaling $N_x \propto a_0/\lambda$ is a consequence of the balance between electrostatic and radiation pressures before electrons return towards the laser pulse. In fact, since the electron density of the compressed skin layer $n_{p0} \gg n_0$ (the initial electron density), the excess number N_x of electrons is almost proportional to the charge-displacement field E_x. Since the electrostatic pressure $P_{es} \propto E_x^2$, by posing $P_{es} = P_{rad} \propto I_L/c \propto a_0^2/\lambda^2$ we obtain $N_x \propto E_x \propto a_0/\lambda$.

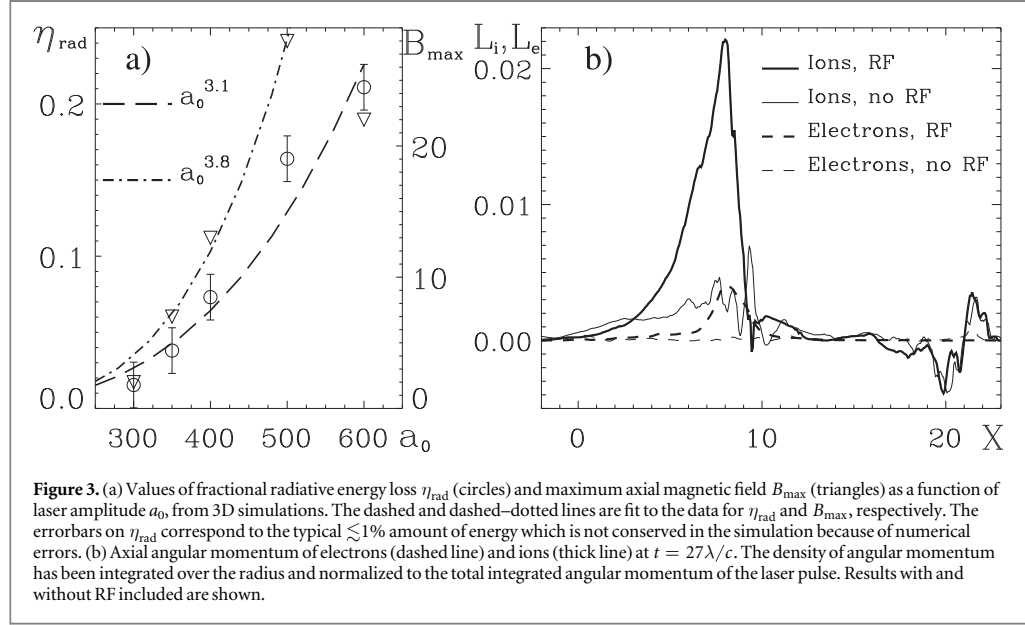**Figure 2.** (a)–(c): Axial magnetic field B_x (normalized to $B_0 = 1.34 \times 10^8$ G) in 3D simulation with a super-Gaussian pulse. Case (a) is without RF, case (b) and (c) are with RF included and for opposite helicities. The field is shown in the *xy* plane $t = 27\lambda/c$ after the beginning of the interaction (very similar patterns are observed in the *xz* plane, not shown). The laser pulse is incident along the *x*-axis from the left side and the thin black lines denote the boundaries of the target. The coordinates are normalized to λ. (d) and (e): B_x averaged over the azimuthal direction comparison for Gaussian (G) and super-Gaussian (SG) pulse profiles. (f): the temporal evolution of the maximum value of B_x on the *x*-axis for both the G (filled dots) and SG (empty diamonds) pulses. The time $t = 0$ corresponds to the laser pulse peak reaching the waist, as in equation (4). The coordinates are normalized to λ.

$$\mathbf{a}(x = 0, r, t) = a_0 (\hat{\mathbf{y}} \cos(\omega t) \pm \hat{\mathbf{z}} \sin(\omega t)) e^{-(r/r_0)^n - (ct/r_L)^4}, \qquad (4)$$

where $r = (y^2 + z^2)^{1/2}$. Both radial profiles with $n = 2$ (Gaussian, G) and $n = 4$ (super-Gaussian, SG) have been used in the simulations. For all the results shown below, we take $r_L = 3\lambda$ and radius $r_0 = 3.8\lambda$. The plus and minus sign in the expression for $\mathbf{a}$ correspond to positive and negative helicity, respectively. The pulse energy is given by $U_L = \mathcal{A} r_0^2 r_L B_0^2 a_0^2$, where $\mathcal{A} = \Gamma(1/4) 2^{-17/2} \simeq 0.19$ and $\mathcal{A} = \pi^{1/2} \Gamma(1/4) 2^{-19/2} \simeq 0.24$ for the G and SG pulse cases, respectively. The target is a plasma of thickness 10λ and electron density $n_0 = 90 n_c$ and charge-to-mass ratio for ions $Z/A = 1/2$. The range of laser amplitudes investigated in the simulation is $a_0 = 200$–600. Assuming $\lambda = 0.8$ μm, the density $n_0 = 1.55 \times 10^{23}$ cm^{-3}, the pulse duration (full-width-half-maximum of the intensity profile) is 14.6 fs and the range for the peak laser intensity $I_L = m_e c^3 n_c a_0^2$ is $(1.9$–$16.7) \times 10^{23}$ W cm^{-2} corresponding to a pulse energy $U_L \simeq (0.38$–$3.4)$ kJ for the G pulse and $U_L \simeq (0.48$–$4.3)$ kJ for the SG pulse. The numerical box had a $30 \times 25 \times 25\lambda^3$ size, with 40 grid cells per λ and 64 particles per cell for each species. The simulations were performed on 480 cores of the JURECA supercomputer at Forschungszentrum Jülich.

Figures 2(a)–(c) show the magnetic field B_x (normalized to $B_0 = 1.34 \times 10^8$ G for $\lambda = 0.8$ μm) along the propagation direction at time $t = 27\lambda/c$ for a simulation (a) where RF is not included and for two simulations (b) and (c) including RF and having positive and negative helicity, respectively; the laser profile was super-Gaussian and $a_0 = 600$ in all the three simulations. Only with RF included an axial magnetic field of maximum amplitude $B_{max} \simeq 22 B_0 = 2.9 \times 10^9$ G, extending over several microns and a polarity inverting with the pulse helicity is generated. The comparison of figures 2(d) and (e) shows that B_x has similar values and extension for a Gaussian pulse. The field is slowly varying over more than a ten laser cycles ($\sim$30 fs) time, with no sign of rapid decay at the end of the simulation, as shown in figure 2(f).

The fraction η_{rad} of the laser energy dissipated by RF reaches values up to $\eta_{rad} \simeq 0.24$ for $a_0 = 600$ as shown in figure 3(a). A fit to the data gives $\eta_{rad} \propto a_0^{3.1}$, close to the $\eta_{rad} \sim a_0^3$ prediction of our model. Figure 3(a) also shows the peak magnetic field B_{max} scaling as $\sim a_0^{3.8}$ up to the highest value $B_{max} \simeq 28 B_0 = 3.75$ GG for $a_0 = 500$. The decrease down to $B_{max} \simeq 22 B_0$ for $a_0 = 600$ is related to the early interruption of the hole boring stage due to the breakthrough of the laser pulse through the target as observed in this case. Notice that we do not show simulations for $a_0 < 200$ since in such case the RF losses become too close to the percentage of energy which is lost due to numerical errors ($\lesssim$1%). However, the inferred scaling would predict $B_{max} \sim 8$ MG for $a_0 = 100$, which may be still detectable making an experimental test closer.

Figure 3. (a) Values of fractional radiative energy loss η_{rad} (circles) and maximum axial magnetic field B_{max} (triangles) as a function of laser amplitude a_0, from 3D simulations. The dashed and dashed–dotted lines are fit to the data for η_{rad} and B_{max}, respectively. The errorbars on η_{rad} correspond to the typical $\lesssim 1\%$ amount of energy which is not conserved in the simulation because of numerical errors. (b) Axial angular momentum of electrons (dashed line) and ions (thick line) at $t = 27\tau\lambda/c$. The density of angular momentum has been integrated over the radius and normalized to the total integrated angular momentum of the laser pulse. Results with and without RF included are shown.

4. Analytical model for IFE

To sketch an analytical model for IFE, let us first observe that the density of angular momentum of the laser pulse $\mathcal{L}_x = (\mathbf{r} \times (\mathbf{E} \times \mathbf{B}))_x / 4\pi c = -r\partial_r I_{\text{L}}(r)/(2c\omega)$, with $I_{\text{L}}(r)$ the radial profile of the intensity, vanishes on axis and has its maximum at the edge of the beam. We thus consider angular momentum absorption to occur in a thin cylindrical shell of radius $R \simeq r_0$, thickness $\delta \ll R$, and length h. The temporal growth of the axial field B_x induces an azimuthal electric field E_ϕ, which in turn allows the absorbed angular momentum to be transferred from electrons to ions. Assuming that the electron and ion shells rotate with angular velocities $\Omega_{\text{e,i}}$, respectively, we may write for the angular momenta $L_{\text{e}} = \mathcal{I}_{\text{e}}\Omega_{\text{e}}$ and $L_{\text{i}} = \mathcal{I}_{\text{i}}\Omega_{\text{i}}$, where $\mathcal{I}_{\text{e}} = 2\pi R^3 \delta h m_{\text{e}} n_{\text{e}}$ and $\mathcal{I}_{\text{i}} = (A m_{\text{p}}/Z m_{\text{e}})\mathcal{I}_{\text{e}}$ are the momenta of inertia for electrons and ions, respectively. The global evolution of the angular momenta of electrons and ions may be described by the equations

$$\mathcal{I}_{\text{e}}\frac{\text{d}\Omega_{\text{e}}}{\text{d}t} = M_{\text{abs}} - M_{\text{E}}, \qquad \mathcal{I}_{\text{i}}\frac{\text{d}\Omega_{\text{i}}}{\text{d}t} = M_{\text{E}}, \tag{5}$$

where M_{abs} is the torque due to angular momentum absorption (related to the absorbed power P_{abs} by $M_{\text{abs}} = P_{\text{abs}}/\omega$) and M_{E} is the torque due to E_ϕ:

$$M_{\text{E}} = \int e E_\phi(r) r n_{\text{e}} \text{d}^3 r \simeq \frac{e E_\phi(R)}{m_{\text{e}} R}\mathcal{I}_{\text{e}}. \tag{6}$$

The rotation of the electrons induces a current density $j_{e\phi} \simeq -e n_{\text{e}} \Omega_{\text{e}} R$. Neglecting the displacement current, in the limiting case $h \gg R$ the field $B_x \simeq 4\pi j_{e\phi}\delta/c$ and it is uniform as in a solenoid. In the opposite limit $h \sim \delta \ll R$, the current distribution may be approximated by a thin wire of cross-section $\sim h\delta$, and $E_\phi(R)$ can be obtained via the self-induction coefficient of a coil [63]. We thus obtain

$$M_{\text{E}} \simeq \mathcal{F}\frac{\omega_{\text{p}}^2 R\delta}{2c^2}\mathcal{I}_{\text{e}}\frac{\text{d}\Omega_{\text{e}}}{\text{d}t} \equiv \mathcal{I}_{\text{e}}'\frac{\text{d}\Omega_{\text{e}}}{\text{d}t}, \tag{7}$$

where $\omega_{\text{p}} = (4\pi n_{\text{e}} e^2/m_{\text{e}})^{1/2}$ is the plasma frequency. The geometrical factor $\mathcal{F} \simeq 1$ if $h \gg R$, and $\mathcal{F} \simeq (h/R)\ln(8R/\sqrt{h\delta})$ if $h \simeq \delta \ll R$. Therefore

$$\Omega_{\text{e}}(t) = \frac{1}{\mathcal{I}_{\text{e}} + \mathcal{I}_{\text{e}}'}\int_0^t M_{\text{abs}}(t')\text{d}t', \tag{8}$$

which shows that the electron rotation follows promptly the temporal profile of $M_{\text{abs}}(t)$, and that effect of the inductive field on electrons is equivalent to effective inertia. Since in our conditions $\mathcal{I}_{\text{e}}' \sim (\omega_{\text{p}}^2/\omega^2)\mathcal{I}_{\text{e}} = (n_{\text{e}}/n_{\text{c}})\mathcal{I}_{\text{e}} \gg \mathcal{I}_{\text{e}}$, and therefore $M_{\text{E}} \simeq \mathcal{I}_{\text{e}}'(\text{d}\Omega_{\text{e}}/\text{d}t) \gg \mathcal{I}_{\text{e}}(\text{d}\Omega_{\text{e}}/\text{d}t)$, the lhs term in equation (5) can be neglected and $M_{\text{E}} \simeq M_{\text{abs}}$ holds. Thus, from equation (5) we obtain

$$L_{\mathrm{i}} \simeq \int_0^t M_{\mathrm{abs}}(t')\,\mathrm{d}t' \simeq \frac{\mathcal{I}'_{\mathrm{e}}}{\mathcal{I}_{\mathrm{e}}}L_{\mathrm{e}} \gg L_{\mathrm{e}}, \tag{9}$$

i.e. the total angular momentum of ions is much larger than that of electrons, in agreement with the simulation results (figure 3(b)).

In turn, posing $M_{\mathrm{E}} \simeq M_{\mathrm{abs}}$ in equation (6) and using $E_\phi(R) \simeq -(R/2c)\mathcal{G}\partial_t B_x(r = 0,\, t)$ (where $\mathcal{G} = 1$ for $h \gg R$ and $\mathcal{G} \simeq (2/\pi)\ln(8R/\sqrt{h\delta})$ for $h \sim \delta \ll R$) we obtain for the final value of the magnetic field on axis $B_{xm} = B_x(r = 0,\, t = \infty)$

$$\frac{\pi e}{c}n_{\mathrm{e}}hR^3\delta\mathcal{G}B_{xm} \simeq \int_0^\infty M_{\mathrm{abs}}(t)\,\mathrm{d}t = L_{\mathrm{abs}}. \tag{10}$$

The total angular momentum absorbed $L_{\mathrm{abs}} = U_{\mathrm{abs}}/\omega$ where the absorbed energy is $U_{\mathrm{abs}} \simeq \eta_{\mathrm{rad}} U_{\mathrm{L}}$, assuming RF as the main source of dissipation. We thus estimate the final magnetic field as

$$\frac{B_{xm}}{B_0} \simeq \frac{\mathcal{A}}{\pi\mathcal{G}}\frac{\eta_{\mathrm{rad}}}{n_{\mathrm{e}}h}\frac{B_0 c}{e\omega}\frac{r_{\mathrm{L}}}{R\delta}a_0^2. \tag{11}$$

The product $n_{\mathrm{e}}h$ is the surface density of the region where dissipation and angular momentum absorption occur. Thus, with reference to figure 1 we may estimate $n_{\mathrm{e}}h \simeq n_{\mathrm{p0}}\ell_{\mathrm{s}} \simeq (I_{\mathrm{L}}/\pi e^2 c)^{1/2} = 2n_{\mathrm{c}}a_0 c/\omega$ (for $n_{\mathrm{p0}} \gg n_0$). Noticing that $B_0/en_{\mathrm{c}} = 2\lambda$ we eventually obtain

$$\frac{B_{xm}}{B_0} \simeq \frac{\mathcal{A}}{\pi\mathcal{G}}\eta_{\mathrm{rad}}\frac{r_{\mathrm{L}}\lambda}{R\delta}a_0. \tag{12}$$

If $\eta_{\mathrm{rad}} \propto a_0^3$ then $B_{xm} \propto a_0^4$, in good agreement with the observed scaling in figure 3(a). If we pose $R \simeq r_0$, the laser initial beam radius, and $\delta \simeq \lambda$, the radial width of the angular momentum density, for $a_0 = 500$, $\eta_{\mathrm{rad}} = 0.16$ and $\mathcal{G} = 1$ equation (12) yields $B_{xm} \simeq 4.8B_0$. The discrepancy with the observed value of $\simeq 28B_0$ may be attributed to the nonlinear evolution and self-channeling of the laser pulse in the course of the hole boring process. For instance, figure 2 shows that the magnetic field is generated in a region of radius $\sim 2\lambda$. Further analysis of the simulation data shows both a slight increase (by a factor ~ 1.2) of the laser amplitude on the axis and a localization of the densities of both EM and mechanical angular momenta in a narrow layer of $\sim 0.5\lambda$ width. Posing $R \simeq 2\lambda$, $\delta \simeq 0.5\lambda$ and an effective $a_0 \simeq 600$ in the above estimate yields $B_{xm} \simeq 23B_0$, which is in fair agreement with the simulation results considering the roughness of the model.

5. Discussion

In our simulations, RF is the dominant dissipative mechanism (if not the only one at all) allowing for the IFE, i.e. angular momentum absorption and magnetic field generation; collisional absorption is suppressed already at intensities $\simeq 10^{18}$ W cm^{-2} even for solid targets, and the comparison between simulations with and without RF shows that collisionless mechanisms (included in the numerical modeling) do not produce any noticeable IFE.

Our simulations use a classical model of RF, based on the LL equation, and do not include quantum electrodynamics (QED) effects. This completely classical approach rises two questions: (a) would a quantum model of RF, which is in principle needed at extremely high intensities, significantly affect the radiative losses and (b) could QED effects including production of electron–positron pairs contribute considerably into absorption of laser radiation, competing with RF as the dominant source of energy dissipation?

Quantum effects on RF are important when the characteristic frequency of emitted photons is comparable to the electron energy, so that the photon recoil is significant. In our case the radiation spectrum peaks at $\omega_{\mathrm{rad}} \simeq a_0^3\omega$ while the electron energy $\simeq a_0 m_{\mathrm{e}}c^2$, so that quantum effects are important at $a_0 \simeq 500$. However, the simulations of the hole boring process performed in [64] under conditions quite similar to our case show that using a quantum corrected model of RF leads at most to a $\simeq 10\%$ reduction of the conversion efficiency into high-energy radiation, without changing the laser–plasma dynamics qualitatively.

For what concerns the role of other QED effects, in the recent simulations of [31] at intensities close to 10^{24} W cm^{-2} it is found that radiative losses are the dominant energy loss mechanism in solid targets (corresponding to 65% of the pulse energy over a 90% total absorption, to be compared with 5% conversion efficiency into electron–positron pairs). For relatively tightly focused pulses as we use in our simulations, intensities of the order of 10^{25} W cm^{-2} (i.e. about one order in magnitude higher than in our case) are required to develop QED cascades of pairs and photons leading to a considerable depletion of a laser pulse (see e.g., [65]).

We are thus quite confident that RF remains the dominant dissipative mechanism even for the highest intensity applied in the simulations, and that the use of a quantum corrected RF model instead of the classical LL equation would not change the results qualitatively. On the other hand, quantitative modifications on the magnetic field may provide a signature of quantum RF.

6. Conclusions

In conclusion, we showed in 3D simulations that in the interaction of superintense, circularly polarized laser pulses with thick, high density targets the strong radiation friction effects lead to angular momentum absorption and generation of multi-gigagauss magnetic fields via the inverse Faraday effect. Simple models for the efficiency of radiative losses, the transfer of angular momentum to ions and the value of the magnetic field are in fair agreement with the simulation results for what concerns both the scaling with intensity and order-of-magnitude estimates. With the advent of multi-petawatt laser systems, the investigated effect may provide a laboratory example of radiation-dominated, strongly magnetized plasmas and a macroscopic signature of RF, providing a test bed for related theories.

Acknowledgments

References

[1] Mourou G A, Tajima T and Bulanov S V 2006 *Rev. Mod. Phys.* **78** 309–71
[2] Di Piazza A, Müller C, Hatsagortsyan K Z and Keitel C H 2012 *Rev. Mod. Phys.* **84** 1177–228
[3] Bulanov S V, Esirkepov T V, Kando M, Koga J K and Bulanov S S 2011 *Phys. Rev. E* **84** 056605
[4] Kravets Y, Noble A and Jaroszynski D 2013 *Phys. Rev.* **88** 011201
[5] Zhidkov A, Koga J, Sasaki A and Uesaka M 2002 *Phys. Rev. Lett.* **88** 185002
[6] Sokolov I V, Naumova N M, Nees J A, Mourou G A and Yanovsky V P 2009 *Phys. Plasmas* **16** 093115
[7] Tamburini M, Pegoraro F, Di Piazza A, Keitel C H and Macchi A 2010 *New J. Phys.* **12** 123005
[8] Chen M, Pukhov A, Yu T P and Sheng Z M 2011 *Plasma Phys. Contr. Fusion* **53** 014004
[9] Vranic M, Martins J, Fonseca R and Silva L 2016 *Comput. Phys. Commun.* **204** 141–51
[10] Jaroschek C H and Hoshino M 2009 *Phys. Rev. Lett.* **103** 075002
[11] Cerutti B, Werner G R, Uzdensky D A and Begelman M C 2013 *Astrophys. J.* **770** 147
[12] Mahajan S M, Asenjo F A and Hazeltine R D 2015 *Mon. Not. R. Astron. Soc* **446** 4112–5
[13] Koga J, Esirkepov T Z and Bulanov S V 2005 *Phys. Plasmas* **12** 093106
[14] Di Piazza A, Hatsagortsyan K Z and Keitel C H 2009 *Phys. Rev. Lett.* **102** 254802
[15] Hadad Y, Labun L, Rafelski J, Elkina N, Klier C and Ruhl H 2010 *Phys. Rev. D* **82** 096012
[16] Neitz N and Di Piazza A 2013 *Phys. Rev. Lett.* **111** 054802
[17] Blackburn T G, Ridgers C P, Kirk J G and Bell A R 2014 *Phys. Rev. Lett.* **112** 015001
[18] Vranic M, Martins J L, Vieira J, Fonseca R A and Silva L O 2014 *Phys. Rev. Lett.* **113** 134801
[19] Li J X, Hatsagortsyan K Z and Keitel C H 2014 *Phys. Rev. Lett.* **113** 044801
[20] Kumar N, Hatsagortsyan K Z and Keitel C H 2013 *Phys. Rev. Lett.* **111** 105001
[21] Tamburini M, Keitel C H and Di Piazza A 2014 *Phys. Rev. E* **89** 021201
[22] Green D G and Harvey C N 2014 *Phys. Rev. Lett.* **112** 164801
[23] Heinzl T, Harvey C, Ilderton A, Marklund M, Bulanov S S, Rykovanov S, Schroeder C B, Esarey E and Leemans W P 2015 *Phys. Rev. E* **91** 023207
[24] Gonoskov A, Bashinov A, Gonoskov I, Harvey C, Ilderton A, Kim A, Marklund M, Mourou G and Sergeev A 2014 *Phys. Rev. Lett.* **113** 014801
[25] Ji L L, Pukhov A, Kostyukov I Y, Shen B F and Akli K 2014 *Phys. Rev. Lett.* **112** 145003
[26] Fedotov A M, Elkina N V, Gelfer E G, Narozhny N B and Ruhl H 2014 *Phys. Rev. A* **90** 053847
[27] Nakamura T, Koga J K, Esirkepov T V, Kando M, Korn G and Bulanov S V 2012 *Phys. Rev. Lett.* **108** 195001
[28] Capdessus R, d'Humières E and Tikhonchuk V T 2013 *Phys. Rev. Lett.* **110** 215003
[29] Capdessus R and McKenna P 2015 *Phys. Rev. E* **91** 053105
[30] Nerush E N and Kostyukov I Y 2015 *Plasma Phys. Contr. Fusion* **57** 035007
[31] Lobet M, Ruyer C, Debayle A, d'Humières E, Grech M, Lemoine M and Gremillet L 2015 *Phys. Rev. Lett.* **115** 215003
[32] Pitaevskii L P 1961 *Sov. Phys.—JETP* **12** 1008–13
[33] Pershan P S 1963 *Phys. Rev.* **130** 919–29
[34] van der Ziel J P, Pershan P S and Malmstrom L D 1965 *Phys. Rev. Lett.* **15** 190–3
[35] Deschamps J, Fitaire M and Lagoutte M 1970 *Phys. Rev. Lett.* **25** 1330–2
[36] Steiger A D and Woods C H 1972 *Phys. Rev. A* **5** 1467
[37] Abdullaev A S and Frolov A A 1981 *Sov. Phys.—JETP* **54** 493
[38] Bychenkov V Y, Demin V I and Tikhonchuk V T 1994 *J. Exp. Theor. Phys.* **78** 62
[39] Sheng Z M and Meyer-ter-Vehn J 1996 *Phys. Rev. E* **54** 1833–42
[40] Berezhiani V I, Mahajan S M and Shatashvili N L 1997 *Phys. Rev. E* **55** 995
[41] Haines M G 2001 *Phys. Rev. Lett.* **87** 135005
[42] Shvets G, Fisch N J and J M 2002 *Phys. Rev. E* **65** 046403
[43] Danson C, Hillier D, Hopps N and Neely D 2015 *High Power Laser Sci. Eng.* **3** e3
[44] Mourou G, Fisch N, Malkin V, Toroker Z, Khazanov E, Sergeev A, Tajima T and Garrec B L 2012 *Opt. Commun.* **285** 720–4

New Journal of Physics

The open access journal at the forefront of physics

PAPER

Efficiency of radiation friction losses in laser-driven 'hole boring' of dense targets

CrossMark

S V Popruzhenko[1,2,7] , T V Liseykina[3,4] and A Macchi[5,6]

1   Max Planck Institute for the Physics of Complex Systems, Dresden, D-01187, Germany
2   National Research Nuclear University MEPhI, Moscow 115409, Russia
3   Institute of Physics, University of Rostock, D-18051 Rostock, Germany
4   On leave from Institute of Computational Mathematics and Mathematical Geophysics SB RAS, 630090 Novosibirsk, Russia
5   CNR/INO (National Institute of Optics), Adriano Gozzini unit, I-56124 Pisa, Italy
6   Enrico Fermi Department of Physics, University of Pisa, largo Bruno Pontecorvo 3, I-56127 Pisa, Italy
7   Prokhorov General Physics Institute of the Russian Academy of Sciences, Vavilova Str. 38, Moscow 119991, Russia

E-mail: sergey.popruzhenko@gmail.com

Keywords: radiation friction force, laser plasma, ultrahigh laser fields

Abstract

In the interaction of laser pulses of extreme intensity ($>10^{23}$ Wcm^{-2}) with high-density, thick plasma targets, simulations show significant radiation friction losses, in contrast to thin targets for which such losses are negligible. We present an analytical calculation, based on classical radiation friction modeling, of the conversion efficiency of the laser energy into incoherent radiation in the case when a circularly polarized pulse interacts with a thick plasma slab of overcritical initial density. By accounting for three effects including the influence of radiation losses on the single electron trajectory, the global 'hole boring' motion of the laser-plasma interaction region under the action of radiation pressure, and the inhomogeneity of the laser field in both longitudinal and transverse direction, we find a good agreement with the results of three-dimensional particle-in-cell simulations. Overall, the collective effects greatly reduce radiation losses with respect to electrons driven by the same laser pulse in vacuum, which also shift the reliability of classical calculations up to higher intensities.

1. Introduction

The continuous progress of laser techniques making higher and higher electromagnetic (EM) intensities accessible for experiments has stimulated the growth of research areas such as relativistic dynamics and nonlinear optics in classical plasmas [1] and quantum electrodynamics in extremely strong fields [2, 3]. Radiation friction (RF) is a problem of central interest in both the above mentioned areas. In the classical context, a modification of the Newton–Lorentz equation of motion for an electron by adding a new force term, named the RF force (RFF) or radiation reaction force, is necessary to make the electron dynamics self-consistent with the emission of radiation. Although the correct form of the RFF has been the subject of intense debate for decades and until recently [4, 5], it now appears that in the classical limit the Landau–Lifshitz (LL) expression [6] gives a correct and consistent description [7, 8]. The LL expression of the RFF has become the basis of classical simulations of superintense laser-plasma interaction [9, 10] where RF losses (corresponding to the escape of high-frequency, incoherent radiation from the plasma) are important enough to affect the plasma dynamics.

When the frequency of the emitted radiation becomes sufficiently high that the energy and momentum of single photons are not negligible with respect to those of the radiating electron, a quantum electrodynamics (QED) description becomes necessary. However, a correct and effective description of 'quantum RF' is an open issue. The first two experiments claiming for evidence of quantum RF signatures in nonlinear Thomson scattering of superintense laser pulses by ultrarelativistic electrons [11, 12] came to somewhat different conclusions about which model better described the experimental results (see [13] for a discussion). Notice that these experiments involved laser-plasma physics in the generation via wakefield acceleration of a dense, short duration bunch of relativistic electrons in order to increase the luminosity in the gamma-ray region; however,

the dynamics of the laser-bunch interaction was of single particle nature. The geometry of these experiments was designed to maximize RF losses in order to make quantum signatures appearing at relatively low intensity. In this regime, such signatures are mostly a reduction of RF losses with respect to the classical calculation because of the spectral cut-off which appears when the emitted photon energy approaches the photon energy. These effects can be reproduced by a semiclassical modeling, similar to what found in a different class of experiments involving high energy electron scattering in crystals [14, 15].

An alternative approach to investigate RF in the laboratory is to search for regimes where *collective* effects in the laser-plasma interaction boost radiation losses, so that RF signatures may become strong and unambiguous. Several simulation works have shown highly efficient radiation losses (a few tens per cent of the laser pulse energy) in the interaction of circularly polarized (CP) pulses with dense thick targets [16–22]. This is in sharp contrast with thin targets accelerated by CP pulses in the so-called 'light sail' (LS) regime, for which the radiation losses are very weak [9, 23, 24]. Strong differences between CP and linear polarization (LP) were also evidenced [9, 23]. Hence, the collective laser-plasma dynamics can play a crucial role in determining the amount of RF losses.

In our previous work [21] we have made a first attempt of a classical model to estimate the conversion efficiency η_{rad} of the laser energy into incoherent radiation in the case when a strong CP pulse interacts with a thick plasma of overcritical initial density. In turn, the efficient absorption of CP light causes a strong transfer of angular momentum to the target, with the generation of ultrahigh magnetic fields (inverse Faraday effect) with strength achieving several Giga-Gauss which can provide a macroscopic signature of RF [21].

In [21] the scaling of η_{rad} with the laser intensity agreed reasonably with the results of three-dimensional (3D) particle-in-cell (PIC) simulations of the laser-plasma interaction, up to intensities approaching 10^{24} W cm^{-2}. Beyond this limit, however, the model predicts unphysical values of $\eta_{\mathrm{rad}} > 1$ because neither the modification of the radiating electron trajectories due to RF nor the depletion of the laser pulse are taken into account. In addition, and more in general, at those intensities the classical description becomes questionable and quantum effects are expected to become relevant.

The aim of this paper is to provide an accurate estimate of η_{rad} for CP fields via analytical modeling assuming that the classical RF regime is retained. First, we use the solution by Zeldovich [25] to take self-consistently into account the effect of RF losses on the electron trajectory. Then, we show that the amount of RF losses is considerably affected by the average motion of the plasma surface, the finite evanescence length of the EM field in the plasma, and the radially inhomogeneous distribution of the laser intensity. By accounting for these effects, analytical estimates in good agreement with the results of 3D simulations are obtained. We also provide an estimate for the value of the quantum parameter and show that, in the present context, the electron dynamics can still be well described within the classical RFF approach.
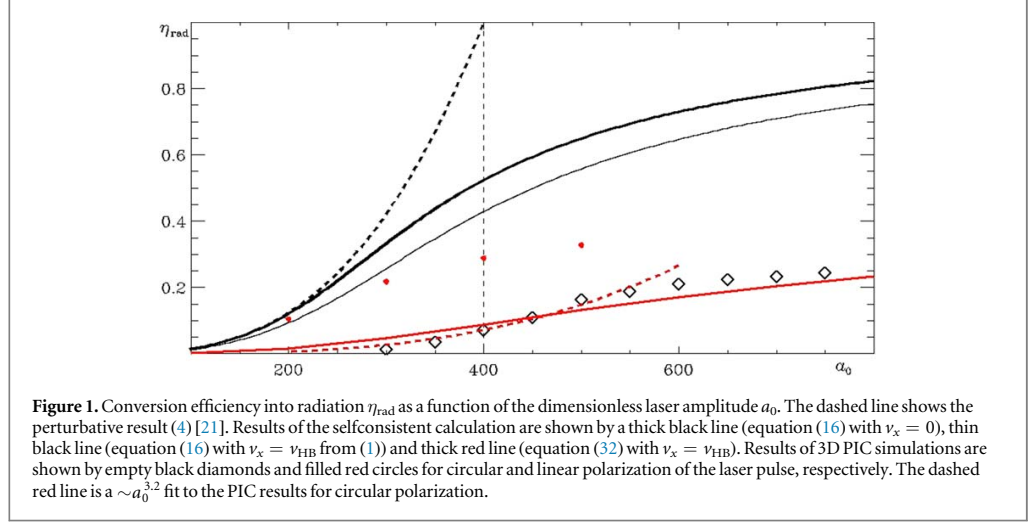
2. Review of previous modeling and its limitations

In the regime of interest here, an ultraintense laser pulse of frequency ω and dimensionless field amplitude $a_0 = eE_L/m_e\omega c$ (with E_L the electric field amplitude) interacts with a strongly overdense (electron density $n_e \gg n_c = m_e\omega^2/4\pi e^2$, the cut-off density) plasma target which remains opaque to the laser light. The radiation pressure of the laser light is high enough to produce 'hole boring' (HB) in the target, i.e. the plasma surface is driven at an average velocity

$$\frac{v_{\mathrm{HB}}}{c} = \frac{\sqrt{\Xi}}{1 + \sqrt{\Xi}}, \qquad \Xi = \frac{I_L}{\rho c^3} = \frac{Zn_c m_e}{An_e m_p}a_0^2, \qquad (1)$$

where $I_L = cE_L^2/4\pi = m_e c^3 n_c a_0^2$ is the laser intensity. Equation (1) can be obtained by balancing the mass and momentum flows at the surface [26] and is valid for total reflection of the laser light *in the frame co-moving with the surface*, i.e. in the absence of dissipative effects. If a fraction η of the laser intensity is dissipated, for example due to RF losses, equation (1) may be modified by replacing I_L with $I_L(1 - \eta/2)$. In the case of our simulations this would lead at most to a $\simeq 5\%$ decrease in v_{HB} at the highest intensity considered ($a_0 = 800$).

In order for the interaction to remain in the HB regime during the whole duration of the laser pulse, the target must be 'thick' enough that $v_{\mathrm{HB}}\tau_L < D$, where τ_L is the laser pulse duration and D is the target thickness. In the opposite 'thin' target limit $v_{\mathrm{HB}}\tau_L \gg D$, the target can be accelerated as a whole and enter the 'LS' regime [27, 28], where the scaling of the velocity v_{LS} with intensity becomes much faster than (1). Thus, the same laser pulse parameters may enable to reach velocities $v_{\mathrm{LS}} \simeq c$ in an ultrathin target while yielding v_{HB} to be a fraction of c in a thick target. In particular, for the parameters of calculations presented below $v_{\mathrm{HB}} \approx (0.3 \div 0.6)c$. The different acceleration regime may therefore explain the huge difference in the radiation efficiency between thick and thin targets. In fact, assuming that the electrons radiate in the field of a plane EM CP wave propagating along x, the radiated power is [29]

Figure 1. Conversion efficiency into radiation η_{rad} as a function of the dimensionless laser amplitude a_0. The dashed line shows the perturbative result (4) [21]. Results of the selfconsistent calculation are shown by a thick black line (equation (16) with $v_x = 0$), thin black line (equation (16) with $v_x = v_{\mathrm{HB}}$ from (1)) and thick red line (equation (32) with $v_x = v_{\mathrm{HB}}$). Results of 3D PIC simulations are shown by empty black diamonds and filled red circles for circular and linear polarization of the laser pulse, respectively. The dashed red line is a $\sim a_0^{3.2}$ fit to the PIC results for circular polarization.

$$P_{\mathrm{rad}} = \frac{2e^2\omega^2\gamma^2 a_0^2}{3c}\left(1 - \frac{v_x}{c}\right)^2, \tag{2}$$

where $\gamma = 1/\sqrt{1 - v^2/c^2}$ and v_x is the velocity component parallel to the wavevector. Assuming that most of the radiating electrons co-move with the target ions, the factor $(1 - v_x/c)^2$ leads to strong suppression of radiation emission for thin targets moving at $v_{\mathrm{LS}} \simeq c$, while the suppression is much less severe for thick targets as far as v_{HB} is significantly smaller than c.

In the thick target case, the laser field penetrates into the skin layer where the electrons pile up under the action of the radiation pressure. The areal density of electrons in the skin layer can be estimated as [21, 30]

$$N_x \simeq \frac{a_0}{r_0\lambda}, \tag{3}$$

where $r_0 = e^2/mc^2$ is the classical electron radius. For $a_0 \gg 1$, by estimating $\gamma \simeq a_0$ we obtain the radiated power per unit surface as $I_{\mathrm{rad}} = N_x P_{\mathrm{rad}} \propto a_0^5$, which implies a $\propto a_0^3$ scaling for the radiation loss efficiency, in good agreement with the simulation results. For $v_x = 0$, and assuming that the duration of the uncoherent high-energy emission is the same as the laser pulse, the conversion efficiency defined as a ratio of the energy emitted by radiating electrons U_{rad} to that of the laser pulse U_{L} is thus given by

$$\eta_{\mathrm{rad}} = \frac{U_{\mathrm{rad}}}{U_{\mathrm{L}}} = \frac{I_{\mathrm{rad}}}{I_{\mathrm{L}}} = \xi a_0^3, \tag{4}$$

where the parameter

$$\xi = \frac{4\pi r_0}{3\lambda} \tag{5}$$

is introduced, and λ is the laser wavelength.

In [21] it was suggested that for thick targets an enhancement of radiation losses may originate from the non-steady dynamics of HB acceleration [30]. In particular, ion acceleration by the space-charge field causes a pulsed 'collapse' of the electron density with the excess electrons returning towards the laser with *negative* velocity $v_x < 0$, enhancing the RF losses by a sequence of radiation bursts. However, it is not straightforward to provide analytical estimates for either the rate of the bursts or the value of v_x for the returning electrons. In particular, estimating v_x would require to find the motion of the returning electrons in an inhomogeneous electric field with the RFF included. For an order-of-magnitude estimate, we simply assumed $(1 - v_x/c)^2 \simeq 1$ and the number of the returning electrons to be $\simeq N_x$ [21] (i.e. most of the electrons in the skin layer to collapse). This leads again to an expression like (4) for the conversion efficiency, apart from a reduction factor < 1 accounting for the fact that the returning electrons radiate only for a fraction of the interaction time.

Apparently, the $\eta_{\mathrm{rad}} \sim a_0^3$ scaling fairly agrees with the results of 3D simulations which give $\eta_{\mathrm{rad}} \sim a_0^{3.2}$ up to intensities $a_0 \simeq 500$, but the absolute value predictions of (4) are much higher than those observed in the simulations (see figure 1 below). This is not surprising since obviously (4) becomes invalid when approaching a critical value of the laser field amplitude

$$a_{\mathrm{cr}} = \xi^{-1/3} \approx 400, \tag{6}$$

where $\eta_{\mathrm{rad}} \simeq 1$, which is unphysical. In the simulation [21], $\eta_{\mathrm{rad}} \approx 0.08$ for $a_0 \simeq 400$. The quantitative disagreement makes also not possible, on the basis of the predicted scaling only, to understand whether the radiation is mostly due to electrons either remaining in the skin layer or returning towards the laser.

The very limited nature of the estimate (4) for the conversion efficiency is due to several underlying shortcomings, such as the neglect of self-consistent RF effects on the electron motion, the absence of a more precise estimate of v_x, and the inhomogeneity of the laser field in both the longitudinal and transverse directions. In the following we show that accounting for these effects, even if still in an approximated way, leads to a considerably smaller growth of the conversion efficiency at high intensities than that given by (4) and therefore substantially improves the agreement with the simulations.

3. Self-consistent electron motion

The model first introduced by Zeldovich [25] describes a stationary electron motion in the field of a strong CP plane wave with RF effects included self-consistently. Since RF allows absorption of momentum from the plane wave, a drag force is exerted on the electron along the direction of wave propagation (x for definiteness). Thus, in order to obtain a stationary solution an electric field E_d along x is introduced in the model balancing the radiation drag. The complete EM fields are thus given by

$$\mathbf{E}(t, x) = (E_d, E_L \cos\varphi, E_L \sin\varphi), \qquad \mathbf{B}(t, x) = (0, -E_L \sin\varphi, E_L \cos\varphi). \tag{7}$$

In the stationary regime an electron moves along a circle in the (y, z) plane and drifts along the x axis with a constant velocity:

$$\mathbf{v}(t) = (v_x, v_0 \sin(\varphi - \theta), -v_0 \cos(\varphi - \theta)), \qquad \varphi = \omega t - kx. \tag{8}$$

The phase shift θ is generated by the RFF. Neglecting the latter in the equations of motion gives $\theta = 0$. For ultra-relativistic particles, the RFF is given by [6]

$$\mathbf{F}_{\mathrm{rad}} = -\frac{P_{\mathrm{rad}}(\mathbf{v})\mathbf{v}}{c^2}, \tag{9}$$

with the radiation power

$$P_{\mathrm{rad}}(\mathbf{v}) = \frac{2e^2\omega^2 v_0^2 \gamma^4}{3c^3}\left(1 - \frac{v_x}{c}\right)^2 \tag{10}$$

which differs from (2) by the replacement $a_0^2 \rightarrow \gamma^2$ reflecting the fact that the circular motion of the electron is now determined jointly by the Lorentz and the RFFs. In the stationary regime the total force (with the centrifugal component included) vanishes. Projecting this condition on the axes of cylindrical coordinates and assuming that the value of the longitudinal electric field E_d is known we obtain three equations which determine the values of γ, θ and v_x:

$$eE_d - \frac{eE_L v_0}{c}\sin\theta - P_{\mathrm{rad}}(\gamma, v_x)\frac{v_x}{c^2} = 0, \tag{11}$$

$$eE_L\left(1 - \frac{v_x}{c}\right)\sin\theta + P_{\mathrm{rad}}(\gamma, v_x)\frac{v_0}{c^2} = 0, \tag{12}$$

$$\gamma m\omega v_0 = eE_L \cos\theta. \tag{13}$$

In principle the system of equations (11)–(13) might be applied to study the motion of electrons in the space-charge field created by the ponderomotive force action, see examples e.g. in [31] where an approximate analytic description for the case of standing waves was developed. However, such space-charge field is highly inhomogeneous, which would already make an analytical estimate difficult. In addition, in the case under investigation the electron density is high enough for screening effects to be non-negligible: considering as an example the contribution of returning electrons, as those located exactly at the plasma-vacuum boundary return towards the incoming laser, the space-charge field is partially canceled so that the electrons filling in inner layers will experience a lower force. A complete description of this scenario would require to resolve the electron plasma dynamics with RFF included.

Since our primary aim is to relate the radiation losses to an average value of v_x determined by the laser-plasma dynamics, we take v_x as a parameter in the system, and following Zeldovich [25] we solve equations (11)–(13) in the reference frame moving with the instant velocity v_x of the radiating electron. In the following, we use the notations γ', v_0', ξ', etc for values measured in this reference frame. Setting $v_x' = 0$ and taking into account that $\gamma' \gg 1$, one may safely put $v_0' \approx c$. Eliminating the angle θ' from equations (12), (13) we obtain an equation determining $\gamma'(\xi', a_0)$ (note that a_0 is relativistically invariant) [25]:

$$\gamma'^2(1 + \xi'^2\gamma'^6) = a_0^2. \tag{14}$$

For low intensities, $a_0 \ll a'_{cr}$ it gives $\gamma' = a_0$, as was used in [21]. In the opposite limit, $a_0 \gg a'_{cr}$, the gamma-factor grows much slower with a_0:

$$\gamma' = \left(\frac{a_0}{\xi'}\right)^{1/4}. \tag{15}$$

Equation (15), previously obtained in [32], corresponds to the limit in which the oscillation energy of the electron in the EM field equals the energy radiated per cycle. Remarkably, this single particle result corresponds, in our model where collective effects enter via (3) for the number of radiating electrons, to a total conversion of the laser pulse energy into radiation from the target. In fact it follows from equations (14), (10) and (3) that

$$\eta_{rad} = \xi'\frac{\gamma'^4}{a_0} = \xi\sqrt{\frac{1 - v_x/c}{1 + v_x/c}}\frac{\gamma'^4}{a_0}, \tag{16}$$

so that $\eta_{rad} \rightarrow 1$ for $a_0 \gg a'_{cr}$. Note that ξ is determined by the laser wavelength measured in the laboratory frame, and the factor $1/2$ is added to take into account that only half of the electrons radiate efficiently [21]. In section 5, we refine the calculation, so that the empirical factor is no longer needed.

We compare predictions of our model to the results of 3D PIC simulations (see [21] for the numerical set-up details) which describe the interaction of a laser pulse with a plasma of thickness $D > 10\lambda$ where $\lambda = 0.8$ μm corresponding to a Ti:Sapphire laser and initial density $n_0 = 90n_c = 1.55 \times 10^{23}$cm^{-3}. The charge-to mass ratio for ions was taken $Z/A = 1/2$. The supergaussian laser pulse is introduced via the time-dependent boundary condition at the plasma surface, $x = 0$, as described in [21]

$$\mathbf{a}(r, x = 0, t) = a_0(\mathbf{y}\cos(\omega t) + \mathbf{z}\sin(\omega t))e^{-(r/r_0)^4 - (ct/r_L)^4}, \tag{17}$$

with $r = \sqrt{y^2 + z^2}$, $r_0 = 3.8\lambda$, $r_L = 3.0\lambda$ and duration (full-width-half-maximum of the intensity profile) 14.6 fs. In our PIC calculations we varied the laser amplitude in the interval $a_0 = 300 \div 750$ which corresponds to the peak intensities $(3.8 \div 23.7) \times 10^{23}$ W cm^{-2} and the total pulse energy (1.08–6.71) kJ. The numerical box had a $[30 \times 25 \times 25]\lambda^3$ size, with 40 grid cells per λ in each direction and 125 particles per cell for each species. The simulations were performed on $5000 \div 10\,000$ cores of the JURECA Cluster Module at NIC (Jülich, Germany).

As is seen on figure 1, the values of η_{rad} obtained from (16) and shown by thick black line for $v_x = 0$ qualitatively reproduce the behavior of conversion efficiency extracted from the PIC simulation (shown by diamonds) in the whole interval of a_0, although the absolute values appear considerably overestimated. Below we identify the sources of these differences and improve the model by accounting for the respective effects. For the sake of comparison, three values of η_{rad} are also shown for a LP pulse at all other parameters identical to those of the CP simulation. As it is seen, the conversion efficiency is considerably higher in the LP case and also reaches its saturation at lower intensities. This is in line with previous observations [9, 23] and can be traced back to effect of the magnetic ($\mathbf{v} \times \mathbf{B}$) force driving longitudinal electron oscillations during which $v_x \rightarrow -c$.

4. Effects of the longitudinal velocity

An analysis of the 3D distribution functions of the radiation power density $\mathcal{P}(x, r, v_x)$ (calculated as $\mathcal{P} = -n_e\mathbf{v} \cdot \mathbf{F}_{rad}$) and of the electron and ion density $n_{e, i}(x, r, v_x)$ extracted from the PIC simulation shows that most of the emitted radiation comes from electrons having velocities $v_x > 0$, and located close to the receding front of the ion density. This is illustrated for the $a_0 = 500$ case in figure 2 where space–time plots in the (x, t) plane are shown for the radiation power and the particle densities at $r = 1\lambda$, where the former has its radial maximum. The density fronts move in the forward direction with average velocity $\simeq 0.41c$, in fair agreement with the value $v_{HB} = 0.47c$ given by equation (1). Small oscillations in the front position are visible in correspondence of the generation of plasma bunches in the forward direction, as discussed in [30]. The power density plot shows that most of the emission originates close to the HB front. Emission due to returning electrons with velocity $\simeq -c$ is visible after $t = 11T_L$, but its contribution to the total emitted power is small, presumably because of the low density in the returning jets (as seen on the $n_e(x, t)$ plot).

As clearly seen from the plot of the x-integrated radiation power shown on the upper panel, spikes of radiation occur in correspondance of the generation of plasma bunches. Such spikes may be explained by the enhanced penetration of the laser field into the plasma at these time instants. Since the spikes remain close to the HB front, no strong modification of v_x is correlated with them. Consistently with these observations, we assume that on the average the radiating electrons move with velocity $v_x = v_{HB}$ given by (1). In this way, we obtain a result shown on figure 1 by a thin black line. The account of the longitudinal motion improves the agreement,

Figure 2. Space–time plots of the radiation power density $\mathcal{P}(x, t)$ (top, logarithmic scale, arbitrary units), ion density $n_i(x, t)$ (middle) and electron density $n_e(x, t)$ (bottom) all evaluated at $r = 1\lambda$ distance from the axis. A white curve on the upper panel shows the radiation power integrated over x.
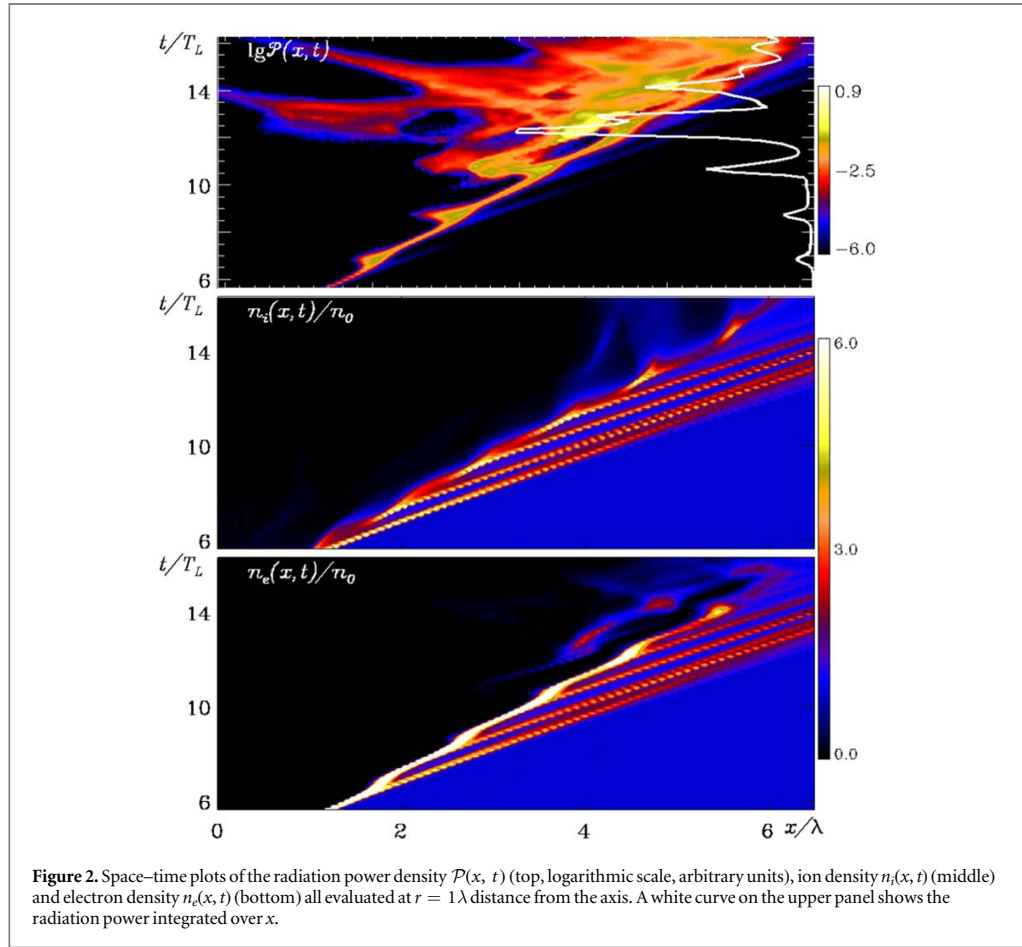
although analytically calculated values still exceed the PIC results by approximately 5 times at $a_0 = 400$ and 3 times at $a_0 = 750$.

5. Effects of field inhomogeneity

Finally, we account for the attenuation of the laser field in the plasma and the dependence of the laser intensity on time and its radial distribution in the focal spot. The laser field amplitude a_0 is not constant within the evanescence length ℓ_s, but dropping down, leading to a considerable decrease of the 'efficient' value of a_0 entering equations (15) and (16). Figure 3 based on the HB model of [30] sketches the electron and the ion density distributions along the propagation direction at the initial stage of the interaction when the electrons are pushed forward by light pressure, while the ions still remain immobile and homogeneously distributed inside the plasma layer. Taking the electron density for $x > d$ in the form

$$n_e(x) = n_0 + (n_{p0} - n_0)e^{-(x-d)/\ell_s}, \tag{18}$$

we replace a step distribution employed in [21] by a decaying exponent. Assuming that $n_{p0} \gg n_0$ with n_{p0} being the maximal density of electrons and n_0 is the initial density equal to that of ions, we obtain for the electric field inside the layer

$$E(x) = 4\pi e(n_{p0} - n_0)l_s e^{-(x-d)/\ell_s} \tag{19}$$

with the maximal value

$$E_d \equiv E(x = d) = 4\pi e(n_{p0} - n_0)\ell_s \approx 4\pi e n_{p0}\ell_s \tag{20}$$

achieved at the electron surface. Taking into account that $n_{p0}\ell_s = N_x \simeq a_0/r_0\lambda'$ (3) we obtain for the maximal longitudinal field

EFFICIENCY OF RADIATION FRICTION LOSSES

Figure 3. Distribution of electron (red line) and ion (blue line) charge densities calculated using the HB model for the initial stage of the charge separation, before the ions started moving under the action of the longitudinal electric field (green curve).
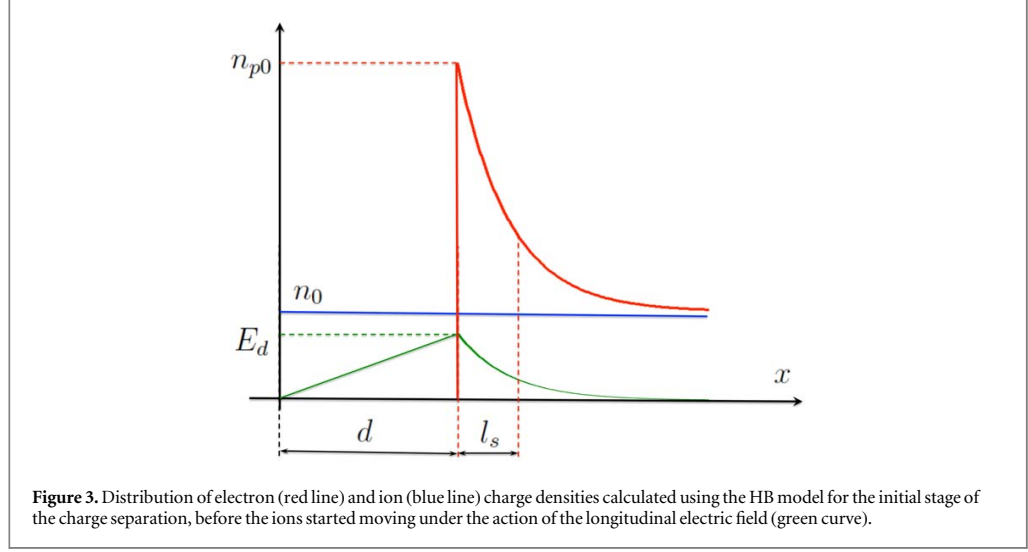
$$E_d \approx 3E_{cl}\xi' a_0, \tag{21}$$

where $E_{cl} = e/r_0^2 = m^2 c^4/e^3 = 1.81 \times 10^{18}$ V cm^{-1} is the critical field of classical electrodynamics which is $1/\alpha = \hbar c/e^2 \approx 137$ times greater than that of QED

$$E_{cr} = \frac{m^2 c^3}{e\hbar}. \tag{22}$$

Note that for $\lambda \simeq 1\ \mu$m, $E_d \simeq E_{cr}$ at $a_0 \simeq (400\xi)^{-1} \approx 1.6 \times 10^5$, according to (21), so that in this case $E_d \simeq E_L \simeq E_{cr}$.

Within the same approximation the local equilibrium condition for the electrons inside the layer requires that the laser field amplitude drops accordingly, $a(x) = a_0 \exp(-(x-d)/\ell_s)$. Then the global equilibrium condition for the whole layer reads

$$(2 - \eta_{rad})\frac{I'_L}{c} = e \int_d^\infty n_e(x)E(x)\mathrm{d}x \approx 2\pi e^2 n_{p0}^2 \ell_s^2. \tag{23}$$

Here we take into account that the intensity of reflected radiation in the reference frame co-moving with the electrons is $(1 - \eta_{rad})I'_L$. The arial radiation power (intensity) is

$$I'_{rad} = \int_d^\infty P'(x, v_x = 0) n_e(x)\mathrm{d}x = \frac{2e^2 \omega'^2 a_0^4 n_{p0}\ell_s}{3c}f(\xi', a_0), \tag{24}$$

where the power $P'(x, v_x = 0)$ is given by (10) in the reference frame co-moving with the electrons and $\gamma'(\xi', a_0)$ is expressed from equation (14), so that

$$f(\xi, a) = \frac{1}{a^5}\int_0^a \gamma^4(\xi, \bar{a})\mathrm{d}\bar{a}. \tag{25}$$

This gives the following equation for the conversion efficiency

$$\eta_{rad} = \frac{I'_{rad}}{I'_L} = 2\sqrt{1 - \eta_{rad}/2}\ \xi' a_0^3 f(\xi', a_0), \tag{26}$$

with an approximate solution

$$\eta_{rad} \approx 2\xi' a_0^3 f(\xi', a_0), \tag{27}$$

which employs the fact that $\eta_{rad}/2 \ll 1$ up to very high values of a_0; in particular, at $a_0 = 750$ which was at the limit of our numerical calculation, $\eta_{rad}/2 \approx 0.11$. In the limiting cases of weak and strong fields the integral in (25) can be solved analytically giving

$$\eta_{rad} \approx \frac{2}{5}\xi a_0^3, \qquad a_0 \ll a_{cr} \tag{28}$$

and

$$\eta_{rad} \to 0.78, \qquad a_0 \to \infty. \tag{29}$$

The latter number is obtained directly from (26), as the approximation $\eta_{rad}/2 \ll 1$ is no longer valid in this limit. As is clearly seen from (28) in the limit of low intensities (which in practice means the laser field amplitude up to $a_0 \simeq 400$), the field attenuation inside the plasma layer leads to further suppression of the radiation losses by a factor $\simeq 0.4$.

Remarkably, when the attenuation of the laser field in the plasma is accounted for along (26), no extra $1/2$ factor introduced in [21] is required to fulfill the requirement $n_{rad} \leqslant 1$. Note that the above results remain rather robust with respect to a particular model for the electron density and field distribution in the emitting layer. As our simulations show, while the distribution of the electron density follows qualitatively that of figure 3, the one for ions appears by far more complicated. However, the only feature of the ion density distribution we practically use for the analytic modeling is that there is a significant number of ions to the left from the sharp electron density profile. These ions, independently of the spatial shape of their distribution, create a quasistatic field E_d which equilibrates the laser light pressure. The electron density profile can also be chosen in different forms, and that given by equation (18) is not unique. The only essential point is that both the electron density and the laser field amplitude drop down on the length ℓ_s which considerably reduces the effective value of a_0 particularly in the low-field regime, $a_0 < a_{cr}$. The value of ℓ_s itself is also not of crucial significance as it enters the equations in the form of $N_x = n_{p0}\ell_s$. Comparing the values of the areal density N_x calculated from (3) and extracted from the simulation we found a reasonably good agreement: for $a_0 = 400$ the simulation and equation (3) give $N_x^{sim} = (1.3 \div 1.5) \times 10^{19} \text{ cm}^{-2}$, and $N_x^{model} = 1.1 \times 10^{19} \text{ cm}^{-2}$ correspondingly; for $a_0 = 500$ these numbers are $N_x^{sim} = (1.4 \div 1.7) \times 10^{19} \text{cm}^{-2}$, and $N_x^{model} = 1.3 \times 10^{19} \text{cm}^{-2}$.

A similar suppression effect emerges due to the laser amplitude dependence on the transverse coordinate and time. Assuming that the dimensionless laser amplitude in the focal waist possess axial symmetry

$$a(r, t) = a_0 g(r/r_0, ct/r_L) \tag{30}$$

and integrating the radiation power over the transverse coordinate and time we obtain that the function $f(\xi', a_0)$ in (27) is replaced by the factor

$$S(\xi', a_0) = \frac{\int g^5(\rho, \tau) f(\xi', a_0 g(\rho, \tau)) d\rho d\tau}{\int g^2(\rho, \tau) d\rho d\tau}, \tag{31}$$

where $\rho = (r/r_0)^2$ and $\tau = ct/r_L$. Finally

$$\eta_{rad} = 2\xi' a_0^3 S(\xi', a_0) \tag{32}$$

apparently leading to additional suppression of the convergence efficiency. For the supergaussian pulse (17) used in the PIC simulations

$$S(\xi', a_0) = \frac{1}{2^{1/4}\sqrt{\pi}\,\Gamma(1/4)} \int_0^1 \frac{dy_1}{y_1\sqrt{-\ln y_1}} \int_0^{y_1} \frac{dy_2 y_2^4}{(-\ln(y_2/y_1))^{3/4}} f(\xi', a_0 y_2). \tag{33}$$

In the strong field limit $f(a) \sim 1/a^3$ so that the integrands in (31) are proportional one to another, leaving the limit (29) unchanged. Instead, in the weak-field limit $f \approx 1/5$, which gives for (33) $S(a_0 \ll a_{cr}) \approx 2^{3/4}/5^{7/4}$, and consequently $\eta_{rad} \approx 0.20 \xi' a_0^3$. The resulting dependence $\eta_{rad}(a_0)$ calculated for a supergaussian pulse (17) along (32) and (33) is shown on figure 1 by a solid red line and demonstrates an impressive improvement of (16): in the interval of intensities $a_0 = 400 \div 800$ the calculated values do not deviate from the PIC result by more than 20%. Residual discrepancies may largely be ascribed to the fact that (1) tends to overestimate the actual recession velocity since complete reflection is assumed. Notice that radiation losses also contribute to decrease the reflectivity $R = 1 - \eta_{rad}$ and hence reduce the recession velocity, which is principle may create a positive feedback for the enhancement of radiation emission. However, since η_{rad} is quite smaller than unity, these effects appear not to play a significant role.

6. Extension of the classical regime of interaction towards higher intensities

Although the radiation losses appear high compared to those in the 'LS' regime, their significant relative suppression caused by the RFF leads to a specific freezing of the electron lateral motion, so that the relativistic γ-factor grows much slower (15) than in the perturbative domain $a_0 \ll a_{cr}$ where the RFF is negligible. This in turn shifts the border between the classical and the quantum regime of interaction to considerably higher intensities. The significance of QED effects is determined by the value of the relativistically invariant quantum parameter

$$\chi = \frac{e\hbar}{m^3 c^4}\sqrt{-(F^{\mu\nu}p_\nu)^2}, \tag{34}$$

where $F^{\mu\nu}$ is the EM field tensor and p^{ν} is the four-momentum vector. The value of (34) can be easily expressed via the parameters in the reference frame moving with $v_x = v_{HB}$ where

$$p^{\mu} \approx mc\gamma'(1, 0, \sin(\varphi - \theta'), -\cos(\varphi - \theta')), \qquad (35)$$

(see equation (8)). Calculating the tensor $F^{\mu\nu}$ for the fields (7) and taking into account equations (11)–(13), we obtain for (34)

$$\chi = \frac{3}{2\alpha}\xi'(\gamma')^2. \qquad (36)$$

In the weak field regime $a_0 \ll a_{cr}$ this gives for $v_{HB} \ll c$ a quantum parameter $\chi = (3/2\alpha)\xi a_0^2$, so that $\chi \simeq 0.1$ already at $a_0 \approx 200$. Recent work has shown that quantum quenching of radiation losses may be already significant at such modest values of χ [24].

However, in our particular conditions, due to (a) RF induced suppression in the growth of γ' (15) and (b) reduction of ξ' with increasing of v_{HB} a further increase in the laser intensity results in a very slow growth of χ starting from $a_0 \simeq a_{cr}$. In the strong field limit, $a_0 \to \infty$ the HB velocity approaches the speed of light, and the parameter

$$\xi' = \xi\sqrt{\frac{1 - v_{HB}/c}{1 + v_{HB}/c}} \simeq \frac{\xi}{\sqrt{2a_0}A^{1/4}}, \qquad (37)$$

where $A = Zn_c m_e/An_e m_p$ (see equation (1)). For parameters of our simulation $A \approx 3 \times 10^{-6}$. This results in the asymptotic value of the quantum parameter

$$\chi_{\infty} \approx \frac{3}{2\alpha}\left(\frac{a_0\xi^2}{2\sqrt{A}}\right)^{1/4}. \qquad (38)$$

In the range $a_0 = 200 \div 800$ the value of χ increases from 0.092 to 0.436, and even for an 'extreme' amplitude of $a_0 = 2000$ we obtain $\chi \approx 0.636$, showing that the onset of a full radiation-dominated regime is prevented. In addition, with regards to the interaction geometry investigated in our case, these estimates neglect the screening of the laser field in the 'skin' layer (section 5) from which most of the radiation is generated. This allows us to predict that, for the specific interaction geometry of CP pulses and thick overdense targets, QED effects will be strongly quenched compared to the case when the laser pulse and electron bunch counter-propagate or at least the longitudinal electron velocity $v_x \simeq 0$ in the laboratory frame.

7. Conclusions

In conclusion, we have presented a self-consistent analytic model for the interaction of superintense CP laser pulses with thick plasma in the HB regime. The inclusion of the RFF along the lines of Zeldovich's work [25] allowed calculating the conversion efficiency of the laser energy into high frequency radiation in the wide range of intensities. After accounting the effects of (a) the global HB motion of the plasma and (b) of the laser field inhomogeneity in space and time, our result demonstrated a good quantitative agreement with the outcome of the PIC simulation. Note that despite of its analytic simplicity the model is robust with respect to assumptions on the particular shape of electron and ion density distributions in the radiating layer. The effect of the RFF, in combination with the factors (a) and (b), results in a much slower (compared to predictions made in [21]) increase of the conversion efficiency with the laser intensity, so that $\eta \approx 0.25$ at $I_L = 3 \times 10^{24}\,\mathrm{W\,cm^{-2}}$. Consequently, the quantum parameter also grows only slowly with increasing of the laser intensity, $\chi \sim a_0^{1/4}$, which may lead to quantum effects not to dominate even at the highest intensities we considered. This prediction may be tested by simulations with QED effects included.

Acknowledgments

ORCID iDs

S V Popruzhenko ● https://orcid.org/0000-0001-6676-7974
T V Liseykina ● https://orcid.org/0000-0002-5070-3543
A Macchi ● https://orcid.org/0000-0002-1835-2544

References

[1] Mourou G A, Tajima T and Bulanov S V 2006 Optics in the relativistic regime *Rev. Mod. Phys.* **78** 309–71
[2] Di Piazza A, Müller C, Hatsagortsyan K Z and Keitel C H 2012 Extremely high-intensity laser interactions with fundamental quantum systems *Rev. Mod. Phys.* **84** 1177–228
[3] Narozhny N and Fedotov A 2015 Extreme light physics *Contemp. Phys.* **56** 249–68
[4] Sokolov I V 2009 Renormalization of the Lorentz–Abraham–Dirac equation for radiation reaction force in classical electrodynamics *J. Exp. Theor. Phys.* **109** 207–12
[5] Zot'ev D B 2016 Critical remarks on Sokolov's equation of the dynamics of a radiating electron *Phys. Plasmas* **23** 093302
[6] Landau L D and Lifshitz E M 1975 *The Classical Theory of Fields* 2nd edn (Amsterdam: Elsevier) ch 76
[7] Krivitski V S and Tsytovich V N 1991 Average radiation-reaction force in quantum electrodynamics *Sov. Phys.—Usp.* **34** 250
[8] Spohn H 2000 The critical manifold of the Lorentz–Dirac equation *Europhys. Lett.* **50** 287
[9] Tamburini M, Pegoraro F, Di Piazza A, Keitel C H and Macchi A 2010 Radiation reaction effects on radiation pressure acceleration *New J. Phys.* **12** 123005
[10] Vranic M, Martins J, Fonseca R and Silva L 2016 Classical radiation reaction in particle-in-cell simulations *Comput. Phys. Commun.* **204** 141–51
[11] Cole J M *et al* 2018 Experimental evidence of radiation reaction in the collision of a high-intensity laser pulse with a laser-wakefield accelerated electron beam *Phys. Rev. X* **8** 011020
[12] Poder K *et al* 2018 Experimental signatures of the quantum nature of radiation reaction in the field of an ultraintense laser *Phys. Rev. X* **8** 031004
[13] Macchi A 2018 Viewpoint: Intense laser sheds light on radiation reaction *Physics* **11** 13
[14] Andersen K K *et al* 2012 Experimental investigations of synchrotron radiation at the onset of the quantum regime *Phys. Rev. D* **86** 072001
[15] Wistisen T N, Di Piazza A, Knudsen V and Uggerhøj U I 2018 Experimental evidence of quantum radiation reaction in aligned crystals *Nat. Commun.* **9** 795
[16] Naumova N, Schlegel T, Tikhonchuk V T, Labaune C, Sokolov I V and Mourou G 2009 Hole boring in a DT pellet and fast-ion ignition with ultraintense laser pulses *Phys. Rev. Lett.* **102** 025002
[17] Schlegel T, Naumova N, Tikhonchuk V T, Labaune C, Sokolov I V and Mourou G 2009 Relativistic laser piston model: Ponderomotive ion acceleration in dense plasmas using ultraintense laser pulses *Phys. Plasmas* **16** 083103
[18] Capdessus R, Lobet M, d'Humières E and Tikhonchuk V T 2014 γ-ray generation enhancement by the charge separation field in laser-target interaction in the radiation dominated regime *Phys. Plasmas* **21** 123120
[19] Capdessus R and McKenna P 2015 Influence of radiation reaction force on ultraintense laser-driven ion acceleration *Phys. Rev. E* **91** 053105
[20] Nerush E N and Kostyukov I Y 2015 Laser-driven hole boring and gamma-ray emission in high-density plasmas *Plasma Phys. Control. Fusion* **57** 035007
[21] Liseykina T V, Popruzhenko S V and Macchi A 2016 Inverse Faraday effect driven by radiation friction *New J. Phys.* **18** 072001
[22] Del Sorbo D *et al* 2018 Efficient ion acceleration and dense electron positron plasma creation in ultra-high intensity laser-solid interactions *New J. Phys.* **20** 033014
[23] Tamburini M, Lyseykina T V, Pegoraro F and Macchi A 2012 Radiation pressure dominant acceleration: polarization and radiation reaction effects and energy increase in three dimensional simulations *Phys. Rev. E* **85** 016407
[24] Zhang P, Ridgers C P and Thomas A G R 2015 The effect of nonlinear quantum electrodynamics on relativistic transparency and laser absorption in ultra-relativistic plasmas *New J. Phys.* **17** 043051
[25] Zeldovitch Y B 1975 Interaction of free electrons with electromagnetic radiation *Sov. Phys.—Usp.* **18** 79
[26] Robinson A P L, Gibbon P, Zepf M, Kar S, Evans R G and Bellei C 2009 Relativistically correct hole-boring and ion acceleration by circularly polarized laser pulses *Plasma Phys. Control. Fusion* **51** 024004
[27] Esirkepov T, Borghesi M, Bulanov S V, Mourou G and Tajima T 2004 Highly efficient relativistic-ion generation in the laser-piston regime *Phys. Rev. Lett.* **92** 175003
[28] Macchi A, Veghini S, Liseykina T V and Pegoraro F 2010 Radiation pressure acceleration of ultrathin foils *New J. Phys.* **12** 045013
[29] Landau L D and Lifshitz E M 1975 *The Classical Theory of Fields* 2nd edn (Amsterdam: Elsevier) ch 78
[30] Macchi A, Cattani F, Liseykina T V and Cornolti F 2005 Laser acceleration of ion bunches at the front surface of overdense plasmas *Phys. Rev. Lett.* **94** 165003
[31] Kostyukov I Y and Nerush E N 2016 Production and dynamics of positrons in ultrahigh intensity laser-foil interactions *Phys. Plasmas* **23** 093119
[32] Bulanov S S, Esirkepov T Z, Thomas A G R, Koga J K and Bulanov S V 2010 Schwinger limit attainability with extreme power lasers *Phys. Rev. Lett.* **105** 220407

5. He-Droplets in intense laser field

The list of publications:

T.V. Liseykina, S. Pirner, D. Bauer, *Relativistic Attosecond Electron Bunches from Laser-Illuminated Droplets*, Phys. Rev. Lett. **104**, 092002 (2010)

T.V. Liseykina, D. Bauer *Plasma-Formation Dynamics in Intense Laser-Droplet Interaction*, Phys. Rev. Lett. **110**, 145003 (2013)

P. Sperling, T. Liseykina, D. Bauer, R. Redmer, *Time-resolved Thomson scattering on high-intensity laser-produced hot dense helium plasmas*, New J. Phys. **15**, 025041 (2013)

Relativistic Attosecond Electron Bunches from Laser-Illuminated Droplets

T. V. Liseykina,[1,2] S. Pirner,[1] and D. Bauer[1,3]

[1]*Max-Planck-Institut für Kernphysik, Postfach 103980, 69029 Heidelberg, Germany*
[2]*Institute for Computational Technologies, SD-RAS, Novosibirsk, Russia*
[3]*Institut für Physik, Universität Rostock, 18051 Rostock, Germany*

The generation of relativistic attosecond electron bunches is observed in three-dimensional, relativistic particle-in-cell simulations of the interaction of intense laser light with droplets. The electron bunches are emitted under certain angles which depend on the ratios of droplet radius to wavelength and plasma frequency to laser frequency. The mechanism behind the multi-MeV attosecond electron bunch generation is investigated using Mie theory. It is shown that the angular distribution and the high electron energies are due to a parameter-sensitive, time-dependent local field enhancement at the droplet surface.

The understanding of the laser energy conversion into fast electrons and ions is of utmost importance for the design of efficient "tabletop" particle accelerators [1–3]. The laser-plasma-based acceleration schemes discussed so far in the pertinent literature may be divided into two groups according to whether the plasma is underdense, i.e., the plasma frequency ω_p is smaller than the laser frequency ω, or vice versa. Wakefield accelerators and the so-called "bubble regime" (see, e.g., [4–6]) fall into the former category while the interaction of intense laser pulses with solid surfaces or thin foils (see, e.g., [7–11]) belongs to the latter, overdense regime. Of particular interest are finite-size targets where fast particles cannot escape into the field-free bulk material but yet the density of the accelerated particles may be sizable. In recent years the nonrelativistic interaction of intense laser light with small, subwavelength-size clusters has been thoroughly investigated [12]. In particular, the efficient absorption of laser energy, leading to high charge states and thus to intense line emission as well as to energetic electrons and ions was studied. In such small clusters of radii $R < \delta \ll \lambda$, where λ is the laser wavelength and δ is the skin depth of the cluster plasma, the effect of the cluster on the propagation of the laser pulse need not be taken into account. Although the plasma, which is created via field ionization on a subcycle time scale, is overdense, screening of the cluster interior only occurs due to polarization but not due to a skin effect. Technically speaking, the dipole approximation can be applied to the nonrelativistically intense laser field, $E(r, t) \simeq E(t)$. As a consequence, the electron dynamics mainly occurs in the laser polarization direction while the $v \times B$ force in laser propagation direction and the influence of the scattered electromagnetic field on the particle dynamics can be safely neglected.

The other extreme of intense laser-matter interaction is constituted by targets of sizes much larger than a wavelength, e.g., a laser beam impinging on a solid surface. The absorption mechanisms in this case have also been exten-

sively investigated [13]. It is well known, for instance, that for perpendicular incidence electrons are accelerated in laser propagation direction (i.e., into the bulk material).

In this Letter we will focus on electron acceleration in the regime where R and λ are of the same order of magnitude (i.e., rather droplets than clusters) and the laser intensity is relativistic, i.e., the ponderomotive energy U_p exceeds the electron rest energy mc^2. By changing the droplet radius from $R \ll \lambda$ (small-cluster limit) to $R \gg \lambda$ (solid-surface limit) the emission angle of electrons is expected to decrease from $\theta = \pi/2$ to 0 with respect to the propagation direction $\hat{k}$. Moreover, the emission is expected to occur in the $(\hat{E}, \hat{k})$ plane for a linearly polarized laser field of amplitude $\hat{E}$.

For a sphere in a plane electromagnetic wave all angles of incidence occur simultaneously. It is known from laser-plasma interaction studies that, depending on the plasma scale length and the laser intensity, there exists an optimal angle of incidence for the absorption of laser energy [14]: the steeper the plasma gradient, the more this optimal angle is pushed towards $\pi/2$, i.e., grazing incidence. For sufficiently large scale lengths, resonance absorption (see, e.g., [1]) can occur most efficiently under a certain optimal angle. Indeed, this effect, resulting in the electron emission *opposite* to the incoming laser pulse, has been observed in experiments with droplets and two-dimensional model simulations [15].

For $R > \delta$ the self-consistent electromagnetic field needs to be calculated. Numerically we do this by means of three-dimensional, electromagnetic, relativistic particle-in-cell (PIC) simulations using a code which originated from the study in [16]. In such PIC simulations the mean-field particle dynamics, the deformation of the target, and the corresponding modification of the field are automatically taken into account. Analytically, the self-consistent electromagnetic field around and inside a laser-illuminated droplet of given dielectric permittivity ε can be calculated using the corresponding solutions to Maxwell's equations

P H Y S I C A L   R E V I E W   L E T T E R S

put forward by Clebsch, Lorenz, Mie, Debye, and others. The electromagnetic scattering by dielectric or metallic spheres is commonly called "Mie theory" [17]. Of course, the self-consistent particle *dynamics* far from equilibrium in very intense laser fields cannot be captured by a dielectric constant and thus is not included in Mie theory while it is included in the PIC simulations. However, we will show that Mie theory is nevertheless capable of explaining the angular distributions observed in the PIC simulations and the high electron energies exceeding the ponderomotive energy significantly.

We start by presenting typical results from PIC simulations of the interaction of an intense plane wave laser pulse with a preionized, cold He droplet. A spatial resolution of $\Delta x = \Delta y = \Delta z = \lambda/100$ and 64 particles per cell for both electrons and ions were used. Absorbing boundary conditions for the fields and for the particles were employed in propagation direction, periodic ones for the other directions. A linearly (in x direction) polarized 16-cycle $\sin^2$-laser pulse enters the numerical box through the boundary $z = 0$ and propagates into the $z > 0$ half-space. The dimensionless vector potential amplitude $a = |e\hat{A}/mc| = |e\hat{E}/m\omega c|$ of the laser pulse ($\lambda = 800$ nm) was $a = 1$, corresponding to a laser intensity $I \simeq 2 \times 10^{18}$ W/cm^2. The initial density of the He droplet was $n_{e0} = 22n_c$, with $n_c = 1.8 \times 10^{21}$ cm^{-3}. Figure 1 shows a snapshot of the electron isocontour surfaces corresponding to 1% of the initial electron droplet density. Electron bunches emitted each half-cycle under plus or minus a certain angle θ (with respect to the propagation axis z) in forward direction are clearly visible. The bunches are mainly confined to the plane of incidence [i.e., the (x, z) plane].

The electron energy and density for the same He droplet in a four-times more intense laser pulse is presented in Fig. 2. Figure 2(a) shows that the bunches consist of electrons with energies up to $\simeq 6$ MeV. The ponderomotive energy $U_p = mc^2(\sqrt{1 + a^2/2} - 1)$ is only $\simeq 0.37$ MeV. As the spatial width of the bunches is much smaller than a wavelength, the temporal bunch structure is already in the attosecond domain. Similar bunches have been observed in PIC simulations of the interaction of ultraintense laser pulses with solid surfaces under grazing incidence or with plasma channels [18]. Such bunches have potential
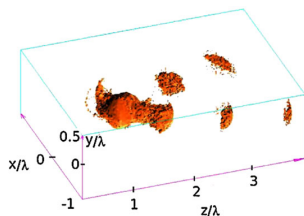
applications in attosecond electron diffraction experiments or the generation of coherent short-wavelength radiation via Thomson scattering.

In the following we will explain the multi-MeV electron energies and their emission angles using Mie theory. The latter gives the analytical electromagnetic field configuration around and inside the (unperturbed) droplet in terms of series expansions over Legendre and Bessel functions [17]. In the case of interest to us, the droplet is conducting ($\varepsilon = 1 - \omega_p^2/\omega^2$), the skin depth $\delta \simeq c/\omega_p \ll R$, and the electric field on the droplet surface is perpendicular to it and quickly decays inside the droplet. Electrons at the droplet surface can be pulled out of the droplet or pushed inside, depending on the time they appear at the surface [7]. Figure 3 shows the absolute value of the radial electric field for an $\omega_p^2/\omega^2 = 22$ times overdense droplet at the droplet surface versus angle θ and time for $R = \lambda/4$ and $R = \lambda/2$ according Mie theory. Note that in our Mie calculations the incident plane wave field is of the form $E_{\text{inc},x}(z, t) = \hat{E}\cos(kz - \omega t)$, i.e., has a constant amplitude. Figure 3 shows that Mie theory predicts certain times and angles at which the electric field at the surface is largest. Moreover, these electric field maxima may exceed the field amplitude $\hat{E}$ [by a factor of 3 in Fig. 3(a) and 2.3 in Fig. 3(b)]. For the bigger droplet the optimal angle is smaller, which means that the maximum electric field occurs more in propagation direction $\theta = 0$. Secondary local maxima are visible at $\theta \simeq 0.45\pi$.

The two panels on the right-hand side of Fig. 3 show the electric vector field in the $y = 0$ plane according to Mie theory at the "optimal" times when the electric field at the surface is highest and points inwards (i.e., it pulls electrons outwards). In Fig. 3(a), for instance, $t \simeq 0.275$ cycles and the largest field occurs under the angle $\theta = 0.27\pi$. It is clear that under the same angle but $x < 0$ the electric field
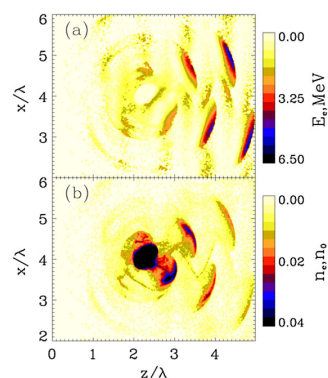

FIG. 2 (color online). Kinetic electron energy (a) and density (b) contour plots (in the $y = 0$ plane) of the He droplet of Fig. 1 in a laser pulse of intensity 8×10^{18} W/cm^2 at $t = 8$ cycles. In the bunch ejected around the pulse maximum, the maximum electron energy is $\simeq 6$ MeV, and 2×10^5 electrons have an energy >3 MeV.

FIG. 1 (color online). Electron isocontour surfaces (1% of n_{e0}) of a $R = \lambda/4$ He droplet in a laser pulse of intensity 2×10^{18} W/cm^2 at $t = 10$ cycles.
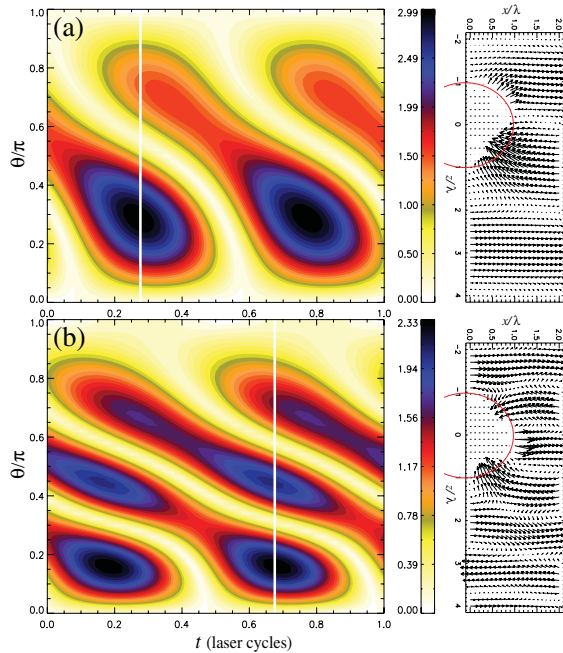
FIG. 3 (color).   Absolute value of the radial electric field for a 22 times overdense droplet at the droplet surface versus angle θ and time, as predicted by Mie theory for $R = \lambda/4$ (a) and $R = \lambda/2$ (b) in the $y = 0$ plane. The color indicates the electric field in units of the incident field strength $\hat{E}$. The plots to the right show the electric vector field in the $y = 0$ plane at the "optimal" times (indicated by white, vertical lines in the left plots) when the electric field at the droplet surface is highest and pointing inwards, i.e., $t = 0.275$ cycles (a) and $t = 0.675$ cycles (b), respectively.

FIG. 4 (color online).   Angle-resolved ion and electron kinetic energy spectra for the $R = \lambda/4$ droplet [(a) ions and (b) electrons] and the $R = \lambda/2$ droplet [(c) ions and (d) electrons] after $t = 9$ cycles in a laser pulse of intensity 2×10^{18} W/cm^2. The emission angle θ [indicated in (c)] was determined as $\theta = \arctan(p_x/p_z)$ with $\boldsymbol{p}$ the momentum. The color coding is proportional to the logarithm of the particle number.

has the same absolute value but points outward. As a consequence, electrons entering from inside the droplet into such a field configuration under this optimal angle will be efficiently accelerated outwards (inwards for $x < 0$). Half a laser cycle later the situation reverses and electrons at $x < 0$ will be accelerated outwards (inwards for $x > 0$). This explains the observation of alternating electron acceleration into two directions each laser cycle.

Figure 4 shows angle-resolved ion and electron energy spectra obtained from the PIC simulations. The spectra were taken at time $t = 9$ cycles when the fast electrons are still inside the simulation box. The ions are hardly set into motion at such an early time. However, the angular distribution of the ions in Figs. 4(a) and 4(c) has already imprinted on them the anisotropy due to the field distribution at the droplet surface. In fact, the emission angles are more easily inferred from the ion distributions than from the electron distributions in Figs. 4(b) and 4(d) because the electrons change their direction as they move away from the droplet. This is why in Figs. 4(b) and 4(d) the energetic electrons are aligned stronger in the forward direction than the slow electrons. The emission angles

inferred from the PIC results in Fig. 4 are $\theta = 0.27\pi$ for the $R = \lambda/4$ droplet and $\theta = 0.14\pi$ for the $R = \lambda/2$ droplet with a secondary maximum at 0.4π. These results are in excellent agreement with the Mie results presented in Fig. 3. We have performed a systematic study, comparing the emission angles predicted by Mie theory with those from the PIC calculations ($a = 2$) for droplet radii between $\lambda/8$ and $\lambda/2$, and in all cases found very good agreement.

The unexpectedly high electron energies can be explained by the field enhancements at the droplet surface. As shown in Fig. 3(a) the field amplitude at the surface of the $R = \lambda/4$ droplet is 3 times the incident field amplitude. We investigated the electron acceleration mechanism by following trajectories of typical PIC electrons ending up in a bunch. We found that for, e.g., the parameters of Fig. 2 the enhanced, radial field at the droplet surface accelerates the bunch electrons over a tenth of a wavelength already up to 90% c. Their subsequent relativistic dynamics is mainly determined by the incoming laser pulse. In particular, the electron bunches remain well-confined in propagation direction as long as they are in the laser pulse. The overdense droplet in essence serves as an electron injector with the enhanced surface field as an efficient preaccelerator. We have also performed test-particle calculations where we placed electrons with zero initial velocity on the droplet surface at various phases with respect to the analytical, time-dependent Mie field configuration. The maximum
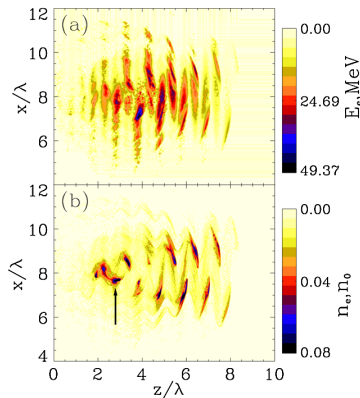
FIG. 5 (color online).   Kinetic electron energy (a) and density (b), as in Fig. 2 but for $a = 20$ (8×10^{20} W/cm²). The arrow in (b) indicates an electron bunch which, after the pulse, acquired an energy of $\simeq 130$ MeV.

kinetic energies acquired by such test electrons are in good agreement with the maximum energies observed in the PIC simulations.

In the limit of small plasma droplets $kR = 2\pi R/\lambda \ll 1$ the maximum radial field at the droplet surface predicted by Mie theory is

$$E_r^{(\text{max})} = 3\hat{E}\,\frac{\omega_p^2/\omega^2 - 1}{\omega_p^2/\omega^2 - 3}. \tag{1}$$

For $\omega_p^2 \gg \omega^2$ one obtains $E_r^{(\text{max})}/\hat{E} = 3$, i.e., a threefold field enhancement, as observed in Fig. 3(a) (although $kR = \pi/2 > 1$ in this case). For, e.g., $\omega_p = 2\omega$, the predicted field enhancement according (1) is $E_r^{(\text{max})}/\hat{E} = 9$, so that one could argue that even more energetic electron bunches can be produced for lower-density droplets. However, only for $a \ll 1$ do the PIC calculations reproduce the predictions of Mie theory as far as the field enhancements at the droplet surface are concerned. This is because for relativistic laser intensities an only few-times overdense droplet quickly dissolves during the rising edge of the laser pulse.

Before concluding we show the simulation result for the droplet of Fig. 2 in an ultraintense laser field of intensity 8×10^{20} W/cm². At the plotting time ($t = 8$ cycles, i.e., at the maximum of the pulse) the highest electron energy observed is $\simeq 50$ MeV. However, if one follows the electron bunch indicated by an arrow in Fig. 5(b), in time one finds a final energy of $\simeq 130$ MeV, i.e., 20 times the ponderomotive energy. From Fig. 5(b) one infers that almost all electrons are removed from the droplet. Nevertheless, the angle under which the electron bunches are emitted is well described by Mie theory. However, the energetic electrons are not only located inside the electron bunches anymore at such high intensities and for such small droplets, as is clearly visible in Fig. 5(a). In order to keep the well-localized electron bunch structure with increasing

laser intensity, the droplet size (or density) should be increased too.

In summary, we showed that multi-MeV attosecond electron bunches are produced when intense laser fields interact with overdense droplets of diameters comparable to the laser wavelength. The attosecond electron bunches are emitted each half-laser cycle under plus or minus a certain angle in the polarization plane. The preferred electron emission angles and the high kinetic energies arise due to local field enhancements at the droplet surface that can be calculated using Mie theory. Relativistic attosecond electron bunches may be used for the generation of short-wavelength radiation, time-resolved structural imaging, or plasma diagnostics.

[1] Paul Gibbon, *Short Pulse Laser Interactions with Matter: An Introduction* (Imperial College Press, London, 2005).
[2] Gerard A. Mourou, Toshiki Tajima, and Sergei V. Bulanov, Rev. Mod. Phys. **78**, 309 (2006).
[3] Yousef I. Salamin *et al.*, Phys. Rep. **427**, 41 (2006).
[4] W. P. Leemans *et al.*, Nature Phys. **2**, 696 (2006).
[5] S. P. D. Mangles *et al.*, Nature (London) **431**, 535 (2004); C. G. R. Geddes *et al.*, *ibid.* **431**, 538 (2004); J. Faure *et al.*, *ibid.* **431**, 541 (2004).
[6] A. Pukhov and J. Meyer-ter-Vehn, Appl. Phys. B **74**, 355 (2002).
[7] F. Brandl *et al.*, Phys. Rev. Lett. **102**, 195001 (2009).
[8] S. Kar *et al.*, Phys. Rev. Lett. **100**, 225004 (2008).
[9] J. Fuchs *et al.*, Phys. Rev. Lett. **99**, 015002 (2007).
[10] J. S. Green *et al.*, Phys. Rev. Lett. **100**, 015003 (2008).
[11] Andrea Macchi *et al.*, Phys. Rev. Lett. **94**, 165003 (2005); F. Pegoraro and S. V. Bulanov, Phys. Rev. Lett. **99**, 065002 (2007).
[12] U. Saalmann, Ch. Siedschlag, and J. M. Rost, J. Phys. B **39** R39 (2006); Th. Fennel *et al.*, arXiv:0904.2706 [Rev. Mod. Phys. (to be published)].
[13] F. Brunel, Phys. Rev. Lett. **59**, 52 (1987); P. Gibbon and A. R. Bell, Phys. Rev. Lett. **68**, 1535 (1992); P. Gibbon, Phys. Rev. Lett. **73**, 664 (1994); S. C. Wilks *et al.*, Phys. Rev. Lett. **69**, 1383 (1992); W. L. Kruer and K. Estabrook, Phys. Fluids **28**, 430 (1985); T.-Y. Bryan Yang *et al.*, Phys. Plasmas **2**, 3146 (1995); M. Cerchez *et al.*, Phys. Rev. Lett. **100**, 245001 (2008); P. Mulser, D. Bauer, and H. Ruhl, Phys. Rev. Lett. **101**, 225002 (2008).
[14] H. Ruhl and P. Mulser, Phys. Lett. A **205**, 388 (1995).
[15] X. Y. Peng *et al.*, Phys. Rev. E **69**, 026414 (2004); Jun Zheng *et al.*, Phys. Plasmas **12**, 113105 (2005); J. Plasma Phys. **72**, 1253 (2006).
[16] V. A. Vshivkov *et al.*, Phys. Plasmas **5**, 2727 (1998).
[17] Max Born and Emil Wolf, *Principles of Optics* (Cambridge University Press, Cambridge, England, 2003).
[18] N. Naumova *et al.*, Phys. Rev. Lett. **93**, 195003 (2004).

Plasma-Formation Dynamics in Intense Laser-Droplet Interaction

T. V. Liseykina[1,2,*] and D. Bauer[1]

[1]*Institut für Physik, Universität Rostock, 18051 Rostock, Germany*
[2]*Institute of Computational Technologies SD RAS, 630090 Novosibirsk, Russia*
(Received 26 September 2012; published 2 April 2013)

We study the ionization dynamics in intense laser-droplet interaction using three-dimensional, relativistic particle-in-cell simulations. Of particular interest is the laser intensity and frequency regime for which initially transparent, wavelength-sized targets are not homogeneously ionized. Instead, the charge distribution changes both in space and in time on a subcycle scale. One may call this the extreme nonlinear Mie-optics regime. We find that—despite the fact that the plasma created at the droplet surface is overdense—oscillating electric fields may penetrate into the droplet under a certain angle, ionize, and propagate in the just generated plasma. This effect can be attributed to the local field enhancements at the droplet surface predicted by standard Mie theory. The penetration of the fields into the droplet leads to the formation of a highly inhomogeneous charge density distribution in the droplet interior, concentrated mostly in the polarization plane. We present a self-similar, exponential fit of the fractional ionization degree which depends only on a dimensionless combination of electric field amplitude, droplet radius, and plasma frequency with only a weak dependence on the laser frequency in the overdense regime.

Introduction.—Spherical, wavelength-sized, homogeneous dielectric or metal objects in plane-wave electromagnetic radiation fall into the realm of Mie theory [1] and are of fundamental importance in optics. Standard Mie theory provides the electromagnetic field configuration inside and outside a homogeneous sphere of a given dielectric constant, assuming an incoming plane wave. However, nowadays available short and intense laser pulses interacting with matter create plasmas on a sublaser period time scale [2,3]. These plasmas, in turn, modify the further propagation of the laser pulse. We call this the extreme nonlinear optics regime, and in the case of (initially) spherical targets, nonlinear Mie optics.

As the laser field propagation is determined by the electron density distribution and the plasma is generated by ionization, the charge state and density distributions are expected to be sensitive to the ionization *dynamics*. In fact, even the strongest present-day lasers cannot directly fully ionize heavier elements so that the assumption of a preformed homogeneous plasma throughout the target with a given dielectric constant, may be inadequate. Furthermore, the skin effect may prevent the laser from penetrating into targets that turn overdense in the course of ionization so that, in general, a richly structured space- and time-dependent charge distribution develops [4]. Such interactions of laser pulses with rapidly self-generated plasmas have already found applications, e.g., as "plasma mirrors," which are routinely used to increase the pulse contrast for intense laser-matter experiments [5,6].

One expects that the part of the laser pulse that is scattered off an overdense target will be mainly determined by the ratio of laser to plasma frequency at the surface whereas possible inhomogeneities inside the target do not play a role. In fact, standard Mie scattering theory assuming a homogeneous, overdense plasma sphere was used to characterize rare gas clusters in recent experiments on a shot-to-shot basis [7,8]. However, *inside* such a sphere, standard Mie theory would predict electric fields only within a narrow skin layer while, in this Letter, we will show that a highly inhomogeneous and temporally changing charge density distribution may be created in the droplet interior. In order to probe such inhomogeneous structures inside the target, laser frequencies greater than the plasma frequency that corresponds to the maximum plasma density in the target should be used. Indeed, Thomson scattering of present-day short-wavelength free-electron laser radiation (from, e.g., DESY in Hamburg, LCLS in Stanford, or SACLA in Japan) is employed to probe overdense plasmas [9–11].

Molecular dynamics is a powerful tool that is widely used to describe the ionization dynamics in small laser-driven clusters [12–14]. However, for wavelength-sized targets such as droplets the influence of the target on the propagation of the incident electromagnetic wave needs to be taken into account self-consistently. This requires the solution of Maxwell's equations together with the equations of motion for the charged particles. In the case of weakly coupled plasmas the problem can be reduced to the solution of the Vlasov-Maxwell system of equations, which is efficiently achieved using particle-in-cell (PIC) codes [2].

Numerically, we study the nonlinear Mie domain by means of a 3D relativistic PIC simulation with ionization included. The code UMKA originated from the study in Ref. [15]. We show that in a certain laser intensity regime the droplet target is neither fully ionized nor are charges

only created at the droplet surface. Instead, fields penetrate under a characteristic angle into the droplet, ionizing atoms in the polarization plane and triggering plasma waves that collide in a focal spot. We present results for the fractional ionization degree at various laser intensities, wavelengths, and densities, that turn out to follow a universal scaling law.

Simulations.—The ionization of an ion with charge state $Z - 1$ and ionization potential I due to the electric field E is implemented using the tunneling ionization rate formula [16]

$$w(E) = \left(\frac{2E_{ch}}{|E|}\right)^{2n^*} \frac{k^2 \hbar}{m} \frac{|E|}{E_{ch}} \exp\left(-\frac{2E_{ch}}{3|E|}\right), \qquad (1)$$

with $k = \frac{\sqrt{2mI}}{\hbar}$, $E_{ch} = \frac{\hbar^2 k^3}{me}$, $n^* = Z\sqrt{\frac{I_H}{I}}$. Here, m is the electron mass and I_H is the ionization potential of atomic hydrogen. When an ionization event takes place a free electron at rest is created at the position of the ion. The energy needed for ionization is taken out of the field via an "ionization current" $\mathbf{j}_{ion}$ parallel to the electric field at the ion location. The value of $\mathbf{j}_{ion}$ is such that $\mathbf{j}_{ion} \cdot \mathbf{E}$ is the work spent on ionization per time step [17,18]. Energy conservation is accounted for during the whole process; if the remaining field energy in a cell is insufficient for further ionization, this cell is not considered anymore during the current time step [19].

We start by presenting typical results from PIC simulations of the interaction of an intense, plane-wave laser pulse with an initially neutral He droplet [20]. A spatial resolution of $\Delta x = \Delta y = \Delta z = \lambda/100$, 125 macroions and 250 macroelectrons per cell were used. Absorbing boundary conditions for the fields and particles were employed in the propagation direction, periodic ones for the other directions. The size of the simulation box was always chosen big enough to rule out any boundary effects on the observables of interest due to reflections or particles leaving the box. A linearly (in the y direction) polarized 10-cycle $\sin^2$-laser pulse of carrier frequency ω_0 enters the numerical box through the boundary $x = 0$ and propagates into the region $x > 0$. The dimensionless vector potential

amplitude $a = |e\hat{A}/mc| = |e\hat{E}/m\omega_0 c|$ was 0.5, corresponding to a laser intensity $I \simeq 5.2 \times 10^{17}$ W/cm², the wavelength $\lambda = 2\pi c/\omega_0$ was 800 nm (i.e., for a laser period $T_L = 2.66$ fs). The density of the $2R = 4\lambda = 3.2$ μm diameter He-droplet was $\rho = 0.14$ g/cm^{-3}. If the droplet was completely preionized such a density would correspond to an electron density $n_{e0} = 24n_{cr}$, where $n_{cr} = 1.8 \times 10^{21}$ cm^{-3} is the critical density for 800-nm wavelength light. The droplet center was located at $x = 4\lambda$, $y = z = 10\lambda$. In the simulations presented in this Letter impact ionization was "switched-off." Test runs showed that for the intensities considered the effect of collisional ionization during the laser pulse is much smaller than that of field ionization. Moreover, self-consistency requires that collisional absorption is taken into account along with the collisional ionization, as in the PIC codes described in Refs. [21–23]. A recently introduced microscopic PIC code [24,25] bridges the gap between PIC and molecular dynamics and is also capable of incorporating collisional ionization and collisional absorption, albeit so far only for smaller targets.

Results.—Figure 1 shows snapshots of the volume distribution of electron and He^{2+} densities. In the beginning the droplet is nonionized and thus transparent for the leading part of the laser pulse. Later, as the field strength of the laser pulse increases in magnitude, ionization becomes more efficient, and an overdense plasma is generated rapidly on the droplet surface as the pulse propagates over it, leading finally to almost full ionization of a thin surface layer. Moreover, we observe that a highly inhomogeneous density distribution inside the droplet is formed, concentrated mostly in the polarization plane. In particular, there seems to be a focal spot [blue area in the polarization plane in Figs. 1(b) and 1(c)]. The fractional ionization degree $I_r = \frac{3}{4\pi R^3 n_{e0}} \int n_e(\mathbf{r}) d^3 r$ of the droplet at the end of the interaction is $\simeq 35\%$.

He^{1+}, He^{2+}, and electron densities in the two perpendicular planes $(\hat{\mathbf{k}}, \hat{\mathbf{E}})$ and $(\hat{\mathbf{k}}, \hat{\mathbf{B}})$ at times $t = 7T_L$ and
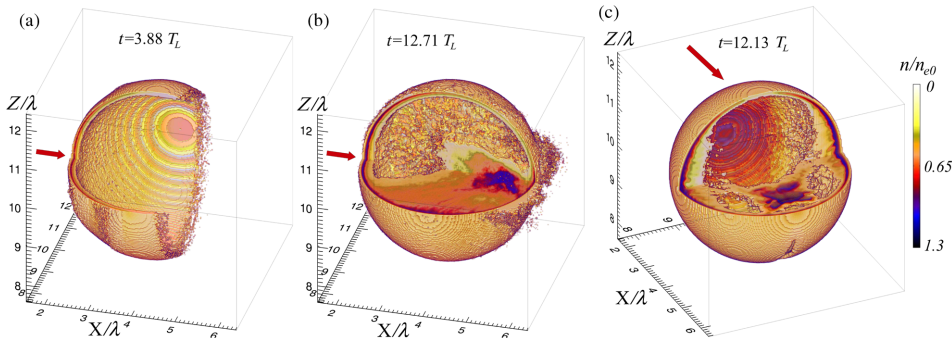

FIG. 1 (color online). Electron density in the beginning (a) and at the end (b) of the interaction with the laser pulse. He^{2+} density (c) at the end of the interaction. For better visualization of the droplet interior a quarter of it was cut out. Laser and droplet parameters are given in the text. The laser propagation direction is indicated by an arrow in each panel.
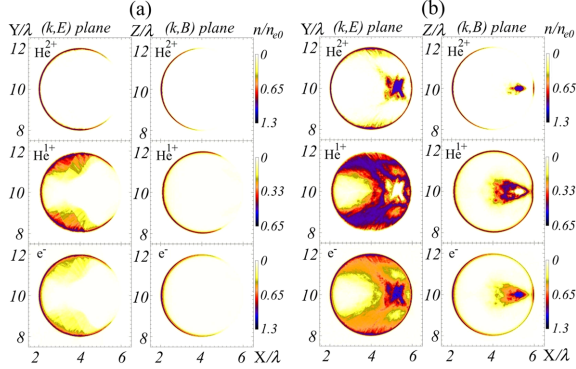
FIG. 2 (color online). Electron (bottom), He^{1+} (middle) and He^{2+} (top) density in two perpendicular planes $(\hat{\mathbf{k}}, \hat{\mathbf{E}})$ (left) and $(\hat{\mathbf{k}}, \hat{\mathbf{B}})$ (right) at $t = 7T_L$ (a) and $t = 12T_L$ (b). Laser and droplet parameters are given in the text.

$t = 12T_L$ are plotted in Fig. 2. Charge density builds up inside the droplet, starting from a certain region on the droplet surface, most clearly seen in the He^{1+}-plot in Fig. 2(a). At the later time in Fig. 2(b) the charge density fronts merged already, creating the focal spot of He^{2+} density. Comparing the charge densities in the two planes shows that the ionization dynamics mainly takes place in the polarization plane $(\hat{\mathbf{k}}, \hat{\mathbf{E}})$. The corresponding distributions of the electric field components (longitudinal E_x and in the polarization direction of the incident laser electric field E_y) are presented in Fig. 3. It is seen that an oscillating electric field penetrates into the droplet, where in Fig. 2 the charge density is created. This is another interesting example for an electric field propagating in a plasma that is created by it in the first place [26]. More precisely, it turns out that the Mie-enhanced field at the surface (discussed in the subsequent paragraph) first results in a deeper penetration and thus more efficient ionization. In addition, the electric field at the surface oscillates and thereby triggers plasma waves which propagate inwards up to the region where plasma has not yet been created. The electric field of the plasma wave then ionizes further, which results in an ionization front propagating inwards.
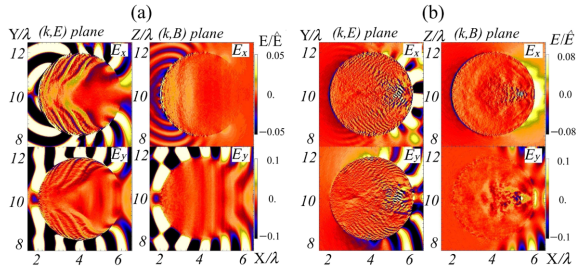
Mie field enhancement.—We attribute the fact that the field and ionization front dynamics originate from a surface region under a certain angle $\theta \gtrsim \pi/2$ (with respect to $\hat{\mathbf{k}}$) to a local, time-dependent field enhancement on the droplet surface. In order to corroborate this statement, we show in Fig. 4 the radial electric field along the droplet surface in the polarization plane vs time and θ as obtained from the PIC simulation (a) and according to Mie theory [1] (b). Standard Mie theory is formulated for plane incident waves. As Mie theory is linear we synthesized our pulse via spectral decomposition and added the fields coherently. In the Mie simulation the droplet is assumed to be homogeneous and conducting, with a dielectric constant $\epsilon = 1 - n_{e0}/n_{cr}$. Under such conditions Mie theory predicts in the strongly overdense regime (where the skin depth is $\delta_e \simeq c/\omega_p \ll R$ with $\omega_p = \sqrt{e^2 n_{e0}/m_e \epsilon_0}$ the electron plasma frequency) that the electric field on the droplet surface is perpendicular to it. In Fig. 4 the time axis has been shifted such that $t = 0$ corresponds to the moment when the maximum of the incident laser pulse arrived at the droplet center. Both the PIC and Mie result predict maxima of the electric field on the droplet surface for angles $\theta/\pi \in [0.4, 0.7]$. The slight disagreement in the field distributions in the forward direction (small θ) is due to the fact that in the Mie calculation the droplet is assumed conducting (i.e., completely ionized) from the very beginning, whereas in the PIC simulation there is not yet plasma at the rear side of the droplet (see Fig. 2). The field enhancement predicted by Mie theory is in excellent agreement with the PIC results ($\simeq 1.9$ times the incident field).

Focused plasma waves.—The propagation direction $\boldsymbol{\chi}$ of the field structures inside the droplet seen in Fig. 3(a) is tilted with respect to $\hat{\mathbf{k}}$, leading to the observed focusing effect. In order to interpret correctly these structures, we project the field components inside the upper half of the droplet onto $\boldsymbol{\chi}$, $E_\tau = E_x \cos\varphi + E_y \sin\varphi$, $E_n = -E_x \sin\varphi + E_y \cos\varphi$, with φ the angle between $\boldsymbol{\chi}$ and $\hat{\mathbf{k}}$ [see Fig. 5(a)].

FIG. 3 (color online). Electric fields (E_x top, E_y bottom) in two perpendicular planes $(\hat{\mathbf{k}}, \hat{\mathbf{E}})$ (left) and $(\hat{\mathbf{k}}, \hat{\mathbf{B}})$ (right) at $t = 7T_L$ (a) and $t = 12T_L$ (b).
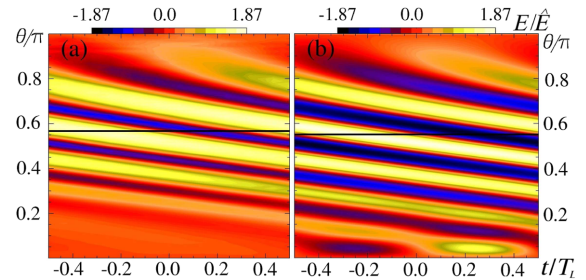

FIG. 4 (color online). Radial electric field along the surface in the polarization plane vs angle θ and time, obtained from the PIC simulation (a) and as predicted by Mie theory (b). The horizontal black lines indicate the angle at which the electric field at the droplet surface is highest.

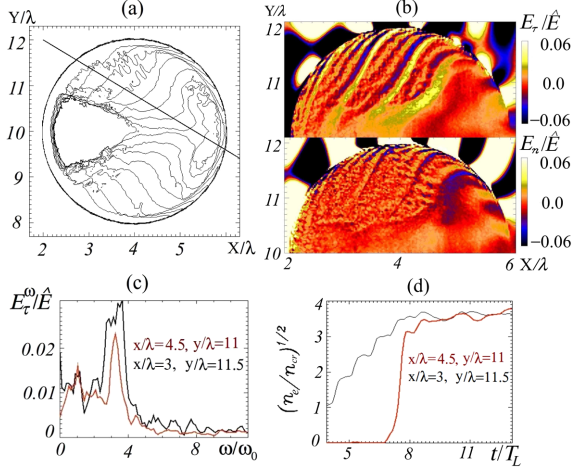P H Y S I C A L   R E V I E W   L E T T E R S

FIG. 5 (color online). (a) The $n = 2.2n_{cr}$ level of the electron density in the droplet central plane $z = 10$ for successive times ($t = 5, 5.4, 6.1, 6.8, 7.4, 8.1, 8.8, 9.4, 10.1T_L$). The straight line indicates the projection direction χ. (b) The distributions of the electric field component E_τ parallel and E_n perpendicular to χ at $t = 8T_L$. (c) Frequency spectra of the electric field E_τ at the points $\mathbf{r}_1 = (3, 11.5, 10)$ and $\mathbf{r}_2 = (4.5, 11, 10)$ inside the droplet. (d) $\sqrt{n_e/n_{cr}}$ vs time at the points $\mathbf{r}_1$ and $\mathbf{r}_2$.

The resulting field distributions for E_τ and E_n are shown in Fig. 5(b). As the values of E_τ are several times bigger than the values of E_n, we identify the field structures as a longitudinal plasma wave. The necessary matching of the plasma wave to the electromagnetic field at the droplet surface results in the tilt of χ with respect to $\hat{\mathbf{k}}$ because the phase velocity of the plasma wave is smaller than c. The frequency spectra of the electric field at two points $x = 3\lambda$, $y = 11.5\lambda$, and $x = 4.5\lambda$, $y = 11\lambda$ inside the droplet are shown in the Fig. 5(c). They peak at the frequency approximately equal to the local plasma frequency, which may be estimated from the plot of the local density vs time in Fig. 5(d).

Fractional ionization degree.—Figure 6 collects all our simulation results for the final fractional ionization degree I_r. Introducing the dimensionless parameter $\eta = a/(R\lambda/\delta_e^2)$, it turns out that for all the various cluster sizes $R > \delta_e$, densities $\omega_p^2 \gg \omega_0^2$, laser intensities and wavelengths simulated, I_r is well described by $I_r \simeq 1 - \exp(-\gamma\eta)$. In our case of He we find $\gamma = 1560$. Note that the species dependence only enters via the ionization potentials I in the tunneling ionization rate formula (1). Inserting the expression for the collisionless skin depth $\delta_e = c/\sqrt{\omega_p^2 - \omega_0^2}$ we obtain $\eta = e\hat{E}/[2\pi mR(\omega_p^2 - \omega_0^2)] \simeq e\hat{E}/(2\pi mR\omega_p^2)$, showing that there is only a weak dependence on the laser frequency. Indeed, for tunneling ionization the electric field amplitude matters, not the laser frequency. For small laser intensity and sufficiently big
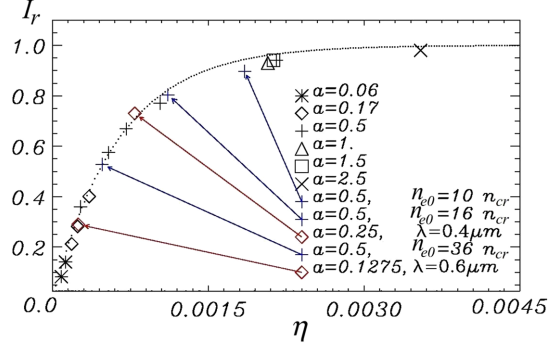

FIG. 6 (color online). Universal curve $I_r = 1 - \exp(-\gamma\eta)$ (dotted) with $\eta = a/(R\lambda/\delta_e^2) = e\hat{E}/[2\pi mR(\omega_p^2 - \omega_0^2)]$ for the final fractional ionization degree of the He droplet after the interaction with a plane-wave laser pulse. The total laser pulse duration in all cases was 26 fs. The symbols for different a are indicated in the plot. For some of them, runs with different density or laser wavelength have been performed, as indicated directly by arrows. The numerical values for a, R/λ, n_{e0}/n_{cr}, and I_r are given in the Supplemental Material [20].

droplets, when only the thin skin layer on the droplet surface gets ionized, one expects $I_r = \frac{4\pi R^2 \delta_e}{4\pi R^3/3} \sim R^{-1}$. In the opposite limit of very high laser intensity or small droplets complete ionization $I_r = 1$ is expected. Both limiting cases are contained in our formula. The chosen exponential interpolation between those two limiting cases matches the simulation results for the fractional ionization degree very well.

Summary.—A strong near-infrared or optical laser pulse interacting with an initially neutral, wavelength-sized He-droplet may generate a charge density distribution that neither is homogeneous throughout the droplet nor created only within a thin skin layer at the surface. Instead, electric fields may penetrate into the droplet interior for certain angles of incidence predicted by standard Mie theory. However, the time-dependent field and density distributions inside the target are not accessible to standard Mie theory but fall into the realm of extreme nonlinear optics. The field penetration causes ionization inside the droplet, mainly confined to the polarization plane. The resulting inhomogeneous charge distribution may be probed via scattering of short-wavelength radiation and should be taken into account when studying typical laser-plasma interaction applications such as ion acceleration or x-ray radiation from recombination in ionized droplets. A particularly high abundance of He^{2+} is observed where the ionization fronts and the trailing plasma waves collide. The fractional ionization degrees for various droplet and laser parameters are found to be in good agreement with a self-similar exponential fit. At higher laser intensities a qualitatively similar ionization dynamics is expected for higher-Z materials as well.

*tatyana.liseykina@uni-rostock.de

[1] M. Born and E. Wolf, *Principles of Optics* (Cambridge University Press, Cambridge, England, 2003).

[2] P. Gibbon, *Short Pulse Laser Interactions with Matter, an Introduction* (Imperial College Press, London 2005).

[3] P. Mulser and D. Bauer, *High-Power Laser-Matter Interaction* (Springer, Berlin, Heidelberg, 2010).

[4] E. C. Jarque, F. Cornolti, and A. Macchi, J. Phys. B **33**, 1 (2000).

[5] H. C. Kapteyn, M. M. Murnane, A. Szoke, and R. W. Falcone, Opt. Lett. **16**, 490 (1991).

[6] C. Thaury, F. Quéré, J.-P. Geindre, A. Levy, T. Ceccotti, P. Monot, M. Bougeard, F. Réau, P. d'Oliveira, P. Audebert, R. Marjoribanks, and Ph. Martin, Nat. Phys. **3**, 424 (2007).

[7] C. Bostedt, E. Eremina, D. Rupp, M. Adolph, H. Thomas, M. Hoener, A. R. B. de Castro, J. Tiggesbäumker, K.-H. Meiwes-Broer, T. Laarmann, H. Wabnitz, E. Plönjes, R. Treusch, J. R. Schneider, and T. Möller, Phys. Rev. Lett. **108**, 093401 (2012).

[8] D. Rupp, M. Adolph, T. Gorkhover, S. Schorb, D. Wolter, R. Hartmann, N. Kimmel, C. Reich, T. Feigl, A. R. B. de Castro, R. Treusch, L. Strüder, T. Möller, and C. Bostedt, New J. Phys. **14**, 055016 (2012).

[9] P. Sperling, T. Liseykina, D. Bauer, and R. Redmer, New J. Phys. **15**, 025041 (2013).

[10] S. H. Glenzer and R. Redmer, Rev. Mod. Phys. **81**, 1625 (2009).

[11] P. Sperling, R. Thiele, B. Holst, C. Fortmann, S. H. Glenzer, S. Toleikis, Th. Tschentscher, and R. Redmer, High Energy Density Phys. **7**, 145 (2011).

[12] T. Döppner, J. P. Müller, A. Przystawik, S. Göde, J. Tiggesbäumker, K.-H. Meiwes-Broer, C. Varin, L. Ramunno, T. Brabec, and T. Fennel, Phys. Rev. Lett. **105**, 053401 (2010).

[13] Th. Fennel, K.-H. Meiwes-Broer, J. Tiggesbäumker, P.-G. Reinhard, P. M. Dinh, and E. Suraud, Rev. Mod. Phys. **82**, 1793 (2010).

[14] A. Mikaberidze, U. Saalmann, and J. M. Rost, Phys. Rev. Lett. **102**, 128102 (2009).

[15] V. A. Vshivkov, N. M. Naumova, F. Pegoraro, and S. V. Bulanov, Phys. Plasmas **5**, 2727 (1998).

[16] V. S. Popov, Phys. Usp. **47**, 855 (2004).

[17] S. C. Rae and K. Burnett, Phys. Rev. A **46**, 2077 (1992).

[18] P. Mulser, F. Cornolti, and D. Bauer, Phys. Plasmas **5**, 4466 (1998).

[19] A. J. Kemp, Y. Sentoku, T. Cowan, J. Fuchs, and H. Ruhl, Phys. Plasmas **11**, L69 (2004).

[20] See Supplemental Material at http://link.aps.org/supplemental/10.1103/PhysRevLett.110.145003 for discussion of the case of focused pulses.

[21] Y. Sentoku and A. J. Kemp, J. Comput. Phys. **227**, 6846 (2008).

[22] R. A. Fonseca, L. O. Silva, F. S. Tsung, V. K. Decyk, W. Lu, C. Ren, W. B. Mori, S. Deng, S. Lee, T. Katsouleas, and J. C. Adam, *Computational Science - ICCS 2002*, Lecture Notes in Computer Science Vol. 2331 (Springer, Berlin, 2002), p. 342.

[23] E. Lefebvre, N. Cochet, S. Fritzler, V. Malka, M.-M. Aleonard, J.-F. Chemin, S. Darbon, L. Disdier, J. Faure, A. Fedotoff, O. Landoas, G. Malka, V. Meot, P. Morel, M. R. Le Gloahec, A. Rouyer, Ch. Rubbelynck, V. Tikhonchuk, R. Wrobel, P. Audebert, and C. Rousseaux, Nucl. Fusion **43**, 629 (2003).

[24] Ch. Varin, Ch. Peltz, Th. Brabec, and Th. Fennel, Phys. Rev. Lett. **108**, 175007 (2012).

[25] C. Peltz, C. Varin, T. Brabec, and T. Fennel, New J. Phys. **14**, 065011 (2012).

[26] A. Debayle and V. T. Tikhonchuk, Phys. Plasmas **14**, 073104 (2007).

New Journal of Physics

Time-resolved Thomson scattering on high-intensity laser-produced hot dense helium plasmas

P Sperling[1], T Liseykina, D Bauer and R Redmer

Institut für Physik, Universität Rostock, D-18051 Rostock, Germany
E-mail: philipp.sperling@uni-rostock.de

Abstract. The introduction of brilliant free-electron lasers enables new pump–probe experiments to characterize warm and hot dense matter states, i.e. systems at solid-like densities and temperatures of one to several hundred eV. Such extreme conditions are relevant for high-energy density studies such as, e.g., in planetary physics and inertial confinement fusion. We consider here a liquid helium jet pumped with a high-intensity optical short-pulse laser that is subsequently probed with brilliant soft x-ray radiation. The optical short-pulse laser generates a strongly inhomogeneous helium plasma which is characterized with particle-in-cell simulations. We derive the respective Thomson scattering spectrum based on the Born–Mermin approximation for the dynamic structure factor considering the full density and temperature-dependent Thomson scattering cross section throughout the target. We observe plasmon modes that are generated in the interior of the target and study their temporal evolution. Such pump–probe experiments are promising tools to measure the important plasma parameters density and temperature. The method described here can be applied to various pump–probe scenarios by combining optical lasers, soft x-rays and hard x-ray sources.

[1] Author to whom any correspondence should be addressed.

2   **IOP** Institute of Physics ⬤ DEUTSCHE PHYSIKALISCHE GESELLSCHAFT

Contents

1. Introduction

Matter at high energy densities occurs in extreme conditions of pressure and/or temperature as relevant for astrophysics, e.g. in the deep interior of planets, in brown dwarfs or in stars [1–3]. Another important example is the concept of intertial confinement fusion, which relies on the full understanding and control of cryogenic deuterium-tritium capsules driven to high energy densities by powerful lasers as used at the National Ignition Facility in Livermore [4] or, in the near future, at the Laser Megajoule near Bordeaux; for a review, see [5].

Such extreme states of matter can be generated using various techniques. For instance, high-energy particle beams (e.g. heavy-ion beams at GSI Darmstadt) or intense short-wavelength radiation from free electron lasers (FELs, e.g. FLASH Hamburg, LCLS Stanford, Elettra Trieste and SACLA Kobe), which are brilliant soft or hard x-ray radiation sources, can be used to heat targets volumetrically. In contrast, optical lasers penetrate only into a thin surface layer (skin depth) of the target. The solid-density plasma that is generated due to rapid tunneling ionization acts as a mirror for optical wavelengths. The electrons can gain relativistic energies in the laser pulse and induce important processes in the plasma such as impact ionization and bremsstrahlung [6–8]. With the planned installation of new high-energy and ultra-short-pulse laser facilities such as the Extreme Light Infrastructure, intensities up to $10^{24}\,\mathrm{W\,cm^{-2}}$ will be accessible in the near future. These intensities enable the production of hot dense matter (HDM) with densities close to solid density up to compressed matter well above solid density, but with electron temperatures T_e above $100\,\mathrm{eV}$ and hence above the warm dense matter regime.

The investigation of such plasmas requires probe lasers that operate at frequencies higher than the plasma frequency $\omega_{pe}^2 = n_e e^2/(\epsilon_0 m_e)$ of the free-electron subsystem, with the free-electron density n_e and the electron mass m_e. Therefore, efficient x-ray sources with high brightness are inevitable for probing plasmas with densities at solid or even higher densities. Energetic optical lasers such as Omega (Rochester), Gekko (Osaka), Titan (Livermore), Vulcan (RAL) or Phelix (Darmstadt) can be used to generate intense but incoherent x-ray radiation. Alternatively, FELs provide brilliant and coherent radiation for such purposes. The FLASH in Hamburg [10, 11] operates in the soft x-ray region, while the LCLS in Stanford and the future European XFEL in Hamburg yield hard x-ray radiation. Simultaneously, x-ray Thomson scattering is a promising tool for the diagnostics of dense strongly correlated plasmas [9] in the HDM region. Therefore, this technique is already implemented at the Matter in Extreme

Conditions (MEC) instrument at LCLS and will be installed at the high energy density (HED) matter experiments instrument at the future XFEL in Hamburg.

Collective x-ray Thomson scattering experiments yield information on the density and temperature of dense plasmas [12]. For a homogeneous density and temperature profile throughout the target, these parameters can be determined directly from the plasmon dispersion and the ratio of the plasmon amplitudes via the detailed balance relation [13]. For laser frequencies below the plasma frequency for solid targets, i.e. optical lasers and energies of about 25–30 eV accessible with FLASH, the target is overdense and the absorption is limited to the skin depth, whereas the excitation by high-frequency FEL radiation generates smoother gradients [14]. The scattering signal represents an average of the local density- and temperature-dependent scattering cross sections weighted with the respective density and temperature profiles [15], which are generated not only by the pump pulse but also by the probe pulse if intense x-ray radiation pulses are used as in the case of the FLASH and LCLS facilities. Therefore, a consistent treatment of the light–matter interaction within pump–probe experiments is crucial for the determination of the plasma density and temperature, their profiles throughout the target and their temporal evolution. Furthermore, the electron–ion equilibration rate can be extracted from the Thomson scattering spectrum by varying the time delay between the pump and probe pulses.

The derivation of an inhomogeneous Thomson scattering signal weighted with the respective density and temperature profiles was shown earlier by Thiele *et al* [16], who investigated the averaged Thomson scattering signal of an inhomogeneous hydrogen plasma produced by an optical laser of wavelength $\lambda = 800$ nm and intensity $I = 10^{15}$ W cm^{-2}. The temporal evolution of a set of plasmon pairs characterizing different regions of the droplet could be monitored. These plasmon pairs stem from the warm dense droplet front generated by the optical laser, whereas a non-collective scattering signal representing the cold interior of the droplet was found to be caused by the FEL.

The goal of the present paper is to demonstrate the capacity of x-ray Thomson scattering experiments for HED studies. Furthermore, the role of inhomogeneities that cannot be avoided in laser–matter interaction on ultra-short time scales is investigated by using small helium droplets as the target material. For this purpose, we study here the interaction of helium droplets with a high-intensity short-pulse laser at medium to high intensities of $I = 10^{15}$, 10^{18} and 10^{19} W cm^{-2}, which generates HDM in different regimes. The x-ray Thomson scattering spectra are calculated in order to test whether the corresponding plasma parameters can be extracted from them.

2. Theory for the dynamic structure factor

We start with the scattered power per solid angle $\mathrm{d}\Omega = \sin\theta \, \mathrm{d}\theta \, \mathrm{d}\varphi$ and per unit frequency interval $\mathrm{d}\omega$ which is experimentally accessible and given by the following expression [15]:

$$\frac{\mathrm{d}^2 P_{sc}}{\mathrm{d}\Omega \mathrm{d}\omega} = \frac{\sigma_T}{A_{rad}} \frac{k_f}{k_i} \int_{-\infty}^{\infty} \frac{\mathrm{d}\omega'}{2\pi} G_{\Delta\omega}(\omega - \omega') \int \mathrm{d}\mathbf{r} \, l(\mathbf{r}) S_{ee}(k, \omega'; T(\mathbf{r}), n(\mathbf{r})) n_e(\mathbf{r}). \quad (1)$$

Here, $\sigma_T = 6.65 \times 10^{-24}$ cm^2 is the Thomson scattering cross-section, k_i and k_f are the initial and final photon wavenumbers, and the energy and momentum transfer are given by $\Delta E = \hbar\omega = \hbar\omega_f - \hbar\omega_i$ and $\hbar\mathbf{k} = \hbar\mathbf{k}_f - \hbar\mathbf{k}_i$. The central quantity for the determination of the scattering signal

is the dynamic structure factor (DSF) $S_{ee}(\mathbf{k}, \omega)$, which can be calculated for given profiles of electron density $n_e(\mathbf{r})$, electron temperature $T_e(\mathbf{r})$, ion density $n_i(\mathbf{r})$ and ion temperature $T_i(\mathbf{r})$, i.e. for the general case of an inhomogeneous target. The momentum transfer is related to the scattering angle θ in the limit $\hbar\omega \ll \hbar\omega_0$ according to $k = 4\pi\sin(\theta/2)/\lambda_0$, with λ_0 being the probe wavelength. $l(\mathbf{r})$ is the $\mathbf{r}$-dependent power density of the probe beam taking into account absorption in the and target, A_{rad} is the irradiated surface of the target. The DSF has to be convoluted with the instrumental function $G_{\Delta\omega}(\omega)$ that models the spectrometer's finite spectral resolution as well as the probe's spectral bandwidth. Usually, a normalized Gaussian distribution is employed with the full-width at half-maximum (FWHM) $\Delta\omega$.

The DSF can be written in terms of free–free, bound–free and bound–bound correlations as proposed by Chihara [17, 18]:

$$S_{ee}(k, \omega) = Z_{free}S_{ee}^0(k, \omega) + |f_i(k) + q(k)|^2 S_{ii}(k, \omega) + Z_c \int_{-\infty}^{\infty} d\omega' S_c(k, \omega) S_s(k, \omega - \omega'). \quad (2)$$

Here, $Z_{free} = n_e/n_i$ is the ionization degree of the plasma and Z_c is the averaged number of core electrons. The three terms in equation (2) are discussed below.

In this paper, we consider the contribution of free electrons $S_{ee}^0(k, \omega)$ (the first term in equation (2)), which is connected with the longitudinal dielectric function $\epsilon(k, \omega)$ via the fluctuation–dissipation theorem

$$S_{ee}^0(k, \omega) = -\frac{\epsilon_0 \hbar k^2}{\pi e^2 n_e} \frac{\operatorname{Im}\epsilon^{-1}(k, \omega)}{1 - \exp\left(-\frac{\hbar\omega}{k_B T_e}\right)}. \quad (3)$$

Considering free electrons without interactions the dielectric function is given by the random phase approximation (RPA) for the one-component plasma. Including interactions between the particles in the plasma via the dynamic electron–ion collision frequency $\nu(\omega)$ [19], the more general approach of Mermin [20] can be applied to the dielectric function, which then reads

$$\epsilon^M(k, \omega) - 1 = \frac{\left(1 + i\frac{\nu(\omega)}{\omega}\right)[\epsilon^{RPA}(k, \omega + i\nu(\omega)) - 1]}{1 + i\frac{\nu(\omega)}{\omega}\frac{\epsilon^{RPA}(k, \omega + i\nu(\omega)) - 1}{\epsilon^{RPA}(k, 0) - 1}}. \quad (4)$$

Calculating the electron–ion collision frequency in Born approximation defines the Born–Mermin approximation (BMA) [13, 21–23].

A further analysis of the DSF for free electrons and the Thomson scattering process on free electrons is possible via the scattering parameter $\alpha = \kappa_e/k$, which relates the inverse screening length κ_e (given below) to the wavenumber k. For $\alpha < 1$ the scattering is non-collective and we can investigate short-range correlations, while long-range correlations are relevant for collective scattering ($\alpha > 1$). In the case of long-range correlations, the DSF $S_{ee}^0(k, \omega)$ shows two particularly pronounced side maxima which are located symmetrically relative to the central ion feature described by the second term of equation (2). These peaks are directly related to the free electron density via the plasmon frequency [12, 13, 21].

For the calculation of the second term in the Chihara formula (2) which characterizes the scattering on bound electrons, we use the atomic form factor $f_i(k)$ [24] and the simple Debye–Hückel ion–ion structure factor for point charges [25]

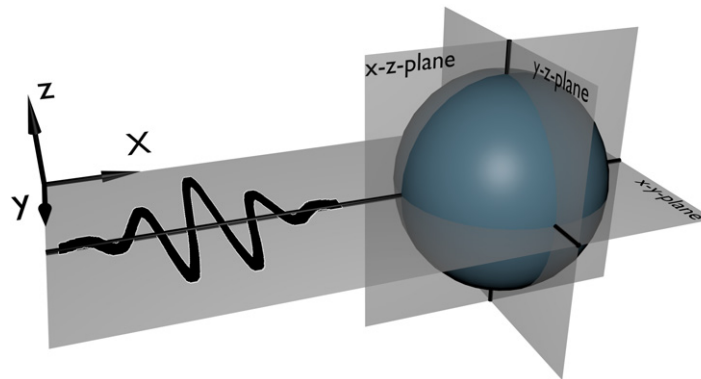$$S_{ii}(k) = \frac{k^2 + \kappa_e^2}{k^2 + \kappa_i^2 + \kappa_e^2} \quad (5)$$

Figure 1. Illustration of the three different spatial planes relative to the pumping, Gaussian-shaped laser pulse.

with the inverse screening length $\kappa_c = \sqrt{e_c^2 n_c/(\epsilon_0 k_B T_c)}$ for species $c = $ e (electrons) and $c = $ i (ions). In the Debye–Hückel picture, the screening cloud can be given with the electron–ion structure factor by $q(k) = \sqrt{Z_{\text{free}}} S_{\text{ei}}(k)/S_{\text{ii}}(k) = Z_{\text{free}} \kappa_e^2/(k^2 + \kappa_e^2)$.

For the last term in equation (2), the contribution of bound–free transitions S_c, we use the formalism of Schumacher *et al* [24, 26]. This part describes Raman-type transitions of inner shell electrons to the continuum which are modulated by the ion motion contained in $S_s(k, \omega)$ [27]. Here, this contribution is to be neglected for the relevant energy range of -10 to 10 eV, where the Thomsons scattering signal of free electrons can be obtained.

3. Plasma generation in helium droplets

As a proposal for future experiments on inhomogeneous HDM states, we describe in this section the interaction between cryogenic helium droplets and a high-intensity short-pulse optical pump laser with different intensities. We consider for this purpose helium droplets of $d = 6.4 \, \mu$m diameter at an initial temperature $T_{\text{ini}} = 20$ K and density $n = 2.2 \times 10^{22} \, \text{cm}^{-3}$. The profiles of electron temperature and density generated in the strongly inhomogeneous helium plasma are simulated with a particle-in-cell (PIC) code [28], where field ionization processes are included via a tunnel ionization rate [29]. The setup of the pump–probe experiment on the helium droplet is illustrated in figure 1.

3.1. A pump laser with an intensity of $10^{15} \, \text{W cm}^{-2}$

First, we consider a linearly polarized optical laser pulse of wavelength $\lambda = 800$ nm, pulse duration $t_{\text{FWHM}} = 30$ fs, energy $E = 3.2 \, \mu$J and focal spot diameter $d_{\text{FWHM}} = 3 \, \mu$m which irradiates a helium droplet. We apply the corresponding intensity of $10^{15} \, \text{W cm}^{-2}$ in order to compare with the previous results for hydrogen given by Thiele *et al* [16]. Note that we use here a three orders of magnitude smaller laser energy than that in [16]. To investigate the interaction of the optical laser with the helium droplet, a PIC simulation in a cubic box of $8 \times 8 \times 8 \, \mu\text{m}^3$ size was performed for a duration up to $t = 400$ fs after the maximum of the optical pump laser pulse. Such long simulation times are necessary to obtain an equilibrated system for the temperature determination. We used $500 \times 500 \times 500$ grid cells with 64 heavy particles each.
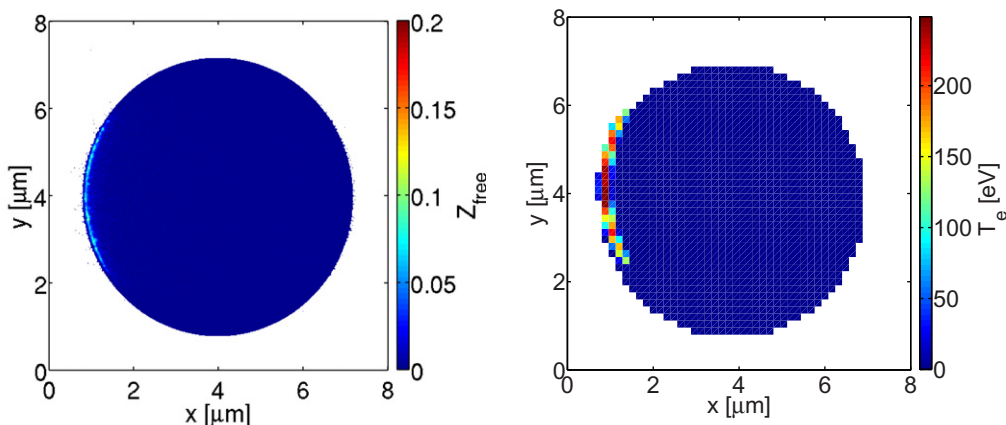
Figure 2. Profiles of the ionization degree Z_{free} (left) and electron temperature T_e (right) at a time of $t = 400\,\text{fs}$ after the pulse maximum. The optical laser irradiates the droplet from the left along the x-axis. Due to the small laser energy $3.2\,\mu\text{J}$ and intensity $10^{15}\,\text{W cm}^{-2}$, only a weakly ionized and thin front is observed at the droplet surface.

The resulting profiles for the electron temperature and the ionization degree are shown in figure 2 for the laser polarization plane at $t = 400\,\text{fs}$ after the maximum of the pump laser pulse. Here, a weakly ionized droplet front of several $10\,\text{nm}$ thickness comparable to the skin depth is observed. Compared to the work of Thiele *et al* [16] for hydrogen a less ionized and less extended plasma front is obtained for helium, which is due to the reduced laser energy and the higher ionization potential of helium atoms. The temperature is determined on a reduced grid of $50 \times 50 \times 50$ cells and adjusted to a Maxwell–Boltzmann statistics via the particle energies.

3.2. A pump laser with an intensity of $10^{18}\,\text{W cm}^{-2}$

To observe a higher ionized plasma we consider the laser–droplet interaction with a more intense laser pulse of $3.2\,\text{mJ}$ energy and $30\,\text{fs}$ duration so that the intensity is $10^{18}\,\text{W cm}^{-2}$. These laser parameters are close to the relativistic regime where the ionized electrons reach relativistic velocities. Such a laser is currently not available at FLASH, but for future experiments at the XFEL in Hamburg or at LCLS in Stanford (where a corresponding short-pulse laser is already installed in the MEC instrument) such setups would be possible. Again the simulation is performed in a cubic box of $8 \times 8 \times 8\,\mu\text{m}^3$ size on $500 \times 500 \times 500$ grid cells with 64 heavy particles each for a duration up to a time of $t = 440\,\text{fs}$ after the maximum of the optical pump laser pulse.

The resulting profiles of the ionization degree are shown in figure 3 for three spatial planes at $t = 80\,\text{fs}$ after the maximum of the pump laser pulse: the laser polarization plane, the x–z plane perpendicular to the laser polarization plane and the y–z plane perpendicular to the laser axis as illustrated in figure 1. The results for the different planes through the droplet center indicate an inhomogeneous, asymmetrical ionization along the laser axis. In the x–z plane perpendicular to the laser polarization plane, we obtain an overcritical, highly ionized front of several tens of nm thickness. In addition, in the polarization plane in the interior of the droplet an ionized plasma is observed due to the penetration of the laser into the droplet. This effect can
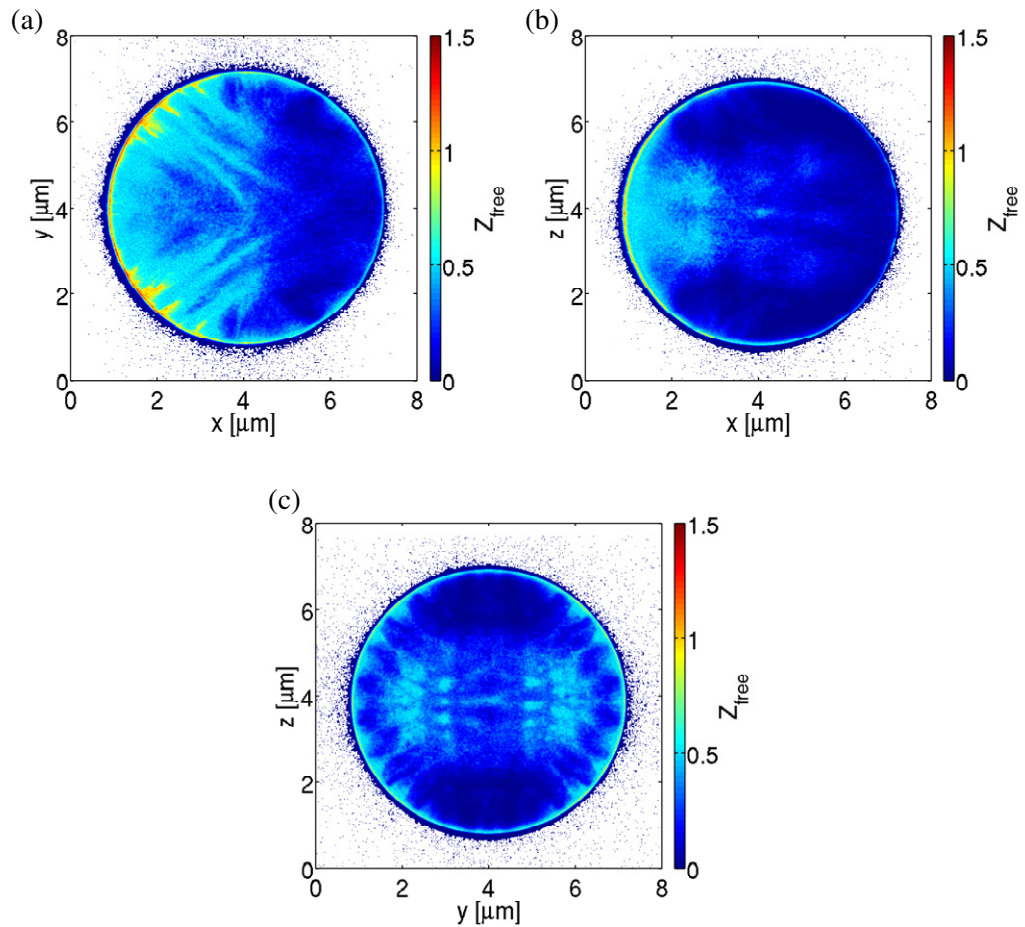
Figure 3. Profile of ionization degree Z_{free} for different planes through the droplet center at a time of $t = 80\,fs$ after the maximum of the optical pump laser pulse with an intensity of $10^{18}\,W\,cm^{-2}$ and an energy of $3.2\,\mu J$. Illustrated are (a) the laser polarization plane, (b) the x–z plane perpendicular to the laser polarization plane and (c) the y–z plane perpendicular to the laser axis. The optical laser has irradiated the droplet from the left along the x-axis. We obtain an asymmetric ionization of the droplet which is caused by a focused penetration of the laser into the droplet. The effect may be understood using Mie theory [30].

be understood in terms of an enhanced electric field at the droplet surface (as predicted by Mie theory) and a plasma wave propagating from there into the target, ionizing also the interior of the droplet; this is investigated in more detail in [30].

For the calculation of Thomson scattering spectra via the BMA temperature and density profiles throughout local thermal equilibrated droplets are necessary. Therefore, results for a substantially longer time $t = 440\,fs$ after the maximum of the pump laser pulse are illustrated in figure 4. Here, the ionization degree is given for the laser polarization plane and the plane perpendicular to the laser axis on the left side of figure 4. The corresponding electron temperature profiles were derived from a reduced grid of $50 \times 50 \times 50$ boxes, see the right side of figure 4. For such longer times we observe a highly ionized droplet front and, in contrast
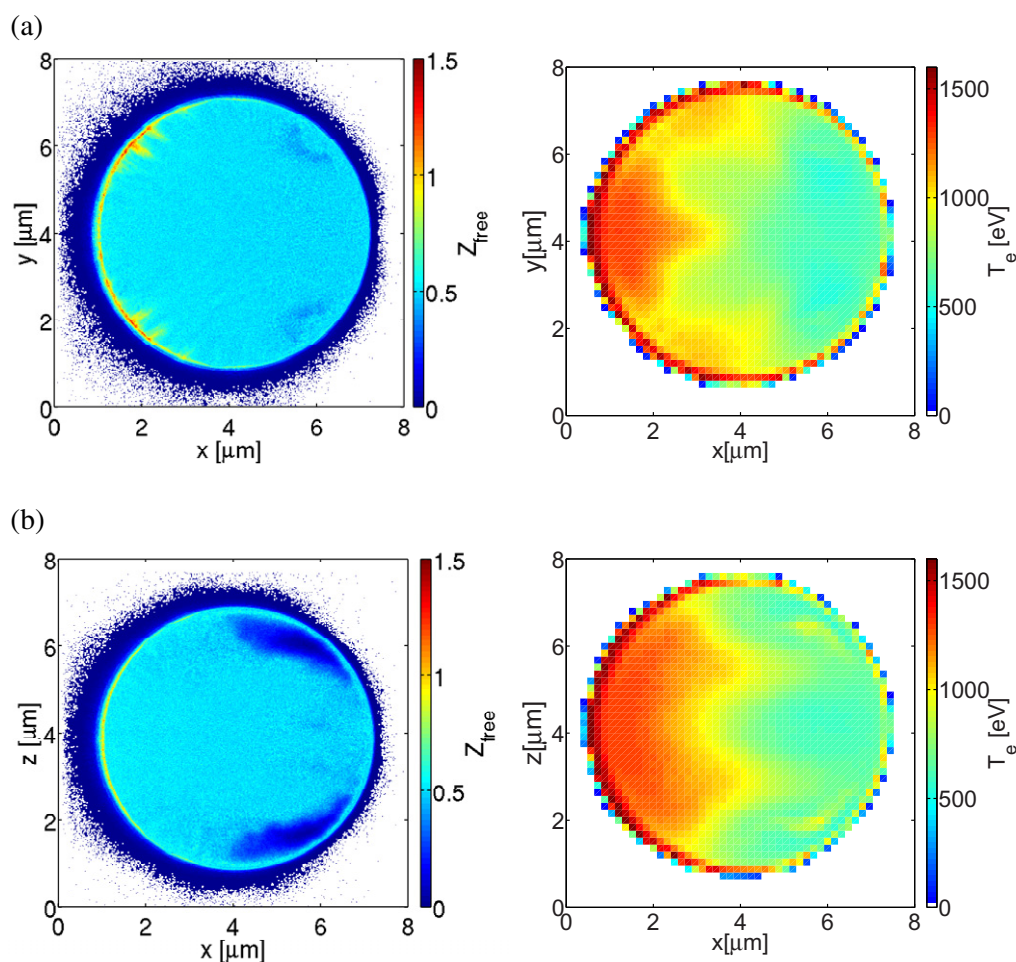
Figure 4. The ionization degree Z_{free} (left) and electron temperature T_e (right) for different droplet planes at a time of $t = 440\,fs$ after the pulse maximum. Illustrated are (a) the laser polarization plane and (b) the x–z plane perpendicular to the polarization plane. The optical laser of intensity $10^{18}\,W\,cm^{-2}$ irradiates the droplet from the left along the x-axis. For this time, we observe an almost homogeneously ionized interior of the droplet with a thin highly ionized front at the surface. Here, we assume an equilibrated system, where a slight decrease of the electron temperature from the front surface to the back surface of the droplet is observed.

to shorter times of $t = 80\,fs$, a more homogeneous interior of the helium droplet. The focusing effect obtained for shorter times is still visible in the droplet front. The temperatures show a decrease of several hundreds of eV from the droplet front to the back of the droplet.

3.3. A pump laser with an intensity of $10^{19}\,W\,cm^{-2}$

As a third case, we study a pump laser with an even higher intensity of $10^{19}\,W\,cm^{-2}$ and an energy of 32 mJ. Due to this high intensity an emission of ions and electrons from the droplet is expected. Therefore, we used a bigger simulation box of $8 \times 18 \times 18\,\mu m^{-3}$ size on
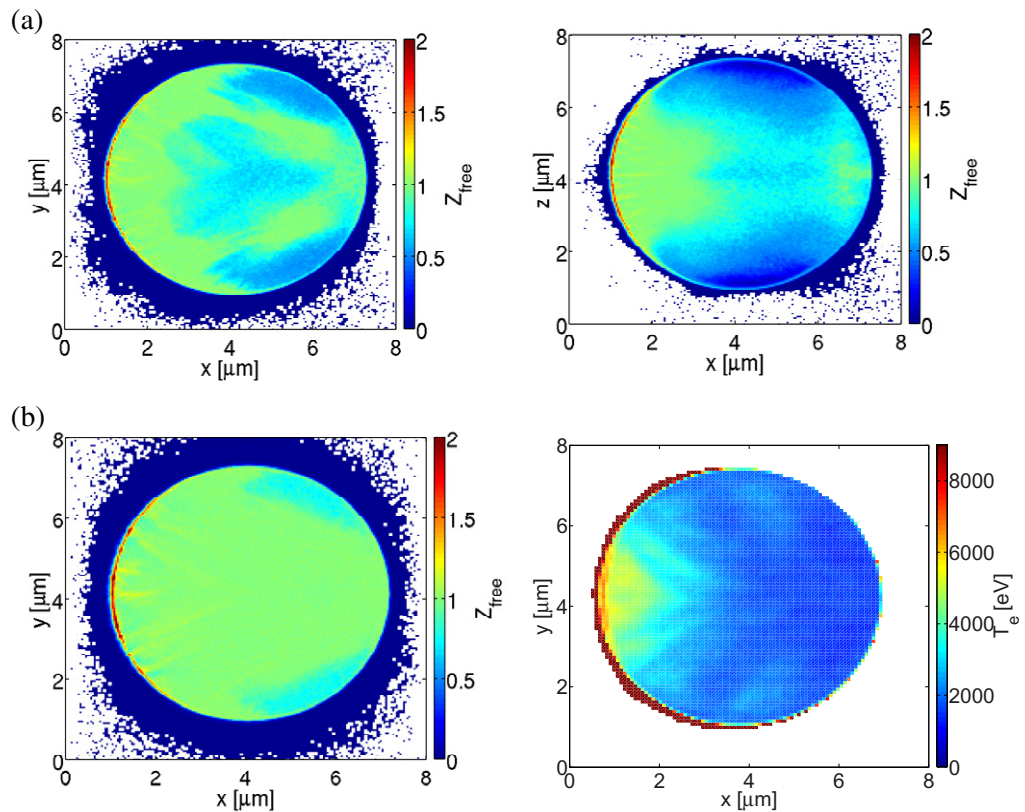
Figure 5. Profiles of (a) ionization degree Z_{free} for two different droplet planes at a time of $t = 50\,\text{fs}$ after the pulse maximum and (b) ionization degree Z_{free} and electron temperature T_e at a time of $t = 90\,\text{fs}$ after pulse maximum. The optical laser irradiates the droplet from the left along the x-axis. In this case of a laser energy $32\,\text{mJ}$ and intensity $10^{19}\,\text{W\,cm}^{-2}$ a high ionization of the droplet is observed.

$500 \times 1125 \times 1125$ grid cells with 64 heavy particles per cell. In this way boundary effects are avoided but the simulation time is substantially increased. Hence, the laser–matter interaction and thereby the ionization degree profile could so far be simulated only up to $90\,\text{fs}$ after the laser pulse maximum; the results are shown in figure 5. In contrast to the simulation of the laser–matter interaction with intensities of $10^{18}\,\text{W\,cm}^{-2}$, an accelerated focused laser penetration into the droplet is observed. This can be explained by the increased laser intensity, which generates faster electrons penetrating the droplet. Moreover, a higher ionization degree at the front as well as the interior of the droplet is obtained due to the higher laser energy.

4. Thomson scattering

We have calculated the overall Thomson scattering spectrum of the helium droplet via the BMA according to section 2 for a probe laser wavelength of $\lambda_0 = 13.5\,\text{nm}$. We use the plasma parameter profiles from the PIC simulations with a laser intensity of 10^{18} and $10^{19}\,\text{W\,cm}^{-2}$, which are illustrated in figures 4 and 5. For the lower intensity of $10^{15}\,\text{W\,cm}^{-2}$ the plasmon signal is very weak because of the low degree of ionization is and completely concealed by the
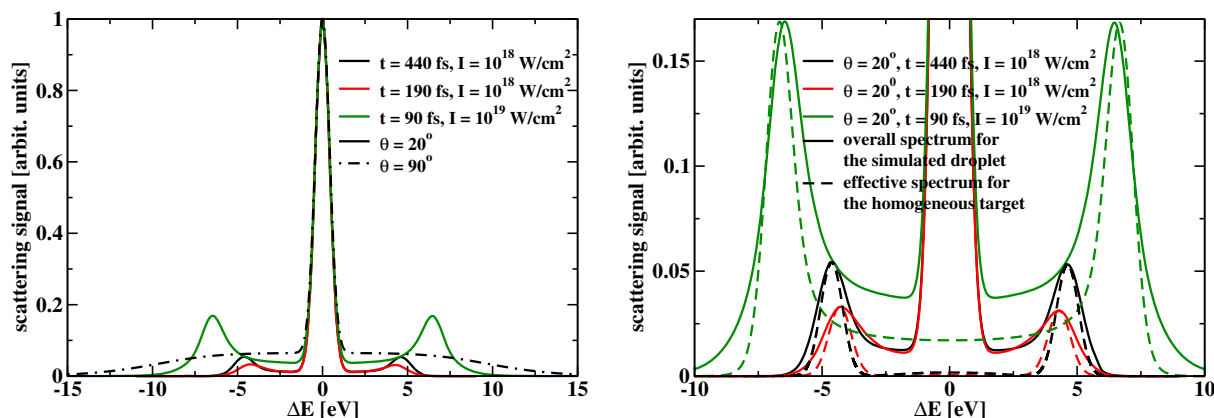
Figure 6. Thomson scattering spectrum as a function of the probe laser energy shift for a scattering angle of $\theta = 20°$ and $90°$ and a laser intensity of 10^{18} and 10^{19} W cm^{-2} at a time of $t = 90$, 190 and 440 fs after the maximum of the pump laser pulse. On the left side the normalized Thomson scattering spectrum is shown and on the right side the Thomson scattering of free electrons is displayed. The solid lines illustrate the overall Thomson scattering spectrum. The broken lines represent the effective Thomson scattering spectrum of a homogeneous plasma with plasma parameters as derived from the plasmon signal of the overall Thomson scattering spectrum for the inhomogeneous droplet at $\theta = 20°$. The broken lines are normalized to the maximal value of the plasmon pair of the corresponding overall Thomson scattering spectrum.

ion feature. In the following, the ion density is fixed at the initial density, the ion temperature is assumed to be equal to the electron temperature and a normalized Gaussian distribution function with the FWHM $\Delta\omega = 1$ eV as the instrumental function is employed. For the BMA calculation, we have used the reduced equidistant grid of $50 \times 50 \times 50$ boxes as for the determination of the electron temperature profile. The overall Thomson scattering spectrum of the helium droplet is derived as the equally weighted sum of the Thomson scattering spectra for each box. Each box is assumed to contain a homogeneous plasma, because FEL absorption effects are neglected due to the high penetration depth of the FEL and the high thermal energy in the system in comparison to the FEL energy.

The overall Thomson scattering spectrum is shown in figure 6 for a laser intensity of 10^{18} W cm^{-2} for two different scattering angles and times $t = 190$ and 440 fs after the maximum of the pump laser pulse and for a laser intensity of 10^{19} W cm^{-2} for one scattering angle and time $t = 90$ fs after the maximum of the pump laser pulse. On the left side of figure 6 the overall Thomson scattering spectrum is covered, whereas on the right side the plasmon peaks representing collective Thomson scattering of free electrons are shown enlarged. Here, we investigate for a scattering angle of $\theta = 90°$ the non-collective and for a scattering angle of $\theta = 20°$ the collective scattering regime. In addition, we observe for each time and intensity at the scattering angle $\theta = 20°$, one plasmon pair which determines the dominating plasma parameters of the droplet. For a laser intensity of 10^{18} W cm^{-2}, the plasmon pair at time $t = 190$ fs at an energy shift $|\Delta E| \approx 4.25$ eV represents a plasma with an effective electron density $n_e \approx 1.3 \times 10^{22}$ cm^{-3} and temperature $T_e \approx 75$ eV, whereas at time $t = 440$ fs the plasmon

pair at an energy shift $|\Delta E| \approx 4.6$ eV specifies a plasma with an effective electron density $n_e \approx 1.4 \times 10^{22}$ cm^{-3} and temperature $T_e \approx 260$ eV. These plasma parameters stem from the interior of the droplet and indicate an evolution of the plasma in which the HDM expands into the droplet. This behavior can also be seen in figures 3 and 4. For a laser intensity of 10^{19} W cm^{-2}, the plasmon pair at an energy shift $|\Delta E| \approx 6.46$ eV identifies a plasma with an effective electron density $n_e \approx 2.15 \times 10^{22}$ cm^{-3} and temperature $T_e \approx 2030$ eV. At a time of about 90 fs after the pump pulse maximum a similar homogeneous interior as in the case of a pump laser with an intensity of 10^{18} W cm^{-2} is observed. However, the ionization degree is in this case about unity and, therefore, two pronounced plasmon peaks are obtained at an energy of $|\Delta E| \approx 6.46$ eV. For comparison, the Thomson scattering spectrum for a homogeneous plasma with these effective plasma parameters is illustrated for $\theta = 20°$ in figure 6. Here, the plasmon peak is normalized to the maximal plasmon peak of the corresponding overall Thomson scattering spectrum. Compared to the effective Thomson scattering spectrum of the homogeneous target, we observe a broadened plasmon peak and higher values for smaller energy shifts ΔE in the overall Thomson scattering spectrum. This indicates that the plasmon pair signal consists of plasma regions with different plasma parameters, which all contribute to the overall Thomson scattering spectrum.

5. Conclusions

In this paper, we have calculated the overall Thomson scattering signal of inhomogeneous helium droplets which are pumped by a short-pulse optical laser of different intensities and probed with brilliant FEL radiation. We have obtained the density and temperature profiles for the pump phase with a 10^{15} W cm^{-2} laser at $t = 400$ fs, a 10^{18} W cm^{-2} laser at $t = 80$, 190 and 440 fs and a 10^{19} W cm^{-2} laser at $t = 50$ and 90 fs after the maximum of the pump laser pulse with a PIC code. The Thomson scattering signal was derived from these density and temperature profiles only for 10^{18} and 10^{19} W cm^{-2} via the BMA, because for 10^{15} W cm^{-2} the plasmon pairs are concealed by the ion feature.

We have shown that the inhomogeneous ionization process in the helium droplets irradiated with a high-intensity short-pulse laser predicted for short time scales in [30] evolves in the interior of the droplet for larger time scales of several hundreds of fs to a plasma with a homogeneous ionized interior and a highly ionized front surface. The evolution of the ionized droplet interior is reflected in the resulting overall Thomson scattering spectrum of this system, where only one plasmon pair dominates. The temporal resolution of this plasmon pair characterizes the evolution of the plasma parameters throughout the helium droplet. The overall Thomson scattering spectrum shows that in contrast to hydrogen droplets irradiated with smaller intensities of $I \approx 10^{15}$ W cm^{-2} as studied by Thiele *et al* [16], the Thomson scattering spectrum is not dominated by the surface of the droplet. In the present work, a plasmon pair can be resolved which stems from the interior of the droplet. The plasma is produced by an intense laser of $I \approx 10^{18}$ W cm^{-2} which can be provided at the MEC station at the LCLS at SLAC or in the future at the HED instrument at the XFEL in Hamburg.

Our calculations show that Thomson scattering on inhomogeneous helium droplets irradiated with high-intensity short-pulse lasers can spatially and temporally resolve the interior heating process in the HDM region. This technique can be extended by applying the calculation of the non-equilibrium DSF to derive the Thomson scattering spectrum in the short-scale heating process of the helium droplet where a strongly inhomogeneous target is observed. At these times

separated plasmon pairs are predicted. In addition, the long-time behavior of the droplet cooling can be observed if a more-dimensional radiation-hydrodynamics code is applied, with the PIC density and temperature profiles as the input.

Acknowledgments

References

[1] Remington B A, Cavallo R M, Edwards M J, Ho D D-M, Lasinski B F, Lorenz K T, Lorenzana H E, Mcnaney J M, Pollaine S M and Smith R F 2005 Accessing high pressure states relevant to core conditions in the giant planets *Astrophys. Space Sci.* **298** 235

[2] Fortney J J, Glenzer S H, Koenig M, Militzer B, Saumon D and Valencia D 2009 Frontiers of the physics of dense plasmas and planetary interiors: experiments, theory, and applications *Phys. Plasmas* **16** 041003

[3] Drake R P 2009 Perspectives on high-energy-density physics *Phys. Plasmas* **16** 055501

[4] Moses E I, Boyd R N, Remington B A, Keane C J and Al-Ayat R 2009 The National Ignition Facility: ushering in a new age for high energy density science *Phys. Plasmas* **16** 041006

[5] Committee on High Energy Density Plasma Physics, Plasma Science Committee and National Research Council 2003 *Frontiers in High Energy Density Physics: The X-Games of Contemporary Science* (Washington, DC: National Academies Press)

[6] Pukhov A 2003 Strong field interaction of laser radiation *Rep. Prog. Phys.* **66** 47–101

[7] Gibbon P 2005 *Short Pulse Laser Interactions with Matter: An Introduction* (Singapore: World Scientific)

[8] Mulser P and Bauer D 2010 *High Power Laser–Matter Interaction* (Berlin: Springer)

[9] Glenzer S H and Redmer R 2009 X-ray Thomson scattering in high energy density plasmas *Rev. Mod. Phys.* **81** 1625

[10] Toleikis S *et al* 2010 Soft x-ray scattering using FEL radiation for probing near-solid density plasmas at few electron volt temperatures *High Energy Density Phys.* **6** 15

[11] Fäustlin R R *et al* 2010 Observation of ultrafast non-equilibrium collective dynamics in warm dense hydrogen *Phys. Rev. Lett.* **104** 125002

[12] Glenzer S H *et al* 2007 Observations of plasmons in warm dense matter *Phys. Rev. Lett.* **98** 065002

[13] Höll A *et al* 2007 Thomson scattering from near-solid density plasmas using soft x-ray free electron lasers *High Energy Density Phys.* **3** 120

[14] Nagler B *et al* 2009 Turning solid aluminium transparent by intense soft x-ray photoionization *Nature Phys.* **5** 693

[15] Baldis H A, Dunn J, Foord M E and Rozmus W 2002 Thomson scattering diagnostic of solid density plasmas using x-ray lasers *Rev. Sci. Instrum.* **73** 4223

[16] Thiele R *et al* 2010 Thomson scattering on inhomogeneous targets *Phys. Rev.* E **82** 056404

[17] Chihara J 1987 Difference in x-ray scattering between metallic and non-metallic liquids due to conduction electrons *J. Phys. F: Met. Phys.* **17** 295

[18] Chihara J 2000 Interaction of photons with plasmas and liquid metals-photoabsorption and scattering *J. Phys.: Condens. Matter* **12** 231

[19] Selchow A, Röpke G, Wierling A, Reinholz H, Pschiwul T and Zwicknagel G 2001 Dynamic structure factor for a two-component model plasma *Phys. Rev.* E **64** 056410

13   **IOP** Institute of Physics Φ DEUTSCHE PHYSIKALISCHE GESELLSCHAFT

[20] Mermin N D 1970 Lindhard dielectric function in the relaxation-time approximation *Phys. Rev.* B **1** 2362

[21] Thiele R, Bornath T, Fortmann C, Höll A, Redmer R, Reinholz H, Röpke G, Wierling A, Glenzer S H and Gregori G 2008 Plasmon resonance in warm dense matter *Phys. Rev.* E **78** 026411

[22] Höll A, Redmer R, Röpke G and Reinholz H 2004 X-ray Thomson scattering in warm dense matter *Eur. Phys. J.* D **29** 159

[23] Redmer R, Reinholz H, Röpke G, Thiele R and Höll A 2005 Theory of x-ray Thomson scattering in dense plasmas *IEEE Trans. Plasma Sci.* **33** 77

[24] Schumacher M, Smend F and Borchert I 1975 Incoherent scattering of gamma rays by inner-shell electrons *J. Phys. B: At. Mol. Phys.* **8** 1428

[25] Sperling P, Thiele R, Holst B, Fortmann C, Glenzer S H, Toleikis S, Tschentscher Th and Redmer R 2011 Two-color Thomson scattering at FLASH *High Energy Density Phys.* **7** 145–9

[26] Gregori G, Glenzer S H, Rogers F J, Pollaine S M, Landen O L, Blancard C, Faussurier G, Renaudin P, Kuhlbrodt S and Redmer R 2004 Electronic structure measurements of dense plasmas *Phys. Plasmas* **11** 2754

[27] Sahoo S, Gribakin G F, Shabbir Naz G, Kohanoff J and Riley D 2008 Compton scatter profiles for warm dense matter *Phys. Rev.* E **77** 046402

[28] Liseykina T V, Pirner S and Bauer D 2010 Relativistic attosecond electron bunches from laser-illuminated droplets *Phys. Rev. Lett.* **104** 095002

[29] Popov V S 2004 Tunnel and multiphoton ionization of atoms and ions in a strong laser field (Keldysh theory) *Phys. Usp.* **47** 855

[30] Liseykina T V and Bauer D 2012 Plasma formation in intense laser–droplet interaction arXiv:1209.5948

6. Numerical support to the experimental studies

The list of publications:

S. Kar, M. Borghesi, C. A. Cecchetti, L. Romagnani, F. Ceccherini, T. V. Liseykina, A. Macchi, R. Jung, J. Osterholz, O. Willi, L. A. Gizzi, A. Schiavi, M. Galimberti and R. Heathcote, *Dynamics of charge-displacement channeling in intense laser-plasma interactions*, New J. Phys. **9**, 402 (2007)

K. Quinn, P. A. Wilson, C. A. Cecchetti, B. Ramakrishna, L. Romagnani, G. Sarri, L. Lancia, J. Fuchs, A. Pipahl, T. Toncian, O. Willi, R. J. Clarke, D. Neely, M. Notley, P. Gallegos, D. C. Carroll, M. N. Quinn, X. H. Yuan, P. McKenna, T. V. Liseykina, A. Macchi, and M. Borghesi, *Laser-driven ultrafast field propagation on solid surfaces*, Phys. Rev. Lett. **102** 194801 (2009)

L. Romagnani, A. Bigongiari, S. Kar, S. V. Bulanov, C. A. Cecchetti, T. Zh. Esirkepov, M. Galimberti, R. Jung, T. V. Liseykina, A. Macchi, J. Osterholz, F. Pegoraro, O. Willi, and M. Borghesi, *Observation of magnetized soliton remnants in the wake of intense laser pulse propagation through plasmas*, Phys. Rev. Lett. **105**, 175002 (2010)

G. Sarri, A. Macchi, C. A. Cecchetti, S. Kar, T. V. Liseykina, X. H. Yang, M. E. Dieckmann, J. Fuchs, M. Galimberti, L. A. Gizzi, R. Jung, I. Kourakis, J. Osterholz, F. Pegoraro, A. P. L. Robinson, L. Romagnani, O. Willi, and M. Borghesi, *Dynamics of self-generated, large amplitude magnetic fields following high-intensity laser matter interaction*, Phys. Rev. Lett. **109**, 205002 (2012)

New Journal of Physics

The open–access journal for physics

Dynamics of charge-displacement channeling in intense laser–plasma interactions

S Kar[1,9]**, M Borghesi**[1]**, C A Cecchetti**[1]**, L Romagnani**[1]**,
F Ceccherini**[2]**, T V Liseykina**[2,7]**, A Macchi**[2,8]**, R Jung**[3]**,
J Osterholz**[3]**, O Willi**[3]**, L A Gizzi**[4]**, A Schiavi**[5]**, M Galimberti**[6]
and R Heathcote[6]

[1] School of Mathematics and Physics, the Queen's University of Belfast,
Belfast BT7 1NN, UK
[2] Dipartimento di Fisica 'E. Fermi', Universit di Pisa, Pisa, Italy
[3] Institut f r Laser-und Plasmaphysik, Heinrich-Heine-Universit t,
D sseldorf, Germany
[4] Intense Laser Irradiation Laboratory, IPCF-CNR, Pisa, Italy
[5] Dipartimento di Energetica, Universit di Roma 1 'La Sapienza', Roma, Italy
[6] Rutherford Appleton Laboratory, Central Laser Facility, Chilton,
OX11 0QX, UK
[7] Institute for Computational Technologies, SD-RAS, Novosibirsk, Russia
[8] PolyLAB, CNR-INFM, Pisa, Italy
E-mail: s.kar@qub.ac.uk

Abstract. The dynamics of transient electric fields generated by the interaction of high intensity laser pulses with underdense plasmas has been studied experimentally with the proton projection imaging technique. The formation of a charged channel, the propagation of its front edge and the late electric field evolution have been characterized with high temporal and spatial resolution. Particle-in-cell simulations and an electrostatic, ponderomotive model reproduce the experimental features and trace them back to the ponderomotive expulsion of electrons and the subsequent ion acceleration.

---

[9] Author to whom any correspondence should be addressed.

---

2   **IOP** Institute of Physics Φ DEUTSCHE PHYSIKALISCHE GESELLSCHAFT

Contents

1. Introduction

The study of the propagation of intense laser pulses in underdense plasmas is relevant to several highly advanced applications, including electron ([1] and references therein) and ion acceleration [2, 3], development of x- and γ-ray sources [4], and fusion neutron production [5]. It is also of fundamental interest, due to the variety of relativistic and nonlinear phenomena which arise in the laser–plasma interaction [6]. Among these, self-focusing and self-channeling of the laser pulse arise in this regime from the intensity dependence of the relativistic index of refraction [7, 8].

Strong space charge electric fields are generated during the early stage of the propagation of a superintense laser pulse through an underdense plasma as the ponderomotive force (PF) acts on electrons, pushing them away from the axis. Thus, for a transient stage the pulse may propagate self-guided in a charged channel [9], while the space-charge field in turn drags and accelerates the ions to MeV energies [3]. So far, experiments have provided evidence of channel formation and explosion using optical diagnostics [9]–[14], or by detecting radially accelerated ions [2, 3, 5, 14], while a direct detection of the space-charge fields has not been obtained yet. The development of the proton projection imaging (PPI) technique [15] has provided a very powerful tool to explore the fast dynamics of plasma phenomena via the detection of the associated transient electric field structures. The technique is based on the use of laser-accelerated multi-MeV protons ([16, 17] and references therein) as a charged probe beam of transient electromagnetic (EM) fields in plasmas, a possibility allowed by the low emittance and high laminarity of the proton source [18, 19], as well as by its ultra-short duration and the straightforward synchronization with an interaction laser pulse. The experimental PPI implementation takes advantage from the broad energy spectrum of protons, since in a time-of-flight arrangement protons of different energy will probe the plasma at different times, and thus an energy-resolved monitoring of the proton probe profile allows single-shot, multi-frame temporal scans of the interaction to be obtained [15]. PPI and the related 'proton deflectometry' technique permit spatial and temporal maps of the electric fields in the plasma to be gathered, and therefore have proven to be an unique tool to explore the picosecond dynamics of laser–plasma phenomena [20]–[22] via the associated space-charge fields.

In this paper, we report on an experiment using the PPI technique to study the formation and subsequent evolution of a charge-displacement channel in an underdense plasma. These investigations have led to the first direct experimental detection of the transient electric fields in the channel, providing an insight of the fundamental physical processes involved. The
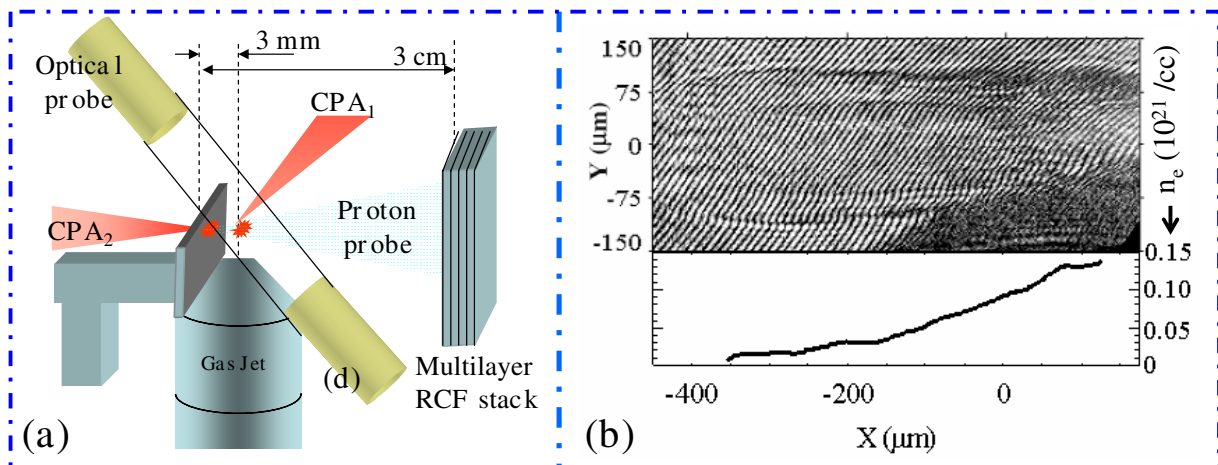
Figure 1. (a) Schematic diagram of the experimental set-up. (b) Top: interferogram of the plasma at 25 ps before the arrival of CPA_1 at its focal plane $x = 0$. The CPA_1 peak intensity was 1.5×10^{19} W cm^{-2}. Bottom: the corresponding electron density profile along the $y = 0$ axis.

comparison of the experimental data with two-dimensional (2D) EM particle-in-cell (PIC) simulations and a simple 1D electrostatic (ES) PIC model allows to characterize in detail the electric field dynamics at different stages of its evolution.

2. Experimental set-up

The experiment was carried out at the Rutherford Appleton Laboratory, employing the VULCAN Nd-glass laser system [23], providing two chirped pulse amplified (CPA) pulses, with 1.054 μm wavelength, synchronized with picosecond precision. Each of the beams delivered approximately 30 J on target in 1.3 ps (full width at half maximum, FWHM) duration. By using $f/6$ off-axis parabolas, the beams were focused to spots of $\sim$8 μm (FWHM) achieving peak intensities up to 1.5×10^{19} W cm^{-2}. The short pulses were preceded by an amplified spontaneous emission (ASE) pedestal of 300 ps duration and a contrast ratio of $\sim 10^6$. One of the beams (CPA_1) was directed to propagate through He gas from a supersonic nozzle, having a 2 mm aperture, driven at 50 bar pressure. The interaction was transversely probed by the proton beam produced from the interaction of the second CPA beam (CPA_2) with a flat foil (a 10 μm thick Au foil was typically used), under the point projection imaging scheme [15]. The schematic of the experimental set-up is shown in figure 1(a). Due to the Bragg peak energy deposition properties of the protons, the use of multilayered stacks of radiochromic film (RCF) detector permits energy-resolved monitoring of the proton probe profile, as each layer will primarily detect protons within a small energy range. This allows to obtain single-shot, multi-frame temporal scans of the interaction in a time-of-flight arrangement [15]. The spatial and temporal resolution of each frame were of the order of a few picoseconds, and of a few microns, respectively, while the magnification was 11.

The interaction region was also diagnosed by Nomarsky interferometry, employing a frequency doubled CPA pulse of low energy. The reconstructed electron density profile along
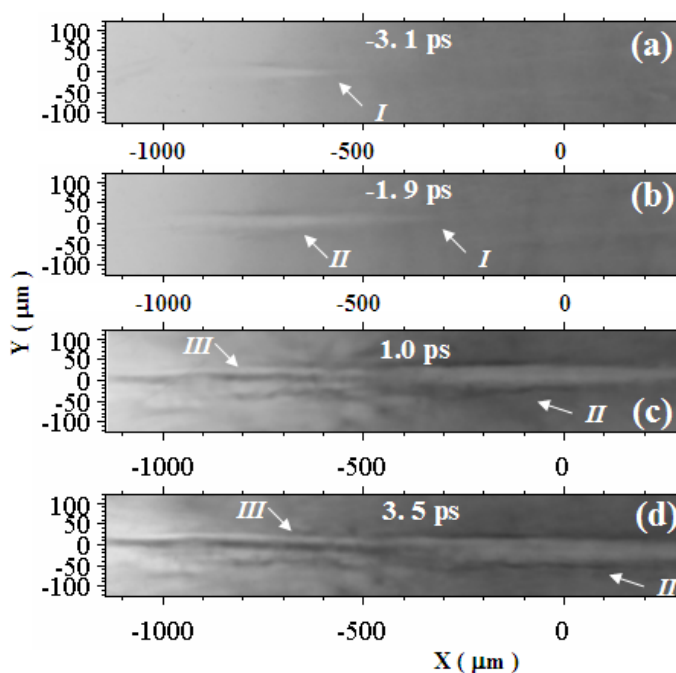
Figure 2. PPIs of the interaction region at different times obtained in two different laser shots. The x and y coordinates refer to the object (interaction) plane, which intersects the probe axis at $(x, y) = (0, 0)$. The images (a) and (b) have been obtained from the same shot at an intensity $I = 4.0 \times 10^{18}$ W cm^{-2}, while (c) and (d) correspond to a shot with $I = 1.5 \times 10^{19}$ W cm^{-2}. The signal in the frames is mainly due to protons (of energies $E = 13, 12.5, 13$ and 12 MeV in (a)–(d), respectively) reaching the Bragg peak within their active layers. The time labels give the probing time of the protons propagating along the probe axis $[t_0(E)]$, relative to the time of arrival of the peak of interaction pulse at the plane $x = 0$ μm. White (dark) regions correspond to lower (higher) proton flux than the background. The labels indicate the most prominent features: (I) the bullet-shaped leading edge and (II) the central region of the 'white', positively charged channel; (III) the 'black' line along the axis, indicating a region of field inversion inside the channel.

the propagation axis before the high-intensity interaction (see figure 1(b)), broadly consistent with the neutral density profile of the gas jet [24] suggests complete ionization of the gas by the ASE prepulse.

3. Experimental results

Figures 2(a)–(d) show four sequential PPIs of the interaction region. The laser pulse propagates from left to right. A 'white' channel with 'dark' boundaries is visible at early times (figures 2(a) and (b)). The leading, 'bullet' shaped edge of the channel, indicated by the label I in figures 2(a) and (b), is seen moving along the laser axis. In the trail of the channel, the proton flux distribution changes qualitatively (figures 2(c) and (d)), showing a dark line along the axis
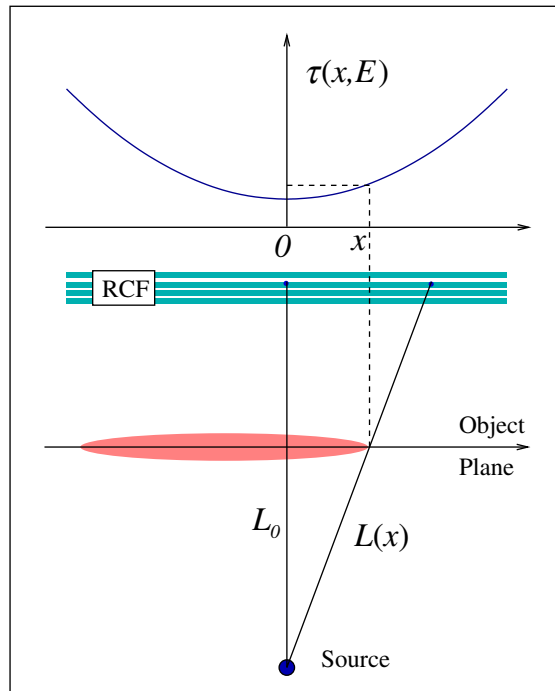
Figure 3. Schematic diagram showing the evaluation of the channel front speed. Protons of energy E from the point-like source cross the channel axis at a distance x from the centre of the object plane at the time $\tau(x, E) = t_0(E) + [L(x) - L_0]/v_{\mathrm{p}}$, where L_0 is the distance between the source and the object plane, $v_{\mathrm{p}} = \sqrt{2E/m_{\mathrm{p}}}$ is the proton velocity, $L(x) = \sqrt{x^2 + L_0^2}$, and $t_0(E)$ is the time at which the protons of energy E directed perpendicularly to the object plane cross the latter, relative to the instant at which the laser pulse peak reaches the focal plane ($x = 0$).

(indicated by the label III), which is observed up to tens of picosecond after the transit of the peak of the pulse. The 'white' channel reveals the presence of a positively charged region around the laser axis, where the electric field points outwards. This can be interpreted as the result of the expulsion of electrons from the central region. The central dark line observed at later times in the channel suggests that at this stage the radial electric field must change its sign, i.e. point inwards, at some radial position. As discussed below, this field inversion is related to the effects of ion motion.

Due to multi-frame capability of the PPI technique with picosecond temporal resolution, it has been possible to estimate the propagation velocity v of the channel front. Critically, one has to take into account that, due to the divergence of the probe beam, the probing time varies along the pulse propagation axis (see figure 3) as $\tau(x, E) \simeq t_0(E) + \tau_0(E)(\sqrt{1 + x^2/L_0^2} - 1)$, where $L_0 \simeq 0.3\,\mathrm{cm}$ is the distance between the plane and the proton source and $\tau_0 = L_0/\sqrt{2E/m_{\mathrm{p}}} \simeq 220\,\mathrm{ps}/\sqrt{E/\mathrm{MeV}}$ is the proton time of flight from the source to the center of the object plane (see figure 3). The reference time $t_0(E)$ is relative to the instant at which the laser pulse peak crosses the focal plane $x = 0$. We divide the displacement of the tip of the channel leading
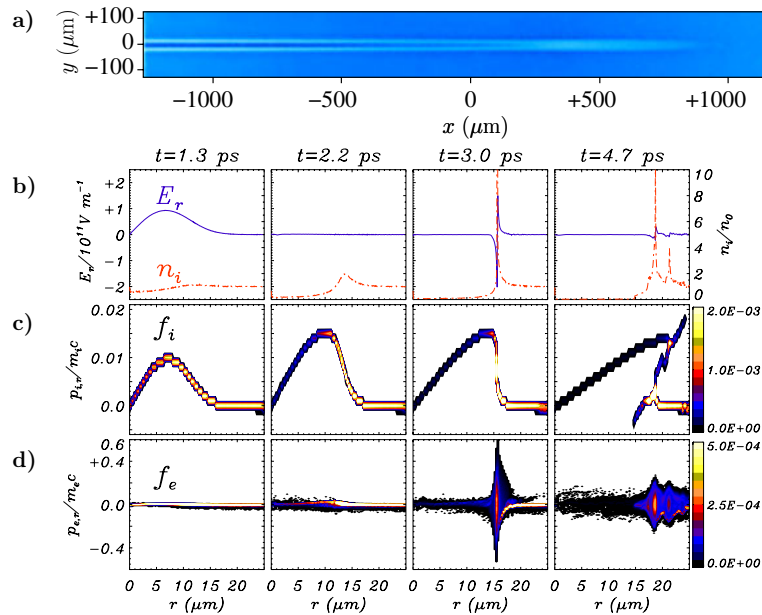
IOP Institute of Physics **Φ** DEUTSCHE PHYSIKALISCHE GESELLSCHAFT

Figure 4. (a) Simulated proton image, obtained from particle tracing simulations of 12 MeV protons (as shown in the data figure 2(d)) in the electric field pattern $\mathbf{E}(r, z, t)$ given by the 1D particle simulations based on the ponderomotive, ES model. (b) Profiles of electric field E_r and ion density n_i (c) and (d): phase space distributions of ions $f_i(r, p_r)$ and electrons $f_e(r, p_r)$, respectively, from the 1D simulation, at various times ($t = 0$ refers to the laser pulse peak).

front from frame (a) to (b), $\Delta X = X_b - X_a \simeq (-300 + 500)\,\mu\text{m} = 200\,\mu\text{m}$ by the difference $\Delta\tau$ in the corresponding probing times $\Delta\tau = \tau(X_b, E_b) - \tau(X_a, E_a) \simeq 0.66\,\text{ps}$ to obtain $v = \Delta X/\Delta\tau \simeq 3 \times 10^8\,\text{m s}^{-1}$. Based on the nominal reference time, we estimate the peak of the pulse to be approximately 0.6 ps behind the tip of the channel front.

4. Data analysis by numerical simulations

In order to unfold the physical mechanisms associated with the dynamics of the charged channel, a 1D ES PIC model in cylindrical geometry was employed, in which the laser action is modeled solely via the PF of a non-evolving laser pulse. A similar approach has been previously used by other authors [12, 14]. The code solves the equation of motion for plasma particles along the radial direction, taking into account the ES field obtained from Poisson's equation and the PF acting on the electrons: $F_r = -m_e c^2 \partial_r [1 + a^2(r, t)/2]^{1/2}$ [25]. Here, $a(r, t) = a_0 e^{-r^2/2r_0^2} f(t)$ and $f(t)$ define the temporal envelope of the laser pulse. For the latter, a 'sin²' profile was used (the use of a Gaussian profile did not yield significant differences).

Figure 4(b) shows the electric field $E_r(r, t)$ and the ion density $n_i(r, t)$ obtained from a simulation with $r_0 = 7.5\lambda$, $a_0 = 2.7$, $\tau_0 = 300\lambda c^{-1}$ and an initial density $0.01 n_c$ (where n_c is the critical density and $n_c = 10^{21}\,\text{cm}^{-3}$ for $\lambda = 1\,\mu\text{m}$). The initial depletion of electrons and the later formation of an ambipolar electric field front are clearly evident. In order to achieve a direct comparison with the experimental data, a 3D particle tracing simulation, employing the

PTRACE code [22], was carried out to obtain the proton images for an electric field given by $\mathbf{E}(x, r, t) = \hat{\mathbf{r}} E_r(r, t - x/c)$. The experimental proton source characteristics (e.g. spectrum and divergence), the detector configuration and dose response were taken into account. A simulated proton image, reproducing well the main features observed in the experiment, is shown in figure 4(a). The tip of the channel front is located 0.75 ps ahead of the pulse peak, in fair agreement with the previous estimate based on the data.

An essential theoretical description of the dynamics observed in the 1D simulations can be given as follows (a detailed description is reported [26]). In the first stage, F_r pushes part of the electrons outwards, quickly creating a positively charged channel along the axis and a radial ES field which holds the electrons back, balancing almost exactly the PF, i.e. $eE_r \simeq F_r$; thus, the electrons are in a quasi–equilibrium state, and no significant electron heating occurs. Meanwhile, the force $ZeE_r \simeq ZF_r$ accelerates the ions producing a depression in n_i around the axis (see figure 4(b)); at the end of the pulse ($t \simeq 2\,\mathrm{ps}$), we find $E_r \simeq 0$ (see figure 4(b)), indicating that the ions and electrons have moved in order to restore the local charge neutrality. However, the ions retain the velocity acquired during the acceleration stage. For $r > r_{\max}$, where $r_{\max}$ is the position of the PF maximum, the force on the ions, and thus the ion final velocity, decrease with r; as a consequence, the ions starting at a position $r_i(0) > r_{\max}$ are ballistically focused towards a narrow region at the edge of the intensity profile, and reach approximately the same position ($r \simeq 15\,\mu\mathrm{m}$) at the same time ($t \simeq 3\,\mathrm{ps}$, i.e. 2 ps after the peak of the laser pulse); here they pile up producing a very sharp peak of n_i. Correspondingly, the ion phase space shows that the fastest ions (with energies $\simeq 400\,\mathrm{keV}$, of the order of the time-averaged ponderomotive potential) overturn the slowest ones and hydrodynamical breaking of the ion fluid occurs. Using a simple model [26], the 'breaking' time and position can be estimated to be $\tau_b \simeq t_p + (\pi/2\sqrt{2})e^{3/4}\sqrt{(A/Z)(m_p/m_e)}(r_0/a_0 c)$ (where $t_p = 1\,\mathrm{ps}$ is the time at which the pulse has maximum amplitude) and $r_b \simeq (3/2)^{3/2} r_0$, yielding $\tau_b - t_p \simeq 1.3\,\mathrm{ps}$ and $r_b \simeq 14\,\mu\mathrm{m}$ for the simulation in figure 4, in good agreement with the numerical results. As inferred from the ion phase space plot at $t = 4.7\,\mathrm{ps}$, a few ions acquire negative velocity after 'breaking'; they return toward the axis and lead to the formation of a local density maximum at $r = 0$ after $t \simeq 15\,\mathrm{ps}$.

The electron phase space shows that at breaking the electrons are strongly heated around the ion density peak, generating a 'hot' electron population with a 'temperature' $T_h \simeq 13\,\mathrm{keV}$ and a density $n_h \simeq 4 \times 10^{19}\,\mathrm{cm}^{-3}$, corresponding to a local Debye length is $\lambda_D = (T_h/4\pi n_h e^2)^{1/2} \simeq 0.13\,\mu\mathrm{m}$. A modeling of the sheath field thus generated around the density spike [26] (whose thickness $d \simeq 0.1\,\mu\mathrm{m}$ is less than both λ_D and the sheath width L) yields a peak field $E_s \simeq 2\pi e n_h d \simeq 6 \times 10^{10}\,\mathrm{V\,m^{-1}}$ and a sheath width $L \simeq 4\lambda_D^2/d \simeq 0.7\,\mu\mathrm{m}$, consistently with the simulation results. The ambipolar field at the 'breaking' location can thus be interpreted as the sheath field resulting from the local electron heating.

The good agreement of the simulated image with the experimental ones indicates that the 1D ponderomotive, ES model contains the essential physics of self-channeling and related electric field dynamics, despite the exclusion of nonlinear pulse evolution due, e.g. to self-focusing, or of the plasma inhomogeneity. To address these issues, we performed EM PIC simulations of the laser–plasma interaction. The simulation were 2D in planar geometry— a fully 3D simulation with spatial and temporal scales close to the experimental ones and adequate numerical resolutions is a way beyond present days computational power. The 2D results can be considered to be qualitative since, for instance, the diffraction length of the laser beam or the scaling with distance of the ES field are different in 3D. Despite
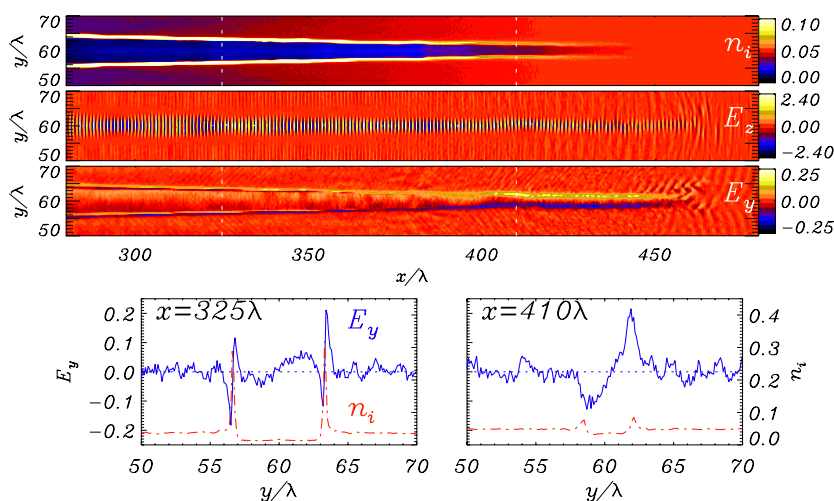
8　**IOP** Institute of Physics ⏀ DEUTSCHE PHYSIKALISCHE GESELLSCHAFT

Figure 5. Top frame: ion density (n_i) and electric field components (E_z and E_y) at $t = 2.0$ ps. Bottom frame: lineout of E_y (blue) and n_i (red) along the y-axis at two different x-positions, showing the transition in the radial field pattern. The density is normalized to $n_c = 10^{21}$ cm^{-3} and the fields to $m_e \omega c/e = 3.2 \times 10^{11}$ V m^{-1}. The initial density profile reproduces the experimental one in figure 1 (b). The laser pulse propagates from left to right along the x-axis and has 1ps duration. The peak amplitude is $a_0 = 2$ in dimensionless units. The laser pulse is s-polarized (i.e. the polarization is perpendicular to the simulation plane). In this configuration E_z is representative of the amplitude of the propagating EM pulse and E_y is generated by the space-charge displacement. The observed increase in E_z by a factor of ~ 1.2 with respect to the peak value in vacuum is due to self-focusing.

of these limitations, the main features of the channel observed in the experimental data are qualitatively reproduced in 2D simulations for a range of parameters close to the experiment. In the simulation of figure 5, the laser pulse has a Gaussian intensity profile both in space and time, with peak dimensionless amplitude $a_0 = 2$, radius $r_0 = 4\lambda$ and duration $\tau_0 = 300\lambda c^{-1}$, where λ is the laser wavelength. For $\lambda = 1\,\mu$m the pulse duration and intensity correspond to 1 ps and 5.5×10^{18} W cm^{-2}, respectively. The charge-to-mass ratio of ions is $Z/A = 1/2$. The electron density grows linearly along the x-axis from zero to the peak value $n_0 = 0.1\,n_c$ over a length of $400\,\lambda$, and then remains uniform for $200\,\lambda$. A 6500×1200 numerical grid, a spatial resolution $\Delta x = \Delta y = \lambda/10$ and 16 particles per cell for both electrons and ions were used.

Figure 5 shows the ion density (n_i) and the components E_y and E_z of the electric field at the time $t = 600\,\lambda c^{-1} \simeq 2.0$ ps. In this simulation, the laser pulse is s-polarized, i.e. the polarization is along the z-axis, perpendicular to the simulation plane. Thus, in figure 5 E_z is a representative of the amplitude of the propagating EM pulse, while E_y is generated by the space-charge displacement. Simulations performed for the case of p-polarization showed no substantial differences in the ES field pattern. The simulation clearly shows the formation of an electron-depleted channel, resulting in an outwardly directed radial space-charge electric field

whose peak value is 6.7×10^{10} V m^{-1} (see the lineout at $x = 410\,\lambda$ in figure 5). In the region behind the peak of the pulse, two narrow ambipolar fronts (one on either side of the propagation axis) are observed. The ambipolar fields have peak values of $\simeq 6 \times 10^{10}$ V m^{-1} (see the lineout at $x = 325\,\lambda$ in figure 5). As shown above, such a radial electric field profile produces a pattern in the proton images similar to that observed in the region (III) of figure 2.

5. Conclusion

We have reported the first direct experimental study of the electric field dynamics in a charge-displacement channel produced by the interaction of a high intensity laser pulse with an underdense plasma. The field profiles observed clearly identify different stages of the channel evolution: the electron depletion near the axis due to the PF, and the following ion acceleration causing a field inversion along the radius. The features observed are reproduced and interpreted by means of 1D ES and 2D EM PIC simulations, followed by a reconstruction of the proton images employing a 3D particle tracing code.

Acknowledgments

References

[1] Malka V *et al* 2005 *Plasma Phys. Control. Fusion* **47** B481
[2] Krushelnick K *et al* 1999 *Phys. Rev. Lett.* **83** 737
    Wei M S *et al* 2004 *Phys. Rev. Lett.* **93** 155003
[3] Willingale L *et al* 2006 *Phys. Rev. Lett.* **96** 245002
[4] Rousse A *et al* 2004 *Phys. Rev. Lett.* **93** 135005
[5] Fritzler S *et al* 2002 *Phys. Rev. Lett.* **89** 165004
[6] Bulanov S V *et al* 2001 *Review of Plasma Physics* vol 22 (Berlin: Springer) p 227
[7] Sun G Z *et al* 1987 *Phys. Fluids* **30** 526
[8] Mori W B *et al* 1988 *Phys. Rev. Lett.* **60** 1298
[9] Borisov A B *et al* 1992 *Phys. Rev. Lett.* **68** 2309
    Borisov A B *et al* 1992 *Phys. Rev. A* **45** 5830
[10] Monot P *et al* 1995 *Phys. Rev. Lett.* **74** 2953
[11] Borghesi M *et al* 1997 *Phys. Rev. Lett.* **78** 879
[12] Krushelnick K *et al* 1997 *Phys. Rev. Lett.* **78** 4047
[13] Sarkisov G S *et al* 1997 *JETP Lett.* **66** 828
[14] Sarkisov G S *et al* 1999 *Phys. Rev. E* **59** 7042
[15] Borghesi M *et al* 2003 *Rev. Sci. Instrum.* **74** 1688
[16] Fuchs J *et al* 2006 *Nat. Phys.* **2** 48–54
[17] Robson L *et al* 2007 *Nat. Phys.* **3** 58
[18] Borghesi M *et al* 2004 *Phys. Rev. Lett.* **92** 055003

10

[19] Cowan T *et al* 2004 *Phys. Rev. Lett.* **92** 204801
[20] Borghesi M *et al* 2002 *Phys. Rev. Lett.* **88** 135002
[21] Borghesi M *et al* 2005 *Phys. Rev. Lett.* **94** 195003
[22] Romagnani L *et al* 2005 *Phys. Rev. Lett.* **95** 195001
[23] Danson C *et al* 1998 *J. Mod. Opt.* **45** 1653
[24] Jung R *et al Central Laser Facility Annual Report* 2004/2005, RAL Report No. RAL-TR-2005-025, p 23
available from http://www.clf.rl.ac.uk/reports/2004-2005/pdf/16.pdf
[25] Bauer D, Mulser P and Steeb W H 1995 *Phys. Rev. Lett.* **75** 4622
[26] Macchi A *et al* 2007 *Preprint* physics/0701139

Laser-Driven Ultrafast Field Propagation on Solid Surfaces

K. Quinn,[1,*] P. A. Wilson,[1] C. A. Cecchetti,[1,†] B. Ramakrishna,[1] L. Romagnani,[1] G. Sarri,[1] L. Lancia,[2] J. Fuchs,[2]
A. Pipahl,[3] T. Toncian,[3] O. Willi,[3] R. J. Clarke,[4] D. Neely,[4] M. Notley,[4] P. Gallegos,[4,5] D. C. Carroll,[5] M. N. Quinn,[5]
X. H. Yuan,[5] P. McKenna,[5] T. V. Liseykina,[6,‡] A. Macchi,[7] and M. Borghesi[1]

[1]*Department of Physics and Astronomy, Queen's University Belfast, Belfast BT7 1NN, United Kingdom*
[2]*Laboratoire pour l'Utilisation des Lasers Intenses, École Polytechnique, 91128 Palaiseau, France*
[3]*Institut für Laser–und Plasmaphysik, Heinrich-Heine-Universität, D-40225 Düsseldorf, Germany*
[4]*Central Laser Facility, Rutherford Appleton Laboratory, Chilton, Oxfordshire OX11 0QX, United Kingdom*
[5]*SUPA, Department of Physics, University of Strathclyde, Glasgow G4 0NG, United Kingdom*
[6]*Max Planck Institute for Nuclear Physics, Heidelberg, Germany*
[7]*CNR/INFM/polyLAB, Dipartimento di Fisica "E. Fermi," Pisa, Italy*
(Received 28 January 2009; published 14 May 2009)

The interaction of a 3×10^{19} W/cm^2 laser pulse with a metallic wire has been investigated using proton radiography. The pulse is observed to drive the propagation of a highly transient field along the wire at the speed of light. Within a temporal window of 20 ps, the current driven by this field rises to its peak magnitude $\sim 10^4$ A before decaying to below measurable levels. Supported by particle-in-cell simulation results and simple theoretical reasoning, the transient field measured is interpreted as a charge-neutralizing disturbance propagated away from the interaction region as a result of the permanent loss of a small fraction of the laser-accelerated hot electron population to vacuum.

The processes by which the relativistic electrons generated in intense ($I > 10^{18}$ W/cm^2) laser-solid interactions transfer their energy from the focal spot to the bulk target remain elusive, yet further investigation into such transport mechanisms is vital, not least of all, to the realization of fast ignition [1]. The incidence of a high-intensity pulse onto a cone-wire target has been used to study the mechanisms by which ignition energy might be delivered to the core [2]. The production of hot electron currents in solid targets is also the basis for the growing field of laser-driven ion acceleration [3]. It has been shown that the adaptation of the divergent, broadband proton beams generated via target normal sheath acceleration (TNSA) [3] to a range of applications [3,4] might be facilitated by the development of one of two schemes for the optimization of a laser-driven proton beam to its minimal bandwidth and divergence angle [5,6], both of which are related to the laser-induced ultrafast (picosecond-time scale) charging of a solid. The development of fast rise-time laser-driven Z pinches, meanwhile, also demands a thorough knowledge of the transient currents induced in laser-wire interactions [7].

While the global charging of a solid irradiated at high intensity has been reported previously [8,9], the propagation mechanism of the related charging fields remains unclear, and local current flows have not yet been directly observed.

In this Letter, we present the experimental observation of the highly transient laser-driven current induced in the interaction of an intense (3×10^{19} W/cm^2) pulse with a metallic wire target. The velocity at which the charge pulse moves along the wire is confidently measured by a novel experimental arrangement to be $\sim c$. The measurements are consistent with a current which rises to a peak magnitude of 8 kA before decaying to below measurable levels over 20 ps. All measurements were performed by employing a TNSA proton beam as a charged particle probe of the electromagnetic fields set up by the interaction pulse in the region of the target. Some 3×10^{11} electrons are calculated to have been drawn toward the interaction region past the cross section of measurement, a figure consistent with a simple model of the target charging.

The proton radiography or imaging technique [10] operates on the principle that the Lorentz deflections impinged upon the constituent protons of the probe beam act as a measure of the E and B fields set up in the interaction region. Dosimetric radiochromic film (RCF) [11] is commonly employed transverse to the incident beam as a proton detector, providing spatially and energetically resolved detection of the incident proton beam when used in a layered configuration. Each RCF layer may then be related to a proton energy E_p by calculating the distance into the film pack at which the Bragg peak occurs as a function of E_p. The probing time assigned to a given layer is then given by $t_{\text{probe}} = d(m_p/2E_p)^{1/2}$, where d is the distance from the proton source to the point of interest at the target and m_p is the proton mass. The evolution of the electric and magnetic fields set up as a result of the interaction pulse may hence be inferred with μm ps spatiotemporal resolution by comparing the experimental proton density behavior at the detector with the results of three-dimensional (3D) particle-tracing simulations [10].

The experiment was conducted on the VULCAN Petawatt laser system [12]. One-tenth of the cross section

of the main 260 J, picosecond-duration, 60 cm beam entering the target chamber was diverted *in situ* via a 235 mm-diameter pickup mirror to provide the interaction pulse CPA$_2$ [13], which was focused down to an $8 \times 4 \ \mu m^2$ spot to give an on-target intensity of 3×10^{19} W/cm^2. The remainder of the main beam (CPA$_1$) was focused down to an area of $5 \times 4 \ \mu m^2$ by a 1 m off-axis parabola onto a 20 μm Au foil to accelerate the proton beam for probing of the interaction. A 50 ps optical delay was applied to CPA$_2$ so that the target was completely enveloped in the probe beam at the time of the interaction. The cutoff energy of the proton beam accelerated by the 4×10^{20} W/cm^2 CPA$_1$ pulse was roughly 25 MeV so that, when combined with the RCF stack, observation of the wire was provided over 40 ps.

We first studied the interaction of CPA$_2$ with a 125 μm-diameter gold wire in a vertical orientation [shot *A*; see Fig. 1(a)]. Measurements were performed at the *zero level* of the probe beam (the level at which protons emitted from the source have no vertical component of velocity). As shown in Fig. 2, over a temporal window of some 20 ps, the extent of the deflections imposed upon the probe protons as they pass the wire increases to its maximum before decaying. This feature is interpreted as being caused by the transient charging and subsequent discharging of the wire as a result of the CPA$_2$ interaction. That this electrical charging is positive is revealed by the fact that proton density "pileups" are visible on either side of the wire image while the central region is depleted (protons have been deflected *away* from the wire).
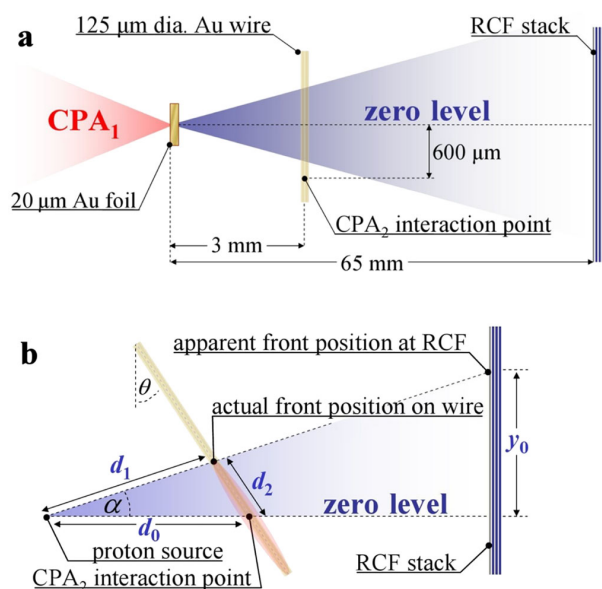
The fields set up as a result of the laser-wire interaction were modeled in the particle tracer. If E_s is the strength of the outwards-pointing radial electric field at the wire surface and r_w the wire radius, then by assuming that (i) positive charge is contained exclusively within the wire and (ii) the negative charge density outside the wire is low compared to the positive charge density inside, the electric field strength at a given radial distance r from the axis may be approximated by $E_s(r_w/r)$ for $r \geq r_w$. The electric field is largely absent for $r < r_w$, meanwhile, falling to $1/e$ of its maximum strength within a skin depth of the wire surface. The azimuthal magnetic field associated with current propagation along the wire is in turn computed via application of Ampère's law, although particle-tracing simulations demonstrated that deflections to the probe protons could be attributed exclusively to the E field as long as the maximum B-field strength did not exceed 100 T.

For each RCF layer, the value of E_s was repeatedly varied in the particle tracer until a match was obtained between the simulated proton density behavior at the detector and that recorded experimentally. The maximum value of E_s was hence determined to be 8×10^9 V/m. Because of the fact that the wire is oriented vertically, d does not vary significantly within the field of view of the probe beam, and each RCF layer in the data set for shot *A* corresponds effectively to a *discrete* probing time. Hence, although there is some indication in Fig. 2 that a charging front might be propagating along the wire, such a front is not clearly resolved.

Relativity dictates that, for the whole target to have become positively charged, such a front must have traversed the wire at some finite velocity $v_f \leq c$. On shot *B*, a small but crucial change was made to the experimental setup to enable the resolution of such a charging front [see Fig. 1(b)]. The experiment was repeated under identical
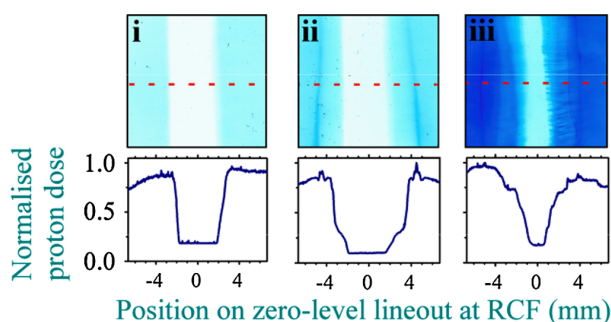

FIG. 1 (color online).   (a) Schematic describing the experimental setup used on shot *A*. (b) The corresponding setup used on shot *B*. In both cases, CPA$_2$ strikes into the page.

FIG. 2 (color online).   Samples of RCF data from shot *A* describing the CPA$_2$ interaction on a vertical 125 μm Au wire. The dashed red line marks the zero level of the probe proton beam. Corresponding proton density lineouts taken across the zero level are shown below each RCF image. Relative to the time of arrival of the CPA$_2$ interaction pulse, the probing times depicted by each layer are (i) 0, (ii) 10, and (iii) 25 ps.

conditions in terms of CPA_2 intensity and pulse duration and wire material and diameter. The wire itself, however, was modified so as to lie an angle $\theta = 30 \pm 0.5°$ to the vertical. As a result, the protons forming the bulk of the signal on a given RCF layer, all traveling at the same velocity, will have probed different points along the wire at different times based on their initial elevation angle relative to the zero level α. In this way, *continuous* observation of the target is provided.

As shown in Fig. 3, the motion of such an electric field front up the wire is easily resolved on shot *B*. It moves away from the CPA_2 interaction point at $v_f = (0.95 \pm 0.05)c$. The data presented here, hence, represent the first experimental measurement of the velocity at which field spreads over a target in an intense laser-solid interaction. With its single-shot, multiframe capabilities, proton radiography is arguably the only diagnostic currently available with which this measurement could have been made.

The observation of the propagation of this field front away from the CPA_2 interaction point at $\sim c$ enables the result of shot *A*, in describing the evolution of the magnitude of the radial electric field at the wire surface $E_s(t)$, to be interpreted as being caused by the flow of a transient current past the zero level, the magnitude of which may be shown by application of Gauss's law and the continuity
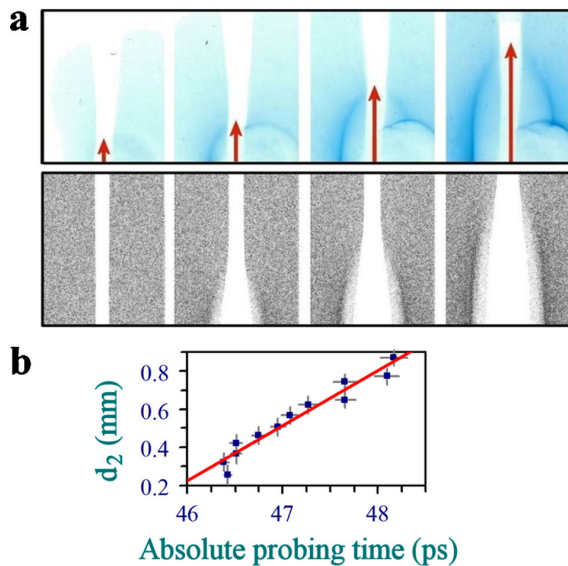

a

b

FIG. 3 (color online).   (a) Selection of experimental (top) and simulated (bottom) RCF data detailing the propagation of the charging front away from interaction point on shot *B*. The front position is indicated by the red arrows. The CPA_2 interaction plasma is visible to the bottom right of each experimental image as a circular area of proton depletion. (b) Measurement of distance from interaction point (d_2) as a function of absolute probing time (relative to the acceleration of the proton beam at the source). The velocity at which the charging front moves along the wire is measured to be $(0.95 \pm 0.05)c$.

equation to be given by $I(t) = 2\pi\epsilon_0 r_w v_f E_s(t)$. This current, then, is calculated to rise to its peak value of 8.1 kA before falling to below measurable levels (~ 1 kA) over a temporal window of some 20 ps. At later times, $I(t)$ will relax further as laser-driven hot electrons recombine with the wire plasma; ultimately, though, global neutralization of the target is facilitated by the flow of negative charge from the effectively infinite electron reservoir of the target mount [6].

Integration of $I(t)$ over time reveals the net total number of electrons moving downwards past the zero level to be $N_0 \simeq 3 \times 10^{11}$. This contrasts starkly with the total number of hot electrons predicted to have been accelerated by CPA_2 at the beam focus. The total number of hot electrons accelerated can be estimated by the energy balance relation $N_{\text{total}} = fE(k_B T_h)^{-1}$ [14], where f is the fraction of laser energy absorbed by hot electrons, E the pulse energy, and $k_B T_h$ the hot electron temperature which is predicted by $I\lambda^2$ scaling to be 1.4 MeV [15]. By assuming 20% absorption of laser energy into hot electrons, then [16], the 30 J CPA_2 pulse is estimated to accelerate some 3×10^{13} hot electrons at its focus. A large positive electrostatic potential, however, will develop in the region of the interaction as the laser-accelerated hot electron population streams to vacuum. Only the most energetic electrons will escape the developing potential well of the target, with the remainder returning to the wire under space-charge separation.

An estimation of the number of electrons escaping to vacuum may be made by developing a simple model of the electrostatic forces at work in this system. If a Maxwellian electron population is released from an initially neutral sphere of radius r_0, the sphere will develop a progressively larger electrostatic potential as more electrons stream to vacuum. By equating the minimum electron energy required for permanent escape to the depth of the electrostatic potential energy well at the sphere surface, the fraction ξ_∞ of the N_{total} laser-accelerated electrons lost to vacuum may be estimated by

$$\frac{\ln\xi_\infty}{\xi_\infty} = -\frac{r_c}{r_0}\frac{m_e c^2}{k_B T_h}N_{\text{total}},$$

where $r_c = 2.82 \times 10^{-15}$ m is the classical electron radius [17,18]. The main source of error in the calculation of ξ_∞ comes from the choice for r_0. With this in mind, by setting the value of r_0 to the average of its maximum and minimum possible values (the 62.5 μm wire radius and 5 μm CPA_2 spot radius, respectively), the total number of electrons escaping to vacuum is estimated to be $\sim 10^{11}$. In agreement with measurements performed under similar experimental conditions [19], the model predicts that $\sim 1\%$ of the hot electrons accelerated at the CPA_2 focus are subsequently lost to vacuum. At 3×10^{11}, then, the total number of electrons measured to have flowed past the zero level toward the interaction point is consistent with
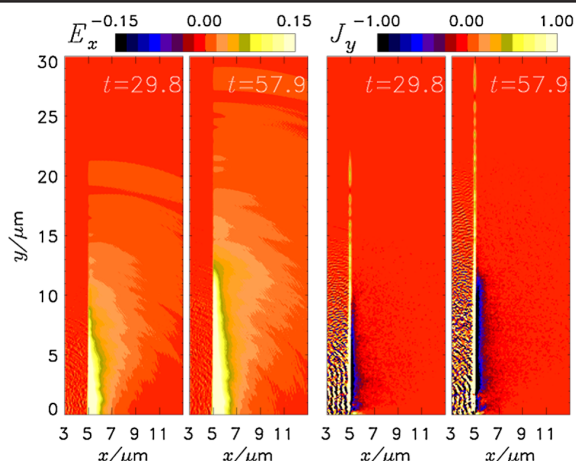
FIG. 4 (color online). PIC simulation results detailing E_x and J_y contours near the target rear surface for two different times (in femtoseconds) relative to the arrival of the pulse peak at the target front surface. The rear surface is located at $x = 5$. E_x is in units of 3.05×10^8 V/cm and J_y in units of 4.8×10^{13} A/cm^2.

the degree of global charge neutralization required following the permanent escape of a small fraction of the laser-accelerated hot electron population to vacuum.

The simulation of a scaled-down model experiment can prove fruitful in investigating the ultrafast electromagnetic dynamics of such a system. A 2D-Cartesian particle-in-cell (PIC) code [20] was hence used to simulate the interaction of a laser pulse of $\lambda = 1$ μm wavelength, 1.2×10^{19} W/cm^2 peak intensity, 100 fs duration, and 4 μm spot diameter normally incident with a plane plasma slab of electron density 10^{22} cm^{-3}. The target plasma extends over $0 < x < 5$ μm, while the pulse strikes from the left-hand side at $x = 0$, $y = 0$.

Figure 4 shows the contour levels of E_x and J_y (the components of the electric field and current density perpendicular and parallel to the target surface, respectively) at the rear side of the target. Only the $y > 0$ region is shown since E_x (J_y) is symmetrical (antisymmetrical) about $y = 0$. A propagation of both E_x and J_y along the target surface, i.e., along y, is observed. Two fronts are visible: an inner front propagating at $0.4c$ over the time interval investigated and an outer one propagating at $\simeq c$. The inner front encompasses a region of strong charge separation and current recirculation, features interpreted as being caused by the refluxing of hot electrons in and around the target. In the outer region, however, J_y is positive and is localized to a thin target surface layer. A similar feature is observed on the front side, i.e., near $x = 0$ (not shown). In our interpretation, this current, corresponding to the flow of negative charge toward the interaction region, is driven by the antennalike electromagnetic disturbance generated by transient charge separation in the region of the interaction.

The disturbance propagates freely in vacuum but penetrates only the skin layer of the target. Its observed propagation velocity ($\simeq c$) and the related vacuum features of E_y and B_z (omitted for brevity) are wholly consistent with this description.

In summary, our measurements quantitatively support previously made postulations that the positive charging of solid targets irradiated at relativistic laser intensities might be attributed to hot electron escape [6–8]. Furthermore, the spread of charge in intense laser-solid interactions, a significant phenomenon for many applications in this intensity regime [1,5–7], has now been resolved directly. Importantly, supported by the results of PIC simulations, a mechanism by which such ultrafast target charging might occur has been identified.

*kquinn09@qub.ac.uk
†Present address: Intense Laser Irradiation Laboratory, IPCF, CNR, Pisa, Italy.
‡On leave from the Institute of Computational Technologies, SD-RAS, Novosibirsk, Russia.

[1] M. Tabak et al., Phys. Plasmas **1**, 1626 (1994).
[2] J. S. Green et al., Nature Phys. **3**, 853 (2007).
[3] M. Borghesi et al., Fusion Sci. Technol. **49**, 412 (2006), and references therein.
[4] V. Malka et al., Nature Phys. **4**, 447 (2008).
[5] T. Toncian et al., Science **312**, 410 (2006).
[6] S. Kar et al., Phys. Rev. Lett. **100**, 105004 (2008).
[7] F. N. Beg et al., Phys. Rev. Lett. **92**, 095001 (2004).
[8] M. Borghesi et al., Appl. Phys. Lett. **82**, 1529 (2003).
[9] P. McKenna et al., Phys. Rev. Lett. **98**, 145001 (2007).
[10] L. Romagnani et al., Laser Part. Beams **26**, 241 (2008).
[11] http://www.gafchromic.com.
[12] C. N. Danson et al., Nucl. Fusion **44**, S239 (2004).
[13] D. Strickland and G. Mourou, Opt. Commun. **56**, 219 (1985).
[14] A. Hauer and R. J. Mason, Phys. Rev. Lett. **51**, 459 (1983).
[15] S. Wilks and W. Kruer, IEEE J. Quantum Electron. **33**, 1954 (1997).
[16] K. B. Wharton et al., Phys. Rev. Lett. **81**, 822 (1998).
[17] E. E. Fill, Phys. Plasmas **12**, 052704 (2005).
[18] V. T. Tikhonchuk, Phys. Plasmas **9**, 1416 (2002).
[19] G. Malka and J. L. Miquel, Phys. Rev. Lett. **77**, 75 (1996).
[20] G. I. Dudnikova et al., Comp. Technol. **10**, 37 (2005).

Dynamics of Self-Generated, Large Amplitude Magnetic Fields Following High-Intensity Laser Matter Interaction

G. Sarri,[1] A. Macchi,[2,3] C. A. Cecchetti,[4] S. Kar,[1] T. V. Liseykina,[5] X. H. Yang,[1] M. E. Dieckmann,[1]
J. Fuchs,[6] M. Galimberti,[7] L. A. Gizzi,[2] R. Jung,[8] I. Kourakis,[1] J. Osterholz,[8] F. Pegoraro,[2,3]
A. P. L. Robinson,[7] L. Romagnani,[6] O. Willi,[8] and M. Borghesi[1]

[1]*School of Mathematics and Physics, The Queen's University of Belfast, Belfast, BT7 1NN, United Kingdom*
[2]*Istituto Nazionale di Ottica, Consiglio Nazionale delle Ricerche, research unit "Adriano Gozzini", 56124 Pisa, Italy*
[3]*Dipartimento di Fisica "E. Fermi", Largo B. Pontecorvo 3, I-56127 Pisa, Italy*
[4]*Light4Tech s.r.l, 50018 Scandicci, Italy*
[5]*Institut für Physik, Universität Rostock, D-18051 Rostock, Germany*
[6]*LULI, Ecole Polytechnique, CNRS, CEA, UPMC, 91128 Palaiseau, France*
[7]*Rutherford Appleton Laboratory, Central Laser Facility, Chilton, OX11 0QX, United Kingdom*
[8]*Institute for Laser and Plasma Physics, Heinrich Heine University, Dusseldorf, Germany*
(Received 9 February 2012; revised manuscript received 30 May 2012; published 13 November 2012)

The dynamics of magnetic fields with an amplitude of several tens of megagauss, generated at both sides of a solid target irradiated with a high-intensity ($\sim 10^{19}$ W/cm^2) picosecond laser pulse, has been spatially and temporally resolved using a proton imaging technique. The amplitude of the magnetic fields is sufficiently large to have a constraining effect on the radial expansion of the plasma sheath at the target surfaces. These results, supported by numerical simulations and simple analytical modeling, may have implications for ion acceleration driven by the plasma sheath at the rear side of the target as well as for the laboratory study of self-collimated high-energy plasma jets.

The generation of magnetic fields in plasmas is a phenomenon of great relevance for a wide range of physical scenarios and it has been studied in laser-produced plasmas since the introduction of high-power lasers, with particular emphasis on their role in inertial confinement fusion [1]. In this scenario, involving nanosecond laser pulses of intensity $I_L \approx 10^{14}$–10^{16} W/cm^2, magnetic field generation is generally described by hydrodynamic modeling [2] and it has been recently characterized by temporally and spatially resolved measurements [3,4]. In the case of shorter ($\leq$ ps) and more intense ($I_L \gtrsim 10^{18}$ W/cm^2) laser pulses, the production of large currents of high energy "hot" electrons requires a more complex modeling [5] and a very intense magnetic field may be generated by, e.g., Weibel-like instabilities [6] or electron recirculation at the plasma boundary (fountain effect) [7]. In this latter case, magnetic fields may influence the emission of multi-MeV proton [8,9] and positron [10] beams. Magnetic fields generated in relativistic laser-produced plasmas are also of central importance in reproducing conditions resembling large-scale astrophysical processes [11] on a laboratory scale such as the self-collimation of relativistic leptonic jets [12] or the upstream-downstream mixing in supernova remnant shocks [13].

Previous experimental work has detected effects induced by such magnetic fields on external optical beams [14] or on the polarization of self-generated harmonics [15]. However, these measurements suffered from limitations, in terms either of the range of plasma density accessible [14] or of spatial and temporal resolution [15]. Furthermore, only the fields generated at the front (laser-irradiated) side of the target have been investigated; the magnetic field generation at the rear side, where proton acceleration in the expanding fast electron sheath takes place [16], is thus yet to be experimentally characterized.

In this Letter, we report on simultaneous measurements of the magnetic fields generated at the front and rear side of a solid target irradiated by a short and intense laser pulse, using a spatially and temporally resolved proton imaging technique [17]. Clear evidence is given of the generation of toroidal magnetic fields [maximum amplitude of ~ 50 megagauss (MG)] that decay in time on a picosecond time scale. Their spatial distribution and amplitude is consistent with the recirculation of the laser-accelerated electrons around the target and they are sufficiently intense to confine the radial plasma expansion.

The experiment was carried out at the Vulcan laser system in the Rutherford Appleton Laboratory [18] using two laser beams both with a central wavelength $\lambda_L = 1.05$ μm, energy $E_L = 50$ J, and duration $\tau_L = 1$ ps. Both beams were preceded by a lower intensity plateau ($I_P \approx 10^{12}$ W/cm^2, duration of ≈ 300 ps), due to amplified spontaneous emission. The first laser beam (CPA$_1$) was focussed, down to a focal spot with radius $r_L \approx 10$ μm, to a peak intensity of $I_L \approx 10^{19}$ W/cm^2 (dimensionless intensity $a_0 \approx 2.7$) onto a $d = 10$ μm thick aluminum foil, with a 45° angle of incidence. Hydrodynamic simulations [19] indicate that the laser prepulse ablates a
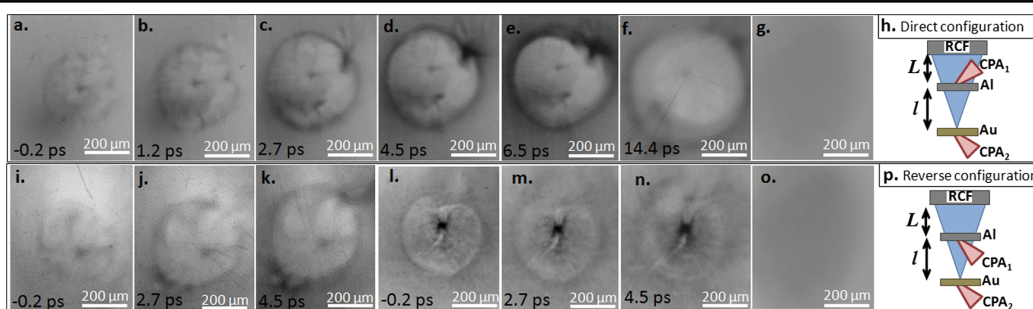
FIG. 1 (color online).   (a)–(f) Proton imaging snapshots in the direct configuration [sketched in frame (h)] and typical image of the unperturbed proton beam (g). (i)–(k) Additional set of images, still obtained in the direct configuration, from a different laser shot. (l)–(n) Proton imaging snapshots in the reverse configuration [sketched in the frame (p)] and typical image of the unperturbed proton beam (o). In all images, the spatial scale refers to the interaction plane and time is relative to the arrival of the peak of the CPA$_1$ pulse on target.

submicron layer of the aluminum foil that expands, in a plasma state, with an exponentially decreasing density profile (scale-length of 2.5 microns) and an electron temperature of ≈ 100 eV. The second laser beam (CPA$_2$) was focussed onto a 20 μm thick gold foil to generate, via target normal sheath acceleration [16], a proton beam with a Boltzmann-like spectrum [temperature of $T_P = 3.0 \pm 0.2$ MeV, and cutoff energy of $E_p \approx 20$ MeV, see Figs. 1(g) and 1(o) for its spatial distribution]. This beam was used as a charged-particle probe [17] and was recorded onto a stack of calibrated radiochromic films (RCFs) [20] giving a pointlike projection of the interaction with a geometrical magnification $M \approx (l + L)/l \approx 11$ with $l \approx 3$ mm and $L \approx 3$ cm the distances between the Au and Al foils and between the Al foil and the RCF respectively, as sketched in Figs. 1(h) and 1(p).

Previous theoretical modeling of high-intensity irradiation of thin solid targets [9] indicates the generation of magnetic fields having a toroidal structure with azimuthal symmetry and field lines parallel to the target surface. The intense electric fields generated in the expanding plasma sheath are almost normal to the target surface and have been directly detected using a probe proton beam parallel to the surface [21]. In the present experiment, in order to maximize the probe proton deflections due to magnetic fields over those due to electric fields, the propagation axis of the probe beam was normal to the target surface. In order to ascertain the magnetic nature of the deflecting fields, two configurations were adopted: the proton beam first encountered either the rear, unirradiated side of the target [*direct* configuration, Fig. 1(h)] or the front, irradiated side [*reverse* configuration, Fig. 1(p)]. For a given polarity of the magnetic field distribution, the two configurations should induce opposite deflections.

A typical set of RCF images, obtained in the direct configuration, are displayed in Figs. 1 [series (a)–(f) and (i)–(k)]. All images depict the presence of two main features: an outer ring (radius of the order of 100–200 μm) and an inner dot (radius of the order of 30–40 μm) of proton

accumulation. The outer ring is seen to slowly expand in time while roughly preserving its amplitude, whereas the inner dot becomes weaker and eventually disappears as time progresses. The reverse configuration [Figs. 1(l)–1(n)] induces an inverse deflection pattern, the central dot being much darker than the outer ring. In the direct configuration, the rear magnetic field focusses the protons propagating near the axis, whereas the front field enhances the divergence of the protons propagating at a wider angle [see Fig. 2(a)]. In the radiographs, this leads to the formation of an accumulation dot produced by the rear field and of an outer ring produced by the front field. In the reverse configuration, the same structures should be expected, yet with a different relative amplitude [Fig. 2(b)], in qualitative agreement with Fig. 1.

For a quantitative analysis of the magnetic field, particle tracing (PT) [22] simulations have been performed. The code follows the propagation of a proton beam, as employed in the experiment, through a prescribed magnetic field distribution and it includes the response of an RCF detector providing synthetic RCF images. The magnetic field is assumed, at both the front and rear sides of the target, as having a cylindrically symmetric toroidal distribution localized at the target surfaces, analogous to the model reported in Ref. [3]. In this model, the magnetic field at each of the two surfaces is described via the following parameters: B (field amplitude), R (radius of the field
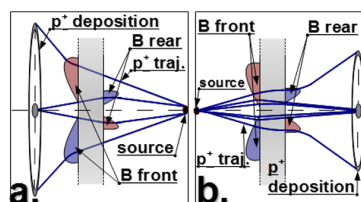

FIG. 2 (color online).   Sketch of the proton deflections induced by the magnetic fields in the direct (a) and reverse (b) configuration.

distribution), and L_r and L_z (field scale length in directions parallel and perpendicular to the target surface, respectively). These parameters were varied independently until a satisfactory match was reached between experimental and synthetic data, in terms of position and amplitude of the optical density peaks observed on RCF in correspondence to the ring and dot proton accumulation regions (see Fig. 3). PT simulations indicate that variations in B and R at both surfaces affect strongly peak amplitude and radius, respectively, while the field scale lengths have only a secondary effect on the synthetic RCF profile. By keeping $L_z = L_r = 10\ \mu$m [consistent with particle-in-cell (PIC) simulations, see later] and varying independently B and R at front and rear, profile matching as shown in Fig. 3 could be obtained, in both the direct and reverse configuration. The matching was considered satisfactory whenever the position and peak value of the simulated optical density maxima reproduced those of the experiment within $\pm 5\ \mu$m and 5%, respectively. These values are of the order of the intrinsic spatial resolution of the proton backlighting [17] and of a typical small-scale nonhomogeneity of the proton density on a beam cross section.

By iteratively applying this method to each RCF layer, it has been possible to simultaneously extract the temporal evolution of the amplitude and radius of the magnetic field at each side of the target (see Fig. 4). In correspondence to the falling edge of the laser pulse, both fields are seen to increase their radius and decrease their amplitude in time. After the laser irradiation ($t \geq 1$ ps in Fig. 4) the front field is seen to rapidly drop down to an almost constant amplitude of $B_F \approx 10$–12 MG while its radius increases up to an approximately constant value of 90 μm. On the other hand, the rear field exponentially decreases in amplitude with a typical time scale of the order of 7 ps. Meanwhile,

its radius increases in time with decreasing radial velocity. The longer persistence of magnetic fields at the front surface might be related to the presence of the underdense preplasma which is able to better support the magnetic field lines [23].

The presence of megagauss magnetic fields of opposite polarity at both sides of the target, is also supported by two-dimensional (2D) PIC simulations. A density profile composed of an exponential ramp reproducing the above mentioned preplasma, followed by a plasma bulk with electron density $n_e = 40 n_c$ and charge-to-mass ratio $Z/A = 9/26$ is assumed. The laser pulse has a Gaussian transverse profile (FWHM = 5 μm), a duration of 250 T (with the laser period $T = 3.3$ fs for 1 μm wavelength), dimensionless peak amplitude $a_0 = 2.7$ on axis and it is incident at 20° with respect to the normal of the target surface. The simulation ran up to 600 T $\simeq$ 2 ps, in order to overlap with the proton radiographs at earlier times. Figure 5 shows the generation of magnetic fields at the front and rear surfaces of the target, both having an approximately antisymmetrical distribution with respect to the axis, and polarity opposite to each other. Near the peak of the laser pulse, the fields reach a maximum amplitude of the order of 50 MG [Fig. 2(a)] and, during the rise of the laser pulse, they propagate in the transverse (y) direction with a constant velocity of $\simeq 2.7 \times 10^8$ m/s (consistent with the scenario experimentally investigated in Ref. [24]) while, as the laser intensity falls down, the field distribution drifts at a much lower velocity of $\sim 2 \times 10^7$ m/s until
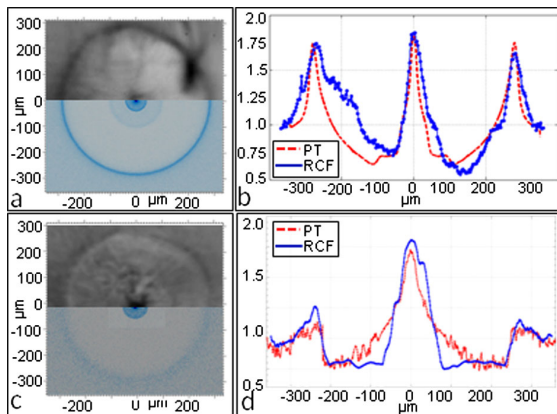

FIG. 3 (color online). Comparison between the experimental proton dose deposition as recorded by the RCF and that resulting from PT simulations assuming magnetic field distributions as the ones depicted in Fig. 5. Spatial scales refer to the interaction plane. Frames (a) and (b) refer to the direct configuration whereas frames (c) and (d) to the reverse one.
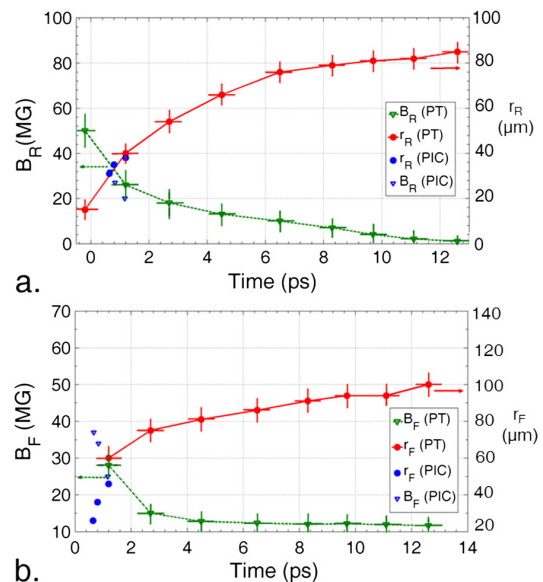

FIG. 4 (color online). Temporal evolution of the magnetic field amplitude and width at the rear (a) and front (b) side of the target as extracted from matching PT simulations, compared with the PIC results. Time refers to the arrival of the peak of CPA$_1$ on target.
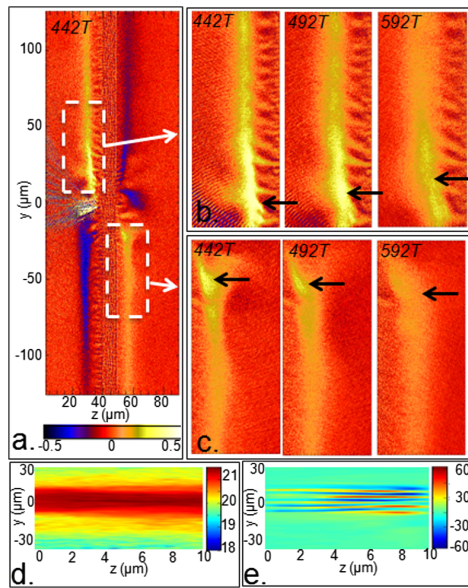
FIG. 5 (color online). (a)–(c): PIC simulation results. The frames show the transverse magnetic field (B_x) at $t = 442$ T in units of $B_0 = m_e \omega c / e = 107$ MG (a), and a zoom of the front (b) and rear (c) regions corresponding to the dashed rectangles in (a) at $t = 442$, 492, and 592 T. The black arrows indicate the position of the field maxima. (d)–(e): transport simulation results. The frames show the hot electron density inside the target in logarithmic scale and units of cm^{-3} (d) and the related magnetic field distribution in units of MG (e), both at $t = 1$ ps after the peak of the pulse.

stagnation is reached ($t \gtrsim 10$ ps). Within the intrinsic approximations that a PIC model unavoidably introduces (such as two-dimensional geometry and noncollisionality) a fair agreement is found between the experimental and numerical results (see Fig. 4). The PIC simulations also indicate that the electrostatic fields at the target's surfaces (not shown for brevity) are almost normal to the original surface (i.e., parallel to the main axis of propagation of the probing proton beam), in agreement with reported experimental observations [21], and allow us to estimate their intensity. The inclusion of such electrostatic fields does not affect significantly the PT images and can thus be neglected.

In principle, strong magnetic fields may also be generated inside the target due to resistive return currents which must balance the fast electron flow. In order to evaluate these fields, 3D simulations of the propagation of an electron beam through aluminium at an initial temperature of 1 eV were performed, using the code ZEPHYROS [25]. The simulation assumed suitable parameters for the electron beam (electron energy of 0.6 MeV, beam density of 4×10^{20} cm^{-3}, initial radius $r_s = 8.5$ μm, divergence $\theta_d \simeq 25°$ [26]) and a background-temperature dependent target resistivity [27]. Simulation results show the growth of small-scale filaments [28] with magnetic fields of

amplitude up to $\simeq 40$ MG and a characteristic spatial scale of 4 μm [Fig. 5(e)] which is below the proton imaging resolution [17]. Indeed, including magnetic fields in the target bulk with these simulated amplitude and spatial distribution induces in PT images the superposition of random fluctuations with amplitude below 5%. In these specific experimental conditions, the proton deflections are thus predominantly induced by the magnetic fields generated at the surfaces of the target.

It is of particular interest to analyze in more detail the field dynamics at the rear side of the target, which are much less explored, and are of direct relevance to the sheath ion acceleration. Here, the intense magnetic fields are generated by hot electron currents which, when crossing the rear surface, can not be balanced anymore by a counterpropagating return current. The expected temperature of hot electrons produced in the interaction is $T_h \simeq 0.6$ MeV, corresponding to a velocity $v_h \simeq 0.9c$ and to a relativistic factor $\gamma \simeq 2$; the hot electron density may be thus roughly estimated by a balance of energy fluxes, $f I_L = n_h v_h T_h$ yielding, for an absorption fraction $f \approx 0.1$ [26], $n_h \simeq 4 \times 10^{20}$ cm^{-3}. The total current due to hot electrons flowing through the target may be estimated as $I_h = e n_h v_h S \simeq 5 \times 10^6$ A, where $S = \pi r_L^2 = 3 \times 10^{-6}$ cm^{-2} is the area of the laser focal spot. The generation of a magnetic field requires a diverging electron flow since, if it were collimated, the large back-holding electric field **E** resulting from charge displacement would cause an equal and antiparallel displacement current $\mathbf{J}_E = \varepsilon_0 \partial_t \mathbf{E}$ of refluxing electrons. In this case, the source term for the magnetic field would exactly vanish. A divergent flow allows part of the current to flow in the radial direction forming loops which fall back to the target where a surface return current may close the circuit. We developed [29] a simple geometrical model of such a "fountain effect" to estimate the peak magnetic field as $B_{max} \simeq \alpha \theta_d B_0$ where $B_0 = \mu_0 I_h / (2\pi r_0)$, $\theta_d \simeq 25°$ is the divergence of the flow, $r_0 \simeq 15$ μm the radius of the electron emitting area, and $\alpha \simeq 8 T_h / (e E r_0)$ with E the typical value of the electric field. By estimating $E \simeq 10^{12}$ V m^{-1}, as suggested both by the PIC simulations and by proton emission data in similar conditions [21], we obtain a peak value of $B_{max} \simeq 70$ MG, in fair agreement with the experimental results. The corresponding value of the Larmor radius $m_e \gamma v_h / e B \simeq 3 B_{10}^{-1}$ μm (where B_{10} is the field in units of 10 MG) is small enough to indicate that electrons would be strongly magnetized in the regions of peak field. In these conditions, the magnetic field lines are frozen in the electron fluid, and the magnetic forces tend to confine the plasma. This tendency may account for the "negative acceleration" in the torus radius versus time $d^2 r_{F,R} / dt^2 < 0$ observed in Fig. 4. The magnetic energy density ($u_m = B^2 / 2\mu_0 = 4 \times 10^5 B_{10}^2$ J cm^{-3}) becomes in fact comparable to the maximum plasma thermal energy density expected at the peak of the laser pulse ($u_t = n_h T_h \simeq 4 \times 10^7$ J cm^{-3}).

Since the typical times for collisional dissipation and magnetic diffusion (of the order of tens of ns) are much longer than the time scales of the observation, the magnetic field value should mainly decay in time because of the sheath expansion and thus be roughly inversely proportional to the square of the observed radius, in agreement with the observations.

In conclusion, temporally and spatially resolved proton imaging indicates the generation of toroidal magnetic fields having tens of megagauss strength on both sides of a foil irradiated by an intense laser pulse. The magnetic fields are strong enough to effectively confine the radial expansion of the plasma region where they are generated, thus possibly affecting the ion acceleration in the expanding sheath. Moreover, the self-confining effect qualitatively resembles the collimation of leptonic astrophysical jets, suggesting that the present framework is suitable to investigate similar mechanisms in down-scaled laboratory experiments.

---

[1] J. A. Stamper, E. A. McLean and B. H. Ripin, Phys. Rev. Lett. **40**, 1177 (1978); A. Raven, O. Willi, and P. Rumsby, *ibid.* **41**, 554 (1978).

[2] M. G. Haines, Can. J. Phys. **64**, 912 (1986).

[3] C. A. Cecchetti *et al.*, Phys. Plasmas **16**, 043102 (2009).

[4] R. D. Petrasso *et al.*, Phys. Rev. Lett. **103**, 085001 (2009); J. R. Rygg *et al.*, Science **319**, 1223 (2008); L. Willingale *et al.*, Phys. Rev. Lett. **105**, 095001 (2010).

[5] R. J. Mason and M. Tabak, Phys. Rev. Lett. **80**, 524 (1998).

[6] U. Wagner *et al.*, Phys. Rev. E **70**, 026401 (2004).

[7] Y. Sakagami, H. Kawakami, S. Nagao, and C. Yamanaka, Phys. Rev. Lett. **42**, 839 (1979).

[8] S. Miyazaki, R. Sonobe, S. Kawata, and T. Kikuchi, Phys. Rev. E **71**, 056403 (2005).

[9] A. Pukhov, Phys. Rev. Lett. **86**, 3562 (2001).

[10] H. Chen *et al.*, Phys. Rev. Lett. **105**, 015003 (2010).

[11] B. A. Remington, D. Arnett, R. P. Drake, and H. Takabe, Science **284**, 1488 (1999).

[12] M. Honda and Y. S. Honda, Astrophys. J. **569**, L39 (2002).

[13] S. F. Martins, R. A. Fonseca, L. O. Silva, and W. B. Mori, Astrophys. J. **695**, L189 (2009).

[14] M. Borghesi, A. J. MacKinnon, A. R. Bell, R. Gaillard, and O. Willi, Phys. Rev. Lett. **81**, 112 (1998).

[15] M. Tatarakis *et al.*, Nature (London) **415**, 280 (2002).

[16] R. A. Snavely *et al.*, Phys. Rev. Lett. **85**, 2945 (2000).

[17] G. Sarri *et al.*, New J. Phys. **12**, 045006 (2010).

[18] C. N. Danson *et al.*, J. Mod. Opt. **45**, 1653 (1998).

[19] J. T. Larsen and S. M. Lane, J. Quant. Spectrosc. Radiat. Transfer **51**, 179 (1994).

[20] J. F. Dempsey, D. A. Low, S. Mutic, J. Markman, A. S. Kirov, G. H. Nussbaum, and J. F. Williamson, Med. Phys. **27**, 2462 (2000).

[21] L. Romagnani *et al.*, Phys. Rev. Lett. **95**, 195001 (2005).

[22] L. Romagnani, Ph.D. thesis, The Queen's University of Belfast, 2005.

[23] A. Frutchman, Phys. Fluids B **3**, 1908 (1991).

[24] K. Quinn *et al.*, Phys. Rev. Lett. **102**, 194801 (2009).

[25] S. Kar, A. Robinson, D. Carroll, O. Lundh, K. Markey, P. McKenna, P. Norreys, and M. Zepf, Phys. Rev. Lett. **102**, 055001 (2009).

[26] J. Fuchs *et al.*, Nat. Phys. **2**, 48 (2005).

[27] J. R. Davies, Phys. Rev. E **65**, 026407 (2002).

[28] X. H. Yuan *et al.*, New J. Phys. **12**, 063018 (2010).

[29] A. Macchi, arXiv:1202.0389v1.

Observation of Magnetized Soliton Remnants in the Wake of Intense
Laser Pulse Propagation through Plasmas

L. Romagnani,[1,2] A. Bigongiari,[1,*] S. Kar,[1] S. V. Bulanov,[3] C. A. Cecchetti,[1,7] T. Zh. Esirkepov,[3] M. Galimberti,[4]
R. Jung,[5] T. V. Liseykina,[6,†] A. Macchi,[7,8] J. Osterholz,[5] F. Pegoraro,[8] O. Willi,[5] and M. Borghesi[1]

[1]*Centre for Plasma Physics, School of Mathematics and Physics, The Queen's University of Belfast, Belfast BT7 1NN, United Kingdom*
[2]*LULI, École Polytechnique, CNRS, CEA, UPMC, route de Saclay, 91128 Palaiseau, France*
[3]*APRC, JAEA, Kizugawa, Kyoto 619-0215, Japan*
[4]*Central Laser Facility, Rutherford Appleton Laboratory, Chilton, United Kingdom*
[5]*Institut für Laser-und Plasmaphysik, Heinrich-Heine-Universität, Düsseldorf, Germany*
[6]*Max-Planck-Institut für Kernphysik, Heidelberg, Germany*
[7]*Istituto Nazionale di Ottica, CNR, Pisa, Italy*
[8]*Dipartimento di Fisica "E. Fermi," Università di Pisa, Pisa, Italy*
(Received 15 January 2010; published 19 October 2010)

Slowly evolving, regularly spaced patterns have been observed in proton projection images of plasma channels drilled by intense ($\gtrsim 10^{19}$ W cm^{-2}) short (~ 1 ps) laser pulses propagating in an ionized gas jet. The nature and geometry of the electromagnetic fields generating such patterns have been inferred by simulating the laser-plasma interaction and the following plasma evolution with a two-dimensional particle-in-cell code and the probe proton deflections by particle tracing. The analysis suggests the formation of rows of magnetized soliton remnants, with a quasistatic magnetic field associated with vortexlike electron currents resembling those of magnetic vortices.

The generation of coherent and ordered structures is one of the most prominent features in the dynamics of nonlinear many-body systems [1]. Theoretical and experimental studies have shown that plasmas interacting with laser pulses at relativistic intensities provide uniquely favorable conditions to investigate a broad class of nonlinear phenomena, the most known examples being arguably stimulated Raman and Brillouin scattering, laser filamentation and self-focusing, or the excitation of large amplitude wake plasma waves (see [2] and references therein). A different but not unrelated class of phenomena which has more recently attracted a great deal of attention includes the generation of organized nonlinear entities such as the so-called electromagnetic (EM) solitons [3–5] and electron vortices [6,7].

EM solitons have been extensively investigated both numerically [3] and in the frame of analytical models [4], and their macroscopic remnants [postsolitons (PSs)] have been experimentally observed to develop following the interaction of an intense laser pulse with a rarefied plasma [5]. Rows of electron vortices [6] and solitary magnetic dipole vortices (MDVs) [7] have been predicted to form in the trail of an intense laser pulse propagating in an underdense plasma. Besides being *per se* relevant as a benchmark for nonlinear plasma theoretical models, the experimental investigation of these phenomena might also have practical implications, as such nonlinear entities may contain a sizable fraction of the initial laser pulse energy [3–5] or be the signature of the development of plasma instabilities [6].

In this Letter we present the experimental observation, employing proton projection imaging (PPI) [8], of slowly evolving, localized EM structures, generated following the interaction at relativistic intensities of a picosecond laser pulse with an underdense plasma. These structures initially appear as a quasiperiodical pattern aligned along the low-density channel drilled by the laser pulse, and evolve on a time scale much longer than the pulse duration, remaining visible for more than 100 ps after the interaction. Simulations of the laser-driven plasma evolution carried out with a two-dimensional (2D) particle-in-cell (PIC) code show the development of EM solitons and their evolution into PSs inside laser-generated plasma channels [9]. Most noticeably the simulations indicate that, besides exhibiting properties typical of solitons (e.g., trapping of EM radiation in their inside and spatial localization consistent with the laser-pulse-depletion generation mechanism), these structures are also accompanied by vortexlike electron currents and quasistatic magnetic field patterns similar to those of MDVs. Extrapolating the results from 2D PIC simulations to the three-dimensional (3D) space, we can infer that in 3D the quasistatic magnetic field would assume a toroidal configuration (see also [3,7]). Particle tracing (PT) simulations [8] of the probe proton deflections show that such a 3D field distribution produces synthetic proton images consistent with the experimental observation.

The experiment was carried out at the Rutherford Appleton Laboratory (RAL), employing the VULCAN Nd-glass laser system operating in the chirped pulse

amplification (CPA) mode. A first laser pulse (1.054 μm wavelength, 1.2 ps duration, and delivering $\sim$30 J energy on target in linear polarization, hereafter named CPA$_1$) was focused at intensities $\gtrsim 10^{19}$ W cm^{-2} onto a supersonic helium (He) jet (2 mm aperture diameter nozzle driven at 50 bar pressure). The main pulse was always preceded by a pedestal (~ 300 ps duration and $\sim 10^6$ contrast ratio) capable of preionizing the interaction region. The electron density profile (linearly ramping along the laser axis up to its peak value $\sim 1.5 \times 10^{20}$ cm^{-3} over a distance of ~ 400 μm and remaining constant after that, see also [10]) was diagnosed by *in situ* frequency-doubled optical interferometry with picosecond time resolution. Comparison of the electron density profile with a separate characterization of the neutral gas density in the gas jet [10] indicates full preionization of the gas.

The EM fields generated in the He plasma in the trail of the CPA$_1$ laser pulse were diagnosed employing a laser-driven transverse proton probe, arranged in a point projection geometry with single-shot temporal multiframe capabilities [8]. The proton beam was accelerated by focusing a second laser pulse (CPA$_2$) (with similar parameters to CPA$_1$) onto a thin metal foil (typically a 10 μm thick Au foil, proton target) and it was detected employing a multilayer stack of radiochromic films (RCFs). The distance of the proton target from the CPA$_1$ propagation axis was $l \sim 3$ mm, and from the RCF pack it was $L \sim 3$ cm, giving a projection magnification $M \simeq L/l \sim 10$. Spatial and temporal resolutions of a few μm and of a few ps, respectively, were achieved.

Typical PPI experimental data are shown in Fig. 1. In the images, regions of a darker (lighter) color compared to the background proton signal correspond to regions of accumulation (depletion) of the probe protons, and for our experimental conditions the proton density variations reflect the EM field gradients in the probed plasma. The laser pulse, linearly polarized in the z direction (i.e., along the normal to the page, z being the symmetry axis of the proton

beam), is impinging from the left and by the earlier probing time $t \sim 3.5$ ps [1(a)] it has already exited the field of view to the right-hand side. In the proton images the channel drilled by the CPA$_1$ laser pulse into the ionized He jet is displayed as a lighter color region along x delimited by two dark lines [1(a)]. An additional dark line is visible near the channel axis on the left-hand side of the images. Longitudinal (i.e., reflecting a dependence of the deflecting fields on x) modulations first appear in the channel at probing times $t \gtrsim 5$ ps [1(b)], and later they evolve into a row of localized bubblelike structures aligned along the plasma channel and particularly evident on the right-hand side of the image 1(c). The localized structures slowly expand, remaining visible until the latest observation times ($t \gtrsim 140$ ps) [Fig. 2(a)], when they have evolved into a cloud of irregularly distributed bubbles. Whenever the plasma channel has split into secondary filaments, bubble structures are also observed inside some of the filaments [2(b)].

In order to infer on the nature of the observed patterns, the interaction of the laser pulse with the He plasma and the following plasma evolution were modeled with 2D PIC simulations [9]. The simulations were performed in a range of plasma densities and laser pulse parameters close to the experimental ones. In the following, lengths are in units of the laser wavelength λ, times in units of the laser period $T_L = \lambda/c = 2\pi/\omega$, densities in units of the critical density $n_c = m_e \omega^2/4\pi e^2$, and field amplitudes are expressed in terms of the dimensionless parameter $a = eE/m_e \omega c$ (see [9] for conversions to standard units). The largest grid employed in the simulations was a 7750×2400 mesh with a spatial resolution of $\lambda/10$, and the simulations were running up to a time $t = 1500 T_L$. The plasma density was linearly ramping from zero at $x = 25\lambda$ to its peak value $n_e = 0.1 n_c$ at $x = 425\lambda$, remaining constant after that. Ions with $Z/A = 1/2$ were assumed. The laser pulse (propagating along x) had a duration of $330 T_L$, it was S polarized (electric field in the z direction, normal to the (x, y) simulation plane), and its field peak amplitude was $a = 2.7$.

In the simulation a low-density channel is ponderomotively bored into the plasma by the laser pulse, with the channel breaking into a number of secondary narrower channels in the higher background density region [9]. Following the initial evolution [9,10] and after the laser pulse has exited the simulation box, both the ion and
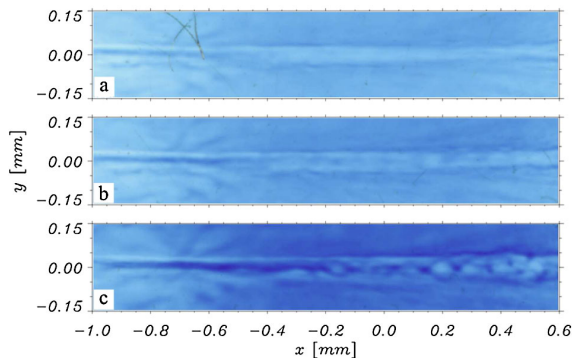

FIG. 1 (color online). Typical PPI data (acquired in a single laser shot). The probing times, relative to the arrival of the peak of the interaction pulse at $x = y = 0$, are (a) $t = 3.5$ ps, (b) $t = 7$ ps, and (c) 17 ps [probe proton energies $\sim$12 MeV (a), $\sim$11 MeV (b) and $\sim$8 MeV (c)].
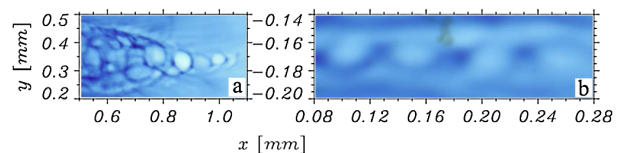

FIG. 2 (color online). (a) Detail of PPI data showing bubble structures at late times ($t \sim 140$ ps, probe proton energy $\sim$8 MeV). (b) Detail of a secondary filament exhibiting a multiple bubble pattern ($t \sim 37$ ps, probe proton energy $\sim$11 MeV).

electron densities are left with a depression on the channel axis while peaking at the channel edges, giving rise to a space-charge separation electric field, mainly in the y direction, E_y. At this stage ($t > 650T_L$) E_y has evolved into two ambipolar fronts on each side of the channel; i.e., it points outwards outside the channel and inwards inside it. An electron current is generated along the channel axis in the wake of the laser pulse (electrons flowing in the pulse propagation direction) and it is compensated by two current sheaths in the opposite direction along the channel edges. Such currents persist until the latest simulation times and produce a quasistatic magnetic field B_z, with $B_z < 0$ (i.e., entering the simulation plane) above the channel axis and $B_z > 0$ below it.

At even later times ($t > 750T_L$) the simulations show the onset of localized modulated patterns in the particle, current, and fields' distributions inside the main and secondary channels. A detail of the EM field distribution in a single localized structure is shown in Fig. 3. The frequency-resolved analysis of the fields reveals an oscillating EM field component (B_x, B_y, E_z) which has a frequency just below the plasma frequency of the surrounding plasma and is therefore trapped inside the structure [3(b) and 3(c)]. The current density forms an antisymmetric double loop, giving rise to a double lobe of quasistatic magnetic field B_z, with $B_z < 0$ above the channel axis and $B_z > 0$ below it [3(d)]. We stress here that this is a constant field, associated with a stationary electron current, differently from the oscillating field observed in other works [3] and also here. The combined effect of the magnetic pressure associated with the static B_z component and of the radiation pressure associated with the oscillating fields drills a density depression in

correspondence with each localized structure. The resulting space-charge separation gives rise to a quasistatic electric field (E_x, E_y) in the radial direction from each structure center [3(a)]. Such field is less pronounced near the channel axis (due to the fact that the plasma density is lower here), and at the latest times ($t > 875T_L$) it tends to overlap with the ambipolar field at the channel edges.

It should be noted here that the presence of a trapped oscillating field is typical of EM solitons and PSs, while the current and quasistatic magnetic field distributions resemble those of MDVs. As these features coexist and the static and oscillating fields are of similar strength, it is difficult to identify the observed structures with either solitons or vortices. However, their position in the plasma channels provides a hint of the mechanism leading to their formation and hence of their primary nature. The localization of the structures towards the end of the channels (both in the experiment and PIC simulations) is qualitatively consistent with estimations of the laser-pulse-depletion length ($l_{\rm depl} \sim cT_L(n_c/n_e) \sim$ mm range) [3], indicating that frequency downshift of the laser pulse and the consequent trapping of EM radiation is likely to be the relevant generation mechanism [3,4]. Hence the observed structures should be regarded as PSs. A likely scenario is that the electron currents readjust according to the density distribution associated with the preformed soliton structure, therefore giving rise to the vortexlike pattern. As these currents will always be present in the wake of a laser pulse propagating in an underdense plasma, a static magnetic field could be an unavoidable feature of laser-excited solitons.

To verify that the field distributions observed in the 2D PIC simulation, extrapolated to a 3D geometry, may produce the observed proton images, PT simulations [8] have been carried out. In PTs the deflections of test protons crossing a given 3D EM field distribution are numerically computed and the particle density in the proton detector is calculated. Only static fields have been considered, as for our experimental conditions the contribution of the oscillating components to the proton deflection is canceled out by integration along the particle trajectories. The input 3D field distribution is extrapolated from the 2D PIC outputs by assuming an azimuthal symmetry around the channel axis, and a reference frame with cylindrical coordinates (ρ, ϕ, x) (x being the channel axis) is considered. The electric field is chosen to be oriented along the radial $\hat{\rho}$ direction and the magnetic field to form closed loops in the azimuthal $\hat{\phi}$ direction.

We first simulated the deflections given by the fields associated with the plasma channel before the longitudinal modulations appear. In the simulation the electric field is taken of the form $E_\rho = f_-(\rho) + f_+(\rho)$, with $f_\pm(\rho) = 2.33E_0[(\rho \pm \alpha)/\beta]\exp\{-[(\rho \pm \alpha)/\beta]^2\}$, and the magnetic field of the form $B_\phi = 2.33B_0(\rho/\gamma) \times \exp[-(\rho/\gamma)^2]$, where the numerical factor 2.33 is chosen in order for E_0 and B_0 to represent the peak fields' amplitudes. The parameters α, β, and γ can be related to the
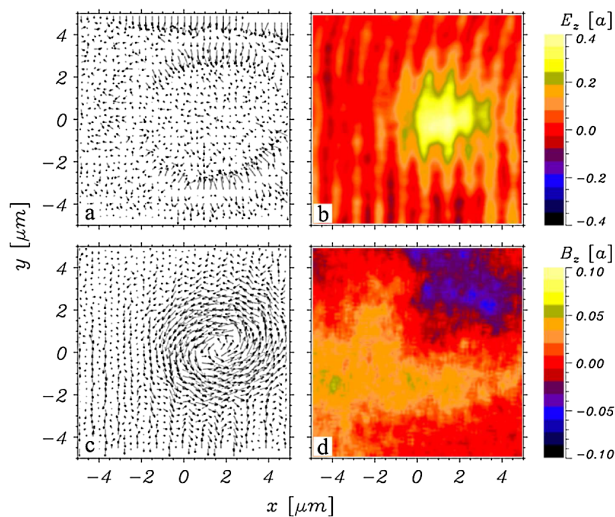

FIG. 3 (color online). Details of the fields' distribution in a single PS from PIC simulations. (a) Quasistatic electric field (E_x, E_y) at $t = 875T_L$, (b) oscillating electric field E_z, (c) oscillating magnetic field (B_x, B_y), and (d) quasistatic magnetic field B_z at $t = 800T_L$.
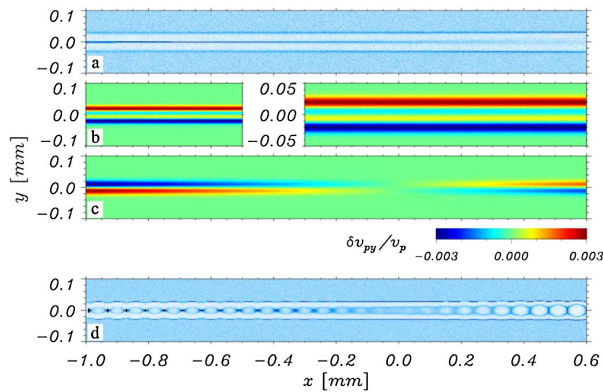
FIG. 4 (color online). Particle tracing simulations. (a) Simulated proton image and (b),(c) maps of the proton deflection $\delta\theta \sim \delta v_{py}/v_p$ arising from (b) the **E** field alone (y scale enlarged for $x > -0.5$ mm to highlight the E_y focusing effect inside the channel) and from (c) the **B** field alone for the unmodulated channel. (d) Simulated proton image for the modulated channel.

spatial characteristics of the PPI image of the channel, yielding $\alpha \simeq \gamma \simeq (15-20)$ μm and $\beta \simeq (5-10)$ μm. The PPI data were best reproduced for $E_0 \simeq (1-2) \times 10^9$ V m^{-1} and $B_0 \simeq (150-300)$ T [Fig. 4(a)], in fair agreement with the values obtained from the PIC simulations. Inspection of the PT results clarifies how the experimental proton images form. The ambipolar E_y field tends to pile up the protons on the channel axis and at the channel edges [see deflection map 4(b)]. The $v_{px}B_z$ component of the $\mathbf{v_p} \times \mathbf{B}$ ($\mathbf{v_p}$ being the proton velocity, with v_{px} mainly arising from the proton beam divergence) force tends to focus the protons on the axis for $x < 0$ (where $v_{px} < 0$, while $B_z < 0$ for $y > 0$ and $B_z > 0$ for $y < 0$), and at the channel edges for $x > 0$ (where $v_{px} > 0$) [4(c)]. Hence E_y gives rise to the dark lines delimiting the channel and contributes to the central dark line visible for $x < 0$. B_z contributes to the central dark line for $x < 0$, while for $x > 0$ it cancels the piling up on the channel axis given by E_y and contributes to the external dark lines.

We next introduce a modulation [described by a $\sin^2$ $(2\pi x/l)$ weight function, where $l \simeq 60$ μm] of B_ϕ along the x direction. Such a field distribution describes a row of tori and represents the simplest possible extrapolation to a 3D geometry of the magnetic field associated with the vortexlike patterns observed in the 2D PIC simulations. The resulting simulated proton image [Fig. 4(d)] is in qualitative agreement with the experimental ones [Figs. 1(c) and 2]. The PT also indicates that the proton deflection in the y direction arises from the same effects described above, with additional longitudinal modulations in the proton density introduced by the B_ϕ dependence on x. We stress here that the presence of a modulated magnetic field, introduced

for consistency with the 2D PIC simulations, is critical in order to reproduce the experimental data and that the proton deflection induced by the electric field alone cannot explain the experimental results.

In conclusion, we have shown that stable modulated patterns observed via PPI inside laser-plasma channels can be identified with the late time remnants of EM solitons observed in PIC simulations. PIC simulations also reveal the simultaneous presence of a quasistatic magnetic field associated with a vortexlike current distribution, and PT simulations evidence that such a magnetic field is essential for their experimental detection. The peculiar features of these structures, such as their magnetic nature, their organization into periodical patterns, and their detailed 3D topology, should be stimulating for further theoretical and numerical investigations.

*Present address: CEA/DSM/IRAMIS/LSI, École Polytechnique, 91128 Palaiseau, France, and LULI, Université Paris VI, 3 rue Galilée, 94200 Ivry-sur-Seine, France.

†Present address: Institut für Physik, Universität Rostock, Rostock, Germany.

[1] T. Dauxois and M. Peyrard, *Physics of Solitons* (Cambridge University Press, Cambridge, England, 2006).

[2] G. A. Morou *et al.*, Rev. Mod. Phys. **78**, 309 (2006).

[3] S. V. Bulanov *et al.*, Phys. Fluids B **4**, 1935 (1992); S. V. Bulanov *et al.*, Phys. Rev. Lett. **82**, 3440 (1999); N. M. Naumova *et al.*, Phys. Rev. Lett. **87**, 185004 (2001); T. Esirkepov *et al.*, Phys. Rev. Lett. **89**, 275002 (2002); T. Esirkepov *et al.*, Phys. Rev. Lett. **92**, 255001 (2004).

[4] V. A. Kozlov *et al.*, Sov. Phys. JETP **49**, 75 (1979); P. K. Kaw, A. Sen, and T. Katsouleas, Phys. Rev. Lett. **68**, 3172 (1992); M. Lontano *et al.*, Phys. Plasmas **10**, 639 (2003).

[5] M. Borghesi *et al.*, Phys. Rev. Lett. **88**, 135002 (2002).

[6] S. V. Bulanov *et al.*, Phys. Rev. Lett. **76**, 3562 (1996); F. Califano, F. Pegoraro, and S. V. Bulanov, Phys. Rev. Lett. **84**, 3602 (2000); A. G. Zhidkov *et al.*, Phys. Rev. E **76**, 016401 (2007).

[7] N. M. Naumova *et al.*, Phys. Plasmas **8**, 4149 (2001); T. Nakamura and K. Mima, Phys. Rev. Lett. **100**, 205006 (2008).

[8] M. Borghesi *et al.*, Appl. Phys. Lett. **82**, 1529 (2003); A. J. Mackinnon *et al.*, Rev. Sci. Instrum. **75**, 3531 (2004).

[9] A. Macchi *et al.*, Plasma Phys. Controlled Fusion **49**, B71 (2007).

[10] S. Kar *et al.*, New J. Phys. **9**, 402 (2007).

Bibliography

[1] D. Strickland, G. Mourou, *Compression of amplified chirped optical pulses*, Opt.Commun. 56, 219 (1985); P. Main, D. Strickland, P. Bado, M. Pessot, G. Mourou, *Generation of ultrahigh peak power pulses by chirped pulse amplification*, IEEE Journal of Quantum Electronics **24**, 398 (1988)

[2] G. Mourou, T. Tajima, S. Bulanov, *Optics in the relativistic regime*, Rev. Mod. Phys. **78**, 309 (2006)

[3] APRI: Advanced Photonics Research Institute, https://apri.gist.ac.kr

[4] SULF: Shanghai super-intense ultrafast laser facility, english.siom.cas.cn; Zh. Guo, L. Yu, J. Wang et al., *Improvement of the focusing ability by double deformable mirrors for 10-PW-level Ti: sapphire chirped pulse amplification laser system*, Optics Express **26** (2018)

[5] Research Center of Laser Fusion, CAEP, https://www.nti.org/learn/facilities/702/

[6] https://www.eli-beams.eu/en/; http://www.eli-np.ro; S. Kühn, M. Dumergue, S. Kahaly et al., *The ELI-ALPS facility: the next generation of attosecond sources*, J. Phys. B: At. Mol. Opt. Phys. **50**, 132002 (2007)

[7] J.P. Zou, C. Le Blanc, D. N. Papadopoulos et al., *Design and current progress of the Apollon 10 PW project*, High Power Laser Sci. Eng. **3**, E2 (2015); D. N. Papadopoulos, J. P. Zou, C. Le Blanc et al., *First commissioning results of the Apollon laser on the 1 PW beam line* in Conference on Lasers and Electro-Optics, OSA Technical Digest (Optical Society of America, 2019), paper STu3E.4.

[8] R. P. Drake, High-energy-fensity physics: fundamentals, inertial fusion, and experimental astro-physics, 1st ed. (Springer, 2006). ISBN-13: 978-3540293149

[9] V.E. Fortov, Extreme states of matter on Earth and in the Cosmos (Springer, 2011). ISBN 978-3-319-18952-9

[10] B. Remington, R. Drake, and D. Ryutov, *Experimental astrophysics with high power lasers and Z pinches*, Ref. Mod. Phys. **78**, 755 (2006)

[11] M. E. Dieckmann, D. Doria, G. Sarri, et al. *Electrostatic shock waves in the laboratory and astrophysics: similarities and differences*, Plasma Phys. Contr. Fusion **60**, 014014 (2018)

[12] J. M. Dawson, *Particle simulation of plasmas*, Ref. Mod. Phys. **55**, 403 (1983)

[13] C.K. Birdsall & A. B. Langdon, Plasma physics via computer simulation (Institute of Physics, Bristol) (1991)

[14] A. Pukhov, *Three-dimensional electromagnetic relativistic particle-in-cell code VLPL (Virtual Laser Plasma Lab)*, J. Plasma Phys. **61**, 425 (1999); Tückmantel, A. Pukhov, *H-VLPL: A three-dimensional relativistic PIC/fluid hybrid code*, J. Plasma Phys. **269**, 168 (2014)

[15] T. D. Arber, K. Bennett, C. S. Brady et al., *Contemporary particle-in-cell approach to laser-plasma modelling*, Plasma Phys. Contr. Fusion **57**, 113001 (2015)

[16] J. Derouillat, A. Beckb, F.Pérez et al., *Smilei : A collaborative, open-source, multi-purpose particle-in-cell code for plasma simulation*, Comp. Phys. Comm. **222**, 351 (2018)

[17] R. A. Fonseca, L. O. Silva, F. S. Tsung et al. *OSIRIS: A three-dimensional, fully relativistic Particle in Cell Code for modeling plasma based accelerators*, Lecture Notes in Computer Science V. 2331, pp 342-351 (2002); F. Fiuza, M. Marti, R. A. Fonseca, L. O. Silva, J. Tonge, J. May, & W. B. Mori, *Efficient modeling of laser–plasma interactions in high energy density scenarios*, Plasma Phys. Contr. Fusion **53**, 074004 (2011)

[18] E. Lefebvre, N. Cochet, S. Fritzler et al., *Electron and photon production from relativistic laser–plasma interactions*, Nucl. Fusion **43**, 629 (2003)

[19] Ch. Varin, Ch. Peltz, Th. Brabec, Th. Fennel, *Attosecond plasma wave dynamics in laser-driven cluster nanoplasmas*, Phys. Rev. Lett. **108**, 175007 (2012)

[20] V.A Vshivkov, N.M. Naumova, F. Pegoraro, S.V. Bulanov, *Nonlinear electrodynamics of the interaction of ultra-intense laser pulses with a thin foil*, Phys. Plasmas **5**, 2727 (1998)

[21] J. Dawson, *On the production of plasma by giant pulse Lasers*, The Physics of Fluids **7**, 981 (1964)

[22] G. Sarri, K. Poder, J.M. Cole et al., *Generation of neutral and high-density electron–positron pair plasmas in the laboratory*, Nature Comm. **6**, 6747 (2015); T. Tajima & J.M. Dawson, *Laser Electron Accelerator*, Phys. Rev. Lett. **43**, 267 (1979); C. McGuffey, A. G. R. Thomas, W. Schumaker el al., *Ionization induced trapping in a Laser wakefield accelerator*, Phys. Rev. Lett. **104**, 025004 (2010)

[23] A. Askar'yan, *Cerenkov radiation and transition radiation from electromagnetic waves*, Soviet Phys. JETP **15**, 943 (1962)

[24] F. Pegoraro, *The world of electromagnetic matter*, 102° Congresso Nazionale - Società Italiana di Fisica, Padova, 2016

[25] D. A. Uzdensky, *Radiative magnetic reconnection*, in In: Gonzalez W., Parker E. (eds) Magnetic Reconnection. Astrophysics and Space Science Library, vol 427. Springer, Cham (2016)

[26] S. P. Hatchett, C. G. Brown, T.E.Cowan et al., *Electron, photon, and ion beams from the relativistic interaction of Petawatt laser pulses with solid targets*, Phys. Plasmas **7**, 2076 (2000)

[27] S. Fritzler, V. Malka, G. Grillon, J.P. Rousseau, *Proton beams generated with high-intensity lasers: Applications to medical isotope production*, Appl. Phys. Lett. **83**, 3039 (2003)

[28] S.V. Bulanov & V.S.Khoroshkov, *Feasibility of using laser ion accelerators in proton therapy*, Plasma Physics Reports **28**, 493-496 (2002); S. V. Bulanov, Ja.J. Wilkens, T.Zh. Esirkepov et al., *Ion acceleration for hadron therapy* Phys.-Usp. **57**, 1149 (2014); L. Karsch, E. Beyreuther, W. Enghardt, et al., *Towards ion beam therapy based on laser plasma accelerators*, Acta Oncol. **56**, 1359 (2017)

[29] G. Rigon, A. Casner, B. Albertazzi et al., *Rayleigh-Taylor instability experiments on the LULI2000 laser in scaled conditions for young supernova remnants*, Phys. Rev. E **100**, 021201(R) (2019); R. D. Petrasso, *Rayleigh's challenge endures*, Nature (London) **367**, 217 (1994); A. Casner, L. Masse, B. Delorme et al., *Progress in indirect and direct-drive planar experiments on hydrodynamic instabilities at the ablation front*, Phys. Plasmas **21**, 122702 (2014); D. S. Clark & M. Tabak, *Acceleration- and deceleration-phase nonlinear Rayleigh-Taylor growth at spherical interfaces*, Phys. Rev. E **72**, 056308 (2005); J. P. Ostriker & Ch. F. McKee *Astrophysical blastwaves*, Ref. Mod. Phys. **60**, 1 (1988)

[30] D. P. Higginson, Ph. Korneev, C. Ruyer et al., *Laboratory investigation of particle acceleration and magnetic field compression in collisionless colliding fast plasma flows*, Commun. Phys. **2**, 60 (2019); Y. Kuramitsu, Y. Sakawa, T. Morita et al., *Laboratory investigations on the origins of cosmic rays*, Plasma Phys. Contr. Fusion **54**, 124049 (2012)

[31] G. Mourou, *Extreme ligh physics and application*, Ref. Mod. Phys. **91**, 030501 (2019)

[32] I. Kostyukov, E. N. Nerush, A. M. Samsonov, A. Golovanov, D. Serebryakov, *Some processes in extremely strong EM fields: from atomic systems and laser-plasma interactions to astrophysical phenomena*, Proceedings of SPIE [0277-786X] **11039**, 1103907 (2019)

[33] F.Z. Sauter, *Über das Verhalten eines Elektrons im homogenen elektrischen Feld nach der relativistischen Theorie Diracs*, Z. Phys. **73**, 547 (1932); W. Heisenberg, H.Z. Euler, *Consequences of Dirac's theory of positrons*, Phys. **98**, 714 (1936;) J. Schwinger, *On Gauge Invariance and Vacuum Polarization*, Phys. Rev. **82**, 664 (1951)

[34] E. N. Nerush, I. Y. Kostyukov, A. M. Fedotov, et al., *Laser field absorption in self-generated electron-positron pair plasma*, Phys. Rev. Lett. **106**, 035001 (2011)

[35] C. H. Jaroschek & M. Hoshino, *Radiation-dominated relativistic current sheets*, Phys. Rev. Lett. **103**, 075002 (2009)

[36] M. Tavani, A. Bulgarelli, V. Vittorini et al., *Discovery of powerful gamma-ray flares from the Crab Nebula*, Science. **331**, 736 (2011); B. Cerruti, D. A. Uzdensky, M. C. Begelman, *Extreme particle acceleration in magnetic reconnection layers: application to the gamma-ray flares in the Crab Nebula*, The Astrophysical Journal, **746**, 178 (2012)

[37] CERN Symposium of high energy accelerators and pion physics, Proceedings v. 1, Gen., 1956: I.B. Fainberg, *The use of plasma waveguides as accelerating structures in linear accelerators*, p. 84; V.I. Veksler, *Coherent principle of acceleration of charged particles*, ibid, p. 80; G.J. Budker, *Relativistic stabilized electron beam*, ibid, p. 68

[38] V. Veksler, *The principle of coherent acceleration of charged particles*, The Soviet Journal of Atomic Energy **2**, 525 (1957)

[39] I. B. Fainberg, *Acceleration of particles in a plasma*, The Soviet Journal of Atomic Energy **6**, 297 (1960)

[40] M. Borghesi, J. Fuchs, S.V. Bulanov et al., *Fast ion generation by high-intensity laser irradiation of solid targets and applications* , Fusion Sci. Tech. **49**, 412 (2006); H. Daido, M. Nishiuchi, A.S. Pirozkhov, *Review of laser-driven ion sources and their applications*, Rep. Prog. Phys. **75**, 056401 (2012)

[41] A. Macchi, M. Borghesi, M. Passoni, *Ion acceleration by superintense laser-plasma interaction*, Ref. Mod. Phys. **85**, 751 (2013)

[42] S. V. Bulanov, N. M. Naumova, & F. Pegoraro, *Interaction of an ultrashort, relativistically strong laser pulse with an overdense plasma*, Phys. Plasmas **1**, 745 (1994); S. V. Bulanov, T. Zh. Esirkepov, N. M. Naumova, & F. Pegoraro, *Evolution of the frequency spectrum of a relativistically strong laser pulse in a plasma*, Phys. Scr. T. **63**, 258 (1996); R. Lichters, J. Meyer-ter-Vehn, & A. Pukhov, *Short-pulse laser harmonics from oscillating plasma surfaces driven at relativistic intensity*, Phys. Plasmas **3**, 3425 (1996); P. Gibbon, *Harmonic generation by femtosecond laser-solid interaction: a coherent "water-window" light source?* Phys. Rev. Lett. **76**, 50 (1996); T. Baeva, S. Gordienko, & A. Pukhov, *Theory of high-order harmonic generation in relativistic laser interaction with overdense plasma*, Phys. Rev. E **74**, 046404 (2006)

[43] U. Teubner, & P. Gibbon, *High-order harmonics from laser-irradiated plasma surfaces*, Ref. Mod. Phys. **81**, 445 (2009); C. Thaury, & F. Quéré, *High-order harmonic and attosecond pulse generation on plasma mirrors: basic mechanisms*, J. Phys. B **43**, 213001 (2010); D. Kormin, A. Borot, G. Ma et al. *Spectral interferometry with waveform-dependent relativistic high-order harmonics from plasma surfaces*, Nature Comm. **9**, 4992 (2018)

[44] A. D. Piliya, *Wave conversion in an inhomogeneous plasma*, Sov. Phys. Tech. Phys. **11**, 609 (1966); H.-J. Kull, *Linear mode conversion in laser plasmas*, Phys. Fluids **26**, 1881 (1983)

[45] W. L. Kruer, The Physics of Laser Plasma Interactions (Addison Wesley, New York, 1988)

[46] F. Cattani, A. Kim, D. Anderson & M. Lisak, *Threshold of induced transparency in the relativistic interaction of an electromagnetic wave with overdense plasmas*, Phys. Rev. E **62**, 1234 (2000)

[47] A.I. Akhiezer, R.V. Polovin, *Theory of Wave Motion of an Electron Plasma*, Sov. Phys. JETP **3**(5), 696 (1956); P. Sprangle, E. Esarey, A. Ting, *Nonlinear theory of intense laser-plasma interactions*, Phys. Rev. Lett. **64**, 2011 (1990)

[48] A. Macchi, S. Veghini, F. Pegoraro, *"Light Sail" acceleration reexamined*, Phys. Rev. Lett. **103**, 085003 (2009)

[49] A. Macchi "A Superintense Laser-Plasma Interaction Theory Primer" (Spriger, Netherlands, 2013)

[50] J.C. Fernández, D.C. Gautier, Ch. Huang et al., *Laser-plasmas in the relativistic-transparency regime: science and applications*, Phys. Plasmas **24**, 056702 (2017)

[51] J. R. Davies, *Laser absorption by overdense plasmas in the relativistic regime*, Plasma Phys. Contr. Fusion **51**, 014006 (2008)

[52] W. Rozmus, V.T. Tikhonchuk & R. Cauble, *A model of ultrashort laser pulse absorption in solid targets*, Phys. Plasmas **3**, 360 (1996)

[53] P. Gibbon, Short Pulse Laser Interaction with Matter (Imperial College Press, London, 2005)

[54] T. Liseykina, M. Mulser, M. Murakami, *Collisionless absorption, hot electron generation, and energy scaling in intense laser-target interaction*, Phys. Plasmas **22**, 033302 (2015)

[55] P. Gibbon & A. R. Bell, *Collisionless absorption in sharp-edged plasmas*, Phys. Rev. Lett. **68**, 1535 (1992); L. M. Chen, J. Zhang, Q. L. Dong et al., *Hot electron generation via vacuum heating process in femtosecond laser–solid interactions*, Phys. Plasmas **8**, 2925 (2001); V. S. Rastunkov & V. P. Krainov, *Electron stochastic heating in the interaction of a short laser pulse with overdense plasma*, Laser Phys. 15, 262 (2005)

[56] Y. Sentoku, V.Y. Bychenkov, K. Flippo et al., *High-energy ion generation in interaction. of short laser pulse with high-density plasma*, Appl. Phys. B **74**, 207 (2002); G. Cristoforetti, P. Londrillo, P. K. Singh, et al. *Transition from coherent to stochastic electron heating in ultrashort relativistic laser interaction with structured targets*, Scientific Reports **7**, 1479 (2017)

[57] D. Umstadter, *Relativistic laser–plasma interactions*, J. Phys. D **36**, R151 (2003); S. Kato, B. Bhattacharyya, A. Nishiguchi & K. Mima, *Wave breaking and absorption efficiency for short pulse p-polarized laser light in a very steep density gradient*, Phys. Fluids B 5, 564 (1993); H.-B. Cai, *Vacuum heating in the interaction of ultrashort, relativistically strong laser pulses with solid targets*, Phys. Plasmas **13**, 063108 (2006)

[58] D. F. Zaretsky, Ph. A. Korneev, S. V. Popruzhenko & W. Becker, *Landau damping in thin films irradiated by a strong laser field*, J. Phys. B **37**, 4817 (2004); Ph. A. Korneev, S. V. Popruzhenko, D. F. Zaretsky & W. Becker, *Collisionless heating of a nanoplasma in laser-irradiated clusters*, Laser Phys. Lett. **2**, 452 (2005)

[59] T.-Y. B. Yang, W. L. Kruer, R. M. More & A. B. Langdon, *Absorption of laser light in overdense plasmas by sheath inverse bremsstrahlung*, Phys. Plasmas **2**, 3146 (1995); W. Rozmus & V.T. Tikhonchuk, *Skin effect and interaction of short laser pulses with dense plasmas*, Phys. Rev. A **42**, 7401 (1990)

[60] F. Brunel, *Not-so-resonant, resonant absorption*, Phys. Rev. Lett. **59**, 52 (1987); *Anomalous absorption of high intensity subpicosecond laser pulses*, Phys. Fluids **31**, 2714 (1988)

[61] A. V. Sofronov & V. P. Krainov, *Relativistic electron drift in underdense plasma produced by a super-intense femtosecond laser pulse*, J. Phys. B **37**, L329 (2004)

[62] A. Pukhov, *Strong field interaction of laser radiation*, Rep. Prog. Phys. **66**, 47 (2003)

[63] W. L. Kruer & K. Estabrook, $J \times B$ *heating by very intense laser light*, Phys. Fluids **28**, 431 (1985)

[64] A. Macchi, F. Cornolti, F. Pegoraro, T. V. Liseikina, H. Ruhl & V. A. Vshivkov, *Surface Oscillations in Overdense Plasmas Irradiated by Ultrashort Laser Pulses*, Phys. Rev. Lett. **87**, 205004 (2001); A. Macchi, F. Cornolti, & F. Pegoraro, *Two-surface wave decay*, Phys. Plasmas **9**, 1704 (2002)

[65] S. Kahaly, S. K. Yadav, W. M. Wang, et al. *Near-complete absorption of intense, ultrashort laser light by sub-λ gratings*, Phys. Rev. Lett. **101**, 14500 (2008)

[66] C. Jungreuthmayer, M. Geissler, J. Zanghellini & T. Brabec, *Microscopic analysis of large-cluster explosion in intense laser fields*, Phys. Rev. Lett. **92**, 133401 (2004)

[67] P. Mulser & D. Bauer, High-Power Laser-Matter Interaction (Springer, Heidelberg, 2010)

[68] A. Macchi, *Surface plasmons in superintense laser-solid interactions*, Phys. Plasmas **25**, 031906 (2018); A. Macchi, G. Cantono, L. Fedeli, F. Pisani, & T. Ceccotti, *Extreme high field plasmonics: electron acceleration and XUV harmonic generation from ultrashort surface plasmons*, Phys. Plasmas **26**, 042114 (2019); A. Sgattoni, L. Fedeli, G. Cantono, T. Ceccotti & A. Macchi, *High field plasmonics and laser-plasma acceleration in solid targets*, Plasma Phys. Contr. Fusion **58**, 014004 (2016)

[69] P. Mulser, S.M. Weng & T. Liseykina, *Analysis of the Brunel model and resulting hot electron spectra*, Phys. Plasmas **19**, 043301 (2012)

[70] M. Cerchez, R. Jung, J. Osterholz et al., *Absorption of ultrashort laser pulses in strongly overdense targets*, Phys. Rev. Lett. **100**, 245001 (2008)

[71] S.C. Wilks, W.L. Kruer, M. Tabak, A.B. Langdon, *Absorption of ultra-intense laser pulses*, Phys. Rev. Lett. **69**, 1383 (1992)

[72] F. N. Beg, A. R. Bell, A. E. Dangor et al., *A study of picosecond laser–solid interactions up to 10^{19} W/cm^2*, Phys. Plasmas **4**, 447 (1997).

[73] C. D. Chen, J. A. King, M. H. Key et al., *A Bremsstrahlung spectrometer using k-edge and differential filters with image plate dosimeters*, Rev. Sci. Instrum. **79**, 10E305 (2008)

[74] A. G. MacPhee, K. U. Akli, F. N. Beg et al., *Diagnostics for fast ignition science*, Rev. Sci. Instrum. **79**, 10F302 (2008)

[75] M. G. Haines, M. S. Wei, F. N. Beg et al. *Hot-Electron Temperature and Laser-Light Absorption in Fast Ignition* , Phys. Rev. Lett. **102**, 045008 (2009)

[76] T. Kluge, T. Cowan, A. Debus et al., *Electron temperature scaling in laser interaction with solids*, Phys. Rev. Lett. **107**, 205003 (2011)

[77] P. Mulser, D. Bauer, & H. Ruhl, *Collisionless laser-energy conversion by anharmonic resonance*, Phys. Rev. Lett. **101**, 225002 (2008)

[78] T. Baeva, S. Gordienko, A. P. L. Robinson, & P. A. Norreys, *The zero vector potential mechanism of attosecond absorption*, Phys. Plasmas **18**, 056702 (2011)

[79] G. Malka and J. L. Miquel, *Experimental confirmation of ponderomotive-force electrons produced by an ultrarelativistic laser pulse on a solid target*, Phys. Rev. Lett. **77**, 75 (1996); P. McKenna, F. Lindau, O. Lundh et al., *Low- and medium-mass ion acceleration driven by petawatt laser plasma interactions*, Plasma Phys. Contr. Fusion **49**, B223 (2007)

[80] Y.-Q. Cui, W.-M. Wang, Z.-M. Sheng et al., *Laser absorption and hot electron temperature scalings in laser–plasma interactions*, Plasma Phys. Contr. Fusion **55**, 085008 (2013)

[81] A. Macchi, T. V. Liseikina, S. Tuveri, S. Veghini, *Theory and simulation of ion acceleration with circularly polarized laser pulses*, Comptes Rendus Physique **10**, 207 (2009)

[82] S. G. Rykovanov, J. Schreiber, J. Meyer-ter-Vehn et al., *Ion acceleration with ultra-thin foils using elliptically polarized laser pulses*, New J. Phys. **10**, 113005 (2008)

[83] H. Ruhl, A. Macchi, P. Mulser, F. Cornolti, S. Hain, *Collective Dynamics and Enhancement of Absorption in Deformed Targets*, Phys. Rev. Lett. **82**, 2095 (1999)

[84] Y. Sentoku, K. Mima, H. Ruhl, Y. Toyama, R. Kogama, T. E. Cowan, *Laser light and hot electron micro focusing using a conical target*, Phys. Plasmas **11**, 3083 (2004)

[85] H. Nakamura, B. Chrisman, T. Tanimoto et al., *Superthermal and Efficient-heating modes in the interaction of a cone target with ultraintense laser light*, Phys. Rev. Lett. **102**, 045009 (2009)

[86] X. H. Yang, W. Yu, H. Xi et al., *Generation of high-energy-density ion bunches by ultraintense laser-cone-target interaction*, Phys. Plasmas **21**, 063105 (2014)

[87] S. A. Gaillard, T. Kluge, K. A. Flippo et al., *Increased laser-accelerated proton energies via direct laser-light-pressure acceleration of electrons in microcone targets*, Phys. Plasmas **18**, 056710 (2011)

[88] O. Budrigă, E. D'Humiéres, *Modeling the ultra-high intensity laser pulse-cone target interaction for ion acceleration at CETAL facility*, Laser and Particle Beams **35**, 458 (2017)

[89] D. B. Zou, A. Pukhov, L.Q.Yi, et al., *Laser-driven ion acceleration from plasma micro-channel targets*, Sci. Rep. **7**, 42666 (2017)

[90] O. Klimo, J. Psikal, J. Limpouch et al., *Short pulse laser interaction with micro-structured targets: simulations of laser absorption and ion acceleration*, New J. Phys. **13**, 053028 (2011)

[91] V. Yanovsky, V. Chvykov, G. Kalinchenko et al., *Ultra-high intensity- 300-TW laser at 0.1 Hz repetition rate.*, Opt. Express **16**, 2109 (2008)

[92] S. V. Bulanov, L. M. Kovrizhnykh, & A. S. Sakharov, *Regular mechanisms of electron and ion acceleration in the interaction of strong electromagnetic waves with a plasma*, Phys. Reports, **186**, 1 (1990); C. E. Clayton, K. A. Marsh, A. Dyson et al., *Ultrahigh-gradient acceleration of injected electrons by laser-excited relativistic electron plasma waves*, Phys. Rev. Lett. **70**, 37 (1993); A. Modena, Z. Najmudin, A. E. Dangor et al., *Electron acceleration from the breaking of relativistic plasma waves*, Nature **377**, 606 (1995); K. Nakajima, D. Fisher, T. Kawakubo et al., *Observation of ultrahigh gradient electron acceleration by a self-modulated intense short laser pulse*, Phys. Rev. Lett. **74**, 4428 (1995); D. Umstadter, S.-Y. Chen, A. Maksimchuk, G. Mourou, R. Wagner,

Nonlinear optics in relativistic plasmas and laser wake field acceleration of electrons, Science **273**, 472 (1996); Chen, S.-Y. et al., Phys. Rev. Lett. **80**, 2610 (1998); D. Gordon, K.C. Tzeng, C.E. Clayton et al., *Observation of electron energies beyond the linear dephasing limit from a laser-excited relativistic plasma wave*, Phys. Rev. Lett. **80**, 2133 (1998); R. Bingham, J. T. Mendonca, & P. K. Shukla, *Plasma based charged-particle accelerators*, Plasma Phys. Contr. Fusion **46**, R1 (2004); V. Malka, S.Fritzler, E. Lefebvre et al., *Electron acceleration by a wake field forced by an intense ultrashort laser pulse*, Science **298**, 1596 (2002); C. G. R. Geddes, *High-quality electron beams from a laser wakefield accelerator using plasma-channel guiding*, Nature **431**, 538 (2004); J. Faure, Y Glinec, A. Pukhov et al., *A laser–plasma accelerator producing monoenergetic electron beams*, Nature **431**, 541 (2004); S. P. D. Mangles, C. D. Murphy, Z.Najmudin et al., *Monoenergetic beams of relativistic electrons from intense laser–plasma interactions*, Nature **431**, 535 (2004); S. Ya. Tochitsky, R. Narang, C. V. Filip, et al., *Enhanced Acceleration of Injected Electrons in a Laser-Beat-Wave-Induced Plasma Channel*, Phys. Rev. Lett. **92**, 095004 (2004)

[93] A. J. Gonsalves, K. Nakamura, J. Daniels, et al., *Petawatt laser guiding and electron beam acceleration to 8 GeV in a laser-heated capillary discharge waveguide*, Phys. Rev. Lett. **122**, 084801 (2019); H. T. Kim, V. B. Pathak, K. H. Pae, et al., *Stable multi-GeV electron accelerator driven by waveform-controlled PW laser pulses*, Sci. Rep. **7**, 10203 (2017)

[94] X. Wang, R. Zgadzaj, N. Fazel, et al., *Quasi-monoenergetic laser-plasma acceleration of electrons to 2 GeV*, Nature Comm. **4**, 1988 (2013)

[95] T. Zh. Esirkepov, Y. Sentoku, K. Mima, et al., *Ion acceleration by superintense laser pulses in plasmas*, JETP Lett. **70**, 82 (1999); K. Krushelnick, E. L. Clark, Z. Najmudin, et al., *Multi-MeV Ion Production from High-Intensity Laser Interactions with Underdense Plasmas*, Phys. Rev. Lett. **83**, 737 (1999); G. S. Sarkisov, V. Yu. Bychenkov, V. N. Novikov, et al., *Self-focusing, channel formation, and high-energy ion generation in interaction of an intense short laser pulse with a He jet*, Phys. Rev. E **59**, 7042 (1999); S. V. Bulanov, T. Th Esirkepov, F. Califano, et al., *Generation of collimated beams of relativistic ions in laser-plasma interactions*, JETP Lett. **71**, 407 (2000); C. Joshi & V. Malka, *Focus on Laser- and Beam-Driven Plasma Accelerators*, New J. Phys. **12**, 045003 (2010); A. Maksimchuk, K. Flippo, H. Krause, et al., *High-energy ion generation by short laser pulses*, Plasma Phys. Rep. **30**, 473 (2004)

[96] E. L. Clark, K. Krushelnik, J. R. Davies et al., *Measurements of energetic proton transport through magnetized plasma from intense laser interactions with solids*, Phys. Rev. Lett. **84**, 670 (2000); R.A. Snavely, M.H. Key, S. P. Hatchett et al., *Intense high-energy proton beams from petawatt-laser irradiation of solids*, Phys. Rev. Lett. **85**, 2945 (2000)

[97] A. Maksimchuk, S. Gu, K. Flippo, D. Umstadter, V. Bychenkov, *Forward ion acceleration in thin films driven by a high-intensity laser*, Phys. Rev. Lett. **84**, 4108 (2000)

[98] F. Wagner, O. Deppert, C. Brabetz et al., *Maximum proton energy above 85 MeV from the relativistic interaction of laser pulses with micrometer thick CH_2 targets*, Phys. Rev. Lett. **116**, 205002 (2016); A. Higginson, R. J. Gray, M. King et al., *Near-100 MeV protons via a laser-driven transparency-enhanced hybrid acceleration scheme*, Nature Comm. **9**, 724 (2018)

[99] S.C. Wilks. A. B. Langdon, T.E. Cowan et al., *Energetic proton generation in ultra-intense laser–solid interactions*, Phys. Plasmas **8**, 542 (2001); P. Mora, *Plasma expansion into a vacuum*, Phys. Rev. Lett. **90**, 185002 (2003)

[100] M. Roth, M. Schollmeier, *Ion Acceleration—Target Normal Sheath Acceleration*, CERN Yellow Reports, [S.l.], v. 1, p. 231, feb. 2016. ISSN 0007-8328

[101] T. Esirkepov, M. Borghesi, S.V. Bulanov, G. Mourou, T. Tajima, *Highly efficient relativistic-ion generation in the laser-piston regime*, Phys. Rev. Lett. **92**, 175003 (2004); T. Esirkepov, M. Yamagiwa, T. Tajima, *Laser ion-acceleration scaling laws seen in multiparametric Particle-in-Cell simulations*, Phys. Rev. Lett. **96**, 105001 (2006)

[102] M. Borghesi, A. Macchi, Laser-Driven Ion Accelerators: State of the Art and Applications, in: Laser-Driven Particle Acceleration Towards Radiobiology and Medicine, Editor: Antonio Giulietti, ISBN: 978-3-319-31561-4 (Print) 978-3-319-31563-8 (Online), Part of the series Biological and Medical Physics, Biomedical Engineering (Springer, 2016), pp. 221-247

[103] A. Macchi, Laser-Driven Ion Acceleration, in: Applications of Laser-Driven Particle Acceleration, ed. by P. R. Bolton, K. Parodi, J. Schreiber (CRC press, 2018)

[104] A.J. Mackinnon, Y. Sentoku, P.K. Patel et al., *Enhancement of proton acceleration by hot-electron recirculation in thin foils irradiated by ultraintense laser pulses*, Phys. Rev. Lett. **88**, 215006 (2002)

[105] M. Hegelich, S. Karsch, G. Pretzler et al., *MeV ion jets from short-pulse-laser interaction with thin foils*, Phys. Rev. Lett. **89**, 085002 (2002)

[106] J. Fuchs, P. Antici, E. d'Humiéres, et al., *Laser-driven proton scaling laws and new paths towards energy increase*, Nat. Phys. **2**, 48 (2006); K. Zeil, S. D. Kraft, S. Bock, et al., *The scaling of proton energies in ultrashort pulse laser plasma acceleration*, New J. Phys. **12**, 045015 (2010); L. Robson, P. T. Simpson, R. J. Clarke et al., *Scaling of proton acceleration driven by petawatt-laser-plasma interactions*, Nat. Phys. **3**, 582 (2007)

[107] T. Ceccotti, A. Lévy, H. Popescu et al., *Proton acceleration with high-intensity ultrahigh-contrast laser pulses*, Phys. Rev. Lett. **99**, 185002 (2007)

[108] A. Macchi, F. Cattani, T.V. Liseykina, F. Cornolti, *Laser acceleration of ion bunches at the front surface of overdense plasmas*, Phys. Rev. Lett. **94**, 165003 (2005)

[109] A.P.L. Robinson, P. Gibbon, M. Zepf et al., *Relativistically correct hole-boring and ion acceleration by circularly polarized laser pulses*, Plasma Phys. Contr. Fusion **51**, 024004 (2009)

[110] T.V. Liseikina, A. Macchi, *Features of ion acceleration by circularly polarized laser pulses*, Appl. Phys. Lett. **91**, 171502, (2007)

[111] A. Macchi & C. Benedetti, *Ion acceleration by radiation pressure in thin and thick targets*, Nucl. Inst. Meth. Phys.Res. A **620**, 41 (2010); A. P. L. Robinson, *Production of high energy protons with hole-boring radiation pressure acceleration*, Phys. Plasmas **18**, 056701 (2011); A. P. L. Robinson, R. M. G. M. Trines, N. P. Dover,and Z. Najmudin, *Hole-boring radiation pressure*

acceleration as a basis for producing high-energy proton bunches, Plasma Phys. Contr. Fusion **54**, 115001 (2012)

[112] C. A. J. Palmer, N. P. Dover, I. Pogorelsky et al., *Monoenergetic proton beams accelerated by a radiation pressure driven shock*, Phys. Rev. Lett. **106**, 014801 (2011)

[113] C. Gong, S. Y. Tochitsky, F. Fiuza et al., *Plasma dynamics near critical density inferred from di-rect measurements of laser hole boring*, Phys. Rev. E **93**, 061202 (2016)

[114] S. Kar, M. Borghesi, S. V. Bulanov et al. *Plasma jets driven by ultraintense-laser interaction with thin foils*, Phys. Rev. Lett. **100**, 225004 (2008); S. Kar, K. F. Kakolee, M. Cerchez et al., *Experimental investigation of hole boring and light sail regimes of RPA by varying laser and target parameters*, Plasma Phys. Contr. Fusion **55**, 124030 (2013)

[115] X. Zhang, B. Shen, X. Li, et al., *Multistaged acceleration of ions by circularly polarized laser pulse: Monoenergetic ion beam generation*, Phys. Plasmas **14**, 073101 (2007); X. Zhang, B. Shen, X. Li et al., *Efficient GeV ion generation by ultraintense circularly polarized laser pulse*, Phys. Plasmas **14**, 123108 (2007)

[116] A.P.L. Robinson, M. Zepf, S. Kar, R.G. Evans, C. Bellei, *Radiation pressure acceleration of thin foils with circularly polarized laser pulses*, New J. Phys. **10**, 13021 (2008)

[117] O. Klimo, J. Psikal, J. Limpouch, V.T. Tikhonchuk, *Monoenergetic ion beams from ultra-thin foils irradiated by ultrahigh-contrast circularly polarized laser pulses*, Phys. Rev. ST Accel. Beams **11**, 031301 (2008)

[118] V. K. Tripathi, C.S. Liu, X. Shao et al., *Laser acceleration of monoenergetic protons in a self-organized double layer from thin foil*, Plasma Phys. Contr. Fusion **51**, 024014 (2009)

[119] X. Q. Yan, C. Lin, Z. M. Sheng et al., *Generating high-current monoenergetic proton beams by a circularly polarized Laser pulse in the phase-stable acceleration regime*, Phys. Rev. Lett. **100**, 135003 (2008); L. Ji, B. Shen, X. Zhang et al. *Comment on "Generating high-current monoenergetic proton beams by a circularly polarized laser pulse in the phase-stablea acceleration regime"*, Phys. Rev. Lett. **102**, 239501 (2009)

[120] F. Pegoraro and S. V. Bulanov, *Photon bubbles and ion acceleration in a plasma dominated by the radiation pressure of an electromagnetic pulse*, Phys. Rev. Lett. **99**, 065002 (2007)

[121] A. Sgattoni, S. Sinigardi, L. Fedeli, F. Pegoraro, and A. Macchi, *Laser-driven Rayleigh-Taylor instability: Plasmonic effects and three-dimensional structures*, Phys. Rev. E **91**, 013106 (2015)

[122] C. A. J. Palmer, J. Schreiber, S. R. Nagel et al. *Rayleigh-Taylor instability of an ultrathin foil accelerated by the radiation pressure of an intense laser*, Phys. Rev. Lett. **108**, 225002 (2012)

[123] B. Aurand, S. Kuschel, O. Jaeckel et al. *Radiation pressure-assisted acceleration of ions using multi-component foils in high-intensity laser-matter interactions*, New J. Phys. **15**, 033031 (2013); F. Dollar, C. Zulick, A. G. R. Thomas et al., *Finite spot effects on radiation pressureacceleration from intense high-contrast laser interactionswith thin targets*, Phys. Rev. Lett. , 108, 175005 (2012); S. Steinke, P. Hilz, M. Schnürer et al. *Stable laser-ion acceleration in the light sail regime*, Phys. Rev. ST Accel. Beams **16**, 011303 (2013)

[124] C. Scullion, D. Doria, L. Romagnani et al., *Polarization dependence of bulk ion acceleration from ultrathin foils irradiated by high-intensity ultrashort laser pulses*, Phys. Rev. Lett. **119**, 054801, (2017)

[125] B. Qiao, S. Kar, M. Geissler et al., *Dominance of radiation pressure in ion acceleration with linearly polarized pulses at intensities of* $10^{21} \mathrm{W/cm^2}$, Phys. Rev. Lett. **108**, 115002 (2012)

[126] T.V. Liseykina, M. Borghesi, M. Macchi, S. Tuveri, *Radiation pressure acceleration by ultraintense laser pulses*, Plasma Phys. Contr. Fusion **50**, 124033 (2008)

[127] A. Marcowith, A. Bret, A. Bykov et al. *The microphysics of collisionless shock waves*, Reports on progress in Physics **79**, 046901 (2016)

[128] V. M. Antonov et al. *A study of the collisionless interaction of interpenetrating super-Alfvén plasma flows*, Journ. of Appl. Mech. and Tech. Phys. **26**, 757 (1985)

[129] A. R. Bell et al. *Collisionless shock in a laser-produced ablating plasma*, Phys. Rev. A **38**, 1363 (1988)

[130] L. Romagnani L et al. *Observation of collisionless shocks in laser-plasma experiments*, Phys. Rev. Lett. **101**, 025004 (2008); H. Ahmed et al. *Time-Resolved Characterization of the Formation of a Collisionless Shock*, Phys. Rev. Lett. **110**, 205001 (2013); Y. Kuramitsu et al. *Laboratory investigations on the origins of cosmic rays*, Plasma Phys. Contr. Fusion **54**, 124049 (2012)

[131] J. Denavit, *Absorption of high-intensity subpicosecond lasers on solid density targets*, Phys. Rev. Lett. **69**, 3052 (1992)

[132] L. O. Silva, M. Marti, J. R. Davies et al., *Proton shock acceleration in laser-plasma interactions*, Phys. Rev. Lett. **92**, 015002 (2004)

[133] D. Haberberger, S. Tochitsky, F. Fiuza et al., *Collisionless shocks in laser-produced plasma generate monoenergetic high-energy proton beams*, Nature Physics **8**, 95 (2012)

[134] S. S. Moiseev & R. Z. Sagdeev, *Collisionless shock waves in a plasma in a weak magnetic field*, J. Nucl. Energy **5**, 43 (1963)

[135] R. Z. Sagdeev, *Cooperative phenomena and shock waves in collisionless plasmas*, Rev. Plasma Phys. **4**, 23 (1966)

[136] A. V. Gurevich, *Distribution of captured particles in a potential well in the absence of collisions*, Sov. J. Exp. Theor. Phys. **26**, 575 (1968)

[137] A. Stockem Novo, M. C. Kaluza, R. A. Fonseca, & L. O. Silva, *Optimizing laser-driven proton acceleration from overdense targets*, Sci. Rep. **6**, 29402 (2016)

[138] S.N.Chen, M. Vranic, T. Gangolf et al., *Collimated protons accelerated from an overdense gas jet irradiated by a 1μm wavelength high-intensity short-pulse laser*, Sci. Rep. **7**, 13505 (2017)

[139] S. Atzeni, M. Temporal, and J. Honrubia, *A first analysis of fast ignition of precompressed ICF fuel by laser-accelerated protons*, Nucl. Fusion **42**, L1 (2002); H. Ruhl, S.V. Bulanov T.E. Cowan, et al., *Computer simulation of the three-dimensional regime of proton acceleration in the interaction of laser radiation with a thin spherical target*, Plasma Physics Reports **27**, 363 (2001)

[140] M. Roth, T. E. Cowan, M. H. Key, et al. *Fast ignition by intense laser-accelerated pro-ton beams*, Phys. Rev. Lett. **86**, 436, (2001)

[141] K. W. D. Ledingham, P. McKenna, and R. P. Singhal, *Applications for nuclear phenomena generated byultra-intense lasers*, Science **300**, 1107 (2003); K. Nemoto, A. Maksimchuk, S. Banerjee, et al., *Laser-triggered ion acceleration and table top isotope production*, Appl. Phys. Lett. **78**, 595 (2001); M. I. K. Santala, M. Zepf, F. N. Beg et al., *Production of radioactive nuclides by energetic protons generated from intense laser-plasma interactions*, Appl. Phys. Lett. **78**, 19 (2001); I. Spencer, K. W. D. Ledingham, R. P. Singhal et al. *Laser generation of proton beams for the production of short-lived positron emitting radioisotopes*, Nucl. Inst. Meth. Phys. Res. B **183**, 449 (2001); A. S. Cucoanes; D. L. Balabanski; F. Canova, et al., *On the potential of laser driven isotope generation at ELI-NP for positron emission tomography*, Proc. SPIE **10239**, Medical Applications of Laser-Generated Beams of Particles IV: Review of Progress and Strategies for the Future, 102390B (2017)

[142] Particle Therapy Co-Operative Group. *Particle therapy facilities in operation.* www.ptcog.ch/index.php/facilities-in-operation; Particle Therapy Co-Operative Group. *Particle therapy facilities under construction.* www.ptcog.ch/index.php/facilities-under-construction

[143] B. G. Bravy, Y. A. Chernyshev, V. M. Gordienko, et al., *Multi-terawatt picoseconds 10μ, O2 laser system: design and parameters' control*, Opt. Express **20**, 25536 (2012); D. Haberberger, S. Tochitsky, and C. Joshi, *"Fifteen terawatt picosecond CO2 laser system*, Opt. Express **18**, 17865 (2010); I. V. Pogorelsky, M. Babzien, I. Ben-Zvi, et al., *BESTIA the next generation ultrafast CO2 laser for advanced accelerator research*, Nucl. Inst. Meth. Phys. Res. A **829**, 432, (2016)

[144] M. Borghesi, A. J. Mackinnon, D. H. Campbell, et al., *Multi-MeV proton source investigations in ultraintense laser-foil interactions*, Phys. Rev. Lett. **92**, 055003, (2004); J. A. Cobble, R. P. Johnson, T. E. Cowan, N. R.-L. Galloudec, and M. Allen, *High resolution laser-driven proton radiography*, J. Appl. Phys. **92**, 1775, (2002); M. Roth, A. Blazevic, M. Geissel et al., *Energetic ions generated by laser pulses: A detailed study on target properties*, Phys. Rev. ST Accel. Beams **5**, 061301, (2002)

[145] M. Borghesi, D. H. Campbell, et al., *lectric field detection in laser-plasma interaction experiments via the proton imaging technique*, Phys. Plasmas **9**, 2214, (2002); A. J. Mackinnon, P. K. Patel, R. P. Town, et al., *Proton radiography as an electromagnetic field and density perturbation diagnostic*, Rev. Sci. Instrum. **75**, 3531 (2004)

[146] L. Romagnani, J. Fuchs, M. Borghesi et al., *Dynamics of electric fields driving the laser acceleration of multi-MeV protons*, Phys. Rev. Lett. **95**, 195001, (2005)

[147] T. Ditmire, T. Donnelly, A. M. Rubenchik et al., *Interaction of intense laser pulses with atomic clusters*, Phys. Rev. A **53**, 3379 (1996); T. Ditmire, J. Zweiback, V. P. Yanovsky et al., *Nuclear fusion in gases of deuterium clusters heated with a femtosecond laser*, Phys. Plasmas **7**, 1993

(2000); *Nuclear fusion from explosions of femtosecond laser-heated deuterium clusters*, Nature **398**, 489 (1999)

[148] T. M. Ostermayr, D. Haffa, P. Hilz et al., *Proton acceleration by irradiation of isolated spheres with an intense laser pulse*, Phys. Rev. E **94**, 033208 (2016)

[149] S. Ter-Avetisyan, B. Ramakrishna, R. Prasad et al., *Generation of a quasi-monoergetic proton beam from laser irradiated sub-micron droplets*, Phys. Plasmas **19**, 073112 (2012)

[150] T. Sokollik, M. Schnürer, S. Steinke et al., *Directional laser-driven ion acceleration from microspheres*, Phys. Rev. Lett. **103**, 135003 (2009)

[151] K. Zeil, J. Metzkes, T. Kluge, et. al., *Robust energy enhancement of ultrashort pulse laser accelerated protons from reduced mass targets*, Plasma Phys. Contr. Fusion **56**, 084004 (2014)

[152] P. Hilz, T. M. Ostermayr, A. Huebl et al., *Isolated proton bunch acceleration by a petawatt laser pulse*, Nature Comm. **9**, 423 (2018)

[153] S. Zherebtsov, Th. Fennel, J. Plenge et al. *Controlled near-field enhanced electron acceleration from dielectric nanospheres with intense few-cycle laser fields*, Nature Physics **7**, 656 (2011)

[154] T.V. Liseykina, S. Pirner, D. Bauer, *Relativistic attosecond electron bunches from laser-illuminated droplets*, Phys. Rev. Lett. **104**, 092002 (2010)

[155] L. Di Lucchio, P. Gibbon, *Relativistic attosecond electron bunch emission from few-cycle laser irradiated nanoscale droplets*, Phys. Rev. ST Accel. Beams **18**, 023402 (2015)

[156] T. P. Yu, Z. M. Sheng, Y. Yin et al., *Dynamics of laser mass-limited foil interaction at ultra-high laser intensities*, Phys. Plasmas **21**, 053105 (2014)

[157] Y. Tong-Pu, H. Li-Xiang, Y. Yan et al., *Bright tunable femtosecond x-ray emission from laser irradiated micro-droplet*, Appl. Phys. Lett. **105**, 114101 (2014)

[158] V. P. Krainov, M. B. Smirnov, *Cluster beams in the super-intense femtosecond laser pulse*, Phys. Rep. **370**, 237 (2002); U. Saalmann, Ch. Siedschlag, & J. M. Rost, *Mechanisms of cluster ionization in strong laser pulses*, J. Phys. B: At. Mol. Opt. Phys. **39**, R3 (2006)

[159] Th. Fennel, K.-H. Meiwes-Broer, J. Tiggesbäumker, P.-G. Reinhard, P. M. Dinh & E. Suraud, *Laser-driven nonlinear cluster dynamics*, Ref. Mod. Phys. **82**, 1793 (2010)

[160] T.V. Liseykina, D. Bauer, *Plasma-Formation Dynamics in Intense Laser-Droplet Interaction*, Phys. Rev. Lett. **110**, 145003 (2013)

[161] P. Sperling, T. Liseykina, D. Bauer, R. Redmer, *Time-resolved Thomson scattering on high-intensity laser-produced hot dense helium plasmas*, New J. Phys. **15**, 025041 (2013)

[162] A. Di Piazza, C. Müller, K. Hatsagortsyan, C.H. Keitel, *Extremely high-intensity laser interactions with fundamental quantum systems*, Ref. Mod. Phys. **84**, 1177 (2012)

[163] N.B. Narozhny, A.M. Fedotov, *Extreme light physics*, Contemporary Phys. **56** (2015)

[164] E. N. Nerush, I. Y. Kostyukov, *Laser-driven hole boring and gamma-ray emission in high-density plasmas*, Plasma Phys. Contr. Fusion **57**, 035007 (2015); I. I. Artemenko, A. A. Golovanov, I. Y. Kostyukov et al., *Formation and dynamics of a plasma in superstrong laser fields including radiative and quantum electrodynamics effects*, JETP Lett. **104**, 883 (2016)

[165] A. V. Bashinov, A. A. Gonoskov, A. V. Kim et al., *New horizons for extreme light physics with mega-science project XCELS*, Eur. Phys. J. ST **223**, 1105 (2014); J. Kawanaka, K. Tsubakimoto, H. Yoshida et al., *Conceptual design of sub-exawatt system by using optical parametric chirped pulse amplification*, J. Phys. Conf. Ser. **688**, 012044 (2016)

[166] C. Danson, D. Hillier, N. Hopps & D. Neely, *Petawatt class lasers worldwide*, High Power Laser Science and Engineering **3**, e3, [ISSN 2052-3289] (2015)

[167] E. Cartlidge, *The light fantastic*, Science **359**, 382 (2018)

[168] A. S. Pirozhkov, Y. Fukuda, M. Nishiuchi, *Approaching the diffraction-limited, bandwidth-limited Petawatt*, Opt. Exp. **25**, 20486 (2017)

[169] J.D. Jackson, "Classical Electrodynamics" 3rd edn (New York: Wiley) (1999)

[170] J. Koga, T. Esirkepov, S.V. Bulanov, *Nonlinear Thomson scattering in the strong radiation damping regime*, Phys. Plasmas **12**, 093106 (2005); A. Di Piazza, K.Z. Hatsagortsyan, C.H. Keitel, *Strong signatures of radiation reaction below the radiation-dominated regime*, Phys. Rev. Lett. **102**, 254802 (2009); Y. Hadad, L. Labun, J. Rafelski et al., *Effects of radiation reaction in relativistic laser acceleration*, Phys. Rev. D **82**, 096012 (2010); T.G. Blackburn, C. P. Ridgers, J. G. Kirk, & A. R. Bell, *Quantum radiation reaction in laser-electron-beam collisions*, Phys. Rev. Lett. **112**, 015001 (2014)

[171] J.X. Li, K. Z. Hatsagortsyan, C.H. Keitel, *Robust signatures of quantum radiation reaction in focused ultrashort laser pulses*, Phys. Rev. Lett. **113**, 044801 (2014)

[172] N. Kumar, K. Z. Hatsagortsyan, C.H. Keitel, *Radiation-reaction-force-induced nonlinear mixing of raman sidebands of an ultraintense laser pulse in a plasma*, Phys. Rev. Lett. **111**, 10500 (2013)

[173] L. L. Ji, A. Pukhov, I. Y. Kostyukov, B. F. Shen, K. Akli, *Radiation-reaction trapping of electrons in extreme laser fields*, Phys. Rev. Lett. **112**, 145003 (20017)

[174] M. Tamburini, C.H. Keitel, A. Di Piazza, *Electron dynamics controlled via self-interaction*, Phys. Rev. E **89**, 021201 (2014); D. G. Green, C. N. Harvey, *Detecting radiation reaction at moderate laser intensities*, Phys. Rev. Lett. **112**, 164801 (2014)

[175] T. Nakamura, J.K. Koga, T. Esirkepov et al., *High-Power γ-ray flash generation in ultraintense laser-plasma interactions*, Phys. Rev. Lett. **108**, 195001 (2012); R. Capdessus, E. d'Humiére, V.T. Tikhonchuk, *Influence of ion mass on laser-energy absorption and synchrotron radiation at ultrahigh laser intensities*, Phys. Rev. Lett. **110**, 215003 (2013)

[176] J. M. Cole, K. T. Behm, E. Gerstmayr, et al. *Experimental evidence of radiation reaction in the collision of a high-intensity laser pulse with a laser-wakefield accelerated electron beam*, Phys. Rev. X **8**, 011020 (2018)

[177] K. Poder, M. Tamburini, G. Sarri, et al., *Experimental signatures of the quantum nature of radiation reaction in the field of an ultraintense laser*, Phys. Rev. X **8**, 031004 (2018)

[178] A. Macchi A *Viewpoint: Intense laser sheds light on radiation reaction*, Physics **11**, 13 (2018)

[179] J. G. Kirk, A. R. Bell & I. Arka, *Pair production in counter-propagating laser beams*, Plasma Phys. Contr. Fusion **51**, 085008 (2009)

[180] T. N. Wistisen, A. Di Piazza, H. V. Knudsen & U. I. Uggerhøj, *Experimental evidence of quantum radiation reaction in aligned crystals*, Nature Comm. **9**, 795 (2018)

[181] T. G. Blackburn, D. Seipt, S. S. Bulanov & M. Marklund, *Benchmarking semiclassical approaches to strong-field qed: Nonlinear compton scattering in intense laser pulses*, Phys. Plasmas **25**, 083108 (2018)

[182] A. Di Piazza, M. Tamburini, S. Meuren & C. H. Keitel, *Implementing nonlinear compton scattering beyond the local-constant-field approximation*, Phys. Rev. A **98**, 012134 (2018)

[183] A. Di Piazza, M. Tamburini, S. Meuren & C. H. Keitel, *Improved local-constant-field approximation for strong-field QED codes*, Phys. Rev. A **99**, 022125 (2019)

[184] I.V. Sokolov, N. M. Naumova, J. A. Nees, & G. A. Mourou, *Pair creation in QED-strong pulsed laser fields interacting with electron beams*, Phys. Rev. Lett. **105**, 105005 (2010); I.V. Sokolov, N. M. Naumova, J. A. Nees, *Numerical modeling of radiation-dominated and quantum-electrodynamically strong regimes of laser-plasma interaction*, Phys. Plasmas **18**, 093109 (2011)

[185] T. Liseykina, S. Popruzhenko, A. Macchi, *Inverse Faraday effect induced by radiation friction*, New J. Phys. **18**, 072001 (2016)

[186] L. P. Pitaevskii, *Electric forces in a transparent dispersive medium*, Sov. Phys.-JETP **12**, 1008 (1961)

[187] M.G. Haines, *Generation of an axial magnetic field from photon spin*, Phys. Rev. Lett. **87**, 135005 (2001)

[188] S. Popruzhenko, T. Liseykina, A. Macchi, *Efficiency of radiation friction losses in laser-driven 'hole boring' of dense target*, New J. Phys. **21**, 033009 (2019)

[189] Y. B. Zel'dovich, *Interaction of free electrons with electromagnetic radiation*, Soviet Physics Uspekhi **18**, 79 (1975)

[190] K.V. Lotov, I.V. Timofeev, E.A. Mesyats, A.V. Snytnikov, V.A. Vshivkov, *Note on quantitatively correct simulations of the kinetic beam-plasma instability*, Phys. Plasmas **22**, 024502 (2015)

[191] A. Pukhov, *Particle-In-Cell codes for plasma-based particle acceleration*, CERN Yellow Reports, [S.l.], v. 1, p. 181, feb. 2016. ISSN 0007-8328

[192] J. Villasenor, O. Buneman, *Rigorous change conservation for electromagnetic field solvers*, Comp. Phys. Comm. **69**, 306 (1992); T. Zh. Esirkepov, *Exact charge conservation scheme for Particle-In-Cell simulations with arbitrary form-factor*, Comp. Phys. Comm. **135**, 144 (2001)

[193] E. C. Jarque, F. Cornolti & A. Macchi, *Ultrashort laser-produced optical microcavities and ionization fronts*, J. Phys. B **33**, 1 (2000)

[194] H. C. Kapteyn, M. M. Murnane, A. Szoke & R.W. Falcone, *Prepulse energy suppression for high-energy ultrashort pulses using self-induced plasma shuttering*, Opt. Lett. **16**, 490 (1991); C. Thaury, F. Quéré, J.-P. Geindre, et al., *Plasma mirrors for ultrahigh-intensity optics*, Nature Physics **3**, 424 (2007); F. Quéré, *Plasma mirrors as attosecond light sources*, in Frontiers in Optics 2014, OSA Technical Digest (online) (Optical Society of America, 2014), paper JTu4E.1.

[195] T. Döppner, J. P. Müller, A. Przystawik, et. al., *Steplike intensity threshold behavior of extreme ionization in laser-driven xenon clusters*, Phys. Rev. Lett. **105**, 053401 (2010); B. Schütte, C. Peltz, D. R. Austin et al. *Low-energy electron emission in the strong-field ionization of rare gas clusters*, Phys. Rev. Lett. **121**, 063202 (2018); L. Seiffert, J. Köhn, C. Peltz, et al., *Signatures and mechanisms of plasmon-enhanced electron emission from clusters in few-cycle laser fields*, J. Phys. B: At. Mol. Opt. Phys. **50**, 224001 (2017)

[196] V.S. Popov, *Tunnel and multiphoton ionization of atoms and ions in a strong laser field (Keldysh theory)*, Phys. Usp. **47**, 855 (2004)

[197] R. Nuter, L. Gremillet, E. Lefebvre, A. Lévy, T. Ceccotti, & P. Martin, *Field ionization model implemented in Particle In Cell code and applied to laser-accelerated carbon ions*, Phys. Plasmas **18**, 033107 (2011)

[198] S. C. Rae, K. Burnett, *Possible production of cold plasmas through optical-field-induced ionization*, Phys. Rev. A **46**, 2077 (1992); P. Mulser, F. Cornolti, *Modeling field ionization in an energy conserving form and resulting nonstandard fluid dynamics*, Phys. Plasmas **5**, 4466 (1998)

[199] A. J. Kemp, Y. Sentoku, T. Cowan, J. Fuchs, H. Ruhl, *Modeling ultrafast laser-driven ionization dynamics with Monte Carlo collisional particle-in-cell simulations*, Phys. Plasmas **11**, L69 (2004)

[200] W. Lotz, *Electron-Impact Ionization Cross-Sections and Ionization Rate Coefficients for Atoms and Ions*, ApJS, 14, 207 (1967); *Electron-impact ionization cross-sections and ionization rate coefficients for atoms and ions from scandium to zinc*, W. Zeitschrift für Physik **206**, 466 (1969)

[201] V. Vahedi & M. Surendra, *A Monte Carlo collision model for the particle-in-cell method: applications to argon and oxygen discharges*, Comp. Phys. Comm. **87**, 199 (1995)

[202] Y. Sentoku & A. J. Kemp, *Numerical methods for particle simulations at extreme densities and temperatures: Weighted particles, relativistic collisions and reduced currents* , J. Comput. Phys. **227**, 6846 (2008)

[203] Ch. Peltz, C. Varin, T. Brabec & T. Fennel, *Fully microscopic analysis of laser-driven finite plasmas using the example of clusters*, New J. Phys. **14**, 065011 (2012)

[204] A. Zhidkov, J. Koga, A. Sasaki & M. Uesaka, *Radiation damping effects on the interaction of ultraintense laser pulses with an overdense plasma*, Phys. Rev. Lett. **88**, 185002 (2002)

[205] F. Rohrlich, *The correct equation of motion of a classical point charge*, Phys. Lett. A **283**, 276 (2001)

[206] L.D. Landau & E.M. Lifshitz, "The classical theory of fields", 2nd edn. (Elsevier, Oxford, 1975)

[207] M. Vranic, J. Martins, R. Fonseca & L. Silva, *Classical radiation reaction in particle-in-cell simulations*, Comp. Phys. Comm. **204**, 141 (2016)

[208] M. Tamburini, F. Pegoraro, A. Di Piazza, C. H. Keitel, A. Macchi, *Radiation reaction effects on radiation pressure acceleration*, New J. Phys. **12**, 123005 (2010)

[209] M. Tamburini, F.Pegoraro, A. Di Piazza, C.H. Keitel, T.V. Liseykina & A. Macchi, *Radiation reaction effects on electron nonlinear dynamics and ion acceleration in laser-solid interaction*, Nuclear Inst. Methods Phys. Research A **653**, 181 (2011)

[210] V. I. Ritus, *Quantum effects on the interaction of elementary particles with an intense electromagnetic field*, J. Russ. Laser Res. **6**, 497(1985); J. G. Kirk A. R. Bell, I. Arka, *Pair production in counter-propagating laser beams plasma*, Plasma Phys. Contr. Fusion **51**, 085008 (2009)

[211] F. Niel, C. Riconda, F. Amiranoff, M. Lobet, J. Derouillat, F. Pérez, T. Vinci M. Grech, *From quantum to classical modeling of radiation reaction: a focus on the radiation spectrum*, Plasma Phys. Contr. Fusion **60**, 094002 (2018)

[212] A. G. R. Thomas, C. P. Ridgers, S. S. Bulanov, B. J. Griffin, S. P. D. Mangles, *Strong radiation-damping effects in a gamma-ray source generated by the interaction of a high-intensity laser with a wakefield-accelerated electron beam*, Phys. Rev. X **2**, 041004 (2012)

[213] M. Passoni, A. Zani, A. Sgattoni et al., *Energetic ions at moderate laser intensities using foam-based multi-layered targets*, Plasma Phys. Contr. Fusion **56**, 045001 (2014)

[214] K. Quinn, P. A. Wilson, C. A. Cecchetti, et al., *Laser-driven ultrafast field propagation on solid surfaces*, Phys. Rev. Lett. **102**, 194801 (2009);

[215] S. Kar, H. Ahmed, R. Prasad et al., *Guided post-acceleration of laser-driven ions by a miniature modular structure*, Nature Comm. **7**, 10792 (2016)

[216] L. Romagnani, A. Bigongiari, S. Kar et al., *Observation of magnetized soliton remnants in the wake of intense laser pulse propagation through plasmas*, Phys. Rev. Lett. **105**, 175002 (2010)

[217] S. Kar, M. Borghesi, C.A. Cecchetti et al., *Dynamics of charge-displacement channeling in intense laser–plasma interactions*, New J. Phys. **9**, 402 (2007)

[218] K. Quinn, L. Romagnani, B. Ramakrishna et al., *Weibel-induced filamentation during an ultrafast laser-driven plasma expansion*, Phys. Rev. Lett. **108**, 135001 (2012)

[219] G. Sarri, A. Macchi, C.A. Cecchetti, *Dynamics of self-generated, large amplitude magnetic fields following high-intensity laser matter interaction*, Phys. Rev. Lett. **109**, 205002 (2012)